Transactions of the ASME®

Technical Editor,
G. K. SEROVY
Associate Technical Editors
Advanced Energy Systems
M. J. MORAN
Environmental Control
H. E. HESKETH
Fuels and Combustion Technologies
D. W. PACER
Gas Turbine
S. A. MOSIER
Internal Combustion Engine
J. A. CATON
Nuclear Engineering
S. M. CHO
Power
R. W. PORTER

BOARD ON COMMUNICATIONS
Chairman and Vice-President
M. E. FRANKE

Members-at-Large
W. BEGELL
T. F. CONRY
T. DEAR
R. L. KASTOR
R. MATES
E. M. PATTON
R. E. REDER
R. D. ROCKE
A. VAN DER SLUYS
A. J. WENNERSTROM
W. O. WINER
B. ZIELS

President, A. E. BERGLES
Executive Director,
D. L. BELDEN
Treasurer, ROBERT A. BENNETT

PUBLISHING STAFF
Mng. Dir., Publ.,
CHARLES W. BEARDSLEY
Managing Editor,
CORNELIA MONAHAN
Sr. Production Editor,
VALERIE WINTERS
Production Assistant,
MARISOL ANDINO

Transactions of the ASME, Journal of Turbomachinery (ISSN 0889-504X) is published quarterly (Jan., Apr., July, Oct.) for $125.00 per year by The American Society of Mechanical Engineers, 345 East 47th Street, New York, NY 10017. Second class postage paid at New York, NY and additional mailing offices. POSTMASTER: Send address change to Transactions of the ASME, Journal of Turbomachinery, c/o THE AMERICAN SOCIETY OF MECHANICAL ENGINEERS, 22 Law Drive, Box 2300, Fairfield, NJ 07007-2300.

CHANGES OF ADDRESS must be received at Society headquarters seven weeks before they are to be effective. Please send old label and new address.

PRICES: To members, $36.00, annually; to nonmembers, $125.00. Add $15.00 for postage to countries outside the United States and Canada.

STATEMENT from By-Laws. The Society shall not be responsible for statements or opinions advanced in papers or . . . printed in its publications (B 7.1, para. 3).

COPYRIGHT © 1990 by The American Society of Mechanical Engineers. Reprints from this publication may be made on condition that full credit be given the TRANSACTIONS OF THE ASME—JOURNAL OF TURBOMACHINERY, and the author, and date of publication be stated.

INDEXED by Applied Mechanics Reviews and Engineering Information, Inc.

Journal of Turbomachinery

Published Quarterly by The American Society of Mechanical Engineers

VOLUME 112 • NUMBER 3 • JULY 1990

TECHNICAL PAPERS

(Contents continued on Inside Back Cover)

Downloaded 01 Jun 2010 to 171.66.16.52. Redistribution subject to ASME license or copyright; see http://www.asme.org/terms/Terms_Use.cfm

(Contents continued)

ANNOUNCEMENTS

Downloaded 01 Jun 2010 to 171.66.16.52. Redistribution subject to ASME license or copyright; see http://www.asme.org/terms/Terms_Use.cfm

Numerical Simulation of the Two-Dimensional Viscous Compressible Flow in Blade Cascades Using a Solution-Adaptive Unstructured Mesh

G. L. D. Sidén
Volvo Flygmotor AB,
Trollhättan, Sweden

W. N. Dawes
Whittle Laboratory,
Cambridge, United Kingdom

P. J. Albråten
Volvo Flygmotor AB,
Trollhättan, Sweden

An explicit finite element procedure has been coupled with an automatic generation procedure for mesh-adaptive steady-state simulations of two-dimensional viscous compressible flows in cascades. Turbulence is modeled by a two-layer algebraic eddy viscosity model. Results show good behavior in comparison with measurements and results of a conventional H-mesh viscous flow solver. Computed loss approaches measured loss as the mesh is refined. Currently, the unstructured solver suffers in efficiency terms because the automatic mesh generator tends to produce inefficient equilateral triangles in the regions of shock waves and boundary layers where stretched elements would be more appropriate. This means that, at least for the Navier–Stokes equations, the unstructured approach is not yet competitive with conventional structured techniques. Nevertheless, this will change once the key advantages of geometric flexibility and user-independent solutions force rapid development.

Introduction

Conventional viscous flow solvers are becoming a routine industrial design tool. These solvers are invariably based on conventional meshes (H-mesh, O-mesh, C-mesh, etc.) with a topologically rectangular structure and usually remain fixed throughout a simulation. Unfortunately, the production of a suitable mesh is not routine. Many, often conflicting issues need to be addressed: the leading edge must be carefully gridded to avoid excessive false entropy creation; highly skewed mesh must be avoided; some attempt must be made to give shocks adequate mesh support; and so on.

By contrast, the solution-adaptive unstructured mesh described in this paper holds out the possibility of user-independent simulations. Provided the user can define the cascade geometry and boundary conditions, the evolution of the solution generates its own appropriate mesh. In the present work the mesh adaption is controlled by two criteria: The magnitude of the static pressure gradient determines the element size in the vicinity of shocks and stagnation points; the local entropy determines the element size in the boundary layer region and in the wake. Pioneering work in this area has been presented (for Euler solvers) by Morgan and Peraire (1987), Löhner et al. (1987), and Holmes et al. (1988).

The solution procedure is based on the two-step explicit Taylor–Galerkin finite element method (Morgan and Peraire, 1987), which has previously proven to be robust and accurate for high-speed compressible flows. Turbulence is modeled by a two-layer algebraic turbulence model (Baldwin and Lomax, 1978) that does not compromise the advantages of the unstructured mesh. This type of turbulence model has the advantage of being computationally inexpensive compared with other candidates such as one or two-equation models. Algebraic models are widely used for turbomachinery simulations and produce good predictions of turbulent boundary layers; however, their performance in large separated regions is questionable.

The flow solver is coupled with an automatic mesh generation procedure (Peraire et al., 1987) that generates a complete new mesh at each refinement. This is a robust way of implementing mesh-adaptive simulations, leaving the user well in control of the number of node points in the refined mesh and allowing the grid to be made coarser as well as more refined where the solution so indicates. The fact that virtually the same mesh has to be regenerated, in areas of small change, from one refinement to the next is not a large constraint since, even though these areas may be large, they usually contain only a minor portion of the mesh points.

Results are presented both for compressor and turbine cascades and comparisons with experiments show improving agreement in loss as the mesh is refined. Comparisons are also

Contributed by the International Gas Turbine Institute and presented at the 34th International Gas Turbine and Aeroengine Congress and Exhibition, Toronto, Ontario, Canada, June 4–8, 1989. Manuscript received at ASME Headquarters February 1, 1989. Paper No. 89-GT-211.

Copyright © 1990 by ASME
Downloaded 01 Jun 2010 to 171.66.16.66. Redistribution subject to ASME license or copyright; see http://www.asme.org/terms/Terms_Use.cfm

made with a conventional H-mesh viscous flow solver (Dawes, 1985).

Equations of Motion

The governing equations for viscous compressible flows may be written in conservation form

$$\frac{\partial U}{\partial t}+\frac{\partial F_i^c}{\partial x_i}=\frac{\partial F_i^v}{\partial x_i} \tag{1}$$

where

$$U=\begin{Bmatrix}\rho\\ \rho u_i\\ \rho e\end{Bmatrix} \quad F_i^c=\begin{Bmatrix}\rho u_i\\ \rho u_i u_j+p\delta_{ij}\\ u_i(\rho e+p)\end{Bmatrix} \quad F_i^v=\begin{Bmatrix}0\\ \sigma_{ji}\\ u_j\sigma_{ji}+k\dfrac{\partial T}{\partial x_i}\end{Bmatrix} \tag{2}$$

Here ρ, p, e, T, k, and δ_{ij} denote density, pressure, total energy, temperature, thermal conductivity, and the Kronecker delta, respectively, and u_i is the component of the fluid velocity in the direction of x_i. The viscous stress tensor σ_{ji} is given by

$$\sigma_{ji}=\mu\left(\frac{\partial u_j}{\partial x_i}+\frac{\partial u_i}{\partial x_j}\right)-\frac{2}{3}\frac{\partial u_k}{\partial x_k}\delta_{ij} \tag{3}$$

where μ is the viscosity. The equation set is completed by the addition of the state equations

$$p=(\gamma-1)\rho\left(e-\frac{1}{2}u_j u_j\right) \tag{4a}$$

$$T=\frac{1}{c_v}\left(e-\frac{1}{2}u_j u_j\right) \tag{4b}$$

Turbulence is accounted for by the inclusion of a two-layer algebraic mixing length eddy viscosity model (Baldwin and Lomax, 1978), in which μ and k consists of a laminar part μ_L and $k_L(k_L=\mu_L/\mathrm{Pr})$, and a turbulent part, μ_T and $k_T(k_T=\mu_T/\mathrm{Pr}_T)$. The model has two layers in which the turbulent viscosity is given by

$$\mu_T=\begin{cases}\mu_{T\text{inner}} & Y\le Y_{\text{crossover}}\\ \mu_{T\text{outer}} & Y>Y_{\text{crossover}}\end{cases} \tag{5}$$

where Y is the normal distance from the nearest wall and $Y_{\text{crossover}}$ is the smallest value of Y at which values from inner and outer formulas are equal. To aid the implementation of the model on the unstructured mesh, at the time of mesh generation, a table is created for each blade surface node of a sequence of nodes nearly normal to the blade surface. This is illustrated in Fig. 1. For each node the normal distance to the blade surface is also computed. Note that as described in the later section on mesh generation a triangular structured O-mesh is deployed close to the blade with about ten nodes normal to the blade (i.e., covering about half the boundary layer). This node sequence is taken to be the "profile" over which the turbulence model is deployed. Although slightly approximate, the strictly "mathematical" error is far less than the uncertainty implicit in turbulence modeling itself. The eddy viscosity in the inner and outer regions is as follows. In the *inner* region

$$\mu_{T\text{inner}}=\rho\lambda^2|\Omega| \tag{6a}$$

where $|\Omega|$ is the magnitude of the vorticity and

$$\lambda=k_\lambda Y\{1-e^{-Y^+/A^+}\} \quad Y^+=\frac{\sqrt{\rho_w\tau_w}Y}{\mu_w} \tag{6b}$$

In the *outer* region

$$\mu_{T\text{outer}}=C_{CL}\rho F_{\text{WAKE}}F_{\text{KLEB}} \tag{7}$$

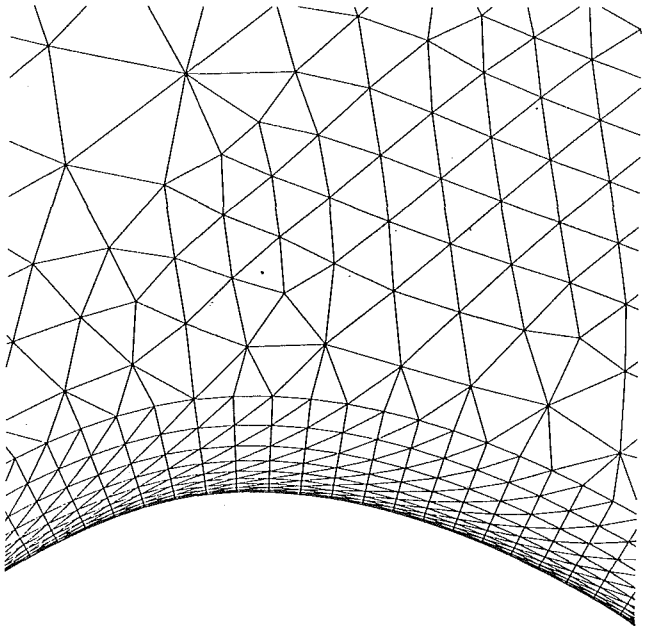

Fig. 1 Structured O-mesh around the blade with a thickness of 10 nodes and 18 elements. This mesh is deployed in order to generate stretched elements in the boundary layer. The solution procedure within the structured mesh is equivalent to the procedure outside.

where

$$F_{\text{WAKE}}=\text{MIN}(Y_{\text{MAX}}F_{\text{MAX}},\ C_{WK}Y_{\text{MAX}}u_{\text{DIFF}}^2/F_{\text{MAX}}) \tag{8}$$

The quantities F_{MAX} and Y_{MAX} are determined from the function

$$F(Y)=Y|\Omega|\{1-e^{-Y^+/A^+}\} \tag{9}$$

F_{MAX} is the maximum value of $F(Y)$ in a given profile and Y_{MAX} is the value of Y at which the maximum occurs. Thus the model length scale is determined from the vorticity distribution. The Klebanoff intermittency factor is given by

$$F_{\text{KLEB}}=\left[1+5.5\left\{\frac{C_{\text{KLEB}}Y}{Y_{\text{MAX}}}\right\}^6\right]^{-1} \tag{10}$$

The value of u_{DIFF} is the difference between maximum and minimum velocity in the given profile. The various constants are taken as

A^+	= 26	C_{CL}	= 0.02688
C_{KLEB}	= 0.3	k_λ	= 0.41
C_{WK}	= 0.25	Pr_T	= 0.9

No special treatment is made of any separated zones. Transition location currently is specified as input data. The wake is effectively modeled by the outer formulation (7).

Solution Strategy

The time domain is divided into finite levels, here denoted by superscript k. For the solution to proceed from time level k to time level $k+1$, the following two-step procedure is used:

Step I

$$U^{k+1/2}=U^k-\frac{\Delta t}{2}\frac{\partial F_i^{c,k}}{\partial x_i} \tag{11a}$$

Step II

$$\Delta U=-\Delta t\frac{\partial F_i^{c,k+1/2}}{\partial x_i}+\Delta t\frac{\partial F_i^{v,k}}{\partial x_i} \tag{11b}$$

where Δt denotes the time step and $\Delta U=U^{k+1}-U^k$. In steady-state calculations the time step varies spatially, such that the

Downloaded 01 Jun 2010 to 171.66.16.66. Redistribution subject to ASME license or copyright; see http://www.asme.org/terms/Terms_Use.cfm

Courant number stability criterion is not exceeded locally

$$(|\mathbf{u}_i| + c)\frac{\Delta t}{\Delta x_i} \leq 1 \tag{12}$$

Above, $|\mathbf{u}_i|$, c, and Δx_i are the magnitude of the fluid velocity, the wave speed, and the shortest element side.

All quantities at the intermediate time level $k+1/2$ are approximated using piecewise constant basis functions, ψ_e, and all quantities at time levels k and $k+1$ are interpolated on linear basis functions, φ_i:

$$U^{k+1/2} \approx U_e^{k+1/2}\psi_e \tag{13a}$$

$$U^k \approx U_j^k \varphi_j \tag{13b}$$

where e and j denote summations over elements and nodes, respectively. The weak formulation takes the form

Step I

$$U_e^{k+1/2}\langle \psi_e \psi_E \rangle = U_j^k \langle \varphi_j \psi_E \rangle - \frac{\Delta t}{2} F_{ij}^{ck} \langle \frac{\partial \varphi_i}{\partial x_i} \psi_E \rangle \tag{14a}$$

Step II

$$\Delta U_j \langle \varphi_j \varphi_l \rangle = \Delta t F_{ie}^{ck+1/2} \langle \psi_e \frac{\partial \varphi_l}{\partial x_i} \rangle - \Delta t \langle F_i^{vk} \frac{\partial \varphi_l}{\partial x_i} \rangle$$

$$- \Delta t \int F_i^{ck+1/2} \varphi_l n_i ds + \Delta t \int F_i^{vk} \varphi_l n_i ds \tag{14b}$$

where n_i is the ith component of the unit normal vector directed outwards, and $\langle\ \rangle$ denotes the inner product:

$$\langle a \cdot b \rangle = \int\int a \cdot b \, dx \, dy \tag{15}$$

The line integrals in (14*a*) and (14*b*) are defined counterclockwise along external boundaries and clockwise along internal boundaries. In the first step the solution is formed directly at the element level, and hence vectorizes directly. The second step, however, involves assembling each element contribution to the nodal fluxes. This operation is somewhat more expensive and in the current version of the code has not been vectorized. To do this elements must be "colored" and sorted into sets to eliminate the data dependencies that prevent automatic vectorization. This will be accomplished in the next version of the code. The second step may be expressed schematically as

$$[M]\Delta U = R \tag{16}$$

where $[M]$ is the consistent mass matrix and R is the assembled flux terms. For steady-state calculations $[M]$ is approximated by the lumped mass matrix, $[M_L]$, which is easily inverted due to its diagonal structure.

$$[M_L]_{ij} = \begin{cases} 0 & i \neq j \\ \sum_k [M]_{ik} & i = j \end{cases} \tag{17}$$

By using the lumped mass matrix the method may be thought of as a Lax–Wendroff predictor-corrector method, which uses shape functions to approximate the primary variables and fluxes within an element.

In order to ensure stable computations in problems involving strong shocks, an artificial viscosity has been applied (Morgan and Peraire, 1987). The solution computed from equation (15*b*) is replaced by the smoothed nodal values, U_s^{k+1}:

$$U_s^{k+1} - U^{k+1} = C_v [M_L]^{-1} \left| \frac{([M] - [M_L])p}{|([M] - [M_L])p|} \right| ([M] - [M_L]) U^{k+1} \tag{18}$$

where C_v is a constant. This is the unstructured mesh implementation of, in finite difference terms, second difference smoothing with a second difference pressure sensing switch. This switch, $|([M] - [M_L])p / |([M] - [M_L])p|\ |$, is of order (mesh spacing)^2 in smooth regions of the flow but of order 1 in the region of shocks. Hence in smooth flow, the term $U_s^{k+1} - U^{k+1}$ is of order (mesh spacing)^3 and does not alter the basic second-order accuracy of the scheme but near shock waves does facilitate shock capture. It should be noted that across boundary layers and wakes the combination of a pressure-driven switch and physically small transverse pressure gradients minimizes false viscosity error. The range of C_v is typically 1–2 in transonic flows and 0.1–0.2 in subsonic flows.

The boundary conditions on the upstream and exit boundaries are applied in a weak sense through the boundary integrals in equation (15*b*). On the upstream boundary total pressure, total enthalpy and the velocity component tangential to the boundary are specified, and on the downstream boundary the static pressure is fixed. These conditions are applied in a nonreflecting manner by making use of characteristic theory (Giles, 1986). On the blade boundary the condition of no normal flux of mass and heat is weakly applied to the continuity and energy equations, whereas the momentum equation is discarded in favor of the strong boundary condition: $\rho u = 0$, $\rho v = 0$.

Mesh Generation and Refinement Strategy

The flow solver is coupled with an advancing front grid generation procedure (Peraire et al., 1987), which is capable of generating an unstructured mesh provided that the geometry and the distribution of local element size δ are given. The boundaries of the domain are prescribed by a number of boundary segments, each defined by a set of boundary points, and the variation of δ is specified at each node point of a given background mesh. The strategy of solution-adaptive refinement for steady-state problems is implemented by the following iterative procedure:

1 generation of a uniform initial mesh (the production of a uniform mesh is trivial; only one background element is needed)
2 computation of steady-state solution
3 if desired accuracy is achieved, stop simulation
4 refinement indicator is computed, at each note point, from the solution
5 generation of new mesh by using the old mesh as a background mesh; local element size is controlled by the indicator
6 initial condition on new mesh is given by the interpolated solution from the old mesh
7 go to (2)

Currently, the indicator used for refinement is a scalar and hence not directional, although it is recognized that by using an indicator that senses element shape as well as element size, stretched elements could be generated. This would be an economical advantage, for example, in boundary layers, where the flow is approximately one dimensional. Here, this issue has been addressed by including a thin layer of structured mesh, consisting of highly stretched elements, in the region near the wall. This is illustrated in Fig. 1. For the present computations (Figs. 7–9, 11) ten nodes were deployed normal to the blade in this O-mesh. Nevertheless, the mesh generator still tends to produce far too many inefficient near-equilateral elements in shocks, boundary layers, and wakes where the flow is essentially one dimensional. It is hoped that further development can alleviate this inefficient use of computer memory, but is is not an easy task.

We have found it convenient first to resolve the boundary layer and wake, which is done using the local entropy as the indicator for refinement

Downloaded 01 Jun 2010 to 171.66.16.66. Redistribution subject to ASME license or copyright; see http://www.asme.org/terms/Terms_Use.cfm

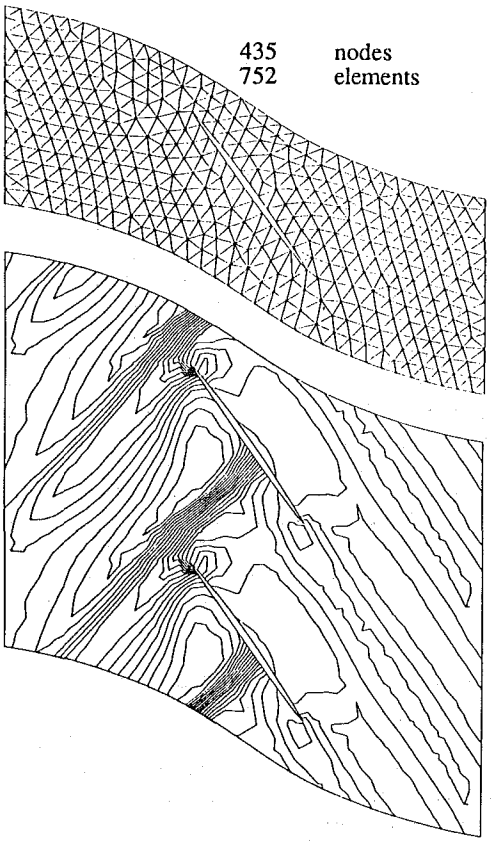

Fig. 2(*a*) Initial finite element mesh for a generic fan blade configuration; (*b*) Mach number contours of the steady-state solution on the initial mesh: $M_{min} = 0.5660$; $M_{max} = 1.3215$; interval = 0.04

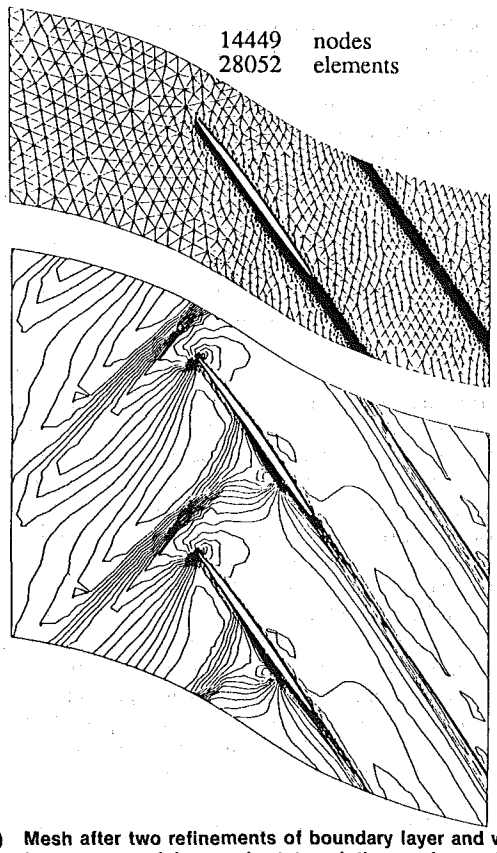

Fig. 3(*a*) Mesh after two refinements of boundary layer and wake; (*b*) Mach number contours of the steady-state solution on the mesh shown in Fig. 3(*a*): $M_{min} = 0.0$; $M_{max} = 1.3707$; interval = 0.04

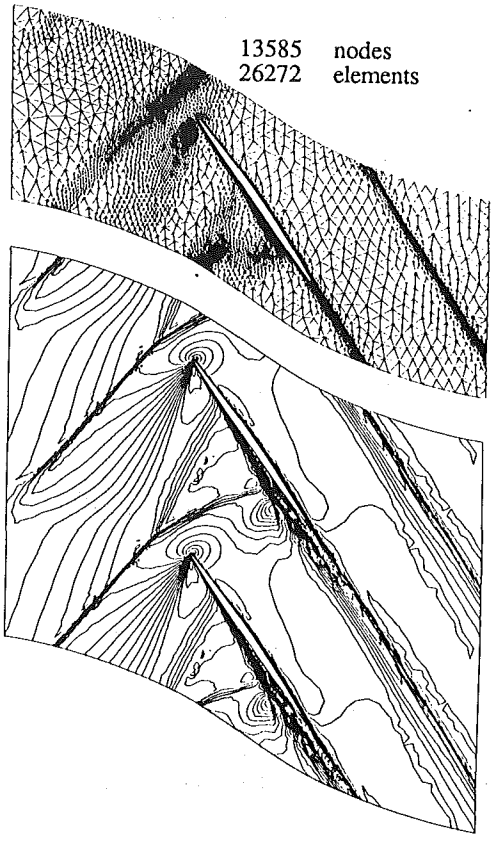

Fig. 4(*a*) Mesh after an additional refinements of shocks and stagnation point; (*b*) Mach number contours of the steady-state solution on the mesh shown in Fig. 4(*a*): $M_{min} = 0.0$; $M_{max} = 1.4628$; interval = 0.04

$$\delta_j = \frac{S_j - S_{\min}}{S_{\max} - S_{\min}}(\delta_{\max} - \delta_{\min}) + \delta_{\min} \tag{19}$$

S_{max}, S_{min}, and S_j are the maximum, minimum, and nodal values of entropy, δ_{max} and δ_{min} are the maximum and minimum specified values of element size, and δ_j is the nodal indicator. Next we refine shocks and stagnation points by also taking into account the magnitude of the static pressure gradient

$$\delta_j = \delta_{\min} \left|\frac{\partial p}{\partial x_i}\right|_{\max} \left|\frac{\partial p_i}{\partial x_i}\right|^{-1} \tag{20}$$

The condition (19) or (20) that produces the smallest value of element size is used locally.

Figures 2–4 show a sequence of refinements for a generic fan blade and the steady-state solution on each respective mesh. Since the initial mesh is too coarse to resolve the boundary layer, the no-slip condition has in this case been replaced by the condition of no flux of mass and heat normal to the blade boundary. This sequence is intended purely to illustrate the concepts of solution adaptive refinement. As the refinement proceeds the blade surface needs increasing definition. This is provided by a sequence of splines to calculate new blade points, thus guaranteeing that blade surface curvature is always properly represented.

Basic Code Validation

The complete validation of a code is extremely expensive and almost invariably carried out in-house (validation is the key investment in CFD). Here we present predictions for a Blasius boundary layer and a transonic aerofoil. Figure 5 compares the predicted laminar flow past a flat plate with zero pressure gradient with the exact Blasius result (Schlichting, 1979). The agreement between the velocity profile (at mid-chord) and skin friction development is perfectly acceptable.

Downloaded 01 Jun 2010 to 171.66.16.66. Redistribution subject to ASME license or copyright; see http://www.asme.org/terms/Terms_Use.cfm

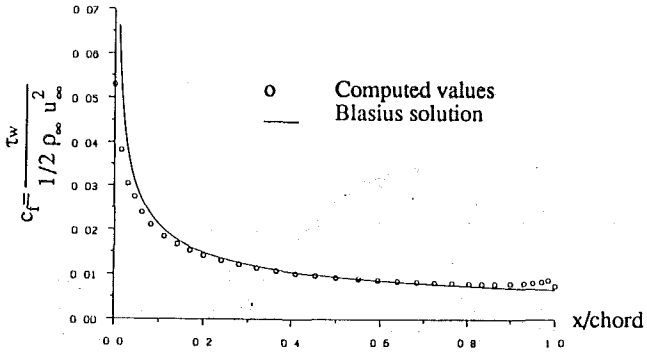

Fig. 5(*a*) Skin friction coefficient versus chord position for the laminar flat plate case compared with the Blasius solution

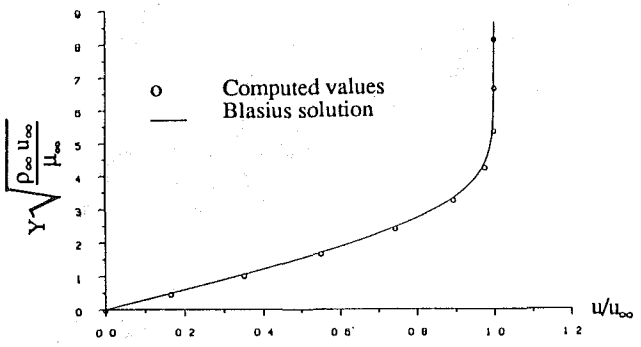

Fig. 5(*b*) Velocity profile at 50 percent of chord for the flat plate case compared with the Blasius solution

The predictions used a mesh of 35 by 33 nodes, a Mach number of 0.2, a Reynolds number of 10^4, and the same value of C_v as for routine blade work.

Figure 6(*a*) shows the mesh (consisting of 2300 nodes) used to predict the flow past a symmetric aerofoil at zero incidence. Only the upper part of the flow was modeled with appropriate symmetry conditions upstream and downstream of the aerofoil. The Mach number is 0.8 and the Reynolds number 1.8×10^6, hence transition is assumed at the leading edge. The comparisons of both surface pressures and skin friction with experimental measurement (Baker and Squire, 1982) and the predictions of a conventional structured mesh solver (Dawes, 1985) are, again, perfectly acceptable (Figs. 6*b–d*).

Sample Application

The capability of the described method is demonstrated by comparing results with measurements and a conventional viscous flow solver (Dawes, 1985), based on the traditional block implicit scheme by Beam and Warming (1977). Two sets of runs have been conducted for a high-speed turbine configuration, for which experimental values of loss and blade surface pressures are available (Kiock et al., 1985). The first simulation considers the turbulent case, whereas the second simulation is laminar. In both cases a Reynolds number of 6.7×10^5, based on the true chord and the flow variables on the exit boundary, is used. Boundary conditions are applied corresponding to a flow angle of 37.9 deg on the upstream boundary and a Mach number of 0.985 on the exit boundary.

The sequence of meshes used is illustrated in Fig. 7 (as in Fig. 1, a structured O-mesh is used near the blade with 10 nodes normal to the blade). The conventional solver uses an entirely structured H-mesh consisting of 50×99 computational cells.

Blade Surface Pressures and General Flow Field. One objective of the simulations is to estimate the load on the blade

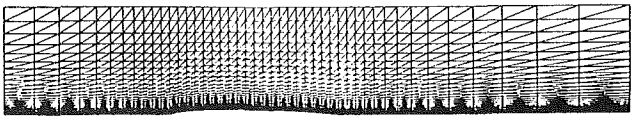

Fig. 6(*a*) Mesh consisting of 2300 nodes used for computation of transonic flow around an aerofoil at zero incidence

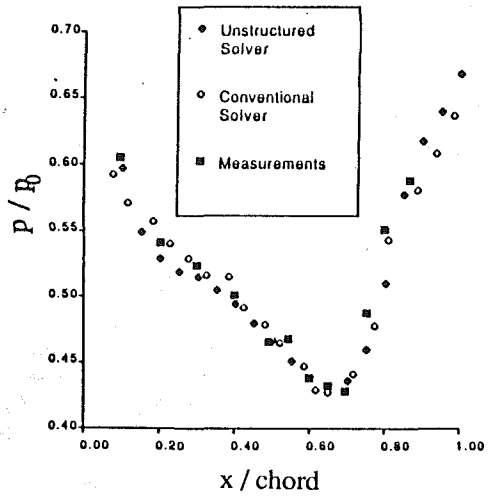

Fig. 6(*b*) Aerofoil surface pressures

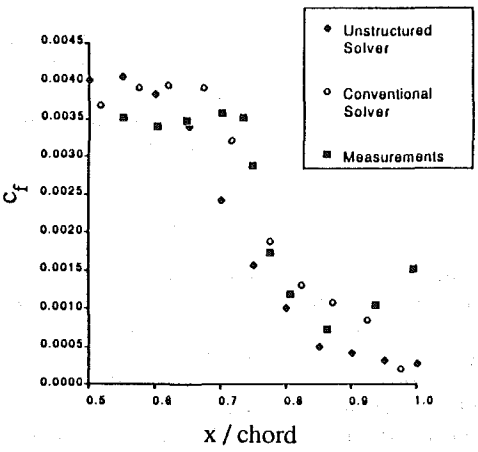

Fig. 6(*c*) Aerofoil skin friction coefficients

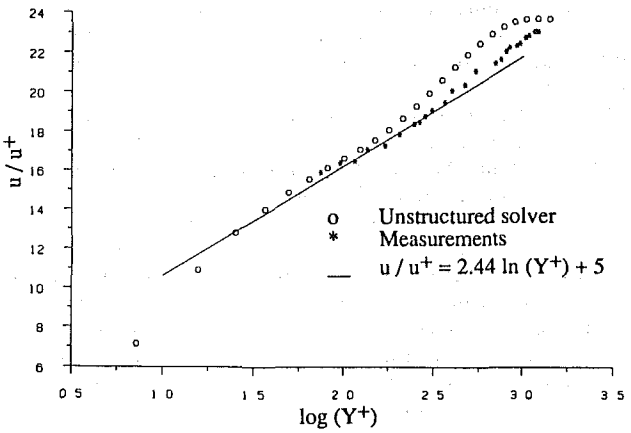

Fig. 6(*d*) Velocity profile at 55 percent of chord

and the distribution of static pressure along the blade surface. In Figs. 8(*a*) and 8(*b*) the surface pressures are plotted versus the blade surface coordinate for the turbulent case and laminar case, respectively. In the turbulent case (Fig. 8*a*) results of both

Downloaded 01 Jun 2010 to 171.66.16.66. Redistribution subject to ASME license or copyright; see http://www.asme.org/terms/Terms_Use.cfm

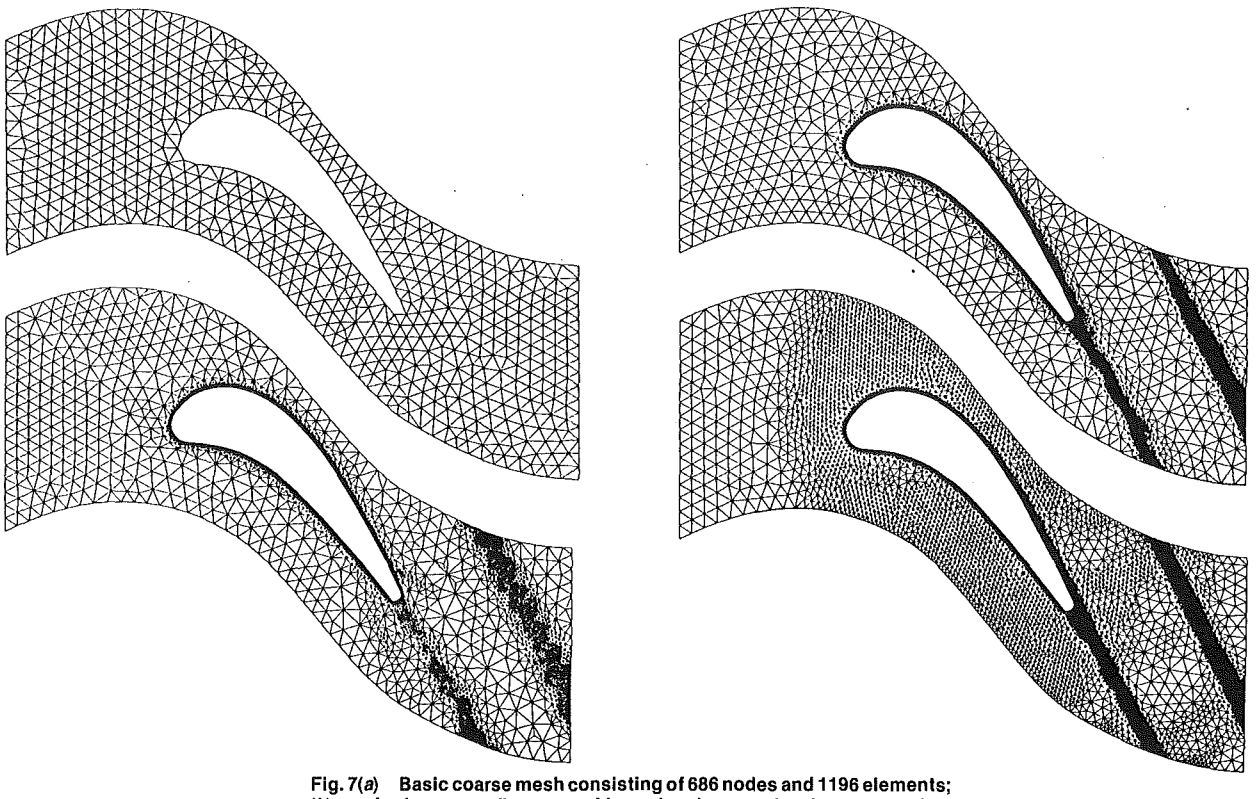

Fig. 7(*a*) Basic coarse mesh consisting of 686 nodes and 1196 elements; (*b*) mesh after one refinement of boundary layer and wake; 8305 nodes; 15,866 elements; (*c*) mesh after two refinements of boundary layer and wake; 12,206 nodes; 26,625 elements; (*d*) mesh after an additional refinement of areas with large static pressure gradients; 15,099 nodes; 29,279 elements

solvers compare well with measured values; the adaptive solver clearly provides better resolution in the shock and trailing edge regions. The results of the laminar simulations (Fig. 8*b*) do not differ much from the turbulent results (Fig. 8*a*), except for the region downstream of the shock on the suction side, indicating that the solution in this area is highly turbulent. The unstructured solver has a tendency to produce small wiggles in the blade surface pressures (see Fig. 8). This is not geometric in origin (as the refined blade surface is always spline fit) but rather is a failure of the numerical smoothing to damp small wiggles propagating from the high-gradient leading edge region. This failure is partly due to using minimal smoothing (i.e., smoothing is too low) but also due to the presence of additional unstable modes on unstructured triangles that are poorly damped by our smoother.

Figures 9(*a–c*) show contour plots of Mach number, static pressures, and entropy for the turbulent solution on the final mesh. These may be compared with the solution on the structured mesh (Figs. 10*a–d*). The two solutions compare in general. But here also, we note discrepancies in the resolution of shocks and in the trailing edge region. The adaptive solver produces much better shock resolution than the conventional solver. In particular the reflection of the trailing edge shock on the suction surface is well predicted by the adaptive solver; the conventional solver has smeared it into the expansion. The shock-boundary layer interaction zone (Fig. 11) shows a well-resolved separation zone (and also illustrates the extend of the resolution of the structured O-mesh local to the blade). The separation bubble itself appears larger than that present in the experiments (Kiock et al., 1985) so this has implications for the loss prediction.

Loss Prediction. Another reason for simulating viscous compressible flows is to predict the loss in a cascade stage under certain flow conditions. The loss ω is defined as

$$\omega = \frac{p_{01} - \bar{p}_{02}}{\bar{p}_{02} - p_2} \tag{21}$$

where p_0 and p are the total and static pressures, respectively; the overbar represents a pitchwise mass average; the subscript 2 denotes the exit value and the subscript 1 is the value at the upstream boundary. In general, numerical schemes tend to overestimate the loss due to numerical viscosity inherent in the method, but are needed in order to stabilize the computations in the vicinity of shocks. Figures 7(*a–d*) show the sequence of meshes used for the turbulent run and Table 1 shows the computed loss as a function of the number of mesh points. As the mesh is refined the experimental loss is approached, although not reached.

It is clear that for a given number of mesh points, the conventional solver is more accurate, according to the losses in Table 1. This is almost entirely due to the present mesh generator, which produces far too many equilateral triangles in regions like shocks, wakes, and boundary layers, which are really one dimensional and would be more efficiently resolved on stretched elements. Overcoming this inherent difficulty with the mesh generator is currently the major pacing item in the code development. This should not be seen as a major restriction for the future. As the mesh refinement increases, the predicted loss falls to a level somewhat above that measured. It is believed that this must be due, at least partly, to numerical smoothing (which should be rather more sophisticated). For the turbulent case the final unstructured and structured loss levels are effectively the same, which is encouraging as they use the same turbulence model and the same model constants.

Conclusion

A solution-adaptive viscous flow solver algorithm is described and applied to high-speed flows in cascades. We have

Downloaded 01 Jun 2010 to 171.66.16.66. Redistribution subject to ASME license or copyright; see http://www.asme.org/terms/Terms_Use.cfm

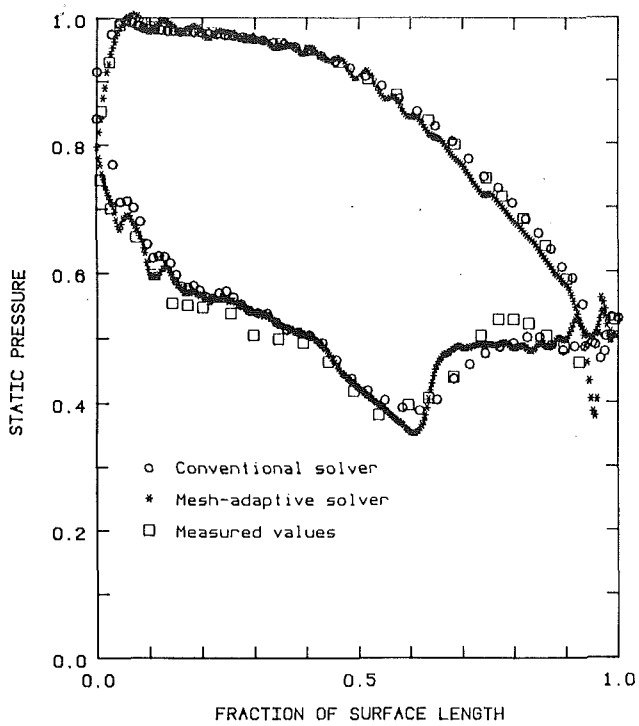

Fig. 8(*a*) Blade surface pressures for turbulent simulation; values are scaled by the upstream stagnation pressure

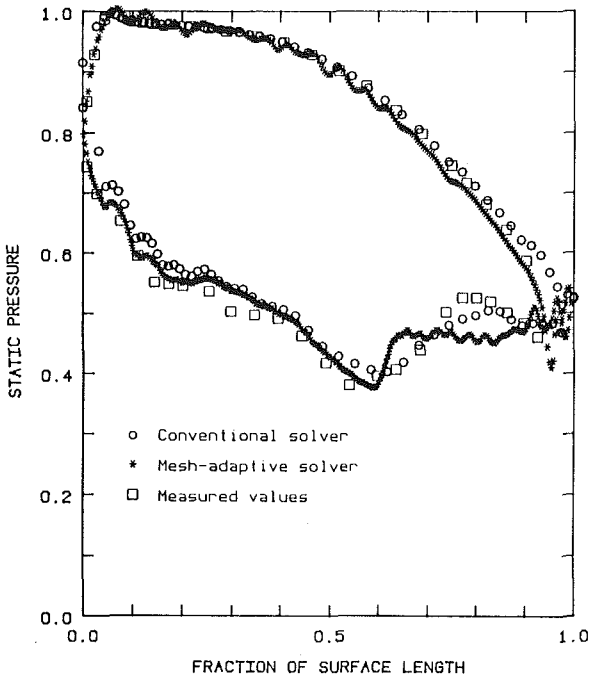

Fig. 8(*b*) Blade surface pressures for laminar simulation; values are scaled by the upstream stagnation pressure

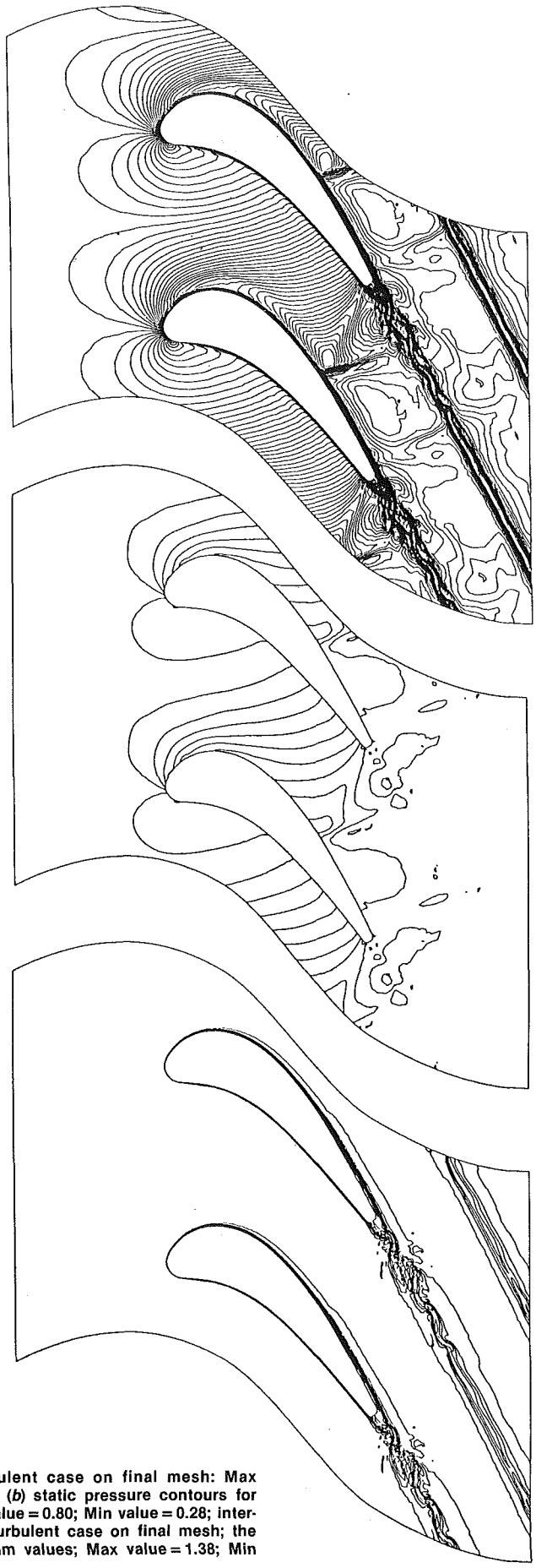

Fig. 9(*a*) Mach contours for turbulent case on final mesh: Max value = 1.28; contour interval = 0.025; (*b*) static pressure contours for turbulent case on final mesh: Max value = 0.80; Min value = 0.28; interval = 0.05; (*c*) entropy contours for turbulent case on final mesh; the entropies are scaled by the upstream values; Max value = 1.38; Min value = 0.96; interval = 0.02

Downloaded 01 Jun 2010 to 171.66.16.66. Redistribution subject to ASME license or copyright; see http://www.asme.org/terms/Terms_Use.cfm

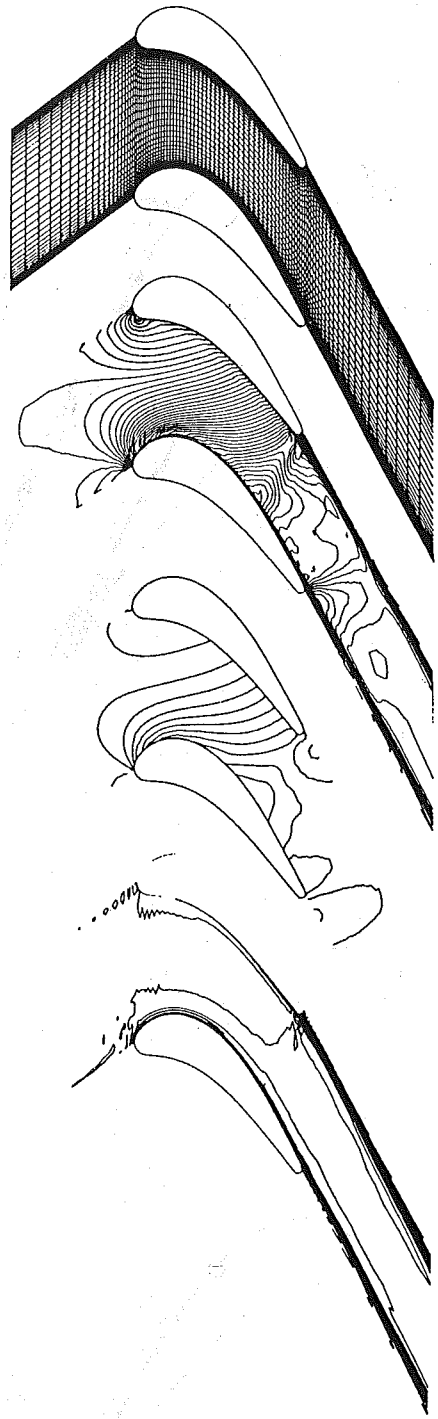

Fig. 10(*a*) Structured H-mesh for conventional flow solver: The mesh consists of 4950 node points; (*b*) Mach contours of steady turbulent solution on the structured mesh: The contour interval is 0.025; (*c*) static pressure contours of steady turbulent solution on the structured mesh: The contour interval is 0.05; (*d*) entropy contours of steady turbulent solution on the structured mesh: The contour interval is 0.02

found three major advantages with this procedure compared with conventional structured mesh flow solvers:

(*i*) The method provides greater generality since the unstructured mesh puts no constraint on the type of geometry that may be encountered. It also allows for adaptive refinement along arbitrary curves or at arbitrary points in the domain. In this way numerical detail may be supplied where, and only where, needed.

(*ii*) The simulations are to a large extent user independent since no knowledge of the solution is required in order to generate the mesh. The mesh is generated automatically from the solution according to given criteria. The only input from the user, except for the geometry and boundary conditions, is minimum and maximum allowed element size.

(*iii*) Any degree of accuracy is achievable without sacrificing good discretization practice. By decreasing the minimum allowed element size it is possible to achieve higher local accuracy without the risk of developing badly deformed or skewed elements.

Results show that the method presented has the ability to resolve local phenomena such as shock/boundary layer interaction.

However, the current code has several disadvantages compared to a conventional, well-developed structured code:

(*i*) The mesh generator produces far too many inefficient equilateral triangles in steep gradient regions like shocks, when correctly aligned stretched elements would drastically reduce the number of nodes required for a given resolution.

(*ii*) More sophisticated smoothing needs to be developed for the unstructured environment.

Table 1 Computed loss versus number of mesh points

method	loss ω
measurement	4.15 %
conventional solver, laminar case	
- 4950 mesh points	5.12 %
conventional solver, turbulent case	
- 4950 mesh points	7.60 %
adaptive solver, laminar case	
- 8305 mesh points	12.7 %
- 12099 mesh points	9.12 %
- 14186 mesh points	6.23 %
adaptive solver, turbulent case	
- 8305 mesh points	12.8 %
- 12206 mesh points	10.3 %
- 15099 mesh points	7.48 %

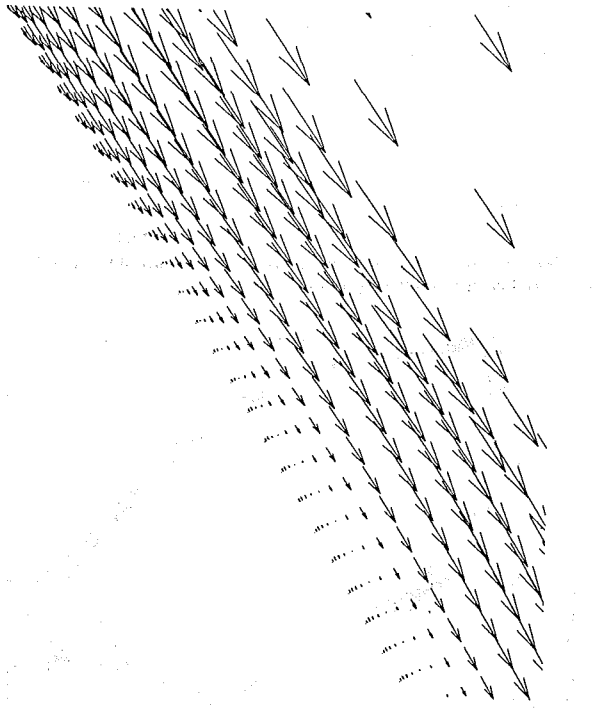

Fig. 11 Vectors of fluid velocity in the turbulent boundary layer separation region, which is located at about 3/4 chord on the suction side

Downloaded 01 Jun 2010 to 171.66.16.66. Redistribution subject to ASME license or copyright; see http://www.asme.org/terms/Terms_Use.cfm

(*iii*) Some implicitness must be introduced into the algorithm to relieve restrictive small time steps in the boundary layer.

(*iv*) The current code is still a research code and so the cpu times do not yet compare favorably with a mature structured code. Nevertheless, the cost per point per time step is comparable and further work on the mesh generator will reduce overall cpu times.

All four issues are currently being addressed.

Acknowledgments

The authors would like to acknowledge the support of Volvo Flygmotor AB.

References

Baker, C. J., and Squire, L. C., 1982, "Turbulent Boundary-Layer Development on a Two-Dimensional Aerofoil With Supercritical Flow at Low Reynolds Number," *The Aeronautical Quarterly*, Vol. 33, pp. 174–198.

Baldwin, B. S., and Lomax, H., 1978, "Thin Layer Approximation and Algebraic Model for Separated Turbulent Flows," AIAA Paper No. 78-257.

Beam, R. M., and Warming, R. F., 1977, "An Implicit Factored Scheme for the Compressible Navier–Stokes Equations," *Proceedings of the AIAA 3rd Computational Fluid Dynamics Conference*, Albuquerque, NM.

Dawes, W. N., 1985, "A Numerical Method for the Analysis of 3D Viscous Compressible Flow in Turbine Cascades; Application to Secondary Flow Development in a Cascade With and Without Dihedral," ASME Paper No. 85-GT-145.

Giles, M. B., 1986, "UNSFLO: A Numerical Method for Calculating Unsteady Stator/Rotor Interaction," Technical Report TR-86-6, MIT Computational Fluid Dynamics Laboratory.

Holmes, D. G., Lamson, S. H., and Connel, S. D., 1988, "Quasi-3D Solutions for Transonic, Inviscid Flows by Adaptive Triangulation," ASME Paper No. 88-GT-83.

Kiock, R., Hoheisel, H., Dietrichs, H. J., and Holmes, A. T., 1985, "The Boundary Layer Behaviour of an Advanced Gas Turbine Rotor Blade Under the Influence of Simulated Film Cooling," AGARD-CP-390.

Löhner, R., Morgan, K., Peraire, J., and Vahdati, M., 1987, "Finite Element Flux-Corrected Transport (FEM-FTC) for the Euler and Navier–Stokes Equations," *Int. J. Num. Meth Fluids*, Vol. 7, pp. 1093–1109.

Morgan, K., and Peraire, J., 1987, "Finite Element Methods for Compressible Flows," von Karman Institute for Fluid Dynamics, Lecture Series 1987-04, *Computational Fluid Dynamics*.

Peraire, J., Peiro, J., Morgan, K., and Zienkiewicz, O. C., 1987, "Finite Element Mesh Generation and Adaptive Procedures for CFD," presented at the GAMNI/SMAI Conference on Automated and Adaptive Mesh Generation, Grenoble, France.

Schlichting, H., 1979, *Boundary-Layer Theory*, 7th ed., McGraw-Hill, New York.

Downloaded 01 Jun 2010 to 171.66.16.66. Redistribution subject to ASME license or copyright; see http://www.asme.org/terms/Terms_Use.cfm

Throughflow Theory for Nonaxisymmetric Turbomachinery Flow: Part I—Formulation

R. P. Dring
United Technologies Research Center,
E. Hartford, CT 06108

G. C. Oates
University of Washington,
Seattle, WA

Throughflow theory has been limited in its applicability and in its accuracy by the fact that it has not historically been cast in a form that can account for the nonaxisymmetries that naturally arise in turbomachinery flow due to the presence of finite numbers of rotor and stator airfoils. The attempt to circumvent this limitation by the introduction of an aerodynamic blockage factor has been demonstrated in earlier work to produce fundamental inconsistencies in the calculation, which lead to significant errors in the regions of the flow where the nonaxisymmetries are severe. The formulation in Part I of the present work is a derivation of a system of throughflow equations for nonaxisymmetric flow. A benchmark database is used in Part II to provide input to the calculation and to help identify the dominant terms. It is demonstrated that the dominant effect of nonaxisymmetry is contained in two terms that relate the total pressure of the averaged flow to the mass-averaged total pressure. It also is demonstrated that the present formulation produces a result that is more accurate than that obtained with the historical blockage-based formulation.

Introduction

Throughflow theory in turbomachinery design is a two-dimensional, axisymmetric calculation describing the spanwise variation of the flow at various streamwise locations, both within and between the rotor and stator airfoil rows, from the inlet of the compressor or turbine to its discharge. The calculation is at the heart of the design process since it determines the incident flow conditions of Mach number and flow angle and the downstream flow conditions of total pressure loss, exit flow angle, and axial velocity-density ratio (AVDR) that the rotor and stator airfoils must be designed to produce.

Although highly sophisticated fully three-dimensional Navier–Stokes solution algorithms are beginning to appear, which have the potential to attack turbomachinery flows in full generality, the basis of most contemporary design systems is a sequence of two-dimensional calculations, most notably, the throughflow prediction and the airfoil potential flow prediction. Because of their speed and efficiency, these two-dimensional calculations will continue to play an important role in the aerodynamic design of multistage compressors. For this reason, there is great incentive to improve the physical model on which throughflow theory is based.

Throughflow theory, as it has historically been used, is based on an axisymmetric treatment of circumferentially averaged flow. It has long been recognized, however, that there are major nonaxisymmetries present in the flows exiting rotor and stator airfoil rows and that these nonaxisymmetries have a powerful impact on the flow. As an example, Fig. 1 illustrates the nature of the total pressure distributions downstream of the second-stage rotor and stator of a two-stage compressor operating at near-stall conditions. Strong nonaxisymmetries are present in the flow due to the rotor tip leakage, profile wake, and hub corner separation, and due to the stator profile wake and hub corner separation.

The strong first-order effects of nonaxisymmetries such as these are normally modeled by introducing a "blockage factor" into the throughflow analysis. This aerodynamic blockage factor is usually thought of in much the same way as the mechanical blockage caused by the tangential thickness of the airfoils. Blockage in the present context is what has been referred to as "tangential" blockage and not "endwall" blockage (AGARD, 1981). Tangential blockage is intended to account for the department of the actual flow field from the axisymmetric treatment in the theory.

Over the years, a number of investigators have looked at the effect of nonaxisymmetries on throughflow theory (Ruden, 1944; Smith, 1966; Hirsch, 1975; Hirsch and Warzee, 1976, 1979; Sehra and Kerrebrock, 1979; Hirsch and Dring, 1987). The major conclusion from this work is that nonaxisymmetries do have the potential to impact the flow, especially near the endwalls.

In an effort to quantify the impact of nonaxisymmetries on a throughflow prediction, a number of detailed analytical/experimental comparisons have been carried out making use of an extensive benchmark data set for a two-stage compressor and utilizing the throughflow calculation of Habashi (1980) and Habashi and Youngson (1983). These assessments were carried out with the compressor operating both at nominal

Contributed by the International Gas Turbine Institute and presented at the 34th International Gas Turbine and Aeroengine Congress and Exhibition, Toronto, Ontario, Canada, June 4–8, 1989. Manuscript received at ASME Headquarters February 21, 1989. Paper No. 89-GT-304.

Copyright © 1990 by ASME
Downloaded 01 Jun 2010 to 171.66.16.66. Redistribution subject to ASME license or copyright; see http://www.asme.org/terms/Terms_Use.cfm

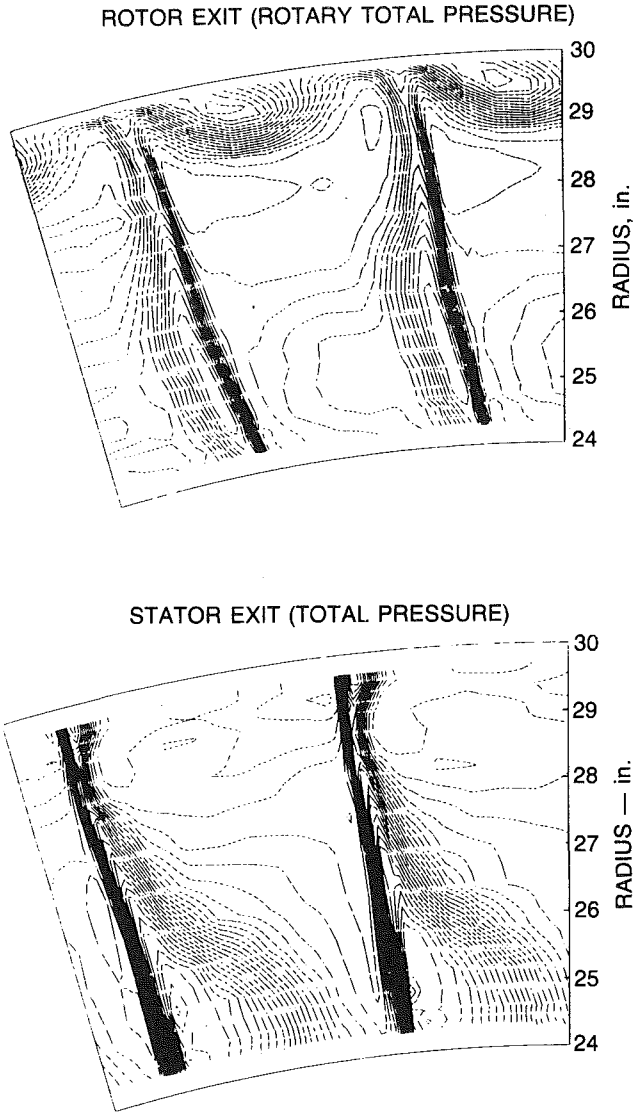

Fig. 1 Second-stage rotor and stator exit total pressure contours, ΔC_{PT} = 0.025

design point conditions (Dring and Joslyn, 1985, 1986a, 1986b, 1986c), and at near-stall conditions (Dring and Joslyn, 1986d, 1987). These assessments have indicated that throughflow theory becomes inaccurate in regions where the aerodynamic blockage is high and that the accuracy of the prediction is very sensitive to the detailed spanwise distributions of blockage.

The objective of the present work is to derive and assess an improved formulation of throughflow theory that accounts for the nonaxisymmetry of the flow.

Derivation

To a great extent, the present work is an extension of the throughflow formulation of Hirsch and Warzee (1979). It also is an extension of the discussion of the implications of the various circumferential averaging processes presented by Hirsch and Dring (1987). One final note of caution with respect to these previous works and the present work is that in this derivation the notation for the various averaging processes has been changed in an attempt to make the work more readable.

The essential concept in applying throughflow theory to nonaxisymmetric flow is that the variables can be dealt with on some suitable circumferentially averaged basis. The nature of the most suitable averaging process depends on the particular equation or variable being averaged. The equations that will be employed in this formulation include the continuity equation, the equation of state, and the radial projection of the momentum equation. In addition to these, the averaging process also must be applied to the variables normally considered to be conserved along stream surfaces, i.e., absolute angular momentum, entropy, and rothalpy. As a result of all this, three different averages will be utilized. The need for each average will become apparent as the derivation develops. These three circumferential averages are as follows for any function $f(\theta)$:

Area Average

$$\bar{f}^a \equiv \int_{\theta_p}^{\theta_s} f d\theta \Big/ \int_{\theta_p}^{\theta_s} d\theta \tag{1}$$

Density Average

$$\bar{f}^d \equiv \int_{\theta_p}^{\theta_s} \rho f d\theta \Big/ \int_{\theta_p}^{\theta_s} \rho d\theta \tag{2a}$$

$$= \overline{\rho f}^a / \bar{\rho}^a \tag{2b}$$

Mass Average

$$\bar{f}^m \equiv \int_{\theta_p}^{\theta_s} \rho C_x f d\theta \Big/ \int_{\theta_p}^{\theta_s} \rho C_x d\theta \tag{3a}$$

$$= \overline{\rho C_x f}^a / \overline{\rho C_x}^a = \overline{C_x f}^d / \overline{C_x}^d \tag{3b}$$

In these definitions note that for incompressible flow or compressible flow at low Mach numbers the density and area averages are equal, or very nearly so.

Nomenclature

b = mechanical blockage
C = absolute flow speed
f = any general function
F_b = airfoil pressure force
F_f = airfoil friction force
H = total enthalpy
h = static enthalpy
I = rothalpy
N = number of airfoils in a row
P = static pressure
R = gas constant
r = radial coordinate
s = entropy
T = static temperature
t = airfoil tangential thickness
W = relative flow speed
x = axial coordinate
α = absolute yaw angle, equation (25)
β = relative yaw angle, equation (26)
θ_l = mean camber line lean angle
φ = stream function
ρ = density
τ = airfoil pitch
θ = angular coordinate

Subscripts

abs = absolute
s = airfoil suction surface
p = airfoil pressure surface
r = radial component
rel = relative
rot = rotary total
x = axial component
0 = total
θ = circumferential component

Superscripts

$\bar{}^a$ = pitchwise area average, equation (1)
$\bar{}^d$ = pitchwise density average, equation (2)
$\bar{}^m$ = pitchwise mass average, equation (3)
$\hat{}$ = defined in equations (14) and (28a)
$'$ = fluctuation from the density average

Downloaded 01 Jun 2010 to 171.66.16.66. Redistribution subject to ASME license or copyright; see http://www.asme.org/terms/Terms_Use.cfm

Continuity Equation. It has been demonstrated by Hirsch and Warzee (1979) that the continuity equation can be integrated circumferentially to produce the following averaged form:

$$\frac{\partial}{\partial r}\left(rb\overline{\rho}^{a}\,\overline{C_r}^{d}\right)+\frac{\partial}{\partial x}\left(rb\overline{\rho}^{a}\,\overline{C_x}^{d}\right)=0 \tag{4}$$

In this expression b is the tangential blockage factor due to the airfoil tangential thickness

$$b=1-(t/\tau) \tag{5}$$

Note that in the axial gaps between adjacent airfoil rows and in the ducts up and downstream of the compressor or turbine (where there are no airfoils), the mechanical blockage is unity. A stream function may be defined based on these area and density-averaged variables.

$$\overline{C_x}^{d}=\frac{1}{rb\overline{\rho}^{a}}\left(\frac{\partial\varphi}{\partial r}\right) \tag{6a}$$

$$\overline{C_r}^{d}=\frac{-1}{rb\overline{\rho}^{a}}\left(\frac{\partial\varphi}{\partial x}\right) \tag{6b}$$

Equation of State. The equation of state also may be circumferentially averaged as follows:

$$\overline{P}^{a}=R\left(\overline{\rho T}^{a}\right)=\overline{\rho}^{a}R\overline{T}^{d} \tag{7}$$

From the continuity equation and the equation of state it can be seen that each variable is emerging in its own preferred circumferentially averaged form, either a density average or an area average.

Momentum Equation. It has been demonstrated by Hirsch and Warzee (1979) that the radial projection of the momentum equation can be integrated circumferentially to produce an equation similar to the following:

$$\overline{C}_x^{d}\left[\frac{\partial}{\partial r}\left(\frac{1}{rb\overline{\rho}^{a}}\frac{\partial\varphi}{\partial r}\right)+\frac{\partial}{\partial x}\left(\frac{1}{rb\overline{\rho}^{a}}\frac{\partial\varphi}{\partial x}\right)\right] \tag{8a}$$

$$=\frac{1}{\overline{\rho}^{a}}\frac{\partial\overline{P}^{a}}{\partial r} \tag{8b}$$

$$+\frac{\partial}{\partial r}\left[\frac{1}{2}\left(\overline{C_r}^{2d}+\overline{W_\theta}^{2d}+\overline{C_x}^{2d}-\Omega^2r^2\right)\right] \tag{8c}$$

$$-\frac{\overline{W_\theta}^{d}}{r}\frac{\partial}{\partial r}\left(r\,\overline{C_\theta}^{d}\right) \tag{8d}$$

$$-F_{f,r}/\overline{\rho}^{a} \tag{8e}$$

$$+\left(\frac{1}{br\overline{\rho}^{a}}\right)\frac{\partial}{\partial r}\left(br\overline{\rho}^{a}\,\overline{W_r'W_r'}^{d}\right) \tag{8f}$$

$$+\left(\frac{1}{br\overline{\rho}^{a}}\right)\frac{\partial}{\partial x}\left(br\overline{\rho}^{a}\,\overline{W_r'W_x'}^{d}\right) \tag{8g}$$

$$-\frac{1}{r}\left(\overline{W_\theta'W_\theta'}^{d}\right) \tag{8h}$$

In this form, the terms (8f), (8g), and (8h) are identical to N_1, N_2, and N_3 in the Hirsch and Warzee (1979) formulation. The primed velocity components C_x', W_θ', and C_r' are the circumferential variations from the density-averaged components. These have been called "perturbation terms" but they are not necessarily small.

The term describing the area-averaged radial pressure gradient may be treated in several ways. Hirsch and Warzee [1976, equation (66)] expanded it in terms of the radial component of the airfoil pressure force and the radial derivative of blockage as follows:

$$\frac{\partial\overline{P}^{a}}{\partial r}=\frac{\partial}{\partial r}\left(\overline{P}^{a}\right)-F_{b,r}+\frac{1}{b}\frac{\partial b}{\partial r}\left(\overline{P}^{a}-\frac{1}{2}\left[P_s+P_p\right]\right) \tag{9}$$

Jennions and Stow [1985, equations (71) and (72)] expanded the same term slightly differently, i.e., in terms of the radial derivative of the airfoil suction and pressure surface angular locations as follows:

$$\frac{\partial\overline{P}^{a}}{\partial r}=\frac{\partial}{\partial r}\left(\overline{P}^{a}\right)+\frac{N}{2\pi b}\left[\left(P_p-\overline{P}^{a}\right)\frac{\partial\theta_p}{\partial r}+\left(\overline{P}^{a}-P_s\right)\frac{\partial\theta_s}{\partial r}\right] \tag{10}$$

This latter form is more convenient to evaluate from measured data in terms of airfoil pressure distributions and airfoil geometry.

Returning to equation (8), it is necessary to eliminate the averaged radial static pressure gradient equation (8b) in favor of radial gradients of rothalpy (I) and entropy (s). These two variables offer the advantage that on some averaged basis they are conserved, or vary in a prescribed manner, along stream surfaces. The radial pressure gradient will be expanded with the Gibbs' equation

$$\frac{\partial P}{\partial r}=-\rho T\left(\frac{\partial s}{\partial r}\right)+\rho\left(\frac{\partial h}{\partial r}\right) \tag{11}$$

The circumferential average of this equation is as follows

$$\frac{\partial\overline{P}^{a}}{\partial r}=-\overline{\rho}^{a}\left(\overline{T\frac{\partial s}{\partial r}}^{d}\right)+\overline{\rho}^{a}\left(\overline{\frac{\partial h}{\partial r}}^{d}\right) \tag{12}$$

Expanding these terms and introducing the fluctuation of each variable from its density average (as demonstrated by Hirsch and Warzee, 1979) results in the following expression when combined with equations (9) and (10) (Dring and Oates, 1988):

$$\overline{C_x}^{d}\left[\frac{\partial}{\partial r}\left(\frac{1}{rb\overline{\rho}^{a}}\frac{\partial\varphi}{\partial r}\right)+\frac{\partial}{\partial x}\left(\frac{1}{rb\overline{\rho}^{a}}\frac{\partial\varphi}{\partial x}\right)\right] \tag{13a}$$

$$=-\overline{T}^{d}\frac{\partial\overline{s}^{d}}{\partial r} \tag{13b}$$

$$+\frac{\partial\overline{h}^{d}}{\partial r}+\frac{\partial}{\partial r}\left[\frac{1}{2}\left(\overline{C}_r^{2d}+\overline{W}_\theta^{2d}+\overline{C}_x^{2d}-\Omega^2r^2\right)\right] \tag{13c}$$

$$-\left(\overline{W}_\theta^{d}/r\right)\frac{\partial}{\partial r}\left(r\,\overline{C}_\theta^{d}\right) \tag{13d}$$

$$-\left(F_{f,r}/\overline{\rho}^{a}\right) \tag{13e}$$

$$+\frac{1}{br\overline{\rho}^{a}}\frac{\partial}{\partial r}\left(br\overline{\rho}^{a}\,\overline{W_r'W_r'}^{d}\right) \tag{13f}$$

$$+\frac{1}{br\overline{\rho}^{a}}\frac{\partial}{\partial x}\left(br\overline{\rho}^{a}\,\overline{W_r'W_x'}^{d}\right) \tag{13g}$$

$$-\frac{1}{r}\left(\overline{W_\theta'W_\theta'}^{d}\right) \tag{13h}$$

$$+\frac{N}{2\pi b\overline{\rho}^{a}}\left[\left(P_p-\overline{P}^{a}\right)\frac{\partial\theta_p}{\partial r}+\left(\overline{P}^{a}-P_s\right)\frac{\partial\theta_s}{\partial r}\right] \tag{13i}$$

$$+\left[\overline{\left(\overline{T}^{d}s'-h'\right)\frac{\partial\rho^{a}}{\partial r}}-\left(\overline{\rho T'\frac{\partial s}{\partial r}}^{a}\right)\right]\Bigg/\overline{\rho}^{a} \tag{13j}$$

Note that the two terms in equation (13c) can be combined to form a type of rothalpy

$$\hat{I}\equiv\overline{h}^{d}+\frac{1}{2}\left(\overline{C}_r^{2d}+\overline{W}_\theta^{2d}+\overline{Cd}_x^{2d}-\Omega^2r^2\right) \tag{14}$$

This expression for rothalpy, $\hat{I}$, is the rothalpy of the density-averaged flow. It is not the density-averaged rothalpy. It is not conserved along stream surfaces (Hirsch and Dring, 1987).

Downloaded 01 Jun 2010 to 171.66.16.66. Redistribution subject to ASME license or copyright; see http://www.asme.org/terms/Terms_Use.cfm

Conservation Conditions. At this stage in the analysis, the continuity equation (4), the equation of state (7), and the radial projection of the momentum equation (13) have all been derived in terms of circumferentially averaged variables and the fluctuations from these averages. These three equations, however, are still not sufficient to describe the flow fully. Several conservation conditions must be incorporated into the system of equations. These conservation conditions account for the fact that three variables, the rothalpy, entropy, and absolute angular momentum, are conserved along stream surfaces. These conditions are one of the mechanisms [along with the elliptic or hyperbolic nature of equation (13)] whereby information is transmitted (convected) in the streamwise direction. Care must be taken, however, in the exact way in which these conditions are incorporated into the averaged system of equations.

For a steady three-dimensional flow, if any quantify (f) is conserved along streamlines this can be expressed as follows:

$$\nabla \cdot (\rho \mathbf{W} f) = 0 \tag{15}$$

The convenience of this form lies in the fact that it can be circumferentially averaged in the same manner as Hirsch and Warzee (1979) did for the continuity equation. As demonstrated by Hirsch and Dring (1987) and by James (1987) this leads to the following averaged conservation equation:

$$\frac{\partial}{\partial r}\left(rb\overline{\rho C_r f}^a\right) + \frac{\partial}{\partial x}\left(rb\overline{\rho C_x f}^a\right) = 0 \tag{16}$$

Rewriting this expression in terms of the mass average defined in equations (3a) and (3b) leads to the following:

$$\frac{\partial}{\partial r}\left(rb\overline{\rho}^a \overline{C}_x^d \left[\frac{\overline{C_r}}{\overline{C_x}} \overline{f}^m\right]\right) + \frac{\partial}{\partial x}\left(rb\overline{\rho}^a \overline{C}_x^d \overline{f}^m\right) = 0 \tag{17}$$

If it is assumed that C_r and C_x are proportional as they vary in the circumferential direction, then this equation simplifies into a very convenient form (Hirsch and Dring, 1987; James, 1987). This assumption is equivalent to assuming that stream surfaces remain axisymmetric. Under this assumption, equation (17) becomes the following:

$$\overline{C}_r^d \frac{\partial}{\partial r}\left(\overline{f}^m\right) + \overline{C}_x^d \frac{\partial}{\partial x}\left(\overline{f}^m\right) = 0 \tag{18}$$

Thus the mass average of a quantity (which is conserved along streamlines in an inviscid three-dimensional flow) is conserved along stream surfaces based on the density-averaged velocity components if the stream surfaces of the three-dimensional flow remain axisymmetric, i.e., if C_x and C_r are proportional in their circumferential variation.

This assumption of axisymmetric stream surfaces in the three-dimensional (noncircumferentially averaged) flow is important in this development since it provides the necessary conservation conditions in a very convenient form, equation (18). This, however, is only an assumption and no doubt there are occasions where it is not an appropriate assumption. However, Adkins and Smith (1982) have provided an excellent and exhaustive treatment of the physics of spanwise mixing by stream surface rotation due to deterministic secondary flows. The assumption has been made in the present analysis that the flow was inviscid, i.e., that the effects of diffusion were negligible. However, the analysis of Gallimore and Cumpsty (1986a, 1986b) provides an excellent model for the inclusion of this mechanism. In summary then, physical models are available that can account for the effects of diffusion and stream surface rotation.

Applying the conservation condition in equation (18) for flows with axisymmetric stream surfaces to the conserved variables required for equation (13), i.e., rothalpy, entropy, and absolute angular momentum, provides the following:

$$\left.\begin{aligned} \overline{I}^m &= \text{const} \\ \overline{s}^m &= \text{const} \\ r\overline{C}_\theta^m &= \text{const} \end{aligned}\right\} \text{ along } \varphi = \text{const} \tag{19, 20, 21}$$

The fact should be kept in mind that within airfoil rows these parameters may not be constant due to the airfoil forces. The mass-averaged entropy will change in response to the prescribed airfoil total pressure loss distribution and the mass-averaged absolute angular momentum will change in response to the prescribed airfoil turning distribution.

It is the three conservation conditions that permit the calculation of the three radial gradient terms on the right-hand side of the momentum equation, i.e., equations (13b), (13c) and (13d). With the introduction of three additional correction terms the momentum equation can be written in terms of radial gradients of the mass-averaged quantities as follows:

$$\overline{C}_x^d \left[\frac{\partial}{\partial r}\left(\frac{1}{rb\overline{\rho}^a}\frac{\partial \varphi}{\partial r}\right) + \frac{\partial}{\partial x}\left(\frac{1}{rb\overline{\rho}^a}\frac{\partial \varphi}{\partial x}\right)\right] \tag{22a}$$

$$= \frac{\partial \overline{I}^m}{\partial r} - \overline{T}^d \frac{\partial \overline{s}^m}{\partial r} \tag{22b}$$

$$- (\overline{W}_\theta^d / r)\frac{\partial r\overline{C}_\theta^m}{\partial r} \tag{22c}$$

$$- (F_{f,r}/\overline{\rho}^a) \tag{22d}$$

$$+ \frac{1}{br\overline{\rho}^a}\frac{\partial}{\partial r}\left(br\overline{\rho}^a \overline{W_r' W_r'}^d\right) \tag{22e}$$

$$+ \frac{1}{br\overline{\rho}^a}\frac{\partial}{\partial x}\left(br\overline{\rho}^a \overline{W_r' W_r'}^d\right) \tag{22f}$$

$$- \frac{1}{r}\left(\overline{W_\theta' W_\theta'}^d\right) \tag{22g}$$

$$+ \frac{N}{2\pi b\overline{\rho}^a}\left[(P_p - \overline{P}^a)\frac{\partial \theta_p}{\partial r} + (\overline{P}^a - P_s)\frac{\partial \theta_s}{\partial r}\right] \tag{22h}$$

$$+ \left[\overline{(\overline{T}^d s' - h')\frac{\partial \rho}{\partial r}}^a - \left(\overline{\rho T' \frac{\partial s}{\partial r}}\right)^a\right] \Big/ \overline{\rho}^a \tag{22i}$$

$$+ \left[\frac{\partial}{\partial r}(\hat{I} - \overline{I}^m) - \overline{T}^d \frac{\partial}{\partial r}(\overline{s}^d - \overline{s}^m)\right] \tag{22j}$$

$$- (\overline{W}_\theta^d / r)\frac{\partial}{\partial r}\left[r(\overline{C}_\theta^d - \overline{C}_\theta^m)\right] \tag{22k}$$

A convenient relationship exists between equation (22k) and the first term in equation (22j). This relationship comes about because of the connection between the rothalpy and the relative and absolute enthalpies. This is demonstrated as follows:

$$I = H_{\text{rel}} - \frac{1}{2}U^2 = H_{\text{abs}} - UC_\theta \tag{23}$$

From this, the following relations may be derived:

$$(\hat{I} - \overline{I}^m) = (\hat{H}_{\text{rel}} - \overline{H}^m{}_{\text{rel}}) \tag{24a}$$

$$= (\hat{H}_{\text{abs}} - \overline{H}^m_{\text{abs}}) - U(\overline{C}_\theta^d - \overline{C}_\theta^m) \tag{24b}$$

Thus the impact of nonaxisymmetry on the rothalpy (and on the relative total enthalpy) is related to its impact on the absolute total enthalpy and on the absolute swirl velocity.

The final closure issue to be addressed is related to whether the static pressure should be density or area-averaged. If the static pressure is calculated by applying the isentropic relations to the total and static enthalpies of the density-averaged flow, equation (14), then a density-averaged static pressure would result. The averaged equation of state, however, gives rise to

Downloaded 01 Jun 2010 to 171.66.16.66. Redistribution subject to ASME license or copyright; see http://www.asme.org/terms/Terms_Use.cfm

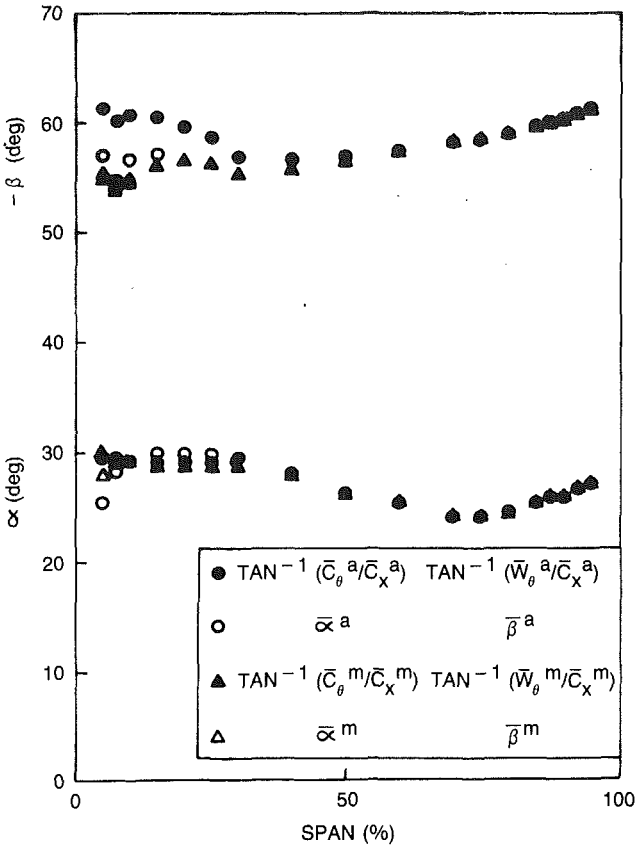

Fig. 2 First-stage stator exit flow angles, ϕ = 0.45

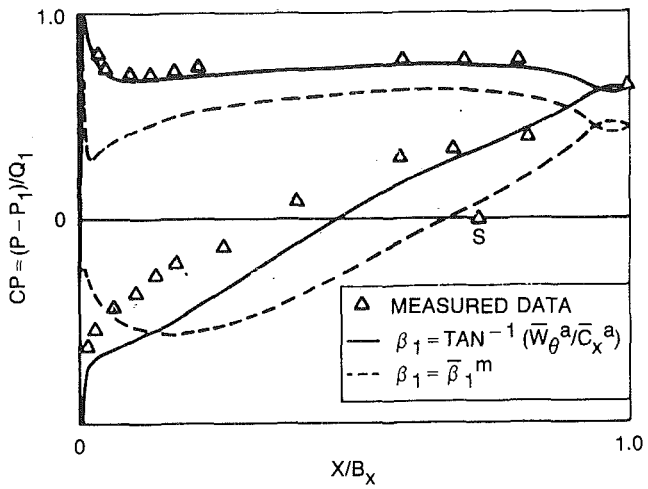

Fig. 3 Second-stage rotor pressure distribution, ϕ = 0.45, 3.2 percent span (*S* = separation location)

an area-averaged static pressure, equation (7). It seems probable, however, that in the vast majority of applications the difference between these two averaged static pressures would be inconsequential in the axial regions between adjacent airfoil rows because of the relatively weak circumferential variations of static pressure in these regions (e.g., Dring and Joslyn, 1986*a*, Fig. 1). There may, however, be significant effects within airfoil rows where the static pressure and density may vary strongly.

Flow Angle Definitions. The input flow angles are neither area nor density nor mass average. In fact, averaged angles have no significance at all. The input angles must be based on the density-averaged velocity components since these angles are used to relate the swirl component of velocity to the axial component of velocity (which appear as density averages)

$$\alpha \equiv \tan^{-1}(\bar{C}_\theta^d/\bar{C}_x^d) \tag{25}$$

$$\beta \equiv \tan^{-1}(\bar{W}_\theta^d/\bar{C}_x^d) \tag{26}$$

Figure 2 contains spanwise distributions of absolute and relative flow angles as calculated by several averaging procedures. It is based on traverse data acquired downstream of the first-stage stator in a two-stage compressor (Dring and Joslyn, 1987) operating at near-stall conditions. The open symbols represent area and mass-averaged angles. The relative and absolute flow angles based on the mass and area averages of the various velocity components are plotted as the solid symbols.

One is led to question why the relative flow angle based on area-averaged velocity components is larger than the other relative flow angle profiles in the region from the hub out to 30 percent span. This behavior is related to the differences that exist between the mass and area-averaged velocity components in this region due to the wide and deep stator wakes. For example, at the 10 percent span location, the area-averaged axial velocity and absolute swirl velocity components are both approximately 85 percent of the mass-averaged values and hence the absolute flow angles based on these mass and area-averaged velocity components are very close ($\approx$ 29.3 deg). When the wheel speed is subtracted, however, the area and mass-averaged relative velocity components produce relative flow angles that are very different (-60.6 deg and -54.8 deg). Thus significantly different relative flow angles can result even when the absolute flow angles are nearly equal.

While it is clear that flow angles based on density-averaged velocity components are the only correct input for a throughflow analysis it is still not clear which of these angle definitions should be used in computing the pressure distributions on the airfoils (Smith and Jennions, 1988). The second-stage rotor was chosen as a basis on which to examine this question. Since the range of relative angles based on the various definitions was large ($\approx$6 deg) in the flow aft of the first stator near the hub (Fig. 2), and since the hub corner separation on the second rotor was small (relative to those on the stators), this airfoil provides a good basis on which to examine this flow angle question.

The results in Fig. 3 include both the measured surface static pressure distribution and the computed potential flow distributions for two inlet flow angles at the 3.2 percent span location on the second-stage rotor. The two inlet flow angles used were the mass-averaged angle (55.4 deg) and the angle based on the area-averaged velocity components (61.8 deg), a difference of 6.4 deg. The agreement between the measured data and the computed results is clearly superior for the angle based on averaged velocity components, especially on the pressure surface. The agreement on the suction surface also is better for this case but it is far from perfect due to the hub corner separation on this rotor. Similar results were demonstrated both at the 12.5 and 25 percent span locations where the differences between the two angle definitions were 5.3 and 2.4 deg, respectively.

The conclusion here is that not only are the flow angles based on averaged velocity components necessary for an accurate throughflow analysis, but they also give a more accurate result in the airfoil potential flow analysis.

Incompressible Flow. For incompressible flow a somewhat simplified form of the momentum equation can be derived by combining equations (8) and (10), by noting that area and density averages are equivalent, and by utilizing rotary total pressure (Hawthorne, 1974) as the conserved quantity instead of rothalpy and entropy. The following form results for incompressible flow:

Downloaded 01 Jun 2010 to 171.66.16.66. Redistribution subject to ASME license or copyright; see http://www.asme.org/terms/Terms_Use.cfm

$$\overline{C}_x^a\left[\frac{\partial}{\partial r}\left(\frac{1}{rb}\frac{\partial \varphi}{\partial r}\right)+\frac{\partial}{\partial x}\left(\frac{1}{rb}\frac{\partial \varphi}{\partial x}\right)\right] \tag{27a}$$

$$=\frac{\partial}{\partial r}\left(\overline{P}_{0,\mathrm{rot}}^m\right) \tag{27b}$$

$$-\rho\frac{\overline{W_\theta}^a}{r}\frac{\partial}{\partial r}\left(r\,\overline{C}_\theta^m\right) \tag{27c}$$

$$-F_{f,r} \tag{27d}$$

$$+\frac{\rho}{rb}\frac{\partial}{\partial r}\left(br\,\overline{W_r'W_r'}^a\right) \tag{27e}$$

$$+\frac{\rho}{rb}\frac{\partial}{\partial x}\left(br\,\overline{W_r'W_x'}^a\right) \tag{27f}$$

$$-(\rho/r)\left(\overline{W_\theta'W_\theta'}^a\right) \tag{27g}$$

$$+\frac{N}{2\pi b}\left[(P_p-\overline{P}^a)\frac{\partial\theta_p}{\partial r}+(\overline{P}^a-P_s)\frac{\partial\theta_s}{\partial r}\right] \tag{27h}$$

$$+\frac{\partial}{\partial r}\left(\hat{P}_{0,\mathrm{rot}}-\overline{P}_{0,\mathrm{rot}}^m\right) \tag{27i}$$

$$-(\rho\overline{W}^a/r)\frac{\partial}{\partial r}\left(r\overline{C}_\theta^a-r\overline{C}_\theta^m\right) \tag{27j}$$

where

$$\hat{P}_{0,\mathrm{rot}}=\overline{P}^a+\frac{1}{2}\rho(\overline{C}_x^{2a}+\overline{W}_\theta^{2a}+\overline{C}_r^{2a}-\Omega^2r^2) \tag{28a}$$

and

$$\overline{P}_{0,\mathrm{rot}}^m=\text{constant along }\varphi=\text{constant} \tag{28b}$$

In comparing the fully compressible form, equation (22), with the incompressible form, equation (27), it can be seen that the effects of rothalpy and entropy have been absorbed by the rotary total pressure. In addition, the fluctuation contribution in equation (22*i*) has been completely eliminated.

Another feature of the incompressible form of the momentum equation (27) that is noteworthy is that the contribution of the fluctuation terms, equations (27*e*)–(27*i*), can be thought of as a single additive term. The contributions of the individual terms are of no consequence. Only the sum is important and nothing in the sum is calculated as part of the throughflow solution. The same cannot be said for the last term, equation (27*j*), since this term also involves the relative swirl velocity ($\overline{W}_\theta^a$) which would be calculated as part of the solution.

Finally, equations (22*h*) and (27*h*) can be written in a somewhat simpler albeit approximate form if it is assumed that the airfoils are sufficiently thin such that the radial derivatives of the suction and pressure surface angular locations (θ_s and θ_p) are both equal to the radial derivative of the airfoil mean camber line angular location (θ_l). In this case, equation (27*h*) can be written as follows

$$\frac{N}{2\pi b}(P_p-P_s)\frac{\partial\theta_l}{\partial r} \tag{29}$$

For flows through airfoil rows where only the airfoil surface pressures are known, equation (29) can be estimated far more accurately than equations (22*h*) or (27*h*).

Conclusions

A formulation of a throughflow theory for nonaxisymmetric flow in turbomachinery has been derived. The formulation satisfies both the mass flow requirements through the use of density-averaged velocity components, as well as the thermodynamic requirements through the use of mass-averaged conservation conditions. The theory does not require aerodynamic blockage as input. Specific conclusions are as follows:

1 Nonaxisymmetric effects should be modeled as the difference between (*a*) the rothalpy, entropy, and angular momentum of the density (or area)-averaged flow and (*b*) the mass-averaged rothalpy, entropy, and angular momentum.

2 Modeling nonaxisymmetric effects with a multiplier on the continuity equation (blockage) is inconsistent.

3 Total pressure losses must be mass averaged.

4 Flow angles must be defined as the arc tangent of the density-averaged tangential velocity component divided by the density-averaged axial velocity component, equations (25) and (26), and not as averaged angles.

5 Not only are the flow angles based on averaged velocity components necessary for an accurate throughflow analysis, but they also give a more accurate result in the airfoil potential flow analysis.

6 The choice of the definition of the flow angles can significantly alter airfoil incidence.

Acknowledgments

The authors are indebted to Prof. Dr. Ir. Charles Hirsch of the Vrije Universiteit Brussel not only for his work in Hirsch and Warzee (1976, 1979) but also for many very helpful discussions over the past few years on the subject of this work. We are also indebted to Mr. Frank Paoletti of Pratt & Whitney Canada Ltd. for his skill in helping us to incorporate a multitude of changes into the computer code. This formulation of throughflow theory for nonaxisymmetric flow was carried out under Navy funding under the direction of Dr. Raymond Shreeve, Contract No. N62271-86-M-0272. Professor Oates passed away on November 1, 1986. We certainly shall miss him.

References

Adkins, G. G., and Smith, L. H., 1982, "Spanwise Mixing in Axial-Flow Turbomachines," ASME *Journal of Engineering for Power*, Vol. 104, No.1, pp. 97–110.

AGARD Advisory Report No.175, 1981, Propulsion and Energetics Panel Working Group 12 on Through-Flow Calculations in Axial Turbomachines, AGARD-AR-175.

Dring, R. P., and Joslyn, H. D., 1985, "An Assessment of Single- and Multi-Stage Compressor Flow Modeling, Part I—Design Conditions," AD-B102 101, final report for Naval Air Systems Command, Contract No. N00014-84-C-0354.

Dring, R. P., and Joslyn, H. D., 1986a, "Throughflow Modeling of Axial Turbomachinery," ASME *Journal of Engineering for Gas Turbines and Power*, Vol. 108, No. 2, pp. 246–253.

Dring, R. P., and Joslyn, H. D., 1986b, "Through-Flow Modeling of a Multistage Compressor: Part I—Aerodynamic Input," ASME JOURNAL OF TURBOMACHINERY, Vol. 108, No. 1, pp. 17–22.

Dring, R. P., and Joslyn, H. D., 1986c, "Through-Flow Modeling of a Multistage Compressor: Part II—Analytical-Experimental Comparisons," ASME JOURNAL OF TURBOMACHINERY, Vol. 108, No. 1, pp. 23–31.

Dring, R. P., and Joslyn, H. D., 1986d, "An Assessment of Single- and Multistage Compressor Flow Modeling, Part II—Near-Stall Conditions," Final Report, Naval Air Systems Command, Contract No. N00014-85-C-0657.

Dring, R. P., and Joslyn, H. D., 1987, "Throughflow Analysis of a Multistage Compressor Operating at Near-Stall Conditions," ASME JOURNAL OF TURBOMACHINERY, Vol. 109, No. 4, pp. 483–491.

Dring, R. P., and Oates, G. C., 1988, "Through-Flow Theory for Nonaxisymmetric Turbomachinery Flow," final report for Naval Air Systems Command, Contract Nos. N62271-86-M-0272 and N62271-87-M-0200.

Dring, R. P., and Oates, G. C., 1990, "Throughflow Theory for Nonaxisymmetric Turbomachinery Flow: Part II—Assessment," ASME JOURNAL OF TURBOMACHINERY, Vol. 112, this issue.

Gallimore, S. J., and Cumpsty, N. A., 1986a, "Spanwise Mixing in Multistage Axial Flow Compressors: Part I—Experimental Investigation," ASME JOURNAL OF TURBOMACHINERY, Vol. 108, No. 1, pp. 2–9.

Gallimore, S. J., and Cumpsty, N. A., 1986b, "Spanwise Mixing in Multistage Axial Flow Compressors: Part II—Throughflow Calculations Including Mixing," ASME JOURNAL OF TURBOMACHINERY, Vol. 108, No. 1, pp. 10–16.

Habashi, W. G., 1980, "Numerical Methods for Turbomachinery," in: *Recent Advances in Numerical Methods in Fluids*, C. Taylor and K. Morgan, eds., Pineridge Press, United Kingdom, Chap. 8.

Habashi, W. G., and Youngson, G. C., 1983, "A Transonic Quasi-3D Analysis for Gas Turbine Engines Including Split-Flow Capability for Turbofans," *Int. Journal for Num. Meth. in Fluids*, Vol. 3, pp. 1–21.

Downloaded 01 Jun 2010 to 171.66.16.66. Redistribution subject to ASME license or copyright; see http://www.asme.org/terms/Terms_Use.cfm

Hawthorne, W. R., 1974, "Secondary Vorticity in Stratified Compressible Flow in Rotating Systems," Cambridge University, CUED/A-Turbo/TR 63.

Hirsch, C., 1975, "Unsteady Contributions to Steady Radial Equilibrium Flow Equations," presented at the AGARD Conference on Unsteady Phenomena in Turbomachinery, CP-177, No. 13.

Hirsch, C., and Warzee, G., 1976, "A Finite Element Method for Through-flow Calculations in Turbomachines," ASME *Journal of Fluids Engineering*, pp. 403–421.

Hirsch, C., and Warzee, G., 1979, "An Integrated Quasi-3D Finite Element Calculation Program for Turbomachinery Flows," ASME *Journal of Engineering for Power*, pp. 141–148.

Hirsch, C., and Dring, R. P., 1987, "Through-Flow Models for Mass and Momentum-Averaged Variables," ASME JOURNAL OF TURBOMACHINERY, Vol. 109, No. 3, pp. 362–370.

James, P. W., 1987, "A Note on Spanwise Mixing," ASME JOURNAL OF TURBOMACHINERY, Vol. 110, No. 1, pp. 153–154.

Jennions, I. K., and Stow, P., 1985, "A Quasi-Three-Dimensional Turbomachinery Blade Design System: Part I—Throughflow Analysis," ASME *Journal of Engineering for Gas Turbines and Power*, Vol. 107, No. 2, pp. 301–307.

Ruden, P., 1944, "Investigation of Single-Stage Axial Fans," NACA TM 1062.

Sehra, A. K., and Kerrebrock, J. L., 1979, "The Effect of Blade-to-Blade Flow Variations on the Mean Flow-Field of a Transonic Compressor," AIAA Paper No. 79-1515, AIAA 12th Fluid and Plasma Dynamic Conference.

Smith, L. H., 1966, "The Radial Equilibrium Equation of Turbomachinery," ASME *Journal of Engineering for Power*, Vol. 88, No. 1.

Smith, L. H., and Jennions, I., 1988, Private Communication.

Downloaded 01 Jun 2010 to 171.66.16.66. Redistribution subject to ASME license or copyright; see http://www.asme.org/terms/Terms_Use.cfm

Hawthorne, W. R., 1974, "Secondary Vorticity in Stratified Compressible Flow in Rotating Systems," Cambridge University, CUED/A-Turbo/TR 63.

Hirsch, C., 1975, "Unsteady Contributions to Steady Radial Equilibrium Flow Equations," presented at the AGARD Conference on Unsteady Phenomena in Turbomachinery, CP-177, No. 13.

Hirsch, C., and Warzee, G., 1976, "A Finite Element Method for Through-flow Calculations in Turbomachines," ASME *Journal of Fluids Engineering*, pp. 403–421.

Hirsch, C., and Warzee, G., 1979, "An Integrated Quasi-3D Finite Element Calculation Program for Turbomachinery Flows," ASME *Journal of Engineering for Power*, pp. 141–148.

Hirsch, C., and Dring, R. P., 1987, "Through-Flow Models for Mass and Momentum-Averaged Variables," ASME JOURNAL OF TURBOMACHINERY, Vol. 109, No. 3, pp. 362–370.

James, P. W., 1987, "A Note on Spanwise Mixing," ASME JOURNAL OF TURBOMACHINERY, Vol. 110, No. 1, pp. 153–154.

Jennions, I. K., and Stow, P., 1985, "A Quasi-Three-Dimensional Turbomachinery Blade Design System: Part I—Throughflow Analysis," ASME *Journal of Engineering for Gas Turbines and Power*, Vol. 107, No. 2, pp. 301–307.

Ruden, P., 1944, "Investigation of Single-Stage Axial Fans," NACA TM 1062.

Sehra, A. K., and Kerrebrock, J. L., 1979, "The Effect of Blade-to-Blade Flow Variations on the Mean Flow-Field of a Transonic Compressor," AIAA Paper No. 79-1515, AIAA 12th Fluid and Plasma Dynamic Conference.

Smith, L. H., 1966, "The Radial Equilibrium Equation of Turbomachinery," ASME *Journal of Engineering for Power*, Vol. 88, No. 1.

Smith, L. H., and Jennions, I., 1988, Private Communication.

DISCUSSION

C. Hirsch[1]

The authors have done excellent work in attempting to clarify the question of which are the most appropriate, and/or consistent, set of averaged quantities to be used in throughflow and quasi-3D, axisymmetric formulations.

This clarification would, however, be incomplete without stressing some aspects of the blockage approach and its relation to the choice between density (or area) and mass-averaged flow quantities. The main contribution that this discussion aims at expressing is that the throughflow equations can be written and treated in a totally consistent way, with either type of averaged variables. The difference between these two options lies in the definition of the quantities introduced in the axisymmetric throughflow equations in order to express the contributions arising from the nonaxisymmetric flow components and the associated set of approximations. In the author's approach, two quantities, DPR and DPA, are needed as empirical input along the spanwise direction at each station, while in the simplified tangential blockage approach a single quantity, namely, the tangential blockage distribution, is required. The latter corresponds to a different way of expressing the nonaxisymmetric contributions and since it summarizes these effects in a single quantity, instead of two, the validity conditions of this approach might be more severe.

In order to specify this point more clearly, we summarize some essential aspects of the blockage formulation, as derived by Hirsch and Dring (1987), using the notations of the present paper.

The blockage formulation results from the different ways the average of velocity products can be expressed as products of averaged velocities. For instance the following momentum flux, appearing in the radial component of the throughflow equations, can be written as:

$$\overline{\rho c_r c_x} = \overline{\rho}^a \overline{c}_r^d \overline{c}_x^d + \overline{\rho c_r' c_x'} \tag{1}$$

where the second term in the right-hand side, expressed as an averaged product of nonaxisymmetric velocity components, measures the nonaxisymmetric contributions. An alternative way can be considered, introducing momentum averages, as follows:

$$\overline{\rho c_r c_x} = \overline{\rho}^a \overline{c}_r^d \overline{\overline{c}}_x^{(r)} = \overline{\rho}^a \overline{c}_x^d \overline{\overline{c}}_r^{(x)} \tag{2}$$

The differences between the momentum-averaged velocities $\overline{\overline{c}}_x^{(r)}$ and $\overline{\overline{c}}_r^{(x)}$ and the corresponding density averages contain the same information as the fluctuation term in the first equation. The second form of the foregoing equation contains the mass-averaged radial velocity component and can be written as

$$\overline{\rho c_r c_x} = \overline{\rho}^a \overline{c}_x^d \overline{c}_r^m \tag{3}$$

Hence, the ratio between the density and mass-averaged radial velocities is a measure of the fluctuation term of equation (1) and can be represented by the quantity

$$K_{rx} = \frac{\overline{\rho c_x c_r}}{\overline{\rho}^a \overline{c}_x^d \overline{c}_r^d} = \frac{\overline{c}_r^m}{\overline{c}_r^d} = 1 + \frac{\overline{\rho c_x' c_r'}}{\overline{\rho}^a \overline{c}_x^d \overline{c}_r^d} \tag{4}$$

With the general definition of the momentum flux ratios

$$K_{ij} = \frac{\overline{\rho c_i c_j}}{\overline{\rho}^a \overline{c}_i^d \overline{c}_j^d} = \frac{\overline{\overline{c}}_j^{(i)}}{\overline{c}_j^d} \tag{5}$$

where i, j indicates any component r, θ, x, one can rewrite the continuity equation, equation (4) of Part I, as follows in function of mass-averaged quantities

$$\frac{\partial}{\partial r}(\overline{\rho}^a br\, K_{rx} \overline{c}_r^m) + \frac{\partial}{\partial x}(\overline{\rho}^a br\, K_{xx} \overline{c}_x^m) = 0 \tag{6}$$

This form of the continuity equation is completely rigorous and consistent. The assumption behind the tangential blockage formulation is that all the K_{ij}-coefficients are equal.

The radial momentum equation can be written in a similar rigorous way as equation (3.13) of Hirsch and Dring (1987)

$$\frac{\partial}{\partial r}(\overline{\rho}^a br\, \overline{c}_r^d \overline{\overline{c}}_r^{(r)}) + \frac{\partial}{\partial x}(\overline{\rho}^a br\, \overline{c}_x^d \overline{c}_r^m) - \overline{\rho}^a b\, \overline{c}_\theta^d \overline{\overline{c}}_\theta^{(\theta)} = -br\frac{\partial \overline{p}}{\partial r} + \overline{\rho}^a b(F_{f,r} + F_{b,r}) \tag{7}$$

and can be transformed to a formulation depending only on mass-averaged quantities if all the K_{ij} coefficients are equal, equation (3.23) of Hirsch and Dring (1987).

The authors' analysis and results might be an indication that this assumption is too severe. Some additional clarifications and consistency checks in the authors' analysis might however be welcome, in order to confirm this indication.

(*i*) The stream function is defined on the basis of the density-averaged velocities, while the mass-averaged rothalpy requires the mass-averaged velocities to derive the static thermodynamic variables from their stagnation values. How has the relation between these velocity components been introduced in the authors' calculations?

(*ii*) In the previously reported analysis based on the blockage formulation (Dring and Joslyn, 1986d, 1987), the tangential blockage factor has to be introduced in the definition of the mass-averaged velocity components based on the stream function, as seen from equation (6) of this Discussion. Also the rothalpy $\hat{I}$ is not constant along a streamline. Have these effects been taken into account in the previous analysis?

(*iii*) What is the validity of the assumptions of potential flow in the highly three-dimensional, viscous dominated end-wall regions and of the resulting derivation of the $\overline{\rho w_\theta' w_\theta'}$ term based on potential flow computations?

[1]Vrije Universiteit Brussel, Department of Fluid Mechanics, Pleinlan 2, 1050 Brussels, Belgium.

Copyright © 1990 by ASME

Downloaded 01 Jun 2010 to 171.66.16.66. Redistribution subject to ASME license or copyright; see http://www.asme.org/terms/Terms_Use.cfm

Authors' Closure

We are indebted to Professor Hirsch for the time and effort that he spent in examining our work, particularly in light of his considerable background in this area.

From Prof. Hirsch's equations (2), (3), (4*a*), and (5), one can arrive at equations (6) and (7). He is correct in pointing out that "if all the K_{ij} coefficients are equal" the equations are greatly simplified. However, the data presented by Hirsch and Dring (1987) in their Figs. 6(*a–c*) showed that while the K_{ij} terms that only involved the axial and tangential components of velocity were relatively uniform, the K_{ij} terms involving the radial component of velocity varied very widely and erratically. This variation in the K_{ij} terms suggests, as Prof. Hirsch pointed out, that the assumption of equality "might be too severe."

Some of Prof. Hirsch's more specific questions are addressed as follows:

(*i*) The mass-averaged rothalpy is not related to the static variables through the mass-averaged velocities. The relationship between the stagnation and static variables is established through equations (14), (24), and (28*a*) in Part I of Dring and Oates (1990) and in equations (10), (11), (17) and (18) in Part II. The issue of how the static pressure is determined is discussed in Part I following equation (24). The only mass-averaged velocity component in the analysis is in the absolute angular momentum ($r \cdot C_{\theta}^{-m}$), which is conserved along stream surfaces (Part I, equation (21)).

(*ii*) Yes. Both of these effects are accounted for rigorously.

(*iii*) I agree with Prof. Hirsch that the validity of applying potential flow to estimate the $\overline{W'_{\theta} W'_{\theta}}$ term in the highly three-dimensional and viscous endwall flow within the airfoil rows is certainly threadbare. However, given the fact that the contribution of this term in the present assessment was very small (see Part I, Sensitivity Analysis, Case *A*: Neglecting H_C), this very simple approach was deemed to be sufficiently accurate.

Copyright © 1990 by ASME

Downloaded 01 Jun 2010 to 171.66.16.66. Redistribution subject to ASME license or copyright; see http://www.asme.org/terms/Terms_Use.cfm

Throughflow Theory for Nonaxisymmetric Turbomachinery Flow: Part II—Assessment

R. P. Dring
United Technologies Research Center,
E. Hartford, CT 06108

G. C. Oates
University of Washington,
Seattle, WA

Throughflow theory has been limited in its applicability and in its accuracy by the fact that it has not historically been cast in a form that can account for the nonaxisymmetries that naturally arise in turbomachinery flow due to the presence of finite numbers of rotor and stator airfoils. The attempt to circumvent this limitation by the introduction of an aerodynamic blockage factor has been demonstrated in earlier work to produce fundamental inconsistencies in the calculation, which lead to significant errors in the regions of the flow where the nonaxisymmetries are severe. The formulation in Part I of the present work is a derivation of a system of throughflow equations for nonaxisymmetric flow. A benchmark database is used in Part II to provide input to the calculation and to help identify the dominant terms. It is demonstrated that the dominant effect of nonaxisymmetry is contained in two terms that relate the total pressure of the averaged flow to the mass-averaged total pressure. It also is demonstrated that the present formulation produces a result that is more accurate than that obtained with the historical blockage-based formulation.

Background

Nondimensionalization. The assessment of the throughflow formulation for nonaxisymmetric flow in turbomachinery formulated Part I of this paper will be based on an existing finite element throughflow analysis suitably modified to include the effects of nonaxisymmetry in the flow. The analysis that will be used is that of Habashi and Youngson (1983). The axisymmetric version of this code solves equations (22 *a*, *b*, *c*) in Part I of this paper. The remaining terms in equation (22) were added in the present analysis.

The experimental data that will provide the input as well as the experimental data for the assessment of the computed results are the low-speed two-stage compressor data of Dring and Joslyn (1986d and 1987). These data were acquired with the compressor operating at near-stall conditions where the effects of the nonaxisymmetries in the flow were most severe. In spite of the fact that the flow in this compressor was nearly incompressible ($M<0.2$), the assessment of the analytical model will utilize the fully compressible form of the equations. This was done in an effort to minimize the number of approximations and also in an effort to facilitate any future assessments with high-speed (compressible) data. However, in light of the nearly incompressible nature of the flow, the rothalpy-entropy correction term [Part I, equation (22*j*)] will be replaced with the rotary total pressure correction term, Part I, equation (27*i*) (divided by density).

It is very convenient, both experimentally and analytically, to utilize dimensionless input to the calculation and also to carry out the analytical/experimental comparisons on a dimensionless basis. For this reason, the following reference quantities will be used as a basis for nondimensionalization:

$$R_m = (R_{\text{tip}} + R_{\text{hub}})/2 \tag{1}$$

$$U_m = \Omega R_m \tag{2}$$

$$Q_{U_m} = \frac{1}{2}\rho_i U_m^2 \tag{3}$$

where ρ_i is the inlet static density. Pressures will be expressed in terms of a pressure coefficient based on the absolute pressure at the inlet and on Q_{U_m}

$$C_p = \left(\frac{P - P_{0i}}{Q_{U_m}}\right) \tag{4}$$

The various pieces of input data required by the new formulation will now be discussed.

Total Pressure Loss. Total pressure loss was calculated by circumferentially averaging the full-span traverse data, e.g., Part I, Fig. 1. The spanwise distribution of total pressure loss across each airfoil row was determined by taking the difference between the mass-averaged absolute (or relative) total pressures at the stator (or rotor) inlet and exit. This difference was taken at a fixed radius and it was used in the analysis in a consistent manner, i.e., as the difference at a fixed radius. Loss was not taken along streamlines since their location is not known *a priori*. As shown by Dring and Joslyn (1986d, 1987) and elsewhere, loss may appear to be locally negative (i.e., an apparent total pressure rise) due to radial transport of the flow in and between wakes. Loss at a fixed radius also may be negative due to radial displacement of stream surfaces. This

Contributed by the International Gas Turbine Institute and presented at the 34th International Gas Turbine and Aeroengine Congress and Exhibition, Toronto, Ontario, Canada, June 4–8, 1989. Manuscript received at ASME Headquarters February 21, 1989. Paper No. 89-GT-305.

Copyright © 1990 by ASME
Downloaded 01 Jun 2010 to 171.66.16.66. Redistribution subject to ASME license or copyright; see http://www.asme.org/terms/Terms_Use.cfm

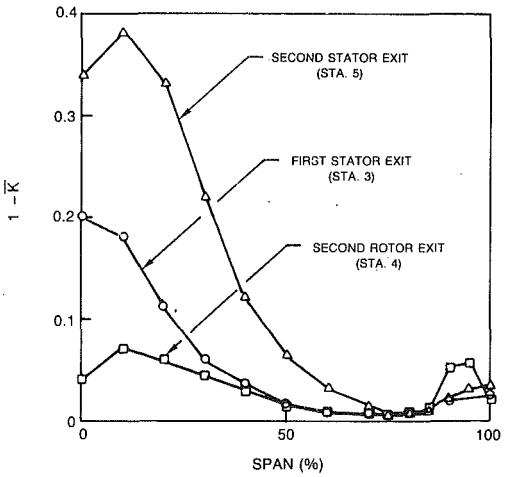

Fig. 1 Spanwise distributions of blockage

can only occur, however, where there are radial gradients in total pressure. Although the loss was based on measurements at traverse planes some distance upstream of the airfoil leading edge and some distance downstream of the trailing edge, in the present calculation the loss was assumed to increase linearly from zero at the airfoil leading edge to the measured value at its trailing edge.

Finally, recall that the assumption of axisymmetric stream surfaces was necessitated in the derivation of the conservation conditions. This assumption is equivalent to neglecting transport across stream surfaces by either deterministic secondary flows or by random diffusion (James, 1987; Adkins and Smith, 1982; Gallimore and Cumpsty, 1986a, 1986b). However, the method by which the total pressure loss is being calculated from the measured data includes these effects. As just stated, both experimentally and analytically the loss is the net total pressure change due to all the mechanisms involved, i.e., skin friction, stream surface rotation, diffusion, and so on.

Exit Flow Angle. The spanwise distributions of airfoil exit flow angle were determined from the density-averaged velocity components according to equations (25) and (26) of Part I of this paper. The importance of using the correct flow angle definition can be seen from Fig. 2 of Part I where absolute and relative flow angles have been calculated from the data acquired in the absolute frame of reference at the first stator exit. Significantly different angles can be calculated depending on the definition chosen.

As suggested by the results of Popovski and Lakshminarayana (1986), turning within each airfoil row was distributed linearly from the leading edge to the trailing edge.

Airfoil Radial Frictional Forces. The radial component of the airfoil frictional forces, $F_{f,r}$, equation (22*d*), was neglected in this assessment. This is justified on the basis that the flow over the airfoils in the regions where the flow is attached, i.e., outside of the regions of corner separation, has only a very small radial component.

Velocity Fluctuation Terms. The spanwise distributions of these three terms [Part I, equations (22*e–g*) were calculated from the velocity component data available at the traverse planes downstream of each airfoil row. The following three dimensionless parameters were calculated from the data:

$$\mathrm{DRR} \equiv (\overline{W_r{}' W_r{}'^d})/U_m^2 \tag{5}$$

$$\mathrm{DRX} \equiv (\overline{W_r{}' W_x{}'^d})/U_m^2 \tag{6}$$

$$\mathrm{DTT} \equiv (\overline{W_\theta{}' W_\theta{}'^d})/U_m^2 \tag{7}$$

It should be noted that while DRR, DRX, and DTT could be calculated from the measured data at the traverse planes

Nomenclature

b = mechanical blockage
C = absolute flow speed
cl/B = rotor tip clearance to chord ratio
C_p = pressure coefficient, equation (4)
CPS = static pressure coefficient
CPTA = absolute total pressure coefficient
CPTR = relative total pressure coefficient
D = diffusion factor, equation (19)
DHA = absolute total enthalpy correction term
DHR = rothalpy correction term, equation (15)
DPA = absolute total pressure correction term, equation (11)
DPR = rotary total pressure correction term, equation (10)
DRR = fluctuation term, equation (5)
DRX = fluctuation term, equation (6)
DTT = fluctuation term, equation (7)
DWT = absolute swirl correction term, equations (12) and (13)
F_b = airfoil pressure force
F_f = airfoil friction force
H = total enthalpy
h = static enthalpy
H_c = composite interaction term, equation (9)
I = rothalpy
$\bar{K}$ = blockage
L = scaling length, equation (8)
N = number of airfoils in a row
P = static pressure
Q_{U_m} = dynamic pressure based on U_m
R = gas constant
r = radial coordinate
R_m = radius at midspan
s = entropy
T = static temperature
U_m = wheel speed at midspan
W = relative flow speed
x = axial coordinate
α = absolute yaw angle
β = relative yaw angle
θ = angular coordinate
θ_l = mean camber line lean angle
ρ = density
σ = pitch/chord ratio
τ = airfoil pitch
φ = stream function
ϕ = flow coefficient = (C_x/U_m)
Ω = rotation rate

Subscripts

abs = absolute
i = inlet
p = airfoil pressure surface
r = radial component
s = airfoil suction surface
rel = relative
rot = rotary total
x = axial component
0 = total
θ = circumferential component

Superscripts

$-a$ = pitchwise area average
$-d$ = pitchwise density average
$-m$ = pitchwise mass average
$\hat{}$ = defined in equations (4) and (28) of Part I
$'$ = fluctuation from the density average

Downloaded 01 Jun 2010 to 171.66.16.66. Redistribution subject to ASME license or copyright; see http://www.asme.org/terms/Terms_Use.cfm

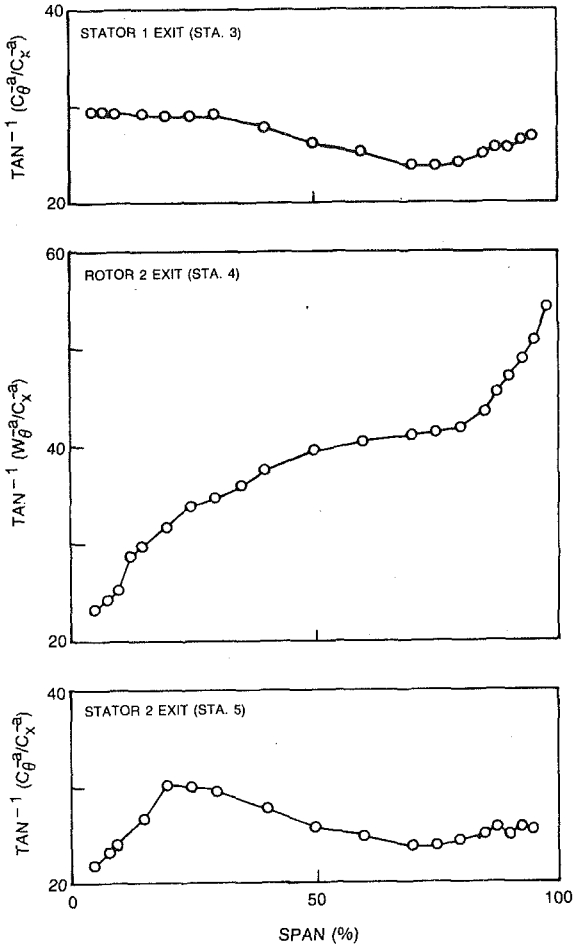

Fig. 2 Spanwise distributions of exit flow angle

between adjacent airfoil rows, there was no intrarow data available for their estimation within the airfoil rows. For this reason, DRR and DRX were assumed to be zero within the airfoil rows. DTT, however, was estimated within the airfoil rows based on the airfoil potential flow analyses available from hub to tip. This was done in spite of the fact that the pressure distributions near the endwalls showed significant departures from potential flow due to corner separation and rotor tip leakage.

The axial derivative in equation (22*f*) of Part I and the evaluation of the fluctuation terms at calculation planes up and downstream of the traverse planes were based on the assumption of an exponential decay of the three parameters. For example

$$\mathrm{DRX}(X) = \mathrm{DRX}(X_0)\exp(-(X-X_0)/L) \tag{8}$$

In this expression, L is a scaling length that models the decay rate of the measured data and it was taken to be half of the airfoil chord.

Airfoil Radial Pressure Forces. The radial component of the airfoil pressure force was treated in the form derived by Jennions and Stow (1985) as in equation (22*h*) (Part I). Although the flow in the core flow region produced rotor and stator pressure distributions which were very close to potential flow (Dring and Joslyn, (1986d) the flow in the endwall regions had major deviations from potential flow (due to hub corner separation and rotor tip leakage). Thus, in the core flow region, a potential flow calculation could have been used to determine $(P_p - \overline{P}^a)$ and $(\overline{P}^a - P_s)$ in equation (22*h*) (Part I). In the endwall regions, however, such a calculation would have been subject to grave doubt. Since the full-span pressure distributions were measured on both the rotor and the stator, an alternative approach was taken utilizing equation (29) of Part I. In this form $(P_p - P_s)$ was available directly from the measured airfoil pressure distributions and the radial derivatives of the airfoil mean camber line angular location (θ_l) was determined from the airfoil geometry.

Thermodynamic Fluctuation Term. The thermodynamic fluctuation term, Part I, equation (22*i*), involves the circumferential variations of entropy, enthalpy and temperature. However, since the present comparison is based on a low-speed experiment ($M \approx 0.2$) with only very small density and temperature variations, and since this term does not appear in the incompressible form of the averaged momentum equation, Part I, equation (27), it was neglected.

As was mentioned in Part I, the velocity fluctuation terms can be combined with the airfoil radial pressure force term to form a single additive term on the right-hand side of the momentum equation. This is possible because, aside from density, these terms contain no computed information. Hence, for the present nearly incompressible case, these four terms have been collected into a single dimensionless term as follows:

$$H_c = \frac{R_m}{U_m^2}\left\{\left(\frac{1}{br\bar{\rho}^a}\right)\frac{\partial}{\partial r}\left(br\bar{\rho}^a \cdot \mathrm{DRR} \cdot U_m^2\right) + \left(\frac{1}{br\bar{\rho}^a}\right)\frac{\partial}{\partial x}\left(br\bar{\rho}^a \cdot \mathrm{DRX} \cdot U_m^2\right) - \frac{1}{r}\left(\mathrm{DTT} \cdot U_m^2\right) + \frac{N}{2\pi b\bar{\rho}^a}\left(C_p(p) - C_p(s)\right)Q_{U_m} \cdot \frac{\partial \theta_l}{\partial r}\right\} \tag{9}$$

Rothalpy/Entropy Average Term. This is the term, Part I, equation (22*j*), that reconciles the different natures of the averaged rothalpy and entropy that arise in the momentum and conservation equations. Since the database for the present assessment is for a virtually incompressible flow, this term will be evaluated based on rotary total pressure (Hawthorne, 1974) instead of rothalpy and entropy. This is the naturally occurring variable for incompressible flow, Part I, equations (27*b*) and (27*i*). For this reason, the following dimensionless parameter was determined from the data at the traverse planes between adjacent airfoil rows for the rotating frame of reference:

$$\mathrm{DPR} \equiv (\hat{P}_{0,\,\mathrm{rot}} - \overline{P}^m_{0,\,\mathrm{rot}})/Q_{U_m} \tag{10}$$

for the absolute frame of reference one must use the following in place of equation (10):

$$\mathrm{DPA} = (\hat{P}_{0,\,\mathrm{abs}} - \overline{P}^m_{0,\,\mathrm{abs}})/Q_{U_m} \tag{11}$$

Both DPR and DPA also were assumed to vary with axial distance up and downstream of the traverse planes in the same exponential manner as DRX in equation (8). Note that, as with H_c, equation (9), aside from the effects of density, these terms, equations (10) and (11), are also only additive terms on the right-hand side of the momentum equation. They play no active role in the iterative process, that is, aside from density they contain no computed information.

Absolute Angular Momentum Average Term. This is the term, Part I, equation (22*k*), that reconciles the naturally occurring density-averaged absolute swirl that arises in the momentum equation with the mass average that occurs in the conservation equation. The following dimensionless parameter was determined from the traverse data between adjacent airfoil rows:

Downloaded 01 Jun 2010 to 171.66.16.66. Redistribution subject to ASME license or copyright; see http://www.asme.org/terms/Terms_Use.cfm

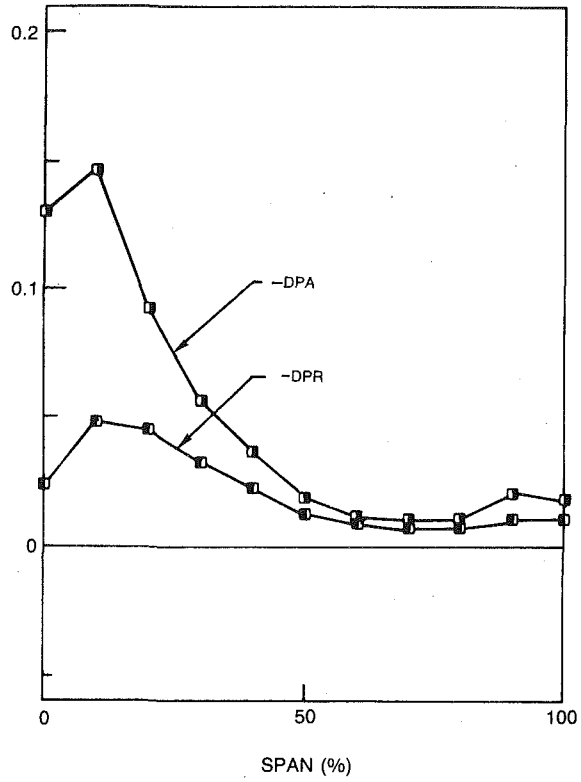

Fig. 3 Spanwise distributions of the relative and absolute total pressure distortion terms at the first stator exit

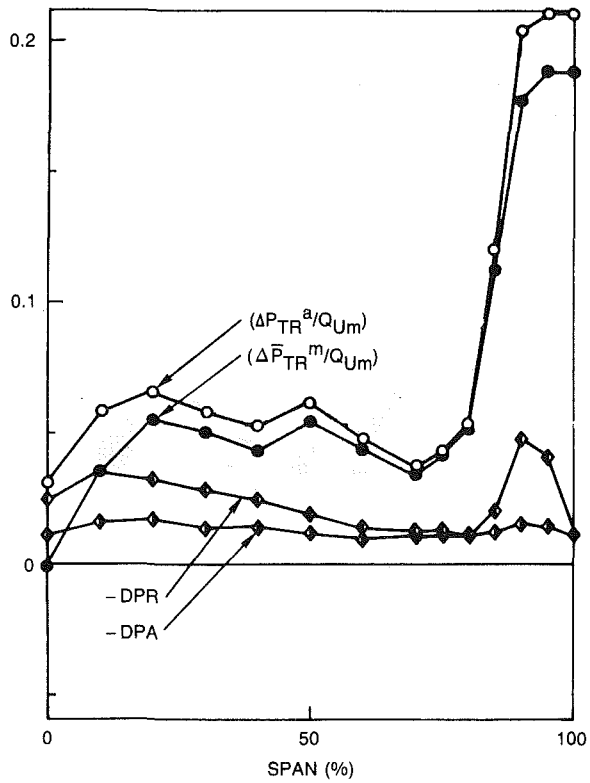

Fig. 4 Spanwise distributions of the relative and absolute total pressure distortion terms and the relative total pressure loss at the second rotor exit.

$$\mathrm{DWT} = (\overline{W}_\theta^d - \overline{W}_\theta{}^m)/U_m \tag{12}$$

$$= (\overline{C}_\theta^d - \overline{C}_\theta^m)/U_m \tag{13}$$

Unlike the previous fluctuation terms, which were essentially

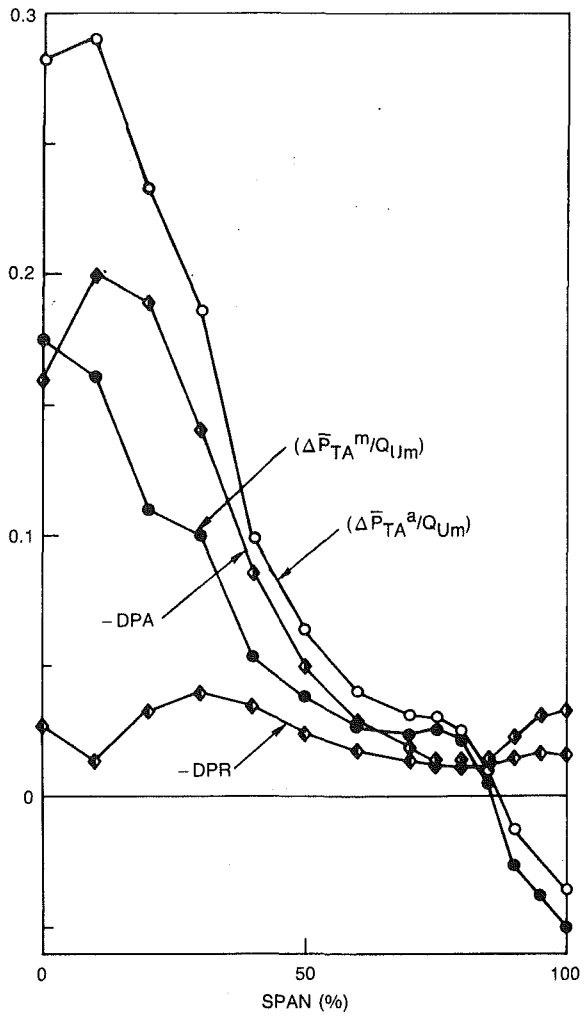

Fig. 5 Spanwise distributions of the relative and absolute total pressure distortion terms and the absolute total pressure loss at the second stator exit.

only additive terms on the right-hand side of the momentum equation, this term does play an active role in the calculation. This is because of the presence of $\overline{W}_\theta^d$ in equation (22*k*) (Part I), which is not known *a priori* and which is determined as part of the solution iteration.

The final form of the averaged radial projection of the momentum equation being employed in this low Mach number assessment is as follows for the rotating frame of reference:

$$\overline{C}_x^d\left[\frac{\partial}{\partial r}\left(\frac{1}{rb\bar{\rho}^a}\frac{\partial \varphi}{\partial r}\right)+\frac{\partial}{\partial x}\left(\frac{1}{br\bar{\rho}^a}\frac{\partial \varphi}{\partial x}\right)\right] \tag{14a}$$

$$=\left(\frac{\partial \bar{I}^m}{\partial r}\right)-\overline{T}^d\left(\frac{\partial \bar{s}^m}{\partial r}\right)-\frac{\overline{W}_\theta^d}{r}\left(\frac{\partial r\overline{C}_\theta^m}{\partial r}\right) \tag{14b}$$

$$+H_c\cdot\frac{U_m{}^2}{R_m} \tag{14c}$$

$$+\frac{1}{\bar{\rho}^a}\frac{\partial}{\partial r}(\mathrm{DPR}\cdot Q_{U_m}) \tag{14d}$$

$$-\frac{\overline{W}_\theta^d}{r}\frac{\partial}{\partial r}(r\cdot\mathrm{DWT}\cdot U_m) \tag{14e}$$

Some Additional Relationships. Since, as was previously stated, this assessment will be based on the compressible form of the equations and not on the incompressible form, some accommodation must be made to relate the relative and absolute

Downloaded 01 Jun 2010 to 171.66.16.66. Redistribution subject to ASME license or copyright; see http://www.asme.org/terms/Terms_Use.cfm

total pressure correction terms (DPR and DPA) to analogous correction terms for the total relative and absolute enthalpy (and rothalpy). This is required since, for the compressible flow calculation, the static and total enthalpies are related directly to velocities, (Part I, equation (14), and the static and total pressures are calculated from them.

Defining DHR in a manner analogous to DPR

$$\mathrm{DHR} \equiv (\hat{I} - \bar{I}^m)/\frac{1}{2} U_m^2 \tag{15}$$

it can be shown that (Dring and Oates, 1988)

$$\mathrm{DPR} = (\bar{\rho}^a/\rho_i)\mathrm{DHR} \tag{16}$$

With this expression, even the small changes in density that occur between the inlet static density and the density at some location within the compressor can to some extent be accounted for. The same expression also can be derived for the total enthalpy and pressure correction terms in the absolute frame of reference. The absolute and relative correction terms are related through equation (24) of Part I as follows:

$$\mathrm{DHR} = \mathrm{DHA} - 2(\mathrm{DWT})(r/R_m) \tag{17}$$

$$\mathrm{DPR} = \mathrm{DPA} - 2(\mathrm{DWT})(r/R_m)(\bar{\rho}^a/\rho_i) \tag{18}$$

In the present calculations DWT will be calculated from the measured distributions of DPR and DPA.

Assessment

Input Data. This formulation of throughflow theory will be assessed by utilizing a benchmark database acquired on a large-scale, low-speed, two-stage axial compressor.The database consists of full-span, stationary, and rotating frame traverse data acquired in planes downstream of the first-stage stator, and downstream of the second-stage rotor and stator. These will be referred to as planes 3, 4, and 5, respectively. This section will provide a summary of these input data for the case of the compressor operating at its near-stall flow coefficient ($\phi = 0.45$) with a large second-stage rotor tip clearance ($cl/B = 0.041$). This case was chosen for the assessment since it had the highest degree of nonaxisymmetry in the flow and, hence, it would be a severe test case for the new formulation.

In order to provide some perspective as to where the effects of nonaxisymmetry are most important, the aerodynamic blockage profiles are presented in Fig. 1. The definition of this expression for aerodynamic blockage is given by Dring (1984). These profiles were not used in the present assessment but they do show that the regions of most severe nonaxisymmetry in the flow (i.e., the regions of highest blockage) were at the hub, and especially in the regions aft of the stators (see Part I, Fig. 1). The nature of the flow in this compressor has already been discussed extensively in the literature (Dring and Joslyn, 1983, 1984, 1985, 1986b, 1986c, 1986d, 1987).

The spanwise distributions of the flow angles measured at the traverse planes downstream of each airfoil row are shown in Fig. 2. They are based on the flow angle definition in equations (25) and (26) of Part I.

The spanwise profiles of DPR and DPA, equations (10) and (11), input to the calculation at the traverse planes, are shown in Figs. 3-5. In order to provide some indication of the magnitude of these terms, the spanwise distributions of the area and mass-averaged total pressure loss also are included on the plots for the traverse planes downstream of the second-stage rotor and stator. Several things are evident in these results: (1) The area and mass-averaged total pressure losses are significantly different. Recall that only the mass-averaged loss is consistent with the formulation. (2) DPR and DPA are always negative. This is because, for these data, the mass-averaged total pressure is always greater than the total pressure of the density-averaged flow, equations (10) and (11). The generality of this observation, however, remains to be demonstrated. (3) DPA is greater than DPR aft of stators and DPR is greater than DPA aft of rotors. (4) Finally, the magnitudes of DPR and DPA are comparable to the total pressure loss across each row. Recall that DWT was calculated from DPR and DPA according to equation (18) and that the decay of these terms up and downstream of the traverse planes was assumed to be exponential, according to equation (8).

Parenthetically, it was demonstrated that the contribution of the static pressure distortion to DPR and DPA (i.e, $(\bar{P}_s^a - \bar{P}_s^m)/Q_{U_m}$) was generally much smaller than that of the dynamic pressure. This fact may be seen in the data presented by Hirsch and Dring (1987), in Figs. 3(a–c) of that work, where a similar observation was made. This suggests that DPR and DPA may be accurately determined from velocity measurements, such as laser or hot-film anemometry data, acquired between the airfoil rows of a compressor. This approximation would be even more accurate at less severe conditions farther from stall.

The term that includes all of the interaction terms derived by Hirsch and Warzee (1979), H_c in equations (9) and (14c), was determined from potential flow calculations and from measured airfoil pressure distributions within the airfoil rows and from traverse data in the regions between adjacent airfoil rows.

Comparison of Measured and Computed Results. The comparison of the measured and computed results is shown in Figs. 6–10. In varying degrees, the agreement obtained with the present formulation of the throughflow equations was better than that obtained with the blockage formulation. In some respects, the predictions were similar but in others there were significant local differences.

The measured and predicted hub and tip static pressure distributions are shown in Fig. 6. The measured data are indicated by sets of three symbols representing the maximum, average, and minimum in the circumferential variation of static pressure. These circumferential variations are due to the pressure distributions of the rotor and stator airfoils.

The agreement between the measured and the computed static pressure results is, in general quite good. It also is comparable to the agreement that was obtained with the blockage

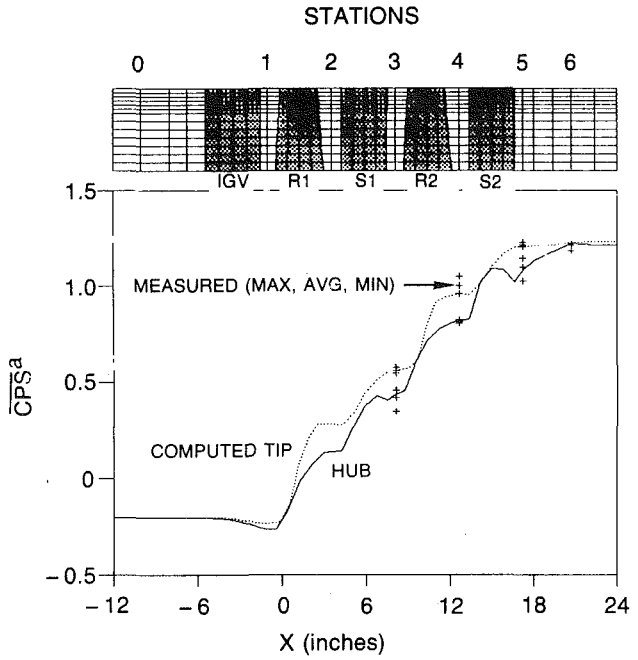

Fig. 6 Finite element grid and the hub and tip static pressure distributions

Downloaded 01 Jun 2010 to 171.66.16.66. Redistribution subject to ASME license or copyright; see http://www.asme.org/terms/Terms_Use.cfm

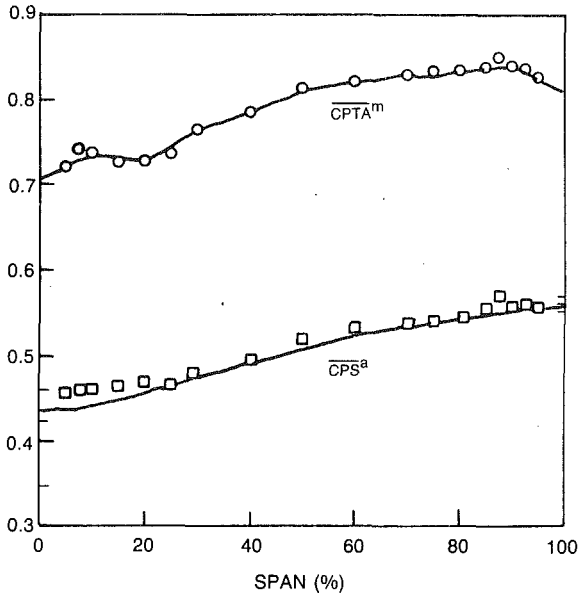

Fig. 7 Spanwise distributions of the total and static pressures at the first stator exit

formulation (Dring and Joslyn, 1986d, 1987). The prediction is below the data at Plane 4 (aft of the second rotor) at the tip. This has been demonstrated to be due to the large rotor tip clearance in this test ($cl/B = 0.041$). The other area of disagreement is at Plane 6, far downstream of the second stator trailing edge. The slightly high predicted static pressure at the hub at Plane 6 may be a result of letting DPR and DPA decay too quickly. Recall that the decay length (L) used in the calculations (equation 8), for locations upstream and downstream of the traverse planes was half of the airfoil chord. A longer decay length would have caused the hub static pressure at Plane 6 to be lower. In summary, an accurate prediction of the flow path static pressure has been achieved with the new formulation without the use of aerodynamic blockage.

Since measured data were only available beginning at the first stator exit (Plane 3), the computed spanwise total pressure distribution at this location was matched to the data by adjusting the loss and deviation in the first-stage rotor and stator (Fig. 7). The excellent agreement between the measured and computed static pressure distribution, however, is a result of the throughflow model. Once the total pressure is set, the static pressure is determined by the stator exit flow angle (Fig. 2) and by DPR and DPA (Fig. 3). The minimum, average, and maximum hub and tip static pressures also are shown in Fig. 7 at 0 percent and 100 percent span.

The spanwise distributions of the remainder of the computed results at the first stator exit (Plane 3) are shown in Fig. 8. The relative flow angle, Fig. 8(*a*), is well predicted, even near the hub where the nonaxisymmetry was strong (Fig. 1). The agreement in this region is better than that obtained with the blockage formulation (Dring and Joslyn, 1987, Fig. 5). The angle errors for that case where two to three times as great as those in Fig. 8(*a*). The main reason for this improvement is due to the more consistent angle definitions in the present formulation, equations (25) and (26) of Part I. The axial velocity component is well predicted (Fig. 8*b*). Agreement at the hub and at the tip is slightly better than with the blockage formulation (Dring and Joslyn, 1987, Fig. 5). The relative total pressure also is predicted accurately (Fig. 8*c*). Agreement is comparable to that with the blockage formulation.

The spanwise distributions of the computed results aft of the rotor (Plane 4) are shown in Fig. 9. Recall that the degree of nonaxisymmetry produced by the second-stage rotor is

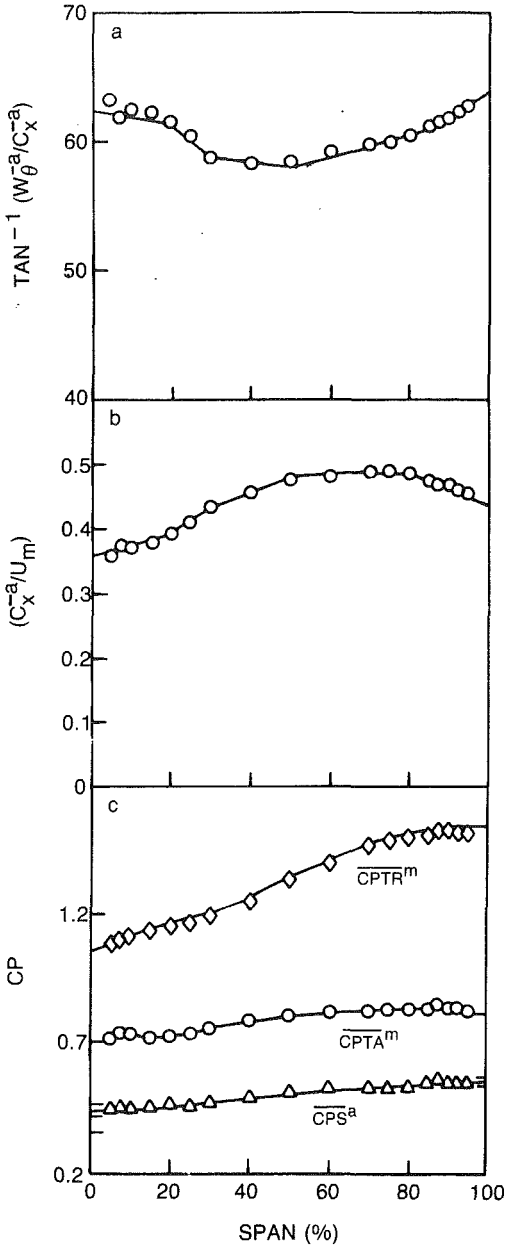

Fig. 8 Spanwise distributions of the relative flow angle, the axial component of velocity, and the absolute and relative total and static pressures at the first stator exit.

significantly less than that produced by either of the stators. This can be seen by the magnitudes of the blockage ($1-\bar{K}$), and DPR and DPA (Figs. 1, 3, 4, and 5). It is not surprising then that the agreement between the prediction and the data at this plane is excellent and that the prediction is only slightly better than that of the blockage formulation (Dring and Joslyn, 1987, Fig. 7). Both predictions of the absolute flow angle close to the tip fall short of the data (Fig. 9*a*) due to the large rotor tip clearance and the strongly three-dimensional flow that it produces (Part I, Fig. 1). This also can be seen in Fig. 9(*c*) where the prediction closely follows the static pressure out to about 90 percent span. The large tip clearance causes a slightly increased gradient from there to the tip, which the prediction does not capture. This effect also was mentioned with regard to the computed tip static pressure at this plane in Fig. 6.

The spanwise distributions of the computed results aft of the second stator (Plane 5) are shown in Fig. 10. Recall that the degree of nonaxisymmetry produced by the second stator

Downloaded 01 Jun 2010 to 171.66.16.66. Redistribution subject to ASME license or copyright; see http://www.asme.org/terms/Terms_Use.cfm

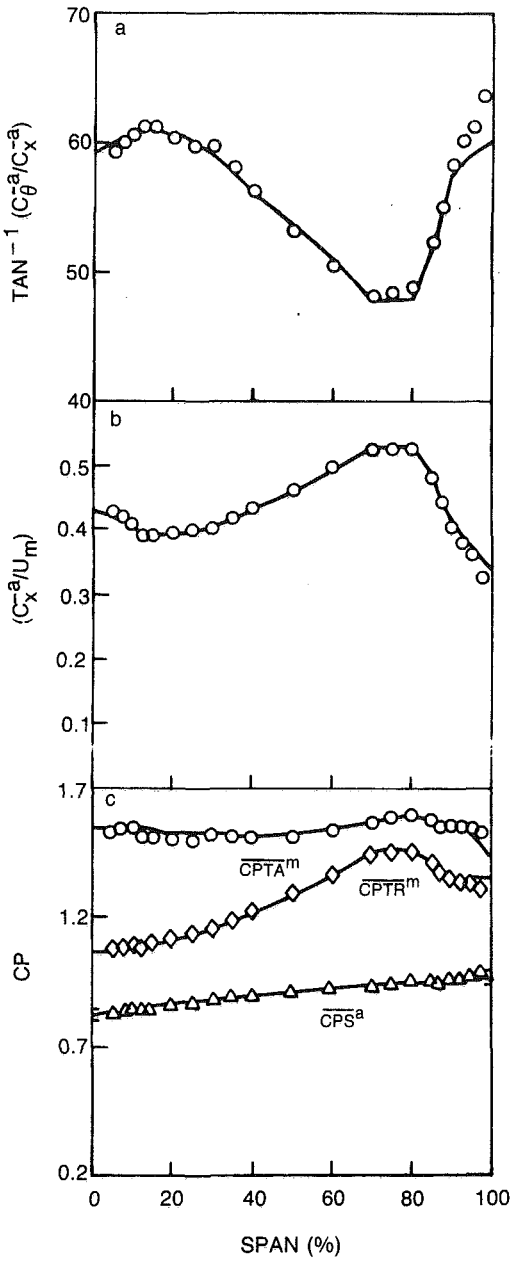

Fig. 9 Spanwise distributions of the relative flow angle, the axial component of velocity, and the absolute and relative total and static pressures at the second rotor exit.

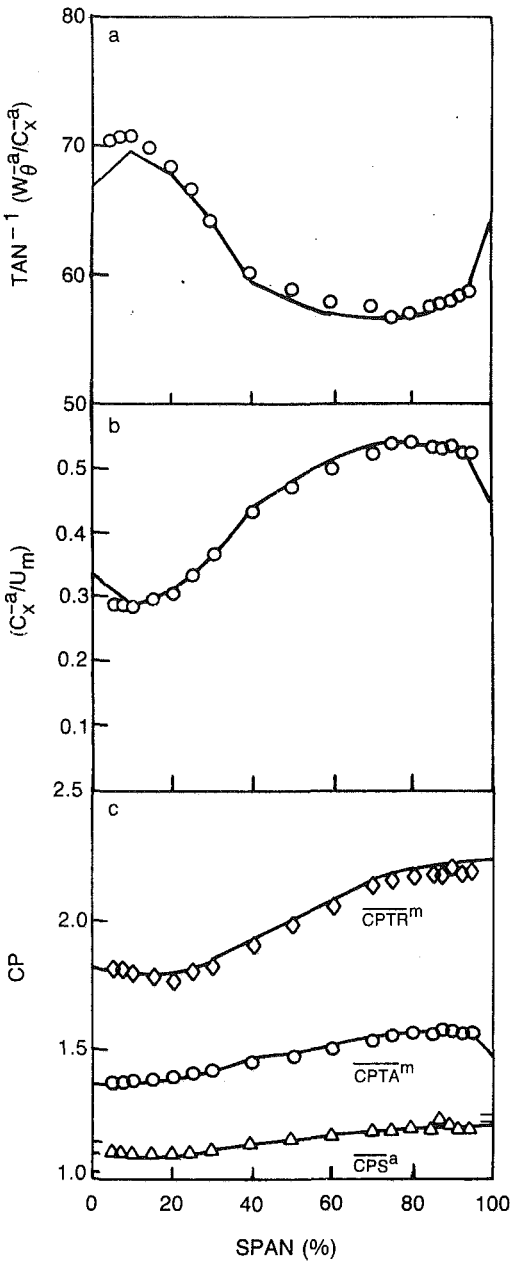

Fig. 10 Spanwise distributions of the relative flow angle, the axial component of velocity, and the absolute and relative total and static pressures of the second stator exit.

is far greater than that produced by any of the other airfoils. This can be seen by the magnitudes of the blockage $(1-\bar{K})$, and DPR and DPA (Figs. 1, 3, 4, and 5). Note that the blockage near the hub at this plane approaches 40 percent. The data at this plane, therefore, represent the severest test of the prediction in this assessment.

The agreement between the measured and computed relative flow angles out to 30 percent span is much better with the present formulation (Fig. 10*a*), than with the blockage formulation (Dring and Joslyn, 1987, Fig. 9) where local errors approached 6 deg. The main reason for this improvement is due to the more consistent angle definitions in the present formulation, equations (25) and (26) of Part I. As discussed earlier, and as shown in Fig. 2 of Part I, the magnitude of the relative flow angle depends strongly on how it is defined. The axial component of velocity, and the static, absolute, and relative total pressures are all in better agreement with the data with the present formulation than with the blockage formulation. This is especially true near the hub and tip where nonaxisymmetry is the strongest.

In summary, the present formulation gave an accurate prediction of nearly every feature of the flow at this challenging near-stall flow condition.

By way of global accuracy, at midspan both formulations were about 1 percent high in predicting the second-stage static pressure rise, 2 percent high in predicting the absolute total pressure rise, and 4 percent high in predicting the relative total pressure rise. It is difficult to say whether this discrepancy lies in the data or in the formulation.

Airfoil loading parameters calculated in the throughflow analysis that are of particular interest to compressor designers include the dimensionless static pressure rise, $\Delta P/Q$, and the diffusion factor, "D" (Johnsen and Bullock, 1956), defined as follows:

$$D=(1-V_2/V_1)+(\Delta V_T/2\sigma V_1) \tag{19}$$

Downloaded 01 Jun 2010 to 171.66.16.66. Redistribution subject to ASME license or copyright; see http://www.asme.org/terms/Terms_Use.cfm

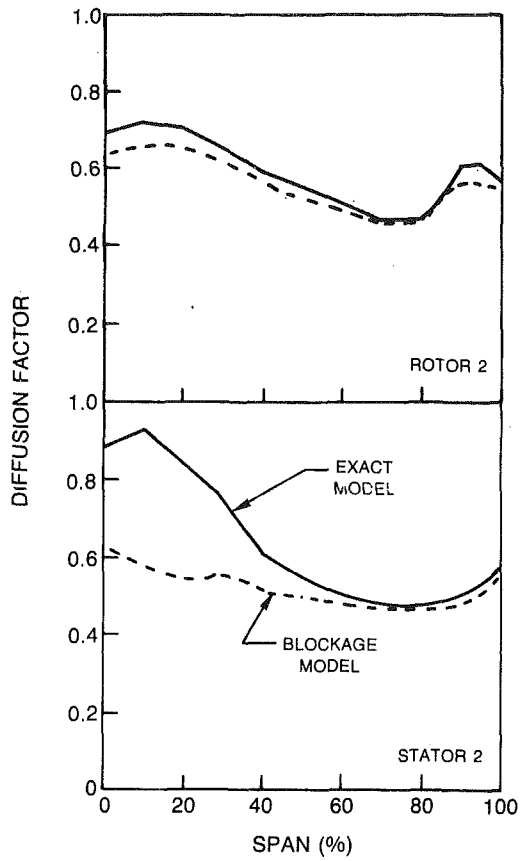

Fig. 11 Spanwise distributions of the diffusion factor for the second-stage rotor and stator

V_1 = inlet velocity
V_2 = exit velocity
ΔV_T = tangential velocity change
σ = pitch/chord ratio

The predicted static pressure rise parameter distributions for the rotor and the stator were similar for the two formulations. The diffusion factors, however, were very different (Fig. 11). This difference was greatest for the second stator, near the hub. This is a critical difference in diffusion factor since airfoil total pressure loss begins to increase dramatically as the diffusion factor rises beyond 0.6. The reason for the difference in the diffusion factors for the two formulations is that in the blockage formulation the velocities (V_1, V_2, and ΔV_T) are usually based on "blocked" velocity components (which are similar to mass averages). These may be converted to unblocked" velocity components (which are similar to area averages) by multiplying them by the local blockage factor ($\bar{K}$). In the present formulation, the velocities are based on the density-averaged velocity components (which are close to area averages in this low-speed assessment). An example of the impact of using these different velocities is as follows for the 10 percent span location for the second-stage rotor and stator.

Blockage Formulation:	Rotor 2	Stator 2
"D" factor with blocked velocities (*)	0.661	0.591
"D" factor with unblocked velocities	0.571	0.854
Present Formulation:		
"D" factor	0.720	0.930
(change relative to *)	(+9 percent)	(+57 percent)

If the blockages at a particular spanwise location at the inlet and at the exit of an airfoil row are equal then the effects of blockage will cancel in the calculation of "D". Hence, the blocked and unblocked "D" factors will be equal. However, if the blockages at the inlet and at the exit of an airfoil row are not equal, they will change the "D" factor. This is the case in the foregoing examples at 10 percent span (at Planes 3-5, $1-\bar{K}=0.821$, 0.928, and 0.617).

The important aspect of this discussion is not which "D" factor distribution is correct but rather it is that widely different "D" factors can be calculated depending on the assumptions used. It is important that the "D" factor used in any loss correlation be consistent with the one calculated in the throughflow analysis.

Sensitivity Analysis. A series of calculations were carried out to determine the sensitivity of the computed results to various simplifying assumptions. This step was felt to be essential due to the very large amount of input data required by the present formulation. In its complete form, the input data require the specification of spanwise distributions of most of the terms on the right-hand side of equation (14).

With this much input, the exact formulation could never be used as a practical design analysis. A major simplification would be achieved if some assumption would be made about the many terms collected into the single term H_c, equation (9), in equation (14). This and other attempts to simplify the input are discussed next and they are judged in terms of the errors that they produce relative to the base case just discussed.

Case A: Neglecting H_c. The most powerful simplifying assumption with regard to H_c is to neglect it completely, i.e., by setting $H_c=0$. Both the local as well as the global effects of this assumption were seen to be extremely small. The changes to the static and to the relative and absolute total pressures at midspan were less than 0.1 percent of the stage pressure rise and less than 0.5 percent for the rest of the flow field. The changes in incidence were small fractions of a degree. These observations were consistent with the fact that the contribution of H_c to the right-hand side of the throughflow equation was typically very small, i.e., about 2 percent.

The insensitivity of the computed results to H_c indicates that the main influence of the nonaxisymmetry of the flow on the computed results is through DPR and DPA. After neglecting H_c, the input to a calculation would consist of only the total pressure loss, the exit flow angle, and DPR and DPA. The potential of further simplifying the input by specifying either DPR or DPA was explored as discussed next.

Case B: Neglecting DPR or DPA. Since DPR was larger than DPA in the region aft of the rotor (Fig. 4) and since DPA was larger than DPR in the regions aft of the stators (Figs. 3 and 5) a calculation was carried out neglecting the smaller of the two correction terms at each calculation plane, i.e., setting DPA = 0 in the region aft of the rotor and setting DRP = 0 in the regions aft of the stators. The objective here was to reduce the amount of input required by the present formulation to be equal to that required by the blockage formulation. The impact of this simplification was to produce errors in the stage static, and absolute and relative total pressure rises of from 4 to 7 percent. In all cases, these errors were negative, i.e., reductions in pressure rise. The errors in incidence were typically ±1 deg. These errors may seem unacceptable but it should be kept in mind that this is a very severe near-stall flow condition and that the errors at design flow conditions could be much smaller.

Case C: Neglecting DPR *and* DPA. A calculation was carried out with DPR and DPA set to zero at all locations. The impact of this simplification was to produce errors in the stage static , and absolute and relative total pressure rises of from 5 to 14 percent. In all cases, these errors were positive, i.e., in-

Downloaded 01 Jun 2010 to 171.66.16.66. Redistribution subject to ASME license or copyright; see http://www.asme.org/terms/Terms_Use.cfm

creases in pressure rise. The errors in incidence were typically +3 deg to −6 deg.

Case D: Blockage Calculation With Consistent Angles. A final comparison was carried out based on the blockage formulation. However, instead of using mass-averaged exit angles [as had been done previously, Dring and Joslyn, 1986d, 1987], the exit angles were based on the mass- (and not area) averaged velocity components. The differences between these definitions are very small at the first stage stator exit and at the second-stage rotor exit. For the second-stage stator exit, however, the differences are large near the hub (up to 4 deg).

For this compressor, it made very little difference which angle definition was used. Where the agreement has been poor, as at the second stator exit near the hub, the blockage formulation gave similar poor agreement regardless of the differences in the input data. The previous assessment of the blockage formulation (Dring and Joslyn, 1986d, 1987) indicated that the error between the measured and the computed results in this region was typically 5 deg. The impact of using the more consistent angle definition was very small (≈ 1 percent in pressure rise and ≈ 0.3 deg in incidence). Using a more consistent angle definition in a basically inconsistent formulation doesn't appear to improve it significantly.

Conclusions

A formulation of a throughflow theory for nonaxisymmetric flow in turbomachinery has been assessed (1) against a benchmark database for a low-speed two-stage compressor operating at near-stall conditions, and (2) against an approximate throughflow formulation based on aerodynamic blockage factors. The present formulation satisfies both the mass flow requirements through the use of density-averaged velocity components, as well as the thermodynamic requirements through the use of mass-averaged conservation conditions. While the theory does not require aerodynamic blockage as input, it does require the specification of at least two parameters describing the nonaxisymmetric nature of the flow (DPR and DPA). Specific conclusions are as follows:

1 The present formulation produces a result that is significantly more accurate than that of the approximate blockage formulation.

2 Modeling nonaxisymmetric effects with a multiplier on the continuity equation (blockage) is inconsistent and inaccurate.

3 Nonaxisymmetric effects should be modeled as correction terms for the quantities that are conserved on stream surfaces (entropy, rothalpy, and angular momentum). These corrections could be based on detailed documentation of the flow field, as in the present assessment. Where such detail is not available, they could be inferred from the data that is available in the same manner as has historically been done for blockage.

4 Flow angles must be defined as the arctangent of the density-averaged tangential velocity component divided by the density-averaged axial velocity component, equations (25) and (26) of Part I), and not as averaged angles.

5 The choice of the definition of the flow angles can significantly alter airfoil incidence.

6 Not only are the flow angles based on averaged velocity components necessary for an accurate throughflow analysis, but they also give a more accurate result in the airfoil potential flow analysis.

7 Total pressure losses must be mass-averaged. There are significant differences between area and mass-averaged losses.

8 The terms DPR and DPA, equations (10) and (11), are sufficient to describe the effects of the nonaxisymmetry in the flow accurately.

9 Care must be taken when using the diffusion factor calculated in a throughflow analysis as a measure of airfoil loading. The value that is calculated depends strongly on the nature of the throughflow formulation (present versus blockage). Local differences approaching 60 percent were demonstrated.

10 The magnitude of the diffusion factor calculated in the blockage formulation depends strongly on whether it is based on blocked or unblocked velocities. Local differences approaching 45 percent were demonstrated.

Acknowledgments

The authors are indebted to Prof. Dr. Ir. Charles Hirsch of the Vrije Universiteit Brussel not only for his work in Hirsch and Warzee (1976, 1979) but also for many very helpful discussions over the past few years on the subject of this work. We are also indebted to Mr. Frank Paoletti of Pratt & Whitney Canada Ltd. for his skill in helping us to incorporate a multitude of changes into the computer code. This assessment of throughflow theory for nonaxisymmetric flow was carried out under Navy funding under the direction of Dr. Raymond Shreeve, Contract No. N62271-87-M-0200. Professor Oates passed away on November 1, 1986. We certainly shall miss him.

References

Adkins, G. G., and Smith, L. H., 1982, "Spanwise Mixing in Axial-Flow Turbomachines," ASME *Journal of Engineering for Power*, Vol. 104, No. 1, pp. 97–110.

Dring, R. P., Joslyn, H. D., and Wagner, J. H., 1983, "Compressor Rotor Aerodynamics," AGARD-CP-351, Viscous Effects in Turbomachines, Copenhagen, Denmark, Paper No. 24.

Dring, R. P., 1984, Blockage in Axial Compressors," ASME *Journal of Engineering for Gas Turbines and Power*, Vol. 106, No. 3, pp. 712–714.

Dring, R. P., and Joslyn, H. D., 1985, "An Assessment of Single- and Multi-Stage Compressor Flow Modeling, Part I, Design Conditions," AD-B102 101, final report for Naval Air Systems Command, Contract No. N00014-84-C-0354.

Dring, R. P., and Joslyn, H. D., 1986a, "Through Flow Modeling of Axial Turbomachinery," ASME *Journal of Engineering for Gas Turbines and Power*, Vol. 108, No. 2, pp. 246–253,

Dring, R. P., and Joslyn, H. D., 1986b, Through-Flow Modeling of a Multistage Compressor: Part I—Aerodynamic Input," ASME JOURNAL OF TURBOMACHINERY, Vol. 108, No. 1, pp. 17–22.

Dring, R. P., and Joslyn, H. D., 1986c, "Through-Flow Modeling of a Multistage Compressor: Part II—Analytical-Experimental Comparisons," ASME JOURNAL OF TURBOMACHINERY, Vol. 108, No. 1, pp. 23–31.

Dring, R. P., and Joslyn, H. D., 1986d, "An Assessment of Single- and Multistage Compressor Flow Modeling, Part II—Near-Stall Conditions," Final Report, Naval Air Systems Command, Contract No. N00014-85-C-0657.

Dring, R. P., and Joslyn, H. D., 1987, "Throughflow Analysis of a Multistage Compressor Operating at Near-Stall Conditions," ASME JOURNAL OF TURBOMACHINERY, Vol. 109, No. 4, pp. 483–491.

Dring, R. P., and Oates, G. C., 1988, "Through-Flow Theory for Nonaxisymmetric Turbomachinery Flow, final report for Naval Air Systems Command, Contract Nos. N62271-86-M-0272 and N62271-87-M-0200.

Dring, R. P., and Oates, G. C., 1990, "Throughflow Theory for Nonaxisymmetric Turbomachinery Flow: Part I—Formulation," ASME JOURNAL OF TURBOMACHINERY, Vol. 112, this issue.

Gallimore, S. J., and Cumpsty, N. A., 1986a, "Spanwise Mixing in Multistage Axial Flow Compressors: Part I—Experimental Investigation," ASME JOURNAL OF TURBOMACHINERY, Vol. 108, No. 1, pp. 2–9.

Gallimore, S. J., and Cumpsty, N. A., 1986b, "Spanwise Mixing in Multistage Axial Flow Compressors: Part II—Throughflow Calculations Including Mixing," ASME JOURNAL OF TURBOMACHINERY, Vol. 108, No. 1, pp. 10–16.

Habashi, W. G., 1980, "Numerical Methods for Turbomachinery," in: *Recent Advances in Numerical Methods in Fluids*, C. Taylor and K. Morgan, eds., Pineridge Press, U. K., Chap. 8.

Habashi, W. G., and Youngson, G. C., 1983, "A Transonic Quasi-3D Analysis for Gas Turbine Engines Including Split-Flow Capability for Turbofans," *International Journal for Num. Meth. in Fluids*, Vol. 3, pp. 1–21.

Hawthorne, W. R., 1974, "Secondary Vorticity in Stratified Compressible Flow in Rotating Systems," Cambridge University, CUED/A-Turbo/TR 63.

Hirsch, C., and Warzee, G., 1976, "A Finite Element Method for Throughflow Calculations in Turbomachines," ASME *Journal of Fluids Engineering*, pp. 403–421.

Hirsch, C., and Warzee, G., 1979, "An Integrated Quasi-3D Finite Element Calculation Program for Turbomachinery Flows," ASME *Journal of Engineering for Power*, Vol. 101, pp. 141–148.

Hirsch, C., and Dring, R. P., 1987, "Through-Flow Models for Mass and

Downloaded 01 Jun 2010 to 171.66.16.66. Redistribution subject to ASME license or copyright; see http://www.asme.org/terms/Terms_Use.cfm

Momentum-Averaged Variables," ASME JOURNAL OF TURBOMACHINERY, Vol. 110, No. 1, pp. 362–370.

James, P. W., 1987, "A Note on Spanwise Mixing," ASME JOURNAL OF TURBOMACHINERY, Vol. 110, No. 1, pp. 153–154.

Jennions, I. K., and Stow, P., 1985, "Quasi-Three-Dimensional Turbomachinery Blade Design System: Part I—Throughflow Analysis," ASME *Journal of Engineering for Gas Turbines and Power*, Vol. 107, No. 2, pp. 301–307.

Johnsen, I. A., and Bullock, R. O., 1956, "Aerodynamic Design of Axial-Flow Compressors, Revised," NASA SP-36.

Joslyn, H. D., and Dring, R. P., 1985, "Axial Compressor Stator Aerodynamics," ASME *Journal of Engineering for Gas Turbines and Power*, Vol. 107, pp. 485–493.

Popovski, P., and Lakshminarayana, B., 1986, "Laser Anemometer Measurements in a Compressor Rotor Flowfield at Off-Design Conditions," *AIAA Journal*, Vol. 24, No. 8, pp. 1337–1345.

Downloaded 01 Jun 2010 to 171.66.16.66. Redistribution subject to ASME license or copyright; see http://www.asme.org/terms/Terms_Use.cfm

A Parametric Study of Radial Turbomachinery Blade Design in Three-Dimensional Subsonic Flow

W. S. Ghaly
Mechanical Engineering Department,
Ecole Polytechnique de Montreal,
Montreal, Quebec, Canada

An aerodynamic design method is described and used to implement a parametric study of radial turbomachinery blade design in three-dimensional subsonic flow. Given the impeller hub and shroud, the number of blades and their stacking position, the design method gives the detailed blade shape, flow, and pressure fields that would produce a prescribed tangentially averaged swirl schedule. The results from that study show that decreasing the number of blades increases the blade wrap, and that the blade loading is strongly affected by the rate of change of mean swirl along the mean streamlines. The results also show that the blade shape and the pressure field are rather sensitive to the prescribed mean swirl schedule, which suggests that, by carefully tailoring the swirl schedule, one might be able to control the blade shape and the pressure field and hence secondary flow.

1 Introduction

There are two approaches to solving the flow in a turbomachine. In the first one, known as the direct problem, the geometric configuration is specified and the flow and pressure fields are sought. The second approach, called the design (indirect or inverse) problem, is based on specifying part of the geometry and part of the flow or pressure field, and the solution provides the remaining part.

There exist many methods for designing blades in the meridional plane (plane r–z, Fig. 1(a)) and in the blade-to-blade plane (Projection AA, Fig. 1(b)). There are also some quasi-three-dimensional methods where two design methods (one in the meridional plane and one in the blade-to-blade plane) are combined (e.g., Jennions and Stow, 1985a; Kashiwabara, 1973). A fully three-dimensional inverse design method for lightly loaded blades has been developed by Okurounmu and McCune (1974a); another three-dimensional design method for high solidity cascades has been reported by Zhao et al. (1985).

A theory for turbomachinery blade design for large deflection in three-dimensional flow is described by Hawthorne et al. (1983) and Tan et al. (1982, 1983). In that theory, it is possible to determine the blade shape that would produce a prescribed tangential averaged (or mean) swirl schedule. Dang (1985) extended that theory to rotational flows; he solved the flow in a rectilinear cascade and devised a method to control secondary flow. Using the same theory, Borges (1986) developed a computer code for designing a low-speed radial inflow turbine (RIT); his work showed that his newly designed impeller achieved an improved efficiency over a rather wide operating range. Ghaly (1986) further extended the theory to the subsonic flow in a turbomachine of arbitrary hub and shroud profiles. In a recent progress report on the design method, Hawthorne and Tan (1987) presented the design of an axial compressor stage as well as that of a marine propeller with two counterrotating rotors.

In this paper, we present a preliminary design study of the influence of the mean swirl distribution, the number of blades, and their stacking position upon the blade shape and the pressure distribution for a radial turbine. Two projections of a typical low-speed radial turbine impeller are given in Fig. 1. Note, however, that the present study was carried out for a hypothetical impeller in which the hub and shroud surfaces form two concentric circular arcs in the meridional projection. The flow is assumed to be steady and irrotational, the fluid inviscid and non-heat conducting. The blades are assumed to be infinitely thin and set at zero angle of attack. In the design approach to be described here, the hub and shroud profiles are specified, the number of blades, their stacking position, and the tangential averaged (or mean) swirl schedule is prescribed in the blade region, and the blade shape and flow field (other than the mean tangential velocity) are sought. In this paper, the mean swirl schedule is taken to be of the free vortex type. The blade shape is determined iteratively from the blade boundary condition, which requires that the flow should be tangent to the blades.

2 Analytical Formulation

2.1 Governing Equations. With the abovementioned assumptions and in the absence of shocks, the flow may be considered homentropic and homenergetic (the entropy and the rothalpy are constant everywhere in the flow field). Thus, the continuity equation, Crocco's equation, the energy equations, and the equation of state may be written, respectively, as

Contributed by the International Gas Turbine Institute and presented at the 34th International Gas Turbine and Aeroengine Congress and Exhibition, Toronto, Ontario, Canada, June 4–8, 1989. Manuscript received at ASME Headquarters January 17, 1989. Paper No. 89-GT-84.

Copyright © 1990 by ASME
Downloaded 01 Jun 2010 to 171.66.16.66. Redistribution subject to ASME license or copyright; see http://www.asme.org/terms/Terms_Use.cfm

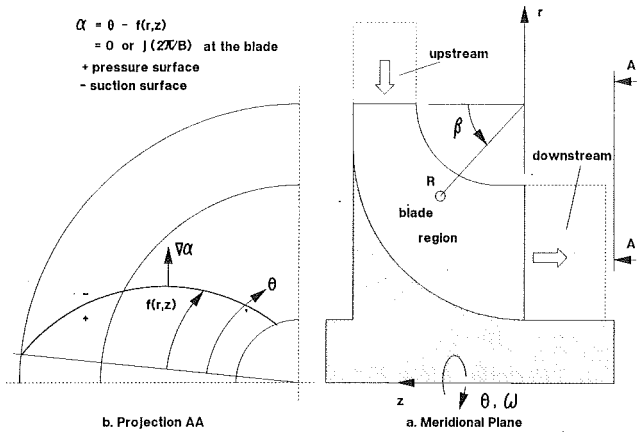

Fig. 1 Schematic diagram of a typical low-speed RIT impeller

$$\nabla \cdot \rho \mathbf{W} = 0 \tag{1}$$

$$\mathbf{W} \times \Omega = \nabla H_t^* - T \nabla Se = 0 \tag{2}$$

$$H_t^* \equiv H_t - \omega r V_\Theta = \text{const} \tag{3}$$

$$P = \rho R T \tag{4}$$

and, for a homentropic flow of an ideal gas (thermally and calorically perfect), the isentropic relation holds so that

$$\left(\frac{P}{P_t^*}\right) = \left(\frac{\rho}{\rho_t^*}\right)^\gamma = \left(\frac{T}{T_t^*}\right)^{\gamma/(\gamma-1)} \tag{5}$$

where P, ρ, T are the fluid pressure, density, and temperature, $\mathbf{V}$ is the velocity vector in the absolute frame of reference, $\mathbf{W}$ is the velocity vector relative to the impeller ($\mathbf{W} = \mathbf{V} - \omega r \mathbf{e}_\Theta$), Ω is the vorticity vector, H_t^* and H_t are the rothalpy and total enthalpy ($H_t = H + 0.5V^2$), H is the static enthalpy, γ is the ratio of specific heats at constant pressure and at constant volume, $\omega r \mathbf{e}_\Theta$ is the impeller velocity, and (r, Θ, z) denotes the right-handed cylindrical coordinate system.

In the limit of an incompressible fluid flow ($\rho = \text{const}$), the density drops out from the continuity equation and the enthalpy H is replaced by P/ρ.

2.2 The Clebsch Approach. In the Clebsch formulation, the velocity is kinematically decomposed into a potential and a rotational part in the following form (Lamb, 1945):

$$\mathbf{V} = \nabla \phi + \sigma \nabla \tau \tag{6}$$

where $\phi(r, \Theta, z)$, $\sigma(r, \Theta, z)$, and $\tau(r, \Theta, z)$ are the Clebsch variables. In the present problem, they can be identified with the mean swirl schedule and a function of the blade shape so that the vorticity field Ω may be written as (Ghaly, 1986; Tan et al., 1983)

$$\Omega \equiv \nabla \times \mathbf{V} \tag{7a}$$

$$= \nabla \sigma \times \nabla \tau \tag{7b}$$

$$= \nabla r \bar{V}_\Theta \times \nabla \alpha \delta_p(\alpha) \tag{7c}$$

where the blade surface $\alpha(r, \Theta, z)$ can, without loss of generality, be written (e.g., in the blade region) as

$$\alpha(r, \Theta, z) = \Theta - f(r, z) = \pm j(2\pi/B) \tag{8}$$

where j is an integer and B is the number of blades (see Fig. 1(*b*)). The $\delta_p(\alpha)$ in equation (7*c*) is the periodic delta function (Lighthill, 1969) given as

$$\delta_p(\alpha) = \sum_{j=-\infty}^{j=+\infty} e^{ijB\alpha} \tag{9}$$

where $i = \sqrt[2]{-1}$. An overbar defines a tangential average or mean, so that for any variable $A(r, \Theta, z)$

$$\bar{A}(r, z) = \frac{1}{(2\pi/B)} \int_0^{2\pi/B} A(r, \Theta, z) d\Theta \tag{10}$$

With the assumptions prescribed here, the flow upstream and downstream of the blade row is irrotational so that all the vorticity will be contained in the blades; thus the vorticity as given in equation (7*c*) will represent the vorticity in the entire flow field and it will vanish outside the blade.

As the flow is periodic in the circumferential direction, it is convenient to express the flow variables as a sum of a mean part ($\bar{}$) and a periodic part ($\tilde{}$). This sum corresponds to the mathematical representation of the flow variables by a Fourier series in which the mean part, e.g. $\bar{\Omega}$, is the zeroth harmonic while the periodic part $\tilde{\Omega}$ constitutes the nonzeroth harmonic. Integrating Ω given by equation (7*c*), the velocity field may be written as (Ghaly, 1986; Tan, 1983)

$$\mathbf{V} = \nabla \phi + r \bar{V}_\Theta \nabla \alpha - S(\alpha) \nabla r \bar{V}_\Theta \tag{11}$$

where the mean and periodic parts of the velocity field can be written as

Nomenclature

B = number of blades
C_P = reduced static pressure coefficient, equation (29)
$\mathbf{e}$ = unit vector
f = blade shape
H = enthalpy
m = distance along streamlines of the mean flow
P = pressure
(r, Θ, z) = cylindrical coordinates
RIT = radial inflow turbine
$S(\alpha)$ = sawtooth function, equation (14)
Se = entropy
T = temperature
$\mathbf{V}, \mathbf{W}$ = absolute and relative velocity vectors
$\tilde{\mathbf{v}}$ = absolute periodic velocity vector
α = blade surface, equation (8)
Γ = blade circulation
γ = specific heat ratio
$\delta_p(\alpha)$ = periodic delta function, equation (9)
ρ = density
ρ_{av} = average density, equation (17)
$\tilde{\Phi}$ = periodic scalar potential function harmonics, equation (23)
ϕ = scalar potential function, equation (11)
ψ = Stokes stream function, equation (19)
Ω = vorticity vector
ω = impeller rotational speed

Subscripts

bl = at the blade
LE = blade leading edge
m = meridional plane, r–z plane, Fig. 1(*a*)
ref = mean line value at the blade LE
r, Θ, z = the r, Θ, z component
st = stacking position
TE = blade trailing edge
t = total, stagnation

Superscripts

$+/-$ = blade pressure/suction surface, Fig. 1(*b*)
$*$ = rotary
($\bar{}$) = tangential average, equation (10)
($\tilde{}$) = periodic part

Downloaded 01 Jun 2010 to 171.66.16.66. Redistribution subject to ASME license or copyright; see http://www.asme.org/terms/Terms_Use.cfm

$$\bar{\mathbf{V}} = \nabla\bar{\phi} + r\bar{V}_\theta \nabla\alpha \tag{12a}$$

$$\tilde{\mathbf{v}} = \nabla\tilde{\phi} - S(\alpha)\nabla r\bar{V}_\theta \tag{13a}$$

in the blade region; and since in the upstream and downstream regions the flow field is irrotationa, it follows that

$$\bar{\mathbf{V}} = \nabla\bar{\phi} \tag{12b}$$

$$\tilde{\mathbf{v}} = \nabla\tilde{\phi} \tag{13b}$$

In equation (13*a*), $S(\alpha)$ is the sawtooth function (Lighthill, 1969) given as

$$S(\alpha) = \sum_{\substack{j=-\infty \\ \neq 0}}^{j=+\infty} \frac{e^{ijB\alpha}}{ijB} \tag{14}$$

The entire flow field, with the assumptions stated above, can now be computed in terms of the Clebsch variables $\tilde{\phi}$, $\bar{\phi}$, and α ($r\bar{V}_\theta$ being prescribed in the design problem). The governing equations for the mean and periodic flow are derived in the next section.

2.3 Flow Equations

2.3.1 Mean Flow Equations. The continuity equation may be rewritten as

$$\nabla\cdot\mathbf{W} = -\mathbf{W}\cdot\nabla\ln(\rho/\rho_t^*) \tag{15}$$

the pitch average of which gives

$$\nabla\cdot\bar{\mathbf{V}} \equiv \nabla\cdot\bar{\mathbf{W}} = -\overline{\mathbf{W}\cdot\nabla\ln(\rho/\rho_t^*)} \tag{16}$$

The right-hand side is a nonlinear term that couples the periodic flow field with the mean as a result of compressibility.

For computational reasons, the mean flow is formulated in terms of Stokes' stream function ψ rather than the scalar potential $\bar{\phi}$ given in equation (12). In using ψ to describe the mean flow, it is convenient to define a fictitious "average" density $\rho_{av}(r, z)$ ($\rho_{av} \neq \bar{\rho}$) that satisfies

$$\nabla\cdot\rho_{av}\bar{\mathbf{V}} = 0 \tag{17}$$

Comparing equation (17) with equation (16) we obtain a governing equation for ρ_{av} as

$$\bar{\mathbf{V}}\cdot\nabla\ln(\rho_{av}/\rho_t^*) = \overline{\mathbf{W}\cdot\nabla\ln(\rho/\rho_t^*)} \tag{18}$$

which yields the "average" density ρ_{av} (when solved with an appropriate initial condition).

Equation (17) can now be satisfied by introducing the Stokes' stream function $\psi(r, z)$

$$\rho_{av}\bar{V}_r = -\frac{\rho_t^*}{r}\frac{\partial\psi}{\partial z} \text{ and } \rho_{av}\bar{V}_z = \frac{\rho_t^*}{r}\frac{\partial\psi}{\partial r} \tag{19}$$

The governing equation for ψ is obtained by equating the definition of $\bar{\Omega}_\theta$ from equation (17*a*) to that from equation (7*c*) using equation (19); this gives

$$(L-N)\psi = -(\rho_{av}/\rho_t^*)\bar{\Omega}_\theta \tag{20}$$

where

$$L = \frac{\partial}{\partial r}\left(\frac{1}{r}\frac{\partial}{\partial r}\right) + \frac{\partial}{\partial z}\left(\frac{1}{r}\frac{\partial}{\partial z}\right)$$

$$N = \frac{1}{r}\left[\frac{\partial\ln}{\partial r}(\rho_{av}/\rho_t^*)\frac{\partial}{\partial r} + \frac{\partial\ln}{\partial z}(\rho_{av}/\rho_t^*)\frac{\partial}{\partial z}\right]$$

and

$$\bar{\Omega}_\theta = \frac{\partial r\bar{V}_\theta}{\partial r}\frac{\partial f}{\partial z} - \frac{\partial r\bar{V}_\theta}{\partial z}\frac{\partial f}{\partial r}$$

Equation (20) is elliptic when the flow is subsonic and hyperbolic when the flow becomes supersonic. Note that the right-hand side vanishes outside the blade region as the flow is irrotational there.

The boundary conditions for equation (20), when the flow is subsonic, are:

- along the inflow and outflow sections, $\partial\psi/\partial n = 0$
- along the hub and the shroud, ψ is constant (no flow normal to the wall).

A useful flow model, the Bladed Actuator Duct (Tan et al., 1983), is obtained when the number of blades B becomes infinite, while $r\bar{V}_\theta$ is kept fixed. In the Bladed Actuator Duct ($B\to\infty$), the periodic part of the flow vanishes, hence $\tilde{\mathbf{v}} = 0$, $\bar{\rho} = \rho_{av}$, and equation (18) is identically satisfied. In that limit, a blade shape can still be determined, as will be described in Sec. 2.4.

2.3.2 Periodic Flow Equation. The continuity equation for the periodic part of the flow is obtained by sutracting the pitch-averaged continuity equation in equation (16) from the continuity equation in equation (15), yielding

$$\nabla\cdot\tilde{\mathbf{v}} = -\mathbf{W}\cdot\nabla\ln(\rho/\rho_t^*) + \overline{\mathbf{W}\cdot\nabla\ln(\rho/\rho_t^*)} \tag{21}$$

Substituting for $\tilde{\mathbf{v}}$ in terms of its Clebsch variables from equation (13) we obtain

$$\nabla^2\tilde{\phi} = \nabla\cdot\{S(\alpha)\nabla r\bar{V}_\theta\} - \mathbf{W}\cdot\nabla\ln(\rho/\rho_t^*) + \overline{\mathbf{W}\cdot\nabla\ln(\rho/\rho_t^*)} \tag{22}$$

where ∇^2 is the Laplacian. The first term on the right-hand side vanishes outside the blade region as the flow is assumed to be irrotational there, while the other two terms vanish in the incompressible flow limit.

The boundary conditions for equation (22), when the flow is subsonic, are:

- along the inflow and outflow sections, $\tilde{\mathbf{v}}(=\nabla\tilde{\phi})$ is assumed to be negligibly small so that $\partial\tilde{\phi}/\partial n$ is approximately zero there;
- along the hub and shroud, there should be no flow normal to the wall so that $\partial\tilde{\phi}/\partial n$ vanishes there (Ghaly, 1986).

Equation (22) can readily be solved for $\tilde{\phi}(r, \Theta, z)$ if the right-hand side is known. As mentioned in the above, because of inherent periodicity in the Θ direction, a Fourier series is used to represent the Θ dependence of any of the flow variables. Accordingly, $\tilde{\phi}$ may be approximated with a truncated Fourier series of the form

$$\tilde{\phi}(r, \Theta, z) = \sum_{\substack{j=-N \\ \neq 0}}^{j=N-1} \tilde{\phi}_j(r, z)e^{ijB\Theta} \tag{23}$$

where $i = \sqrt{-1}$. Substituting for $\tilde{\phi}$ from equation (23) into equation (22) and by making use of the orthogonality property of the Fourier series, a set of equations for the Fourier coefficients $\tilde{\phi}_j(r, z)$ is obtained; thus, the flow periodicity in the Θ direction has been used to reduce a three-dimensional elliptic problem (equations (20), (22)) into a set of two-dimensional ones. The Finite Element Method is used to solve the equations describing the mean and the periodic flows.

2.4 Blade Boundary Condition. The remaining boundary condition is the blade boundary condition, which states that the velocity normal to the blade surfaces vanishes. Since $\nabla\alpha$ is normal to the blade surfaces, the blade boundary condition on the pressure and suction sides of the blades may be written as

$$\mathbf{W}^+\cdot\nabla\alpha = 0 \quad \text{and} \quad \mathbf{W}^-\cdot\nabla\alpha = 0 \tag{24}$$

Adding and subtracting the above equations, we obtain

$$\mathbf{W}_{bl}\cdot\nabla\alpha = 0 \tag{25a}$$

$$\Delta\mathbf{W}\cdot\nabla\alpha = 0 \tag{26}$$

where the velocity at the blades is defined as $\mathbf{W}_{bl} \equiv 1/2(\mathbf{W}^+ + \mathbf{W}^-)$ and the velocity jump across the blades is given as $\Delta\mathbf{W} = \mathbf{W}^+ - \mathbf{W}^-$. Equation (26) is identically

Downloaded 01 Jun 2010 to 171.66.16.66. Redistribution subject to ASME license or copyright; see http://www.asme.org/terms/Terms_Use.cfm

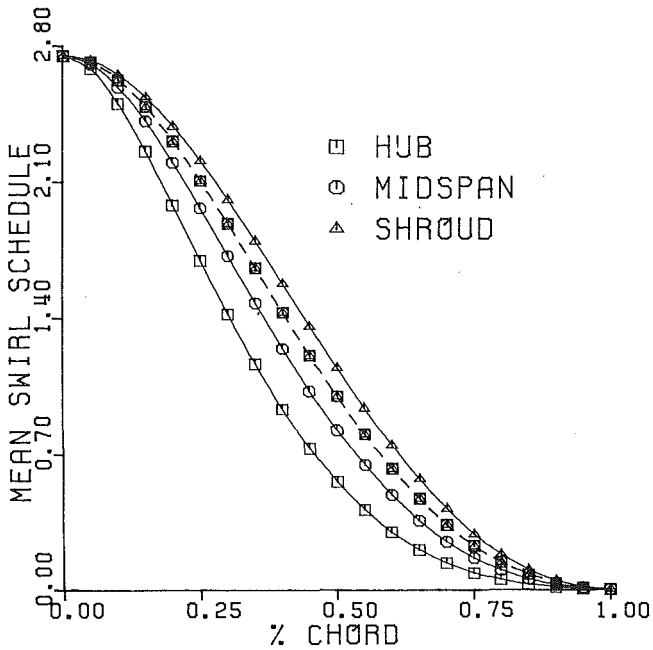

Fig. 2 Original (dashed lines) and modified $r\bar{V}_\theta$; every other node shown

satisfied since $\Delta\mathbf{W}$ is a measure of the bound vorticity, which lies in the blade surface.

Equation (25*a*) may appropriately be integrated to obtain the blade shape $f(r, z)$. It may also be written as

$$\bar{V}_m \frac{\partial f}{\partial m} \equiv \bar{\mathbf{V}} \cdot \nabla f = \bar{W}_\theta / r + \bar{v}_{bl} \cdot \nabla \alpha \qquad (25b)$$

where m denotes distance along the streamlines of the mean meridional flow. When the number of blades $B \to \infty$, the equation reduces to

$$\bar{V}_m \frac{\partial f}{\partial m} = \bar{W}_\theta / r \qquad (25c)$$

The integration of equation (25) requires the specification of an integration constant for f as

$$f_{st} = f(r_{st}, z_{st}) \qquad (25d)$$

f_{st} must be given along a line going from hub to shroud (not coinciding with any of the streamlines). This specification is called the blade stacking position (Tan et al., 1983).

2.5 The Kutta Condition. The Kutta condition ensures smooth flow at a sharp trailing edge. This translates to the fact that, in subsonic flow, the pressure must be continuous at the trailing edge. Accordingly, the swirl schedule should be such as to satisfy this condition. The homentropic assumption implies that all the thermodynamic properties will be continuous if either P or ρ or T is. Hence, by requiring that the enthalpy jump across the blade trailing edge vanishes, the temperature and hence pressure will all be continuous.

As the rothalpy is uniform, it follows that

$$H^+ - H^- = 0.5(\mathbf{W}^-)^2 - 0.5(\mathbf{W}^+)^2 \qquad (27a)$$

$$= -\mathbf{W}_{bl} \cdot \Delta\mathbf{W}$$

Using the definition of $\mathbf{W}_{bl}$, and substituting for $\Delta\mathbf{W}$ in terms of the bound vorticity, and using the blade boundary condition (equation (25*a*)) we obtain

$$H^+ - H^- = \frac{2\pi}{B} \mathbf{W}_{bl} \cdot \nabla r \bar{V}_\theta \qquad (27b)$$

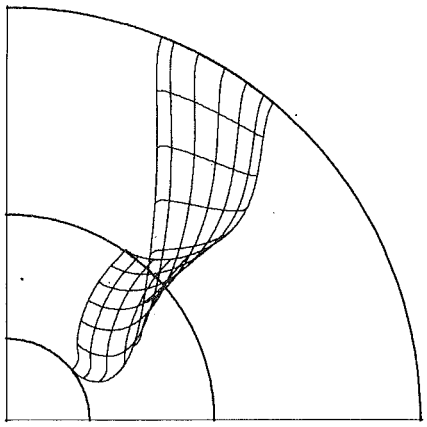

Fig. 3(a) Impeller blade original design

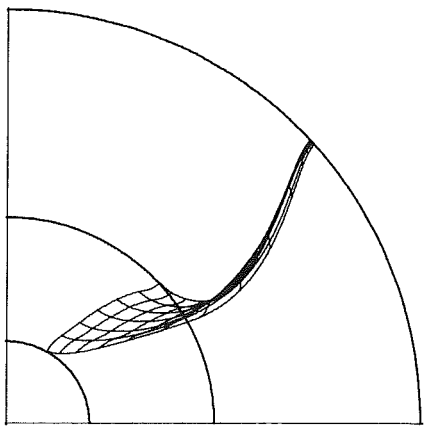

Fig. 3(*b*) Impeller blade modified design

so that the Kutta condition can be directly satisfied by setting the right-hand side of the above equation to zero, i.e.,

$$\mathbf{W}_{bl} \cdot \nabla r \bar{V}_\theta = 0 \qquad (28)$$

It is worthy to note that, as the incidence angle at the blade leading edge (LE) is assumed to be zero, the pressure there should be continuous in a way similar to that at the TE. Therefore, the condition of zero incidence at the blade LE implies that $r\bar{V}_\theta$ should satisfy equation (28) at the LE as well.

3 Results and Discussion

In a radial impeller, the blade wrap should be as small as possible for ease of manufacture as well as for mechanical stress considerations; also, the pressure distribution on the hub, the shroud, and the blade surfaces will determine, in a viscous flow situation, the secondary flow motion and the accompanying losses.

In this section, we present preliminary results on the parametric influence of a few design variables (e.g., the mean swirl distribution, the number of blades, and their stacking position) on the blade shape and the pressure field.

As mentioned earlier, the impeller hub and shroud profiles form concentric circular arcs. Such a geometric configuration is to be considered as hypothetical (as the ratio of cross-sectional area at LE to that at TE is about 3); however, it still serves the purpose of examining the parametric influence of the few relevant design variables.

The results on the parametric influence of the $r\bar{V}_\theta$ distribution, the number of blades, and their stacking position are for situations where the flow is further assumed to be incom-

Downloaded 01 Jun 2010 to 171.66.16.66. Redistribution subject to ASME license or copyright; see http://www.asme.org/terms/Terms_Use.cfm

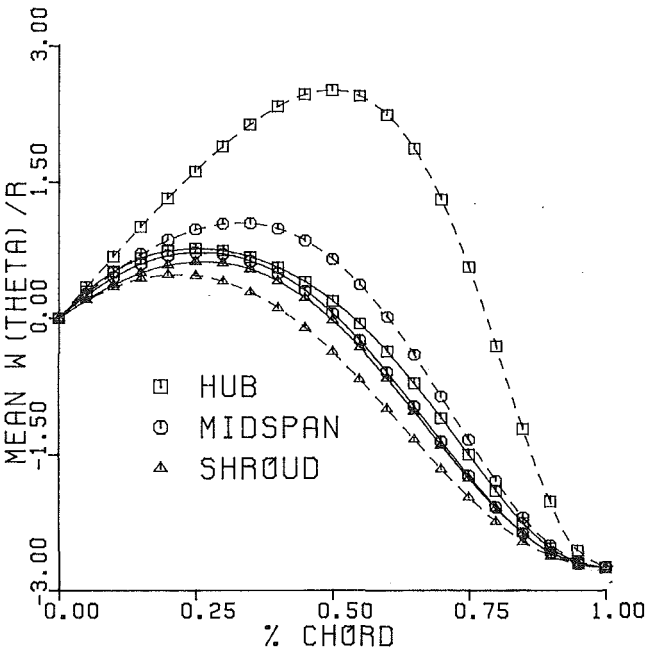

Fig. 4 Original (dashed lines) and modified $\bar{W}_\theta/r$

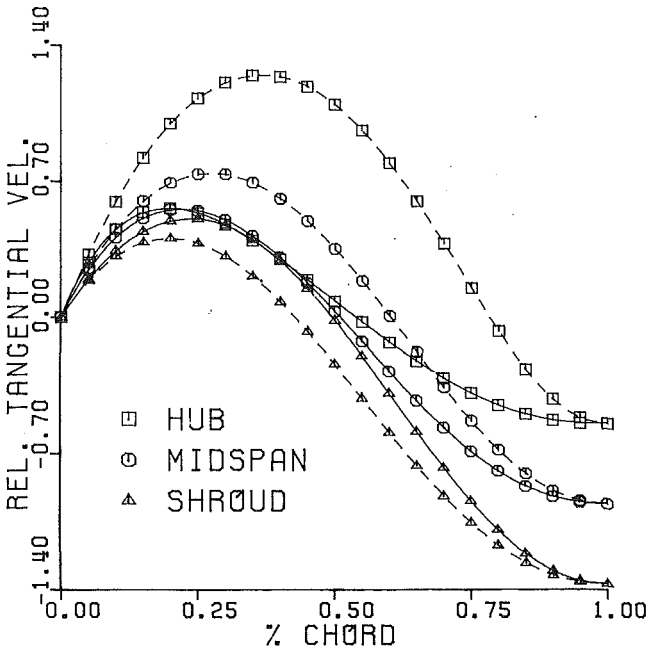

Fig. 6 Original (dashed lines) and modified $\bar{W}_\theta$

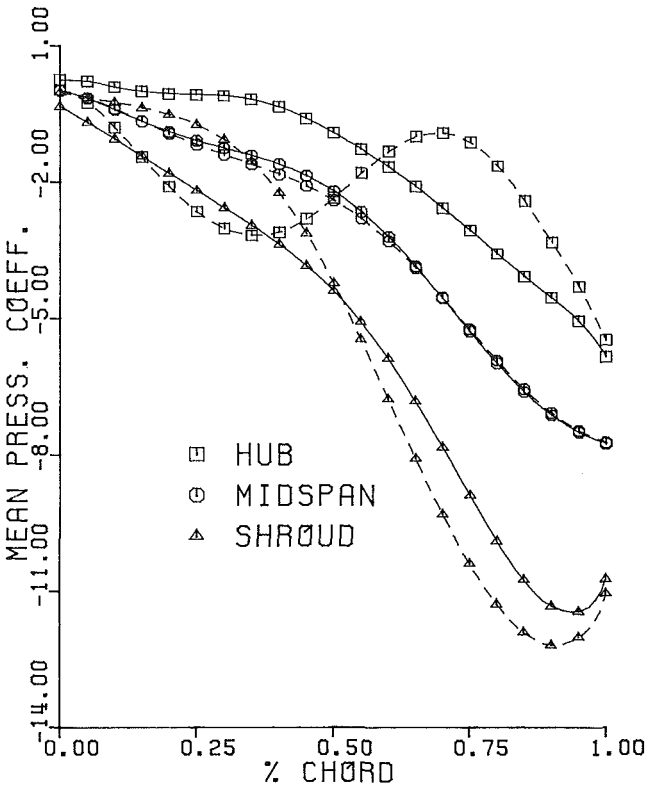

Fig. 5 Original (dashed lines) and modified mean pressure coefficient

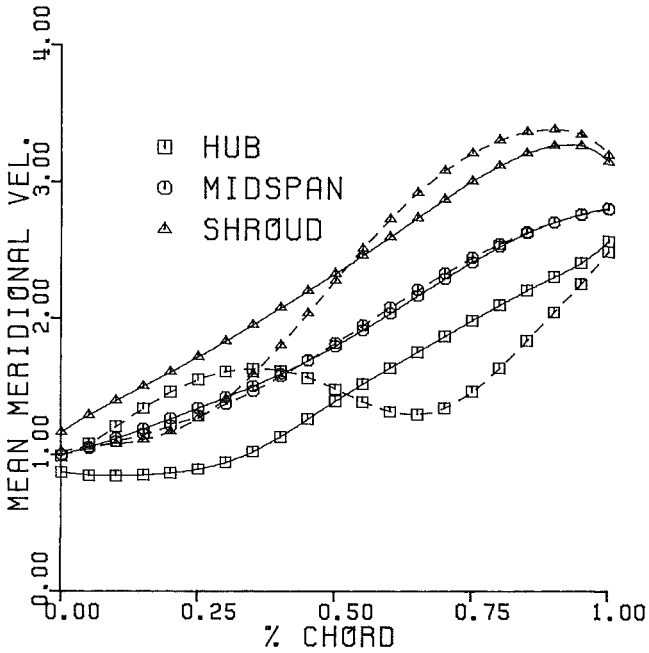

Fig. 7 Original (dashed lines) and modified $\bar{V}_m$

pressible. The effect of compressibility will be examined separately.

In the following analysis, the variables are normalized using the radius and radial velocity at the blade LE, and the rotary stagnation state (which is reached when the flow is decelerated insentropically to a stagnation state in the relative frame) is used as a reference state for the thermodynamic variables. The relative dynamic head $0.5(\rho W^2)_{\text{ref}}$ at the blade LE (based on a mean line calculation) is used to normalize the pressure, so that the reduced static pressure coefficient C_P may be defined as

$$C_P \equiv \frac{P^* - P^*_{\text{ref}}}{0.5(\rho W^2)_{\text{ref}}} \tag{29}$$

The relevance of the reduced static pressure coefficient, as opposed to the static pressure coefficient, stems from the fact that, in a viscous flow situation, the low-momentum fluid in the boundary layer near the walls will tend to move from high to low-pressure regions along the lines of maximum reduced pressure gradient.

3.1 Effect of the Mean Swirl Schedule $r\bar{V}_\theta(r, z)$. To illustrate how the swirl schedule may be tailored to control the pressure distribution along the blade surfaces and, at the same time, keep the blade wrap at an acceptable level, two designs of a RIT impeller having 15 blades, with the stacking position specified as $f_{st} = 0$ along the midchord quasi-orthogonal line,

Downloaded 01 Jun 2010 to 171.66.16.66. Redistribution subject to ASME license or copyright; see http://www.asme.org/terms/Terms_Use.cfm

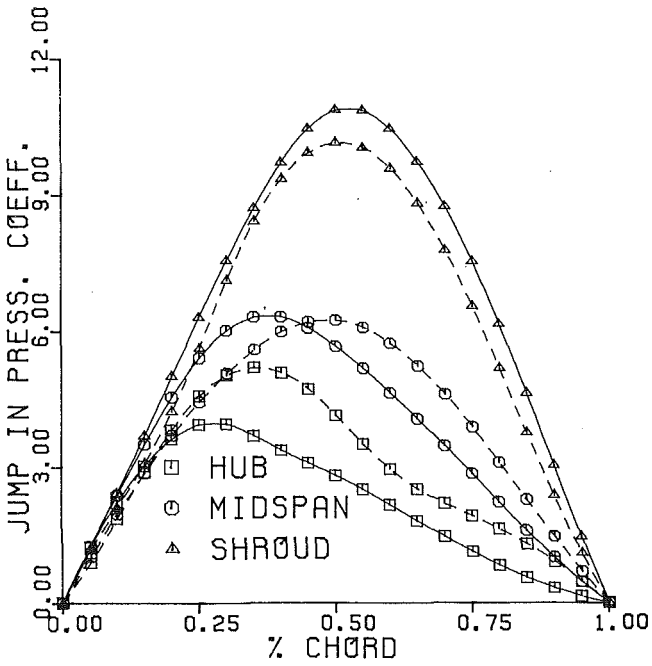

Fig. 8 Jump in pressure coefficient across the blades for the original (dashed lines) and modified designs

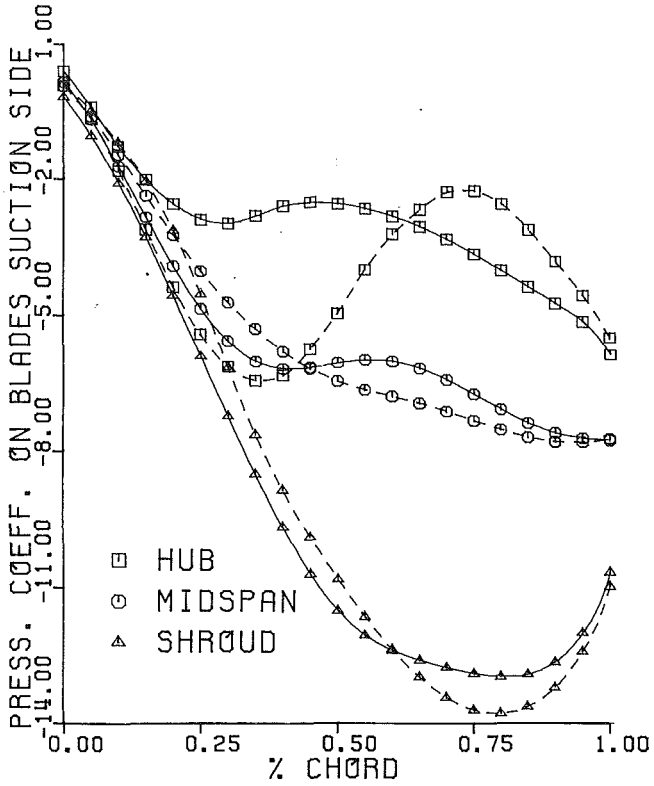

Fig. 9 Original (dashed lines) and modified $C_{\bar{p}}$

but with a slightly different $r\bar{V}_\theta$ distribution within the blade region, are presented. These $r\bar{V}_\theta$ distributions are chosen in such a way that the overall change in $r\bar{V}_\theta$ from the leading edge to the trailing edge is the same, i.e., both impellers accomplish the same change in total pressure.

In these designs, the swirl schedule takes the following form:

$$r\bar{V}_\theta(r, z) = c_1(R)(a(R) \sin 2\beta + 2 \cos 2\beta)e^{-a(R)\beta} + c_2(R) \tag{30}$$

and

$$\partial r\bar{V}_\theta/\partial s = c_3(R)e^{-a(R)\beta} \sin 2\beta$$

where $c_3(R) = c_1(R)(a^2(R)+4)/R$, $s = R\beta$, and R and β are shown in Fig. 1(*a*). The exponent $a(R)$ allows for changing the swirl schedule within the blade region and the constants c_1 and c_2 are calculated from the known values of $r\bar{V}_\theta$ at the blade LE and TE. In the original design, $a(R) = 1$ throughout the blade region, while in the modified one $a(R)$ assumes the new values 2.5 along the hub and 0.5 along the shroud, and a linear variation in between. The original and modified $r\bar{V}_\theta$ are given in Fig. 2.

Figure 3 shows the original and modified impeller blades. The modified blades are less wrapped than the original ones in the streamwise direction and are almost straight in the spanwise direction. Equation (25*b*) indicates that, when $\bar{V}_m$ is of order one (which is the case in a good design), the blade wrap/shape is primarily controlled by the mean swirl schedule $r\bar{V}_\theta$. Consequently, it was possible to reduce the blade wrap $f(r, z)$ by reducing $|\bar{W}_\theta/r|$ (through our choice of $r\bar{V}_\theta$); the latter is shown in Fig. 4 for both original and modified designs.

The pressure field on the blade suction and pressure surfaces is studied by examining the mean pressure field and the pressure jump across the blades. The variation in mean reduced static pressure coefficient $\bar{C}_P (= 1 - \bar{W}^2$ in incompressible flow) from the leading edge to the trailing edge for the original and the modified designs is shown in Fig. 5. These results may be interpreted in terms of the mean relative velocity $\bar{W}^2$ as follows: Fig. 6 shows that the absolute value of the modified relative velocity is significantly reduced in the first half chord, and Fig. 7 shows that the modified $\bar{V}_m$ (particularly along the hub) varies in a monotonic way compared to that of the original design. This change in $\bar{V}_m$ is due to a decrease in $\bar{\Omega}_\theta$ resulting from the decreased blade wrap; the latter is responsible for the change observed in the mean meridional velocity $\bar{V}_m$ along the hub as it induces a relatively smaller velocity there. The changes in the prescribed $\bar{W}_\theta$ and in $\bar{V}_m$, which is a result of modifying $r\bar{V}_\theta$, are responsible for removing the region of adverse pressure gradient along the hub surface.

The numerical results show that the jump in pressure coefficient ΔC_P, given in Fig. 8, is primarily affected by the product of the gradient of the mean swirl schedule along the mean streamlines $\partial r\bar{V}_\theta/\partial m$ and W_{bl}; this agrees with equation (27*b*) where H is replaced by P/ρ in incompressible flow. In the modified design, the point of maximum loading along the hub is shifted upstream so as to avoid a region of adverse pressure gradient present in the original design. The reduced static pressure coefficient on the blade suction surface is given in Fig. 9, which shows that the modified design has, to a large extent, eliminated a region of adverse pressure gradient along the hub.

We can thus conclude from this rather simple example that, by carefuly tailoring the $r\bar{V}_\theta$ distribution, one can control the blade shape and the pressure distribution and hence the resulting secondary flow.

3.2 Effect of the Number of Blades *B*. As B is decreased while keeping all other parameters fixed, it is expected that the load per blade would increase; this would lead to a subsequent increase in the blade wrap and in the pressure jump across the blades, which will be apparent from the following example.

The presence of a blade may be represented by a bound vortex of strength Γ ($= 2\pi r\bar{V}_\theta/B$). When $r\bar{V}_\theta$ is fixed and B decreases, Γ will increase so that the velocity induced by that bound vortex would increase, thus resulting in a larger turning angle, as shown in Fig. 10; these results also show the

Downloaded 01 Jun 2010 to 171.66.16.66. Redistribution subject to ASME license or copyright; see http://www.asme.org/terms/Terms_Use.cfm

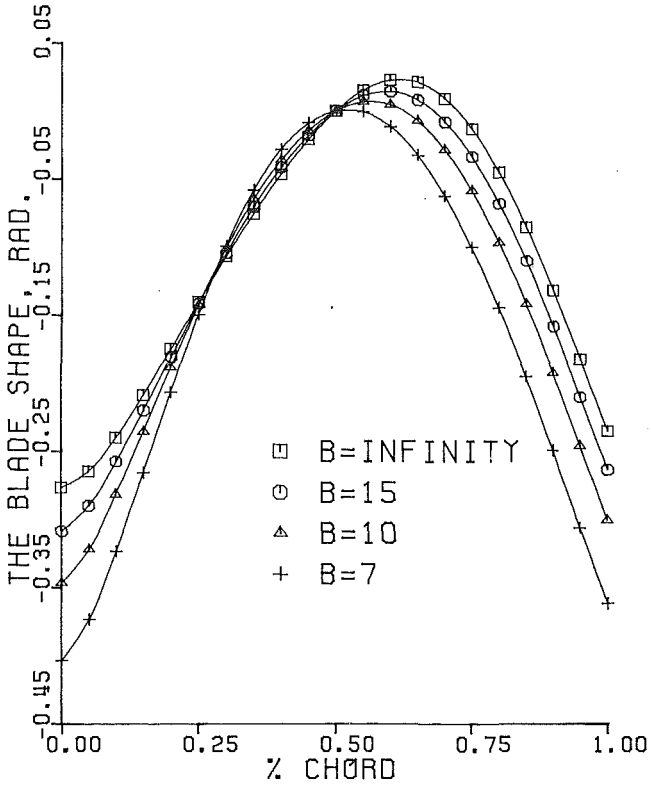

Fig. 10 Blade shape along midspan for different numbers of blades

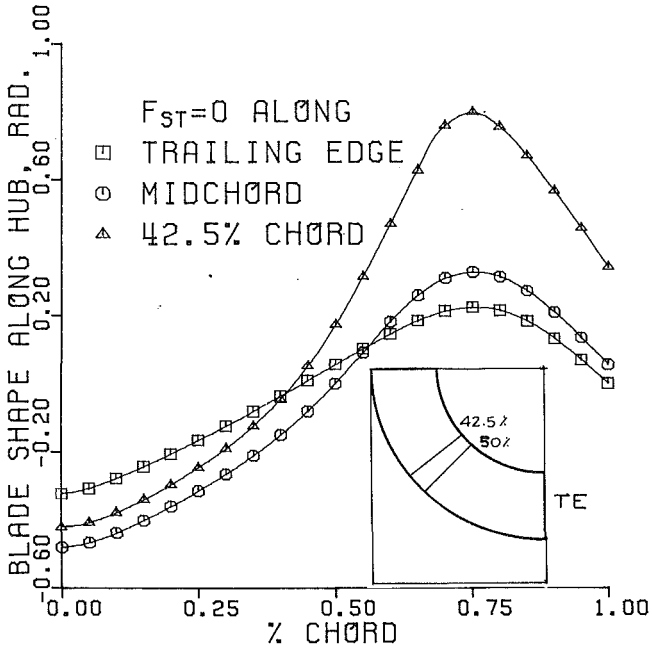

Fig. 11 Blade shape along the hub for different stacking positions

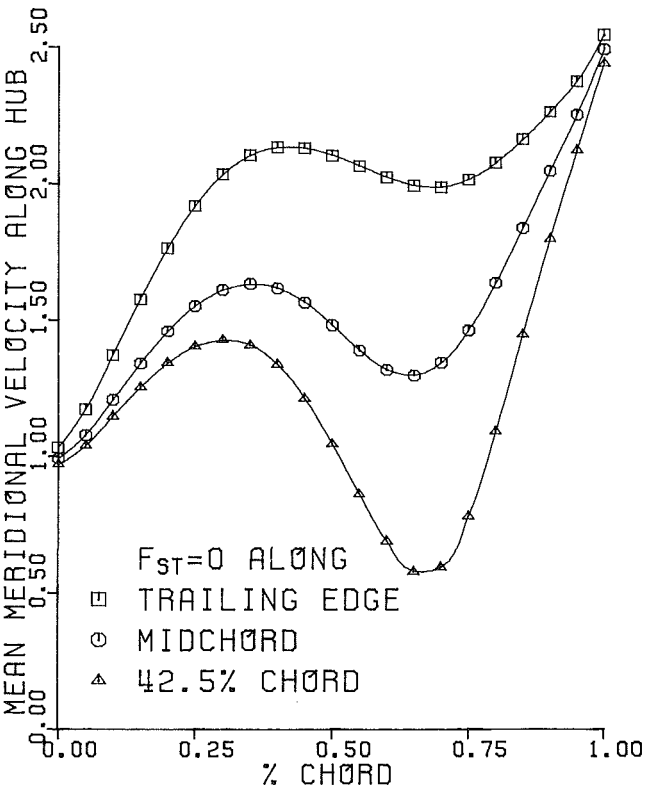

Fig. 12 $\bar{V}_m$ along the hub for different stacking positions

significance of the three-dimensional (blade-to-blade) effects on the blade shape.

3.3 Effect of the Blade Stacking Position. The results in Fig. 11 show that a change in the blade stacking position, specified as $f_{st}=0$ along three different quasi-orthogonal lines, can result in a different blade shape $f(r, z)$ (hence ∇f), thus the velocity and pressure fields will change as well. (Note, however, that $\bar{\Omega}_r$ and $\bar{\Omega}_z$ remain the same as $r\bar{V}_\theta$ is the same.)

The numerical study that has so far been carried out shows that the mean meridional velocity is sensitive to f_{st}. In the original design, when the stacking position, specified as $f_{st}=0$, is moved from the blade TE to midchord to 42.5 percent chord (see Fig. 11 for the definition of stacking position) the mean meridional velocity along the hub, shown in Fig. 12, approaches zero. This is due to the fact that, for this particular stacking, $\bar{\Omega}_\theta$ is such that the velocity induced by the bound vorticity is so strong that it annihilates the oncoming flow relative velocity at some point along the hub. This behavior has also been reported by Tan et al. (1983) for the design problem of an axial flow turbine.

3.4 Effect of Compressibility. A rudimentary study on compressibility effects has been implemented. The results thus obtained concur with those of Hawthorne and Tan (1987) in that, for a given set of parameters, the wrap angle of the blade decreases with increasing Mach number.

4 Conclusion

A design method for turbomachinery blading in three-dimensional subsonic flow has been presented. It has been used to carry out a parametric study of the response of the blade shape, flow field, and pressure field to a few design variables.

During the course of this study, it was found that the resulting blade shape and pressure field are rather sensitive to the changes in the prescribed mean swirl distribution. For a given change in mean swirl between the blades LE and TE, it was possible to decrease the blade wrap by reducing $|\bar{W}_\theta/r|$. The number of blades, when decreased, caused an increase in blade wrap. On the other hand, the blade loading was shown to be related to, and strongly affected by, the rate of change of mean swirl along streamlines of the mean flow. The results also indicate the significance of the blade stacking position.

The present study appears to indicate that one might be able to tailor the mean swirl distribution to control the blade shape

Downloaded 01 Jun 2010 to 171.66.16.66. Redistribution subject to ASME license or copyright; see http://www.asme.org/terms/Terms_Use.cfm

and the pressure distribution and hence the secondary flow motion.

Acknowledgments

The authors are grateful to Professor Sir W. R. Hawthorne of Cambridge University for his valuable suggestions during the course of this work. This work was supported by Cummins Engine Company, Inc., when the first author was working on his Ph. D. program at MIT. The cases presented in this paper were run on the main frame of the Ecole Polytechnique de Montreal.

References

Borges, J. E., 1986, "Three-Dimensional Design of Turbomachinery," Ph. D. Dissertation, Engineering Department, Cambridge University, United Kingdom.

Dang, T. Q., 1985, "A Three-Dimensional Blade Design Method to Control Secondary Flow," Ph. D. Thesis, Aeronautics and Astronautics Department, MIT, Cambridge, MA.

Ghaly, W. S., 1986, "A Study and Design of Radial Turbomachinery Blading in Three-Dimensional Flow," Ph. D. Thesis, Aeronautics and Astronautics Department, MIT, Cambridge, MA.

Hawthorne, W. R., Wang, C., Tan, C. S., and McCune, J. E., 1983, "Theory of Blade Design for Large Deflections: Part I—Two-Dimensional Cascade," ASME *Journal of Engineering for Gas Turbines and Power*, Vol. 106, No. 2, pp. 346-353.

Hawthorne, W. R., and Tan, C. S., 1987, "Design of Turbomachinery Blading in Three-Dimensional Flow by the Circulation Method: A Progress Report," *Proceedings, International Conference on Inverse Design Concepts and Optimization in Engineering Sciences*, G. S. Dulicravitch, ed.

Jennions, I. K., and Stow, P., 1985a, "A Quasi-Three-Dimensional Turbomachinery Blade Design System: Part I—Throughflow Analysis," ASME *Journal of Engineering for Gas Turbines and Power*, Vol. 107, pp. 301-307.

Jennions, I. K., and Stow, P., 1985b, "A Quasi-Three-Dimensional Turbomachinery Blade Design System: Part II—Computerized System," ASME *Journal of Engineering for Gas Turbines and Power*, Vol. 107, pp. 308-316.

Kashiwabara, Y., 1973, "Theory on Blades of Axial, Mixed, and Radial Turbomachines by Inverse Method," *Bulletin of the JSME*, Vol. 16, No. 92, pp. 272-281.

Lamb, H., 1945, *Hydrodynamics*, 6th ed., Dover, New York, p. 248.

Lighthill, M. J., 1969, *An Introduction to Fourier Analysis and Generalized Functions*, Cambridge University Press, United Kingdom.

Okurounmu, O., and McCune, J. E., 1974a, "Lifting Surface Theory of Axial Compressor Blade Rows: Part I—Subsonic Compressor," *AIAA Journal*, Vol. 12, No. 10, pp. 1363-1372.

Okurounmu, O., and McCune, J. E., 1974b, "Lifting Surface Theory of Axial Compressor Blade Rows: Part II—Transonic Compressor," *AIAA Journal*, Vol. 12, No. 10, pp. 1372-1380.

Tan, C. S., Wang, C., McCune, J. E., and Hawthorne, W. R., 1982, "Three-Dimensional Blade Design for Large Deflections Using an Analytical Theory," MIT GT&PDL Report No. 168, MIT; also CUED/A-Turbo/TR 115, Cambridge University, United Kingdom.

Tan, C. S., Hawthorne, W. R., McCune, J. E., and Wang, C., 1983, "Theory of Blade Design for Large Deflections: Part II—Annular Cascades," ASME *Journal of Engineering for Gas Turbines and Power*, Vol. 106, No. 2, pp. 354-365.

Zhao, X.-L., Sun, C.-L., and Wu, C.-H., 1985, "A Simple Method for Solving Three-Dimensional Inverse Problems of Turbomachine Flow and the Annular Constraint Condition," ASME *Journal of Engineering for Gas Turbines and Power*, Vol. 107, pp. 293-300.

Downloaded 01 Jun 2010 to 171.66.16.66. Redistribution subject to ASME license or copyright; see http://www.asme.org/terms/Terms_Use.cfm

A Three-Dimensional Inverse Method for Turbomachinery: Part I—Theory

J. E. Borges
Department of Mechanical Engineering,
Instituto Superior Técnico,
1096 Lisboa Codex, Portugal

There are surprisingly few inverse methods described in the literature that are truly three dimensional. Here, one such method is presented. This technique uses as input a prescribed distribution of the mean swirl, i.e., radius times mean tangential velocity, given throughout the meridional section of the machine. In the present implementation the flow is considered inviscid and incompressible and is assumed irrotational at the inlet to the blade row. In order to evaluate the velocity field inside the turbomachine, the blades (supposed infinitely thin) are replaced by sheets of vorticity, whose strength is related to the specified mean swirl. Some advice on the choice of a suitable mean swirl distribution is given. In order to assess the usefulness of the present procedure, it was decided to apply it to the design of an impeller for a low-speed radial-inflow turbine. The results of the tests are described in the second part of this paper.

1 Introduction

In the field of turbomachinery there are two different ways of viewing the problem of fluid dynamic calculations. In the first instance, called the "direct" or "analysis" problem, we seek to determine the flow field produced by a certain blade shape. In the second way of treating the problem, called the "inverse" or "design" problem, the emphasis is different since, in this case, the effort is directed toward finding a suitable blade geometry that will achieve certain conditions for the flow field, given as input data.

The restriction of the inverse problem to two-dimensional blade-to-blade cases has been tackled in many different ways. Examples of such methods are provided by Lewis (1982) who used surface vorticity for modeling the flow, Lighthill (1945) who based his method on a conformal transformation, and Garabedian and Korn (1976) who solved the equations in the hodograph plane and used a method of characteristics in finite difference form. Other instances are Schmidt (1980) who worked with a streamfunction Ψ and a potential Φ as independent variables, while Sobieczky and Dulikravich (1982) adapted a potential analysis program to the design of transonic blades. Wang (1985) presented a solution based on the use of a streamfunction concept and the artificial compressibility technique. An inverse procedure based on a time-marching method is described by Meauzé (1974). Novak and Haymann-Haber (1983) used a fourth-order Taylor series expansion to solve the flow equations. It is possible to fill pages with other examples of two-dimensional blade-to-blade methods, such is the wealth of existing methods in the open literature. However, since our only intention is to give some brief examples, no further references will be presented for the two-dimensional blade-to-blade case.

The solution of the indirect problem was also tried in the hub-to-shroud plane and using a quasi-three-dimensional approach although the examples are fewer. Wright and Novak (1960), Jansen and Kirschner (1974), and Weber and Mulloy (1982) present examples of two-dimensional hub-to-shroud methods. All of them are based on streamline curvature techniques, and also have in common the fact that they use as input data for the design procedure a specification of mean swirl $r\bar{V}_\theta$ (i.e., radius times mean tangential velocity) or quantities that are closely related to the mean swirl (case of Jansen and Kirschner, 1974, who impose the blade loading). There is also very little work done on quasi-three-dimensional inverse methods, and it is difficult to find an example that is characteristic of this approach. One of the best instances is the work described by Jennions and Stow (1984), although only the blade-to-blade component of the software package described in this paper can be considered as a truly inverse technique.

The next step in difficulty is given by truly three-dimensional inverse techniques. Here, the scarcity of published methods is even more marked than for hub-to-shroud and quasi-three-dimensional solutions.

One of the few existing approaches to this subject is provided by Tan et al. (1984), who developed a technique for the design of annular cascades of infinitely thin blades with constant hub and tip radius. The blades are modeled by surface vorticity and the input to the program consisted of a specification of mean swirl, $r\bar{V}_\theta$. Dang and McCune (1984a) extended this approach to the case of rotational inlet flow through a linear cascade. In this case, there is vorticity moving with the fluid, in addition to the vorticity used to model the blades.

Recently, a totally different method was published by Zhao

Contributed by the International Gas Turbine Institute and presented at the 34th International Gas Turbine and Aeroengine Congress and Exhibition, Toronto, Ontario, Canada, June 4–8, 1989. Manuscript received at ASME Headquarters January 23, 1989. Paper No. 89-GT-136.

Copyright © 1990 by ASME
Downloaded 01 Jun 2010 to 171.66.16.66. Redistribution subject to ASME license or copyright; see http://www.asme.org/terms/Terms_Use.cfm

et al. (1985), who used a Taylor series expansion in the circumferential direction for the solution of the flow equations. In spite of being a completely fresh form of treating the problem, this method also uses as input a sort of mean swirl (the value of rV_θ at the mean streamsurface).

From this, necessarily brief, description of the work done it is clear that, only recently, the three-dimensional approach to the indirect problem started to receive some attention and is being tackled. It is in this domain that the work described in this paper will fit.

Why is there so little work done on this field? Well, it is difficult to give a simple answer without being controversial, but nevertheless there is one point one should focus on when trying to answer. In fact, in addition to the normal problems associated with analysis procedures, in indirect techniques it is essential to specify the input data carefully in order to avoid ill-posed problems with no solution. For example, even in a simple two-dimensional situation, it is impossible to specify at the same time and independently the velocity on the whole contour of the blade and the far-upstream and far-downstream velocity. It is for this reason that it is necessary to impose certain constraints to the initial specifications, a fact well known by everybody working in this field (see, e.g., Lighthill, 1945; note that these constraints involve an integral and so it is difficult to know if they are satisfied a priori).

The way out of this difficulty is to specify the input data in such a way that does not lead to ill-posed problems. This approach is the one taken in most of the two-dimensional indirect methods, for example, by specifying only the velocity on the suction surface of the blade together with a suitable thickness. Another input specification that does not require complicated constraints is a specification of mean swirl $r\bar{V}_\theta$ and blade thickness (see Dang and McCune, 1984b, who implemented this sort of input in a two-dimensional situation). This last design specification may seem rather odd at first sight, but it is one of the specifications best suited to a truly three-dimensional situation, since there are no complicated constraints to be imposed and since the value of $r\bar{V}_\theta$ plays an important physical role. In fact, this quantity gives the mean angular momentum per unit mass and so is related to the way the work is imparted to the fluid as it moves through the machine. As the mean angular momentum can only be changed by a tangential force, the way it varies along a streamline gives us an idea of the variation of the pressure loading across the blades. The importance of the mean swirl is so marked and the desirability of using it for three-dimensional inverse methods so clear, that the most recent attempts at the solution of the three-dimensional problem (Tan et al., 1984; Dang and McCune, 1984a; Zhao et al., 1984) use as input a specification of mean swirl. This sort of specification was also adopted in the present work.

The use of a mean swirl distribution, $r\bar{V}_\theta$, has other advantages, namely the simple kinematic relationship existing between its value and the vorticity bound to the blades. This relationship plays a central part in the procedure described herein. In fact, the basic idea of this design method consists in replacing the action of the blades by sheets of vorticity (it is this vorticity that causes the jump in velocity when one goes from the suction surface to the pressure surface). The strength of this vorticity is related to the specified values of $r\bar{V}_\theta$ through an expression also involving the blade coordinates. The knowledge of the vorticity present in the flow region permits us to calculate the corresponding velocity field, which is done, in our case, using the Clebsch formulation. Afterward, the blade shape is determined by requiring it to be aligned with the local velocity vector throughout its length. Since the vorticity also depends on the blade shape it is necessary to solve the problem iteratively.

This idea is the same as the one described by Tan et al. (1984). However, the method described by Tan et al. (1984) was applied only to annular cascades of constant tip and hub radius and with a specification of mean swirl that was only a function of the axial distance. In the present study we consider the extension of this method to radial turbomachinery with an arbitrary meridional geometry (see Fig. 1) and a general $r\bar{V}_\theta$ distribution, which can vary both with r and z. In order to be able to deal with these extensions, the numerical techniques used to solve the equations must be different from those used by Tan et al. (1984).

As an example of a possible application, the design of a rotor of a radial-inflow turbine will be presented and discussed in detail in the last section of this paper.

2 Description of Design Method

The following method uses the usual right-handed cylindrical polar coordinate system defined by (r, θ, z), where r is the radius, θ the angular coordinate, and z the axial distance. In addition, an auxiliary coordinate α will be introduced, defined by

$$\alpha = \theta - f(r, z) \tag{1}$$

where $f(r, z)$ is the angular coordinate of a point on the blade camber surface. Some manufacturers of radial-inflow turbines call f the wrap angle and that convention will be adopted here, for brevity's sake. The variable α can be interpreted as a sort of helical angular coordinate; for values of α given by $\alpha = 2m\pi/B$, $m = \ldots, -1, 0, 1, 2, \ldots$ the equation of the blade surface is obtained (the blade surfaces are coincident with the

Nomenclature

B = number of blades
C_p = pressure coefficient; see equation (19)
f = angular coordinate of blade surface (wrap angle), rad
k, m = integers
N = number of harmonics used
p = static pressure
r = radius
$r\bar{V}_\theta$ = mean swirl
s = coordinate along the streamline
S = saw-tooth function
U = blade speed
$\mathbf{V}$ = absolute velocity
$\bar{V}_\theta$ = mean tangential velocity
$v_{\theta bl}$ = periodic tangential velocity at the blade; see equation (17)
$\mathbf{W}$ = relative velocity
z = axial coordinate
α = auxiliary coordinate; see equation (1)
δ_p = periodic delta function
η = coordinate in the transformed domain
θ = angular coordinate
ξ = coordinate in the transformed domain
ρ = density
Φ = potential
Ψ = streamfunction
ω = rotational speed
Ω = vorticity

Subscripts

bl = referring to blade
k = kth harmonic
r = in the radial direction
ref = reference value
tip = tip of impeller
z = in the axial direction
θ = in the tangential direction
o = mean value

Superscripts

c = cosine harmonic
s = sine harmonic
$+$ = upper surface of blade (facing positive θ)
$-$ = lower surface of blade (facing negative θ)

Downloaded 01 Jun 2010 to 171.66.16.66. Redistribution subject to ASME license or copyright; see http://www.asme.org/terms/Terms_Use.cfm

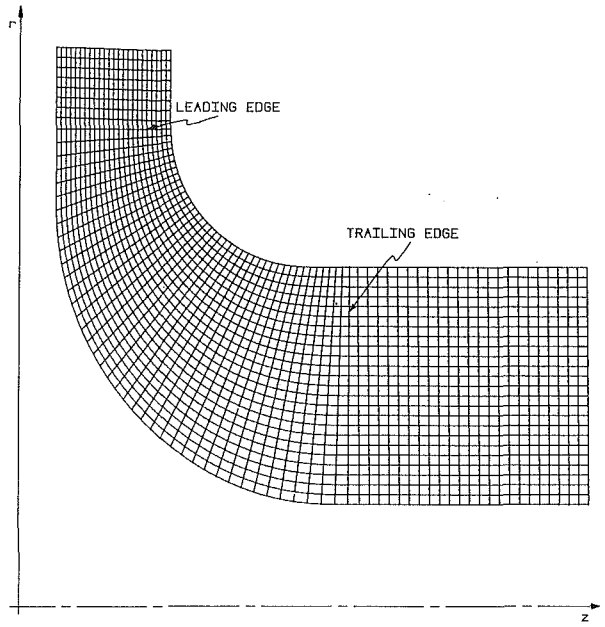

Fig. 1 Grid in physical plane

blade camber surface because it is supposed that the blades have zero thickness). In the following, vectors will be denoted by bold characters and mean values will be indicated with an overbar.

2.1 Calculation of the Velocity Field. Since in the present method the velocity will be calculated from the knowledge of the vorticity, the first piece of information to be discussed is the strength and location of all the vorticity existing in the flow field, which will be done immediately. It will be assumed that the flow is inviscid and irrotational at inlet to the turbomachine. In addition, our attention will be focused only on designs that impose constant work along the span, because this presents some advantages, as will be discussed later on. For these conditions and according to Kelvin's theorem, the flow is everywhere irrotational. So, if there is any vorticity at all, it must be bound to the blade surfaces. This implies that the expression for the vorticity vector must have a dependence on the angular coordinate given by the periodic delta function, δ_p. Moreover, it is known that the vorticity field is solenoidal, or $\nabla \cdot \Omega = 0$, and therefore can be written as the cross product of two gradients of scalar functions. One of the factors in this product may be $\nabla\alpha$ because the vorticity is lying on the blade surface and therefore is normal to $\nabla\alpha$. The other factor turns out to be $\nabla r\bar{V}_\theta$ as is shown in more detail by Tan et al. (1984) or Borges (1986). Therefore, the final expression for the vorticity vector is

$$\Omega = [\nabla r\bar{V}_\theta \times \nabla\alpha]\delta_p(\alpha) \tag{2}$$

where the Fourier expansion of the periodic delta function is given by

$$\delta_p(\alpha) = 1 + \sum_{k=1}^{\infty} 2\cos(kB\alpha) \tag{3}$$

Now that all the vorticity existing in the flow field is known, the velocity induced by this vorticity can be evaluated. In order to do that the Clebsch formulation of the problem will be used. This basically consists in writing the velocity in such a form that it satisfies identically the vorticity expression (2). The adopted expression must depend on an unknown scalar function Φ, which is then evaluated by satisfying the continuity equation.

Executing the first step of the above idea, the velocity will be written as

$$\mathbf{V} = \nabla\Phi(r, \theta, z) + r\bar{V}_\theta\nabla\alpha - S(\alpha)\nabla r\bar{V}_\theta \tag{4a}$$

inside the blade region and as

$$\mathbf{V} = \nabla\Phi(r, \theta, z) \tag{4b}$$

outside it. The function $S(\alpha)$ is such that the curl of the above expression (4) must be equal to the vorticity as calculated from expression (2). So, taking the curl of (4) we obtain

$$\Omega = [\nabla \times \mathbf{V}] = [S'(\alpha) + 1]\nabla r\bar{V}_\theta \times \nabla\alpha \tag{5}$$

and the only way for equation (5) to be equal to equation (2) is to have

$$S'(\alpha) = \delta_p(\alpha) - 1 \tag{6}$$

or, in other words, $S(\alpha)$ must be the periodic sawtooth function with zero mean value. Notice that what we have done so far is to determine the unknown function $S(\alpha)$ using one of the conditions that expression (4) must satisfy. For the calculation of the unknown scalar function $\Phi(r, \theta, z)$ we are going to use the other condition left, i.e., the continuity equation. For incompressible flow, the continuity equation takes the form

$$\nabla \cdot \mathbf{V} = 0 \tag{7}$$

Substituting the value (4) for the velocity $\mathbf{V}$, we arrive at

$$\nabla^2\Phi = -r\bar{V}_\theta\nabla^2\alpha + [S'(\alpha) + 1]\nabla\alpha \cdot \nabla r\bar{V}_\theta + S(\alpha)\nabla^2 r\bar{V}_\theta \tag{8a}$$

inside the blade passage and

$$\nabla^2\Phi = 0 \tag{8b}$$

upstream and downstream of the blade row.

In order to solve this equation in Φ, we are going to expand both Φ and the right-hand side of equation (8) in a Fourier series in the tangential direction. The corresponding harmonics must be equal, which gives us a second-order differential equation for each of the harmonics of Φ. For example, for the mean value of Φ, $\Phi_o(r, z)$, it is necessary to solve

$$\frac{\partial^2\Phi_o}{\partial r^2} + \frac{1}{r}\frac{\partial\Phi_o}{\partial r} + \frac{\partial^2\Phi_o}{\partial z^2} = \frac{1}{r}\frac{\partial}{\partial r}\left[r^2\bar{V}_\theta\frac{\partial f}{\partial r}\right] + \frac{\partial}{\partial z}\left[r\bar{V}_\theta\frac{\partial f}{\partial z}\right] \tag{9a}$$

inside the blade passage, and outside it

$$\frac{\partial^2\Phi_o}{\partial r^2} + \frac{1}{r}\frac{\partial\Phi_o}{\partial r} + \frac{\partial^2\Phi_o}{\partial z^2} = 0 \tag{9b}$$

which is a Poisson equation. For the kth cosine harmonic, the equation to solve is

$$\frac{\partial^2\Phi_k^c}{\partial r^2} + \frac{1}{r}\frac{\partial\Phi_k^c}{\partial r} + \frac{\partial^2\Phi_k^c}{\partial z^2} - \frac{k^2B^2}{r^2}\Phi_k^c = -[\nabla^2 r\bar{V}_\theta]\frac{2\sin(kBf)}{kB} + [\nabla\alpha \cdot \nabla r\bar{V}_\theta]2\cos(kBf) \tag{10a}$$

inside the blade passage;

$$\frac{\partial^2\Phi_k^c}{\partial r^2} + \frac{1}{r}\frac{\partial\Phi_k^c}{\partial r} + \frac{\partial^2\Phi_k^c}{\partial z^2} - \frac{k^2B^2}{r^2}\Phi_k^c = 0 \tag{10b}$$

outside the bladed region. Similarly, for the kth sine harmonic it is required to solve

$$\frac{\partial^2\Phi_k^s}{\partial r^2} + \frac{1}{r}\frac{\partial\Phi_k^s}{\partial r} + \frac{\partial^2\Phi_k^s}{\partial z^2} - \frac{k^2B^2}{r^2}\Phi_k^s = [\nabla^2 r\bar{V}_\theta]\frac{2\cos(kBf)}{kB} + [\nabla\alpha \cdot \nabla r\bar{V}_\theta]2\sin(kBf) \tag{11a}$$

inside the blade passage;

$$\frac{\partial^2\Phi_k^s}{\partial r^2} + \frac{1}{r}\frac{\partial\Phi_k^s}{\partial r} + \frac{\partial^2\Phi_k^s}{\partial z^2} - \frac{k^2B^2}{r^2}\Phi_k^s = 0 \tag{11b}$$

outside the blade passage.

Downloaded 01 Jun 2010 to 171.66.16.66. Redistribution subject to ASME license or copyright; see http://www.asme.org/terms/Terms_Use.cfm

Equations (10) and (11) are Helmholtz-type equations which, like equation (9), can be solved in the meridional section of the blade row provided use is made of the appropriate boundary conditions at the endwalls and far-upstream and far-downstream boundaries. At the endwalls, the condition of no flow is used, and at the far-upstream and far-downstream boundary, uniform flow is imposed (see Borges, 1986).

In order to calculate the pressure loading on the blades, it is necessary to estimate the jump in velocity across the blade ($\mathbf{W}^+ - \mathbf{W}^-$). Tan et al. (1984) and Borges (1986) show that this jump is given by

$$\mathbf{W}^+ - \mathbf{W}^- = \frac{2\pi}{B} \frac{(\nabla r\bar{V}_\theta \times \nabla\alpha)\times \nabla\alpha}{\nabla\alpha \cdot \nabla\alpha} \tag{12}$$

This expression is physically plausible as it gives a jump in velocity that lies on the blade (since it is normal to $\nabla\alpha$, a vector normal to the blade) and is also normal to the vorticity vector, $\frac{2\pi}{B}(\nabla r\bar{V}_\theta \times \nabla\alpha)$, which is causing the jump. The pressure loading on the blades can be determined if we assume irrotational flow and use Bernoulli's equation. The final expression is (see Tan et al., 1984, and Borges, 1986):

$$p^+ - p^- = \frac{2\pi}{B} \rho \mathbf{W}_{bl} \cdot \nabla r\bar{V}_\theta \tag{13}$$

where ρ is the density of the fluid and p^+ and p^- are, respectively, the static pressures on the upper and lower surfaces of the blade.

As is well known, the Kutta–Joukowski condition states that at the trailing edge of a blade, $p^+ = p^-$. Using equation (13), this implies that

$$\mathbf{W}_{bl} \cdot \nabla r\bar{V}_\theta = 0 \tag{14}$$

or, in other words, the component of the gradient of $r\bar{V}_\theta$ along the meridional projection of the blade streamline must be zero. This is logical, since downstream of a blade row the mean angular momentum per unit mass ($r\bar{V}_\theta$) cannot change because there are no tangential forces actuating there. The same can be said at the trailing edge since the Kutta–Joukowski condition imposes zero tangential pressure loading there, as well.

In the method described here, this condition is satisfied by specifying an $r\bar{V}_\theta$ distribution with zero gradient at the trailing edge, thus automatically satisfying condition (14). A similar condition is also imposed at the leading edge. This corresponds to designing a blade row that is exactly aligned with the local velocity vector at the leading edge (zero local incidence angle) so that the tangential loading there is zero.

2.2 Calculation of Blade Camber. The blade shape is calculated using the condition that the blade must be aligned with the local velocity vector. This can be expressed as

$$\mathbf{W}_{bl} \cdot \nabla\alpha = 0 \tag{15}$$

by noting again that $\nabla\alpha$ is a vector normal to the blade camber surface. Expanding equation (15), we arrive at

$$V_{zbl}\frac{\partial f}{\partial z} + V_{rbl}\frac{\partial f}{\partial r} = \frac{W_{\theta bl}}{r} \tag{16}$$

where f is the wrap angle and the blade relative tangential velocity, $W_{\theta bl}$, is defined as equal to

$$W_{\theta bl} = \bar{V}_\theta + v_{\theta bl} - \omega r \tag{17}$$

Here ω is the rotational speed of the blade row and $v_{\theta bl}$ is the value of the periodic tangential velocity at the blade (difference between the tangential velocity at the blade and the mean tangential velocity $\bar{V}_\theta$ specified as input).

The blade boundary condition (as equation (16) will be called from now on) is a first-order partial differential equation with characteristic lines coincident with the meridional projection of the blade streamlines. In order to integrate this differential equation, some initial data (values of f) must be specified along a line roughly perpendicular to these characteristic lines and extending from hub to shroud. These initial data on f will be called the stacking condition of the blade. In our method this stacking condition is implemented by giving as input the values of blade wrap angle f along a quasi-orthogonal, for example, at the leading edge. After the stacking condition is specified, we can integrate equation (16), since all the velocities that appear in it are known from the previous iteration by using the equations described in the last subsection.

2.3 Numerical Procedure. The design method described here requires the solution of partial differential equations like (9), (10), (11), and (16) on the meridional section of the machine. For a radial turbomachine, the meridional section has a complicated geometry with curved endwalls. For this reason, it was decided to do a transformation of coordinates from (r, z) to a body-fitted curvilinear coordinate system (ξ, η). A discussion of this technique and some examples of its practical application to the solution of partial differential equations can be found from Thompson et al. (1977). Ideally, this coordinate system should be easy to generate and require little computational time. For this reason it was decided to use an algebraic transformation with the points equally distributed along quasi-orthogonals, extending from hub to shroud (see Borges, 1986). Since the transformation is always the same for all the partial differential equations to be solved, it is only necessary to calculate it once, at the very beginning of the process. It is recognized that the use of an algebraic transformation of coordinates may lead to a grid that is nonorthogonal in the physical plane (see Fig. 1), but this fact is taken into account when doing the transformation.

The equations obtained from (9), (10), and (11) after the transformation (see appendix) are solved using finite difference techniques. Second-order accurate, central difference formulae and a nine-point numerical molecule are used throughout. In our program this was implemented in conjunction with a multigrid technique in order to accelerate the convergence rate of the solution. A good description of multigrid methods can be found in Brandt (1977), the relaxation subroutines used in our program being a slightly modified version of the ones presented there.

The multigrid method discretizes the problem on several grids, which become increasingly coarser as one moves from one grid level to the next. The desired solution is the one obtained in the finer mesh, because the truncation errors are smaller at this level. The coarser meshes are used to accelerate the convergence of the solution by efficiently eliminating the low-frequency (long-wavelength) errors in the solution. As the solution on the coarser grids requires much less work than in the finest grid, the attenuation of low-frequency errors is done very cheaply. The highest frequency errors are also liquidated inexpensively because their wavelength is of the same order as the mesh size and therefore the information about changes only has to travel a few mesh nodes.

The blade boundary condition (16) (see appendix for the form it takes in the transformed domain) will also be solved using finite-difference techniques. However, since it is a first-order differential equation, it must be solved using a different numerical scheme that respects the direction of the characteristic lines. For this reason it was decided to solve the blade boundary condition using an Euler's modified method (see Roache, 1982). This is an implicit numerical scheme that has a truncation error of second order in $\Delta\xi$ and $\Delta\eta$ and is consistent and stable. In order to start this method the values of wrap angle f must be known along an initial quasi-orthogonal. This information is provided by the stacking condition.

Downloaded 01 Jun 2010 to 171.66.16.66. Redistribution subject to ASME license or copyright; see http://www.asme.org/terms/Terms_Use.cfm

The calculations must be done iteratively since the vorticity depends on the blade shape, which is not known at the start. So, after the input of the initial data and generation of the body-fitted curvilinear coordinate system, a first estimate for the blade shape f is obtained, assuming that the blade velocity is equal to the value one would have if the velocity profile was uniform along a quasi-orthogonal. Then, an iterative loop is entered, where the blade velocity is calculated (this step requires the solution of equations (9), (10) and (11)), followed by the calculation of the blade shape f (this step requires the solution of equation (16)). After convergence is achieved, the blade shape is output. For further information on the numerical procedure see Borges (1986).

3 Results

The inverse method just presented is fully three-dimensional. Therefore, the most appropriate way of really testing it is by using it to design a blade row with significant three-dimensional effects. For this reason, it was decided to apply this method to the design of a low-speed rotor (with 17 blades) of a radial-inflow turbine. We considered a low-speed rotor because the developed indirect method only applies to incompressible flow, as yet.

For the application of the procedure, a grid consisting of 145 quasi-orthogonals and 49 quasi-streamlines was fitted to the meridional section of the radial-inflow turbine, the geometry of this meridional section being treated as an input to the program. Every other line of the grid used is shown in Fig. 1. The leading and trailing edges of the blade row are also indicated in the figure, in order to demonstrate that, in the solution to be described, a region upstream and downstream of the blade row was considered, there being 81 quasi-orthogonals inside the blade region. In the Fourier expansion for the velocity, 15 harmonics were considered, each harmonic having one sine and one cosine component.

The other fundamental input for the present inverse method is a mean-swirl distribution, specified throughout the entire meridional projection of the blade row. In the following we will explain, in detail, how this input was chosen, because this is one of the first instances of the use of such design specification.

The necessary values of $r\bar{V}_\theta$ along the leading and trailing edges are determined during the preliminary one-dimensional design stage through a consideration of the amount of energy per unit mass of fluid that is to be exchanged in the blade row as a whole. These values must be taken as constant along the leading and trailing edges, since this gives a blade that produces constant work along the span and this has the advantage of not introducing trailing vorticity into the exit flow. In the present example, the value of $r\bar{V}_\theta$ was considered equal to $r\bar{V}_\theta = 0.882\omega r_{tip}^2$ at inlet, and at exit, a zero value of swirl was imposed. At the trailing edge the derivative of $r\bar{V}_\theta$ along the quasi-streamlines was taken as equal to zero ($\partial r\bar{V}_\theta/\partial\xi = 0$) because that was necessary in order to satisfy the Kutta–Joukowski condition. At the leading edge a similar restraint was imposed on the derivative of $r\bar{V}_\theta$ for the reasons discussed above.

Now the problem of choosing an $r\bar{V}_\theta$ distribution reduces to the fitting of a smooth variation of $r\bar{V}_\theta$ between these initial and final values of $r\bar{V}_\theta$ and its derivatives. There are mainly two types of arguments that must be considered during this task. One concerns the evolution of the loading throughout the machine, and the other is related to the amount of twist of the blades, which must be kept within reasonable limits for manufacturing and stress reasons.

According to equation (13), the blade loading (difference in pressure between suction and pressure surfaces) is proportional to the product of the modulus of the relative velocity and the value of the derivative of $r\bar{V}_\theta$ along the meridional projection of the blade streamline, or

$$p^+ - p^- = \frac{2\pi}{B}\,\rho\,|\mathbf{W}_{bl}|\,\frac{\partial r\bar{V}_\theta}{\partial s} \tag{18}$$

where s is distance along the meridional projection of the blade streamline. This means that the pressure loading is essentially determined by the absolute value of $|\mathbf{W}_{bl}|$ and $\partial r\bar{V}_\theta/\partial s$. The first term should vary smoothly from inlet to outlet in a machine well designed. So, the variation in $|\mathbf{W}_{bl}|$ is not going to affect the overall evolution of the pressure loading significantly. Therefore, we can conclude that the pressure loading will roughly follow the value of the derivative of $r\bar{V}_\theta$ along the streamlines. In addition, in a well-designed machine, the direction of the streamlines should be approximately the same as the direction of the quasi-streamlines. This implies that in the above argument, it is reasonable to substitute the derivative of $r\bar{V}_\theta$ along the streamlines by the value of the derivative along the quasi-streamline ($\partial r\bar{V}_\theta/\partial\xi$), and say that the evolution of the pressure loading will follow roughly the shape of the derivative of $r\bar{V}_\theta$ along the quasi-streamlines. This fact provides us with some control over the pressure loading on the blade surfaces since the derivative of $r\bar{V}_\theta$ along the quasi-streamlines can be evaluated from the input and, so, is known from the start. For example, if it is desired to design a blade with a big loading near the leading edge, then the derivatives of the $r\bar{V}_\theta$ distribution along the quasi-streamlines should have large values near the leading edge.

Since the most heavily loaded streamsurface in the rotor of a radial-inflow turbine is the shroud, the behavior of the derivatives of $r\bar{V}_\theta$ should be watched with special care there, specifying an $r\bar{V}_\theta$ distribution with a smooth first derivative.

In addition to providing some control over the pressure distribution on the blade surfaces, the specification of $r\bar{V}_\theta$ also gives some control over the amount of blade twist. That is important, since for stress considerations and for ease of manufacture it is convenient to avoid a highly twisted blade; see, e.g., Jansen and Kirschner (1974). To see how this control comes about, let us take a fresh look at equation (16). This equation implies that the variation in wrap angle along a streamline is proportional to the integral of the blade tangential relative velocity divided by r and the meridional blade velocity, or $(\bar{V}_\theta + v_{\theta bl} - \omega r)/(rV_{mbl})$ (see equation (17)). We do not have any control over the periodic blade tangential velocity $v_{\theta bl}$ since it is a result of the calculations. However, it should be recognized that this term is an order of magnitude smaller than the other two components on the right-hand side of (17), in regions where the flow is well guided. In fact, if the velocity profile in the tangential direction presented a linear variation between the suction and the pressure surfaces, the value of $v_{\theta bl}$ would be zero and the blade tangential relative velocity would be coincident with the mean tangential relative velocity. Since for a radial-inflow turbine the flow can be considered as well guided for most of the flow path, it follows that the term $v_{\theta bl}$ can safely be neglected in this argument. Thus, it can be concluded that the variation in wrap angle along a streamline is approximately proportional to the integral of the mean tangential relative velocity. In other words, if it is desired to avoid large variations in wrap angle, it is necessary to keep the value of $\bar{W}_\theta$ as low as possible by imposing an $r\bar{V}_\theta$ distribution obtained considering a value for $\bar{V}_\theta$ that follows closely the local value of the blade speed ωr. The fact that in the above integral the radius r and the meridional blade velocity appear in the denominator, means that it is more important to keep the mean tangential relative velocity, $\bar{W}_\theta$, small where the radius and the meridional blade velocity are small. So, from the point of view of highly twisted blades, the most critical streamsurface is the hub, not only because there the radius and meridional blade velocity take the lowest values, but also because the meridional flow path is usually much longer along the hub than anywhere else in the machine. For this reason it is advisable to specify

Downloaded 01 Jun 2010 to 171.66.16.66. Redistribution subject to ASME license or copyright; see http://www.asme.org/terms/Terms_Use.cfm

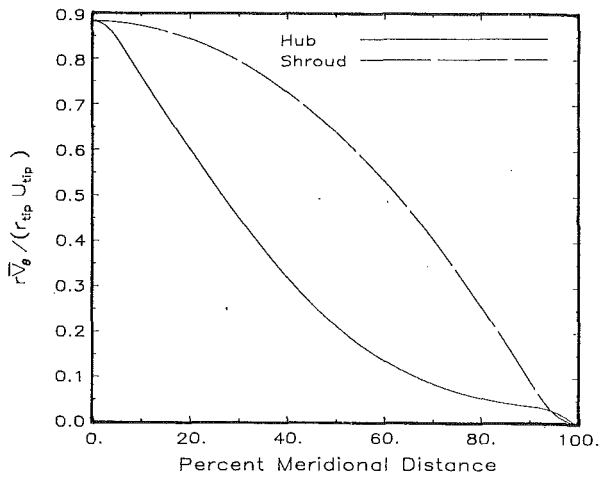

Fig. 2 Input mean swirl distribution at hub and shroud

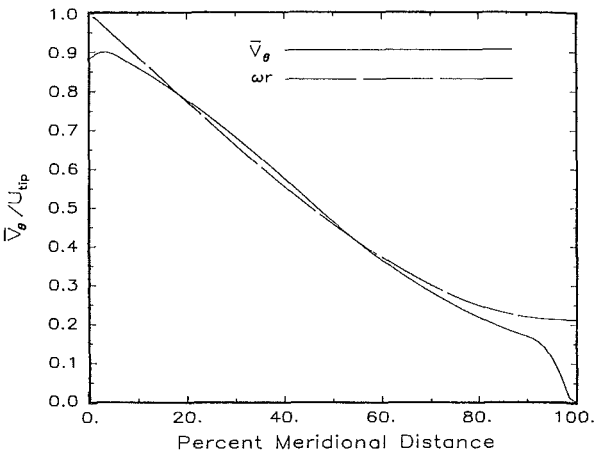

Fig. 3 Mean tangential velocity and blade speed at hub

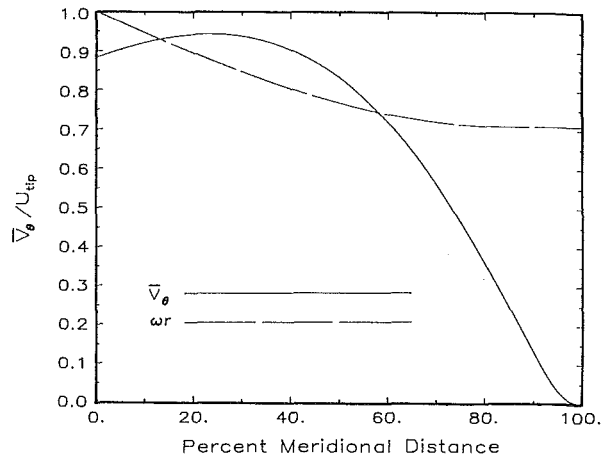

Fig. 4 Mean tangential velocity and blade speed at shroud

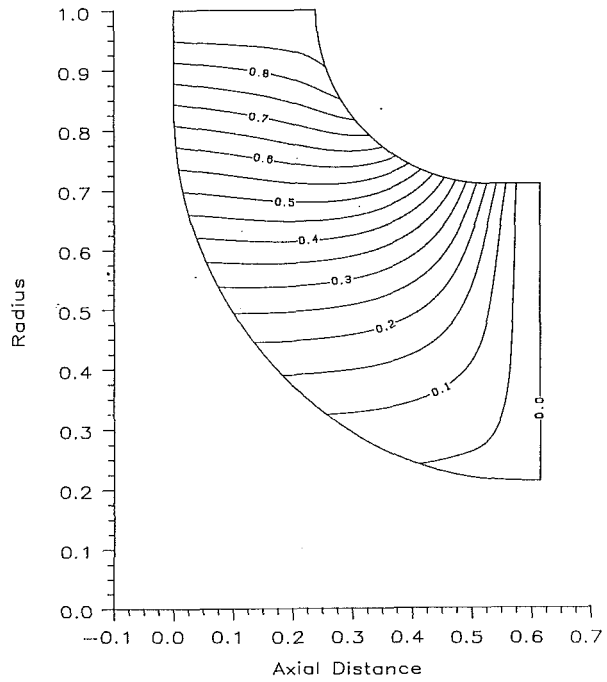

Fig. 5 Contours of the input mean swirl distribution (defined as $r\bar{V}_\theta/(r_{tip}U_{tip})$)

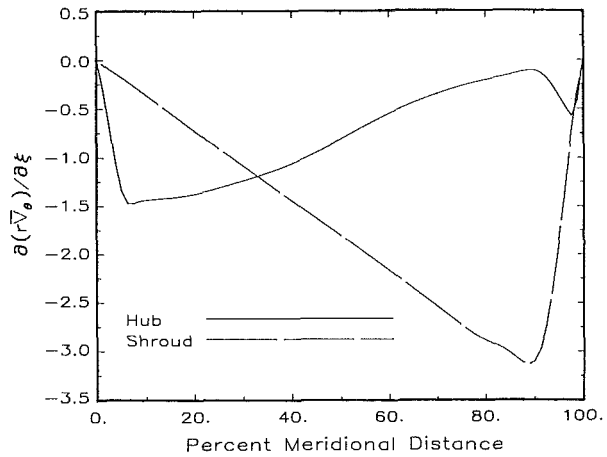

Fig. 6 Derivatives of the input mean swirl distribution

at hub an $r\bar{V}_\theta$ distribution that gives a mean tangential absolute velocity, $\bar{V}_\theta$, similar to the local value of ωr.

The final distribution of $r\bar{V}_\theta$ chosen for a particular design is in general a tradeoff between these two conflicting requirements. As already mentioned, at the shroud, preference should be given to the pressure distribution on the blade surfaces, and at the hub, the principal objective should be to avoid a large variation of wrap angle. Usually this compromise results in a blade that is heavily loaded at the hub inlet, while at the shroud most of the load is concentrated near the trailing edge.

The present application is no exception to this. In Fig. 2, the chosen $r\bar{V}_\theta$ distribution on hub and shroud is plotted as a function of percent meridional distance (here and in the following, flow properties will be nondimensionalized using the tip radius and tip blade speed, unless otherwise stated). Figure 3 is a graph of the specified value of $\bar{V}_\theta$ at hub compared with the local blade speed ωr. This figure shows that at the hub it was necessary to impose a value of $\bar{V}_\theta$ that followed closely the curve of ωr in order to avoid a highly twisted blade. The same does not apply to the shroud, as the next plot, Fig. 4, clearly demonstrates. The next figure, Fig. 5, shows contours of the $r\bar{V}_\theta$ distribution used, and, as can be seen, the imposed variation is smooth everywhere. Finally in Fig. 6 the values of the derivatives of the swirl distribution in the direction of the quasi-streamlines are presented. Notice the smooth and monotonic variation of the derivative of $r\bar{V}_\theta$ at shroud. At the hub, that variation is not monotonic and is less smooth because at the hub the $r\bar{V}_\theta$ distribution was chosen with the main objective of keeping the variation of wrap angle as low as possible.

The program developed was run using these input data, and the blade shape was obtained as output. Figure 7 is a plot of the contours of wrap angle f, on the meridional section of the

Downloaded 01 Jun 2010 to 171.66.16.66. Redistribution subject to ASME license or copyright; see http://www.asme.org/terms/Terms_Use.cfm

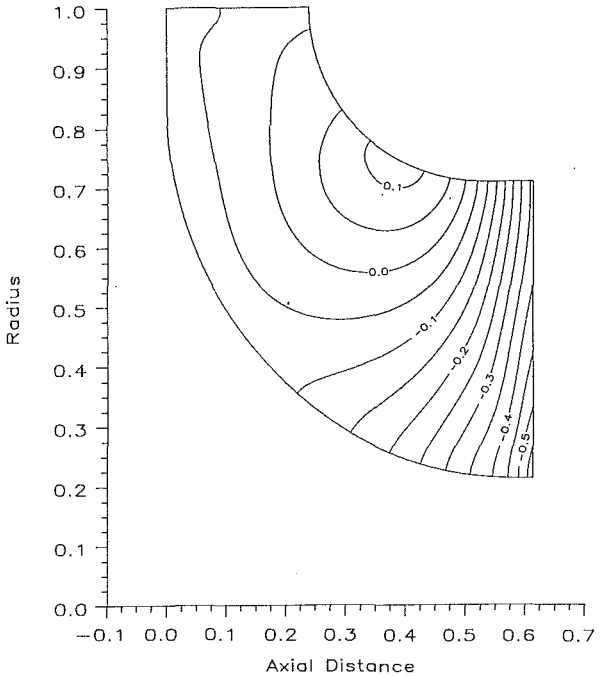

Fig. 7 Contours of wrap angle, f (in rad)

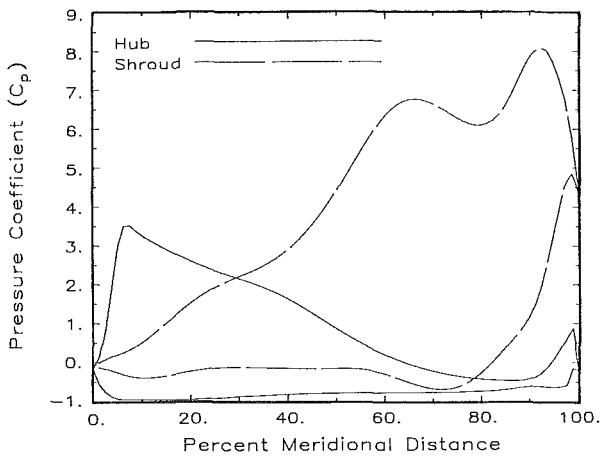

Fig. 8 Pressure distribution on hub and shroud

turbine. From it, it is possible to conclude that the maximum variation of wrap angle is not excessive and is less than two blade pitches. Notice that the resulting blade shape has double curvature and so, it would be very difficult, if not impossible, for a designer to guess such a blade shape. Therefore it is unlikely that this design could ever be reached by an approach of the sort of "cut and try." This fact illustrates one of the advantages of the present indirect technique.

The output of the program also includes the pressure distribution on the blade surfaces, which is presented in the next plot, Fig. 8. The definition of the pressure coefficient used in this plot is

$$C_p = \left[\frac{W}{W_{\text{ref}}} \right]^2 - 1 \tag{19}$$

where W_{ref} was taken as the relative velocity at the intersection of the leading edge with hub (for the present case $W_{\text{ref}} = 0.278\omega r_{\text{tip}}$).

The pressure distribution, shown in Fig. 8, has a reasonable shape throughout, except at the shroud, where it presents a dip in the region near the trailing edge. This dip is caused by

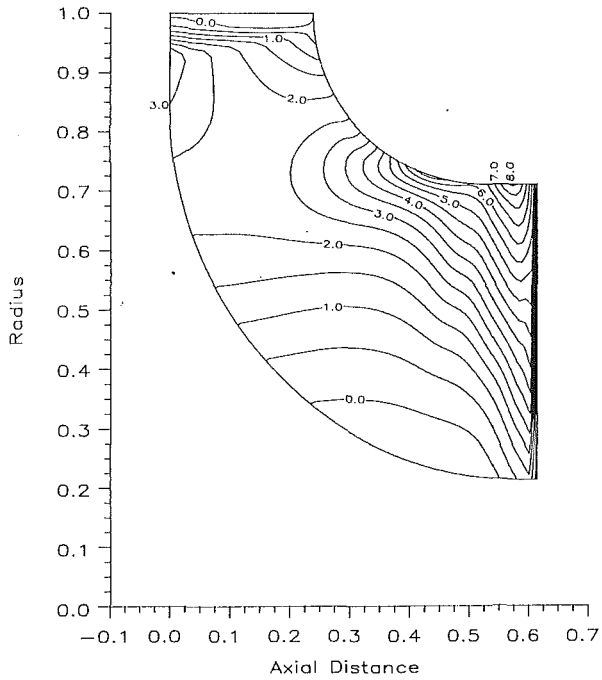

Fig. 9 Contours of pressure coefficient C_p on suction surface

a change of radius of curvature of the shroud profile in the meridional plane (this point corresponds to the intersection of a circular arc and a straight line in the meridional section of the turbine). As this dip is connected with the meridional shape of the turbine, it would be difficult to specify an $r\bar{V}_\theta$ distribution that would avoid it. Therefore, this pressure distribution and the associated mean swirl distribution were accepted. The next plot, Fig. 9, gives the contours of pressure coefficient, C_p, on the suction surface of the blade. As can be seen, the pressure is smooth on the main part of the blade, there being a rapid variation near the trailing edge that is due to the necessary rapid unloading existent there.

It is illuminating to compare the plot of the pressure distribution, Fig. 8, with Fig. 6, giving the derivatives of $r\bar{V}_\theta$. It is seen that the trends of both the blade loading (difference in pressure between suction and pressure surface) and the curves of the $r\bar{V}_\theta$ derivatives are the same, which bears out the comments made previously. In fact, notice that the regions where the $r\bar{V}_\theta$ derivatives are larger (in modulus) correspond to regions in the C_p plot with large values for the pressure loading (at the hub the pressure loading and the $r\bar{V}_\theta$ derivative are larger near the leading edge, while at shroud the opposite happens).

It should be stressed once more that it is not pretended that the present design has an ideal pressure distribution. In fact, the pressure distribution could be improved by a convenient alteration of the meridional section and the $r\bar{V}_\theta$ distribution. This route was not pursued further since the meridional section of the turbine was fixed (it was intended to compare this design with an existing machine). Nevertheless, it is recognized that this particular point needs a lot more research work and that the definition of the best $r\bar{V}_\theta$ distribution for a given meridional section is a desirable extension of the present work.

Another desirable extension of the present work is the inclusion of thickness in the present design program. Nevertheless, it is possible to estimate some of the consequences of the introduction of thickness, namely the effects of blockage introduced into the flow field. This added blockage will increase the blade meridional velocity and consequently, the total velocity. This fact implies that the pressure coefficient will take higher values than those indicated in Figs. 8 and 9, the dif-

Downloaded 01 Jun 2010 to 171.66.16.66. Redistribution subject to ASME license or copyright; see http://www.asme.org/terms/Terms_Use.cfm

ference being bigger where the relative blade blockage is higher, which occurs in the last half of the flowpath near the hub. Therefore, the change in the pressure coefficient at the shroud will be small, and at the hub, the biggest difference will be a reduction in the steepness of the adverse pressure gradient existing there (see Fig. 8). In what concerns the blade shape, the effect of blockage will be a reduction in the total amount of wrap angle variation. This is so because the blade meridional velocity will be increased, thus reducing the value of the integral that gives the variation of wrap angle (see the above discussion on the control over blade twist). This effect is more marked near the hub, which is the most critical streamsurface from the point of view of highly twisted blades. So, it can be concluded that the effect of blockage will ease the difficulties linked with the total amount of blade twist.

4 Conclusions

The present study was motivated by the need for a three-dimensional inverse method. As shown, this is a virtually unexplored field at the present, in spite of the fact that a three-dimensional indirect method is an essential tool for the design of blade rows with significant three-dimensional effects such as rotors for radial turbomachinery.

One such possible three-dimensional inverse method has been successfully developed and is described here. This inverse method was applied to the design of a radial-inflow turbine rotor with the intention of testing the program with a difficult test case and so assessing its usefulness. As far as the author is aware, this is one of the first examples of the design of a rotor for a radial-inflow turbine using a fully three-dimensional inverse method.

The present indirect method uses as design specification an imposition of mean swirl ($r\bar{V}_\theta$) given throughout the meridional section of the turbomachine, and some advice on how to choose this specification was included here. It was shown that the pressure loading on the blades is directly connected to the derivatives of the imposed $r\bar{V}_\theta$. On the other hand, the integral of the difference between the specified value of $\bar{V}_\theta$ and the local blade speed (i.e., the mean relative tangential velocity) is closely linked with the amount of blade twist, a fact that provides us with some control over the variation of wrap angle. This advice was put into practice in the example described here. It was demonstrated that it is possible to obtain a final design with a reasonable pressure distribution on the blade surfaces while keeping the total amount of blade twist within acceptable limits.

Based on the work done, we strongly advise the use of three-dimensional inverse programs to assist in the design of turbomachines with significant three-dimensional effects.

Acknowledgments

This work was supervised by Professor Sir W. R. Hawthorne and done while the author was at the Whittle Laboratory. The help of the staff of this laboratory is gratefully acknowledged. The author is also grateful to Holset Engineering Co. Ltd (England), Churchill College (Cambridge, England), and Junta Nacional de Investigação Científica e Tecnológica—INVOTAN (Portugal) for the financial support they gave to this project.

References

Borges, J. E., 1986, "Three-Dimensional Design of Turbomachinery," Ph.D. Thesis, Cambridge University, Cambridge, U.K.

Brandt, A., 1977, "Multi-Level Adaptive Solutions to Boundary-Value Problems," *Mathematics of Computation*, Vol. 31, No. 138, pp. 333–390.

Dang, T. Q., and McCune, J. E., 1984a, "A Three-Dimensional Blade Design Method in Rotational Flow," *Proceedings, International Conference on Inverse Design Concepts in Engineering Sciences (ICIDES)*, G. S. Dulikravich, ed., University of Texas, Austin, TX.

Dang, T. Q., and McCune, J. E., 1984b, "Design Methods for Highly-Loaded Blades With Blockage in Cascade," *Proceedings, ASME Conference Computation of Internal Flows: Methods and Applications*, P. M. Sockel and K. N. Ghia, eds., pp. 129–136.

Garabedian, P., and Korn, D., 1976, "A Systematic Method for Computer Design of Supercritical Airfoils in Cascade," *Comm. Pure Appl. Math.*, Vol. 29, pp. 369–382.

Jansen, W., and Kirschner, A. M., 1974, "Impeller Blade Design Method for Centrifugal Compressors," NASA SP 304, Pt. 2, pp. 537–563.

Jennions, I. K., and Stow, P., 1984, "A Quasi-Three-Dimensional Turbomachinery Blade Design System: Part I—Throughflow Analysis; Part II—Computerized System," ASME *Journal of Engineering for Gas Turbines and Power*, Vol. 107, No. 2, pp. 301–316.

Lewis, R. I., 1982, "A Method for Inverse Aerofoil and Cascade Design by Surface Vorticity," ASME Paper No. 82-GT-154.

Lighthill, M. J., 1945, "A Mathematical Method of Cascade Design," ARC Rep. & Mem. 2104.

Meauzé, G., and Lesain, A., 1984, "Use of an Inverse Method for the Design of High Efficiency Compressor and Turbine Blades With Large Change in Radius," ASME Paper No. 84-GT-167.

Novak, R. A., and Haymann-Haber, G., 1983, "A Mixed-Flow Cascade Passage Design Procedure Based on a Power Series Expansion," ASME *Journal of Engineering for Power*, Vol. 105, pp. 231–242.

Roache, P. J., 1982, *Computational Fluid Dynamics*, Hermosa Publishers, Albuquerque, NM, pp. 84–85.

Schmidt, E., 1980, "Computation of Supercritical Compressor and Turbine Cascades With a Design Method for Transonic Flows," ASME *Journal of Engineering for Power*, Vol. 102, No.1, pp. 68–74.

Sobieczky, H., and Dulikravich, D. S., 1982, "A Computational Design Method for Transonic Turbomachinery Cascades," ASME Paper No. 82-GT-117.

Tan, C. S., Hawthorne, W. R., McCune, J. E., and Wang, C., 1984, "Theory of Blade Design for Large Deflections: Part II—Annular Cascades," ASME *Journal of Engineering for Gas Turbines and Power*, Vol. 106, No. 2, pp. 354–365.

Thompson, J. F., Thames, F. C., and Mastin, C. W., 1977, "Boundary-Fitted Coordinate Systems for Numerical Solution of Partial Differential Equations on Fields Containing Any Number of Arbitrary Two-Dimensional Bodies," NASA CR 2729.

Wang, Z., 1985, "Inverse Design Calculations for Transonic Cascades," ASME Paper No. 85-GT-6.

Weber, H. G., and Mulloy, J., 1983, Private Communication, Cummins Engine Co.

Wright, L. C., and Novak, R. A., 1960, "Aerodynamic Design and Development of the General Electric CJ805-23 Aft Fan Component," ASME Paper No. 60-WA-270.

Zhao, X.-L., Sun, C.-L., and Wu, C.-H., 1985, "A Simple Method for Solving Three-Dimensional Inverse Problems of Turbomachine Flow and the Annular Constraint Condition," ASME *Journal of Engineering for Gas Turbines and Power*, Vol. 107, pp. 293–300.

APPENDIX

The generation of the numerical grid gives us a relation of the form

$$r = r(\xi, \eta) \qquad z = z(\xi, \eta) \tag{20}$$

where (r, z) are the coordinates in the physical domain and (ξ, η) are the coordinates in the numerical plane. Then, in this numerical plane, equation (10) takes the form

$$\delta\Phi^c_{\xi\xi} - 2\beta\Phi^c_{\xi\eta} + \gamma\Phi^c_{\eta\eta} + \Phi^c_\xi\left[\frac{z_\eta Dy - r_\eta Dx}{J} - \frac{Jz_\eta}{r}\right] + \Phi^c_\eta\left[\frac{r_\xi Dx - z_\xi Dy}{J} + \frac{Jz_\xi}{r}\right] - \left[\frac{JkB}{r}\right]^2\Phi^c = -[\nabla^2 r\bar{V}_\theta]\frac{2\sin(kBf)}{kB} + [\nabla\alpha\cdot\nabla r\bar{V}_\theta]2\cos(kBf) \tag{21}$$

and equation (11) transforms into

$$\delta\Phi^s_{\xi\xi} - 2\beta\Phi^s_{\xi\eta} + \gamma\Phi^s_{\eta\eta} + \Phi^s_\xi\left[\frac{z_\eta Dy - r_\eta Dx}{J} - \frac{Jz_\eta}{r}\right] + \Phi^s_\eta\left[\frac{r_\xi Dx - z_\xi Dy}{J} + \frac{Jz_\xi}{r}\right] - \left[\frac{JkB}{r}\right]^2\Phi^s = [\nabla^2 r\bar{V}_\theta]\frac{2\cos(kBf)}{kB} + [\nabla\alpha\cdot\nabla r\bar{V}_\theta]2\sin(kBf) \tag{22}$$

Downloaded 01 Jun 2010 to 171.66.16.66. Redistribution subject to ASME license or copyright; see http://www.asme.org/terms/Terms_Use.cfm

with the transformation parameters used in these equations defined as

$$\begin{aligned} J &= z_\xi r_\eta - z_\eta r_\xi \\ \delta &= z_\eta^2 + r_\eta^2 \\ \beta &= z_\xi z_\eta + r_\xi r_\eta \\ \gamma &= z_\xi^2 + r_\xi^2 \\ Dx &= \delta z_{\xi\xi} - 2\beta z_{\xi\eta} + \gamma z_{\eta\eta} \\ Dy &= \delta r_{\xi\xi} - 2\beta r_{\xi\eta} + \gamma r_{\eta\eta} \end{aligned} \tag{23}$$

and where a subscript denotes differentiation with respect to that variable.

The mean flow can be solved using the potential or the streamfunction concept, both approaches being equivalent. Although in the main text the equation for the potential was presented (equation (9)), in the program preference was given to the equation using the streamfunction concept (see Borges, 1986). So, in the transformed plane, the equation to be solved for the mean flow is

$$\delta\Psi_{\xi\xi} - 2\beta\Psi_{\xi\eta} + \gamma\Psi_{\eta\eta} + \Psi_\xi\left[\frac{z_\eta Dy - r_\eta dx}{J} + \frac{Jz_\eta}{r}\right] + \Psi_\eta\left[\frac{r_\xi Dx - z_\xi Dy}{J} - \frac{Jz_\xi}{r}\right] = -rJ[f_\xi(r\bar{V}_\theta)_\eta - f_\eta(r\bar{V}_\theta)_\xi] \tag{24}$$

The blade boundary condition (equation (16)), used to update the blade shape f, is transformed into

$$[\bar{V}_\xi + v_{\xi bl}]f_\xi + [\bar{V}_\eta + v_{\eta bl}]\, f_\eta = J\left[\frac{r\bar{V}_\theta}{r^2} + \frac{v_{\theta bl}}{r} - \omega\right] \tag{25}$$

with $\bar{V}_\xi$, $\bar{V}_\eta$, $v_{\xi bl}$, $v_{\eta bl}$, and $v_{\theta bl}$ calculated with the help of the following formulae:

$$\bar{V}_\xi = \frac{J\Psi_\eta}{r} \tag{26}$$

$$\bar{V}_\eta = -\frac{J\Psi_\xi}{r} \tag{27}$$

$$v_{\xi bl} = \sum_{k=1}^{N} [\delta\Phi_\xi^c - \beta\Phi_\eta^c]\cos(kBf) + \sum_{k=1}^{N} [\delta\Phi_\xi^s - \beta\Phi_\eta^s]\sin(kBf) \tag{28}$$

$$v_{\eta bl} = \sum_{k=1}^{N} [\delta\Phi_\eta^c - \beta\Phi_\xi^c]\cos(kBf) + \sum_{k=1}^{N} [\delta\Phi_\eta^s - \beta\Phi_\xi^s]\sin(kBf) \tag{29}$$

$$v_{\theta bl} = \sum_{k=1}^{N} \frac{kB}{r}\Phi_k^c\cos(kBf) + \sum_{k=1}^{N} \frac{kB}{r}\Phi_k^s\sin(kBf) \tag{30}$$

Note that in equations (28) and (29) we omitted the subscript k from Φ for clarity's sake.

Downloaded 01 Jun 2010 to 171.66.16.66. Redistribution subject to ASME license or copyright; see http://www.asme.org/terms/Terms_Use.cfm

A Three-Dimensional Inverse Method for Turbomachinery: Part II—Experimental Verification

J. E. Borges
Department of Mechanical Engineering,
Instituto Superior Técnico,
1096 Lisboa Codex, Portugal

The performance of an impeller of a low-speed radial-inflow turbine, designed using a three-dimensional inverse technique, was evaluated experimentally. This performance was compared with that achieved by a rotor typical of the present technology. Besides measuring overall quantities, in special efficiency, some traverses of flow velocity were carried out. The results of the tests showed that the new design had a peak total-to-static efficiency 1.4 points better than the conventional build. The traverses indicated that the level of swirl at exhaust of the new impeller was only half as big as that for the conventional rotor, in spite of the fact that both impellers were designed to have zero swirl at outlet. It is also shown that the rotor loss for the new impeller is considerably lower than for the conventional wheel. This research points to the desirability of using a three-dimensional inverse method for the design of turbomachines with significant three-dimensional flows.

1 Introduction

In Part I (Borges, 1990), a three-dimensional inverse method was described that used as design specification a mean swirl (radius times mean tangential velocity, $r\bar{V}_\theta$) distribution given throughout the meridional section of the blade row. This method can be applied to turbomachines with an arbitrary meridional section and any amount of fluid deflection. The application of this indirect technique to the design of a rotor for a radial-inflow turbine was also discussed in that paper. This particular kind of turbomachine was chosen because it is a machine with significant three-dimensional flows, therefore providing a good test case of the developed program.

The rotor designed using this inverse technique was built and tested. It is the objective of the present paper to describe the experimental results obtained. The experimental program consisted of the comparison of the overall performance of the new rotor, designed using the described inverse method, with that given by a rotor designed using methods typical of the present state of the art. By doing this comparison, a simple and accurate assessment of the usefulness of the developed inverse method can be done.

The tests were done using a large-scale, low-speed model of a radial-inflow turbine. This means that the velocities were kept at a low level, leading to incompressible flow, one of the conditions of applicability of the inverse method described. The large dimensions also had the additional bonus of permitting good accuracy for the measurements to be made. In addition to the measurement of the overall performance, some detailed flow measurements were made with the intention of clarifying the differences observed in the overall performance of both rotors.

2 Experimental Apparatus and Geometry of Rotors

The layout of the test rig is presented in Fig. 1. Air is sucked through a bellmouth into the turbine directly from the atmosphere. Then it moves radially through section A, where the volume flow passing through the turbine is evaluated by measuring the local static pressure relative to atmospheric. This is followed by the stator (formed by 31 blades with a chord of 64 mm) which deflect the air flow to a direction almost tangential (making a design angle of 74 deg with the radius). Some measurements of the velocity field were made at station B, in the interspace between rotor and stator. Following the stator comes the rotor, where the energy is extracted from the air flow. After the rotor, the air enters the outlet duct. The initial length (around 400 mm) of this exit duct has the shape of an annular duct, which was achieved by introducing a center body fixed to the external duct by a series of struts. It was decided to put the center body into the exit duct to avoid a sudden expansion in the flow path. This abrupt expansion would lead to a separation and a very complicated three-dimensional flow, which would be very difficult to measure and analyze accurately. Downstream of the rotor, provision was made for the measurement of the static pressure at the station marked C in Fig. 1. There were three pressure tappings equally spaced circumferentially on the center body and another three equally spaced pressure tappings on the external duct. The three tappings on the center body were interconnected and the same was done for the tappings on the outer diameter. The pressure indicated by these two groups of tappings was measured separately. The value of downstream static pressure used in the calculation of the overall per-

Contributed by the International Gas Turbine Institute and presented at the 34th International Gas Turbine and Aeroengine Congress and Exhibition, Toronto, Ontario, Canada, June 4–8, 1989. Manuscript received at ASME Headquarters January 23, 1989. Paper No. 89-GT-137.

Copyright © 1990 by ASME
Downloaded 01 Jun 2010 to 171.66.16.66. Redistribution subject to ASME license or copyright; see http://www.asme.org/terms/Terms_Use.cfm

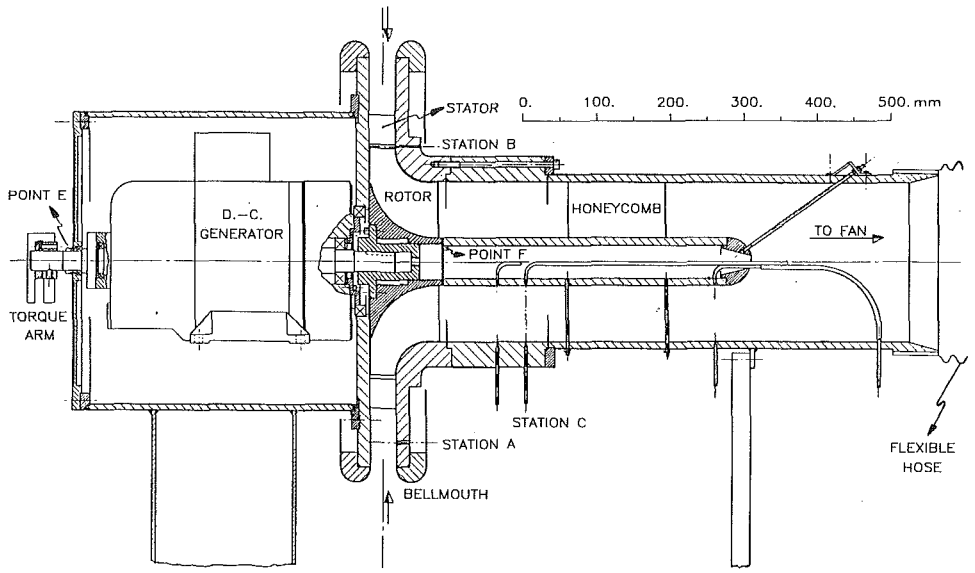

Fig. 1 Layout of rig

formance was the average of the center body and outer diameter pressures. This was done because, as is well known, at exit from a radial-inflow turbine the static pressure is not uniform radially, even for peak efficiency conditions (see Kofskey and Wasserbauer, 1966; Kofskey and Nusbaum, 1972; and Sasaki et al., 1977).

It was also possible to make a radial traverse for the measurement of velocity field and total pressure, using a three-hole probe, at this same station C. Following this station was a section of annular duct filled with a honeycomb, which had the function of extracting any swirl present at the outlet of the rotor. The end of the outlet duct was connected to a flexible hose that led the air flow into a radial fan, which sucked the air through the turbine.

The work done by the turbine was absorbed by a d-c electric motor-generator. The stator frame of this generator was cradle-mounted, allowing the measurement of the torque with the help of a torque arm (see Fig. 1). As the rotor of the turbine was mounted directly onto the shaft of the generator, the rotational speed was measured using an optical pickup placed on the center body, point F (Fig. 1). Care was taken in order to avoid leaks of air into the flow path. For example, the generator was enclosed in a cylindrical box sealed from the atmosphere at the point furthest removed from the turbine—point E in Fig. 1.

Since we are going to compare the performance of both impellers quantitatively, it is important to discuss the error involved in the measurements of the overall performance in order to make sure that any differences present are significant and not due to experimental errors. Borges (1986) presents an estimate for the errors involved in the different physical quantities and concludes that the maximum relative error in each individual measurement of efficiency is 2.5 percent (to this value corresponds a probable error of 1.3 percent). This level of relative errors is typical of what can be achieved when testing small power radial-inflow turbines, judging by other examples and estimates presented in the open literature (see, for example, Futral et al., 1969). As the expected differences between the rotors were small, it was important to make the influence of the experimental errors as small as possible and to quantify their effect accurately. So, in order to minimize the deleterious effects of these experimental errors, the curve of efficiency was calculated using a large number of points as will be shown later on. In this way, a clear idea of the scatter present in the data will be obtained.

In what follows, we will also report the results of some traverses made with a three-hole probe used in the null-yaw mode and mounted in a manually driven traverse gear. This three-hole probe was calibrated against a standard pitot tube in a separate low-speed wind tunnel, for the same range of speeds likely to be found in the tests. Based on the results of the calibrations, it is estimated that the maximum error in the measurement of velocity is 1 percent and in the velocity direction is 1.5 deg. For points near the endwalls (within a distance of about 2.2 mm) the errors involved in the measurements of velocity and flow angle may be bigger than those just mentioned due to wall proximity effects (the experimental data were not corrected for this effect). The estimated error in the positioning of the probe is 0.5 mm in the radial direction. For further information on the test rig and the three hole probe see Borges (1986).

The radial-inflow turbine tested in the above rig was designed so that it is typical of small gas turbine practice. The specific speed defined as

Nomenclature

D = tip diameter of rotor
f = angular coordinate of blade surface (wrap angle), deg
N_s = specific speed (nondimensional; see equation (1))
p = pressure
Q = volume flow
r = radius
$r\bar{V}_\theta$ = mean swirl
Re = Reynolds number
U = blade speed
V = absolute velocity
z = axial coordinate
η = efficiency
ν = kinematic viscosity
ρ = density
ω = rotational speed

Subscripts

o = stagnation value
tip = tip of impeller
1 = conditions at inlet to the stator
2 = conditions at inlet to the rotor
3 = conditions at exit from the rotor

Downloaded 01 Jun 2010 to 171.66.16.66. Redistribution subject to ASME license or copyright; see http://www.asme.org/terms/Terms_Use.cfm

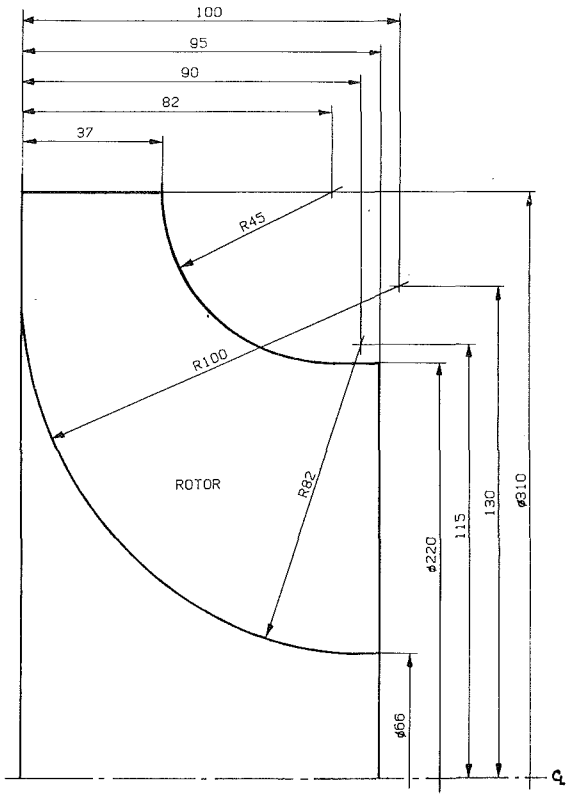

Fig. 2(*a*) Meridional geometry of rotor (common to both rotors); dimensions are in mm

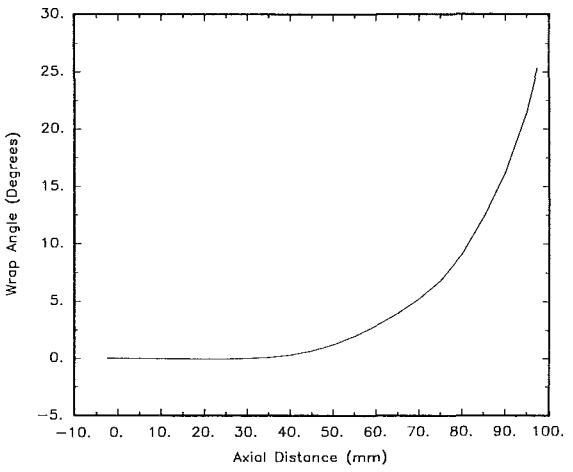

Fig. 2(*b*) Wrap angle (*f*(*z*)) distribution for conventional rotor (wrap angle in deg and axial distance in mm)

$$N_s = \frac{\omega\sqrt{Q}}{\left[\frac{(p_{o1}-p_{o3})}{\rho}\right]^{3/4}} \tag{1}$$

was chosen equal to 0.6, since it is for a specific speed around this value that one can expect the best level for the static-to-total efficiency in radial-inflow turbines. The preliminary one-dimensional design of this turbine was based on the theory advanced by Rohlik (1968), choosing for the tip diameter of the rotors a value of 310 mm.

As already mentioned, two different impellers were tested in this radial-inflow turbine rig. The first one, which will be called the conventional rotor from now on, was designed using iteratively an analysis program and is characterized by having radial blades. The program used was a streamline curvature through-flow program based on the method described by Vanco (1972). This analysis program was used to predict the flow field for slightly different geometries (but maintaining always the restriction of radial blades). The final geometry chosen was the one that gave the best distribution for the velocities on the blade surfaces and an exit swirl equal to zero. This geometry is defined in Fig. 2(*a*) where the meridional geometry is given (note that the meridional geometry was kept the same for both rotors) and in Fig. 2(*b*) where the wrap angle distribution used is plotted (since the conventional rotor has radial blades, the wrap angle is only a function of the axial distance, z. The function $f(z)$ is plotted in Fig. 2*b*).

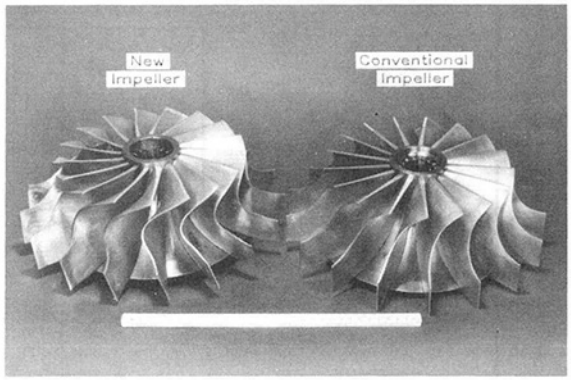

Fig. 3 Rotors side by side

The second impeller, which will be called the new rotor from now on, was designed using the method described in Part 1 of this paper (Borges, 1990), and its geometry is defined in more detail there. Further information on the design of both rotors can be found in Borges (1986).

A photograph of the two impellers side by side is presented in Fig. 3, and it can be seen that they are quite different. Therefore this work has the additional interest of presenting experimental results for two very different rotors, designed using two completely different philosophies.

As the tip gap could have a major effect on the rotor performance, it is convenient to indicate its value for the tests done. The inlet tip clearance was equal to 0.56 mm (1.5 percent of span) and the exit tip clearance was equal to 0.58 mm (0.75 percent of span). A more careful check, made only for the new impeller, showed that the exit tip clearance varied in the circumferential direction from a minimum value of 0.41 mm to a maximum value of 0.64 mm (0.83 percent of span). These measured values of tip clearance are so small that they will not have significant effects on the efficiency, according to the conclusions advanced in Futral and Holeski (1970).

3 Experimental Results

The first set of experimental results to be shown consists in all the measured points for the total-to-static efficiency of both rotors as a function of volume flow, presented in Fig. 4. In this figure, the volume flow was made nondimensional by dividing it by ωD^3 (D is the tip diameter of the impellers). For nominal conditions, the Reynolds number, defined as $\mathrm{Re} = (\omega D^2/\nu)$, was equal to 2.1×10^6.

It can be seen from Fig. 4 that the conventional rotor shows a mean peak value for the total-to-static efficiency of around 0.876 percent. This value compares quite favorably with what can be achieved with the current technology. In fact, Rohlik (1968) predicts a maximum value of the total-to-static efficiency of 0.87 percent for a specific speed around 0.6. Published experimental results corroborate this conclusion. For exam-

Downloaded 01 Jun 2010 to 171.66.16.66. Redistribution subject to ASME license or copyright; see http://www.asme.org/terms/Terms_Use.cfm

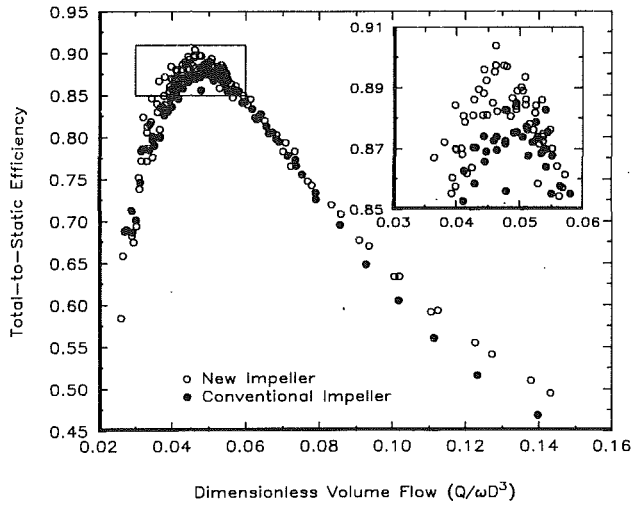

Fig. 4 Measured total-to-static efficiency (the Reynolds number for nominal conditions is $Re = 2.1 \times 10^6$)

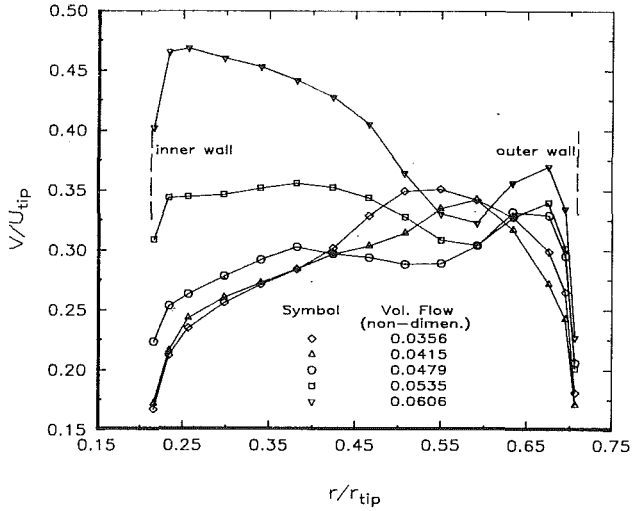

Fig. 5(a) Absolute velocity profile downstream of rotor at station C; conventional impeller

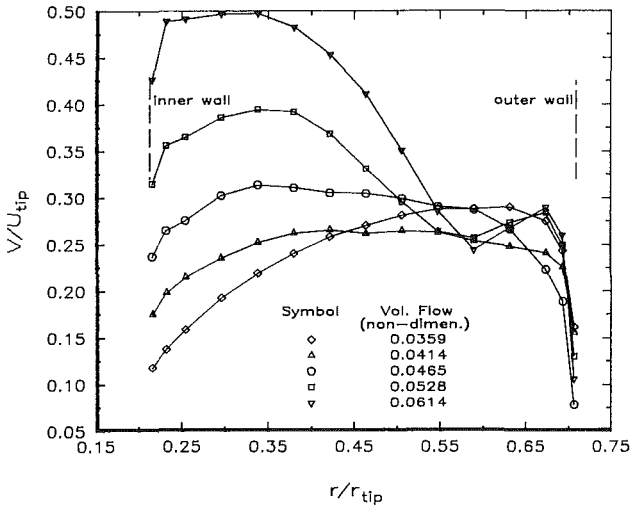

Fig. 5(b) Absolute velocity profile downstream of rotor at station C; new impeller

ple, Kofskey and Wasserbauer (1966) measured an absolute maximum total-to-static efficiency of 0.87 percent for a specific speed of 0.67 and Kofskey and Nusbaum (1972) reported a value of 0.880 percent for a specific speed of 0.59. More recently Ribaud and Mischel (1986) measured a maximum value of 0.883 percent for the total-to-static efficiency of a radial-inflow turbine characterized by a specific speed equal to 0.58. All these results indicate that the efficiency levels obtained in our tests are typical of the present know-how. Therefore, the conventional rotor provides a good standard against which to compare the performance of the new impeller.

Doing this comparison, it is seen that the new rotor shows a mean peak value for the total-to-static efficiency of around 0.890 percent, which is 1.4 percent better than the corresponding value for the conventional impeller. This difference between the efficiency of the two rotors is significant since it is greater than the probable error (1.3 percent) in the measurement of efficiency. Reflecting this conclusion is the fact that all the measured points for the new rotor fall systematically above those obtained for the conventional rotor, near peak efficiency conditions ($Q/(\omega D^3) \simeq 0.046$; see inset in figure). Notice that the efficiency near peak efficiency conditions was measured for a good number of points in order to be able to ascertain the scatter in the experimental points as accurately as possible.

The comparison of the efficiency levels of both impellers also show that the gains were achieved over most of the tested range of volume flows, although for volume flows smaller than nominal conditions and in the range $0.055 < Q/(\omega D^3) < 0.08$, the difference between both impellers is small. For very large volume flows ($Q/(\omega D^3) > 0.08$) the gains in efficiency increase again, reaching a value of 3.4 percent for the highest volume flows tested ($Q/(\omega D^3) \simeq 0.14$).

Now that an improvement in the total-to-static efficiency has been demonstrated, the next question that arises is why it is so, and the reasons for these differences. A complete answer to this question would require detailed flow measurements made inside the rotors, measurements that were not carried out. Nevertheless, it is possible to shed some light on this question by analyzing the results of measurements obtained downstream of the rotors (at station C). This will be our aim in the following.

The first set of results (Figs. 5*a*, *b*) to be presented give the measured absolute velocity downstream of the rotors. Figure 5(*a*) shows the velocity profiles obtained with the conventional rotor for five different volume flows, their values being indicated in the figure (peak efficiency conditions corresponding to $(Q/(\omega D^3) = 0.0479)$. Figure 5(*b*) presents the corresponding results for the new rotor (peak efficiency conditions are obtained for a value of $Q/(\omega D^3) = 0.0466$). In these plots, the radius was made nondimensional, dividing it by the tip radius of the impellers (r_{tip}), and the velocity was nondimensionalized using the blade tip speed ($U_{tip} = \omega r_{tip}$).

The results for both rotors show similar trends. In fact, the overall shape of the velocity profiles change a lot, becoming more nonuniform for larger volume flows. As the volume flow increases, the general level of the absolute velocity increases markedly near the hub, while remaining roughly the same near the shroud. Notice also that the velocity profiles for both impellers are not uniform in the spanwise direction even for peak efficiency conditions. Nevertheless, for peak efficiency conditions, the new impeller shows a more uniform profile than the conventional rotor.

An important variable in the inverse method described here is the mean swirl, $r\bar{V}_\theta$. So, it is interesting to evaluate its value from the results of the downstream traverses and to compare it for both rotors. That is done in the next two figures, Fig. 6(*a*), giving the measured values of mean swirl for the conventional rotor, and Fig. 6(*b*) for the new impeller. A positive value of $r\bar{V}_\theta$ corresponds to a component of $\bar{V}_\theta$ in the direction of rotation of the impeller, the radius and velocity being made nondimensional in the same way as in Fig. 5.

Downloaded 01 Jun 2010 to 171.66.16.66. Redistribution subject to ASME license or copyright; see http://www.asme.org/terms/Terms_Use.cfm

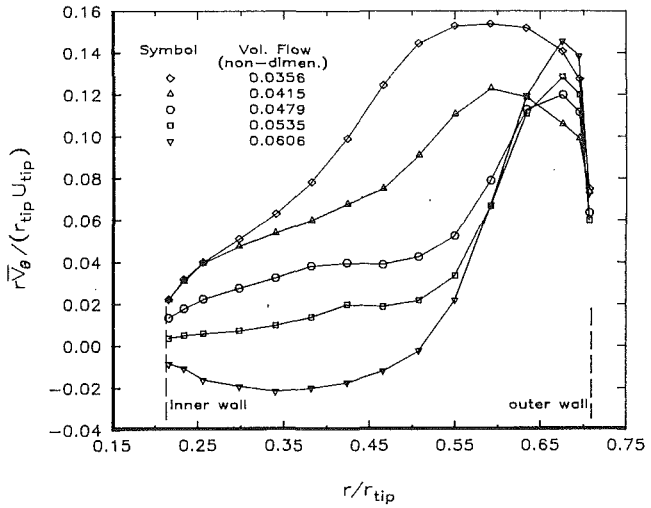

Fig. 6(*a*) Swirl downstream of rotor at station C; conventional impeller

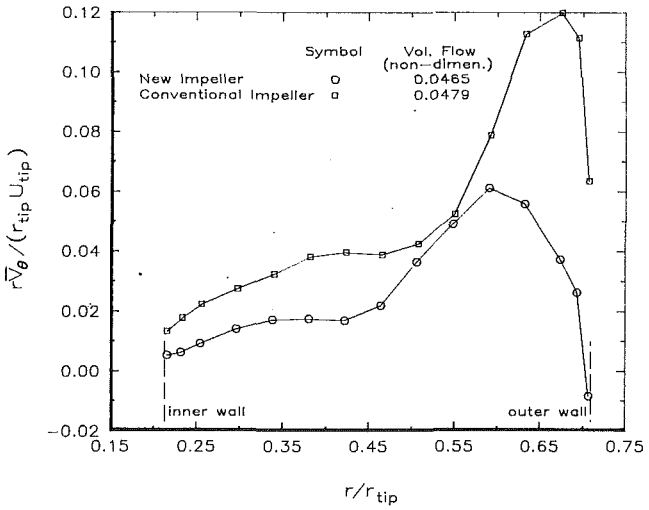

Fig. 7 Comparison of downstream swirl for peak-efficiency conditions

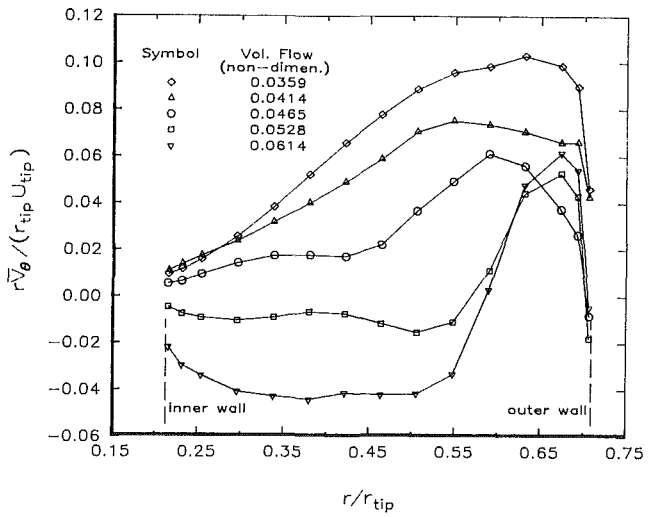

Fig. 6(*b*) Swirl downstream of rotor at station C; new impeller

Both set of results (Figs. 6*a*, *b*) show that, as the volume flow increases, the general level of $r\bar{V}_\theta$ tends to decrease and that its profile becomes more peaky, with the peak occurring near the shroud. It can also be seen that there are significant portions of the exit flow with values of $r\bar{V}_\theta$ quite different from zero for all volume flows tested (including peak efficiency conditions). It should be emphasized that the nonuniform variation of downstream mean swirl, $r\bar{V}_\theta$, is not peculiar to these particular tests but, rather, seems to be common to other published results. For example, Kofskey and Wasserbauer (1966) concluded that for all the radial-inflow turbines they tested, there was a nonuniform distribution of work in the spanwise direction, with minimum work occurring at the shroud. This is exactly the same trend observed here.

As is well known, the exit tangential component of the absolute velocity is very difficult to recover efficiently, using a downstream axial diffuser. So, the angular momentum associated with this tangential component will be thrown away without taking advantage of the potential it has. Not only is this component lost, but it also has a very unpleasant implication in case the $r\bar{V}_\theta$ is not uniform along the span (as in the present case). In fact, assuming irrotational flow at inlet to the impeller, the nonuniformity of $r\bar{V}_\theta$ will imply that there are trailing vortices being introduced at the trailing edges of the rotor blades. These vortices cause a nonuniform velocity profile, which has a larger kinetic energy than the minimum possible and thus penalizes unnecessarily the total-to-static efficiency. In this connection and corroborating the above statement note that the absolute velocity profiles (Figs. 5*a*, *b*) show a pronounced dip located exactly in the same region where there is a rapid variation of $r\bar{V}_\theta$ (see Figs. 6*a*, *b*). Note also that as the volume flow increases, both effects become more marked.

From the foregoing, it is obvious that it is desirable to have a mean swirl at exit as small and as uniform as possible. Indeed, both rotors were designed for an exit mean swirl constant along the span and equal to zero. In this respect the new rotor performed much better than the conventional rotor as the comparison of the downstream mean swirl for peak efficiency conditions, presented in Fig. 7, clearly shows. In fact, the new impeller shows an $r\bar{V}_\theta$ level that is approximately only half as big as the one observed for the conventional rotor. More significantly, the gradients of $r\bar{V}_\theta$ are smaller for the new design. This smaller level of $r\bar{V}_\theta$ and its gradient suggests that the flow through the turbine was more accurately predicted in the new design, thus implying that the application of this inverse program was a move in the right direction. Notice also that, as was to be expected from the above arguments, the reduced value of the gradients of $r\bar{V}_\theta$ leads to a more uniform measured velocity profile (compare Figs. 5*a*, *b*). This more uniform exit flow not only reflects itself in a better total-to-static efficiency, but also means that all the downstream components will be more easily projected since they receive a cleaner flow. This is particularly true of the downstream diffuser that will perform so much the better the more uniform is the flow at exit of the rotor.

Since the flow conditions were measured both upstream and downstream of the rotors, it is possible to calculate the variation of local loss as a function of radius. This loss is defined as:

$$\left[\text{local loss} = 1 - \frac{\rho[U_2 V_{2\theta} - U_3 V_{3\theta}]_{\text{streamline}}}{[p_{o2} - p_{o3}]_{\text{streamline}}}\right] \qquad (2)$$

where the subscripts 2 and 3 refer to upstream and downstream conditions, respectively, and p_o is the total pressure. The subscript streamline means that both quantities inside the bracket lie along the same streamline. The streamlines were traced back from downstream to upstream by assuming that the volume flow that passed between them and the hub was the same. Upstream conditions were calculated by interpolating in the pitch average profiles of the measured variables (see Borges, 1986).

The variation of local loss with radius for the conventional

Downloaded 01 Jun 2010 to 171.66.16.66. Redistribution subject to ASME license or copyright; see http://www.asme.org/terms/Terms_Use.cfm

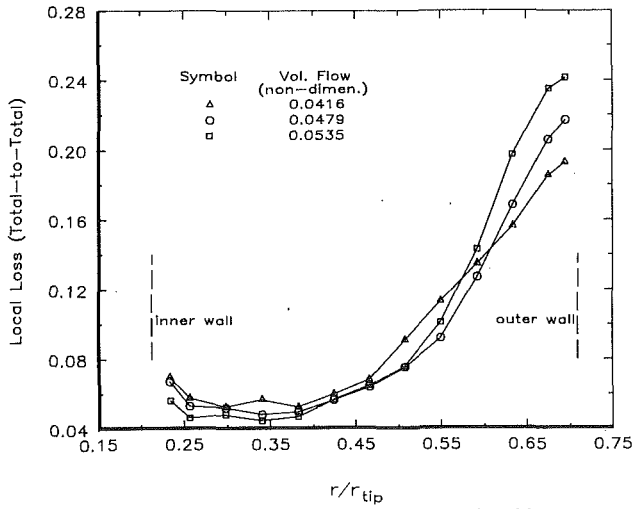

Fig. 8(*a*) Local rotor loss (total-to-total); conventional impeller

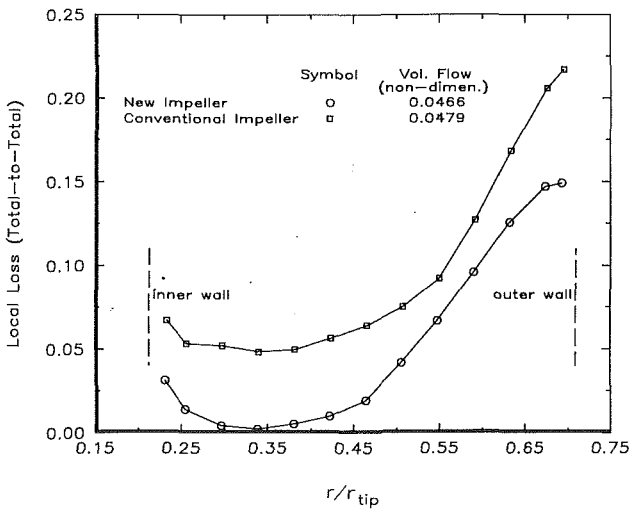

Fig. 9 Comparison of local rotor loss (total-to-total)

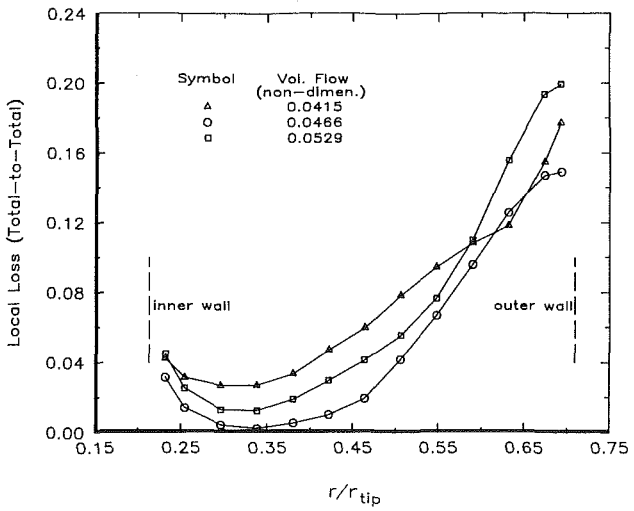

Fig. 8(*b*) Local rotor loss (total-to-total); new impeller

rotor is given in Fig. 8(*a*), and for the new rotor in Fig. 8(*b*). In these two figures, only three different vlaues of volume flow are considered because it is only for these volume flows that traverses were made upstream of the rotors. The exact values of the volume flows considered are indicated in the figures. As can be seen in both figures, the local loss takes, on average, the smallest values for peak efficiency conditions as one would expect.

All the curves for the conventional rotor show the same trend, with the loss increasing sharply near the shroud, and reaching there values much higher than at the hub. This large increase of the rotor loss toward the shroud indicates that something anomalous is happening near the shroud, possibly a flow separation. However, the experimental evidence gathered does not permit us to reach this conclusion with certainty. The general trend described above is also typical of other tests reported in the literature (see Kofskey and Wasserbauer, 1966, and Kofskey and Nusbaum, 1972).

The local loss curves for the new rotor show trends similar to those already discussed above, the biggest difference lying in the lower level for the measured local loss. This can be seen more clearly in Fig. 9, which presents a direct comparison of the local loss for peak efficiency conditions. The curve for the new impeller is consistently below that for the conventional impeller all along the span and not in a concentrated region. It should also be noted that the loss for the new impeller is very small between the hub and midspan, almost reaching a zero value.

Based on the results for the absolute velocity, mean swirl, and local loss, it can be said that the conventional rotor is typical of the present technology, not only in what concerns the measured efficiency level but also with respect to the detailed fluid behaviour inside the rotor. The new rotor presents better efficiency, a smaller mean swirl at exit, smaller local loss, and a slightly more uniform downstream velocity profile. Of course, it is recognized that the new impeller has some disadvantages, in that it is more expensive and difficult to manufacture than the conventional make. Nevertheless, it should find application in situations where efficiency is of paramount importance.

At this point it should be stressed that the above improvement in efficiency and flow field was brought about not based on experimental information from the tests of the conventional rotor but rather based on theoretical considerations and the application of the inverse method. This is exactly the opposite of what is usually done (see, e.g., Sasaki et al., 1977, where the improvements were obtained based on experimental information) and demonstrates the usefulness of the inverse program described in Part I.

4 Summary and Conclusions

Two markedly different impellers were tested and their performance compared in the present work. The first impeller tested, called the conventional impeller, was designed so that it would be characteristic of present-day technology. As such, this rotor has radial element blades and was designed using a throughflow analysis program iteratively. The intention behind the tests of the conventional rotor was to acquire a set of data typical of the performance of currently available radial-inflow turbines. As demonstrated above, this aim was fully achieved. Indeed, the efficiency level obtained with the conventional wheel compares favorably to that being obtained nowadays. The typical nonuniform value of work done along the span (or a nonuniform $r\bar{V}_\theta$ at exit) and the deterioration of local efficiency toward the shroud were observed as well.

The second impeller was designed using the described three-dimensional inverse program and was tested in order to assess the usefulness of this design method. As the geometry of this impeller resulted from the calculations, the blade shape shows double curvature and is not radial.

The tests showed that the new impeller had a peak total-to-static efficiency 1.4 percent bigger than the conventional rotor. There was also an improvement in efficiency for off-

Downloaded 01 Jun 2010 to 171.66.16.66. Redistribution subject to ASME license or copyright; see http://www.asme.org/terms/Terms_Use.cfm

design conditions, the difference reaching a value of 3.4 percent for the biggest nondimensional volume flow tested. It was also demonstrated that, for peak efficiency conditions, the new rotor had an outlet absolute velocity profile more uniform, an exit mean swirl ($r\bar{V}_\theta$) smaller and more uniform, and a consistently lower value of the local rotor loss than the conventional rotor. The more uniform values of $r\bar{V}_\theta$ indicate that the use of the three-dimensional inverse program was a step in the right direction.

Finally, a link between a more uniform $r\bar{V}_\theta$ downstream value and a more uniform exit velocity profile was established. In fact, the smaller variations of the downstream $r\bar{V}_\theta$ values measured for the new impeller are associated with exit velocity profiles more uniform in the spanwise direction than those observed with the conventional impeller. This fact, in turn, causes a reduction of the exit kinetic energy loss and consequently better total-to-static efficiencies. This argument points to the desirability of designing the rotors of radial-inflow turbines in such a way that they execute constant work along the span. In this respect, note also that for radial-inflow turbines with higher specific speeds than the present case, the possible gains from a more orderly exit flow are probably bigger than those proved in this study. The reason is that the exit kinetic energy loss accounts for a larger proportion of the total loss for radial-inflow turbines with higher specific speeds.

Another factor that could lead to bigger improvements in efficiency than those demonstrated in this work is a more appropriate choice of the input $r\bar{V}_\theta$ schedule. As mentioned by Borges (1990), the $r\bar{V}_\theta$ distribution used in the present design is far from giving an ideal pressure distribution throughout the rotor. It is to be expected that an improvement in pressure distribution obtained by using a better $r\bar{V}_\theta$ distribution would lead to an improvement in efficiency. This is a point on which more research should be done.

This work clearly demonstrates the usefulness of using three-dimensional inverse methods in the design of radial-inflow turbines. In fact, an improvement of 1.4 percent is not something to look down on. Furthermore, the author does not see any physical reason preventing the extrapolation of these results to radial and mixed-flow turbomachines, so that it is believed that this technique could be usefully applied to this sort of machine.

Acknowledgments

This work was supervised by Professor Sir W. R. Hawthorne and done while the author was at the Whittle Laboratory. The help of the staff of this laboratory is gratefully acknowledged. The author is also grateful to Holset Engineering Co. Ltd. (England), Churchill College (Cambridge, England), and Junta Nacional de Investigação Cientifica e Tecnológica—INVOTAN (Portugal) for the financial support they gave to this project.

References

Borges, J. E., 1986, "Three-Dimensional Design of Turbomachinery," PhD Thesis, Cambridge University, Cambridge, United Kingdom.

Borges, J. E., 1990, "A Three-Dimensional Inverse Method for Turbomachinery: Part I—Theory," ASME JOURNAL OF TURBOMACHINERY, Vol. 112, this issue.

Futral, S. M., and Holeski, D. E., 1970, "Experimental Results of Varying the Blade-Shroud Clearance in a 6.02-inch Radial-Inflow Turbine," NASA TN D-5513.

Futral, S. M., Kofskey, M., and Rohlik, H. E., 1969, "Instrumentation Used to Define Performance of Small Size, Low Power Gas Turbines," ASME Paper No. 69-GT-104.

Kofskey, M. G., and Wasserbauer, C. A., 1966, "Experimental Performance Evaluation of a Radial-Inflow Turbine Over a Range of Specific Speeds," NASA TN D-3742.

Kofskey, M. G., and Nusbaum, W. J., 1972, "Effects of Specific Speed on Experimental Performance of a Radial-Inflow Turbine," NASA TN D-6605.

Ribaud, Y., and Mischel, C., 1986, "Study and Experiments of a Small Radial Turbine for Auxiliary Power Units," ASME Paper No. 86-GT-23.

Rohlik, H. E., 1968, "Analytical Determination of Radial Inflow Turbine Design Geometry for Maximum Efficiency," NASA TN D-4384.

Sasaki, S., Takizawa, M., and Mizumachi, N., 1977, "A Development of Advanced Radial Gas Turbine for Automobile," *Proc. 1977 Tokyo Joint Gas Turbine Congress*, Paper No. 29, pp. 241-248.

Vanco, M. R., 1972, "Fortran Program for Calculating Velocities in the Meridional Plane of a Turbomachine. I—Centrifugal Compressor," NASA TN D-6701.

Downloaded 01 Jun 2010 to 171.66.16.66. Redistribution subject to ASME license or copyright; see http://www.asme.org/terms/Terms_Use.cfm

Analysis of Three-Dimensional Turbomachinery Flows on C-Type Grids Using an Implicit Euler Solver

K. F. Weber

D. W. Thoe

R. A. Delaney

Allison Gas Turbine Division,
General Motors Corporation,
Indianapolis, IN 46206-0420

A three-dimensional Euler analysis for turbomachinery flows on a C-type grid is presented. The analysis is based on the Beam and Warming implicit algorithm for solution of the unsteady Euler equations and is derived from the ARC3D code developed by Pulliam at NASA Ames Research Center. Modifications made to convert this code from external flow applications to internal turbomachinery flows are given in detail. These changes include the addition of inflow, outflow, and periodic boundary point calculation procedures. Also presented are the C-grid construction procedures. Finally, results of code experimental verification studies for three-dimensional compressor cascade and rotor flows are presented.

Introduction

Over the past 15 years steady progress has been made in the development of fluid flow analyses for turbomachinery blade rows. The eventual goal of these analyses is a time accurate model of the three-dimensional flow through the blade rows. Solving the full Navier–Stokes equations over the entire flowfield is the most complete model. Although Rai (1985, 1987) has obtained time accurate Navier–Stokes solutions for a single stage, and Adamczyk (1986) has developed an average pass multistage analysis that includes viscous effects, a complete model is still too complex and computationally too costly. This is especially true considering that a highly accurate analysis for any arbitrary compressor blade row does not yet exist.

The three-dimensional analysis methods that have been the most highly developed and have provided the greatest advancements in the turbomachinery field are the time-dependent Euler solvers based on a fully conservative form of the governing equations. They provide a single approach for subsonic, transonic, and supersonic flows, and they inherently provide natural shock capturing capability. In many cases, predicted results from Euler solvers are in good agreement with experimental data and provide accurate information on important flow features such as shock location and static pressure distribution. Most importantly, an accurate and efficient Euler solver forms the basis for an efficient viscous solution procedure. Denton (1974) was the first to develop an Euler solver for turbomachines, and he has since been followed by others, including Van Hove (1984), Shieh and Delaney (1987), and Subramanian and Bozzola (1986). In general, these solvers have been more widely used to predict turbine flows than compressor flows and have been used routinely in the turbine design process throughout the aircraft gas turbine industry.

The method of solution chosen for the compressor analysis presented here is based on the implicit approximate factorization algorithm of Beam and Warming (1976). There are many important aspects to consider when choosing a method to solve the Euler or Navier–Stokes equations. For finite difference schemes, the two classical approaches for time integration are explicit and implicit techniques. Both implicit and explicit methods are capable of computing time accurately, but for steady-state calculations, implicit methods have less stringent stability criteria, allowing larger time steps to be used to speed up convergence to the steady state. The CFL stability criteria for explicit methods are much more limiting for Navier–Stokes than for Euler equations because of the need to resolve the wall region when solving the Navier–Stokes equations on highly clustered grids. This limitation becomes less critical when the Euler equations are considered since Euler solvers do not require high near-wall resolution. However, shock resolution is becoming increasingly important in advanced high Mach number compressors, and small mesh spacings will be required in the region of shocks, making implicit techniques advantageous for Euler solutions. Recent work by Merriam (1987) also indicates that schemes that satisfy a discrete entropy inequality may need to be implicit to achieve second-order accuracy in space.

The coordinate system is perhaps just as important as the flow solver. In recent years there has been considerable progress in the development of body-conforming C- and O-type grids for turbomachinery flow calculations. These grids are capable of providing improved solution accuracy when compared with the H-type grids used by Denton and others. Much of the problem with H grids is due to the singular Jacobian at the leading edge branch point. Body-conforming grids may

Contributed by the International Gas Turbine Institute and presented at the 34th International Gas Turbine and Aeroengine Congress and Exhibition, Toronto, Ontario, Canada, June 4–8, 1989. Manuscript received at ASME Headquarters January 17, 1989. Paper No. 89-GT-85.

Copyright © 1990 by ASME
Downloaded 01 Jun 2010 to 171.66.16.66. Redistribution subject to ASME license or copyright; see http://www.asme.org/terms/Terms_Use.cfm

make it easier to improve leading edge resolution without special procedures. In any event, increasing accuracy and minimizing error at the leading edge is very important because any errors incurred at the leading edge are convected downstream and adversely affect the solution accuracy over the entire airfoil surface.

This paper describes an efficient three-dimensional compressor flow analysis method that incorporates an implicit approximate factorization scheme based on the Beam–Warming algorithm along with body-conforming C-type grids. The method is based on the numerics in the ARC3D code developed by Pulliam (1984) at the NASA Ames Research Center. Included in the paper are descriptions of the governing equations for a rotating Cartesian coordinate system, the grid generation scheme, and an outline of the method of solution. Numerical solution results for two three-dimensional compressor flows are presented and compared with experimental data to demonstrate the predictive capability of the analysis method.

Governing Equations

The differential equations used in this study are the Euler equations for a compressible fluid. If relative Cartesian velocity components are retained as dependent variables in a system attached to a rotating or stationary blade row, the three-dimensional unsteady Euler equations can be expressed in strong conservation form as

$$\frac{\partial \hat{Q}}{\partial t} + \frac{\partial \hat{E}}{\partial x} + \frac{\partial \hat{F}}{\partial y} + \frac{\partial \hat{G}}{\partial z} = \hat{H} \tag{1}$$

where

$$\hat{Q} = \begin{bmatrix} \rho \\ \rho u_r \\ \rho v_r \\ \rho w_r \\ \rho E' \end{bmatrix}, \quad \hat{E} = \begin{bmatrix} \rho u_r \\ \rho u_r^2 + p \\ \rho u_r v_r \\ \rho u_r w_r \\ \rho u_r H \end{bmatrix}, \quad \hat{F} = \begin{bmatrix} \rho v_r \\ \rho v_r u_r \\ \rho v_r^2 + p \\ \rho v_r w_r \\ \rho v_r H \end{bmatrix},$$

$$\hat{G} = \begin{bmatrix} \rho w_r \\ \rho w_r u_r \\ \rho w_r v_r \\ \rho w_r^2 + p \\ \rho w_r H \end{bmatrix}, \quad \hat{H} = \begin{bmatrix} 0 \\ \rho\Omega^2 x - 2\rho\Omega v_r \\ \rho\Omega^2 y + 2\rho\Omega u_r \\ 0 \\ 0 \end{bmatrix} \tag{2}$$

$$E' = \frac{p}{(\gamma-1)\rho} + \frac{1}{2}\left(u_r^2 + v_r^2 + w_r^2\right) - \frac{1}{2}\left(u_c^2 + v_c^2\right) \tag{3}$$

$$H = E' + p/\rho \tag{4}$$

and $u_r = u - u_c$, $v_r = v - v_c$, $w_r = w$ are the relative velocity components; ρ is the density; p, the static pressure; u, v, and w, the absolute velocity components in the x, y, z directions, respectively; Ω, the rotational speed of the blade row; u_c and v_c, the velocity components of the rotating blade row at a given x, y, z location; and E', a rotational energy term.

Equation (1) makes up a system of five equations for five dependent variables ρ, u_r, v_r, w_r, and E'. To solve the system of equations numerically on a body-conforming grid system, they are transformed to an arbitrary curvilinear coordinate system. If the transformation equations are written

$$\begin{aligned} \xi &= \xi(x, y, z, t) \\ \eta &= \eta(x, y, z, t) \\ \zeta &= \zeta(x, y, z, t) \end{aligned} \tag{5}$$

and the chain rule is used for differentiation, with the inertial Cartesian velocity components kept as dependent variables, equation (1) can be rewritten as

$$\frac{\partial Q}{\partial t} + \frac{\partial E}{\partial \xi} + \frac{\partial F}{\partial \eta} + \frac{\partial G}{\partial \zeta} = H \tag{6}$$

where

$$Q = \begin{bmatrix} \rho \\ \rho u \\ \rho v \\ \rho w \\ e \end{bmatrix}, \quad E = J^{-1}\begin{bmatrix} \rho U \\ \rho u U + \xi_x p \\ \rho v U + \xi_y p \\ \rho w U + \xi_z p \\ \rho h U - \xi_t p \end{bmatrix},$$

$$F = J^{-1}\begin{bmatrix} \rho V \\ \rho u V + \eta_x p \\ \rho v V + \eta_y p \\ \rho w V + \eta_z p \\ \rho h V - \eta_t p \end{bmatrix} \quad G = J^{-1}\begin{bmatrix} \rho W \\ \rho u W + \zeta_x p \\ \rho v W + \zeta_z p \\ \rho w W + \zeta_z p \\ \rho h W - \zeta_t p \end{bmatrix},$$

$$H = J^{-1}\begin{bmatrix} 0 \\ -\rho v \Omega \\ +\rho u \Omega \\ 0 \\ 0 \end{bmatrix} \tag{7}$$

and where e is the total energy, and U, V, and W are the contravariant velocity components in the ξ, η, and ζ directions written without metric normalization and given by

Nomenclature

a = speed of sound
a_1 = reference speed of sound (inlet hub)
C_p = specific heat at constant pressure
C_x = blade section axial chord
e = total internal energy
h = enthalpy
j, k, l, n = indices for ξ, η, ζ, and t coordinates, respectively
J = Jacobian of coordinate transformation
M = Mach number
p = pressure
r, θ, z = cylindrical polar coordinates
T_o = total temperature
t = time
U, V, W = contravariant velocity components in the ξ, η, and ζ directions, respectively
u, v, w = absolute velocity components in the x, y, z directions, respectively
$u_c = \Omega y$ = velocity component of rotating coordinate system in x direction
$v_c = -\Omega x$ = velocity component of rotating coordinate system in y direction
u_r, v_r, w_r = relative velocity components in the x, y, z directions, respectively
v_r, v_θ, v_z = velocity components in the r, θ, z directions, equation (18)
x, y, z = Cartesian coordinates
γ = ratio of specific heats
Δ, ∇ = forward and backward difference operators, respectively
ξ, η, ζ = general curvilinear coordinates
ρ = density
ρ_1 = reference density (inlet hub)
Ω = rotational speed of rotor

Downloaded 01 Jun 2010 to 171.66.16.66. Redistribution subject to ASME license or copyright; see http://www.asme.org/terms/Terms_Use.cfm

$$U = \xi_x(u-u_c) + \xi_y(v-v_c) + \xi_z w$$
$$V = \eta_x(u-u_c) + \eta_y(v-v_c) + \eta_z w \quad (8)$$
$$W = \zeta_x(u-u_c) + \zeta_y(v-v_c) + \zeta_z w$$

The inverse Jacobian of the transformation, J^{-1}, is defined as

$$J^{-1} = \begin{vmatrix} x_\xi & x_\eta & x_\zeta \\ y_\xi & y_\eta & y_\zeta \\ z_\xi & z_\eta & z_\zeta \end{vmatrix} \quad (9)$$

and the metrics are given by the equations

$$\begin{aligned} \xi_x &= J(y_\eta z_\zeta - y_\zeta z_\eta) & \eta_x &= J(z_\xi y_\zeta - y_\xi z_\zeta) \\ \xi_y &= J(z_\eta x_\zeta - x_\eta z_\zeta) & \eta_y &= J(x_\xi z_\zeta - x_\zeta z_\xi) \\ \xi_z &= J(x_\eta y_\zeta - y_\eta x_\zeta) & \eta_z &= J(y_\xi x_\zeta - x_\xi y_\zeta) \\ \zeta_x &= J(y_\xi z_\eta - z_\xi y_\eta) & \xi_t &= -x_\tau \xi_x - y_\tau \xi_y - z_\tau \xi_z \\ \zeta_y &= J(x_\eta z_\xi - x_\xi z_\eta) & \eta_t &= -x_\tau \eta_x - y_\tau \eta_y - z_\tau \eta_z \\ \zeta_z &= J(x_\xi y_\eta - y_\xi x_\eta) & \zeta_t &= -x_\tau \zeta_x - y_\tau \zeta_y - z_\tau \zeta_z \end{aligned} \quad (10)$$

The Cartesian velocity components u, v, and w are nondimensionalized with respect to the speed of sound at the inlet of the hub section, a_1; density, ρ, is referenced to the hub inlet density, ρ_1; and the energy and pressure to $\rho_1 a_1^2$. Pressure is defined as

$$p = (\gamma - 1)\,[e - 0.5\rho(u^2 + v^2 + w^2)] \quad (11)$$

with γ as the ratio of specific heats.

Coordinate System

The coordinate system for the three-dimensional analysis is a C-type body-conforming system. This grid is particularly attractive because it affords high resolution of the leading edge region to capture bow shocks and minimize the errors that would be convected downstream. As shown in Fig. 1, this system is constructed by radially stacking two-dimensional, C-type grids on surfaces of revolution.

The grid generator is capable of modeling the complete geometry of compressor blade rows including endwall contour and blade twist. The boundary of the physical passage domain is defined by the hub and shroud endwalls and the inlet and exit boundaries as shown in Fig. 2. The location and shape of the inlet and exit boundaries may be defined as planar surfaces, but are generally constructed to follow the curved contours of the leading and trailing edges of the blade, respectively. The distances between the blade leading edge and inlet boundary and the blade trailing edge and exit boundary are specified as percentages of the blade chord at a given radial location. The two-dimensional blade-to-blade surfaces intermediate to the hub and shroud are surfaces of revolution. C-type grids are constructed on these surfaces using elliptic techniques. In the grid generation process, a mean radius is calculated for each surface, and the surface is then projected onto a cylinder of that radius (see Fig. 2). A grid for each cylindrical section is then found by solving an elliptic system of partial differential equations (Thompson et al., 1985) to produce blade conforming two-dimensional grids. Controlling functions are introduced to enforce orthogonality. Grid point locations on the blade surface are determined by imposing orthogonality at the surface. All of these steps are performed in an interactive manner, so that the user is able to monitor the generation and alter the grid by varying parameters.

Numerical Algorithm

The algorithm used to solve the system of equations (6) is an implicit approximate factorization finite difference scheme. The scheme was developed by Beam and Warming (1976) and was used initially by Steger (1977) and subsequently by Pulliam and Steger (1980). Explicit and implicit artificial dissipation terms are added to attain nonlinear stability, and a spatially variable time step is used to accelerate convergence for steady-state calculations. The diagonal form of the algorithm is used because it allows for the use of fourth-order implicit dissipation and produces a robust, rapidly converging scheme in most cases.

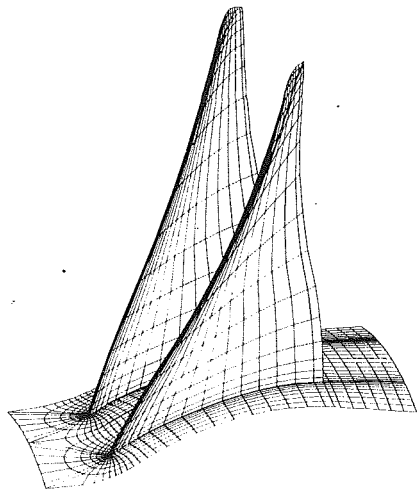

Fig. 1 Three-dimensional grid constructed by stacking two-dimensional grids on surfaces of revolution

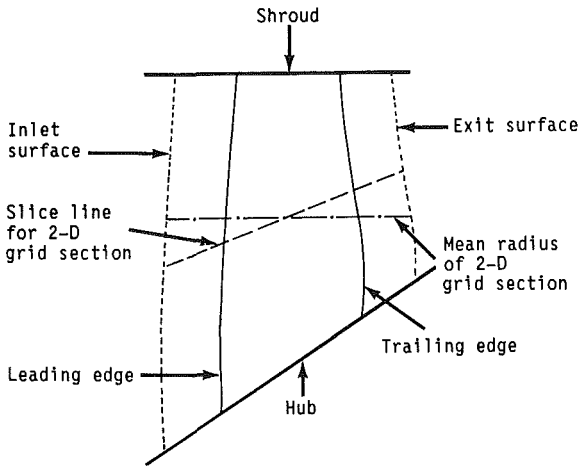

Fig. 2 Schematic diagram showing meridional view of the physical grid domain

By applying implicit time differencing, local time linearizations, and approximate factorization as shown by Pulliam (1984), equation (6) can be written as

$$(I + h\delta_\xi A^n)(I + h\delta_\eta B^n)(I + h\delta_\zeta C^n)\Delta Q^n = -h[\delta_\xi E^n + \delta_\eta F^n + \delta_\zeta G^n - H] \quad (12)$$

where $A = \partial E/\partial Q$, $B = \partial F/\partial Q$, and $C = \partial G/\partial Q$ are the flux Jacobians, each of which has real eigenvalues and a complete set of eigenvectors. The term h is the spatially variable time step, given as $dt/(1. + \sqrt{J})$. The development of the method of solution and the algorithm are given in detail in papers by Beam and Warming (1976), Steger (1977), Pulliam (1984), and Pulliam and Steger (1985). Equation (12) consists of an implicit (left) side and an explicit (right) side. The left side has three implicit operators, each of which is block tridiagonal. The spatial derivative terms are approximated with second-order central differences. The computational work can be decreased

Downloaded 01 Jun 2010 to 171.66.16.66. Redistribution subject to ASME license or copyright; see http://www.asme.org/terms/Terms_Use.cfm

by introducing a diagonalization of the blocks in the implicit operators as developed by Pulliam and Chaussee (1981). The eigensystem of the flux Jacobians A, B, and C is used in this development. Because the flux Jacobians have real eigenvalues and a complete set of eigenvectors, the matrices can be diagonalized (Warming et al., 1975; Turkel, 1973), i.e.,

$$\Lambda_\xi = T_\xi^{-1} A T_\xi, \qquad \Lambda_\eta = T_\eta^{-1} B T_\eta, \qquad \Lambda_\zeta = T_\zeta^{-1} C T_\zeta \quad (13)$$

where T_ξ, T_η, and T_ζ are the matrices whose columns are the eigenvectors of A, B, and C. Replacing A, B, and C in equation (13) by their eigensystem decomposition yields

$$[T_\xi T_\xi^{-1} + h\delta_\xi(T_\xi \Lambda_\xi T_\xi^{-1})][T_\eta T_\eta^{-1} + h\delta_\eta(T_\eta \Lambda_\eta T_\eta^{-1})] [T_\zeta T_\zeta^{-1} + h\delta_\zeta(T_\zeta \Lambda_\zeta T_\zeta^{-1})]\Delta Q^n \quad (14)$$

$$= \text{explicit right-hand side of equation (12)} = R^n$$

A modified version of equation (14) can be obtained by factoring the T_ξ, T_η, and T_ζ eigenvector matrices outside the spatial derivative terms δ_ξ, δ_η, δ_ζ. The resulting equations are

$$T_\xi[I + h\delta_\xi \Lambda_\xi] N [I + h\delta_\eta \Lambda_\eta] P [I + h\delta_\zeta \Lambda_\zeta] T_\zeta^{-1} \Delta Q^n = R^n \quad (15)$$

where $N = T_\xi^{-1} T_\eta$ and $P = T_\eta^{-1} T_\zeta$.

The explicit side of the diagonal algorithm is the set of steady-state finite difference equations and is exactly the same as the original algorithm. In addition, computational experiments by Pulliam and Chaussee (1981) have shown that the convergence and stability limits of the diagonal algorithm are similar to those of the block tridiagonal algorithm. The diagonal algorithm reduces the block tridiagonal inversion to four 5×5 matrix multiples and three scalar tridiagonal inversions, with an overall savings in computational work that can be as high as 40 percent (Pulliam, 1986a).

Code Developments

The turbomachinery flow code that has been developed is based on the external flow code ARC3D, which was written at the NASA Ames Research Center. The original ARC3D code is capable of calculating the flow about bodies with bilateral symmetry in an external environment. The steps used to adapt the code and algorithm to turbomachinery flow are outlined in this section.

The first step in this adaptation was the reformulation of the Euler equations in a rotating Cartesian frame of reference. This involved the inclusion of terms to account for velocities and accelerations in the relative system. The second step was the transformation of the equations to generalized curvilinear coordinates. This yielded equation (6), which is very similar to the form of the equations shown by Pulliam and Steger (1980) or Pulliam (1986a) where the algorithm is given in more detail. The major difference is the presence of source terms to account for relative accelerations. At this point, it was possible to follow the development shown in detail by Pulliam (1984) and briefly in this paper to arrive at the diagonal form of the algorithm.

The next step involved code modification to account for the relative terms. The form of the code that had been obtained did not account for these terms in a global sense. The changes to the original code were extensive and were implemented in a general manner. The code defines the velocity of the rotating coordinate system at each point and calculates the relative velocity and acceleration components when required.

Although the changes in a Cartesian system formulation to account for rotation are more extensive than those in a polar coordinate system formulation, the truncation error in a Cartesian formulation is not a function of radius as it is with the polar coordinate formulation. This advantage may become more important as the accuracy required from the analysis increases.

After the equations had been reformulated and the basic code has been modified, the far field external flow boundary point calculations from ARC3D were replaced by three-dimensional calculations for the treatment of periodic, inlet, and exit boundaries. With the modifications to the boundary procedures and those to account for the relative system of reference, the code was qualified for axial turbomachinery flow computations.

In addition to the major modifications for turbomachinery flow calculations, some algorithm modifications or upgrades were also implemented. First, the mixed second- and fourth-order damping scheme of Jameson (1981) was extended from one to all three coordinate directions. This scheme is explained in the section on the nonlinear artificial dissipation model. Second, an alternate procedure for calculation of the metrics was added because central differencing for the calculation of three-dimensional metrics introduces errors resulting from nonzero metric invariants. This procedure, described by Pulliam and Steger (1980), can be used to ensure that the metric invariants are exactly zero. Basically, this is a weighted averaging that computes the metrics in a finite volume manner. The alternative is to subtract out the local error term that arises when the strong conservation form of the equations is used as a source term on the explicit right-hand side. This is not the same as the approach of Pulliam and Steger for maintaining the free stream. However, it is the approach that contributed most toward improving the three-dimensional solutions.

Boundary Conditions

As with the ARC3D flow code, the dependent variables are updated explicitly, which means that there is a first-order error in time at the boundaries. Because the boundary procedures are a modular element of the code, they can be altered or replaced without interfering with the implicit algorithm. The far field boundary procedures in ARC3D were replaced with three-dimensional turbomachinery boundary procedures. For three-dimensional turbomachinery calculations, there are six boundaries. Figure 3 is a schematic diagram of a two-dimensional C-grid section. Three of the boundaries, the hub and tip section and the blade, are solid surfaces. The other three boundaries are the inlet, exit, and periodic boundaries.

At the inlet, an extension of the two-dimensional procedure used by Chima (1985) that allows for the specification of total temperature, total pressure, and the radial and tangential velocity components is used. Nonuniform radial distributions of any of these properties can be specified. The procedure uses a characteristic boundary condition similar to that used by Jameson and Baker (1983) where the upstream-running Riemann invariant R^-, based on the total velocity q, is extrapolated from the interior to the boundary, i.e.,

$$R^- = (q - 2c/(\gamma - 1))_{\text{ext}} \quad (16)$$

where $c = (\gamma p/\rho)^{1/2}$ is the speed of sound. Total temperature,

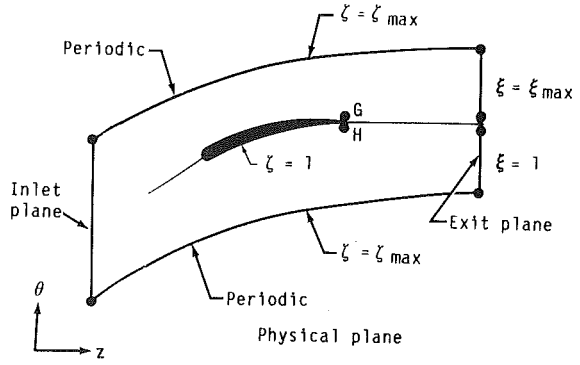

Fig. 3 Schematic diagram of a two-dimensional C-grid section showing inlet, exit, and periodic boundaries

Downloaded 01 Jun 2010 to 171.66.16.66. Redistribution subject to ASME license or copyright; see http://www.asme.org/terms/Terms_Use.cfm

T_o, and isentropic relations are then used to determine q_{in}, the total velocity

$$q_{in} = \left[(\gamma-1)R^- + \sqrt{4(\gamma+1)C_pT_o - 2(\gamma-1)(R^-)^2}\right]/(\gamma+1) \tag{17}$$

The axial velocity component is found from trigonometric relations, and pressure and density are determined using isentropic relations.

At the exit boundary points, the static pressure is specified, and ρ, u, v, and w are extrapolated from the inner field. The pressure at the hub surface is set and the radial pressure distribution is determined using a simplified version of the radial equilibrium equation

$$\frac{\partial_p}{\partial_r} = \rho\left(\frac{v_\theta^2}{r} - v_r\frac{\partial v_r}{\partial_r} - v_z\frac{\partial v_r}{\partial_z}\right) \tag{18}$$

This equation is integrated at each time step following the extrapolation of the other flow variables. The calculated pressure distribution is then imposed as a boundary condition at the next time step. Initially when the relative difference between the back pressure and the inner field pressure is large, the nonreflective procedure of Rudy and Strikwerda (1980) is used because the specified pressure is imposed asymptotically, and the flow field is not immediately presented with a sharp discontinuity.

On the hub and shroud endwalls, and the blade surface, solid surface boundary procedures very similar to those outlined by Pulliam and Steger (1980) or Chima (1985) are implemented. For example, on the blade surface, ζ = const, the flow tangency condition is enforced by setting the normal contravariant velocity component, $W = 0$, and extrapolating the other two contravariant components, U and V. The Cartesian velocity components are found using metric relations, i.e.,

$$\begin{bmatrix} u \\ v \\ w \end{bmatrix} = J^{-1}\begin{bmatrix} (\eta_y\zeta_z - \eta_z\zeta_y) & -(\xi_y\zeta_z - \xi_z\zeta_y) & (\xi_y\eta_z - \eta_y\xi_z) \\ (\eta_x\zeta_z - \eta_z\zeta_x) & (\xi_x\zeta_z - \xi_z\zeta_x) & -(\xi_x\eta_z - \xi_z\eta_x) \\ (\eta_x\zeta_y - \eta_y\zeta_x) & (\xi_x\zeta_y - \xi_y\zeta_x) & (\xi_x\eta_y - \xi_y\eta_x) \end{bmatrix}\begin{bmatrix} U - \xi_t \\ V - \eta_t \\ W - \zeta_t \end{bmatrix} \tag{19}$$

Pressure is found using the normal momentum relation, which is a combination of the three transformed momentum equations given by

$$\begin{aligned} p_n\left(\zeta_x^2+\zeta_y^2+\zeta_z^2\right)^{1/2} &= (\xi_x\zeta_x+\xi_y\zeta_y+\xi_z\zeta_z)p_\xi \\ &\quad + (\eta_x\zeta_x+\eta_y\zeta_y+\eta_z\zeta_z)p_\eta \\ &\quad + (\zeta_x^2+\zeta_y^2+\zeta_z^2)p_\zeta \\ &= \rho[\partial_\tau\zeta_t + u\partial_t\zeta_x + v\partial_t\zeta_y + w\partial_t\zeta_z] \\ &\quad - \rho U(\zeta_x u_\xi + \zeta_y v_\xi + \zeta_z w_\xi) \\ &\quad - \rho V(\zeta_x u_\eta + \zeta_y v_\eta + \zeta_z w_\eta) \\ &\quad + \rho\Omega\zeta_y u - \rho\Omega\zeta_x v \end{aligned} \tag{20}$$

where n is the normal direction to the ζ = const solid surface. In this form, the boundary conditions are applicable to steady or unsteady motion. Surface densities are found using a boundary condition suggested by Chima (1985) and by Barton and Pulliam (1984). The entropy expressed as $S = p/\rho^\gamma$ is extrapolated to the body and used to find the density. This condition is very stable and conserves total pressure or entropy better than a boundary condition in which rothalpy or total enthalpy is specified.

Nonlinear Artificial Dissipation Model

One of the important aspects of compressor aerodynamics is the ability to capture shocks and predict shock losses. MacCormack and Baldwin (1975) used a second-difference dissipation operator for the solution of the Navier–Stokes equations for flow with shocks. More recent work by Jameson et al. (1981) and Pulliam (1986a, 1986b) shows that a mixed second- and fourth-order dissipation model with appropriate coefficients should give a central difference scheme good shock capturing capability. The model used in this analysis is the combined second- and fourth-order model first proposed by Jameson et al. (1981). The model expressed in simplified notation for the ξ direction is written

$$\nabla_\xi(\sigma_{j+1}J_{j+1}^{-1} + \sigma_jJ_j^{-1})(\epsilon_j^{(2)}\Delta_\xi Q_j - \epsilon_j^{(4)}\Delta_\xi\nabla_\xi\Delta_\xi Q_j)$$

with

$$\epsilon_j^{(2)} = K_2\Delta t\,\max(\Upsilon_{j-1}, \Upsilon_j, \Upsilon_{j+1}),\quad \Upsilon_j = \frac{|p_{j+1}-2p_j+p_{j-1}|}{p_{j+1}+2p_j+p_{j-1}}$$

$$\epsilon_j^{(4)} = \max(0, K_4\Delta t - \epsilon_j^{(2)})$$

$$\sigma_j = |U| + a\sqrt{\xi_x^2+\xi_y^2+\xi_z^2} + |V| + a\sqrt{\eta_x^2+\eta_y^2+\eta_z^2} + |W| + a\sqrt{\zeta_x^2+\zeta_y^2+\zeta_z^2} \tag{21}$$

which is the sum of the spectral radii of the flux Jacobians A, B, and C. For simplicity of presentation, only the j subscripts, which correspond to the ξ direction, have been presented. The suggested values for the constants are $K_2 = 1/4$ and $K_4 = 1/100$.

The first term is a second-order dissipation model with an extra pressure gradient coefficient to increase its value near shocks. The second term is a fourth-order model where the logic to compute $\epsilon_j^{(4)}$ switches it off when the second-order nonlinear coefficient is larger than the constant fourth-order coefficient. This occurs very near a shock. Near computational boundaries, the fourth-order dissipation term is modified to maintain a dissipative term. A derivation and analysis of various boundary treatments for dissipation models is given by Pulliam (1986b).

Results and Discussion

Numerical solution results for a compressor cascade and an isolated rotor are presented and compared with experimental data. The solutions were started from uniform inlet hub conditions with the hub exit static pressure set at the desired steady-state value. The final values of the damping coefficients for the rotor solution were $K_2 = 1/3$ and $K_4 = 1/50$, which were above the suggested (Pulliam, 1986a, 1986b) values of $K_2 = 1/4$ and $K_4 = 1/100$. The solutions were assumed to be converged when the root-mean-square average of the right-hand side residual had been reduced more than three orders of magnitude; however, this is more a rule of thumb than an absolute criterion.

Controlled Diffusion Airfoil. The accuracy of the three-dimensional code was tested during its development by comparison of solutions with experimental data. The initial verification was carried out using data for a rectilinear cascade of supercritical airfoils. The cascade data were used to validate the turbomachinery boundary point calculations.

Downloaded 01 Jun 2010 to 171.66.16.66. Redistribution subject to ASME license or copyright; see http://www.asme.org/terms/Terms_Use.cfm

The rectilinear cascade, shown in Fig. 4, was tested by Stephens and Hobbs (1979) over a range of inlet Mach numbers and incidence angles. Sample experimental midspan airfoil Mach number distributions are presented in Fig. 5. Two-dimensional and three-dimensional flow predictions were made for the design operating condition with inlet Mach number $M_1 = 0.735$ and incidence $i = 0$ deg. The three-dimensional analysis accounted for the endwall boundary layer blockage by linearly contracting the endwalls by the axial velocity density ratio (AVDR) of 1.17, whereas the two-dimensional analysis, determined using the same numerical scheme, did not account for blockage. As shown in Fig. 5, the three-dimensional predictions more closely match the experimental data. The oscillations in the solution near $X/Cx = 1.0$ result from the use of a C-type grid that approximates the trailing edge geometry as a wedge.

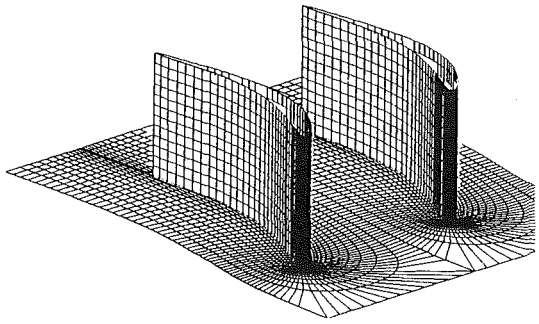

Fig. 4 Three-dimensional coordinate system for a rectilinear supercritical airfoil cascade

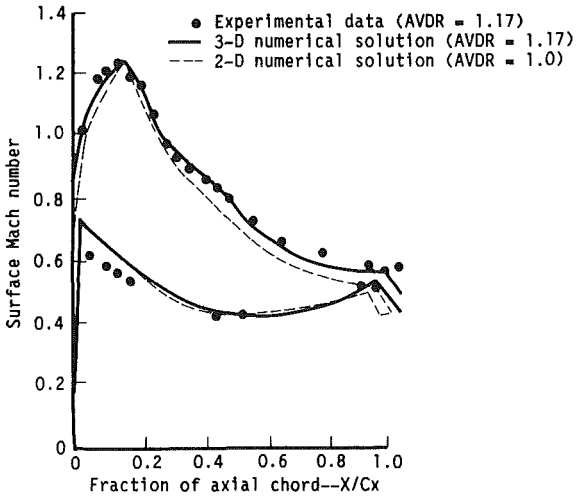

Fig. 5 Airfoil surface Mach number distribution for the midspan section of a supercritical airfoil cascade ($M_1 = 0.735$; $i = 0$ deg; $P_2/P_1 = 1.15$)

NASA Fan Rotor 67. The capability of the code to predict flows in rotating blade rows was established and the solution accuracy verified by comparing predicted results with experimental data for NASA fan Rotor 67, shown in Fig. 6. This rotor provided a rigorous test for the grid generator and the flow solver. The highly loaded rotor was tested at the NASA-Lewis Research Center and reported by Pierzga and Wood (1985). The rotor has 22 low aspect ratio (1.56) blades rotating at 16,042 rpm with a relative tip Mach number of 1.38 at the design speed of 1407.2 ft/sec and flow rate of 73.3 lb/sec. As Fig. 6 reveals, this rotor has a large amount of twist from hub to tip, which produces a highly three-dimensional flow field. The C-type grid contains 121 normals, 21 contours, and 17 sections hub to tip. The solutions converged three orders of

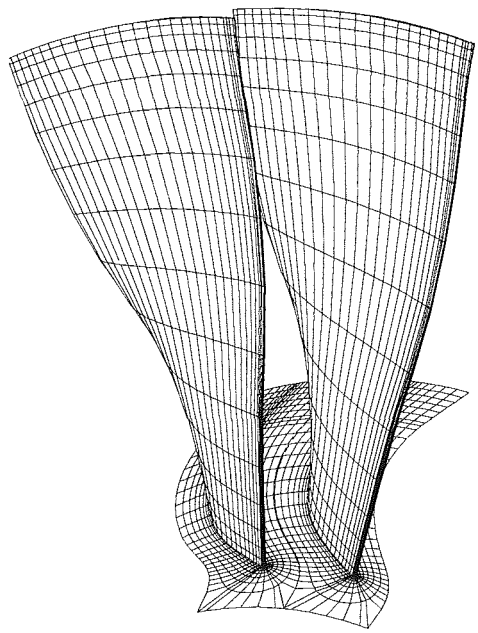

Fig. 6 Hidden line plot of the three-dimensional grid for NASA Rotor 67 showing the blade passage and the high amount of blade twist

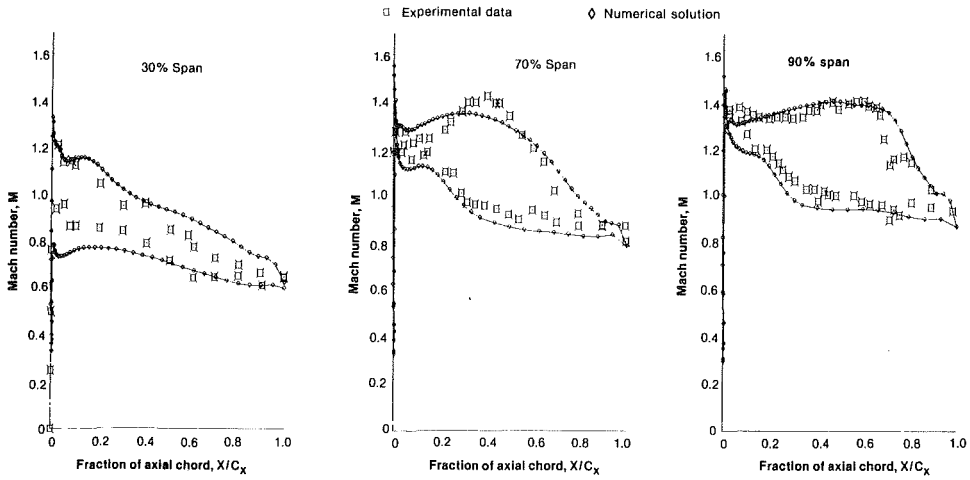

Fig. 7 Predicted and experimental Mach number distributions for NASA Rotor 67 at the peak efficiency operating condition

Downloaded 01 Jun 2010 to 171.66.16.66. Redistribution subject to ASME license or copyright; see http://www.asme.org/terms/Terms_Use.cfm

magnitude in approximately 500 iterations and required 10 min of CPU time on a CRAY X-MP vector computer.

The analysis was used to simulate the flow at the peak efficiency and near-stall operating points.

Figure 7 shows predicted surface relative Mach number and experimental near-surface relative Mach number distributions for the peak efficiency operating point. The comparisons are made at 30, 70, and 90 percent span, measured from the hub. The predicted static pressure contours at the same spanwise locations are presented in Fig. 8. Although the agreement is better at 90 and 70 percent span, overall agreement is good. The solution was obtained by adjusting the hub exit static pressure to obtain the best overall agreement. At peak efficiency, this was 1.4 percent higher than the reported hub exit static pressure. Figure 8 clearly shows the shock structure within the blade row at the near-tip sections.

Results for the near-stall operating point are presented in Figs. 9 and 10. Figure 9 compares the predicted surface and experimental near surface relative Mach number distributions at 30, 70, and 90 percent span. Figure 10 shows the predicted static pressure contours at 30, 70, and 90 percent span. Starting with the peak efficiency solution, the exit static pressure was raised until the best overall comparison was obtained for the near stall operating point. In this case, the hub exit static pressure was 2 percent higher than the reported hub exit static pressure. Overall agreement is fairly good. The discrepancies between the predicted results and data on the pressure surface near the leading edge may be due to inadequate mesh density in that high gradient region. The static pressure contour plots at 70 and 90 percent span show that at the near-stall operating point, the passage normal shock has been driven upstream and has combined with the leading edge bow shock.

Summary

An efficient three-dimensional turbomachinery flow analysis method has been presented. The method, based on the implicit approximate factorization finite difference scheme of Beam and Warming, combines Pulliam's diagonal form of the algorithm for solution of the three-dimensional time-dependent Euler equations with body conforming C-type grids. Explicit and implicit artificial dissipation terms were added to attain nonlinear stability. The grids were constructed by stacking two-dimensional C-type grids on surfaces of revolution. Numerical solution results for two three-dimensional compressor flows have been presented. The solution for a cascade of supercritical airfoils and for NASA fan Rotor 67 are compared with experimental data to demonstrate the accuracy of the analysis method.

References

Adamczyk, J. J., 1986, "Model Equation for Simulating Flows in Multistage Turbomachinery," ASME Paper No. 85-GT-226.

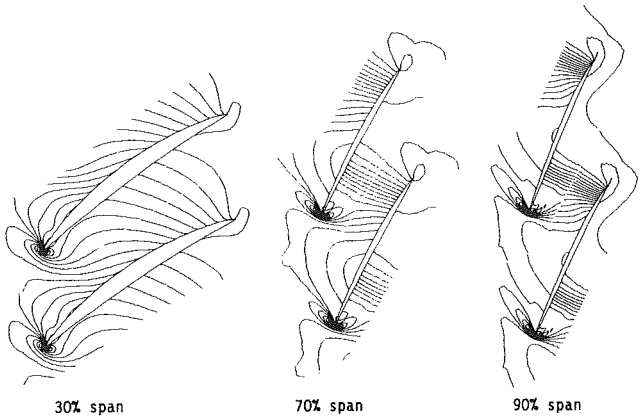

Fig. 8 Static pressure contour plots for NASA Rotor 67 at 30, 70, and 90 percent span at the peak efficiency operating condition

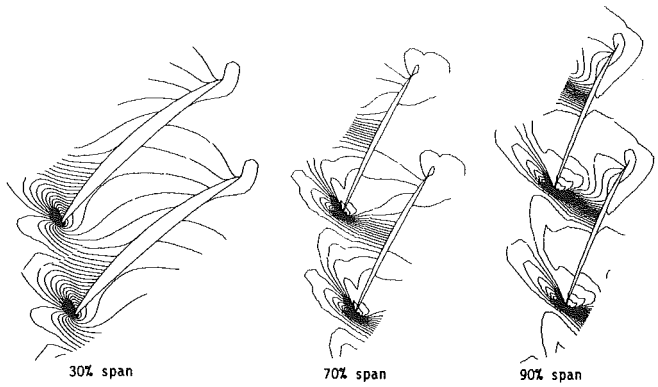

Fig. 10 Static pressure contour plots for NASA Rotor 67 at 30, 70, and 90 percent span at the near-stall operating condition

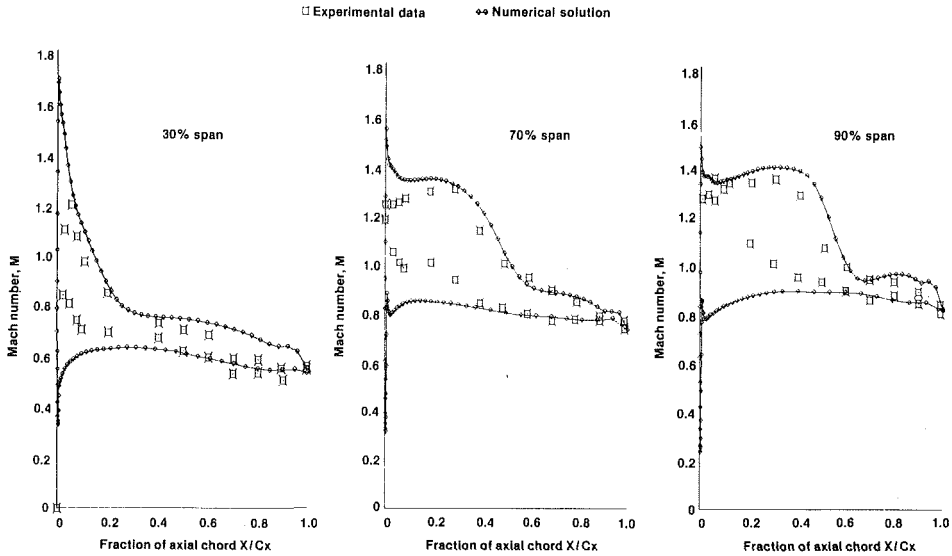

Fig. 9 Predicted and experimental Mach number distributions for NASA Rotor 67 at the near-stall operating condition

Downloaded 01 Jun 2010 to 171.66.16.66. Redistribution subject to ASME license or copyright; see http://www.asme.org/terms/Terms_Use.cfm

Barton, J. T., and Pulliam, T. H., 1984, "Airfoil Computations at High Angles of Attack, Inviscid and Viscous Phenomena," AIAA Paper No. 84-0524.

Beam, R., and Warming, R. F., 1976, "An Implicit Finite-Difference Algorithm for Hyperbolic Systems in Conservation Law Form," *Journal of Computational Physics*, Vol. 22, pp. 87–110.

Chima, R. V., 1985, "Inviscid and Viscous Flows in Cascades With an Explicit Multiple Grid Algorithm," *AIAA Journal*, Vol. 23, pp. 1556–1563.

Denton, J. D., 1974, "A Time Marching Method for Two-Dimensional and Three-Dimensional Blade to Blade Flows," ARC R&M 3775.

Jameson, A., Schmidt, W., and Turkel, E., 1981, "Numerical Solution of the Euler Equations by Finite Volume Methods Using Runge-Kutta Time Stepping Schemes," presented at the AIAA 14th Fluid and Plasma Dynamics Conference, Palo Alto, CA, Paper No. 81-1259.

Jameson, A., and Baker, T. J., 1983, "Solution of the Euler Equations for Complex Configurations," AIAA Paper No. 83-1929.

MacCormack, R., and Baldwin, B., 1975, "A Numerical Method for Solving the Navier-Stokes Equations with Application to Shock Boundary Layer Interactions," AIAA Paper No. 75-1.

Merriam, M. L., 1987, "Smoothing and the Second Law," *Computer Methods in Applied Mechanics and Engineering*, Vol. 64, pp. 177–193.

Pierzga, M. J., and Wood, J. R., 1985, "Investigation of the Three-Dimensional Flow Field Within a Transonic Fan Rotor: Experiment and Analysis," ASME *Journal of Engineering for Gas Turbines and Power*, Vol. 107, pp. 436–449.

Pulliam, T. H., and Steger, J. L., 1980, "On Implicit Finite Difference Simulations of Three Dimensional Compressible Flow," *AIAA Journal*, Vol. 18, p. 159.

Pulliam, T. H., and Chaussee, D. S., 1981, "A Diagonal Form of an Implicit Approximate Factorization Algorithm," *Journal of Computational Physics*, Vol. 39.

Pulliam, T., 1984, "Euler and Thin Layer Navier-Stokes Codes: ARC2D, ARC3D," Notes for Computational Dynamics Users Workshop, UTSI E02-4005-023-84, Mar.

Pulliam, T. H., and Steger, J. L., 1985, "Recent Improvements in Efficiency, Accuracy, and Convergence for Implicit Approximate Factorization Algorithms," AIAA Paper No. 85-0360.

Pulliam, T. H., 1986a, "Implicit Solution Methods in Computational Fluid Dynamics," *Applied Numerical Mathematics*, Vol. 2, pp. 441–474.

Pulliam, T. H., 1986b, "Artificial Dissipation Models for the Euler Equations," *AIAA Journal*, Vol. 24.

Rai, M. M., 1985, "Navier-Stokes Simulations of Rotor-Stator Interaction Using Patched and Overlaid Grids," AIAA Paper No. 85-1519.

Rai, M. M., 1987, "Unsteady Three-Dimensional Navier-Stokes Simulations of Turbine Rotor-Stator Interaction," AIAA Paper No. 87-2058.

Rudy, D. H., and Strikwerda, J. C., 1980, "A Nonreflecting Outflow Boundary Condition for Subsonic Navier-Stokes Calculations," *Journal of Computational Physics*, Vol. 36, pp. 159–167.

Shieh, C. F., and Delaney, R. A., 1987, "An Accurate and Efficient Euler Solver for Three-Dimensional Turbomachinery Flows," ASME JOURNAL OF TURBOMACHINERY, Vol. 109, pp. 346–353.

Steger, J. L., 1977, "Implicit Finite Difference Simulation of Flow About Arbitrary Geometries With Application to Airfoils," AIAA Paper No. 77-665.

Stephens, H. E., and Hobbs, D. E., 1979, *Design and Performance Evaluation of Supercritical Airfoils for Axial Flow Compressors*, Final Report, Naval Air Systems Command Contract N00019-77-C-0546, Feb.

Subramanian, S. V., and Bozzola, R., 1986, "Computation of Three-Dimensional Flow Through Turbomachinery Blade Rows for Improved Aerodynamic Design Studies," ASME Paper No. 86-GT-26.

Thompson, J. F., Warsi, Z. U. A., and Mastin, C. W., 1985, *Numerical Grid Generation—Foundations and Applications*, Elsevier Science Publishing Co., pp. 188–192.

Turkel, E., 1973, "Symmetrization of the Fluid Dynamics Equations With Applications," *Mathematical Computations*, Vol. 27, p. 729.

Van Hove, W., 1984, "Calculation of Three-Dimensional, Inviscid, Rotational Flow in Axial Turbine Blade Rows," ASME *Journal of Engineering for Gas Turbines and Power*, Vol. 106, pp. 430–436.

Warming, R. F., Beam, R., and Hyett, B. J., 1975, "Diagonalization and Simultaneous Symmetrization of the Gas Dynamic Matrices," *Mathematical Computations*, Vol. 29, p. 1037.

Downloaded 01 Jun 2010 to 171.66.16.66. Redistribution subject to ASME license or copyright; see http://www.asme.org/terms/Terms_Use.cfm

J. J. Adamczyk
NASA Lewis Research Center,
Cleveland, OH 44135

M. L. Celestina

T. A. Beach

Sverdrup Technologies, Inc.,
NASA Lewis Research Center Group,
Cleveland, OH 44135

M. Barnett
United Technologies Research Center,
Hartford, CT 06108

Simulation of Three-Dimensional Viscous Flow Within a Multistage Turbine

This work outlines a procedure for simulating the flow field within multistage turbomachinery, which includes the effects of unsteadiness, compressibility, and viscosity. The associated modeling equations are the average passage equation system, which governs the time-averaged flow field within a typical passage of a blade row embedded within a multistage configuration. The results from a simulation of a low aspect ratio stage and one-half turbine will be presented and compared with experimental measurements. It will be shown that the secondary flow field generated by the rotor causes the aerodynamic performance of the downstream vane to be significantly different from that of an isolated blade row.

Introduction

A goal of computational fluid dynamics for turbomachinery is the prediction of performance parameters and the flow processes that set their values. Achieving this goal for multistage devices is made difficult by the wide range of length and time scales in the associated flow fields. Currently the procedure used in design and off-design analysis is based on a quasi-three-dimensional flow model whose origins can be traced back to the late forties and early fifties (e.g., Wu, 1952; Smith, 1966). This model requires calculations to be executed on two orthogonal surfaces within a blade row passage of a multistage configuration. One of these surfaces is an axisymmetric surface of revolution whose intersection with a blade row defines a cascade. The flow field relative to this cascade is assumed to be steady in time. In practice, a finite number of such surfaces are chosen to define a series of cascade flows from hub to shroud. The other surface represents a meridional throughflow surface. The flow associated with this surface is an axisymmetric representation of the flow field within the machine. This flow field is also assumed to be steady. The flow fields on both surfaces are coupled and are solved iteratively. The effects of unsteadiness, turbulence, and endwall secondary flows are introduced through empirical correlations.

Although proven to be very useful, this flow model has its limitations. Among these is off-design performance analysis, and the ability to analyze unconventional machinery where extrapolation of the underlying empirical database is required. Other problems arise whenever there are large local variations in the radial velocity component within a blade passage. Such variations can be brought about by in-passage shock waves, separated boundary layers, and endwall secondary flows. It is generally agreed upon that a way of overcoming these shortcomings is the development of a true three-dimensional flow model.

Two three-dimensional flow models have been proposed for the simulation and analysis of multiple blade row flows. The first (Denton, 1979; Adamczyk, 1984; Ni, 1987), referred to as the average passage flow modeled by Adamczyk (1986), simulates the time-averaged flow field within a typical passage of the blade row. The second simulates the unsteady deterministic flow field within the machine. Although a number of unsteady simulations of single-stage turbine configurations and counterrotating propellers have been reported (Rai, 1987; Whitfield et al., 1987), executing an unsteady simulation of a multistage configuration of practical interest is far beyond the capabilities of today's advanced supercomputers. Furthermore, it is by no means obvious that performance prediction requires such a high degree of flow resolution. However, because unsteady simulations of an idealized configuration may prove to be a useful means of investigating the closure issue associated with time-averaged flow models, this activity should be pursued. In this work it will be shown that the simulation of the time-averaged flow field within multistage machinery is within the capabilities of today's advanced computers and that the average passage flow model gives more insight into the flow phenomena that control the performance of multistage machinery than today's quasi-three-dimensional flow models.

The objective of this paper is to outline a procedure for simulating the time-averaged flow field within a typical passage of a blade row within a multistage machine. This model includes the effects of viscosity and compressibility, and the influence of neighboring blade rows. The mathematical formulation upon which this model is based has been outlined by Adamczyk (1984). The algorithm used to solve the inviscid form of the governing equations is reported by Celestina (1986), and Adamczyk et al. (1986). The current work outlines a nu-

Contributed by the International Gas Turbine Institute and presented at the 34th International Gas Turbine and Aeroengine Congress and Exhibition, Toronto, Ontario, Canada, June 4–8, 1989. Manuscript received at ASME Headquarters January 25, 1989. Paper No. 89-GT-152.

Copyright © 1990 by ASME
Downloaded 01 Jun 2010 to 171.66.16.66. Redistribution subject to ASME license or copyright; see http://www.asme.org/terms/Terms_Use.cfm

merical solution procedure for the viscous form of these equations and an acceleration technique to enhance convergence. In addition, a comparison will be made between experimental data recorded during tests of a one and one-half stage, large-scale, low-speed, axial flow research turbine and simulation prediction. The underlying steady flow physics that appears to control the performance of the second vane of this machine will also be discussed.

Governing Equation

A complete derivation of the three-dimensional average-passage equation system is presented by Adamczyk (1984). These equations were derived by filtering the Navier–Stokes equation in both space and time to remove all information except that associated with the time-averaged flow field within a typical passage of a blade row of a multistage configuration. With respect to this blade row, the integral form of these equations can be written

$$\int \frac{\partial}{\partial t}(\lambda q)d\forall + L(\lambda q) = \int \lambda S\, d\forall + \int \lambda k\, d\forall + L_v(\lambda q) \tag{1}$$

The vector q contains the variables density, axial and radial momenta, angular momenta, and total internal energy. λ is the neighboring blade row blockage factor and ranges between zero and unity, unity being the value associated with zero blade thickness. This parameter explicitly introduces the effect of the neighboring blade row blade thickness. The operator $L(\lambda q)$ balances the mass, axial and radial momenta, angular momentum, and energy through a control volume. $\int \lambda k\, d\forall$ is a source term due to the cylindrical coordinate system and $\int \lambda S d\forall$ contains the body forces, energy sources, momenta, and energy temporal and spatial mixing correlations associated with the neighboring blade rows. A procedure for estimating S has been outlined by Adamczyk et al. (1986) and is extended here to include the effects of viscosity. The operator $L_v(\lambda q)$ contains the viscous and heat transfer terms. The vector q and the operators L and L_v are defined as

$$q = [\rho,\ \rho v_z,\ \rho v_r,\ r\rho v_\theta,\ \rho e_o]^T \tag{2}$$

$$L = \int_{dA} [\lambda \overline{F}\, dA_z + \lambda \overline{G}\, dA_r + \lambda \overline{H}\, dA_\theta] \tag{3}$$

and

$$L_v = \int_{dA} [\lambda \overline{F}_v\, dA_z + \lambda \overline{G}_v\, dA_r + \lambda \overline{H}_v\, dA_\theta] \tag{4}$$

where

$$\overline{F} = [\rho v_z,\ \rho v_z^2 + P,\ \rho v_z v_r,\ r\rho v_z v_\theta,\ \rho H v_z]^T \tag{5}$$

$$\overline{G} = [\rho v_r,\ \rho v_2 v_r,\ p v_r^2 + P,\ r\rho v_r v_\theta,\ \rho H v_r]^T \tag{6}$$

$$\overline{H} = [v n_\theta,\ \rho v_\theta v_z,\ \rho v_\theta v_r,\ r(\rho v_\theta^2 + P),\ \rho H v_\theta]^T \tag{7}$$

$$\overline{F}_r = [0,\ \tau_{rr},\ \tau_{zr},\ \tau_{z\theta},\ q_z]^T \tag{8}$$

$$\overline{G}_r = [0,\ \tau_{zr},\ \tau_{rr},\ \tau_{r\theta},\ q_r]^T \tag{9}$$

$$\overline{H}_v = [0,\ \tau_{\theta z},\ \tau_{\theta r},\ \tau_{\theta\theta},\ q_\theta]^T \tag{10}$$

$$\overline{\tau}_{zz} = 2\mu \frac{\partial v_z}{\partial z} + \lambda_v \nabla \cdot \mathbf{V} \tag{11}$$

$$\tau_{zr} = \tau_{r2} = \mu \left(\frac{\partial v_r}{\partial z}\right) + \left(\frac{\partial v_z}{\partial r}\right) \tag{12}$$

$$\tau_{z\theta} = \tau_{\theta z} = \mu \left(\frac{1}{r}\frac{\partial v_r}{\partial \theta}\right) + \left(\frac{\partial v_\theta}{\partial z}\right) \tag{13}$$

$$\tau_{rr} = 2\mu \left(\frac{\partial v_r}{\partial r}\right) + \lambda_v \nabla \cdot \mathbf{V} \tag{14}$$

$$\tau_{r\theta} = \tau_{\theta r} = \mu \left(\frac{1}{r}\frac{\partial v_r}{\partial z} + \frac{\partial v_\theta}{\partial r} - \frac{v_o}{r}\right) \tag{15}$$

$$\tau_{\theta\theta} = 2\mu \left(\frac{1}{r}\frac{\partial v_\theta}{\partial \theta} + \frac{v_r}{r}\right) + \lambda_v \nabla \cdot \mathbf{V} \tag{16}$$

$$q_z = \nu_z \tau_{zz} + \nu_r \tau_{zr} + \nu_\theta \tau_{z\theta} k \frac{\partial T}{\partial z} \tag{17}$$

$$q_r = \nu_z \tau_{rz} + \nu_r \tau_{rr} + \nu_\theta \tau_{r\theta} + k \frac{\partial T}{\partial r} \tag{18}$$

$$q_o = v_z \tau_{\theta z} + v_\theta \tau_{\theta r} + v_\theta \tau_{\theta\theta} + k \frac{1}{r}\frac{\partial T}{\partial \theta} \tag{19}$$

$$k = \left[0,\ 0,\ \frac{p v_\theta^2 + P}{r} - \tau_{\theta\theta},\ 0,\ 0\right]^T \tag{20}$$

In the above equations ρ represents the density, $\mathbf{V}$ the absolute velocity vector, p the pressure, and T the temperature. The differential $d\forall$ is the volume of the control volume and dA_z, dA_r, dA_θ are the differential areas of its sides. From the equation of state, the total internal energy is related to pressure through the equation

$$e_o = \frac{P}{\rho(\gamma - 1)} + \frac{1}{2}|\mathbf{v}|^2 \tag{21}$$

and the total enthalpy, H, is related to p and e_o by

$$H = e_o + \frac{p}{\rho} \tag{22}$$

Sutherland's law is used to determine the molecular viscosity coefficient, and Stokes' hypothesis gives $\lambda_v = -2/3\ \mu_l$. Turbulence is accounted for by adding a turbulent viscosity μ_t to the molecular viscosity μ_l

$$\mu = \mu_l + \mu_t \tag{23}$$

In a similar manner, the molecular thermal conductivity k is replaced by

$$k = C_p\left[\frac{\mu}{P_r}\bigg|_l + \frac{\mu}{P_r}\bigg|_t\right] \tag{24}$$

where C_p is the specific heat at constant pressure and $P_r|_l + P_r|_t$ is the laminar and turbulent Prandtl number, respectively. The two-layer algebraic model of Baldwin and Lomax (1978) is used to model μ_t.

All lengths in the above equations are nondimensionalized by a reference length normally taken as the largest blade row diameter. The velocity components are nondimensionalized by a reference speed of sound, a_{ref}/γ where γ is the ratio of specific heats. Pressure and density are nondimensionalized by their respective reference values.

For rotating flows, the absolute (fixed) reference frame is transformed to the relative (rotating) frame by the transformation

$$\theta_{\text{ABSOLUTE}} = \theta_{\text{RELATIVE}} + \Omega t \tag{25}$$

where Ω is the rotational wheel speed. Introducing equation (24) into equation (1) transforms L and L_V to

$$L = \int_{dA}\left(\lambda \overline{F}\, dA_z + \lambda \overline{G}_v dA_r + \lambda(\overline{H} - r\Omega q)dA_\theta\right) \tag{26}$$

and

$$L_v = \int_{dA}\left(\lambda \overline{F}_v\, dA_z + \lambda \overline{G}_v dA_r + \lambda(\overline{H}_v - r\Omega q)dA_\theta\right) \tag{27}$$

Discretization of the inviscid portion of equation (1) including estimates of the surface area and volume is presented by Celestina et al. (1986). The viscous and heat transfer portion of equation (1) is discretized by evaluating the shear stress and the heat flux at the center of each face. The shear stresses and

Downloaded 01 Jun 2010 to 171.66.16.66. Redistribution subject to ASME license or copyright; see http://www.asme.org/terms/Terms_Use.cfm

heat flux are estimated using central differences of the velocity and the temperature field.

Artificial Dissipation

To suppress odd-even point decoupling of the solution to the discretized equations, dissipative terms are added to the equations. The operator L_v is replaced in the discretized form of equation (1) with $D(\lambda q)$

$$D(\lambda q) = D_I(q) + L_v(\lambda q) \tag{28}$$

where $D_I(q)$ is the added artificial dissipation operator needed to prevent decoupling of the solution within inviscid regions of the flow. The operator D_I is patterned after the model developed by Jameson et al. (1981) and is composed of three spatial operators

$$D_I(q) = (D_z + D_r + D_\theta)q \tag{29}$$

which can be evaluated separately. The dissipation in, for example, the axial direction (and similarly for the others) is expressed as follows:

$$D_z = d_{i+1/2,j,k} - d_{i-1/2,j,k} \tag{30}$$

where

$$d_{i+1/2,j,k} = \epsilon^{(2)}_{i+1/2,j,k}(\Delta_z q_{i+1/2,j,k}) - \epsilon^{(4)}_{i+1/2,j,k}\left(\Delta_z^2(\Delta_z q_{i+1/2,j,k})\right) \tag{31}$$

$$\epsilon^{(2)}_{i+1/2,j,k} = \kappa^{(2)}_i \beta_{i+1/2,j,k} \min(\nu_{i,j,k};\ \nu_{i+1,j,k};\ 0.5) \times \min\left(\frac{\mathrm{M}_{i+1/2,j,k}}{\overline{\mathrm{M}}},\ 1\right) \tag{32}$$

$$\epsilon^{(4)}_{i+1/2,j,k} = \max\left(0,\ \kappa^{(4)}\beta_{i+1/2,j,k}, \min\left(\frac{\mathrm{M}_{i+1/2,j,k}}{\overline{\mathrm{M}}},\ 1\right) - \epsilon^{(2)}_{i+1/2,j,k}\right) \tag{33}$$

and $\kappa^{(2)}$, $\kappa^{(4)}$ are constants set at 1/8 and 1/512, respectively. The symbols Δ and Δ^2 denote the first and second difference operators, while β is the maximum eigenvalue of the Jacobian matrix formed from $\overline{F}$. The coefficient $\nu_{i,j,k}$ is defined as

$$\nu_{i,j,k} = \left|\frac{P_{i+1,j,k} - 2P_{i,j,k} + P_{i-1,j,k}}{P_{i+1,j,k} + 2P_{i,j,k} + P_{i-1,j,k}}\right| \tag{34}$$

and is used primarily to prevent oscillations near stagnation points and shocks.

Vasta and Wedan (1988) scaled the Jameson artificial dissipation operator by a function of the local Mach number to reduce its effect within viscous regions of the flow. The present work uses the local meridional Mach number $\overline{\mathrm{M}}$ normalized by a reference upstream meridional Mach number $\overline{\mathrm{M}}$ to accomplish this task. To prevent this function from increasing the level of dissipation in the inviscid flow regions, the maximum value of this function is taken as unity. To reduce the level of artificial viscosity resulting from highly stretched mesh cells, we also adopted what is referred to by Vasta and Wedan as individual eigenvalue scaling of the artificial dissipation operator.

Solution Procedure

The discretized forms of the equations associated with the averaged passage flow model are solved using a dimensional sequencing algorithm. The motivation for the present algorithm came from observing the evolution of the error history associated with the algorithm reported in Celestina (1986). For many cases the magnitude of the error associated with the axisymmetric component of a variable was a significant fraction of the magnitude of the error associated with the variable itself. It thus seems reasonable to expect that a solution algorithm that explicitly reduced the error of the axisymmetric component of the flow field would enhance the convergence of the three-dimensional field. With the body forces assumed known (i.e., S assumed known), the present algorithm iterates between the three-dimensional flow equations and the corresponding throughflow equations to enhance the rate of convergence to the three-dimensional time asymptotic flow problem. The construction of this algorithm is as follows. First, the throughflow equations compatible with equation (1) are derived by summing equation (1), as modified according to the discussion in the preceding sections, over the tangential index k. This is accomplished by premultiplying equation (1) by the operator

$$\mathfrak{L} = \frac{1}{k}\sum_{k=1}^{k} \tag{35}$$

where K is the number of control volumes spanning the pitch. The result may be written as

$$\frac{d}{dt}\overline{\lambda q}\, d\overline{\forall} + \overline{L}(\overline{q}) - \overline{D}(\overline{q}) = \int \overline{\lambda}\,\overline{k}\, d\overline{\forall} + \mathfrak{L}\int S\, d\forall + \left\{\mathfrak{L}\int \lambda k\, dv - \int \overline{\lambda}\,\overline{k}\,\overline{d}\forall + \overline{L}(\tilde{\mathfrak{L}}q) - L(q) - \overline{D}(\tilde{\mathfrak{L}}q) + \mathfrak{L}D(q)\right\} \tag{36}$$

where $d\forall$, $\overline{\lambda}$, $\overline{q}$ are defined as (37)

$$\mathfrak{L}\lambda\, d\forall = \overline{\lambda}\, d\overline{\forall} \tag{38}$$

$$\mathfrak{L}\lambda\, d\forall = \overline{\lambda q}\, d\overline{\forall} \tag{39}$$

while the operators $\tilde{\mathfrak{L}}$, $\overline{L}$, and $\overline{D}$ are

$$\tilde{\mathfrak{L}}\, q = \frac{\lambda q\, d\forall}{\overline{\lambda}\, d\overline{\forall}} = \overline{q} \tag{40}$$

$$\overline{L}(\overline{q}) = \mathfrak{L}L(\overline{q}) \tag{41}$$

$$\overline{D}(\overline{q}) = \mathfrak{L}D(\overline{q}) \tag{42}$$

The terms that appear on the right-hand side of equation (36) are treated as forcing functions and are estimated using the most recent value of the three-dimensional flow variables. Note that the expressions that appear within brackets vanish by construction in regions of the flow where $q = \overline{q}$, and upon convergence of equation (36) (i.e., $\partial/\partial t\ \lambda q\, d\forall = 0$), $\tilde{\mathfrak{L}}\, q = \overline{q}$. The time asymptotic solution of equation (36) is thus identical to the axisymmetric average of the time asymptotic solution to equation (1). The steady-state solution of equation (1) can thus be obtained by cycling between a time-advancing algorithm for equation (1) and a similar algorithm for equation (36).

The discretized form of equation (1) is advanced in time using the four-stage Runge–Kutta algorithm of Jameson et al. (1981). Local time stepping (i.e., constant C.F.L. number) and residual averaging are employed to enhance convergence. Upon completion of a fixed number of temporal relaxation cycles, the three-dimensional flow variables are used to evaluate the right-hand side of equation (36). This equation is then advanced in time using the same integration procedure as that for the three-dimensional system. After a fixed number of time steps, the value of q is updated according to the equation

$$q = \overline{q} + (q - \tilde{\mathfrak{L}}q) \tag{43}$$

where the q's within the brackets are those that were used to evaluate the right-hand side of equation (36).

The three-dimensional residual error based on the updated value of q (i.e., equation (43)) is generally found to be largest within the blade passage region. Prior to initiating the next three-dimensional iteration cycle, the residual is reduced by performing a fixed number of three-dimensional iteration cycles (between five and ten iterations) over a local three-dimensional

Downloaded 01 Jun 2010 to 171.66.16.66. Redistribution subject to ASME license or copyright; see http://www.asme.org/terms/Terms_Use.cfm

flow region, which extends a modest distance upstream and downstream of the blade passage leading and trailing edges. The inlet and exit boundaries of this reduced flow domain are located in a region where the sum of the bracketed terms in equation (36) is small. The inlet and exit boundary conditions associated with the reduced flow domain are derived using the updated variables obtained from equation (43). Within this region of flow the values of q obtained from relaxing the reduced flow domain equations replace those obtained from equation (43).

The outlined solution procedure is a multigrid algorithm of the form introduced by Brandt (1982). It was specially constructed to reduce the axisymmetric component of the error vector, which at the start of the solution procedure is often large. It also recognizes the spatial relaxation of the three-dimensional flow field to an axisymmetric field away from the blade row of interest. This recognition reduces the computational work required to obtain a solution relative to a more traditional multigrid strategy.

The solution procedure outlined above has been implemented in both a V and W cycle framework. In the V cycle strategy, one proceeds directly from the three-dimensional solver to the throughflow solver to the reduced flow solver before going back to the three-dimensional solver. In the W cycle, one proceeds from the three-dimensional solver to the throughflow solver to the reduced flow solver and then cycles between the throughflow solver and the reduced flow solver before going back to the three-dimensional flow solver. The simulation to be reported was executed using the V cycle strategy. Experience with the W cycle is limited and needs further development. However, a preliminary analysis showed the W cycle strategy to require less computational work than the V cycle to converge to a fixed tolerance level.

When the three-dimensional flow field converges to a predetermined level, the body forces and energy sources required as input to simulations of the remaining blade rows can be estimated using the procedure outlined in Jameson et al. (1981). The cycling of information between the simulated blade rows of the multiblade row machine is carried out until the tangential averages of the simulated blade row flow fields agree with each other to a predetermined tolerance.

Boundary Conditions

All solid surfaces are modeled as rigid, nonslip, and impermeable. The surfaces are also assumed to be adiabatic. These conditions imply that the velocity relative to a solid surface is zero and that the temperature gradient normal to the surface is also zero. The pressure at a solid surface is obtained from the normal momentum equation evaluated at the surface. At the inlet, either the mass flow or the total pressure is specified along with the total temperatures and the radial and tangential velocity components. The one-dimensional Reinmann invariant C^- is extrapolated from the interior to the boundary; with the specified flow variables, it defines the incoming pressure, axial velocity component, and temperature. The shear stresses and heat flux at the inlet are also set to zero. At the exit radial equilibrium, with the pressure specified at the hub, is used to establish the radial pressure distribution. The flow quantities ρ, ρv_z, ρv_r, ρv_θ are extrapolated from the interior.

Grid Generation

As discussed by Celestina et al. (1986), the averaged passage equation system requires that a mesh be specified for each blade row of a multistage machine. In addition, the meshes must have a common meridional mesh in order to eliminate the need for interpolating the body forces and correlations from grid to grid. To capture shear layers and stagnation points properly a fine mesh spacing is required in a direction normal to solid surfaces and in the blade leading and trailing edge regions. A mesh generator capable of generating these features is discussed in detail by Mulac (1986).

Results and Discussion

The simulation executed used the Low-Speed Rotating Rig at United Technologies Research Center. The Low-Speed Rotating Rig (LSRR) is a stage-and-a-half turbine consisting of an inlet guide vane, a rotor, and a stator. The inlet guide vane contains 22 blades and the rotor and stator both contain 28 blades. The flow coefficient ϕ is 0.78 and the spacing between blades, B_x is 0.5. The LSRR grid contains 228 axial, 25 radial, and 41 circumferential points. Each blade row contains 40 axial points distributed along the chord with 26 axial points between each blade row, the inlet and exit.

The results to be presented required 11 h of Cray 2 C.P.U. time. They represent but a small fraction of the information obtained from the simulation. They are intended to illustrate the degree to which one can quantitatively predict performance parameters of interest to designers, and to reveal qualitative information identifying flow phenomena that may have an impact on performance. These results also reflect the current state of model development. The first series of results shows the predicted pressure distribution on the surface of each blade row of the turbine as a function of axial chord length and percent of span height. The span locations measured from the hub are 1.3, 12.5, 50, 87.5, and 98.7 percent, respectively. The experimental measurements taken at these locations are also shown. Experimental data were also available for 25 and 75 percent of span but were not utilized since they provided little additional information relative to the current discussion. The results for the first vane are shown in Fig. 1. The predicted loading level is seen to be in good agreement with the measurements of Dring (1988). The predicted pressure surface pressure distribution is in excellent agreement with the experimental results. For the suction surface, the agreement between measurement and simulation is good for the region forward of the minimum pressure peak. Aft of the peak, the agreement between experiment and simulation deteriorates. This deterioration is believed to be related to viscous effects (i.e., turbulence and transition modeling) whose modeling could be improved. Some exploratory calculations suggest that the boundary layer aft of the suction surface minimum pressure is growing too rapidly and, as a result of the radial pressure gradient, is being transported toward the hub to an extent greater than that suggested by a flow visualization studies. Improvements in the agreement between simulation and experiment have been obtained by incorporating a simple transition model in which the flow remains laminar forward of the minimum pressure peak and Baldwin Lomax turbulence model as implemented by

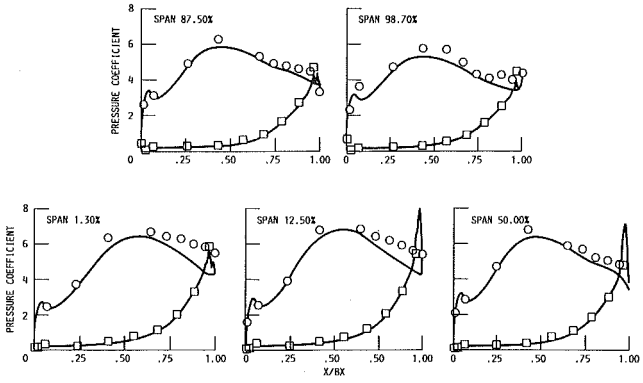

Fig. 1 First blade pressure distributions

Downloaded 01 Jun 2010 to 171.66.16.66. Redistribution subject to ASME license or copyright; see http://www.asme.org/terms/Terms_Use.cfm

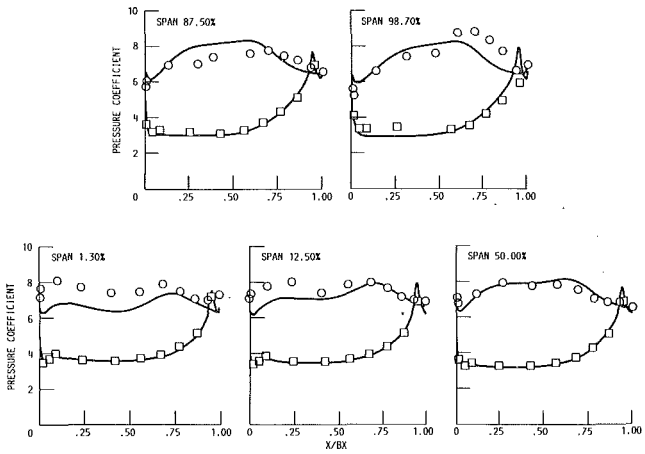

Fig. 2 Rotor pressure distributions

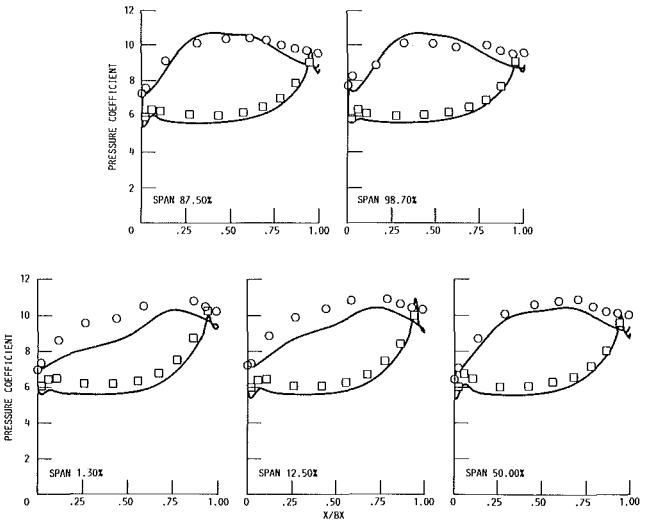

Fig. 3 Second blade pressure distributions

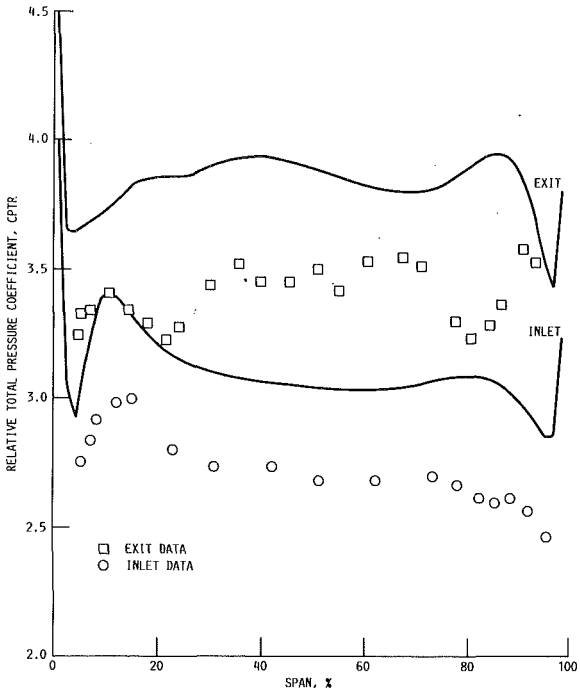

Fig. 4 Rotor relative total pressure coefficient versus span

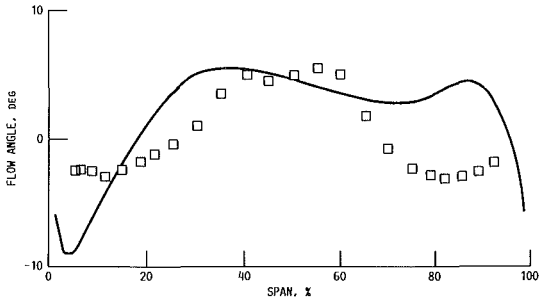

Fig. 5 Rotor relative exit flow angle versus span

Dawes (1986). The current simulation assumes the flow to be fully turbulent from the leading edge of each blade. Work on this problem is continuing. The next figure shows the predicted and measured pressure distribution for the rotor. The predicted loading levels appear to be in good agreement with measurements, with the exception of the hub and tip region. The present simulation does not include a clearance region, which should account for some of the discrepancy in the tip region. The pressure distribution along the pressure surface is once more in excellent agreement with the measurements. At the midspan and at 25 and 75 percent (not shown) of span the predicted pressure distribution along the suction surface is in good agreement with the data. At 1.3 percent and 12.5 percent of span, the suction surface pressure coefficient is lower than that measured. As a result the loading is lower over the forward portion of the rotor than what has been measured. Although the cause of this discrepancy is unknown at the present time, one could speculate that it may be due to an overestimate of the magnitude and extent of the low-momentum fluid exiting the first vane.

The pressure distribution for the last vane is shown in Fig. 3. Once again the loading level is well predicted with the exception of the location at 1.3 percent of span. The underpredicted suction surface pressure coefficient at 1.3 and 12.5 percent of span suggests that the flow incidence to these sections is underestimated. There also appears to be a shift of the predicted pressure distribution relative to the measured distribution. This shift is believed to be caused by an overestimate of the loss generated by the first two blade rows. With the exception of this discrepancy, the pressure distribution on the pressure surface is in good agreement with measurements. Similarly, the predicted suction surface distribution at midspan agrees well with the experimental distribution. The next figure shows the predicted relative total pressure coefficient forward and aft of the rotor as a function of span. The measured distribution reported by Sharma et al. (1988) is also shown. The magnitude of the predicted coefficient for the inlet flow is higher than measured; however, the shape of the curve is consistent with the data. The magnitude of the predicted exit flow coefficient is also higher than measured. The influence of the secondary vortices generated within the rotor passage on the exit flow coefficient is more evident in the experimental data than in the simulation result. The data of Sharma et al. (1988) suggest that the secondary vortices exit the rotor at approximately 30 and 70 percent of span. The local minimums in the measured exit flow distribution at 25 and 85 percent of span are a consequence of the velocity field induced by these vortices. The location of the tip vortex as suggested by the experimental data is significantly inboard of the location 90 percent span suggested by the simulation. The difference is believed to be due to the tip leakage flow, which was not accounted for. It appears that this flow drives the tip secondary vortex inward toward the hub.

Downloaded 01 Jun 2010 to 171.66.16.66. Redistribution subject to ASME license or copyright; see http://www.asme.org/terms/Terms_Use.cfm

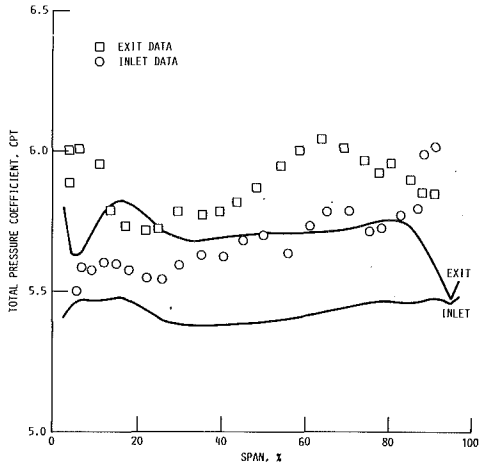

Fig. 6 Second blade total pressure coefficient versus span

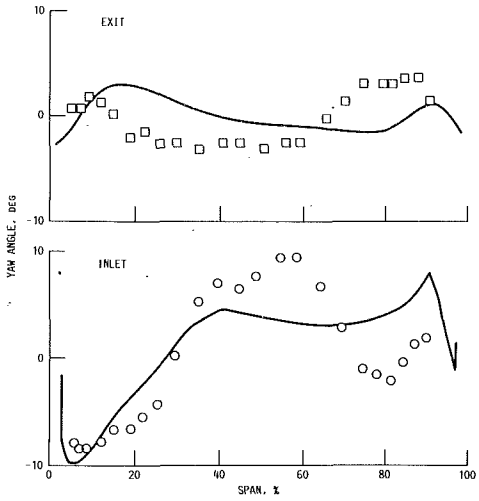

Fig. 7 Second stator flow angle distribution

The simulation results place the hub secondary flow vortex at 25 percent of span at the exit of the rotor, which is in good agreement with measurements. This vortex, however, appears to be more diffuse than measured, which may account for the lack of a local minimum in the exit flow relative total pressure coefficient at 25 percent of span.

The deviation from the design intent of the rotor relative exit flow angle is shown in Fig. 5. This angle is plotted as a function of span, with the solid curve representing the simulation and the open symbols the measured data from Sharma et al. (1988). The agreement between the two is reasonable, with the exception of the tip region, where the result of neglecting the tip leakage flow is quite evident. The noticeable overturning of the flow near the endwalls and the subsequent underturning in the region of midspan caused by the secondary vortices is clearly seen in both the data and the prediction. The flow physics that leads to this result appears to be well captured.

Recently the authors became aware of data acquired under A.F.O.S.R. sponsorship by United Technologies Research Center that show the agreement between simulation and measurement to be better than that indicated by Figs. 4 and 5. An evaluation of the present results in light of these data will have to await its publication.

The next two figures are for the second vane. The first, Fig. 6, shows the predicted total pressure coefficient forward and aft of the second vane as a function of span. Also shown are the data from Sharma et al. (1988).

The predicted total pressure coefficients are lower than measured, which, as previously noted, is the result of overestimating the loss produced by the first two blade rows. The difference between these two curves is a measure of the loss across the blade row. It too appears to be overestimated. With the exception of the flow region strongly influenced by the tip leakage flow from the rotor, the indicated trends agree with the experiment. Judging by the shape of the incoming total pressure field (either from the data or the prediction), it does not appear that the secondary vortices generated by the rotor would have a significant effect on the performance of the second vane. The next figure, which shows the flow angle entering and leaving the second vane relative to the design intent, leads to a far different conclusion. The large variation in the inlet flow angle between 10 and 40 percent of span seen in both the experimental data and prediction clearly is caused by the rotor hub secondary vortex. The time-averaged signature of this vortical structure is a region of shear whose vorticity vector is nearly aligned with the incoming time-averaged velocity field. The tip secondary vortex appears to generate a similar structure; however, the measurements suggest it occurs inboard of that predicted. This entering shear flow causes the second vane to behave aerodynamically differently than it would in isolation.

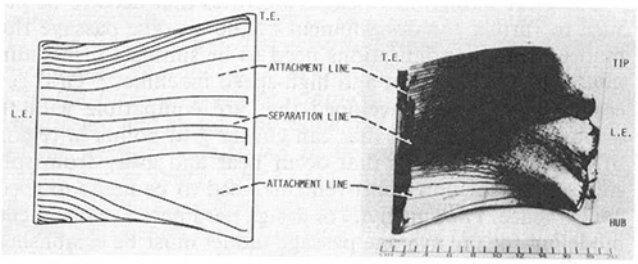

Fig. 8 Second blade pressure surface limiting streamline pattern

The results shown in Fig. 7 indicate that the simulation predictions are in reasonable agreement with data. The simulation captures the underturning of the flow near the endwalls, and in the midspan region, the tendency for the flow to overturn. This behavior is partly due to the time-averaged shear flow produced by the rotor secondary vortices.

The last figure shows the limiting streamline pattern associated with the time-averaged flow adjacent to the second vane pressure surface. Also shown is the corresponding flow visualization result of Langston (1988). These results are presented to show that the time-averaged effect of the unsteady vorticity field entering a blade row has a major influence on the flow field within the blade row. Near midspan, the incoming shear flow causes a contraction of the streamlines, suggesting the existence of a line of flow separation. Near both endwalls, the time-averaged vorticity field entering the second vane interacts with the secondary vortices generated within the vane to generate two lines of flow attachment. This flow pattern is far more complicated than that for an isolated blade row and the ability of the present model to capture its structure is very encouraging. Finally, in closing it is suggested that the enhanced heat transfer observed at midspan of the suction surface reported by Sharma et al. (1988) is caused by the secondary vortices generated within the rotor.

Summary and Conclusion

Given the early state of the average passage model development, the results presented in this report are very encouraging. The amount of empirical information used in the stage and one-half turbine simulation is considerably less than that

Downloaded 01 Jun 2010 to 171.66.16.66. Redistribution subject to ASME license or copyright; see http://www.asme.org/terms/Terms_Use.cfm

required to achieve comparable results using today's quasi-three-dimensional flow models. The average passage flow model also appears to be able to capture the physical features of the secondary flow field generated within a multistage turbine configuration. It appears that an accurate model of the time-averaged vorticity field produced by the unsteady secondary vorticity exiting a blade row is required to establish the performance of the downstream blade row. The outlined closure procedure, unlike some others that have been suggested, insures that the unsteady vorticity field exiting a blade row is consistent with exiting time-averaged vorticity field. Hence, no spurious vorticity is produced as a result of coupling one blade row to another.

The simulation of the stage and one-half turbine has shown the complex nature of the endwall flow in a low-aspect-ratio turbine. In the rotor, the secondary vortices generated within the endwalls affect the flow at midspan. They cause the endwall fluid to be deposited on the suction surface. This transport of low-momentum fluid leads to significant spanwise mixing across the axisymmetric stream surface. It is doubtful that an endwall boundary layer model could be used to predict this phenomenon.

There are numerous research activities that need to be pursued to further the development of the average passage flow model. Other configurations need to be simulated, including multistage compressors and high-speed machinery. Grid generators need to be developed that are compatible with the average passage model that can cluster grid points in regions of high flow gradients that occur near and away from solid surfaces. Algorithm improvements need to be made to speed convergence. The sensitivity of design parameters to turbulence modeling for the average passage model must be established. Finally, experimental and analytical work in support of closure modeling must be pursued to establish the models for generalized Reynolds stresses and the associated energy correlations.

Acknowledgments

The authors wish to express their gratitude to Professor E. M. Greitzer of the Massachusetts Institute of Technology and to Dr. O. P. Sharma of Pratt & Whitney Aircraft for their many useful suggestions during the course of this work. The authors would also like to thank Dr. R. P. Dring of the United Technologies Research Center for providing the experimental pressure distribution data and Dr. L. S. Langston of the University of Connecticut for his flow visualization results.

References

Adamczyk, J. J., 1984, "Model Equation for Simulating Flows in Multistage Turbomachinery," ASME Paper No. 85-GT-226; NASA TM-86869.

Adamczyk, J. J., Mulac, R. A., and Celestina, M. L., 1986, "A Model for Closing the Inviscid Form of the Average Passage Equation System," ASME Paper No. 86-GT-227; NASA TM-87199.

Baldwin, B. S., and Lomax, H., 1978, "Thin Layer Approximation and Algebraic Model for Separated Turbulent Flows," AIAA Paper No. 78-257.

Brandt, A., 1982, "Guide to Multigrid Development," *Multigrid Methods*, Springer-Verlag, New York.

Celestina, M. L., Mulac, R. A., and Adamczyk, J. J., 1986, "A Numerical Simulation of the Inviscid Flow Through a Counterrotating Propeller," ASME JOURNAL OF TURBOMACHINERY, Vol. 108.

Dawes, W. N., 1986, "Application of Full Navier-Stokes Solvers to Turbomachinery Flow Problems," *Numerical Techniques for Viscous Flow Calculation in Turbomachinery Bladings*, VKI-LS-1986-02, Von Karman Institute for Fluid Dynamics, Rhode-Saint-Genese, Belgium.

Denton, J. D., and Singh, U. K., 1979, "Time Marching Methods for Turbomachinery Flow Calculations," *Application of Numerical Methods to Flow Calculations in Turbomachines*, VKI-LEC-SER-1979-7, Von Karman Institute for Fluid Dynamics, Rhode-Saint-Genese, Belgium.

Dring, R. P., 1988, United Technologies Research Center, Private Communication.

Jameson, A., Rizzi, A., Schmidt, W., and Turkel, E., 1981, "Numerical Solutions of the Euler Equations by Finite Volume Methods Using Runge-Kutta Time-Stepping Schemes," AIAA Paper No. 81-1259.

Langston, L. S., 1988, University of Connecticut, Private Communication.

Mulac, R. A., 1986, "A Multistage Mesh Generator for Solving the Average Passage Equation System," NASA CR-179539.

Ni, R. H., 1987, "Flow Simulation in Multistage Turbine," presented at the NASA Marshall Space Flight Center Computational Fluid Dynamics Workshop, Apr.

Rai, M. M., 1987, "Unsteady Three-Dimensional Simulations of Turbine Rotor-Stator Interaction," AIAA Paper No. 87-2058.

Sharma, O. P., Renaud, E., Butler, T. L., Millsaps, K., Jr., Dring, R. P., and Joslyn, H. G., 1988, "Rotor-Stator Interaction in Multi-stage Axial-Flow Turbines," AIAA Paper No. 88-3013.

Smith, L. H., Jr., 1966, "The Radial-Equilibrium Equation of Turbomachinery," ASME *Journal of Engineering for Power*, Vol. 88, No. 1, pp. 1-12 (discussion in Vol. 88, No. 3, p. 282).

Vatsa, V. N., and Wedan, B. W., 1988, "Navier-Stokes Solutions for Transonic Flow Over a Wing Mounted in a Tunnel," AIAA Paper No. 88-0102.

Whitfield, D. L., Swafford, T. W., Janus, J. M., Mulac, R. A., and Belk, D. M., 1987, "Three-Dimensional Unsteady Euler Solutions for Propfans and Counter-rotating Propfans in Transonic Flow," AIAA Paper No. 87-1197.

Wu, Chung-Hua, 1952, "A General Theory of Three-Dimensional Flow in Subsonic and Supersonic Turbomachines of Axial-, Radial-, and Mixed-Flow Types," NACA TN 2604.

Downloaded 01 Jun 2010 to 171.66.16.66. Redistribution subject to ASME license or copyright; see http://www.asme.org/terms/Terms_Use.cfm

Multi-Airfoil Navier-Stokes Simulations of Turbine Rotor-Stator Interaction

M. M. Rai
Research Scientist,
Applied Computational Fluids Branch.

N. K. Madavan
Principal Analyst,
Sterling Federal Systems.

NASA Ames Research Center,
Moffett Field, CA 94035

An accurate numerical analysis of the flows associated with rotor-stator configurations in turbomachinery can be extremely helpful in optimizing the performance of turbomachinery. In this study the unsteady, thin-layer, Navier-Stokes equations in two spatial dimensions are solved on a system of patched and overlaid grids for an axial-turbine rotor-stator configuration. The governing equations are solved using a finite-difference, upwind algorithm that is set in an iterative, implicit framework. Results are presented in the form of pressure contours, time-averaged pressures, unsteady pressures, amplitudes, and phase. The numerical results are compared with experimental data and the agreement is found to be good. The results are also compared with those of an earlier study, which used only one rotor and one stator airfoil. The current study uses multiple rotor and stator airfoils and a pitch ratio that is much closer to the experimental ratio. Consequently, the results of this study are found to be closer to the experimental data.

Introduction

Flows within turbomachinery are generally unsteady in nature and are therefore difficult to compute. The unsteadiness is caused by (*a*) the interaction of the rotor airfoils with the wakes and passage vortices generated by upstream airfoils, (*b*) the relative motion of the rotors with respect to the stators (potential effect), and (*c*) the shedding of vortices by the airfoils because of blunt trailing edges. Computation of such flows is further complicated by the relative motion between the rotor and stator airfoils and the periodic transition of the flow from laminar to turbulent. Nevertheless, a clear understanding of the unsteady processes within turbomachinery is essential to improving current design procedures.

Several calculations of cascade flow already exist in the literature. These studies include two- and three-dimensional calculations using both the Euler and Navier-Stokes equations. While analyses of flows through isolated rows can be used to study many of the fluid-dynamic phenomena in turbomachinery, such analyses do not yield any information regarding the unsteadiness arising out of the interaction of moving and stationary rows of airfoils. These interaction effects become increasingly important as the distance between successive rows is decreased. The experimental results of Dring et al. (1982) show that the temporal pressure fluctuation near the leading edge of the rotor airfoil can be as much as 72 percent of the exit dynamic pressure when the axial gap is reduced to 15 percent of the chord length (for the operating conditions and geometry chosen). Thus, the need is obvious for treating the rotor and stator airfoils as a system in cases where interaction effects are predominant.

Rai (1987a) presents two-dimensional rotor-stator interaction results for an axial turbine. The airfoil geometry and flow conditions used are the same as those in the experiments of Dring et al. (1982). The unsteady, thin-layer, Navier-Stokes equations are solved in a time-accurate manner to obtain the unsteady flow field associated with this configuration. The governing equations are solved on a system of patched and overlaid grids with information transfer from grid to grid taking place at the zonal boundaries. The numerically obtained results are compared with the experimental results of Dring et al. (1982). A good comparison between theory and experiment is obtained in the case of time-averaged pressures on the rotor and stator airfoils. Pressure amplitudes (corresponding to the pressure variation in time) were found to compare reasonably well with experiment, thereby indicating the validity of the computed unsteady component of the flow.

In Rai (1987b) the approximation of two-dimensionality is removed and fully three-dimensional airfoil geometries are used. In addition, the hub, outer casing, and rotor tip clearance are all included in the calculation. As in Rai (1987a), a system of patched and overlaid grids is used to discretize the rather complex geometry of the three-dimensional configuration. An implicit, upwind third-order-accurate method is used in all the patches (the calculation of Rai, 1987a, used a hybrid upwind/central difference scheme near the surface boundaries). The equations solved are the unsteady, thin-layer, Navier-Stokes equations in three dimensions. As in Rai (1987a), time-averaged airfoil surface pressures were found to compare well with experiment, but numerically obtained pressure amplitudes were only reasonably close to experimental data.

Contributed by the International Gas Turbine Institute and presented at the AIAA 26th Aerospace Sciences Meeting, Reno, Nevada, January 11-14, 1988. Manuscript received at ASME Headquarters February 5, 1990. Paper No. AIAA-88-0361.

Copyright © 1990 by ASME
Downloaded 01 Jun 2010 to 171.66.16.66. Redistribution subject to ASME license or copyright; see http://www.asme.org/terms/Terms_Use.cfm

One approximation that was made by Rai (1987a, 1987b) was a rescaling of the rotor geometry. The experimental turbine of Dring et al. (1982) has 22 airfoils in the stator row and 28 airfoils in the rotor row. Therefore an accurate calculation would require a minimum of 25 airfoils (11 in the stator row and 14 in the rotor row). In order to avoid the computational expense involved in simulating the flow associated with 25 airfoils, the rotor airfoil was enlarged by a factor of 28/22, keeping the pitch-to-chord ratio the same. It was then assumed that there were 22 airfoils in the rotor row. This assumption makes it possible to perform a calculation with only one rotor and one stator, thus reducing computation time by more than an order of magnitude. Whereas this approximation has little or no effect on time-averaged pressure distributions, it does affect the temporal variations of the flow variables. Far-field acoustics are significantly altered when the configuration is changed to have an equal number of rotor and stator airfoils.

This study presents results obtained using a new computer program that can simulate flow in a stage with an unequal number of rotor and stator airfoils. The calculations are performed with the unsteady, thin-layer, Navier–Stokes equations in two dimensions. The region of interest is discretized with the help of multiple patched and overlaid grids as in Rai (1987a, 1987b). Results in the form of time-averaged pressures, as well as pressure amplitudes and phase for the rotor and stator airfoils, are presented for both the one-rotor/one-stator and the multirotor/multistator (three stator and four rotor airfoils) cases. The time-averaged pressures are almost identical for the two cases. However, a significant improvement is obtained in pressure amplitude and phase for the multirotor/multistator case. This improvement is to be expected because the ratio of rotors to stators in the multi-airfoil calculation (4/3) is much closer to the experimental value (28/22). The degree of rotor rescaling required to keep the blockage effects the same is much smaller.

The following sections describe the grids used in the calculation, the integration method, the various boundary conditions, and the results obtained.

Grid System for the Rotor–Stator Configuration

A combination of patched and overlaid grids is used to discretize the regions surrounding the rotor–stator configuration. The region can be discretized using only patched grids. However, the number of zones required to solve the problem accurately would be twice as many as that required when both patched and overlaid grids are used in conjunction. Overlaid grid calculations are difficult to make conservative at the overlay boundaries. Since the current calculation is entirely subsonic and free of flow discontinuities (the maximum Mach number in the system is less than 0.35), physically meaningful solutions can be obtained even with the use of the nonconservative form of the equations. Therefore nonconservative overlap boundary conditions can be expected to yield accurate solutions.

The airfoil geometry used in the current study is the same as that used in the experimental investigation of Dring et al. (1982). The geometry consists of 22 stator airfoils and 28 rotor airfoils. An accurate simulation of this configuration would require at least 11 stator airfoils and 14 rotor airfoils, thus making the computation extremely expensive. Therefore the rescaling strategy of Rai (1987a) was used to reduce the number of airfoils. In the one-rotor/one-stator case this was done by enlarging the rotor by the factor 28/22 and then assuming that there were only 22 rotor airfoils. The pitch-to-chord ratio of the rotor was not changed during the enlargement process. Similarly, in the four-rotor/three-stator case it was assumed that there were 21 stators and 28 rotors and the stator was enlarged by the factor 22/21. Figure 1 shows the rotor–stator geometry of Dring et al. (1982) at midspan.

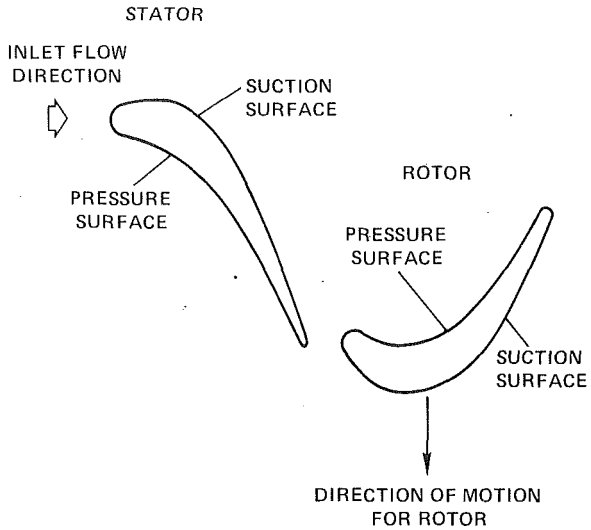

Fig. 1 Rotor–stator geometry of Dring et al. (1982)

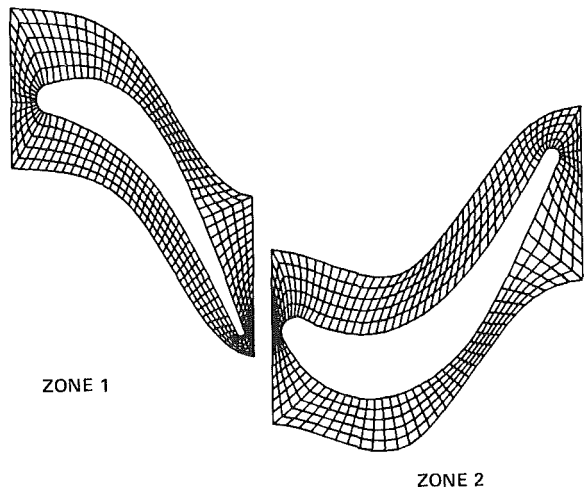

Fig. 2 "O" type grids for zones 1 and 2

The multizone grid used to discretize the region consists of four zones. Figure 2 shows the first two zones. The first zone contains the stator and is discretized with an "O" grid. The second zone contains the rotor and is also discretized with an "O" grid. The grids in these two zones were generated using an elliptic grid generator of the type developed by Steger and Sorenson (1979). Although the actual grids used for the calculation are very dense near the airfoil surfaces (to resolve the viscous effects), for the purpose of clarity Fig. 2 shows grids in which the points are equispaced in the direction normal to the airfoil surfaces.

Figure 3 shows zones 3 and 4. The grids for zones 3 and 4 were generated using an algebraic grid generator. Zone 3 contains the inner stator zone and zone 4 contains the inner rotor zone. In fact the inner boundary of zone 3 corresponds to the outer boundary of zone 1 and similarly the inner boundary of zone 4 corresponds to the outer boundary of zone 2. This positioning of the inner and outer stator zones (and the inner and outer rotor zones) facilitates information transfer between these zones. The outer zones abut each other along the patch boundary ABCD and slip past each other as the rotor airfoil moves downward. It is advantageous to use a patch boundary (as opposed to an area of overlay) where one system of grids moves relative to another system of grids because both time accuracy and conservation can be more easily controlled in patched-grid calculations.

Downloaded 01 Jun 2010 to 171.66.16.66. Redistribution subject to ASME license or copyright; see http://www.asme.org/terms/Terms_Use.cfm

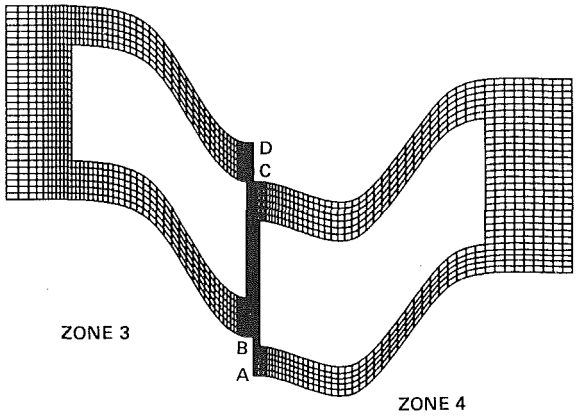

Fig. 3 Algebraically generated grids for zones 3 and 4

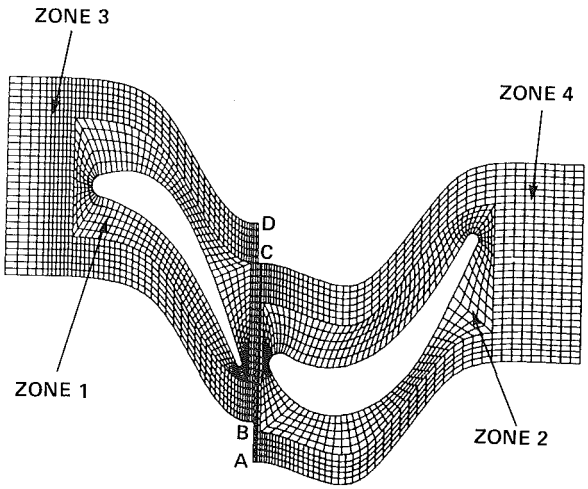

Fig. 4 Composite grid containing zones 1–4

Note in Fig. 3 that zones 3 and 4 do not align with each other. The segment AB of zone 4 does not seem to align with any part of the patch boundary of zone 3 and similarly the segment CD of zone 3 does not seem to align with any part of the patch boundary of zone 4. However, the periodicity boundary condition can be used to solve this problem, the result being that the segment AB is matched with the segment CD. Figure 4 shows all the zones and the corresponding grids used in the calculation. Figure 5 shows a similar system of grids for the four-rotor/three-stator calculation.

Numerical Methodology

The unsteady, thin-layer, Navier–Stokes equations in two spatial dimensions are solved using an upwind finite-difference algorithm.This algorithm is third-order accurate in space and second-order accurate in time. It is set in an iterative, factored, implicit framework wherein several iterations are performed at each time step so that the fully implicit finite-difference equations are solved. In this scheme, factorization and linearization errors can be driven to zero at each step. Details regarding the method can be found from Rai (1987b).

The use of multiple grids in simulating the flow over the rotor–stator configuration shown in Fig. 4 results in several computational boundaries. The boundary condition used at each of these boundaries is briefly outlined below.

The inner boundaries of the two "O" grids correspond to the airfoil surfaces and, hence, the "no-slip" condition and adiabatic wall conditions (or wall temperature) are imposed at these boundaries. It should be noted that in the case of the rotor airfoil no-slip does not imply zero absolute velocity at the surface of the airfoil, but rather zero relative velocity. In addition to the no-slip condition, the derivative of pressure in the direction normal to the wall surface is set to zero.

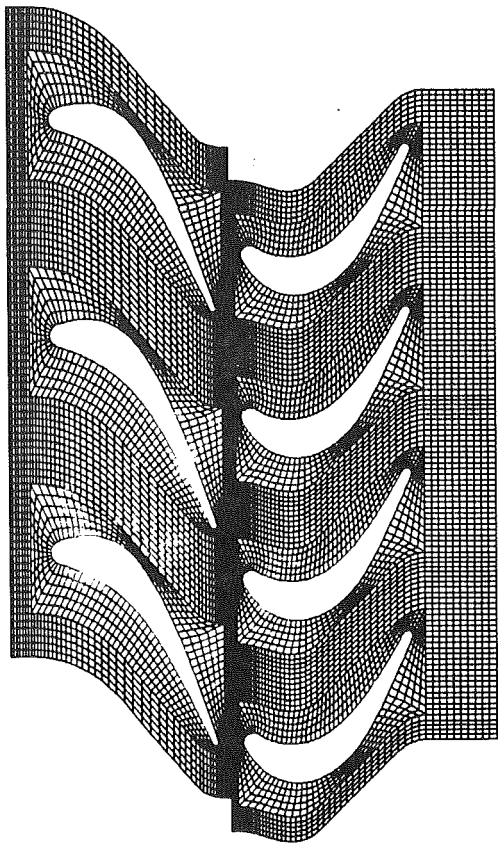

Fig. 5 Composite grid for the four-rotor/three-stator case

The left boundary of zone 3 is a subsonic inlet boundary. Three quantities need to be specified at this boundary. The three chosen for this study are the Riemann invariants

$$R_1 = u + \frac{2c}{\gamma - 1} \qquad R_3 = \frac{p}{\rho^\gamma} \tag{1}$$

and the inlet flow angle, which in this case is equivalent to

$$v_{\text{inlet}} = 0 \tag{2}$$

In the above equations the quantities u and v are the velocities in the x and y directions, respectively, p is the pressure, ρ is the density, and c the local speed of sound. The fourth quantity (which is necessary to update the points on this boundary) is also a Riemann invariant

$$R_2 = u - \frac{2c}{\gamma - 1} \tag{3}$$

and is extrapolated from the interior of zone 3.

The calculation assumes that there are an infinite number of rotor and stator airfoils in the positive and negative y directions in Fig. 4. Hence, a simple periodicity boundary condition is imposed on the upper and lower boundaries of zones 3 and 4. The implicit implementation of this boundary condition is straightforward and will not be discussed here. In the four-rotor/three-stator case periodicity is imposed over a distance in the y direction corresponding to three stator airfoils (or four rotor airfoils). The lower boundary (outer stator zone) of the first stator is assumed to have the same dependent variable values as the upper boundary (outer stator zone) of the third stator. A similar procedure is adopted for the rotor row.

Downloaded 01 Jun 2010 to 171.66.16.66. Redistribution subject to ASME license or copyright; see http://www.asme.org/terms/Terms_Use.cfm

The right boundary of zone 4 is a subsonic exit boundary. A simple implicit extrapolation procedure is used at this boundary. The implicit extrapolation is followed by a postupdate correction wherein the exit static pressure is specified. This type of boundary condition reflects the pressure waves that reach the exit boundary back into the system. The effect of this reflective property of the exit boundary is discussed later.

A second exit boundary condition used in this study is a partially nonreflective procedure developed by Erdos et al. (1977). This exit boundary condition is obtained from a quasi-one-dimensional analysis and amounts to specifying the Riemann invariant

$$R_2 = u - \frac{2c}{\gamma - 1}$$

at the exit boundary. This boundary condition is nonreflective for waves or components of waves that are perpendicular to the exit boundary (pressure variations in the x direction only) and is reflective for waves that are parallel to the exit boundary (pressure variations in the x direction only) and is reflective for waves that are parallel to the exit boundary (pressure variations in the y direction only). A shortcoming of this approach is that the specification of the Reimann invariant R_2 does not result in a good control over the mass flow rate through the turbine. The correct pressure drop across the turbine has to be obtained through an iterative process in which R_2 is varied until the right average exit static pressure is obtained. It may be possible to obtain a completely nonreflective boundary condition by using a hybrid approach wherein the variation of R_2 along the grid line $imax - 1$ is transferred to the grid line $imax$.

The present calculation uses both patched grids (grids that come together along common lines) and overlaid grids (grids that have a common area of overlap). The region of overlay is not clear from Fig. 4. Although information from zone 3 is transferred to zone 1 at the patch boundary (clearly seen in Fig. 4), the information from zone 1 is transferred to zone 3 at grid points of zone 3 that lie in zone 1. This is possible because the zone 3 grid exists under the zone 1 grid, though this overlap is not shown in Fig. 4 for the purpose of clarity. The boundary conditions used to transfer information from grid to grid are discussed by Rai (1987b) and, in the interest of brevity, are not included here.

Results

In this section the results obtained for the rotor–stator configuration shown in Fig. 1 are presented. These results were obtained by integrating the equations of motion and the boundary conditions described earlier. Three iterations were performed at each step. Approximately seven cycles (a cycle corresponds to the motion of the rotor through an angle equal to $2\pi/N$ where N is the number of stator airfoils) were required to eliminate the initial transients and establish a solution that was periodic in time. The calculation was performed at a constant time step value of about 0.04 (this translates into 2000 time steps per cycle).

The dependent variables are nondimensionalized with respect to the inlet pressure (p_∞) and density (ρ_∞). This yields

$$u_\infty = \mathrm{M}_\infty \sqrt{\gamma}$$
$$v_\infty = 0 \text{ (inlet flow is axial)}$$

where M_∞ is the inlet Mach number. The inlet Mach number used for this calculation was 0.07. The Riemann invariants that are prescribed at the inlet are determined using the dependent variables defined above. The rotor velocity ω is determined from the desired flow coefficient u_∞/ω (0.78 in this case) and the inlet axial velocity (u_∞). Since the quantities that are prescribed at the inlet boundary are the Riemann invariants

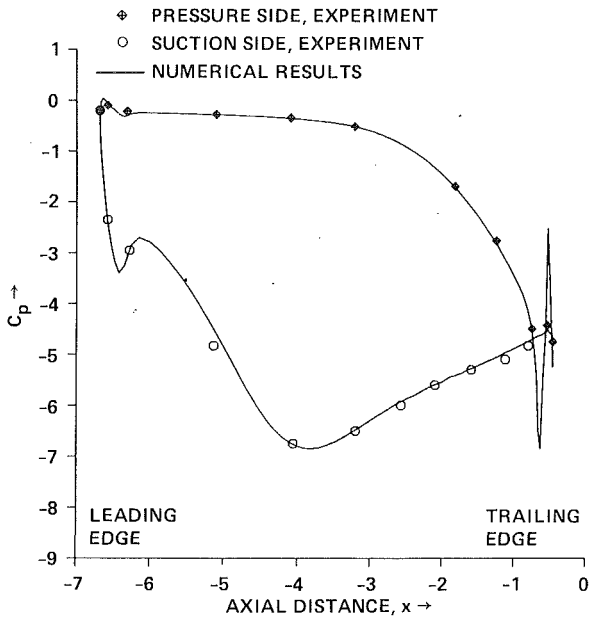

Fig. 6 Time-averaged pressure distribution on the stator

and not the dependent variables themselves, the values of u, v, ρ, and p obtained at the inlet, when the solution becomes periodic in time, are different from those used to determine the Riemann invariants. Hence, the rotor velocity needs to be recomputed and the calculation needs to be continued for a few more cycles (which then establishes a slightly different time-periodic solution). This iterative process must be continued until the calculated flow coefficient is equal to the required flow coefficient within certain limits of tolerance. The iterative process was not carried out for the calculations presented in this study because the right value of the rotor velocity (to obtain a flow coefficient of 0.78) was known a priori from the two-dimensional calculation of Rai (1987a).

The Reynolds number used for this calculation was 100,000/in. This value of the Reynolds number is close to the experimental value but not exactly so (because of the rescaling of the rotor geometry). The Baldwin–Lomax model (Baldwin and Lomax, 1978) was used to determine the eddy viscosity. The kinematic viscosity was calculated using Sutherland's law.

A One-Rotor/One-Stator Calculation. The first calculation was performed assuming that there were equal numbers of rotor and stator airfoils (22 of each). This permitted a calculation with only one rotor and one stator airfoil. The rotor airfoil was enlarged by the factor 28/22 to keep the blockage effects the same as in the experiment. The pitch-to-chord ratio was not changed during the enlargement process.

Figures 6–9 depict results obtained using a fixed exit, static-pressure condition (totally reflective exit boundary condition). Figure 6 shows the time-averaged pressure coefficient (C_p) as a function of the axial distance along the stator. The pressure coefficient is defined as

$$C_p = \frac{p_{\mathrm{avg}} - (p_t)_{\mathrm{inlet}}}{\frac{1}{2}\rho_{\mathrm{inlet}}\omega^2}$$

where p_{avg} is the static pressure averaged over one cycle, $(p_t)_{\mathrm{inlet}}$ is the average total pressure at the inlet, and ρ_{inlet} is the average density at the inlet. Clearly there is good agreement between theory and experiment. A small separation bubble was found on the pressure side of the stator in the numerical results. This is seen as a sharp dip and rise of C_p toward the trailing edge on the pressure side. The experimental data also indicate such

Downloaded 01 Jun 2010 to 171.66.16.66. Redistribution subject to ASME license or copyright; see http://www.asme.org/terms/Terms_Use.cfm

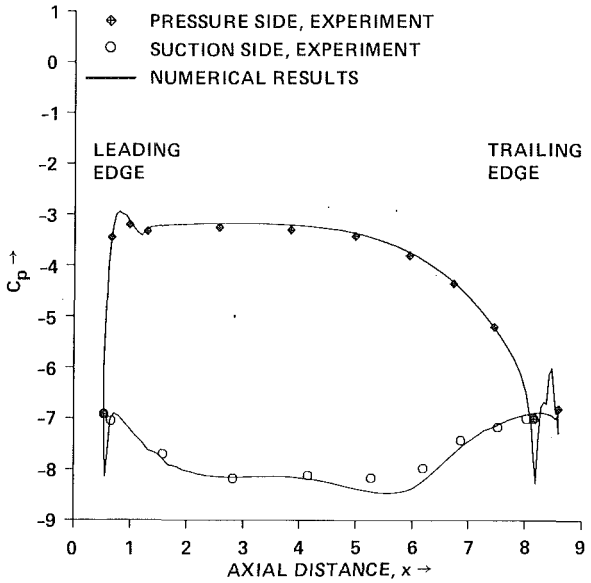

Fig. 7 Time-averaged pressure distribution on the rotor

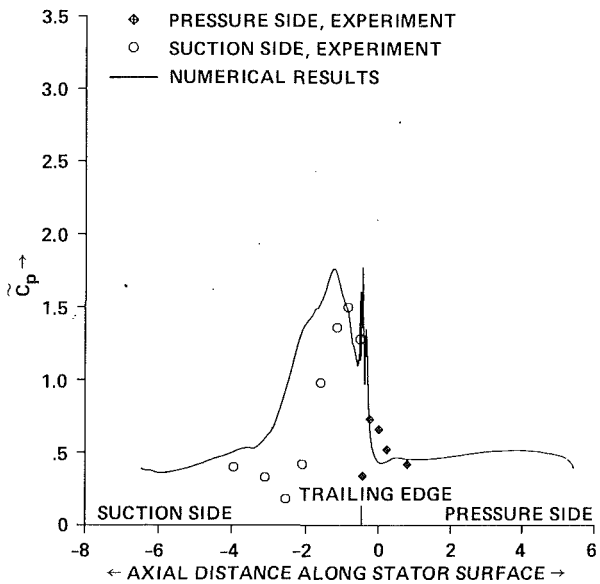

Fig. 8 Pressure amplitude distribution on the stator

a separation. However, the magnitude of the pressure fluctuation obtained numerically may be suspect because the turbulence model was not tailored to yield accurate estimates of the eddy viscosity in such regions.

Figure 7 shows the time-averaged C_p distribution for the rotor. The agreement is good except on the suction side of the rotor toward the trailing edge ($4.0 \leq x \leq 7.0$). This difference between the calculated and experimental results is because of the three dimensionality of the real flow. The disappearance of this difference between theory and experiment with a three-dimensional calculation is documented by Rai (1987b). A small separation bubble was found on the trailing edge circle as in the case of the stator. The bubble is seen as a spatial fluctuation in pressure.

The amplitude of the temporal pressure fluctuation is a measure of the unsteadiness of the flow. Figure 8 shows pressure amplitudes $\tilde{C}_p$ on the surface of the stator plotted as a function of the axial distance. The quantity $\tilde{C}_p$ is defined as

$$\tilde{C}_p = \frac{p_{\max} - p_{\min}}{\frac{1}{2}\rho_{\text{inlet}}\omega^2}$$

where $p_{\max}$ and $p_{\min}$ are the maximum and minimum pressures that occur over a cycle at a given point. The numerical amplitude distribution shows most of the qualitative features that are found in the experimental results. However, the numerical data seem to form a wider large amplitude region than that found experimentally. In addition, the predicted peak is to the left of the experimental peak, and the pressure amplitude minimum on the suction side seen in the experimental results ($x = -2.4$) is absent in the calculated results. These distortions occur because of the following reasons.

The current calculation uses an equal number of stator and rotor airfoils. An acoustic analysis (Tyler and Sofrin, 1962) shows that in such a situation every harmonic in time (if one were to perform a Fourier decomposition of the unsteady pressures in the region between the stator and rotor) results in a propagating wave in the axial direction. In the experimental configuration there are 22 stator airfoils and 28 rotor airfoils. This results in only the higher harmonics in time giving rise to propagating waves; the lower harmonics give rise to decaying signals. Since the higher harmonics are much smaller in magnitude, the unsteady pressures that reach the exit boundary are much smaller in the case of the experiment. The reflective

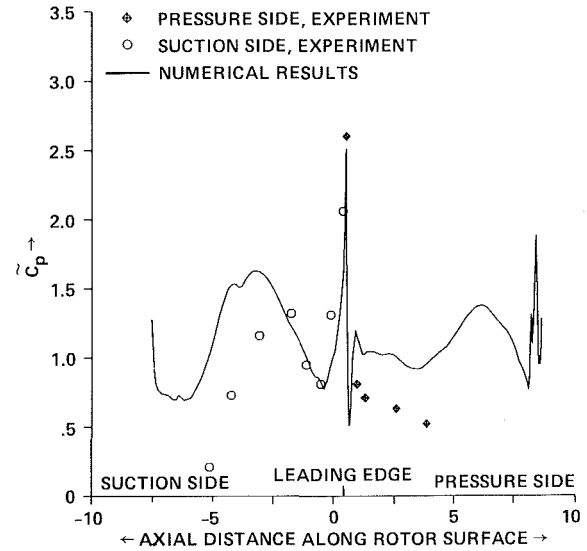

Fig. 9 Pressure amplitude distribution on the rotor

exit boundary condition used in the calculation reflects the relatively large calculated pressure waves that reach the exit boundary back into the system, thus distorting the unsteady pressures everywhere in the system.

Figure 9 shows the $\tilde{C}_p$ distribution on the rotor. The agreement between theory and experiment is not as good as in the case of the stator. The suction side amplitude peak is shifted to the left of the experimental one. A sizable portion of the pressure side peak toward the trailing edge is due to strong pressure waves being reflected back from the exit boundary. The stator pressure amplitude distributions tend to be predicted better because the rotor airfoils partially shield the stator airfoils from the reflected pressure waves (reflected off the exit boundary). However, the numerical data shown in Fig. 9 do predict all the qualitative features shown by the experiment.

The problem can be solved only to a limited extent by developing a nonreflective boundary condition. This is because the pressure signals being generated by the one-rotor/one-stator system are different from those that would be generated by a multirotor/multistator system. The right approach is to perform a multirotor/multistator calculation (the reflective

Downloaded 01 Jun 2010 to 171.66.16.66. Redistribution subject to ASME license or copyright; see http://www.asme.org/terms/Terms_Use.cfm

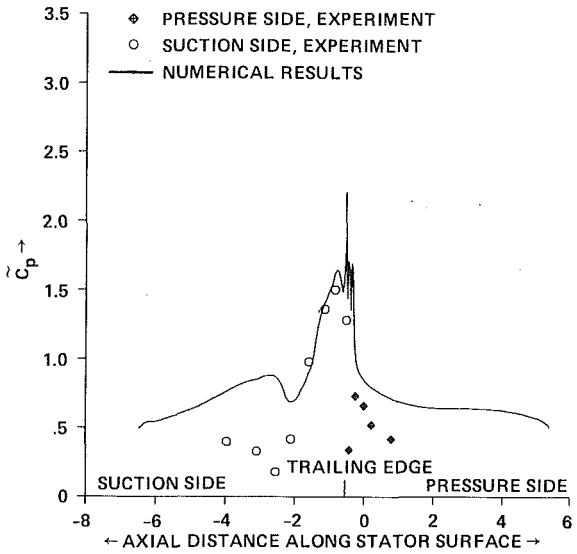

Fig. 10 Pressure amplitude distribution on the stator (nonreflective boundary condition of Erdos et al., 1977)

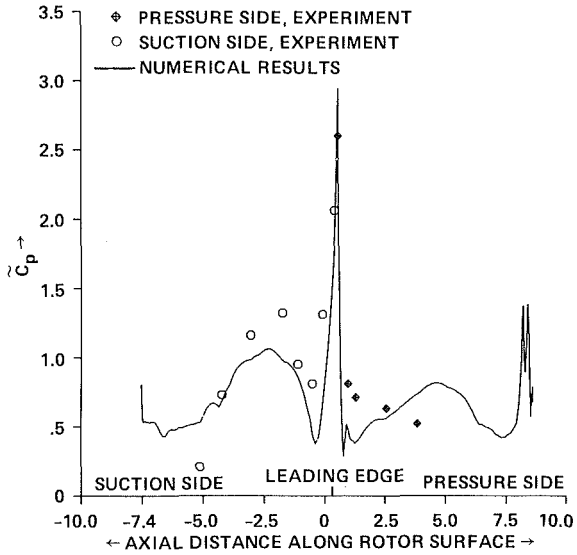

Fig. 11 Pressure amplitude distribution on the rotor (nonreflective boundary condition of Erdos et al., 1977)

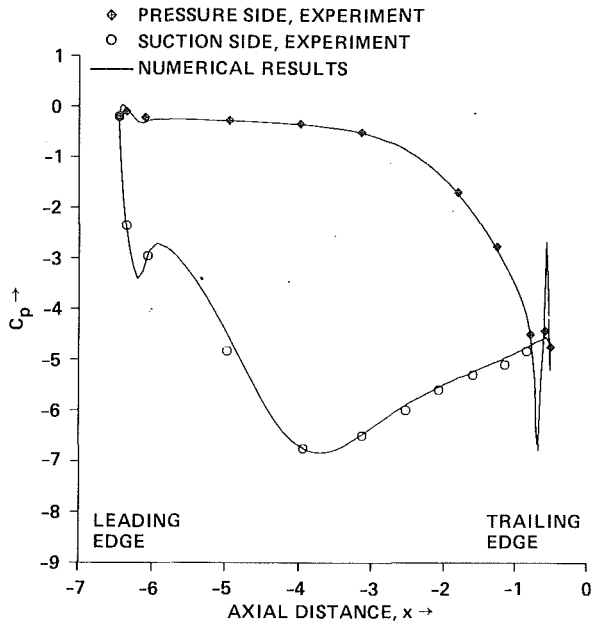

Fig. 12 Time-averaged pressure distribution on the stator (four-rotor/three-stator case)

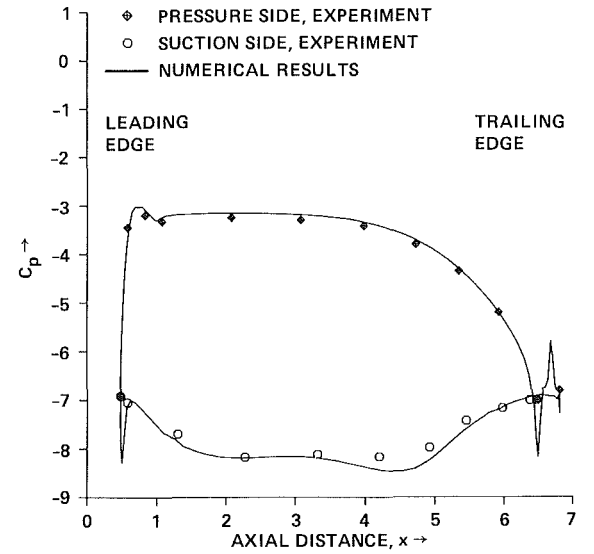

Fig. 13 Time-averaged pressure distribution on the rotor (four-rotor/three-stator case)

properties of the exit boundary condition will be relatively less important for more realistic rotor and stator airfoil counts).

Figure 10 shows the pressure amplitude curve obtained with a nonreflective boundary condition of the type developed by Erdos (1977). This boundary condition permits plane waves (pressure waves that are one-dimensional, that is, pressure variations only in the x direction) to exit the system without distortion. According to the theory of Tyler and Sofrin (1962), most of the unsteadiness can be expected to be one-dimensional and aligned with the x axis in the one-rotor/one-stator case. Hence, this boundary condition should be sufficient for the one-rotor/one-stator case. However, it is clear from Fig. 10 that the improvement in pressure amplitudes with the use of the nonreflective boundary condition is marginal. In fact the difference between theory and experiment is greater on the pressure side in Fig. 10 than it is in Fig. 8. Figure 11 shows the pressure amplitude variation for the rotor obtained with the nonreflective exit boundary condition. Whereas the use of the nonreflective exit boundary condition alters the rotor pressure amplitudes considerably, the numerical results of Fig. 11 are not any closer to the experimental data than in Fig. 9. This calculation indicates that nonreflective boundary conditions alone cannot yield the right pressure amplitudes. It is important that the mechanism that generates the unsteady pressures, that is, the rotor–stator geometry with the right airfoil count, needs to be used in order to obtain numerical results that are close to the experimental data.

A Four-Rotor/Three-Stator Calculation. The next calculation was performed with three stator airfoils and four rotor airfoils. The resulting ratio of rotor to stator airfoils (4/3) is much closer to the experimental ratio (28/22) than is the ratio obtained for the one-rotor/one-stator case. Consequently the amount of rescaling is also much smaller. In addition, it can be shown that only the higher harmonics result in propagating pressure signals. The lower harmonics result in decaying pressure signals. Since the higher harmonics are much smaller in magnitude than the lower harmonics, the pressure signals reaching the exit boundary can also be expected to be much smaller in magnitude. Hence the reflective properties of the

Downloaded 01 Jun 2010 to 171.66.16.66. Redistribution subject to ASME license or copyright; see http://www.asme.org/terms/Terms_Use.cfm

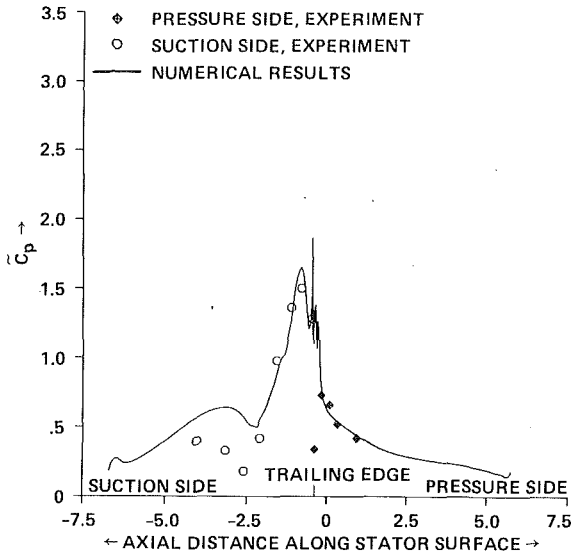

Fig. 14 Pressure amplitude distribution on the stator (four-rotor/three-stator case)

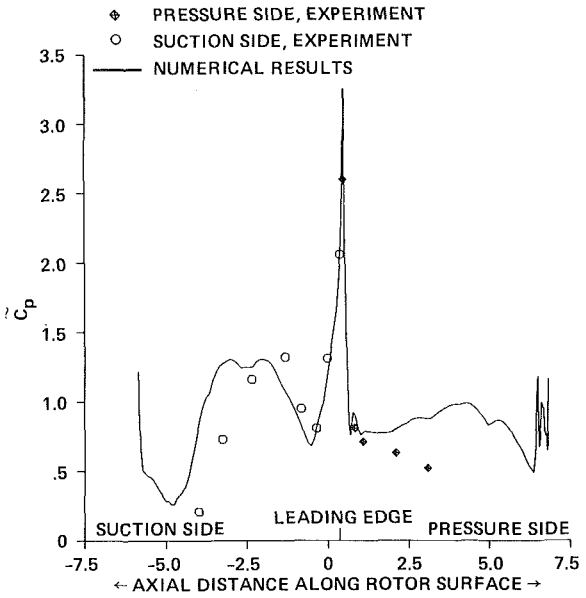

Fig. 15 Pressure amplitude distribution on the rotor (four-rotor/three-stator case)

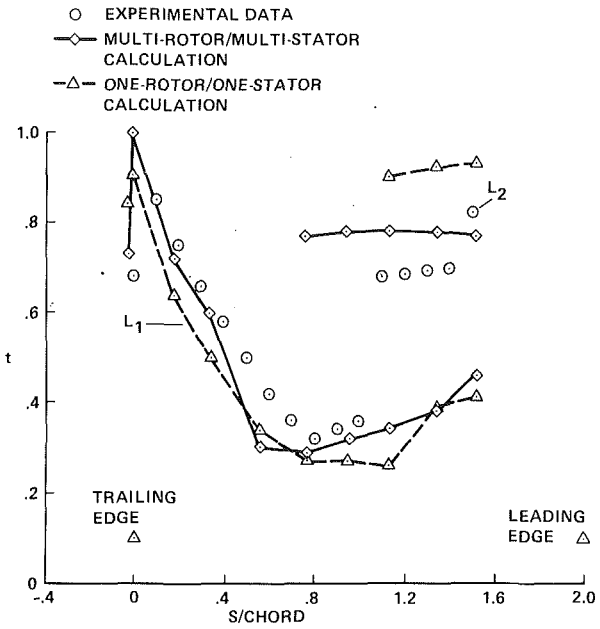

Fig. 16 Phase of the low-pressure peak

exit boundary condition play a smaller role in determining the unsteady pressures on the airfoils.

Figures 12 and 13 show the time-averaged pressure distributions on the stator and rotor airfoils, respectively. The agreement between theory and experiment is good and of the same quality as that obtained in the one-rotor/one-stator case. Figure 14 shows the pressure amplitude distribution obtained on the stator. Clearly there is a marked improvement over the numerical results depicted in Fig. 8. The wider large amplitude region in Fig. 8 now almost exactly matches the experimental data. The positions of the experimental and numerical peaks are in much better agreement. The numerical data show an amplitude minimum on the suction side, as do the experimental data. However, there is some difference between theory and experiment on the suction side of the stator and this may be, once again, because of the small difference between experimental and numerical rotor/stator pitch ratios or because of three-dimensional effects.

Figure 15 shows pressure amplitudes on the rotor. As in the case of the stator, the numerical results for the four-rotor/three-stator case are considerably closer to the experimental results than those obtained for the one-rotor/one-stator case (Fig. 9). The pressure side peak of Fig. 9 has decreased in magnitude, resulting in much better comparisons between theory and experiment. Similar improvements can also be seen on the suction side of the rotor. However, just as in the case of the stator, there are still some quantitative differences between theory and experiment.

The pressure amplitude variation along the surfaces of the airfoils is one measure of the unsteady component of the flow. A second, and more sensitive, measure is the phase of the pressure variation in time as a function of the position on the airfoil surfaces. Figure 16 shows the time at which a pressure minimum occurs on the stator suction surface. The initial position ($t = 0$) for the rotor and stator is shown in Fig. 1 and corresponds to the instant when the stator trailing edge circle center is in line with the rotor leading edge circle. The figure indicates a low pressure peak traveling from about 40 percent chord toward the trailing edge (L1) and a second low pressure peak traveling upstream (L2). This phenomenon is described in greater detail by Dring et al. (1982). In general the multi-rotor/multistator calculation is seen to be much closer to the experimental data.

Figures 17–20 show pressure contours at various time instants for the four-rotor/three-stator configuration. These figures clearly show the main features of the time-averaged pressure distributions of Figs. 12 and 13, namely, the expansion and subsequent recompression of the flow on the suction side of the stator and rotor, and the almost constant pressure region followed by an expansion on the pressure side of the stator and rotor. Unlike the one-rotor/one-stator results of Rai (1987a) the pressures in the different rotor and stator channels are out of phase. These figures also show small-amplitude, high-frequency oscillations superimposed on the contours. These oscillations are caused by the tendency of the continuity, momentum, and energy equations to decouple at low Mach numbers and will disappear for calculations at higher Mach numbers. A comparison of the contours presented in Figs. 17–20 and those of Rai (1987a) shows a considerable reduction in the amount of oscillations in the present study. This improvement in the quality of the pressure contours is believed to be due to the integration method used in this study (high-order-

Downloaded 01 Jun 2010 to 171.66.16.66. Redistribution subject to ASME license or copyright; see http://www.asme.org/terms/Terms_Use.cfm

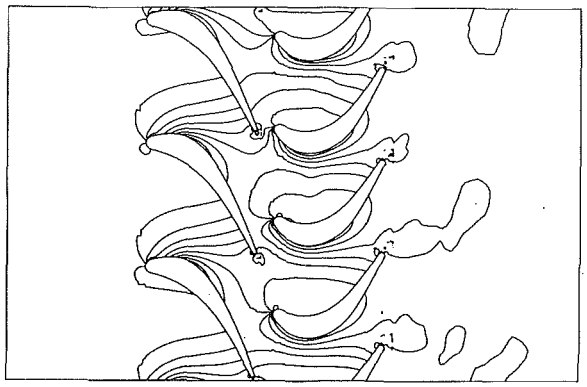

Fig. 17 Pressure contours (t = 0.00)

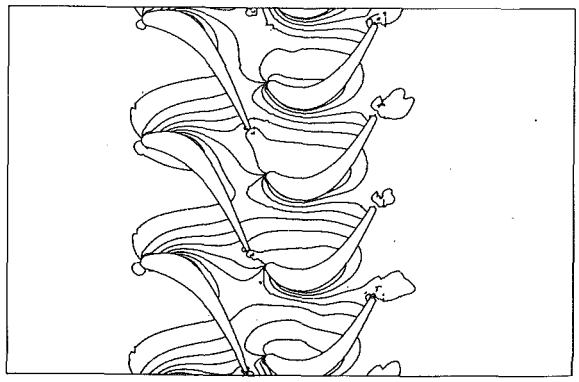

Fig. 19 Pressure contours (t = 0.50)

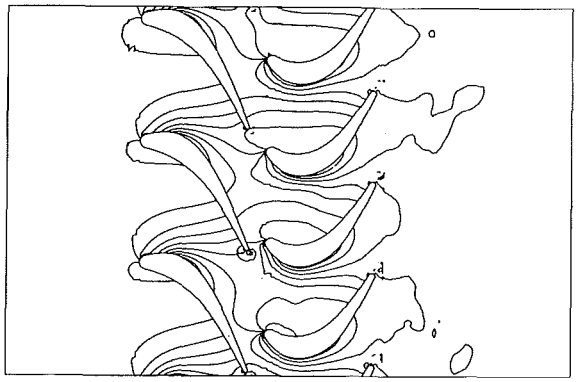

Fig. 18 Pressure contours (t = 0.25)

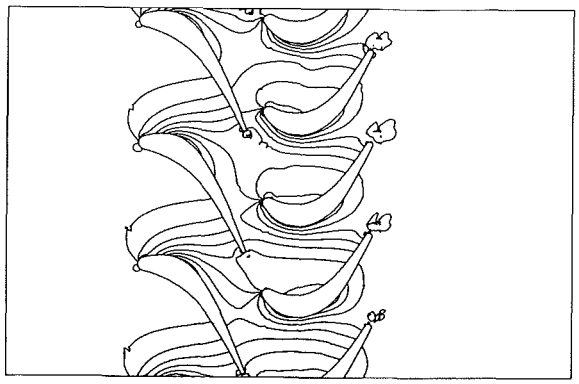

Fig. 20 Pressure contours (t = 0.75)

accurate upwind method instead of a hybrid central/upwind scheme).

Summary

An unsteady, thin-layer, Navier–Stokes code has been developed to study two-dimensional rotor–stator interaction problems. The code uses patched and overlaid grids that move relative to each other to simulate the motion of the rotor airfoils with respect to the stator airfoils. The integration method is a spatially third-order accurate and temporally second-order accurate, upwind finite-difference scheme that is set in an iterative implicit framework. The code was used to simulate subsonic flow past a turbine stage for which considerable data exist.

The code permits the use of an arbitrary number of rotor and stator airfoils. Numerical results were obtained for a one-rotor/one-stator configuration and for a four-rotor/three-stator configuration. The four-rotor/three-stator case had a pitch ratio much closer to the experimental one. Results in the form of time-averaged surface pressures, surface pressure amplitudes (corresponding to the pressure fluctuations in time), pressure phase relationships, and instantaneous passage pressure contours are presented for the two configurations. The time-averaged surface pressures for the two configurations are almost identical and agree well with the experimental data. The surface pressure amplitudes and phase predicted by the four-rotor/three-stator configuration are found to agree much better with the experimental data than do the calculated data obtained with the one-rotor/one-stator configuration.

References

Baldwin, B. S., and Lomax, H., 1978, "Thin Layer Approximation and Algebraic Model for Separated Turbulent Flow," AIAA 16th Aerospace Sciences Meeting, Huntsville, AL, Jan. 16–18, Paper No. 78-257.

Dring, R. P., Joslyn, H. D., Hardin, L. W., and Wagner, J. H., 1982, "Turbine Rotor–Stator Interaction," ASME *Journal of Engineering for Power*, Vol. 104, pp. 729–742.

Erdos, J. I., Alzner, E., and McNally, W., 1977, "Numerical Solution of Periodic Transonic Flow Through a Fan Stage," *AIAA Journal*, Vol. 15, No. 11, pp. 1559–1568.

Rai, M. M., 1987a, "Navier–Stokes Simulations of Rotor–Stator Interaction Using Patched and Overlaid Grids," *AIAA Journal of Propulsion and Power*, Vol. 3, No. 5, pp. 387–396.

Rai, M. M., 1987b, "Unsteady Three-Dimensional Navier–Stokes Simulations of Turbine Rotor–Stator Interaction," presented at the AIAA/SAE/ASME/ASEE 23rd Joint Propulsion Conference, San Diego, CA, June 29–July 2, AIAA Paper No. 87-2058.

Steger, J. L., and Sorenson, R. L., 1979, "Automatic Mesh-Point Clustering Near a Boundary in Grid Generation With Elliptic Partial Differential Equations," *Journal of Computational Physics*, Vol. 33, No. 3, pp. 405–410.

Tyler, J. M., and Sofrin, T. G., 1962, "Axial Flow Compressor Noise Studies," *SAE Transactions*, Vol. 70, pp. 309–332.

Downloaded 01 Jun 2010 to 171.66.16.66. Redistribution subject to ASME license or copyright; see http://www.asme.org/terms/Terms_Use.cfm

The Extension and Application of Three-Dimensional Time-Marching Analyses to Incompressible Turbomachinery Flows

P. J. Walker[1]
Rolls-Royce plc.,
Derby, United Kingdom

W. N. Dawes
Whittle Laboratory,
Cambridge, United Kingdom

Conventional time-marching flow solvers perform poorly when integrating compressible flow equations at low Mach number levels. This is shown to be due to unfavorable interaction between long-wavelength errors and the inflow and outflow boundaries. Chorin's method of artificial compressibility is adopted to extend the range of Denton's inviscid flow solver and Dawes' three-dimensional Navier–Stokes solver to zero Mach number flows. The paper makes a new contribution by showing how to choose the artificial acoustic speed systematically to optimize convergence rate with regard to the error wave–boundary interactions. Applications to a turbine rotor and generic water pump geometry are presented.

Introduction

An important class of analysis tools for the three-dimensional flows in turbomachinery solves, by time marching, the compressible equations of motion expressed in general form as

$$\frac{\partial}{\partial t}\begin{bmatrix}\rho\\ \rho\bar{U}\\ \rho E\end{bmatrix}+\sum\begin{matrix}\text{CELL}\\ \text{FLUX}\\ \text{SUMS}\end{matrix}\begin{bmatrix}\text{Continuity}\\ \text{Momentum}\\ \text{Energy}\end{bmatrix}=0 \qquad (1)$$

The major cost in producing a robust, reliable design tool is not in writing the code itself but in its validation. This cost is high in part because many different comparisons must be made between predictions and measurement for many different configurations. Another reason the validation cost is high is that realistic, high-speed experiments are expensive to conduct. It would be attractive to use relatively inexpensive low-speed (i.e., low Mach number) experiments to help validate the time-marching codes. However, this can often lead to irritating problems with the codes themselves, which either "do not run" at low Mach numbers or suffer severe reduction in convergence rate.

There is nothing wrong, physically, with the unsteady compressible equations of motion (1) at low Mach numbers. After all, mass, momentum, and energy are always conserved. The numerical problems associated with time-marching algorithms at low Mach numbers are threefold. First, extra precision must be used as the density variations become smaller (maybe even 128 bit words). Second, the Courant–Freidrichs–Lewy time step limit becomes increasingly restrictive as the acoustic waves dominate the convective waves so that an increasing number of time steps is required to reach a given physical time (i.e., to converge). Third, most significantly, the long-wavelength errors present in the solution find increasing difficulty interacting with the inflow and outflow boundaries as the Mach number levels become smaller. The decay of the long-wavelength errors becomes increasingly retarded and convergence is slowed or even prevented.

The purpose of this paper is first to describe and quantify the poor interaction between long-wavelength errors and boundaries and the effect on convergence rate. Then Chorin's (1967) well-known method of artificial compressibility will be adopted as a means of extending the range of applicability of two time-marching codes (Dawes, 1986; Denton, 1986) to low Mach numbers. The key contributions of the paper will be to remove the previous ad hoc guess work of a suitable artificial acoustic speed by optimizing this speed with respect to long-wavelength error–boundary interaction. A range of realistic applications will be presented.

Low Mach Number Convergence Properties

In all time-marching algorithms solving compressible equations of motion, the time step size and artificial viscosity magnitudes affect only the local rate of decay of errors. Long-term convergence rate is dominated by long-wavelength errors, which travel up and down the flow domain interacting with the inflow and outflow boundaries. We may study this essentially one-dimensional process with the one-dimensional Euler equations written in isentropic quasi-linear form:

[1]Former address: Whittle Laboratory, Cambridge, United Kingdom.

Contributed by the International Gas Turbine Institute and presented at the 34th International Gas Turbine and Aeroengine Congress and Exhibition, Toronto, Ontario, Canada, June 4–8, 1989. Manuscript received at ASME Headquarters February 1, 1989. Paper No. 89-GT-212.

Copyright © 1990 by ASME
Downloaded 01 Jun 2010 to 171.66.16.66. Redistribution subject to ASME license or copyright; see http://www.asme.org/terms/Terms_Use.cfm

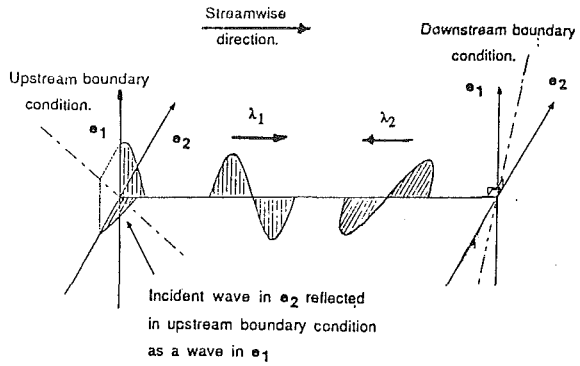

Fig. 1 Numerical information flow

$$\frac{\partial}{\partial t}\begin{bmatrix}\rho\\ u\end{bmatrix}+\begin{bmatrix}u & \rho\\ a^2/\rho & u\end{bmatrix}\frac{\partial}{\partial x}\begin{bmatrix}\rho\\ u\end{bmatrix}=0 \tag{2}$$

This system has eigenvalues λ, and corresponding Riemann invariants e

$$\lambda_1 = u+a, \qquad e_1 = \delta p + \rho a \delta u$$
$$\lambda_2 = u-a, \qquad e_2 = \delta p - \rho a \delta u \tag{3}$$

Information propagates in the numerical simulation by downstream running waves e_1, with speed λ_1, and upstream waves e_2 at speed λ_2. The boundary conditions constrain particular linear combinations of e_1 and e_2. The outflow boundary condition of constant static pressure, $\delta p = 0$, is equivalent to setting $|e_2| = -|e_1|$ at the outflow boundary. The inflow boundary condition of constant stagnation pressure $\delta p + \rho u \delta u = 0$, is easily shown to be equivalent to setting $|e_1| = -[(1-M)/(1+M)]\,|e_2|$, where $M = u/a$, at the inflow boundary. This information flow is illustrated in Fig. 1. More details are given by Walker (1988).

The key deduction from the use of this particular combination of inflow and outflow boundary conditions is that a given error wave, initially running downstream (say) has its magnitude modified by a factor of $(1-M)/(1+M)$ after one reflection from the outflow boundary and one reflection from the inflow boundary. Consequently, at low Mach numbers the long-wavelength errors tend not to decay (not at all in the limit $M = 0$) and so convergence is impeded (or prevented). It must be stressed again that time step size, artificial viscosity, and even the algorithm itself can damp errors in the solution only locally and that it is the long-wavelength errors, which are accurately convected by any solution method, which can dominate ultimate convergence rate.

To illustrate the deterioration of convergence rate with Mach number level, Fig. 2 shows plots obtained from Denton's well-known method for a low reaction turbine rotor blade (impulse bucket). Below a Mach number level of around 0.1 convergence is dramatically slowed.

Application of Artificial Compressibility

To solve for essentially incompressible flow via time-marching strategies (rather than adopting complicated pressure correction methodologies) Chorin (1967) introduced the idea of artificial compressibility. The equation of mass continuity is used to drive pressure (rather than density) via an artificial acoustic speed $\sqrt{\beta}$

$$\delta p = \beta \cdot \delta \rho \tag{4}$$

The "compressible" equations become

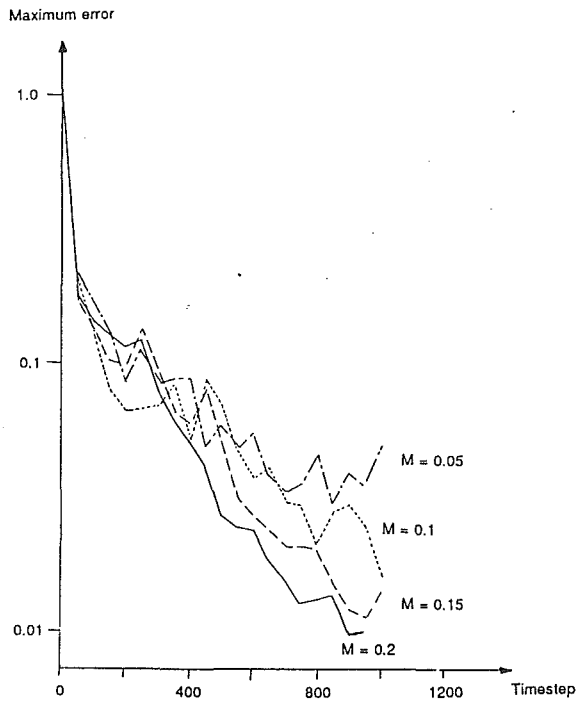

Fig. 2 Convergence rate with Mach number of Denton code for impulse bucket

$$\frac{\partial}{\partial t}\begin{bmatrix}p\\ \rho\bar{U}\\ \rho E\end{bmatrix}+\begin{bmatrix}\beta & 0 & 0\\ 0 & 1 & 0\\ 0 & 0 & 1\end{bmatrix}\sum\begin{matrix}\text{CELL}\\ \text{FLUX}\\ \text{SUMS}\end{matrix}\begin{bmatrix}\text{Continuity}\\ \text{Momentum}\\ \text{Energy}\end{bmatrix}=0 \tag{5}$$

(Note that there is now no coupling between the energy equation and the flow dynamics.) At convergence, the time derivative term is zero, and so the desired incompressible flux balances are recovered. Any time-marching code can be adapted to solve these equations. The approach is only practical for *steady* flows, since to compute accurate *un*steady flow, β must be very large to force $\text{div} \cdot \bar{u} = 0$ during the transients. This was Chorin's original motivation and choice, but it simply reproduces one of the numerical problems we are trying to avoid (excessive "stiffness").

The choice of the acoustic speed, β, is critical and until now has been chosen on ad hoc grounds. Rizzi et al. (1985) used values of β/u^2 in the range 1 to 5. Kwak et al. (1984) defined upper and lower values of β/u^2 dependent on the geometry and the Reynolds number in the range 0.1 to 10. Choi et al. (1984) and Michelossi et al. (1986) claimed that numerical experiments showed β/u^2 around unity was optimal in terms of convergence rate. The principal contribution of this paper is to show how to choose β rationally based on optimizing the interaction of long-wavelength errors with the inflow and outflow boundaries and thus maximizing convergence rate.

In a similar manner to the previous section we consider the one-dimensional artificial compressibility equations of motion in quasi-linear form (with $\rho = \text{const}$) for zero Mach numbers

$$\frac{\partial}{\partial t}\begin{bmatrix}p\\ \rho u\end{bmatrix}+\begin{bmatrix}0 & \beta\\ 1 & 2u\end{bmatrix}\frac{\partial}{\partial x}\begin{bmatrix}p\\ \rho u\end{bmatrix}=0 \tag{6}$$

This system has eigenvalues λ and corresponding Riemann invariants e

Downloaded 01 Jun 2010 to 171.66.16.66. Redistribution subject to ASME license or copyright; see http://www.asme.org/terms/Terms_Use.cfm

$$\lambda_1 = u + \sqrt{u^2+\beta}, \qquad e_1 = \delta p + \rho\sqrt{u^2+\beta}\,\delta u$$

$$\lambda_2 = u - \sqrt{u^2+\beta}, \qquad e_2 = \delta p - \rho\sqrt{u^2+\beta}\,\delta u \tag{7}$$

Consider an initial error wave e_1 running downstream. At a fixed static pressure outflow boundary a wave must be generated running upstream with magnitude $|e_2| = -|e_1|$ so that $\delta p = 0$. Similarly, this wave must reflect from the inflow boundary of fixed stagnation pressure, $\delta p + \rho u \delta u = 0$ as a wave in e_1 with magnitude $|e_1| = -|e_2| * [(\sqrt{u^2+\beta} - u)/(\sqrt{u^2+\beta} + u)]$. Thus the "loop gain," L, for a single cycle of such wave-boundary interactions is

$$L = \frac{\alpha - 1}{\alpha + 1} \text{ where } \alpha = \sqrt{1 + \frac{\beta}{u^2}} \tag{8}$$

This represents the factor by which the magnitude of an initially downstream running error wave is modified by one reflection from a fixed static pressure outflow boundary and one reflection from the fixed stagnation pressure inflow boundary.

Now, if C is the CFL number used for the time marching, l_x the length of the computational domain, and Δx the mesh spacing, then the stable time step is

$$\Delta t = C\Delta x/\lambda_1 \tag{9}$$

(since $|\lambda_1| > |\lambda_2|$). The number of time steps for a wave to travel from inflow to outflow is

$$n_1 = l_x/C\Delta x \tag{10}$$

and from outflow back to inflow it is

$$n_2 = (-\lambda_1/\lambda_2) l_x/C\Delta x \tag{11}$$

(note that $\lambda_2 < 0$). Therefore the total number of time steps for a complete loop $N = n_1 + n_2$ is

$$N = X(\lambda_2 - \lambda_1)/\lambda_2 \text{ where } X = l_x/C\Delta x \tag{12}$$

Substitution for λ_1 and λ_2 gives

$$N = 2\alpha X/(\alpha - 1) \tag{13}$$

Thus, the amplification of the error wave magnitude per time step, ν, is

$$\nu = L^{1/N} = \left(\frac{\alpha - 1}{\alpha + 1}\right)^{(\alpha-1)/2\alpha X} \tag{14}$$

It can be shown (Walker, 1988) that the minimum of ν occurs at $\alpha = 1.7719$ (i.e., maximum damping of error wave) *and* that this value is independent of x (i.e., independent of CFL chosen). Hence, the optimum artificial acoustic speed is

$$\beta_{\text{opt}} = 2.1395u^2 \tag{15}$$

A rather more general analysis (Walker, 1988) without the assumption of zero Mach number replaces equation (6) by

$$\frac{\partial}{\partial t}\begin{bmatrix} p \\ \rho u \end{bmatrix} + \begin{bmatrix} 0 & \beta \\ 1 - M^2 & 2u \end{bmatrix} \frac{\partial}{\partial x}\begin{bmatrix} p \\ \rho u \end{bmatrix} = 0 \tag{16}$$

with M the Mach number and shows the optimum artificial acoustic speed to be

$$\beta_{\text{opt}} = 2.1395u^2/(1 - M^2) \tag{17}$$

(In this nonzero Mach number context, the application of artificial compressibility is equivalent to assuming a modified equation of state for the gas: $p = \beta\rho$; this effectively permits a modified and optimal time integration path.)

As discussed earlier, this is only valid for *steady* flows (where $\text{div} \cdot \bar{u} = 0$ by virtue of $\partial p/\partial t = 0$, rather than $\beta \to \infty$). This is *also* only valid for wholly subsonic flow since wave propagation is, of course, quite different in supersonic (or transonic) flow.

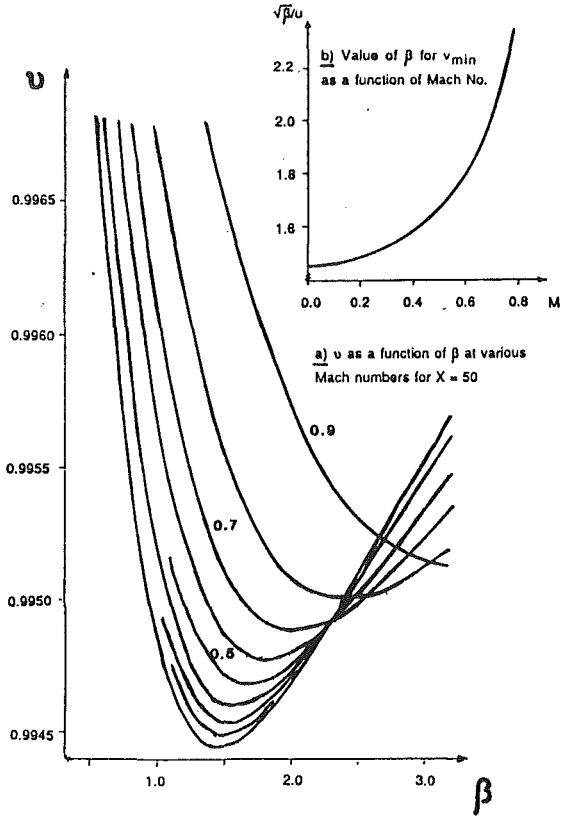

Fig. 3 Wave damping per time step

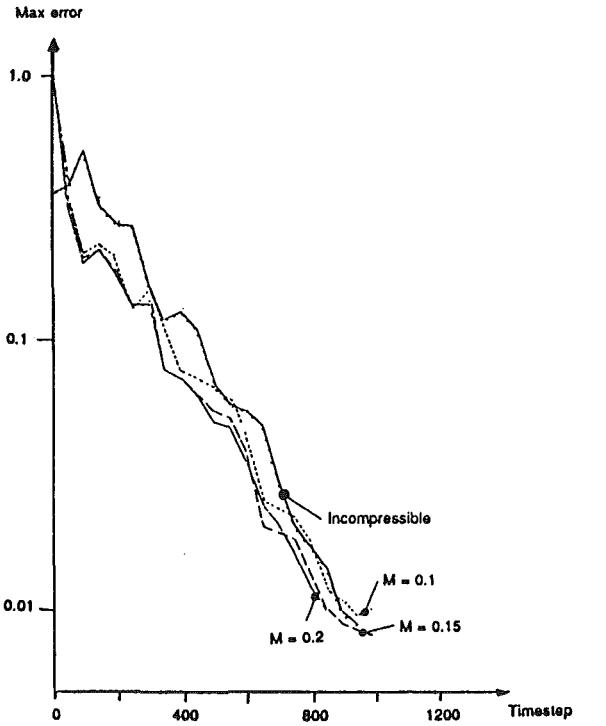

Fig. 4 Convergence rate of the Denton code with artificial compressibility for the impulse bucket

Plots of ν, the error wave damping per time step, as a function of β/u^2 for varying Mach numbers are shown in Fig. 3. The significant result is the unexpectedly narrow range over which β/u^2 can be allowed to vary and still produce optimal convergence rate.

Downloaded 01 Jun 2010 to 171.66.16.66. Redistribution subject to ASME license or copyright; see http://www.asme.org/terms/Terms_Use.cfm

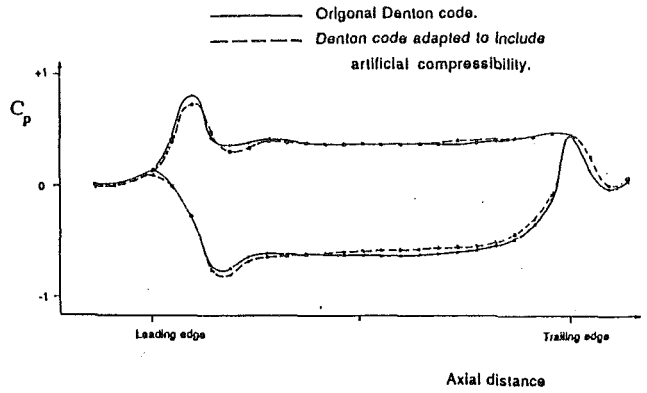

Fig. 5 Comparison of impulse bucket surface pressures; standard code and modified code at M = 0.2

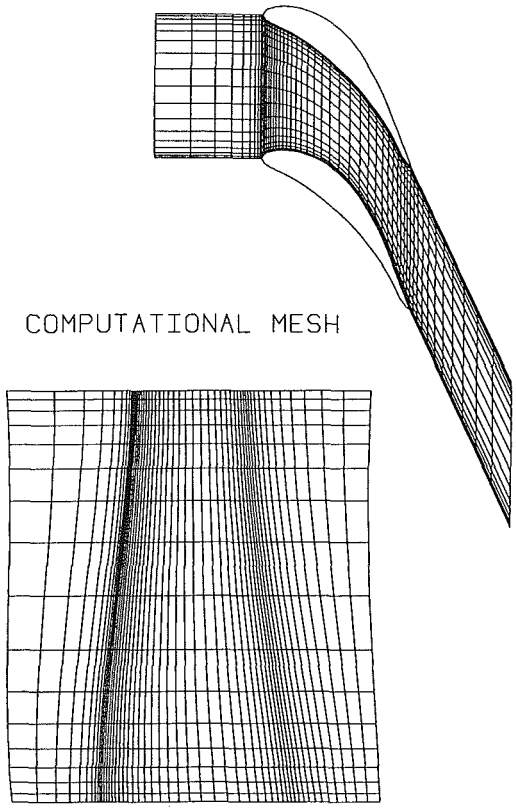

Fig. 6 Reaction blade; 17 x 51 x 17 mesh; meridional view and midspan blade-blade view

Numerical Results

Denton (1986) Inviscid Code. The artificial compressibility method outlined above was programmed into Denton's standard time-marching code and applied to the impulse bucket referred to earlier. The value of β was computed locally at each mesh point. The convergence history for a range of Mach numbers is shown in Fig. 4. The convergence rate is essentially identical for all Mach numbers down to zero; this should be compared to the progressive deterioration of convergence rate for the same blade with the standard code in Fig. 2. Blade surface pressures are compared in Fig. 5 for the standard code and the modified code at a Mach number level of 0.2. The agreement is satisfactory. Hence at low Mach numbers the artificial compressibility approach permits far more economical solutions: first because the convergence rate is maintained, minimizing the required time steps; second because the absence of the energy equation reduces the cpu time per point per time step by 20 percent (in three dimensions).

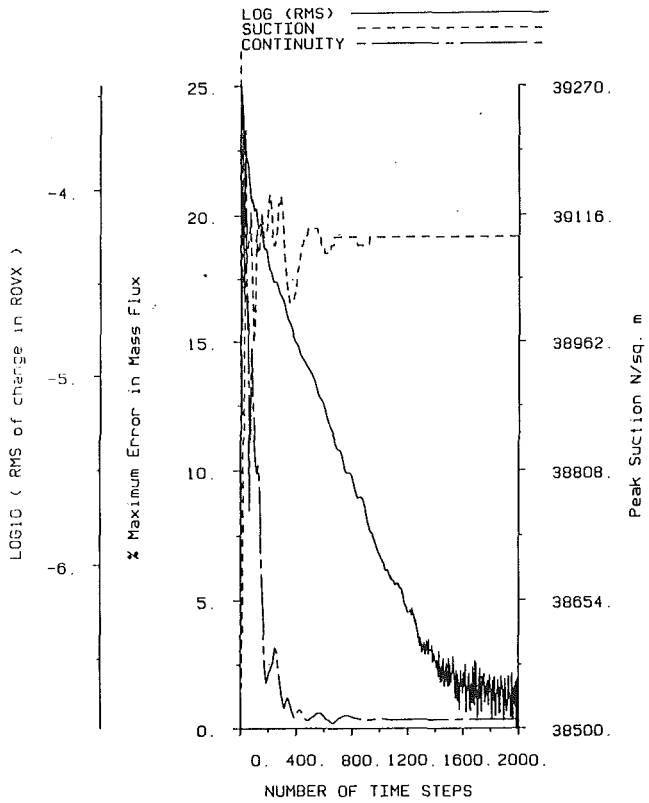

Fig. 7 Convergence history for reaction blade

Dawes (1986) Navier-Stokes Code. The artificial compressibility method is equally applicable to the Navier-Stokes equations (since viscosity affects only local propagation of information and so does not alter the optimum value of β described earlier). Accordingly, an incompressible version was produced of the Dawes (1986) three-dimensional Navier-Stokes solver with the values of β computed locally from equation (15). The code no longer solves the unnecessary energy equation (so saving 20 percent on computer time) but otherwise remains standard as described by Dawes (1986), including the use of multigrid. There is no adverse interaction between the multigrid and long-wavelength error propagation; in fact quite the opposite. The role of multigrid is really to make long waves look like shorter ones (on an appropriate mesh) to increase the spectrum of waves damped efficiently by the algorithm itself. Thus the more efficient transport of the long-wavelength errors by the artificial compressibility scheme simply enhances this basic process. Sample applications are presented here for a 50 percent reaction axial turbine rotor blade and a generic water pump geometry.

50 Percent Reaction Axial Turbine Rotor. Results are presented for the rotor installed as part of a stage in a large low-speed air turbine at the Whittle Laboratory (Hodson, 1983). The stage data are:

	Stator	Rotor
$Re \times 10^5$	4.2	3.2
Loading (stage) = $\Delta ho/Um2$	-----	1
rpm	-----	530
Inlet axial velocity, m/s	17.95	-----
Flow coefficient = Ux/Um	-----	0.495
Blade inlet angle, deg	0	0
Blade exit angle, deg	65	−65
Chord, mm	152.4	114.3
Pitch-chord ratio	0.742	0.698
Aspect ratio	1.5	2.0
Mean radius	0.647	0.647
Stagger, deg	44.5	4.45

Downloaded 01 Jun 2010 to 171.66.16.66. Redistribution subject to ASME license or copyright; see http://www.asme.org/terms/Terms_Use.cfm

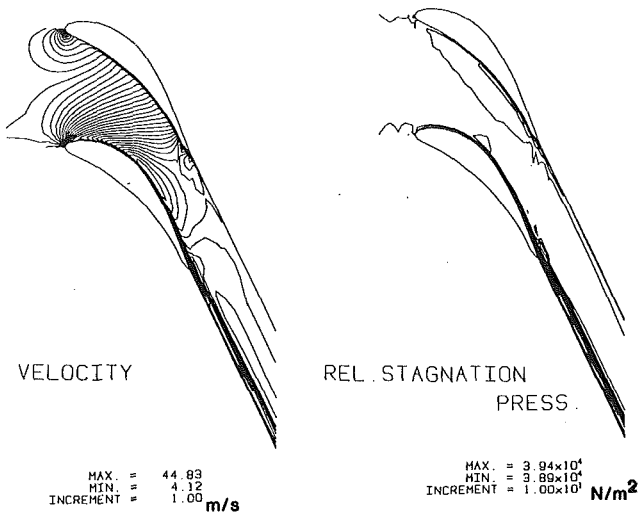

Fig. 8 Predicted midspan velocities and relative stagnation pressures

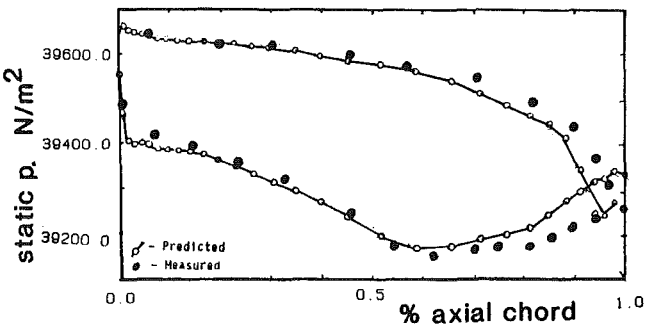

Fig. 9 Measured and predicted midspan pressure distribution

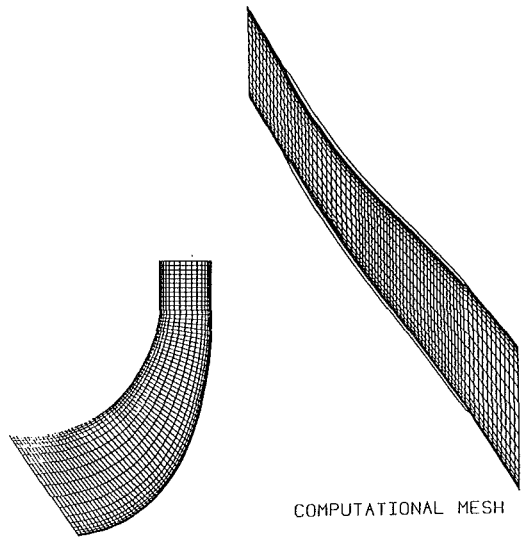

Fig. 10 Generic water pump; 19 × 97 × 19 mesh

The (relatively coarse) $17 \times 51 \times 17$ computational mesh is shown in Fig. 6. For contractual reasons only midspan geometry (and hence results) can be presented; the simulation was, however, fully three dimensional. The convergence history is plotted in Fig. 7; convergence to machine zero (as evidenced by the flat and oscillatory rms residue asymptote) is essentially achieved after 1600 time steps (with one level of multigrid). Figure 8 shows the predicted midspan velocities and relative stagnation pressures. Figure 9 compares measured

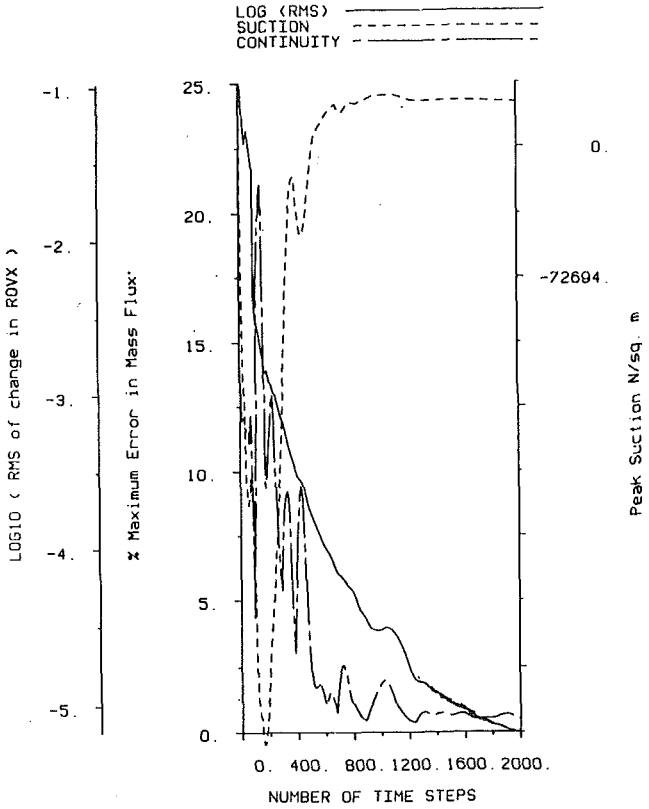

Fig. 11 Water pump convergence history

and predicted midspan blade surface pressure distributions; the agreement is satisfactory. The rotor relative losses compare as follows:

	Rotor relative loss coefficient $\Delta po_{rel}/1/2\ \rho v^2_{exit}$, rel, percent
Predicted	2.4
Measured in stage	2.6
Measured in cascade (midspan section)	1.8

The agreement is acceptable for such a coarse mesh.

Generic Water Pump Geometry. The $19 \times 93 \times 19$ mesh for a generic water pump geometry is shown in Fig. 10. The main geometric parameters are:

Re	5×10^5
Density, kg/m^3	1000
Hub radius LE, mm	94.3
Hub radius TE, mm	201.2
Shroud radius LE, mm	140.0
Shroud radius TE, mm	201.2
rpm	1000
Static/total pressure rise $= p_2/p_{01}$	2.5

The convergence history is shown in Fig. 11; the rms residue decreases by four orders of magnitude in 2000 steps (one level of multigrid). Figures 12 (velocity contours), 13 (velocity vectors), and 14 (relative stagnation pressure) show the expected flow features, in particular the strong secondary flows leading to the development of jet-wake structure.

Downloaded 01 Jun 2010 to 171.66.16.66. Redistribution subject to ASME license or copyright; see http://www.asme.org/terms/Terms_Use.cfm

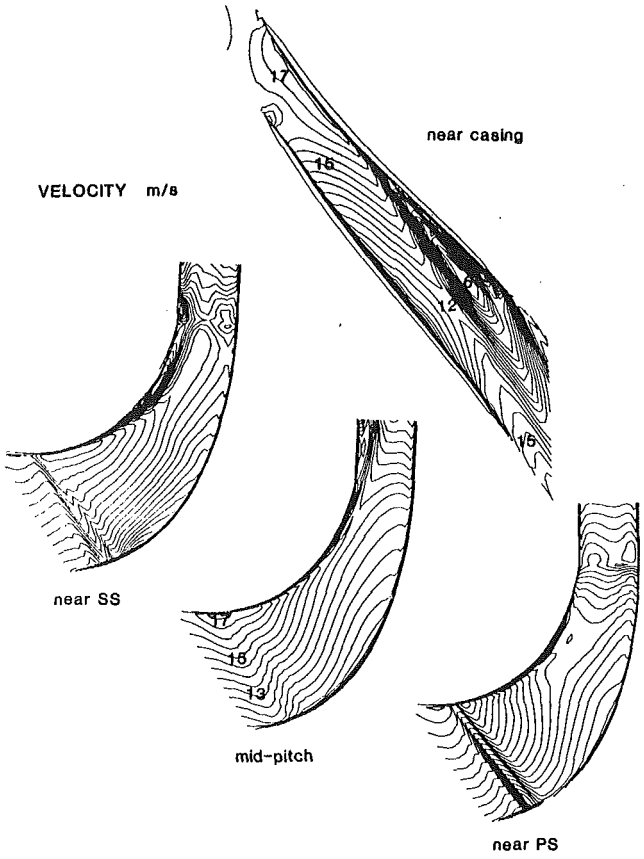

Fig. 12 Predicted velocity contours

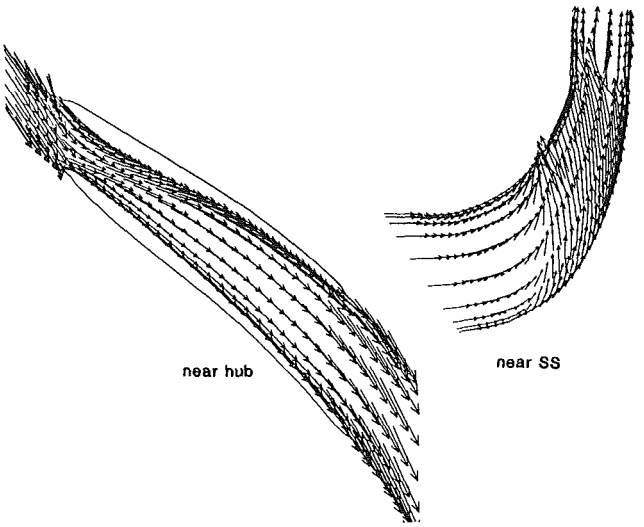

Fig. 13 Predicted velocity vectors

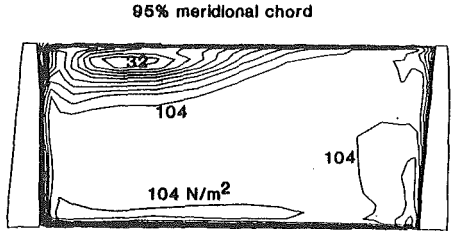

Fig. 14 Predicted relative stagnation pressure

Concluding Remarks

The poor performance of conventional time-marching solvers of the compressible flow equations at low Mach numbers has been analyzed and shown to be caused by the interaction of long-wavelength error waves with the inflow and outflow boundaries. Chorin's artificial compressibility method has been adopted to extend the range of applicability of two conventional flow solvers down to zero Mach number. This paper makes a new contribution to the literature by showing how to choose the artificial acoustic speed systematically to optimize convergence rate. Applications to a turbine rotor and a generic water pump geometry produced encouraging results.

Acknowledgments

The first author was supported during this Ph.D. work by an SERC CASE studentship (jointly with the CEGB).

References

Choi, D., and Merkle, C. L., 1984, "Application of Time-Iterative Schemes to Incompressible Flow," AIAA Paper No. 84-1638.

Chorin, A. J., 1967, "A Numerical Method for Solving Incompressible Viscous Flow Problems," *Journal of Computational Physics*, Vol. 2, pp. 12–26.

Dawes, W. N., 1986, "Application of Full Navier–Stokes Solvers to Turbomachinery Flow Problems," *Numerical Techniques for Viscous Flow Calculation in Turbomachinery Blading*, V.K.I. Lecture Series 2.

Denton, J. D., 1986, "The Calculation of Fully Three-Dimensional Flow Through Any Type of Turbomachinery Blade Row," *Three-Dimensional Computation Techniques Applied to Internal Flows in Propulsion Systems*, AGARD Lecture Series No. 140.

Hodson, H. P., 1983, "Unsteady Boundary Layers on Axial Flow Turbine Rotor Blades," Ph.D. Thesis, Cambridge University, United Kingdom.

Kwak, D., and Chakravarthy, S. R., 1984, "A Three-Dimensional Incompressible Navier–Stokes Flow Solver Using Primitive Variables," AIAA Paper No. 84-0253.

Michelossi, V., and Berocci, C., 1986, "Solution of the Steady State Incompressible Navier–Stokes Equations in Curvilinear Nonorthogonal Coordinates," Von Karman Institute for Fluid Dynamics, Technical Note 158.

Rizzi, A., and Eriksson, L., 1985, "Computation of Inviscid Incompressible Flow With Rotation," *Journal of Fluid Mechanics*, Vol. 153, pp. 257–312.

Walker, P. J., 1988, "The Effect of Lean in Axial Turbines," Ph.D. Thesis, Cambridge Univeristy, United Kingdom.

Downloaded 01 Jun 2010 to 171.66.16.66. Redistribution subject to ASME license or copyright; see http://www.asme.org/terms/Terms_Use.cfm

Three-Dimensional Solutions for Inviscid Incompressible Flow in Turbomachines

S. Abdallah

C. F. Smith

Applied Research Laboratory,
Penn State University,
State College, PA 16804

A primitive variable formulation is used for the solution of the incompressible Euler equation. In particular, the pressure Poisson equation approach using a nonstaggered grid is considered. In this approach, the velocity field is calculated from the unsteady momentum equation by marching in time. The continuity equation is replaced by a Poisson-type equation for the pressure with Neumann boundary conditions. A consistent finite-difference method, which insures the satisfaction of a compatibility condition necessary for convergence, is used in the solution of the pressure equation on a nonstaggered grid. Numerical solutions of the momentum equations are obtained using the second-order upwind differencing scheme, while the pressure Poisson equation is solved using the line successive overrelaxation method. Three turbomachinery rotors are tested to validate the numerical procedure. The three rotor blades have been designed to have similar loading distributions but different amounts of dihedral. Numerical solutions are obtained and compared with experimental data in terms of the velocity components and exit swirl angles. The computed results are in good agreement with the experimental data.

Introduction

The flow through a turbomachinery blade passage is very complex. The flow can be dominated by three-dimensional effects, such as secondary flows caused by the vorticity distribution of the incoming boundary layer. Quasi-three-dimensional methods do not account for these effects adequately (Wu, 1951; Katsanis, 1973; Novak, 1977; Abdallah et al., 1988). An improved approach to these flow problems is the solution of the three-dimensional Euler equation. Several formulations have been developed for the solution of the incompressible Euler equation. These methods can be classified into two groups: primitive variable and nonprimitive variable formulations.

The nonprimitive variable formulations are based upon introducing new dependent variables other than velocity and pressure. Under this category, the vector potential function method, the two stream function method, and the vorticity-velocity method can be classified. In the first two methods, the velocity is expressed as the curl of a vector potential function and the cross product of the gradient of two stream functions, respectively. These expressions satisfy the continuity equation identically. The substitution of the velocity expressions in the definition of vorticity gives three second-order elliptic differential equations. The major drawback of these formulations is the difficulty in determining boundary conditions for the new dependent variables. In two dimensions, both formulations reduce to the well-known vorticity-stream function formulation. In the vorticity-velocity formulation, three second-order elliptic differential equations for the velocity components are obtained from the continuity and the definition of vorticity equations. It should be mentioned here that only derivatives of the continuity equation are satisfied in the resulting governing equations. In all nonprimitive variable formulations, the vorticity components are computed from the vorticity-transport equations. The vorticity-transport equations are derived from the momentum equation by eliminating the pressure. After the velocity field is computed, the pressure can be recovered from a Poisson-type equation with Neumann boundary conditions (Roache, 1982).

The nonprimitive variable formulations are inefficient because they solve a large number of differential equations (about twice the number as that of the primitive variable formulation for three-dimensional flows) and this becomes excessively expensive. On the other hand, the primitive-variable formulations solve the Euler equations directly. Also, the boundary conditions are simpler to implement in the primitive variable formulation. Two formulations that are well known for solving the incompressible Euler equations in primitive variables are the artificial compressibility method (Kwak and Chakravarthy, 1986; Choi and Merkle, 1984) and the pressure Poisson equation approach (Harlow and Welch, 1965). In the former, a time-dependent pressure term is added to the continuity equation. The continuity equation is then coupled with the momentum equations and the system is solved with an implicit procedure (Beam and Warming, 1978).

Contributed by the International Gas Turbine Institute and presented at the 34th International Gas Turbine and Aeroengine Congress and Exhibition, Toronto, Ontario, Canada, June 4–8, 1989. Manuscript received at ASME Headquarters January 23, 1989. Paper No. 89-GT-140.

Copyright © 1990 by ASME
Downloaded 01 Jun 2010 to 171.66.16.66. Redistribution subject to ASME license or copyright; see http://www.asme.org/terms/Terms_Use.cfm

In the pressure Poisson equation approach, the momentum equations are solved for the velocity field by marching in time. The continuity equation is replaced by a Poisson-type equation for the pressure. Solutions for the pressure Poisson equation exist only if a compatibility condition is satisfied. This condition is automatically satisfied on staggered grids (Harlow and Welch, 1965); however, this is not the case on nonstaggered grids. A consistent finite-difference approach is developed by Abdallah (1987a), which satisfies the compatibility condition on nonstaggered grids. This method is extended here to three-dimensional curvilinear coordinates. Details of the analysis and numerical solutions for three rotors are presented. The numerical results are compared to experimental data and the comparisons are in good agreement.

Governing Equations

The continuity and momentum equations for inviscid incompressible flow are written in rotating cylindrical coordinates r, θ, and z as shown below.

Continuity Equation:

$$\frac{\partial}{\partial r}(rw_r)+\frac{\partial}{\partial \theta}(w_\theta)+\frac{\partial}{\partial z}(rw_z)=0 \tag{1}$$

Momentum Equation:

$$\frac{\partial Q'}{\partial t}+\frac{\partial E'}{\partial r}+\frac{\partial F'}{\partial \theta}+\frac{\partial G'}{\partial z}+H' \tag{2}$$

where

$$Q'=(rw_r,\ rw_\theta,\ rw_z)^T$$

$$E'=(rw_r^2,\ rw_rw_\theta,\ rw_rw_z)^T$$

$$F'=(rw_rw_\theta,\ rw_\theta^2,\ rw_zw_\theta)^T$$

$$G'=(rw_rw_z,\ rw_zw_\theta,\ rw_z^2)^T$$

$$H'=\left[\left(V_\theta^2-r\frac{\partial P}{\partial r}\right),\ -\left(w_rw_\theta+2\omega rw_r+\frac{\partial}{\partial \theta}\right),-\left(r\frac{\partial P}{\partial z}\right)\right]^T \tag{2a}$$

The relative velocity components w_r, w_θ, and w_z are in the directions r, θ, and z, respectively, P is the static pressure divided by the density, and ω is the wheel speed. The superscript T indicates the transpose matrix.

The absolute tangential velocity component V_θ is given by

$$V_\theta=w_\theta+\bar{\omega}\times\bar{r} \tag{2b}$$

Numerical solutions for equations (1) and (2) using standard compressible flow techniques (Beam and Warming, 1978) are not possible because of the absence of the density time derivative terms from equation (1). In the present study, the continuity equation (1) is replaced by a Poisson-type equation for the pressure. This equations derived from the divergence of the momentum equation.

Pressure Poisson Equation

The divergence of the momentum equation is given by

$$\frac{\partial}{\partial r}\left(r\frac{\partial P}{\partial r}\right)+\frac{1}{r}\frac{\partial}{\partial \theta}\left(\frac{\partial P}{\partial \theta}\right)+\frac{\partial}{\partial z}\left(r\frac{\partial P}{\partial z}\right)=-f' \tag{3}$$

where

$$f'=\frac{\partial}{\partial r}\left[\frac{\partial}{\partial r}(rw_r^2)+\frac{1}{r}\frac{\partial}{\partial \theta}(rw_rw_\theta)+\frac{\partial}{\partial z}(rw_rw_z)-V_\theta^2\right]$$

$$+\frac{1}{r}\frac{\partial}{\partial \theta}\left[\frac{\partial}{\partial r}(rw_rw_\theta)+\frac{1}{r}\frac{\partial}{\partial \theta}(rw_\theta^2)+\frac{\partial}{\partial z}(rw_zw_\theta)+w_rw_\theta+2\omega rw_r\right]$$

$$+\frac{\partial}{\partial z}\left[\frac{\partial}{\partial r}(rw_rw_z)+\frac{1}{r}\frac{\partial}{\partial \theta}(rw_zw_\theta)+\frac{\partial}{\partial z}(rw_z^2)\right]+\frac{\partial D'}{\partial t} \tag{3a}$$

and

$$D'=\frac{\partial}{\partial r}(rw_r)+\frac{1}{r}\frac{\partial}{\partial \theta}(rw_\theta)+\frac{\partial}{\partial z}(rw_z) \tag{3b}$$

The time derivative term in equation (3a) is approximated as follows:

$$\frac{\partial D'}{\partial t}=\frac{D'(t+\Delta t)-D'(t)}{\Delta t} \tag{4}$$

In order to satisfy the continuity equation (1), $D'(t+\Delta t)$ is set equal to zero in equation (4) (Harlo and Welch, 1965); thus

Nomenclature

D, F = source terms in pressure Poisson equation
E, F, G, H = terms in momentum equation
i, j, k = computational indices for the ξ, η, and ζ directions, respectively
J = Jacobian for coordinate transformation
$\bar{n}$ = unit normal vector
P = static pressure divided by density
Q = primitive variable matrix in curvilinear coordinates
r, θ, z = radial, tangential, and axial directions, respectively
t = time
V_θ, V_z = tangential and axial absolute velocities, respectively
VINF = free-stream velocity
$\bar{w}$ = relative velocity vector
w_r, w_θ, w_z = radial, tangential, and axial relative velocities, respectively
ξ, η, ζ = computational domain coordinates
$\Delta\xi, \Delta\eta, \Delta\zeta$ = increments of the computational coordinates
$\alpha, \beta, \gamma, \sigma, \mu, \epsilon$ = metric terms in transformed Pressure Poisson Equation
Δt = time increment
ω = angular velocity

Subscripts

e, w = east $(i+1/2)$ and west $(i-1/2)$ directions, respectively
r, θ, z = radial, tangential, and axial directions, respectively

Superscripts

T = transpose indicator
ξ, η, ζ = computational domain coordinate directions
$'$ = refers to terms in cylindrical coordinates

Downloaded 01 Jun 2010 to 171.66.16.66. Redistribution subject to ASME license or copyright; see http://www.asme.org/terms/Terms_Use.cfm

$$\frac{\partial D'}{\partial t} = -\frac{D'(t)}{\Delta t} \tag{4a}$$

where Δt is the time marching step.

Boundary Conditions

1 Velocity. For inviscid flow, the no-flux condition is satisfied at the solid boundaries

$$\bar{w} \cdot \bar{n} = 0 \tag{5}$$

where $\bar{n}$ is the unit vector normal to the boundary.

2 Pressure. Neumann boundary conditions are obtained for the pressure by using the normal component of the momentum equation at all boundaries.

Compatibility Condition

Solutions for the pressure Poisson equation (3) with Neumann boundary conditions exist only if a compatibility condition is satisfied. This condition results from Green's theorem

$$\iint -f' r dr d\theta dz = \oint \frac{\partial P}{\partial n} dS \tag{6}$$

where n is the outward unit vector normal to the boundary contour S enclosing the volume of the solution domain.

The integral constraint (6) is automatically satisfied when using staggered grids (Harlow and Welch, 1965). In order to satisfy the compatibility condition on nonstaggered grids, the consistent finite-difference method (Abdallah, 1987a, 1987b) is used in the numerical solutions.

The governing equations (2) and (3) are written in general curvilinear coordinates $\xi(r, \theta, z)$, $\eta(r, \theta, z)$, and $\zeta(r, \theta, z)$ using the chain rule. They are given by:

Momentum Equation:

$$\frac{\partial Q}{\partial t} + \frac{\partial E}{\partial \xi} + \frac{\partial F}{\partial \eta} + \frac{\partial G}{\partial \zeta} = H \tag{7}$$

where

$$Q = \frac{1}{J}(w_r, w_\theta, w_z)^T \tag{7a}$$

$$E = \frac{1}{J}(w^\xi w_r, w^\xi w_\theta, w^\xi w_z)^T \tag{7b}$$

$$F = \frac{1}{J}(w^\eta w_r, w^\eta w_\theta, w^\eta w_z)^T \tag{7c}$$

$$G = \frac{1}{J}(w^\zeta w_r, w^\zeta w_\theta, w^\zeta w_z)^T \tag{7d}$$

$$H = \frac{1}{J}\left[\left(\frac{1}{r}V_\theta^2 - P_\xi \xi_r - P_\eta \eta_r - P_\zeta \zeta_r\right), -\frac{1}{r}(w_r w_\theta + 2\omega r w_r + P_\xi \xi_\theta + P_\eta \eta_\theta + P_\zeta \zeta_\theta), -P_\xi \xi_z + P_\eta \eta_z + P_\zeta \zeta_z)\right]^T \tag{7e}$$

The contravariant velocity components w^ξ, w^η, and w^ζ defined in terms of the cylindrical velocity components are

$$w^\xi = \bar{w} \cdot \nabla \xi, \; w^\eta = \bar{w} \cdot \nabla \eta, \; w^\zeta = \bar{w} \cdot \nabla \zeta \tag{8}$$

The Jacobian of transformation J is

$$J = 1/\frac{\partial(r, \theta, z)}{\partial(\xi, \theta, \zeta)} \tag{9}$$

In all equations above, the subscripts r, θ, z refer to partial derivatives when associated with pressure P and the curvilinear coordinates ξ, θ, and ζ.

The pressure Poisson equation in generalized coordinates is given by

$$\frac{\partial}{\partial \xi}(\alpha P_\xi + \beta P_\eta + \gamma P_\zeta) + \frac{\partial}{\partial \eta}(\beta P_\xi + \sigma P_\eta + \mu P_\zeta) + \frac{\partial}{\partial \zeta}(\gamma P_\xi + \mu P_\eta + \epsilon P_\zeta) = -f \tag{10}$$

where

$$\alpha = \frac{1}{J}\nabla \xi \cdot \nabla \xi, \; \beta = \frac{1}{J}\nabla \xi \cdot \nabla \eta,$$

$$\gamma = \frac{1}{J} Yn \cdot \nabla \zeta, \; \sigma = \frac{1}{J}\nabla \eta \cdot \nabla \eta,$$

$$\mu = \frac{1}{J}\nabla \eta \cdot \nabla \zeta, \; \epsilon = \frac{1}{J}\nabla \zeta \cdot \nabla \zeta$$

$$f = \frac{\partial}{\partial \xi}(\bar{S} \cdot \nabla \xi) + \frac{\partial}{\partial \eta}(\bar{S} \cdot \nabla \eta) + \frac{\partial}{\partial \zeta}(\bar{S} \cdot \nabla_z) - \frac{1}{\Delta t} D(t) \tag{10a}$$

The vector function $\bar{S}$ is defined by

$$\bar{S} = \left[\frac{\partial}{\partial \xi}\left(\frac{w^\xi w_r}{J}\right) + \frac{\partial}{\partial \eta}\left(\frac{w^\eta w_r}{J}\right) + \frac{\partial}{\partial \zeta}\left(\frac{w^\zeta w_r}{J}\right) - \frac{v_\theta^2}{Jr}, \frac{\partial}{\partial \xi}\left(\frac{w^\xi w_\theta}{J}\right) + \frac{\partial}{\partial \eta}\left(\frac{w^\eta w_\theta}{J}\right) + \frac{\partial}{\partial \zeta}\left(\frac{w^\zeta w_\theta}{J}\right) + \frac{1}{Jr}(w_r w_\theta + 2\omega r w_r), \frac{\partial}{\partial \xi}\left(\frac{w^\xi w_z}{J}\right) + \frac{\partial}{\partial \eta}\left(\frac{w^\eta w_z}{J}\right) + \frac{\partial}{\partial \zeta}\left(\frac{w^\zeta w_z}{J}\right)\right] \tag{10b}$$

The dilatation term D is

$$D = \frac{\partial}{\partial \xi}\left(\frac{w^\xi}{J}\right) + \frac{\partial}{\partial \eta}\left(\frac{w^\eta}{J}\right) + \frac{\partial}{\partial \zeta}\left(\frac{w^\zeta}{J}\right) \tag{10c}$$

Boundary Conditions

1 Velocity. Boundary conditions for the velocity are obtained from the no-flux condition at the solid boundary. The velocity components w_r, w_θ, and w_z are computed from the contravariant velocity components w^ξ, w^η, and w^ζ using equation (8).

$$\begin{bmatrix} w_r \\ w_\theta \\ w_z \end{bmatrix} = \begin{bmatrix} \xi_r & \frac{1}{r}\xi_\theta & \xi_z \\ \eta_r & \frac{1}{r}\eta_\theta & \eta_z \\ \zeta_r & \frac{1}{r}\xi_\theta & \zeta_z \end{bmatrix}^{-1} \begin{bmatrix} w^\xi \\ w^\eta \\ w^\zeta \end{bmatrix} \tag{11}$$

The contravariant velocity components in the right-hand side of equation (11) are computed from the interior grid points by linear extrapolation (Barton et al., 1987). The appropriate contravariant component is set equal to zero in the right-hand side of equation (11).

2 Pressure. The Neumann boundary conditions for the pressure are obtained using the normal component of the momentum equation. For example at η = const

$$\beta P_\xi + \sigma P_\eta + \mu P_\zeta = -\bar{S} \cdot \nabla \eta \tag{12}$$

Downloaded 01 Jun 2010 to 171.66.16.66. Redistribution subject to ASME license or copyright; see http://www.asme.org/terms/Terms_Use.cfm

Numerical Solutions

The governing equations (7) and (10) with the boundary conditions (11) and (12) are solved using finite-difference techniques. Although the governing equations are written in conservative form, the numerical solutions are obtained for the nonconservative form because it is more suitable for the upwind differencing scheme used here.

Finite-Difference Approximation for Equation (7). The momentum equation (7) is solved using the second-order upwind scheme (Roache, 1982). Depending upon the sign of the contravariant velocity components, the velocity derivatives are approximated using three grid points either upstream or downstream of the grid point under consideration. For example $\partial E/\partial \xi$ is approximated by

For $w^\xi(i, j, k) > 0$

$$\frac{w^\xi}{J}\left(\frac{\partial \phi}{\partial \xi}\right) = w^\xi(i, j, k)\,[\phi(i, j, k) - \phi(i-1, j, k)]/ \times \Delta\xi J(i, j, k) + w^\xi(i, j, k)[\phi(i, j, k) - 2\phi(i-1, j, k) + \phi(i-2, j, k)]/2\Delta\xi\, J(i, j, k) \quad (13a)$$

For $w^\xi(i, j, k) < 0$

$$\frac{w^\xi}{J}\left(\frac{\partial \phi}{\partial \xi}\right) = w^\xi(i, j, k)\,[\phi(i+1, j, k) - \phi(i, j, k)]/ \times \Delta\xi J(i, j, k) - w^\xi(i, j, k)[\phi(i, j, k) - 2\phi(i+1, j, k) + \phi(i+2, j, k)]/2\Delta\xi\, J(i, j, k) \quad (13b)$$

where ϕ represents w_r, w_θ, and w_z. Similar expressions are derived for $\partial F/\partial \eta$ and $\partial G/\partial \zeta$ using the same method.

The pressure derivatives in the right-hand side of equation (7) are approximated using central second-order accurate formulas

$$\frac{\partial P}{\partial \xi} = [P(i+1, j, k) - P(i-1, j, k)]/2\Delta\xi \quad (14a)$$

$$\frac{\partial P}{\partial \eta} = [P(i, j+1, k) - P(i, j-1, k)]/2\Delta\eta \quad (14b)$$

and

$$\frac{\partial P}{\partial \zeta} = [P(i, j, k+1) - P(i, j, k-1)]/2\Delta\zeta \quad (14c)$$

where i, j, and k are the grid points in ξ, η, and ζ, respectively.

Also, the time derivative terms in equation (7) is approximated using first-order accurate formula

$$\frac{1}{J}\frac{\partial \phi}{\partial t} = [\phi^{n+1}(i, j, k) - \phi^n(i, j, k)]/\Delta t \cdot J(i, j, k) \quad (15)$$

where the superscripts n and $n+1$ refer to the time levels t and $t+\Delta t$, respectively.

Finite-Difference Approximation for Equation (10). The pressure Poisson equation (10) and the boundary condition equation (12) are approximated using the method developed by Abdallah (1987a). The method consists of two steps for inviscid flow. First, the pressure equation is written in conservative form. Second, the Neumann boundary conditions (12) are applied at one-half grid away from the boundaries. The finite-difference expressions for the first term in equation (10) are written as (see Fig. 1)

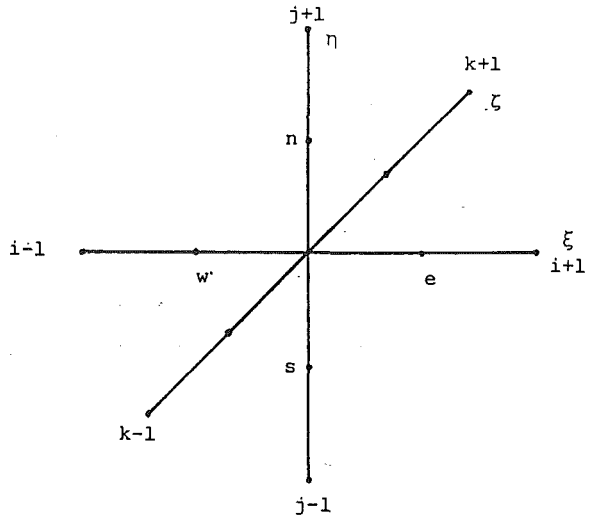

Fig. 1 Finite-difference grid

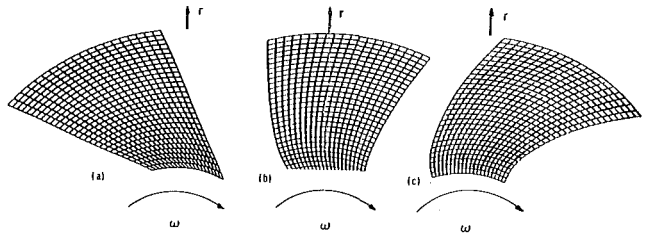

Fig. 2 Trailing edge upstream views: (*a*) Rotor 1; (*b*) Rotor 2; (*c*) Rotor 3

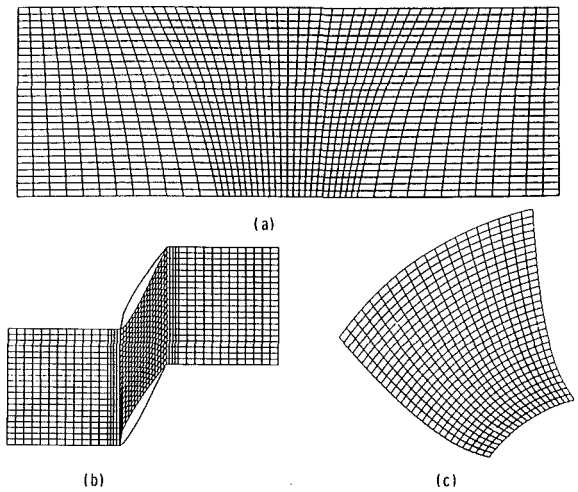

Fig. 3 Typical computational grid sections: (*a*) meridional view; (*b*) blade-to-blade view; (*c*) hub-to-tip view

$$\frac{\partial}{\partial \xi}(\alpha P_\xi) = \alpha_e[P((i+1, j, k) - P(i, j, k)]/\Delta\xi^2 - \alpha_w[P(i, j, k) - P(i-1, j, k)]/\Delta\xi^2 \quad (16a)$$

$$\frac{\partial}{\partial \xi}(\beta P_\eta) = \beta_e[P(i+1, j+1, k) + P(i, j+1, k) - P(i+1, j-1, k) - P(i, j-1, k)/ \times 4\Delta\xi\,\Delta\eta - \beta_w[P(i, j+1, k) + P(i-1, j+1, k) - P(i, j-1, k) - P(i-1, j-1, k)]/4\,\Delta\xi\,\Delta\eta \quad (16b)$$

Downloaded 01 Jun 2010 to 171.66.16.66. Redistribution subject to ASME license or copyright; see http://www.asme.org/terms/Terms_Use.cfm

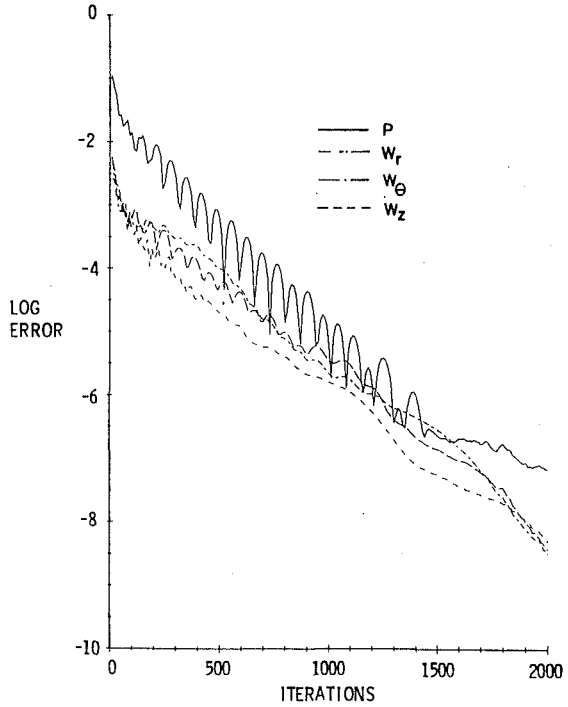

Fig. 4 Typical convergence history

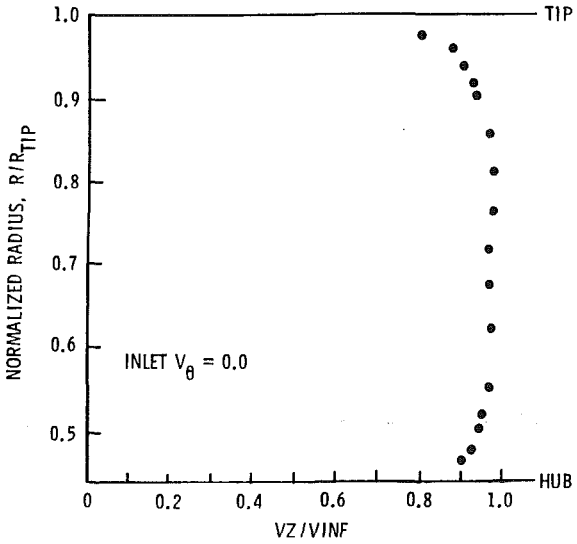

Fig. 5 Inlet velocity profile

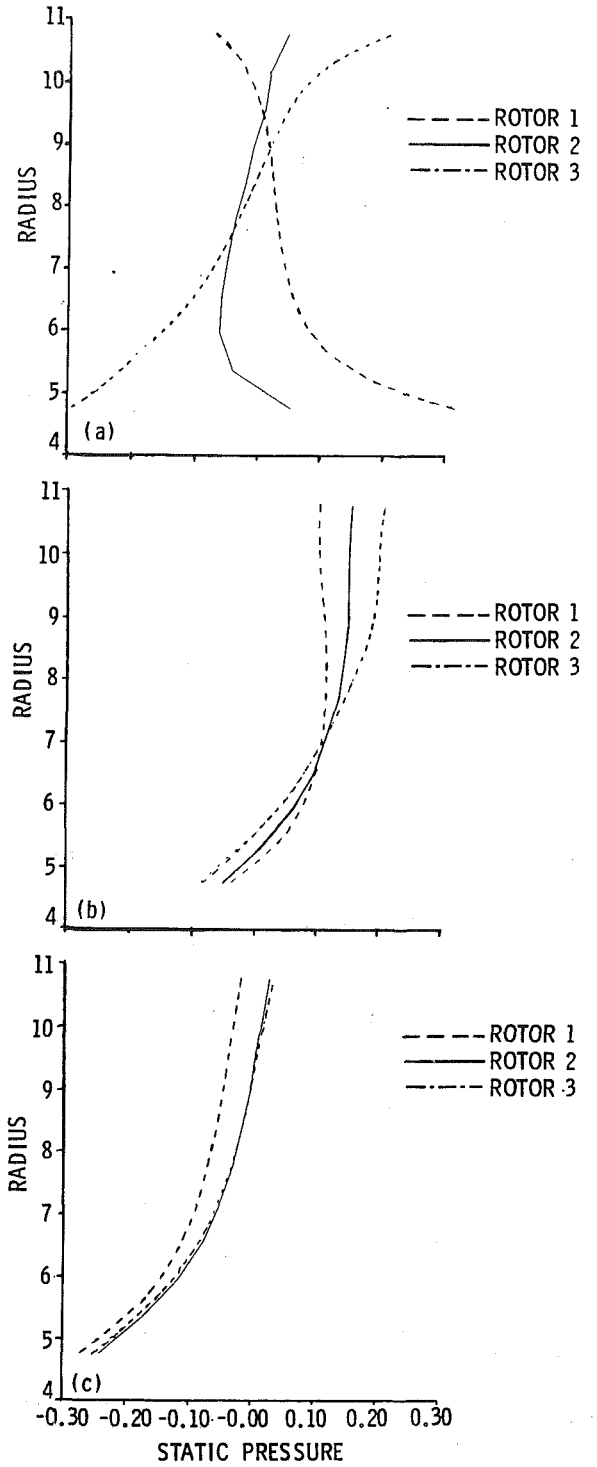

Fig. 6 Static pressure profiles for Rotors 1, 2, and 3: (*a*) leading edge; (*b*) trailing edge; (*c*) downstream exit

$$\frac{\partial}{\partial \xi}(\gamma P_\gamma) = \gamma_e[P(i+1, j, k+1) + P(i, j, k+1) - P(i+1, j, k-1) - P(i, j, k-1) \times 4\,\Delta\xi\,\Delta\zeta - \gamma_w[P(i, j, k+1) + P(i-1, j, k+1) - P(i, j, k-1) - P(i-1, j, k-1)]/4\,\Delta\xi\,\Delta\zeta \quad (16c)$$

where the subscripts e and w refer to the grid points $i + 1/2$ and $i - 1/2$, respectively.

Similar expressions are obtained, using the same method, for the rest of the derivatives in equation (10).

The source term f in the right-hand side of equation (10) is approximated using central finite-difference formulas. Consider for example the first term in the source f:

$$\frac{\partial}{\partial \xi}(\bar{S} \cdot \nabla \xi) = [(S_1\xi_r + S_2\xi_\theta/r + S_3\xi_z)_e - (S_1\xi_r + S_2\xi_\theta/r + S_3\xi_z)_w]/\Delta\xi \quad (17)$$

where S_1, S_2, and S_3 are the components of the vector S, equation (10*b*). With reference to Fig. 1, the terms in equation (17) are approximated as follows:

Downloaded 01 Jun 2010 to 171.66.16.66. Redistribution subject to ASME license or copyright; see http://www.asme.org/terms/Terms_Use.cfm

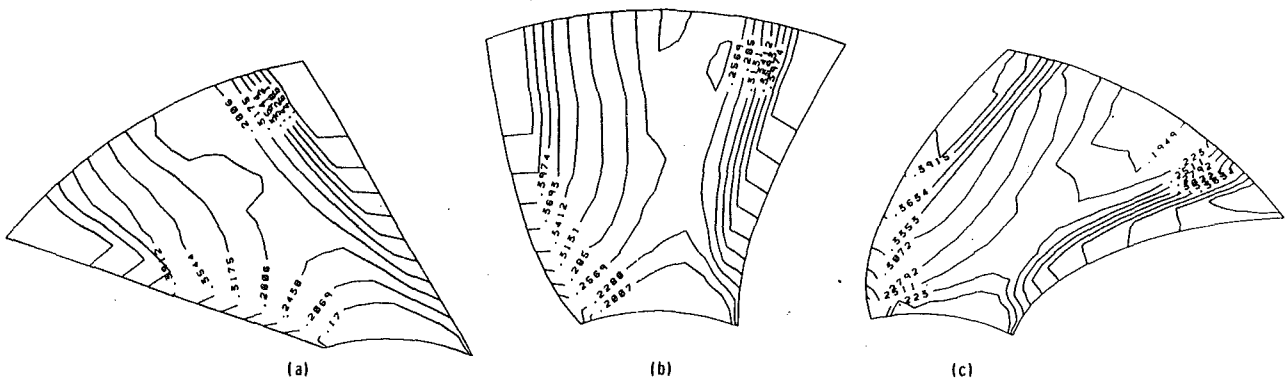

Fig. 7 Static pressure contours at the trailing edge station: (*a*) Rotor 1; (*b*) Rotor 2; (*c*) Rotor 3

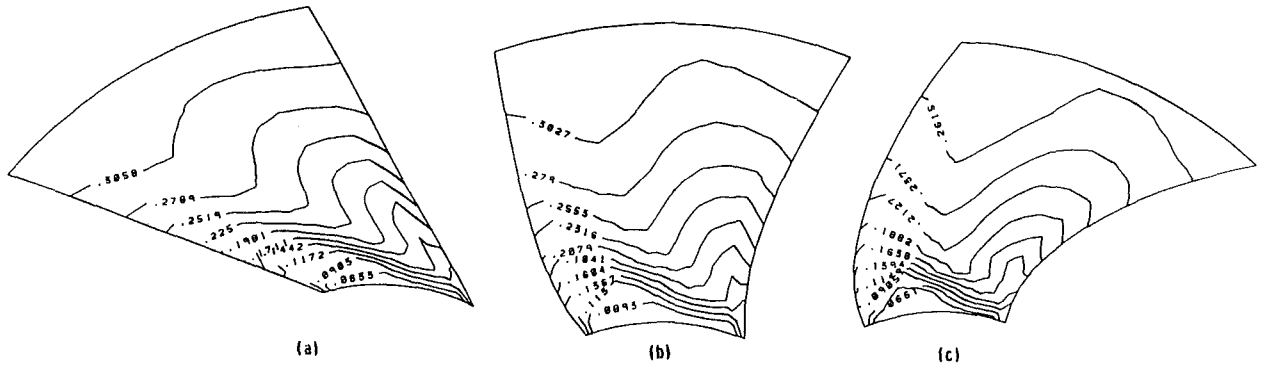

Fig. 8 Static pressure contours at the downstream exit station: (*a*) Rotor 1; (*b*) Rotor 2; (*c*) Rotor 3

$$(S_1\xi_r)_e = (\xi_r)_e \Bigg\{ \left[\left(\frac{w^\xi w_r}{J}\right)_{i+1,\,j,\,k} - \left(\frac{w^\xi w_r}{J}\right)_{i,\,j,\,k} \right] /\Delta\xi + \left[\left(\frac{w^\eta w_r}{J}\right)_{i+1,\,j+1,\,k} + \left(\frac{w^\eta w_r}{J}\right)_{i,\,j+1,\,k} - \left(\frac{w^\eta w_r}{J}\right)_{i+1,\,j-1,\,k} - \left(\frac{w^\eta w_r}{J}\right)_{i,\,j-1,\,k} \right] /4\,\Delta\eta + \left[\left(\frac{w^\zeta w_r}{J}\right)_{i+1,\,j+1,\,k+1} + \left(\frac{w^\zeta w_r}{J}\right)_{i,\,j,\,k+1} + \left(\frac{w^\zeta w_r}{J}\right)_{i+1,\,j,\,k} - \left(\frac{w^\zeta w_r}{J}\right)_{i,\,j,\,k-1} \right] /4\,\Delta\zeta \Bigg\}$$

Similar approximations for the rest of the terms in equation (17) are obtained using the same method.

Boundary Conditions for Equation (12). Equation (12) is applied at the boundaries η = const (Abdallah, 1987a). The boundary conditions are applied at $j = 3/2$ and $j = j\,\text{maximum} - 1/2$.

For example at $j = 3/2$

$$\sigma_{i,\,\frac{3}{2},\,k}\,[P(i,\,2,\,k) - P(i,\,1,\,k)]/\Delta\eta =$$

$$-\beta_{i,\,\frac{3}{2},\,k}[P(i+1,\,2,\,k) + P(i+1,\,1,\,k) - P(i-1,\,2,\,k) - P(i-1,\,1,\,k)]/4\,\Delta\xi - \mu_{i,\,\frac{3}{2},\,k} \times [P(i,\,2,\,k+1) + P(i,\,1,\,k+1) - P(i,\,2,\,k-1) - P(i,\,1,\,k-1)]/4\,\Delta\zeta - (S\cdot\nabla\eta)_{i,\,\frac{3}{2},\,k} \qquad (18)$$

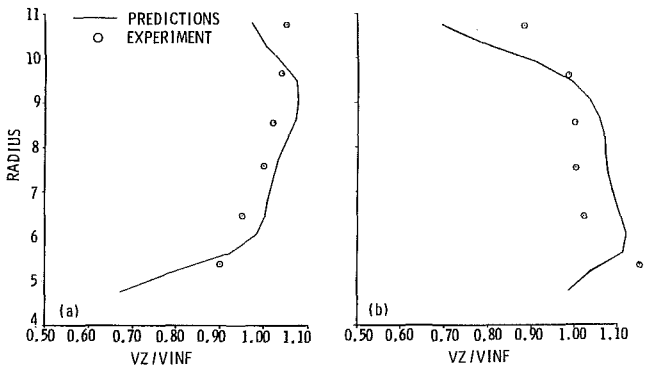

Fig. 9 Axial velocity profiles at the leading edge: (*a*) Rotor 3; (*b*) Rotor 1

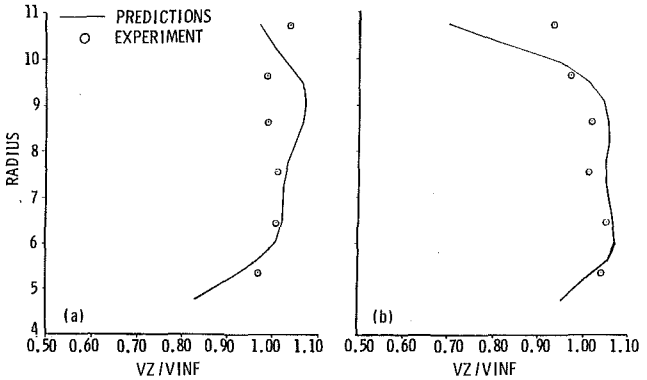

Fig. 10 Axial velocity profiles at the trailing edge: (*a*) Rotor 3; (*b*) Rotor 1

Downloaded 01 Jun 2010 to 171.66.16.66. Redistribution subject to ASME license or copyright; see http://www.asme.org/terms/Terms_Use.cfm

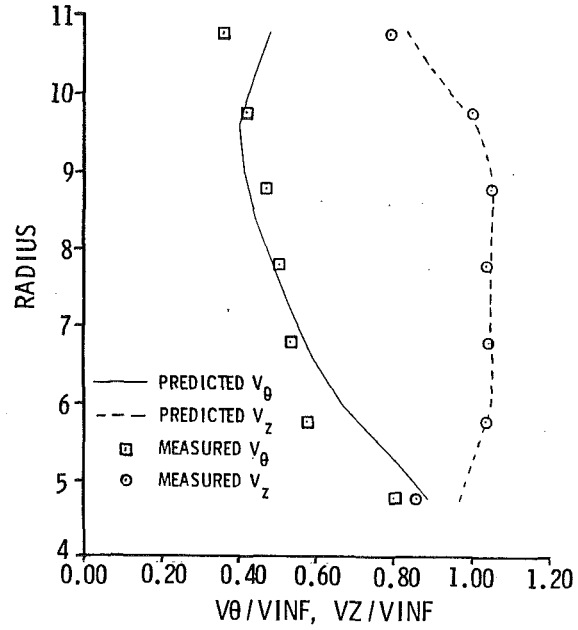

Fig. 11 Velocity profiles at the downstream exit for Rotor 2

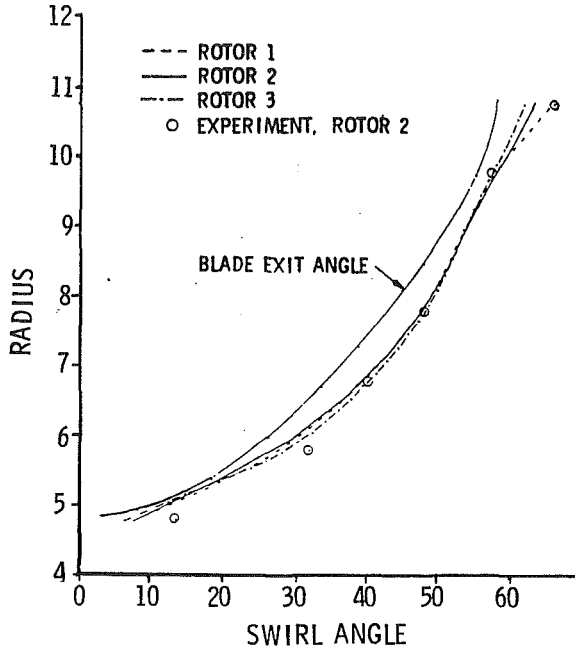

Fig. 12 Downstream relative flow angles

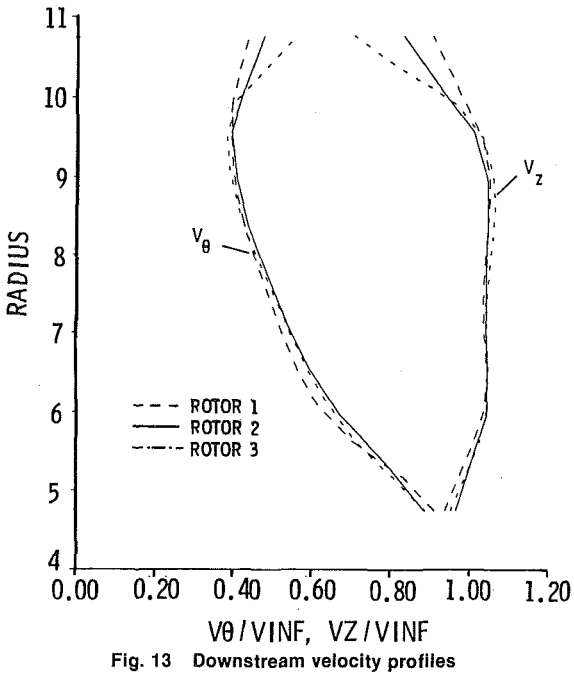

Fig. 13 Downstream velocity profiles

Similar expressions at $j = j$ maximum $- 1/2$, $i = 3/2$, $i = i$ maximum $- 1/2$, $k = 3/2$, and $k = k$ maximum $- 1/2$ are obtained using the same method.

Numerical Results. Numerical solutions for the governing equations (2) and (3) are obtained for three rotors (Pierzga, 1980). These blades have been designed to have similar loading distributions and wheel speed ($\omega = 64.6$ rad/s), but different amounts of dihedral. The upstream views (i.e., looking upstream) of these rotors are shown in Fig. 2. As can be seen from these views, the stackup lines of rotors 1 and 3 depart significantly from the radial direction. This creates a fairly complex geometry to model.

Two iterative cycles are used in the numerical solutions of the governing equations. In the outer cycle, the momentum equations are advanced in time from t to $t+\Delta t$ using forward finite-difference approximation for the time derivatives. The spatial derivatives are approximated using the second-order upwind scheme at time level t (explicit solution). At each time level $(t+\Delta t)$ the pressure Poisson equation is solved for the pressure using the line successive overrelaxation method. The iterative process of solving the Poisson equation is the inner cycle. Since we are interested in the steady-state solution, only one iteration is performed in the inner cycle. The advancement of the momentum equation one time step and the solution of the pressure equation at this step complete one outer cycle. The process is continued in time until convergence is achieved. The convergence criterion is that the residues in velocity and pressure are less than a specified small number (10^{-4}). The residues in velocity and pressure are the average difference between two successive outer cycles.

The computed results are obtained using $15 \times 11 \times 25$ grid points in the radial, tangential, and axial directions, respectively. Two-dimensional grids on surfaces of constant radius are stacked geometrically in the radial direction to form a three-dimensional grid. Typical two-dimensional grid sections are shown in Fig. 3.

It is important to mention here that twice the number of the grid points, used in the numerical solutions, are shown in Figs. 2 and 3. These extra grid points are generated in order to compute the metric coefficients at $i+1/2$, $i-1/2$, $j+1/2$, $j-1/2$, $k+1/2$, and $k-1/2$.

A typical convergence behavior for the velocity components w_r, w_θ, w_z and the pressure P is shown in Fig. 4 for the first rotor. The iteration number in Fig. 4 refers to the time steps, while the vertical coordinate is the residue. The average computational time required to obtain a solution for each rotor on a VAX 11/782 computer is eight hours, for 2000 iterations.

Numerical results are obtained for the three rotors using the measured inlet velocity profile shown in Fig. 5. The effect of different amounts of dihedral in the rotor blade is the imposition of different pressure gradients on the flow field. These effects can be seen in the computer pressure profiles shown in Fig. 6. The pressure at the hub increases as one compares rotors 1, 2, and 3, sequentially. At the tip, this trend is reversed. As can be seen in Fig. 6(*c*), downstream of the blades, the pressure profiles from hub to tip are very similar for the three rotors. These trends are also apparent in the computed pressure contours shown in Figs. 7 and 8, for the trailing edge station

Downloaded 01 Jun 2010 to 171.66.16.66. Redistribution subject to ASME license or copyright; see http://www.asme.org/terms/Terms_Use.cfm

and downstream exit station, respectively. No pressure measurements are available for comparison with the computed pressure results.

Comparisons of measured axial velocities with numerical results are shown in Figs. 9 and 10, for the leading and trailing edge regions, respectively. Although the agreement is fair, the trends are correct. For Rotor 3, the static pressure is higher at the hub than at the tip, and the corresponding velocity profiles, shown in Figs. 9(*a*) and 10(*a*), indicate lower velocity at the hub than at the tip, as expected. From Fig. 6, it can be seen that Rotor 1 has a lower pressure at the hub than at the tip and the corresponding velocity profiles shown in Figs. 9(*b*) and 10(*b*) indicate a reverse trend from hub to tip. One source for the differences between the measurements and the numerical results shown in Figs. 9 and 10 may be due to the error associated with the measurements made very near the blades' leading and trailing edge regions.

Measurements of the downstream axial and tangential velocity components were available for Rotor 2. The comparisons of the predictions with experimental data are in good agreement, as shown in Fig. 11. The computed downstream flow angles for the three rotors are almost identical, as shown in Fig. 12. Also shown in Fig. 12 are the relative flow angles for Rotor 2, which were determined from the measured velocity components. These data agree well with the predicted flow angles for Rotor 2. The calculated downstream axial and tangential velocity components for the three rotors are shown in Fig. 13. It can be seen from Fig. 13 that the three rotors have approximately the same tangential velocity distribution. This is consistent with the design procedure of specifying the same amount of turning for the three blades, but different amounts of dihedral.

Conclusions

Three-dimensional solutions are obtained for the inviscid incompressible Euler equations using the primitive variable approach. The governing equations are solved in general curvilinear coordinates using nonstaggered grids. The method developed by Abdallah (1987a, 1987b) is applied in three dimensions to satisfy the compatibility condition, necessary for convergence of the pressure Poisson equation. The numerical results are compared with experimental data of three turbomachinery rotors.

The calculations made at a downstream station compare very well with the experimental data. Predictions made at the leading and trailing edge stations are in fair agreement with the measurements made at these locations. These differences may be due to the error incurred in obtaining data at the leading and trailing edge locations. In general, predicted trends in the radial variation of velocity and pressure are consistent with the differences in the geometries of each rotor.

Acknowledgments

This work was sponsored by the Office of Naval Research, Code 12, under the direction of Dr. James Fein.

References

Abdallah, S., 1987a, "Numerical Solutions for the Pressure-Poisson Equation With Neumann Boundary Conditions Using Non-staggered Grid I," *Journal of Computational Physics*, Vol. 70, pp. 182–192.

Abdallah, S., 1987b, "Numerical Solutions for the Incompressible Navier–Stokes Equations in Primitive Variables Using a Non-staggered Grid II," *Journal of Computational Physics*, Vol. 70, pp. 193–202.

Abdallah, S., Smith, C. F., and McBride, M. W., 1988, "Unified Equation of Motion (UEM) Approach as Applied to S1 Turbomachinery Problems," ASME *Journal of Fluids Engineering*, Vol. 110, pp. 251–256.

Barton, O. M., Yamamoto, O., and Bober, L. J., 1987, "Euler Analysis of Transonic Propeller Flows," *Journal of Propulsion*, Vol. 3, No. 3.

Beam, R. M., and Warming, R. F., 1978, "An Implicit Factored Scheme for the Compressible Navier–Stokes Equations," *AIAA Journal*, Vol. 16, pp. 393–401.

Choi, D., and Merkle, C. L., 1984, "Application of Time Derivative Schemes to Incompressible Flow," AIAA 17th Fluid Dynamics, Plasma Dynamics, and Lasers Conference, Snowmass, CO, Paper No. 84–1638.

Harlow, F. H., and Welch, J. E., 1965, "Numerical Calculation of Time-Dependent Viscous Incompressible Flow With Free Surfaces," *Physics of Fluids*, Vol. 8, No. 12, pp. 2182–2185.

Katsanis, T., and McNally, W. D., 1973, "Fortran Program for Calculating Velocities and Streamlines on Hub-Shroud Mid-channel Flow Surface of an Axial or Mixed-Flow Turbomachine," NASA TN D-7343.

Kwak, D., and Chakravarthy, S. R., 1986, "A Three-Dimensional Incompressible Navier–Stokes Flow Solver Using Primitive Variables," *AIAA Journal*, Vol. 24, No. 3.

Novak, R. A., and Hearsey, R. M., 1977, "A Nearly Three-Dimensional Intrablade Computing System for Turbomachinery," ASME *Journal of Fluids Engineering*, Vol. 99, pp. 154–166.

Pierzga, M. J., 1980, "Experimental Verification of the Streamline Curvature Numerical Analysis Method Applied to the Flow Through an Axial Flow Fan," M.S. Thesis, Department of Aerospace Engineering, The Pennsylvania State University, Nov.

Roache, P. J., 1982, *Computational Fluid Dynamics*, Hermosa, Albuquerque, NM.

Wu, Chung-Hua, 1951, "A General Through-Flow Theory of Fluid Flow With Subsonic Velocity in Turbomachines of Arbitrary Hub and Casing Shapes," NACA TN 2302.

Downloaded 01 Jun 2010 to 171.66.16.66. Redistribution subject to ASME license or copyright; see http://www.asme.org/terms/Terms_Use.cfm

Axial Flow Compressor Design Optimization: Part I—Pitchline Analysis and Multivariable Objective Function Influence

A. Massardo

A. Satta

Dipartimento di Ingegneria Energetica,
Universitá di Genova,
Genoa, Italy

The design of an axial flow compressor stage has been formulated as a nonlinear mathematical programming problem with the objective of minimizing the aerodynamic losses and the weight of the stage, while maximizing the compressor stall margin. Aerodynamic as well as mechanical constraints are considered in the problem formulation. A method of evaluating the objective function and constraints of the problem with a pitchline analysis is presented. The optimization problem is solved by using the penalty function method in which the Davidon-Fletcher-Powell variable metric minimization technique is employed. Designs involving the optimization of efficiency, weight of the stage, and stall margin are presented and the results discussed with particular reference to a multivariable objective function.

Introduction

In order to introduce a design system for axial flow compressor stages, some criteria for a good design should be stated. The first goal of a design system should be to generate a compressor geometry that will produce the design point total pressure ratio when the design point mass flow rate exists in each stage of the compressor. Design point pressure ratio, flow rate, and rotational speed must be obtained within the aerodynamic and aeromechanical design requirements of the machine with an acceptable level of compressor thermodynamic efficiency, an adequate surge margin, and a reduced weight.

The compressor designer must therefore develop a compressor geometry that demonstrates stable aerodynamic and aeromechanical operation, including sufficient surge margin, no excessive blade or disk vibrations, and acceptable thermodynamic efficiency for all expected operating conditions.

Subject to these constraints, the compressor configuration should be designed for the maximum possible mass flow rate per unit frontal area, the highest possible average pressure ratio per stage, the minimum values of axial stage length, and the minimum number of blades specified for each row.

These characteristics lead to the minimization of compressor stage weight and cost.

The design system must include a procedure for determining potentially satisfactory flow path geometries capable of stable and efficient operation at the design flow rate and at a tip peripheral velocity acceptable to the mechanical system designers; a procedure for predicting the flowfield through the compressor at the design point; a method for predicting compressor performance at off-design flows and rotational speed; a stress analysis (blade rows, disks, and shrouds); and an aeroelastic analysis.

The abovementioned design method, even if simplified in some parts, can be coupled with techniques of numerical minimization. The goal of the present work is the presentation of this coupling, using objective functions that are composed not only of a single variable, but of a combination of variables. This is done in order to avoid the improvement of a single quantity (efficiency), to the detriment of other important compressor characteristics. The optimization is performed with the appropriate physical constraints; the design limit parameters provide a quantitative basis for predicting the conditions under which unacceptable blade row or overall performance will occur. They are needed in a preliminary design as arbitrary stop signs in setting up a geometric flowfield combination.

Formulation of Optimum Design Problem

Any optimization problem involves the identification of design variables, objective functions and constraints of the problem.

Design Variables. These are preselected variables, which can assume independent values in the design process. The other data of the problem are either given at the beginning of the design process or can be expressed in terms of the design variables.

For the design of an axial flow compressor stage, the following parameters are taken as the design variables:

Contributed by the International Gas Turbine Institute and presented at the 34th International Gas Turbine and Aeroengine Congress and Exhibition, Toronto, Ontario, Canada, June 4–8, 1989. Manuscript received at ASME Headquarters February 1, 1989. Paper No. 89-GT-201.

Copyright © 1990 by ASME
Downloaded 01 Jun 2010 to 171.66.16.66. Redistribution subject to ASME license or copyright; see http://www.asme.org/terms/Terms_Use.cfm

X_1 = stage enthalpy drop (ψ)
X_2 = inlet flow coefficient (φ)
X_3 = outlet flow absolute angle from the stator (α_3)
X_4 = mean diameter of the stage (D_m)
X_5 = axial velocity ratio in the rotor (AVR_R)
X_6 = axial velocity ratio in the stator (AVR_S)
X_7 = solidity of the stator (σ_S)
X_8 = solidity of the rotor (σ_R)
X_9 = ratio of the chord of the rotor blade to the mean diameter (C_R/D_m)
X_{10} = ratio of the chord of the stator blade to the mean diameter (C_S/D_m)
X_{11} = maximum thickness to chord ratio of the stator blade $(t_m/C)_S$
X_{12} = maximum thickness to chord ratio of the rotor blade $(t_m/C)_R$

Variables have been chosen in order to be easily identified in the initial design phase; they are mainly nondimensional (ψ, φ, AVR, σ, t_m/C, C/D_m) or, if dimensional (D_m) they represent the size of the machine to which the stage refers. The angle α_3, even if it was introduced in the design variables, could be easily referred to a fixed design parameter (i.e., $\alpha_3 = 0$ deg or $\alpha_3 = \alpha_1$).

It is necessary to point out that in similar work on turbines (Rao and Gupta, 1980), design angles are confused with flow angles. In the present work the incidence and deviation angles are taken into account for every row. This is done by using design variables and data that make it possible to obtain the flow angles, based on loss and turning correlations. Using the design variables and data in this manner permits the evaluation of the incidence angle for which the minimum losses are achieved and the corresponding deviation angle. This aspect will be discussed in the course of this paper.

Objective Function

A design problem usually has several solutions that may adequately satisfy the specified functional requirements. The objective function in a general optimization problem represents a basis for the choice between various equally acceptable designs.

In the case of an axial-flow compressor used in aerospace applications, the minimization of weight is one of the most important criteria, while in the case of a gas compressor used in stationary power plants, the maximization of efficiency represents a more useful criterion. In both cases, therefore, the machine presents the highest operating capacity. Therefore the compressor could be designed with the widest stall margin.

Thus, in some cases, a mixed (multivariable) objective function representing a linear combination of weight, efficiency, and stall margin would be a more appropriate objective. In this work the multivariable objective function is used so that the optimum design of an aerospace or industrial compressor can be found using the same computer program and ascribing suitable importance to the efficiency, stall margin, and weight of the machine in the objective function.

Objective Function Evaluation

Since the complete objective function comprises three distinct quantities, efficiency (losses), stall margin, and weight of the stage (specific inlet area), each one will be considered separately. The inlet total pressure and temperature, the mass flow rate, and the total-to-total pressure ratio are pre-assigned parameters. The values of the design variables are assumed to be known at the beginning of the analysis and will be modified during the design analysis iterative process (Fig. 1).

Efficiency (Losses) of the Stage. The necessary steps for evaluating the total-to-total stage efficiency are stated sequentially in this section. This involves assuming a trial value of efficiency η_{TTt}, and iterating until the values of stage efficiency in two consecutive iterations are sufficiently close to each other. The free vortex assumption is employed for three-dimensional design consideration (tip and root flow characteristics and relative limits).

After determining the geometric characteristics of the inlet area and the value of the peripheral velocity, the flow angles are evaluated in the light of the axial velocities and the total temperature gradient, which has been estimated on the trial value of the efficiency. This allows prediction of the upstream row flow characteristics and, with the geometry information available from the design data, evaluation of the incidence and deviation angles. Thus it is easy to get the blade angles. The evaluation of the incidence and deviation angles is based on the NASA-SP 36 correlations, assuming that the incidence angle is the one for which there is minimum loss (i^*) and so obtaining the corresponding deviation angle (δ^*). The abovementioned procedure is, of course, iterative (the incidence starting value is set equal to zero). The loss calculation is based on the correlation curves presented by Davis and Miller (1976). Shock losses have been evaluated with the Miller–Lewis–Hartmann method (Miller et al., 1961).

The knowledge of the loss coefficients allows evaluation of the conditions downstream of the stage (and thus also the effi-

Nomenclature

A, A_{sp} = area, specific area = $\dot{m}/A$
AVR = axial velocity ratio
C = chord
C_h = stall margin coefficient
c = absolute velocity
D_m = mean diameter
D_f = diffusion factor
G_η, G_a, G_c = objective function coefficients
H = blade height
h = enthalpy
i, δ = incidence and deviation angle
$\dot{m}$ = mass flow rate
M = Mach number
p = pressure
S = entropy
t_m = maximum blade thickness
T = temperature
U = peripheral velocity
w = relative velocity
x = design variable
α, β = relative and absolute flow angles
β_{TT} = total-to-total pressure ratio
η_{TT} = total-to-total stage efficiency
ρ = density
σ = solidity
τ = tip clearance
φ, ψ = flow and head stage coefficients
ω = total pressure loss coefficient

Subscripts

1, 2, 3 = station number
a = absolute
b = blade
h = hub
m = mid
r = relative
R, S = rotor, stator
t = tip

Superscripts

$\bar{}$ = nondimensional

Downloaded 01 Jun 2010 to 171.66.16.66. Redistribution subject to ASME license or copyright; see http://www.asme.org/terms/Terms_Use.cfm

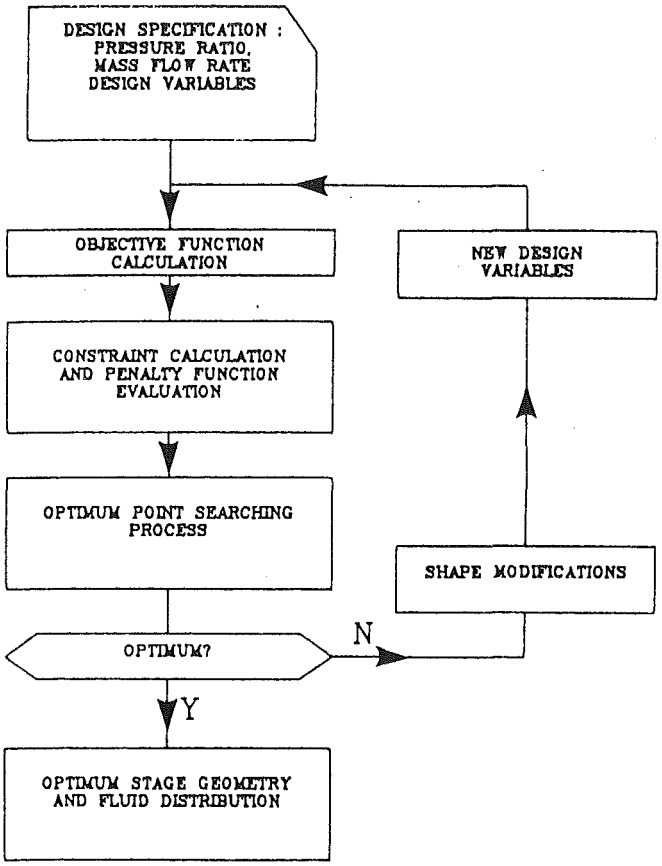

Fig. 1 General optimization flow chart

ciency). Suitable corrections considering the tip loss correlation of Lakshminarayana (1970) are made.

Stall Margin. Great difficulty and expense may be involved in correcting compressor stall margin problems, because detailed refinement and development may not be sufficient to correct the problem if the basic design has not been chosen to permit the required stall margin to be achieved. In the present work a procedure that allows easy and rapid evaluation of the stage "stall margin" is essential. The correlation proposed by Koch (1981) has been chosen because of its simplicity and because it is particularly well suited for preliminary design studies. The term chosen as the primary dependent variable relating to stall pressure rise was the overall stage enthalpy equivalent static pressure rise coefficient C_h. This is based upon stage overall static pressure rise converted to the equivalent isentropic enthalpy rise, minus any enthalpy change attributed to changes in pitchline across the rotor (Koch, 1981).

Note that the stall margin correlations are based upon simplified stage-averaged pitchline quantities, as is the method presented for the stage efficiency calculation.

In the calculation the rotor and stator stall margin values are combined into a weighted averaged stage value in which the blade row inlet dynamic head was used as the weighting factor.

Stage Weight. In the present analysis the evaluation of the stage weight was not easy, considering it was evaluated in a preliminary procedure (pitchline analysis). It is, however, possible to single out a variable that, because of its correlation with the stage weight, can be evaluated more easily. Therefore the stage inlet specific area has been chosen; it is the ratio between the mass flow rate and the inlet stage area ($A_{sp} = \dot{m}/A_1$). Since both of the two other variables that comprise the objective function are, in value, less than unity, we chose to work with a limited variable in this case too. This makes it possible to simplify the choice of the coefficients to be assigned to any single objective in the multivariable objective function. To reduce the specific area value, it has been related to the value it should have in the inlet stage area if sonic conditions were to happen.

Design Constraints

The constraints of the optimized design procedure could be of two different kinds: rectangular constraints, which are directly applied on the design variables and so defined as

$$X_i^l < X_i < X_i^u$$

They are evaluated on previous design data and on the field of the possible applicability of the correlations used in the objective function computation. However, a direct constraining of any single design variable does not assure that, in a particular combination of them, some of the mechanical or fluid dynamic variables could exceed the usual limits.

For this reason, nonrectangular constraints have been chosen: They are related to aerodynamic "loading," flow instability, limiting flow rate through a flow path element, aeroelastic aspect of compressor blade rows, and noise generation.

It is important to observe that, since the objective of the present work was to evaluate the aerodynamic potential of the new design method, stress and vibration analysis for this design stage were limited.

The limits that are used in this work are:

- The rotational velocity of the rotor should be within some upper and lower bounds.
- The aspect ratios of rotor and stator blades should be within some specified upper and lower limits.
- The axial Mach number at stations 1, 2, and 3 should be within specified bounds.
- The included angle of convergence of the compressor annulus walls should not exceed the specified upper limit.
- The tip rotor clearance should be lower than a limit value.
- The ratio between the tip rotor clearance and the rotor height should be within specified bounds.
- The stresses developed at the root of the rotor blade should be less than the permissible value.
- The ratio between the blade height and the mean diameter of the stage should be within specified bounds.
- The rotor and stator blade numbers should be within specified bounds.
- The relative tip rotor Mach number should be less than a permissible value.
- The stator and rotor stall margin should be greater than a specified value.
- The specific inlet area should be greater than a specified value.
- The total-to-total efficiency should be greater than a specified value.

The constraints other than those involving stress and vibration can be specified with the help of the relations utilized to evaluate the objective function. For the purpose of stress computations the rotating blade is idealized as a rectangular cantilever beam having linear taper in depth, breadth, and twist from root to tip and subjected to rotational pressure and gas bending stress.

In the present analysis a method similar to the one proposed by Rao and Gupta (1980) is utilized with some simplification such as using only the centrifugal stress calculation.

Statement of Optimization Problem

The optimization problem (see Fig. 1) can now be stated in

Downloaded 01 Jun 2010 to 171.66.16.66. Redistribution subject to ASME license or copyright; see http://www.asme.org/terms/Terms_Use.cfm

Table 1 Optimization results for three different limits imposed at $X_3 = \alpha_3$

DESIGN VARIABLES	STARTING VALUE	OPTIMUM VALUE		
		$\alpha_3 \leq 20°$	$\alpha_3 \leq 10°$	$\alpha_3 \leq 0°$
ψ	0.4	0.496	0.462	0.438
φ	0.45	0.465	0.471	0.464
α_3(°)	0.9 (0.0)	19.99	9.19	0.0
D_m(m)	0.170	0.163	0.159	0.158
AVR_R	1.15	1.04	1.00	1.00
AVR_S	1.20	1.32	1.40	1.48
σ_S	1.9	1.50	1.50	1.74
σ_R	1.6	1.26	1.36	1.27
C_R/D_m	0.300	0.200	0.200	0.222
C_S/D_m	0.140	0.128	0.13	0.122
t_m/C_R	0.050	0.0518	0.0487	0.0447
t_m/C_S	0.050	0.0498	0.0502	0.0745
OBJ=$(1-\eta_{TT})$	0.875	0.927	0.920	0.917

$\dot{m}$ = 4 kg/s ; β_{TT} = 1.65 ; P_{01} = 101300 Pa ; T_{01} = 300 K ; α_1 = 0°.

Table 2 Design constraints

$0.03 < H_1/D_m < 0.3$	$0.03 < H_2/D_m < 0.3$	$0.03 \leq H_2/D_m \leq 0.3$
$50 < U < 450$ (m/s)	$0.5 < (H_1/C_R) < 4$	$0.5 \leq (H_2/C_S) \leq 3$
$0.1 < M_{a1} < 0.7$	$0.1 < M_{a2} < 0.9$	$0.1 \leq M_{a3} \leq 0.9$
0.1 (mm) $< \tau <$ 1 (mm)	$0.001 \leq \tau/H_1 \leq 0.01$	$\sigma_{stress} \leq \sigma_{AM}$
$15 < Z_R < 50$	$20 \leq Z_S \leq 100$	$M_{rlt} \leq 2.0$
$0.35 < C_{hR}$	$0.35 \leq C_{hS}$	$140 \leq A_{sp}$
$0.75 < \eta_{TT}$	$1. \leq H_1/H_2 \leq 2.5$	$1. \leq H_2/H_3 \leq 1.5$
$0.2 < \varphi < 0.60$	$0.15 \leq \psi \leq 0.5$	$0° \leq \alpha_3 \leq 20°$
$0.15 < D_m < 0.3$ m	$0.8 \leq AVRR \leq 1.5$	$1.0 \leq AVRS \leq 1.5$
$1.0 < \sigma_S < 2.0$	$0.6 \leq \sigma_R \leq 2.0$	$0.2 \leq (C_R/D_m) \leq 0.5$
$0.1 < (C_S/D_m) < 0.5$	$0.035 \leq (t_m/C)_R \leq 0.2$	$0.035 \leq (t_m/C)_S \leq 0.2$

the format of a nonlinear programming problem as follows: Find $[X]$ that minimizes

$$f(X) = G_\eta(1-\eta_{TT}) + G_A(1-\bar{A}_{sp}) + G_C(1-C_h) \qquad (1)$$

subject to the constraints

$$X_i^l < X_i < X_i^u \qquad i = 1, m$$

$$g_j(X) \qquad j = 1, n$$

The details of the method are presented in the part II of this work.

Applications

Before starting up the complete optimized design of the stages of an axial compressor, the method to calculate the efficiency was accurately verified. The method was tested using geometric and experimental data available in the literature.

Table 3 Influence of α_1 value on the optimization (OBJ = $1-\eta_{TT}$; α_3 = 20 deg; DCA blade; β_{TT} = 1.75; *i* = initial; *o* = optimum)

	α_1 = 0°		α_1 = 10°		α_1 = 20°	
	i	o	i	o	i	o
η_{TT}	0.870	0.914	0.884	0.914	0.883	0.910
A_{sp}	180	166	178	178	176	177
C_h	0.541	0.516	0.534	0.512	0.526	0.531
ω_R	0.128	0.082	0.103	0.076	0.088	0.075
ω_s	0.061	0.047	0.069	0.051	0.089	0.063
M_{rlm}	1.224	1.081	1.134	1.089	1.052	1.049
M_{a3}	0.669	0.646	0.664	0.705	0.826	0.780

Table 4 Influence of the kind of blade row on the optimization results (OBJ = $1-\eta_{TT}$; α_3 = 20 deg; *i* = initial; *o* = optimum)

KIND OF BLADE ROW	65-SERIES		C-SERIES		D.C.A.	
--	i	o	i	o	i	o
η_{TT}	0.876	0.919	0.875	0.921	0.883	0.920
A_{sp}	171.8	162	171.9	158.9	171.3	170.2
C_h	0.537	0.488	0.535	0.481	0.541	0.515
α_3	9.00	15.08	9.00	19.99	9.00	19.87
ω_R	0.112	0.068	0.114	0.067	0.103	0.063
ω_s	0.059	0.049	0.059	0.046	0.059	0.051
ϱ_3	1.364	1.352	1.363	1.398	1.368	1.417

The results were generally positive (within 1.0 percent of the measured value at design point) for low and medium stage aspect ratios while, for higher aspect ratios, notable differences from the experimental data were encountered.

The complete optimization method was first used with a single objective function coincident with η_{TT} and then with a multivariable function (η_{TT}, $\bar{A}_{sp}$, C_h).

Single Variable Objective Function. To use the suggested method, we have chosen to design a stage of a small axial compressor ($\dot{m}$ = 4 kg/s) with a high pressure ratio (β_{TT} = 1.65).

The design variables, and the initial and optimized values, are shown in Table 1, while in Table 2 the numerical values of constraints are shown. The optimization has been performed with a single variable objective function, the total-to-total stage efficiency.

The initial stage efficiency value of 0.875 grows up to 0.927 ($\alpha_3 < 20$ deg). This confirms the capacity for improvement in the stage performance using the proposed method.

The optimized results shown in Table 1 have been obtained by imposing different limits to the stage (α_3). As shown, the design variables, particularly φ, ψ, AVR, and σ seem to be particularly sensitive to the α_3 limits. In all three examples, the optimized efficiency seems to be too high if referred to the total pressure ratio of the stage. The optimization procedure has, as seen before, carried out a reduction of the relative inlet Mach number (to which shock losses are related) so permitting a remarkable reduction in the rotor losses (ω_{R_i} = 0.114 and ω_{Ro} = 0.0675).

Additional calculations have been performed by modifying the inlet flow angle (α_1), simulating in this way the presence of

Downloaded 01 Jun 2010 to 171.66.16.66. Redistribution subject to ASME license or copyright; see http://www.asme.org/terms/Terms_Use.cfm

Table 5 Influence of the different coefficient values in the multivariable objective function ($C-$ series; $\dot{m}=4$ kg/s; $\alpha_3 \leq 20$ deg; $\beta_{TT}=1.65$)

G_η	G_A	G_C	η_{TT}	A_{sp}	C_h
-	-	-	0.875	171.98	0.535
1	0	0	0.921	158.88	0.481
0	1	0	0.600	225.74	0.539
0	0	1	0.415	145.72	0.598
1	1	1	0.786	208.95	0.572
1	0	1	0.888	162.04	0.553
1	1	0	0.854	208.60	0.478
0	1	1	0.730	213.90	0.572
1	0.5	1	0.891	187.63	0.577

an IGV or of a stage upstream. As an example, Table 3 shows the results obtained for $\alpha_1 = 0$; 10; 20 deg.

Similarly, the influence of blade profile on the optimization process has been investigated. The correlations used throughout this method consider three different kinds of profiles: DCA, C-series, and C-65. The results obtained are shown in Table 4. Looking at the tables quoted it generally transpires that, whereas η_{TT} increases, the other significant design variables (A_{sp}, C_h) are dramatically reduced. This remarkable feature points out the necessity to operate with mixed objective functions.

Multivariable Objective Function. A design optimization has been performed using a multivariable objective function from equation (1). To achieve this purpose and considering the values of the single variables, which compose the objective function, several calculations have been performed, varying, along the limits of the range 0.0 to 1.0, the coefficients G_η, G_A, and G_C.

Table 5 shows the initial values of η_{TT}, A_{sp}, and C_h, and the final values after the optimization process. It is necessary to point out that in this application, the constraints on the minimum value of η_{TT}, A_{sp}, and C_h have been eliminated, so that the design optimization tendency could be completely manifest. From Table 5 it is evident that if $G_\eta = 0$, the values of η_{TT} are absolutely unsatisfactory, especially in the case where G_A and G_C are unity. For this reason, the efficiency should always be present in the objective function. In the case where $G_\eta = 1$ and $G_C = 0$, a high reduction in the stall margin results (especially if $G_A = 1$).

If $G_\eta = G_A = G_C = 1$, the dominant effect of G_A leads to a large increase in the specific area and also a corresponding decrease in the starting value of efficiency (from 0.87 to 0.78).

It is no doubt necessary to investigate in detail the influence of the three coefficients G_η, G_A, and G_C so that they all have average values between 0 and 1; for instance, looking at the last line of Table 5 where $G_\eta = 1$, $G_A = 0.5$, and $G_C = 1$, an increase in all three functions in the objective function was achieved.

The different values of the three coefficients influence, of course, not only the constituent functions of the objective, but also geometric and fluid compressor parameters. For example, Figs. 2 and 3 show the radial distribution of the relative Mach number along the rotor span at the inlet and the absolute Mach number in the three axial computational stations. In this case the large influence of G_A and G_η is also evident. The lines when $G_\eta = 0$ are plotted on the figures just to compare with each other, because they show excessively low values of the

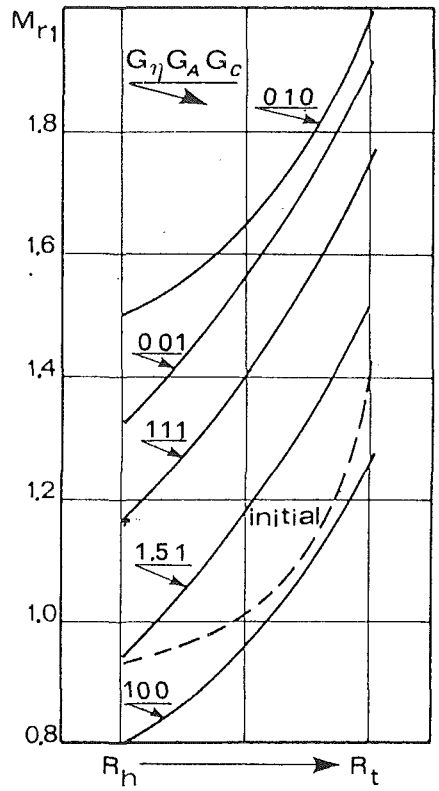

Fig. 2 Influence of G_η, G_A, G_C coefficients on M_{r1}

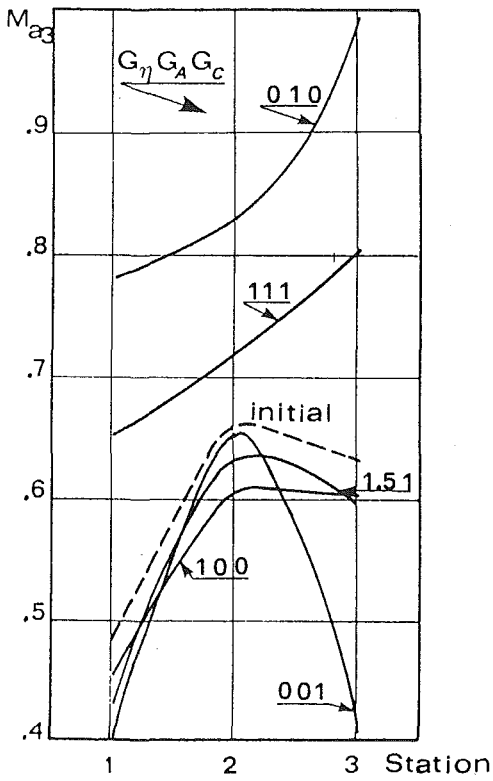

Fig. 3 Influence of G_η, G_A, and G_C coefficients on M_a

stage efficiency. The analysis of the optimization with the multivariable objective function has been finally performed varying G_A from 0 to 1, with G_C as a parameter and $G_\eta = 1$. The behavior of the optimum efficiency is plotted in Fig. 4 (data of Table 1 have the starting values). The optimum effi-

Downloaded 01 Jun 2010 to 171.66.16.66. Redistribution subject to ASME license or copyright; see http://www.asme.org/terms/Terms_Use.cfm

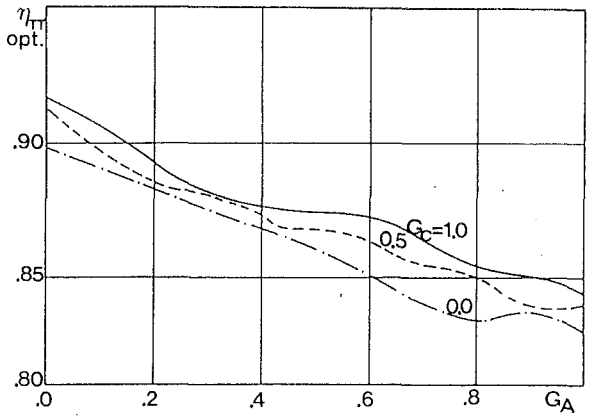

Fig 4 Efficiency for different values of G_A and G_C

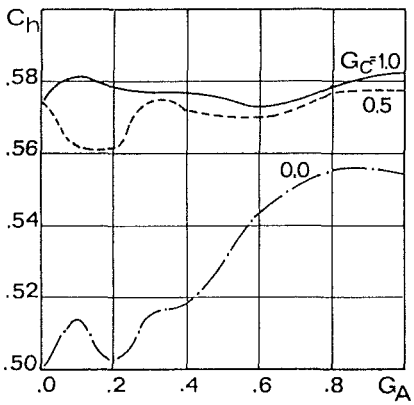

Fig. 5 Influence of G_A and G_C on stall margin coefficient ($G_\eta = 1.0$)

ciency decreases greatly with G_A. The same trend, albeit reduced in effects, is shown by the function of G_C. Figure 5 shows the "stall margin coefficient" C_h; the influence of G_A is negligent for high values of G_C while if $G_C = 0$ the increase in G_A is positive for the stall margin. The specific area A_{sp}, shown in Fig. 6, is slightly influenced by G_C, while it increases greatly if G_A increases too, over its entire variation range.

From what has been said, it can be concluded that the optimum conditions should be defined according to the design requirements. In fact, if $G_A = 0$, η_{TT} could be high with A_{sp} insufficient, and vice versa. The influence of G_C on η_{TT} and A_{sp} seems to be slight but considerable on the stall margin.

Conclusions

The ability to apply optimized design techniques for the development of a compressor stage has been shown.

The choice of the design variables and the constraints, and the calculation of the objective function have been analyzed and described. The possibility of obtaining remarkable results by applying the classic theory of the objective function coincident with the stage efficiency, which is largely employed in turbine studies (Baljè and Binsley, 1968; Macchi and Perdichizzi, 1981; Massardo et al., 1984), has been shown.

Nevertheless, the fact has been pointed out that an increase in efficiency can reduce the values of other significant design variables (weight of the stage, stall margin, etc.). Hence, an optimized design, with a multivariable objective function, has been achieved. The variables selected are the efficiency of the stage, which leads to minimum losses, the stall margin, which allows a wide stable characteristics curve, and finally the inlet specific area, which is related to the weight of the stage.

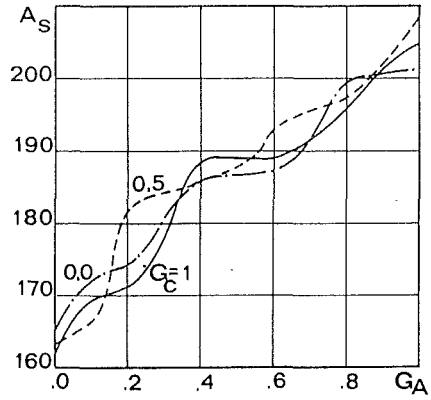

Fig. 6 Influence of G_A and G_C on inlet specific area ($G_\eta = 1.0$)

All variables have been evaluated by a pitchline analysis. The results show the possibility of obtaining optimum design with remarkable increases in all three variables of the objective function or at least in some of them. The process depends strongly on the assumed values of the three coefficients G_A, G_η, and G_C.

Experience shows that the objective function needs G_η to be always equal to 1, while the effect of G_C, which greatly influences the stall margin, is generally less remarkable than G_A. The choice of G_η, G_A, and G_C is made by the designer, based on the particular requirements of the stage design, and by referring to the results shown in Fig. 4 and the subsequent figures.

It should also be pointed out that, while the optimization scheme is extremely rapid, taking about 2 min of CPU on a B-6800 Burroughs Computer, it is limited to the mean diameter geometry.

In Part II of this work (Massardo et al., 1990) an extension of the method to the whole radial geometry distribution, coupled to a throughflow analysis, will be presented.

Acknowledgments

This work was partially financed by the CNR of Italy through grant No. 87.02280.59 PFE2 and by the MPI.

References

Baljè, O., and Binsley, H., 1968, "Axial Turbine Performance Evaluation," ASME *Journal of Engineering for Power*, Vol. 90, pp. 341–360.

Davis, R., and Millar, D., 1976, "Through-flow Calculation Based on Matrix Inversion: Loss Prediction," AGARD CP 195.

Koch, C. C., 1981, "Stalling Pressure Rise Capability of Axial Flow Compressor Stages," ASME *Journal of Engineering for Power*, Vol. 103, pp. 645–656.

Lakshminarayana, B., 1970, "Methods of Predicting the Tip Clearance Effects in Axial Flow Turbomachinery," ASME *Journal of Basic Engineering*, Vol. 92, No. 3, pp. 467–482.

Lieblein, S., et al., 1965, "Aerodynamic Design of Axial Flow Compressor, Revised," NASA SP 36.

Macchi, E., and Perdichizzi, A., 1981, "Efficiency Prediction for Axial Flow Turbines Operating With Nonconventional Fluids," ASME *Journal of Engineering for Power*, Vol. 103, pp. 718–724.

Massardo, A., Pittaluga, F., and Satta, A., 1984, "Design Methods for Optimization of Turbomachine Performances," presented at the International Meeting on Optimization Problems in Engineering, Cassino, Italy.

Massardo, A., Satta, A., and Marini, M., 1990, "Axial Flow Compressor Design Optimization: Part II—Throughflow Analysis," ASME JOURNAL OF TURBOMACHINERY, Vol. 112, this issue.

Miller, G. R., Lewis, G. W., and Hartmann, M. J., 1961, "Shock Losses in Transonic Compressor Blade Rows," ASME *Journal of Engineering for Power*, Vol. 83, No. 3, pp. 235–242.

Rao, S., and Gupta, R., 1980, "Optimum Design of Axial Flow Gas Turbine Stage," ASME *Journal of Engineering for Power*, Vol. 102, pp. 782–797.

Downloaded 01 Jun 2010 to 171.66.16.66. Redistribution subject to ASME license or copyright; see http://www.asme.org/terms/Terms_Use.cfm

A. Massardo

A. Satta

M. Marini

Dipartimento di Ingegneria Energetica,
Universitá di Genova,
Genoa, Italy

Axial Flow Compressor Design Optimization: Part II—Throughflow Analysis

A new technique is presented for the design optimization of an axial-flow compressor stage. The procedure allows for optimization of the complete radial distribution of the geometry, since the variables chosen to represent the three-dimensional geometry of the stage are coefficients of suitable polynomials. Evaluation of the objective function is obtained with a throughflow calculation, which has acceptable speed and stability qualities. Some examples are given of the possibility to use the procedure both for redesign and, together with what was presented in Part I, for the complete design of axial-flow compressor stages.

Introduction

Techniques of design optimization of turbomachines have for the most part been employed in the field of axial-flow turbines (Baljè and Binsley, 1968; Rao and Gupta, 1980; Macchi and Perdichizzi, 1981). In all these cases, as in the procedure on axial-flow compressor stages presented in Part I (Massardo and Satta, 1990), the fluid dynamic analysis, which enables the objective function to be evaluated, referred to the mean diameter of the machine. The simplicity of such a calculation is justified by various considerations, among which are the need for a rapid calculation of the objective function, considering the strong iterative aspect of the optimization research; the need for an immediate definition of the global geometry of the machine; and the possibility to obtain useful general information particularly with regard to preliminary design choices.

Nevertheless, the design result only gives the optimum geometry of the rows at the mean diameter. Instead, the radial distribution of the geometric characteristics between the hub and the shroud remains incompletely defined with respect to the optimum value. In fact, one-dimensional optimization does not provide any information concerning the three-dimensional shape of rotor and stator blade rows. With a view to a complete optimization, it is therefore necessary to optimize the radial distribution of the airfoil geometric characteristics.

To define the radial distribution adequately, substitution of a pitchline analysis with a procedure that provides information concerning the radial distribution of flow within the stage is required. Such analysis contains various aspects that can make the coupling of numerical minimization procedures quite complex. Among these are problems with calculation time, which is undoubtedly larger than the time required for the mean diameter analysis (Massardo and Satta, 1986), and problems of stability (related to the difficult choice of which constraints to apply to design variables). Calculation times are increased since the throughflow analysis requires solutions of an iterative type and this will be used frequently in the optimization calculations. Thus, it is clear that the success of such a coupling resides chiefly in the choice of a rapid throughflow calculation with stability and precision.

Particular attention must be given to the choice of design variables; in previous applications (Massardo and Satta, 1987), the design variables were the geometric characteristics of the blade on three sections along the span. The calculation time was controlled, but the optimum results were not completely sufficient for the correct design of the stage. If more than three sections were analyzed, the optimization provided unacceptable geometric results. This was due to the difficulty in choosing adequate constraints to the numerous design variables. The present work has allowed all of these problems to be eliminated, and also contains interesting results for transonic compressors.

Formulation of Optimum Design Problem

The organization of a design problem using optimization techniques requires the definition of three fundamental parameters: design variables, objective function, and constraints. It is also necessary to predispose a scheme to which the optimization must refer.

Design Variables. While evaluating the objective function with a pitchline analysis, the choice of design variables, although not a simple operation, is a process that is easy to verify. In the case of optimization with a throughflow analysis, the selection becomes much more difficult. In fact, to change from the first to the second case, the first thing to do is to place beside the mean diameter section other sections along the entire blade span from which geometric optimization proceeds. In a previous work (Massardo and Satta, 1987), we chose to work with three radial sections — root, mean, and tip — for a total of ten design variables for each single row,

Contributed by the International Gas Turbine Institute and presented at the 34th International Gas Turbine and Aeroengine Congress and Exhibition, Toronto, Ontario, Canada, June 4–8, 1989. Manuscript received at ASME Headquarters February 1, 1989. Paper No. 89-GT-202.

Copyright © 1990 by ASME
Downloaded 01 Jun 2010 to 171.66.16.66. Redistribution subject to ASME license or copyright; see http://www.asme.org/terms/Terms_Use.cfm

considering the fixed geometry of the meridional section (shroud and hub profiles). The results obtained demonstrated the need for a better definition of the design variables and, therefore, of the row geometry. The number of radial sections was then increased to five. However, the results obtained were unacceptable due to the difficulty of choosing congruent values for the design variable constraints. The solution to the problem lay in choosing as design variables the coefficients of suitable polynominal that represent, in a continuous constructive and mathematical sense, the representative functions of the geometry to be optimized. Therefore, the geometric function can be expressed as

$$f = a_1 + a_2R + a_3R^2 + a_4R^3 + \ldots + a_nR^{n-1} \quad (1)$$

where R is the nondimensional radius.

In turbomachinery problems it was held sufficient to consider only the first three polynomial terms. The design variables that result are defined as follows:

$$\beta_{1b} = a_1 + a_2R + a_3R^2 \quad (2)$$

$$\beta_{2b} = a_4 + a_5R + a_6R^2 \quad (3)$$

$$\sigma = a_7 + a_8R + a_9R^2 \quad (4)$$

$$t_m/C = a_{10} + a_{11}R + a_{12}R^2 \quad (5)$$

$$C = a_{13} \quad (6)$$

The chord is fixed in only one radial position, at the root for instance, and its radial values result from the solidity distribution. The choice of such variables, which result in 13 for each single machine row, moreover permits the throughflow calculation with the desired number of calculation lines along the blade span without encountering problems for the correct recognition of the geometry (in fact, no interpolations are necessary). Furthermore, the choice of constraints for the a_i variables turns out to be extremely simple and effective as the following applications will demonstrate.

The 13 design variables for each single row entail, in the case of one stage, the need to work with 26 variables, and thus, as shown by Massardo and Satta (1987), the need to apply the technique to one stage at a time. This is for two reasons: the calculation times that increase rapidly with the number of variables and the difficulty in searching for the minimum of one function at an elevated number of variables (>40).

Finally, it is possible to observe that in this case, as opposed to the procedure presented in the preliminary design characteristics of Part I (Massardo and Satta, 1990), the design variables are all geometric. This is due to the supposition that the optimization criteria will be applied to a machine of which the design is known, albeit only a preliminary one.

Objective Function

Although the necessity of operating with an objective function with many variables was shown in the first part, here we preferred to conduct the optimization on only one objective function coincident with the stage efficiency (η_{TT}). It turns out, in fact, to be easy to evaluate the function with the throughflow calculation along the entire blade span. On the other hand, the calculation of the stall margin presents difficulties since the correlation used in Part I is typical of preliminary design computations (pitchline analysis) and more complex techniques could excessively burden the design procedure. Finally, as far as the specific inlet section ($A_{sp} = \dot{m}/A_1$) is concerned, it would require the alteration of those variables that, as will be further described, it is preferable to keep constant during optimization (H_1, D_t, D_h, n).

Design Constraints

What was stated in Part I (Massardo and Satta, 1990) concerning optimization constraints holds true in this case also. It must, however, be observed that due also to the fact that some quantities are already fixed (blade span, rpm, shroud and hub radial distributions, tip clearances), the choice of nonrectangular limits turns out to be greatly simplified with respect to the pitchline calculation.

The limits are chosen on the basis of experience since beyond certain values, a realistic blade shape will not result. In addition, certain extreme combinations of variables may cause convergence problems and are therefore best avoided. The constraint functions specified are:

- relative inlet tip rotor Mach number (<1.8)
- maximum stress at rotor root ($<\sigma_{am}$)
- maximum and minimum blade number for rotor and stator rows
- maximum and minimum aspect ratio for rotor and stator rows
- stator and rotor stall margins (calculated at the mean diameter) greater than a specified value.

Throughflow Program

The flow that develops in the axial compressor is evaluated with a throughflow matrix method, which solves the main equation of the stream function. This solution is obtained using a matrix technique; the choice of the above rather than others is due to the fact that with it the control of computational times is possible without a reduction in calculation precision (at least in this application). The matrix technique solves the stream function equation of a fixed network placed in the meridional plane of the machine. This does not change during the repetitive solution of the equation unless the longitudinal

Nomenclature

A = area
A_{sp} = specific area = $\dot{m}/A$
a = polynomial coefficient
$\bar{a}$, $\bar{x}$ = design vectors
b = penalty function constant
C = chord
D = diameter
D_f = diffusion factor
F = objective function
g = constraint
G_η, G_C, G_A = objective function coefficients
H = blade height
i, δ = incidence and deviation angle
$\dot{m}$ = mass flow rate
n = rotational speed
p_o = total pressure
R = nondimensional radius
S_i = current search direction
t_m = maximum blade thickness
T_o = total temperature
α, β = absolute and relative flow angles
β_{TT} = total-to-total pressure ratio
η_{TT} = total-to-total stage efficiency
σ = solidity
ω = total pressure loss coefficient

Subscripts

1, 2 = inlet, outlet
ax = axial
b = blade
h, t = hub, tip

Downloaded 01 Jun 2010 to 171.66.16.66. Redistribution subject to ASME license or copyright; see http://www.asme.org/terms/Terms_Use.cfm

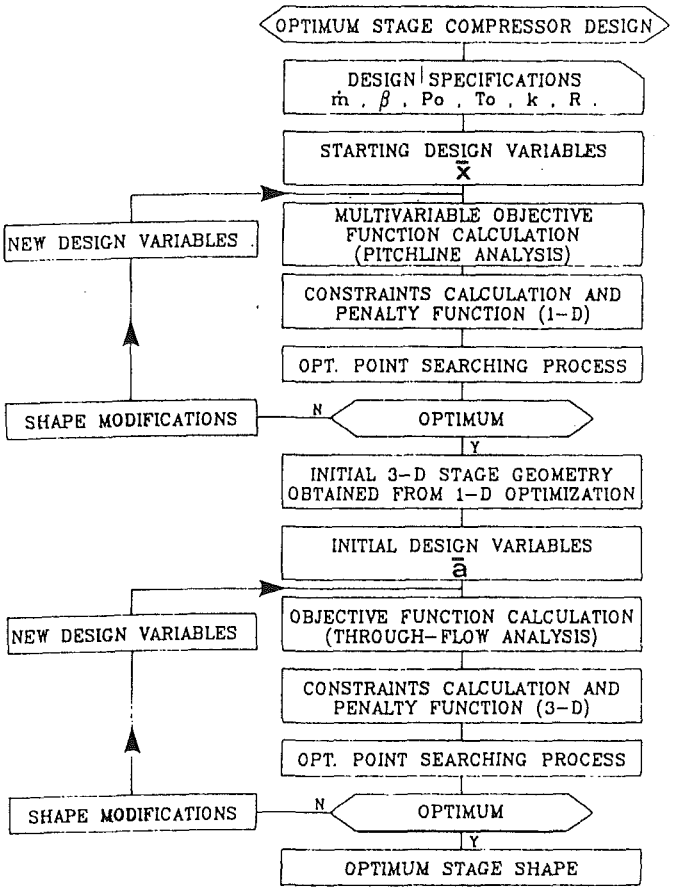

Fig. 1 Optimum complete stage design (pitchline and throughflow analysis)

geometry is altered. Therefore, the calculation of the coefficient matrix and its factorization, whose calculation time is about one half of the entire program time, is performed only once even though the fluid dynamic analysis is developed during the iterative procedure of the minimum research. A description of the matrix method is available from Breschi and Massardo (1982).

Correlations available in the open literature (Davis and Millar, 1976), which have shown reliable results at compressor design conditions, have been used to evaluate the compressor efficiency. For the analysis of the transonic flow, the code was modified and coupled to a solution of the gradient velocity equation, described by Massardo and Praticò (1984); the code furthermore permits, in an automatic way, the calculation of the annulus wall boundary layer with an integral type solution (Perkins and Horlock, 1971) and the calculation of the secondary deviation angle (Massardo and Satta, 1985).

The reasonable reliability of the throughflow code results was evident in many previous applications, in particular with regard to the efficiency prediction at design condition. The latter is chosen as the objective function.

Optimization Scheme

The general scheme illustrated in Fig. 1 of Part I (Massardo and Satta, 1990) is sound, except for the necessary modifications in the throughflow calculation, and for the optimization of the radial distribution of the blade geometry.

If it is thought desirable to couple the two procedures presented here, this is made possible by using the technique illustrated in Fig. 1, where the throughflow procedure presented is made to follow that of preliminary optimum design.

Starting from initial data (p_o, T_o, β_{TT}, $\dot{m}$) and from the mean diameter design variables (X_i), and working with a multivariable objective function, the mean diameter optimum geometry is obtained.

Beginning here, by hypothesizing a law of radial geometry distribution (for example the free vortex), the values of the initial data of the throughflow calculation (D_h, D_t, n) and the new design variables (a_i) are obtained. Using the same algorithm of constrained minimization as in the first part, the procedure continues to complete optimization until the prefixed objective is reached. The throughflow procedure can, of course, be applied to the initial geometry obtained by means of traditional techniques.

Statement of Optimization Problem

The optimization problem can now be stated in the format of a nonlinear programming problem as follows: Find the a that minimizes

$$f(\bar{a}) = G_\eta (1 - \eta_{TT}) \qquad j = 1, n \tag{7}$$

subject to the constraints

$$g_j (\bar{a}) \tag{8}$$

Solution of Optimization Problem

The problem of the optimum design of an axial compressor stage has been formulated and a method of computing the objective function and constraints has been developed. The problem formulated is in the form of a nonlinear mathematical programming problem and can be stated in the standard form:

$$\text{Find the } \bar{a} = \begin{Bmatrix} a_1 \\ a_m \end{Bmatrix} \text{ that minimizes } F(\bar{a}) \tag{9}$$

and satisfies the constraints $g_j(\bar{a}) \leq 0$; $j = 1, n$.

The function $F(\bar{a})$ need not be known analytically, but it is specified by giving its value at any point a in the space of parameters. The space may be limited by physical restrictions on the permitted values of the parameters.

When the problem involves "nonrectangular" constraints (i.e., constraints that cannot be expressed by imposing simple independent limits of the form $A < a < B$), the penalty function method is utilized as follows: Suppose we wish to minimize the function $F(\bar{a})$ subject to the condition $g(\bar{a}) < 0$; then define the objective function value F to be

$$F = F(\bar{a}) \text{ if } g(\bar{a}) < 0 \tag{10}$$

$$F = F(\bar{a}) + b\,[g^2(\bar{a})] \text{ if } g(\bar{a}) > 0 \tag{11}$$

where b is a constant, large compared with F.

Note that this method requires $F(\bar{a})$ to be defined everywhere, and to be continuous at $g(\bar{a}) = 0$, which may sometimes be difficult to arrange. However, the method is usually found to work well and is perfectly general (i.e., independent of the method used for minimization). The penalty function methods are quite reliable and their sequential nature allows a gradual approach to the criticality of constraints.

The previous equations require a feasible starting point. Since each of the designs generated during the optimization process lies inside the acceptable design space, the method is classified as an interior penalty function formulation.

The sequence of minimization of $F(\bar{a})$ is done according to the iteration

$$\bar{a}_{i+1} = \bar{a}_i + \lambda^* S_i \tag{12}$$

where $\bar{a}_{i+1}$ is the design vector corresponding to the minimum value of F along the current search direction S_i, $\bar{a}_i$ is the starting design vector, and λ^* is the minimizing step length in the direction S_i. From the several methods available for finding the search direction S_i, the selected Davidon–Fletcher–Powell variable metric method is a powerful general method for find-

Downloaded 01 Jun 2010 to 171.66.16.66. Redistribution subject to ASME license or copyright; see http://www.asme.org/terms/Terms_Use.cfm

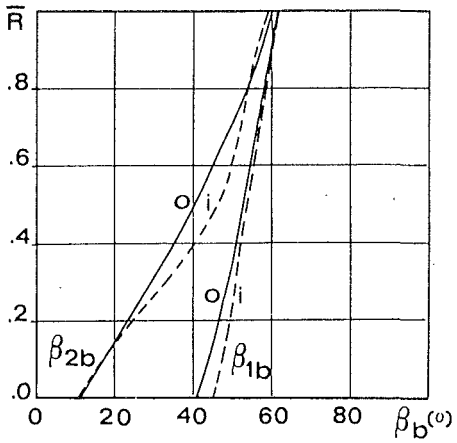

Fig. 2 Starting and optimum radial distributions of the blade angles (*i* = initial; *o* = optimum)

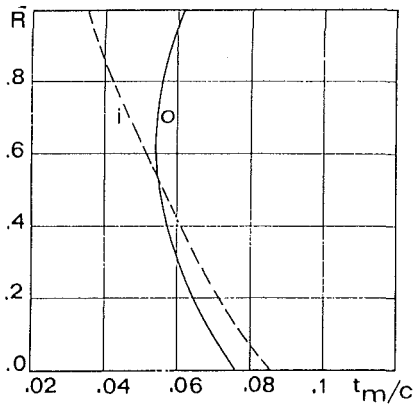

Fig. 3 Starting and optimum radial distributions of the maximum blade thickness (*i* = initial; *o* = optimum)

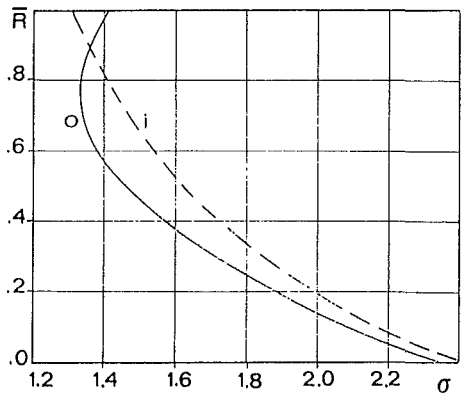

Fig. 4 Starting and optimum radial distributions of the blade row solidity (*i* = initial; *o* = optimum)

ing a local unconstrained minimum of a function of many variables (Fletcher and Powell, 1963).

Applications

The applications of the developed procedure fall into two categories. The first utilizes the process for the redesign of an existing isolated transonic rotor. The second applies the complete procedure shown in Fig. 1. The single transonic rotor described by Seyler and Gostelow (1967) is selected for the verification of the described optimization process. The principle geometric data of the rotor, which coincide with the polynomial functions to be optimized, are shown in Figs. 2, 3, and 4, respectively. The root chord is equal to 0.0838 m

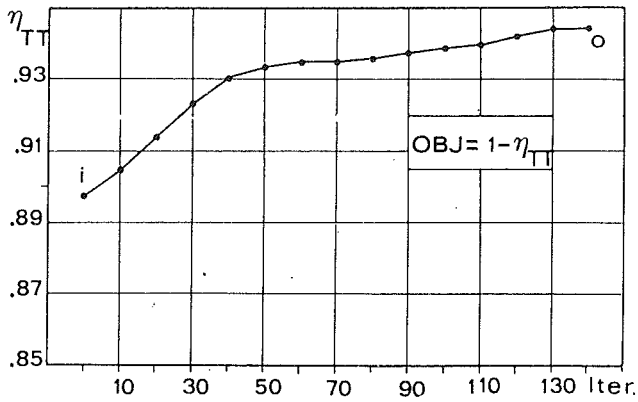

Fig. 5 Optimization history of the rotor total-to-total efficiency

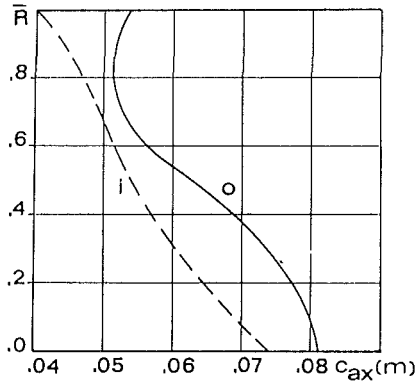

Fig. 6 Initial and optimum radial distributions of the axial blade chord (*i* = initial; *o* = optimum)

and is constant along the entire blade span. The calculation is carried out for the design conditions: $\dot{m} = 96.18$ kg/s and $n = 8870$ rpm. The initial efficiency (original geometry) is equal to 0.897, while the value obtained at the end of the optimization process is 0.943, greater than a 4 percent increase. Figure 5 illustrates the objective function history during optimization.

In Figs. 2, 3, and 4, quoted above, in addition to the initial radial distribution values, optimized values are also given; it is possible to note how the angle β_{1b} has undergone slight variations, particularly in the zone above the blades, while the maximum variation is present at the root, where the change takes the value of approximately 4 deg.

The angle β_{2b} shows shift with respect to the initial value, particularly in the central zone along the span, where the maximum variation is approximately 6 deg. This involves an increase in blade curvature in the central zone with a slight reduction in the extreme zones of the root and the tip. The solidity is reduced along nearly the entire span with the only exception being the tip zone (it passes from 1.30 to 1.41). The maximum thickness/chord has, at the end of optimization, a more uniform radial distribution. Particularly noteworthy is the increase in the upper zone (from 0.035 to 0.051) and the reduction at the root (from 0.085 to 0.075). Such a reduction does not represent a problem from a mechanical resistance point of view since the root chord also increased, passing from 0.0838 m to 0.0910 m. The fact that all of the design variables present continuous and smooth radial distributions is particularly noteworthy.

In addition to the quantities discussed above, it is interesting to study the distributions of other geometric quantities (axial chord) and fluid dynamics (losses, diffusion factor, incidence, and deviation angles).

The axial chord (Fig. 6) indicates higher values in the optimum case with respect to the initial values. The analysis of

Downloaded 01 Jun 2010 to 171.66.16.66. Redistribution subject to ASME license or copyright; see http://www.asme.org/terms/Terms_Use.cfm

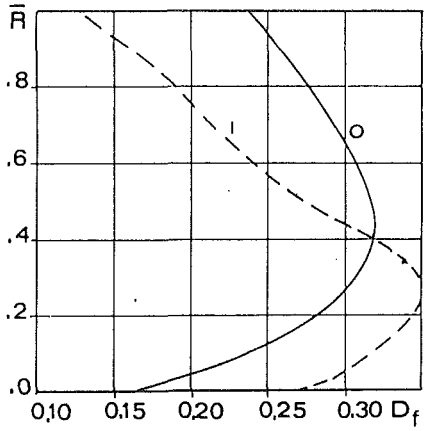

Fig. 7 Initial and optimum radial distributions of diffusion factor (i = initial; o = optimum)

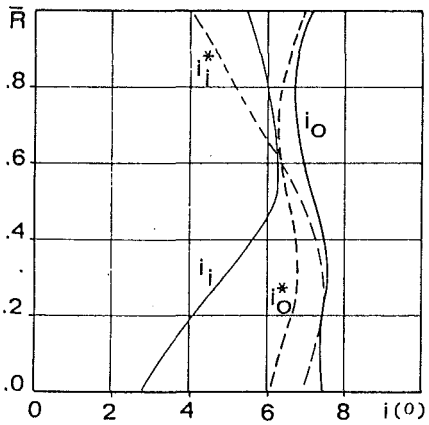

Fig. 9 Initial and optimum radial distributions of incidence angle

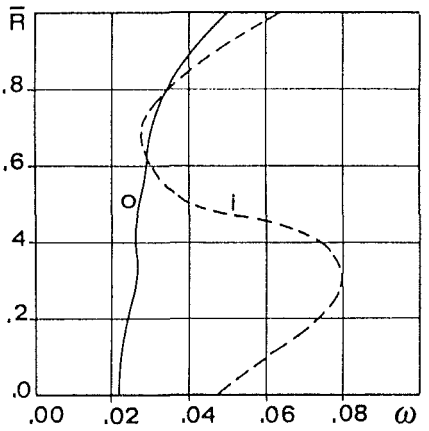

Fig. 8 Initial and optimum radial distributions of total pressure loss coefficient (i = initial; o = optimum)

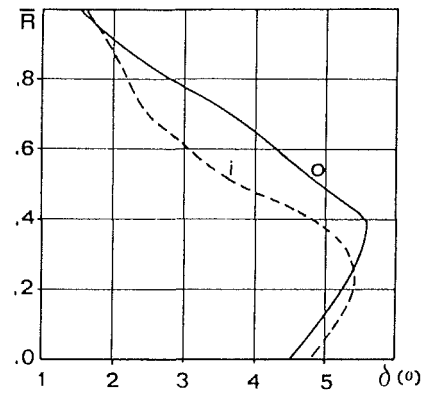

Fig. 10 Initial and optimum radial distributions of deviation angle (i = initial; o = optimum)

the diffusion factor (D_f) is of particular interest (Fig. 7). The optimization operates in the sense of a reduction of D_f in the $R<0.4$ zone, while in the upper area, D_f increases in a significant manner, above all at the tip. Following the D_f distribution directly, except for shock losses, is the radial distribution of the losses (Fig. 8).

For $\bar{R}<0.6$, the loss reduction is significant; for instance at $\bar{R}=0.30$ it passes from $\omega=0.080$ to $\omega=0.027$; in the tip zone, where a great deal of the loss is due to shock, although a reduction occurs (from 0.062 to 0.049), it appears to be more contained. The reduction of ω obviously justifies the noteworthy increase in efficiency.

Finally, Figs. 9 and 10 show the initial and optimum distributions of the incidence and deviation angles. The variation in the radial distribution of the incidence angle is notable, particularly in the region for $\bar{R}<0.5$. The dotted line indicates for the initial and optimum configurations the value of the "star" incidence, obtained with the NASA-SP 36 correlation. As is evident, the difference between i and i^* is reduced significantly with optimization. As far as the deviation is concerned, there is a slight increase where $\bar{R}>0.30$ (resulting from the increase in the profile curvature) and a slight reduction is seen at the root.

The second application envisages the employment of both procedures (pitchline and throughflow). In fact, it is intended to design a stage working from the following information: mass flow rate $\dot{m}=4$ kg/s; pressure ratio $\beta_{TT}=1.60$, $P_{01}=101.3$ kPa, $T_{01}=300$ K. The initial optimization procedure is carried out with an objective function having the following weights: $G_\eta=1.0$; $G_C=0.0$; $G_A=0.0$, and with a higher constraint for α_3 of 10 deg.

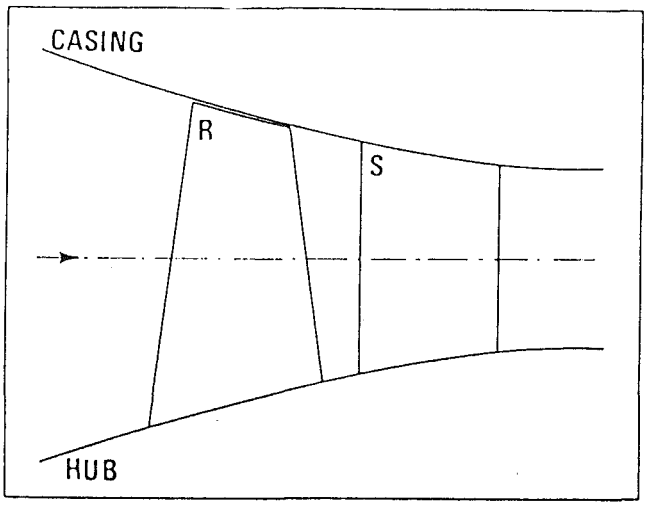

Fig. 11 Meridional section of the axial flow compressor stage optimized with pitchline analysis (Part I)

The meridional section optimized with such a procedure is illustrated in Fig. 11; where the rotational speed is 39,500 rpm. Optimized efficiency is equal to 0.91, the stall margin coefficient is $C_h=0.50$, and the specific inlet area is $A_{sp}=170$. The radial distribution of the blade geometric characteristics, from which the new design variables $\bar{a}$ are obtained, was acquired by hypothesizing the free vortex law for the rotor and inlet section of the stator. For the stator outlet section, the angle α_{3b} was chosen in a different way (see Fig. 12). Optimization

Downloaded 01 Jun 2010 to 171.66.16.66. Redistribution subject to ASME license or copyright; see http://www.asme.org/terms/Terms_Use.cfm

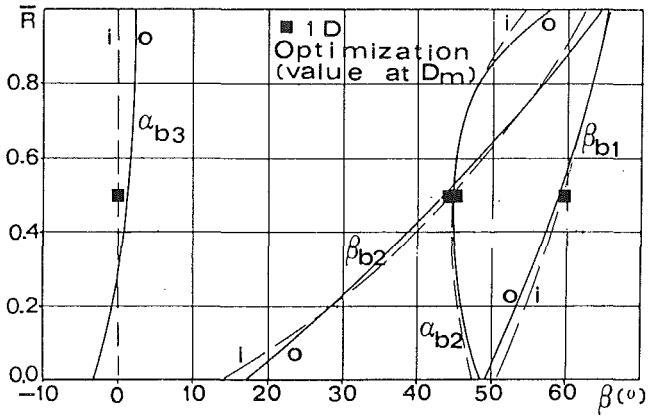

Fig. 12 Initial (*i*) and optimum (*o*) stator and rotor blade angles (throughflow optimization)

results are shown and compared to starting values in the above-mentioned figures.

As far as efficiency is concerned, it must be pointed out that the value calculated with pitchline analysis differs from the initial finding obtained with the throughflow calculation. This latter, however, changes with the second optimization process from 0.844 to 0.905, showing at the same time a sufficiently rapid increase.

The entire calculation process requires approximately 2 min of CPU with one-dimensional analysis and approximately 34 min for the subsequent throughflow optimization. All computations were performed with a Burroughs B-6800 computer at the University of Genoa.

Conclusions

The possibility of coupling techniques of simple fluid dynamic analysis (pitchline analysis) with procedures of numerical optimization has been known for years, particularly in the design of turbines. Moreover, the authors of this paper have also shown the possibility of employing the process in the field of axial flow compressors (Part I, Massardo and Satta, 1990), where the need to operate with a multivariable objective function (efficiency, stall margin, stage weight) was found.

The obvious extension of the above optimization technique to more sophisticated methods of fluid dynamic analysis, the throughflow type for instance, has been presented in this paper. The success of the new optimized design procedure is essentially due to its swiftness — particularly in present applications — and to the stability of the matrix technique chosen (suitably modified so as to allow the evaluation of the zones of transonic flow). Furthermore, it should be noted that the choice of design variables used in previous works has been improved. The new variables are coefficients of suitable polynomials that are employed to represent the three-dimensional geometry of the rows.

It is also clear that this last choice has permitted the simplification of those values to be applied to design constraints, and resulted in continuous results, both in a mathematical and in a constructive sense (radial distributions of the blade angles, the solidity, etc.).

The applications of the proposed procedure for redesign of an existing transonic isolated rotor and for the complete optimum design of a transonic stage have been demonstrated. The technique has shown remarkable swiftness in calculation, ability to forecast accurately the initial characteristics, and a rapid improvement of those data. The same holds true, as is clear, particularly for the objective function (coinciding with machine efficiency).

It must be observed that the findings obtained are obviously correlated to the ability to forecast local phenomena (three-dimensional flow aspects) on the part of the fluid dynamic analysis calculation. Throughflow methods, which have attained widespread use, do not always represent the above phenomena perfectly; however, they can be improved so as to evaluate, for example, the annulus wall boundary layer flow, secondary flow, etc. Moreover, computation times, stemming from throughflow methods, remain quite contained.

The necessity, however, of the throughflow calculation for the evaluation of losses and of the flow angle with semi-empirical correlations, limits in a certain sense its general use. To eliminate this point, a feasible solution might be the coupling of the minimization with an automatic iterative meridional and blade-to-blade code, for instance, the example developed with the aid of the CAD technique (Massardo et al., 1987). The implementation of a similar method for the evaluation of the objective function does in fact allow the recognition of the downstream flow angle and, with suitable calculations of the profile boundary layer, the losses, without resorting to the correlations.

It is further possible that the optimization of the blade profile shapes, beginning from the optimum radial distributions, can be accomplished in a manner analogous to that used by Sanger (1984).

All of the above offers a generalized design procedure with which the blade row shapes can be attained. This fact, however, renders the calculation extremely time consuming, complex, and burdensome, at least at present. It is possible, on the other hand, that with more rapid computers and numerical techniques, the procedure may become feasible.

Acknowledgments

This work was partially financed by the CNR of Italy through grant No. 87.02280.59 PFE2 and by the MPI.

References

Baljè, O., and Binsley, H., 1968, "Axial Turbine Performance Evaluation," ASME *Journal of Engineering for Power*, Vol. 90, pp. 341-360.

Breschi, D., and Massardo, A., 1982, "Metodo matriciale per il calcolo meridiano di un compressore assiale pluristadio," presented at the 37th ATI Conference, Padova, Italy.

Davis, W., and Millar, D., 1976, "Throughflow Calculation Based on Matrix Inversion: Loss Prediction," AGARD CP-195.

Fletcher, R., and Powell, M., 1963, "A Rapidly Converging Descent Method for Minimization," *Computation Journal*, Vol. 6, p. 163.

Macchi, E., and Perdichizzi, A., 1981, "Efficiency Prediction for Axial Flow Turbines Operating With Nonconventional Fluids," ASME *Journal of Engineering for Power*, Vol. 103, pp. 718–724.

Massardo, A., and Praticó, F., 1984, "Un metodo di calcolo della zona viscosa e non viscosa nei compressori assiali transonici," presented at the 39th ATI Conference, L'Aquila, Italy.

Massardo, A., and Satta, A., 1985, "A Correlation for the Secondary Deviation Angle," ASME Paper No. 85-GT-36.

Massardo, A., and Satta, A., 1986, "Procedura di ottimizzazione per il progetto dei compressori assiali," presented at the VIII AIMETA Conference, Torino, Italy.

Massardo, A., and Satta, A., 1987, "The Use of Optimization Technique and Through-Flow Analysis for the Design of Axial Flow Compressor Stages," *Proceedings 8th Turbomachinery Conference*, Budapest, Hungary.

Massardo, A., Novelli, A., Pasini, M., and Satta, A., 1987, "CAD Procedure for a Fully Automatic Meridional and Blade-to-Blade Flow Calculation," presented at the 42 ATI Conference, Genova, Italy.

Massardo, A., and Satta, A., 1990, "Axial Flow Compressor Design Optimization: Part I—Pitchline Analysis and Multivariable Objective Function Influence," ASME JOURNAL OF TURBOMACHINERY, Vol. 112, this issue.

Perkins, H., and Horlock, J., 1976, "Annulus Wall Boundary Layer in Turbomachines," AGARDOGRAPH.

Rao, S., and Gupta, R., 1980, "Optimum Design of Axial Flow Gas Turbine Stage," ASME *Journal of Engineering for Power*, Vol. 102, pp. 782–797.

Sanger, N. L., 1983, "The Use of Optimization Technique to Design Controlled Diffusion Compressor Blading," ASME *Journal of Engineering for Power*, Vol. 105, pp. 256–264.

Seyler, D. R., and Gostelow, J. P., 1967, "Single Stage Experimental Evaluation of High Mach Number Compressor Rotor Blading, Part 2. Performance of Rotor 1-B," NASA CR 582.

Downloaded 01 Jun 2010 to 171.66.16.66. Redistribution subject to ASME license or copyright; see http://www.asme.org/terms/Terms_Use.cfm

Unsteady Lifting Surface Theory for a Rotating Cascade of Swept Blades

H. Kodama
Research and Development Department,
Aero-Engine and Space Operations,
Ishikawajima-Harima Heavy Industries,
Tokyo, Japan

M. Namba
Department of Aeronautical Engineering,
Kyushu University,
Fukuoka, Japan

A lifting surface theory is developed to predict the unsteady three-dimensional aerodynamic characteristics for a rotating subsonic annular cascade of swept blades. A discrete element method is used to solve the integral equation for the unsteady blade loading. Numerical examples are presented to demonstrate effects of the sweep on the blade flutter and on the acoustic field generated by interaction of rotating blades with a convected sinusoidal gust. It is found that increasing the sweep results in decrease of the aerodynamic work on vibrating blades and also remarkable reduction of the modal acoustic power of lower radial orders for both forward and backward sweeps.

Introduction

Recently ducted ultrahigh-bypass engines have been considered as an advanced propulsion system with attractive fuel efficiency. In contrast to unducted propfan engines, the ducted ultrahigh-bypass engines can be mounted under the wings of large transport aircraft. The contrarotating propfan engine with swept blades is one proposal for the ducted ultrahigh-bypass propulsion system, and is considered to combine the positive properties of a conventional turbofan with the advantages of an unducted propfan (Grieb and Eckardt, 1986).

It is expected that incorporation of blade sweep in the ducted fan would result in an improvement in noise reduction similar to the unducted propfan. However, achieving the benefit should require careful design on blade sweep, taking into account the influence of a duct wall. The effect of the sweep on the blade flutter is also one of the important aspects that should be considered in the blade design. Hence an analysis method to predict the unsteady aerodynamic characteristics for swept blades in the duct is required.

At present the computational fluid dynamics for the unsteady aerodynamic problems of high-speed ducted and unducted propfans are still under development. In view of the fact that high-speed propfans are composed of very thin blades, the analytical approach based on the linearized lifting surface theory will be justified as an efficient method to predict the essential features of the three-dimensional unsteady effects for propfans.

However, mathematical formulations, even if linearized, become highly complicated due to the three-dimensional geometry and the time-dependent flow field. Therefore only a limited number of papers have treated the unsteady lifting surface method for rotating blades. Hanson derived the lifting surface integral equations for the unducted propfan (1983) and showed some numerical results for the steady problem (1985).

As for the unsteady problems related to the ducted propfan, there are some available papers dealing with the unsteady lifting surface theory for a rotating annular cascade of unswept blades. Namba and Ishikawa (1983) showed the three-dimensional effects on aerodynamic characteristics for oscillating supersonic and transonic annular cascades, and Namba and Abe (1984) dealt with the problem of interaction with distorted inlet flow for supersonic and transonic annular cascades. However, their analyses were restricted to unswept blades with constant axial chord along the span mainly in order to avoid difficulty in dealing with the integral equation for the unsteady blade loading functions.

This paper gives an analytical method to predict the unsteady aerodynamic characteristics for a rotating annular cascade of swept blades using the unsteady lifting surface theory developed by Namba et al. (1983, 1984). A discrete element method is adopted to solve the integral equation for the unsteady blade loading. Calculations have been carried out on simple blade models to demonstrate effects of the blade sweep on the unsteady lifting pressure of vibrating blades and on the acoustic field generated by interaction of rotating blades with inlet flow distortions. In the present analysis, only the case of entirely subsonic flow is dealt with. The analysis for transonic or supersonic cascades will be reported in future publications.

Theoretical Model

Consider a uniform axial subsonic flow in a cylindrical rigid walled duct of infinite axial extent disturbed by a single annular blade row with N blades rotating at a constant angular velocity ω^* (Fig. 1). The fluid is assumed to be an inviscid and non-heat-conducting perfect gas. The disturbances caused by the blades are assumed to be small. Each blade has no steady loading and no thickness.

Contributed by the International Gas Turbine Institute and presented at the 34th International Gas Turbine and Aeroengine Congress and Exhibition, Toronto, Ontario, Canada, June 4–8, 1989. Manuscript received at ASME Headquarters February 21, 1989. Paper No. 89-GT-306.

Copyright © 1990 by ASME
Downloaded 01 Jun 2010 to 171.66.16.66. Redistribution subject to ASME license or copyright; see http://www.asme.org/terms/Terms_Use.cfm

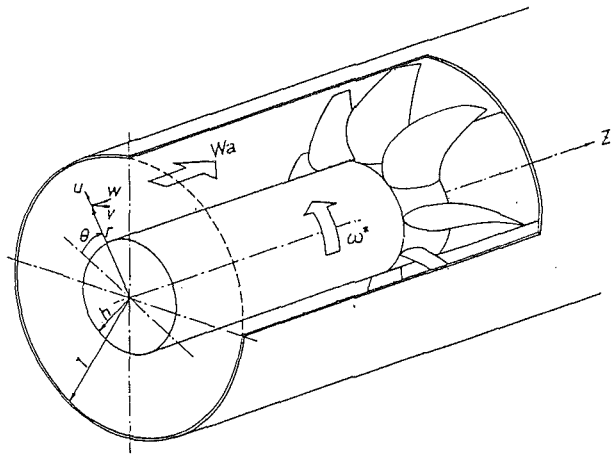

Fig. 1 A rotating annular cascade

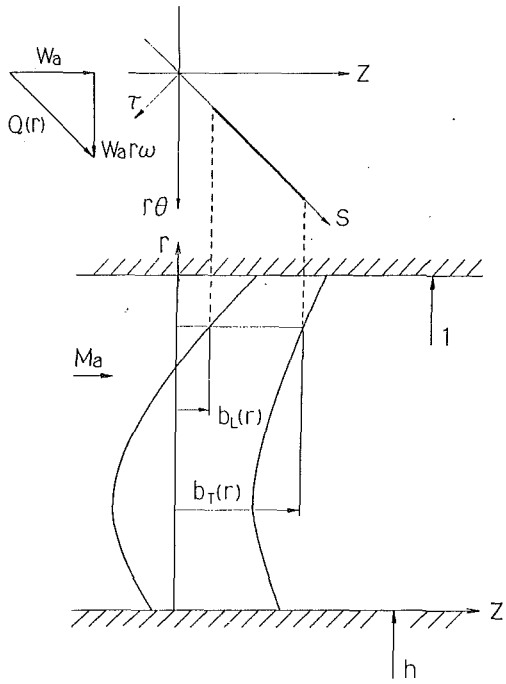

Fig. 2 Coordinate system

A rotor-fixed cylindrical coordinate system (r, θ, z) and a time coordinate t are used. Lengths are normalized by the duct radius r_T^*, and times are normalized by r_T^*/W_a, where W_a is axial velocity of the undisturbed flow. Hence the dimensionless rotor speed ω is defined by $\omega = \omega^* r_T^*/W_a$.

This paper deals with a blade flutter problem, where the blades vibrate at a reduced frequency $\lambda (= \lambda^* r_T^*/W_a)$ with an interblade phase angle $\hat{\sigma}$ $(= 2\pi\sigma/N)$, and also deals with a problem of interaction with a convected sinusoidal gust, where the blades sense the incident gust with a reduced frequency $\lambda (= N_w \omega)$ and an interblade phase angle $\hat{\sigma}$ $(= 2\pi(1 - N_w/N))$. Here N_w denotes the circumferential wave number of the gust. In both cases, the unsteady blade loading is expressed as $\Delta p_B(r, z) e^{i\lambda t + ik\hat{\sigma}}$ $(k = 0, 1, \ldots, N-1)$. Then the rotor-induced pressure field $p(r, \theta', z)e^{i\lambda t}$ can be expressed in the form

$$p(r, \theta', z) = \int_h^1 d\rho \int_{b_L(\rho)}^{b_T(\rho)} \Delta p_B(\rho, \zeta) \times K_p(r, \theta', z - \zeta \,|\rho) d\zeta \quad (1)$$

Here ρ and ζ denote radial and chordwise coordinates, respectively, at a point on the blade surface, and θ' $(= \theta - \omega z)$ denotes a helical coordinate. Further $b_L(\rho)$ and $b_T(\rho)$ denote the axial positions of leading and trailing edges of the blade, respectively, and $K_p(r, \theta', z - \zeta \,|\rho)$ is the pressure kernel function defined in equation (2) of Namba and Ishikawa (1983).

A finite radial eigenfunction series approximation is applied to the expression of pressure field given by equation (1), as has been shown by Namba et al. (1983, 1984). In the present paper the radial eigenfunction specified by the circumferential wave number n is expressed in terms of $R_l^{(\infty)}(r)$ rather than $R_l^{(0)}(r)$ (see Namba and Abe, 1984, and Namba, 1987)

$$R_l^{(n)}(r) = \sum_{k=0}^{L-1} BB_{lk}^{(n)} R_k^{(\infty)}(r) \quad (2)$$

Nomenclature

$a_j^{(b)}(r)$, $a_k^{(t)}(r)$ = spanwise mode shapes of the jth order bending and kth order torsional vibrations
$BB_{lk}^{(n)}$ = coefficients of the finite series expansion of $R_l^{(n)}(r)$ in terms of $R_l^{(\infty)}(r)$, equation (2)
$b^*(r, \tilde{z})$ = defined by equation (21) or (22)
$b_L(r)$ = z coordinate of the leading edge
$b_T(r)$ = z coordinate of the trailing edge
$CB_{lk}^{(n)}$ = coefficients of the series for $R_l^{(n)}(r)/r^2$ expanded in terms of $R_k^{(\infty)}(r)$
$C_a(r)$ = axial length of the blade chord, equation (13)
$C_M(r)$ = z coordinate of the midchord, equation (14)
$DB_{lk}^{(n)}$ = defined by equation (4)
E_-, E_+ = dimensionless total acoustic power in upstream and downstream propagation, respectively
g = $(z - \zeta)\lambda \mathrm{M}^2/\beta_a^2$
h = hub-to-tip ratio
i = $\sqrt{-1}$
K_p = pressure kernel function defined by equation (3)
K_τ = upwash kernel function defined by equation (7)
K_τ^* = K_τ expressed by the locally normalized axial coordinate
$k_l^{(n)}$ = radial eigenvalues
L = number of retained terms in the finite radial eigenfunction series
l = radial order of an acoustic mode
M = axial Mach number
N = number of blades
N_w = circumferential wave number of a convected sinusoidal gust
n = $\nu N + \sigma$ = circumferential wave number of an acoustic mode
$p(r, \theta', z)e^{i\lambda t}$ = disturbance pressure
Q = $W_a\sqrt{1 + \omega^2 r^2}$ = undisturbed fluid velocity relative to rotating blades
$q_\tau(r, \theta', z)e^{i\lambda t}$ = disturbance velocity component normal to blade surfaces
$\tilde{q}_\tau^{(b)}$ = upwash component of the disturbance velocity due to the bending vibration

Downloaded 01 Jun 2010 to 171.66.16.66. Redistribution subject to ASME license or copyright; see http://www.asme.org/terms/Terms_Use.cfm

As shown in Figs. 3 and 4 of Namba and Abe (1984), $R_l^{(\infty)}(r)$ is dominant at $r=1/\kappa_l^{(\infty)}$, and a finite sequence of $1/\kappa_0^{(\infty)}$, $1/\kappa_1^{(\infty)}$, . . . , $1/\kappa_{L-1}^{(\infty)}$ is equally spaced between 1 (tip radius and h (hub radius). Here $\kappa_l^{(\infty)}$ are limit eigenvalues determined from equation (9) of Namba and Abe (1984) by applying $|n|\to\infty$. Because of these properties, a finite radial eigenfunction series approximation by $R_k^{(\infty)}(r)$ gives a clearer view of the structure of the pressure disturbance, and also enables one to give reasonable control points in the numerical integration described later.

Consequently, the pressure kernel function $K_p(r, \theta', z-\zeta|\rho)$ is rewritten as

$$K_p(r,\theta',z-\zeta|\rho)= -\frac{N}{4\pi\beta_a^2}e^{ig\rho}\sum_{j=0}^{L-1}R_j^{(\infty)}(r)\sum_{k=0}^{L-1}R_k^{(\infty)}(\rho) \times\sum_{\nu=-\infty}^{\infty}e^{in\phi}\sum_{l=0}^{L-1}e^{-\Omega_l^{(n)}|z-\zeta|}BB_{lj}^{(n)}DB_{lk}^{(n)} \quad (3)$$

where

$$DB_{lk}^{(n)}=\frac{i}{\Omega_l^{(n)}}\left\{BB_{lk}^{(n)}\frac{M^2}{\beta_a^2}\omega(n\omega+\lambda)-nCB^{(n)}\right\} -BB_{lk}^{(n)}\omega\ \mathrm{sgn}(z-\zeta) \quad (4)$$

$$g=(z-\zeta)\lambda M^2/\beta_a^2,\quad \phi=\theta'+(z-\zeta)\omega/\beta_a^2,\quad \beta_a^2=1-M^2,\quad n=\nu N+\sigma$$

and

$$\left.\begin{aligned}&\{\Omega_l^{(n)}\}^2=[\{k_l^{(n)}\}^2-(n\omega+\lambda)^2M^2/\beta_a^2]/\beta_a^2\\ &\Omega_l^{(n)}=|\Omega_l^{(n)}|\quad\text{for}\quad\{\Omega_l^{(n)}\}^2>0\\ &\text{(cut-off mode)}\\ &\Omega_l^{(n)}=i|\Omega_l^{(n)}|\quad\text{for}\quad\{\Omega_l^{(n)}\}^2<0\\ &\text{(cut-on mode)}\end{aligned}\right\} \quad (5)$$

Furthermore M denotes the axial Mach number of the undisturbed flow, and $k_l^{(n)2}=n^2\kappa_l^{(n)2}$. $CB_{lk}^{(n)}$ are coefficients of a series for $R_l^{(n)}(r)/r^2$ expanded in terms of $R_k^{(\infty)}(r)$. The details of the mathematical metod are given by Namba (1987).

Integral Equation

The velocity component normal to the blade surfaces $q_\tau(r, \theta', z)e^{i\lambda t}$ can be obtained by integrating the linearized equation of motion. The resultant expression is

$$q_\tau(r,\theta',z)=\frac{1}{\rho_0 Q}\int_h^1 d\rho\int_{b_L(\rho)}^{b_T(\rho)}\Delta p_B(\rho,\zeta) \times K_\tau(r,\theta',z-\zeta|\rho)d\zeta \quad (6)$$

where ρ_0 denotes the undisturbed fluid density, $Q=W_a\sqrt{1+\omega^2r^2}$ is the undisturbed local relative velocity, and the $K_\tau(r, \theta', z-\zeta|\rho)$ is the upwash kernel function given by

$$K_\tau(r,\theta',z-\zeta|\rho)=-e^{-i\lambda z}\int_{-\infty}^{z}e^{i\lambda z} \times\left[\left(\frac{1}{r}\frac{\partial}{\partial\theta}-\omega r\frac{\partial}{\partial z}\right)K_p(r,\theta-\omega z,z-\zeta|\rho)\right]_{\theta=\theta'+\omega z}dz \quad (7)$$

The unsteady blade loading $\Delta p_B(\rho, \zeta)$ has to be determined so that the normal component of the relative velocity to the blade surface is zero. In the case of vibrating blades, the boundary condition on the reference blade is expressed as

$$q_\tau(r,0,z)=W_a(i\lambda+\partial/\partial z)\eta(r,z) \quad (8)$$

where $\eta(r, z)e^{i\lambda t}$ is the displacement of the reference blade normal to its surface. For the case of interaction with a sinusoidal gust

$$q_\tau(r,0,z)+\tilde{q}_\tau^{(w)}(r,0,z)e^{-iN_w\omega z}=0 \quad (9)$$

Here $\tilde{q}_\tau^{(w)}(r, 0, z)e^{i\lambda t}$ denotes the upwash component of incident disturbance velocity with no rotation and no radial skew given by

$$\tilde{q}_\tau^{(w)}(r,0,z)=-\epsilon W_a\tilde{w}(r)\omega r/\sqrt{1+\omega^2r^2} \quad (10)$$

Combining equation (6) with equation (8) or (9) yields an integral equation for the lifting pressure $\Delta p_B(\rho, \zeta)$.

Discrete Element Method

Namba et al. (1983, 1984) have applied a double mode func-

Nomenclature (cont.)

$\tilde{q}_\tau^{(w)}$ = upwash component of the incident disturbance velocity
$R_l^{(n)}(r)$ = radial eigenfunctions
r_T^* = radius at the blade tip
(r, θ, z) = cylindrical coordinate system fixed to the rotor
$S_-(\nu, l)$, $S_+(\nu, l)$ = dimensionless acoustic power of mode (ν, l) in upstream and downstream propagation, respectively
t = time
$\bar{W}_j^{(b)}$, $\bar{W}_k^{(t)}$ = dimensionless total aerodynamic work on a blade in the jth order bending and kth order torsional vibrations, respectively
W_a = axial velocity of the undisturbed fluid
$\bar{z}$ = locally normalized axial coordinate, equation (20)
β_a^2 = $1-M^2$
γ = blade sweep angle (backward sweep positive)
$\Delta p_B(r, z)e^{i\lambda t}$ = pressure difference across the reference blade
Δp_B^* = Δp_B expressed by the locally normalized axial coordinate
δ_{ij} = Kronecker delta
ζ = axial coordinate at a point on a blade surface
$\bar{\zeta}$ = locally normalized axial coordinate at a point on a blade surface, equation (12)
$\eta(r, z)e^{i\lambda t}$ = displacement of the reference blade normal to its surface
θ' = $\theta-\omega z$ = helical coordinate
$\kappa_l^{(n)}$ = $k_l^{(n)}/n$
λ = dimensionless angular frequency
ρ = radial coordinate at a point on a blade surface
ρ_0 = undisturbed fluid density
$\hat{\sigma}$ = $2\pi\sigma/N$ = interblade phase angle
ϕ = $\theta'+(z-\zeta)\omega/\beta_a^2$
$\Omega_l^{(n)}$ = axial wave factor defined by equation (5)
ω = dimensionless angular velocity of the rotor

Downloaded 01 Jun 2010 to 171.66.16.66. Redistribution subject to ASME license or copyright; see http://www.asme.org/terms/Terms_Use.cfm

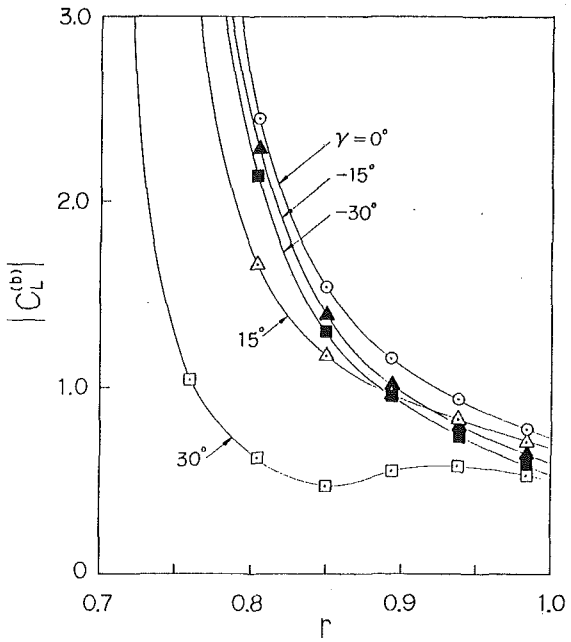

Fig. 3(*a*) Radial variation in the magnitude of the local unsteady lift coefficient for the first-mode bending vibration

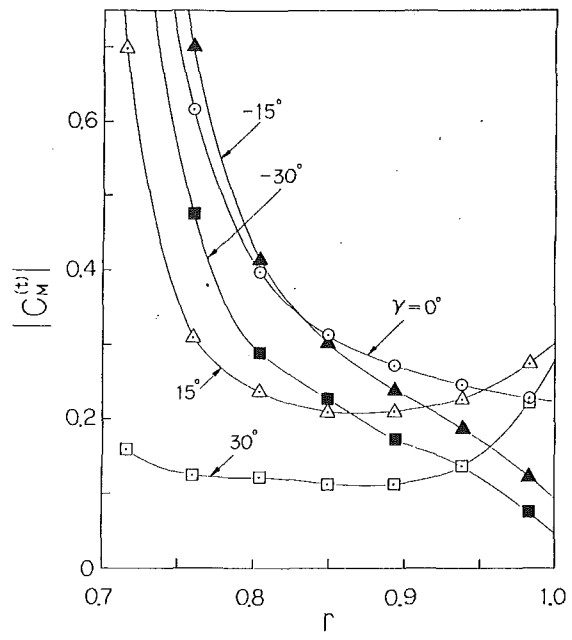

Fig. 4(a) Radial variation in the magnitude of the local unsteady force moment coefficient for the first-mode torsional vibration

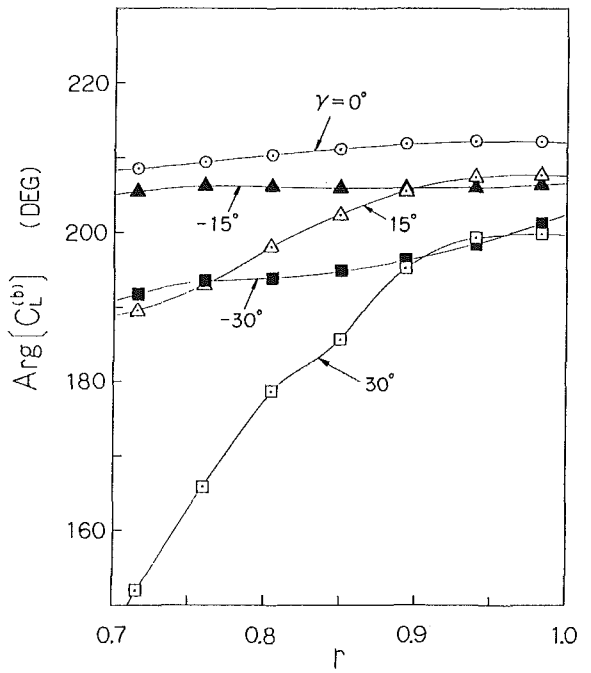

Fig. 3(*b*) Radial variation in the argument of the local unsteady lift coefficient for the first-mode bending vibration

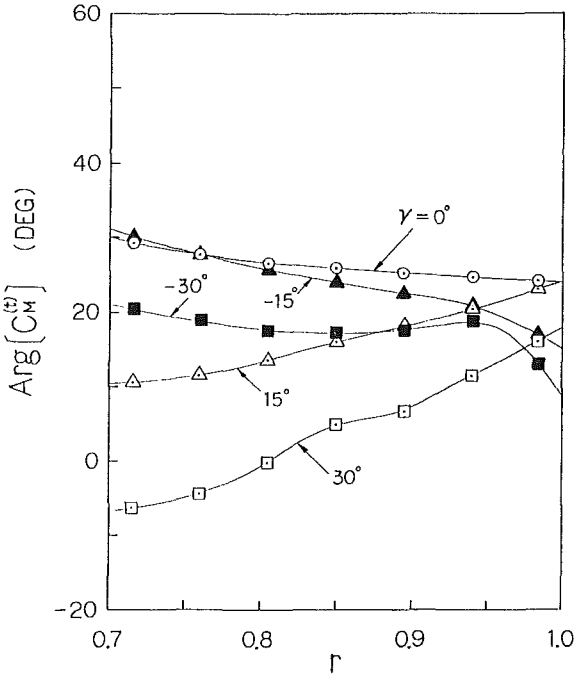

Fig. 4(*b*) Radial variation in the argument of the local unsteady force moment coefficient for the first-mode torsional vibration

tion method to solve the integral equation for the unsteady blade loading by expressing $\Delta p_B(\rho, \zeta)$ in terms of the double series of radial mode functions and chordwise mode functions. In the case of unswept blades with constant axial chord along the span, where $b_L(\rho)$ and $b_T(\rho)$ are constant, the radial integration in equation (6) can be carried out analytically using the relation

$$\int_h^1 r\, R_l^{(n)}(r) R_m^{(n)}(r) dr = \delta_{lm} \tag{11}$$

Here δ_{lm} denotes Kronecker delta. In the case of swept blades, however, the analytical integration cannot be applied because the relative axial position of the blade varies with radius. Therefore there is no advantage in expanding $\Delta p_B(\rho, \zeta)$ in terms of the radial eigenfunction series. Hence, in the present analysis, the integral equation is solved numerically by applying a discrete element method.

The discrete element method consists in determining $\Delta p_B^*(\rho, \bar{\zeta})$ at a finite number of load points.

$$(\rho_j, \bar{\zeta}_i) \qquad i = 1, 2, \ldots, I; \quad j = 1, 2, \ldots, J$$

where $\bar{\zeta}$ is the locally normalized axial coordinate defined by

$$\bar{\zeta} = \{\zeta - C_M(\rho)\}/C_a(\rho) \tag{12}$$

Here

$$C_a(\rho) = b_T(\rho) - b_L(\rho) \tag{13}$$

Downloaded 01 Jun 2010 to 171.66.16.66. Redistribution subject to ASME license or copyright; see http://www.asme.org/terms/Terms_Use.cfm

$$C_M(\rho) = (b_L(\rho) + b_T(\rho))/2 \tag{14}$$

In the case of subsonic flows $\Delta p_B^*(\rho, \bar{\zeta})$ is infinite at the leading edge and $\Delta p_B^*(\rho, 1/2) = 0$ at the trailing edge due to the Kutta condition. Therefore it will be better to set

$$\frac{1}{\rho_0 W_a^2}\Delta p_B^*(\rho, \bar{\zeta}) = P(\rho, \bar{\zeta})\Big/\sqrt{\frac{1}{4} - \bar{\zeta}^2} \tag{15}$$

and determine numerical values of $P(\rho, \bar{\zeta})$. Consequently $P(\rho, \bar{\zeta})$ is allowed to take a finite value at the leading edge and $P(\rho, 1/2) = 0$ at the trailing edge. Then using numerical integrals like

$$\int_{-1/2}^{1/2} f(\bar{\zeta})d\bar{\zeta} \to \sum_{i=1}^{I} f(\bar{\zeta}_i)\Delta\bar{\zeta}_i \tag{16}$$

$$\int_h^1 f(\rho)d\rho \to \sum_{j=1}^{J} f(\rho_j)\Delta\rho_j \tag{17}$$

one can write the integral equation for the lifting pressures as

$$\sum_{j=1}^{J} C_a(\rho_j)\Delta\rho_j \sum_{i=1}^{I} \frac{P(\rho_j, \bar{\zeta}_i)}{\sqrt{\frac{1}{4} - \bar{\zeta}_i^2}} \times K_\tau^*(r_\beta, 0, g(\bar{z}_\alpha, r_\beta) - g(\bar{\zeta}_i, \rho_j)\,|\rho_j)\Delta\bar{\zeta}_i = b^*(r_\beta, \bar{z}_\alpha)(1 + \omega^2 r_\beta^2) \tag{18}$$

where

$$g(\bar{z}, r) = C_a(r)\bar{z} + C_M(r) \tag{19}$$

$$\bar{z} = (z - C_M(r))/C_a(r) \tag{20}$$

and

$$b^*(r_\beta, \bar{z}_\alpha) = \left\{i\lambda + \frac{1}{C_a(r_\beta)}\frac{\partial}{\partial\bar{z}}\right\} \times \eta^*(r_\beta, g(\bar{z}_\alpha, r_\beta))/\sqrt{1 + \omega^2 r_\beta^2} \tag{21}$$

(for the case of vibrating blades)

$$b^*(r_\beta, \bar{z}_\alpha) = \epsilon\bar{w}(r_\beta)\omega r_\beta \times e^{-iN\nu\omega g(\bar{z}_\alpha, r_\beta)}/(1 + \omega^2 r_\beta^2) \tag{22}$$

(for the case of interaction with a convected sinusoidal gust)

It is reasonable to take $J = L$, and

$$\left.\begin{aligned} \rho_j &= 1/\kappa_{j-1}^{\{\infty\}} \qquad j = 1, 2, \ldots, L \\ r_\beta &= 1/\kappa_{\beta-1}^{\{\infty\}} \qquad \beta = 1, 2, \ldots, L \end{aligned}\right\} \tag{23}$$

for the reason that each $R_l^{\{\infty\}}(r)$ is dominant at $r = 1/\kappa_l^{\{\infty\}}$ as described before. As to selection of $\bar{z}_\alpha$ and $\bar{\zeta}_i$, the so-called "1/4-3/4" rule has been chosen.

Numerical Results and Discussion

Practical swept fan blades are likely to have curved leading and trailing edges. The present study, however, is confined to swept blades with straight leading and trailing edges and with constant axial chord length along the span in order to focus attention on the effects of sweep on the unsteady aerodynamic characteristics. The other parameters are fixed as follows: number of blades $N = 30$, dimensionless speed of the rotor $\omega = 2.4744$, hub/tip ratio $h = 0.7$, dimensionless axial chord length $C_a(r) = b_T(r) - b_L(r) = 0.0667$, and the axial Mach number $M = 0.3$. The midchord line $C_M(r)$ defined by equation (14) is expressed as

$$C_M(r) = (r - h)\tan\gamma \tag{24}$$

Here γ denotes the sweep angle of a blade projected on the meridional plane.

In all cases the numbers of radial collocation stations $L = 7$ and chordwise load points $I = 11$ are used.

Vibrating Blades. In the present paper, parametric studies are carried out by changing the sweep angle. In actual cases the blade natural frequencies would decrease with sweep, because the blade span becomes longer with increasing sweep. The vibration modes also would become more complex with increase in the sweep angle. In order to avoid effects other than the blade sweep on the unsteady aerodynamic characteristics, we assume that the blade frequencies and the vibration modes are independent of the sweep angle. The dimensionless frequency and the interblade phase angle parameter are taken as $\lambda = 3$ and $\sigma = 6$, respectively. Here two types of vibration modes are considered: the case of pure bending where the circumferential dispacement of a reference blade is given by $HC_a(r)\,a_j^{\{b\}}(r)\,e^{i\lambda t}$, i.e.,

$$\eta(r, z) = HC_a(r)a_j^{\{b\}}(r)/\sqrt{1 + \omega^2 r^2} \tag{25}$$

and the case of pure torsion about the midchord point $c_M(r)$ where the twist angle of a reference blade is given by $\Theta a_R^{\{t\}}(r)e^{i\lambda t}$

$$\eta(r, z) = \Theta a_k^{\{t\}}(r)\sqrt{1 + \omega^2 r^2}(z - C_M(r)) \tag{26}$$

Here H and Θ denote the displacement and angle amplitudes at the blade tip, respectively, and $a_j^{\{b\}}(r)$ and $a_k^{\{t\}}(r)$ denote the spanwise mode shapes of the jth order bending and kth order torsional vibrations, respectively. The natural mode shapes of a uniform cantilever beam are assumed.

Figures 3(a) and 3(b) show the local unsteady lift coefficient for the first mode bending vibration of unit amplitude $H = 1$. The local unsteady lift coefficient is defined by

$$C_L^{\{b\}}(r) = L(r)/(\pi\rho_0 Q(r)C^*\bar{q}_\tau^{\{b\}}) \tag{27}$$

where

$$\bar{q}_\tau^{\{b\}} = i\epsilon\lambda C_a(r)a_j^{\{b\}}(r)Q(r)/(1 + \omega^2 r^2) \tag{28}$$

and $L(r)$ is the local unsteady lift force per unit span. In addition, $C^* = r_T^*\,C_a(r)\sqrt{1 + \omega^2 r^2}$ denotes the local chord length. Generally the unsteady lift force decreases as the sweep angle increases for both forward and backward sweeps. Especially for the backward sweep, the reduction in the unsteady lift force becomes more remarkable toward the hub, and the radial variation of the local unsteady lift coefficient becomes smaller. In general, incrasing the sweep angle $|\gamma|$ results in decrease of the phase of the unsteady lift coefficient, i.e., Arg $[C_L^{\{b\}}(r)]$.

Figures 4(a) and 4(b) show the local unsteady moment coefficient for the first mode torsional vibration of unit amplitude $\Theta = 1$ defined by

$$C_M^{\{t\}}(r) = \mathrm{M}^{\{t\}}(r)/(\pi\rho_0 Q^2(r)C^{*2}a_k^{\{t\}}(r)) \tag{29}$$

where $\mathrm{M}^{\{t\}}(r)$ denotes the local unsteady moment per unit span about midchord. A similar tendency as seen in $C_L^{\{b\}}(r)$ for the bending mode vibration is observed in $C_M^{\{t\}}(r)$. Again the distinctive reduction of the local unsteady moment near the hub with increasing sweep is seen for the backward sweep.

Figures 5 and 6 show the effect of the blade sweep on the total aerodynamic work coefficients for the first-mode bending vibration $\bar{W}_1^{\{b\}}$ and the first-mode torsional vibration $\bar{W}_1^{\{t\}}$ defined by equation (51) of Namba and Ishikawa (1983). For both forward and backward sweeps, the blade vibrations are stabilized drastically at large sweep angles.

Interaction With a Sinusoidal Gust. Any arbitrary circumferential wake profile can be decomposed into pure harmonic components. Because of the linearized nature of the analysis, one can carry out the calculation for each component and sum the solutions. In the present analysis, the calculation is conducted for only one component to study the effects of blade sweep. The sinusoidal component of the circumferential

Downloaded 01 Jun 2010 to 171.66.16.66. Redistribution subject to ASME license or copyright; see http://www.asme.org/terms/Terms_Use.cfm

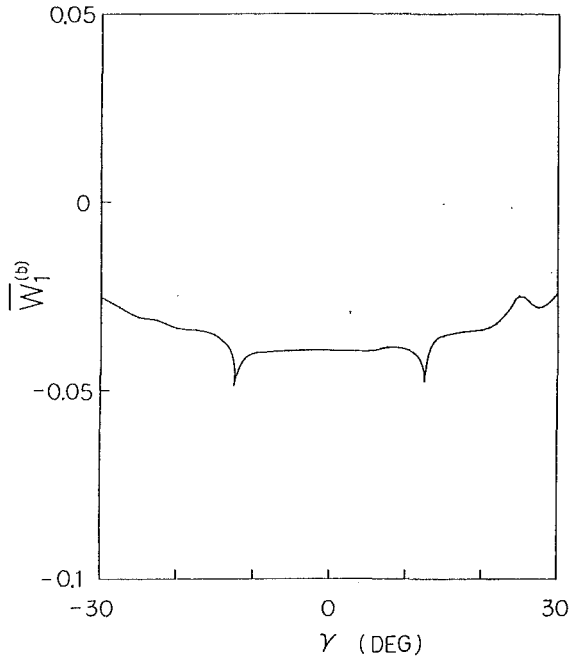

Fig. 5 Effect of sweep angle on the total aerodynamic work coefficient for the first-mode bending vibration

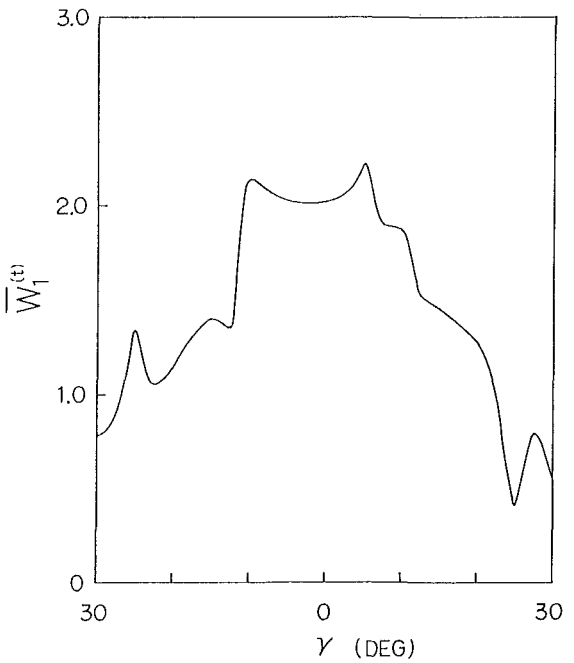

Fig. 6 Effect of sweep angle on the total aerodynamic work coefficient for the first-mode torsional vibration

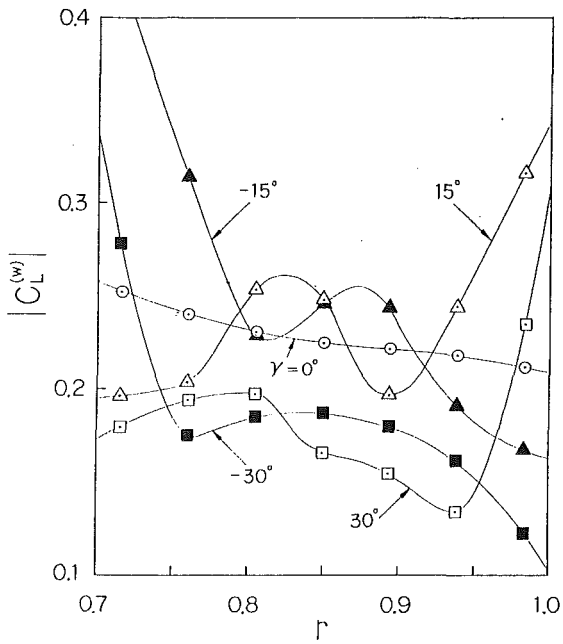

Fig. 7(a) Radial variation in the magnitude of the local lift unsteady coefficient for interaction with a convected sinusoidal gust

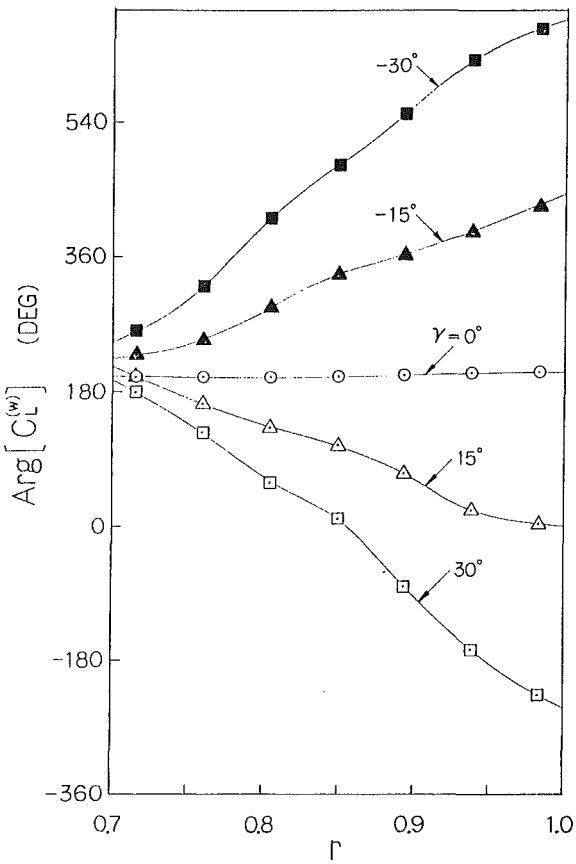

Fig. 7(b) Radial variation in the argument of the local unsteady lift coefficient for interaction with a convected sinusoidal gust

wave number $N_w = 20$ is selected. Hence it is determined that $\lambda = 49.488$ and $\sigma = 10$. Furthermore the incident disturbance flow velocity is assumed to be of constant amplitude $\tilde{w}(r) = 1$.

Figures 7(*a*) and 7(*b*) show the radial variation in the local unsteady lift coefficient defined by

$$C_L^{(w)}(r) = -L(r)/(\pi\rho_0 Q(r) C^* \tilde{q}_\tau^{(w)}) \tag{30}$$

It can be seen that the overall unsteady lift force becomes small at large sweep angles, i.e., $\gamma = +30$ deg or -30 deg. It is worth noticing, however, that the local unsteady lift force becomes large near the hub for larger forward sweep and near the tip for larger backward sweep.

Figure 8 shows the axial components of the total and modal acoustic powers calculated in the same way as shown by Namba (1977). In the figure, the subscripts + and − denote downstream and upstream propagation, respectively, and E_+, E_-, S_+ (ν, l), and S_- (ν, l) are normalized by $(\pi/4) r_T^* \rho_0 W_a^3 \epsilon^2$. A remarkable reduction in the acoustic power is attained by increasing $|\gamma|$ beyond 12.5 deg. There are two main

Downloaded 01 Jun 2010 to 171.66.16.66. Redistribution subject to ASME license or copyright; see http://www.asme.org/terms/Terms_Use.cfm

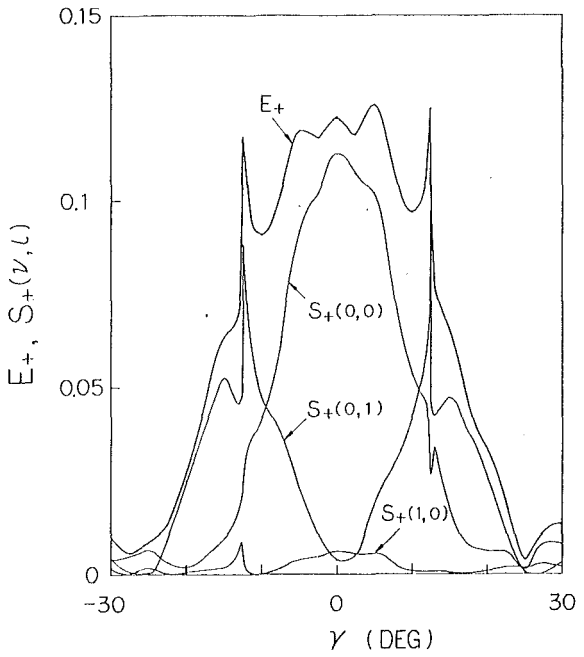

Fig. 8(*a*) Effect of sweep angle on the total and modal acoustic powers

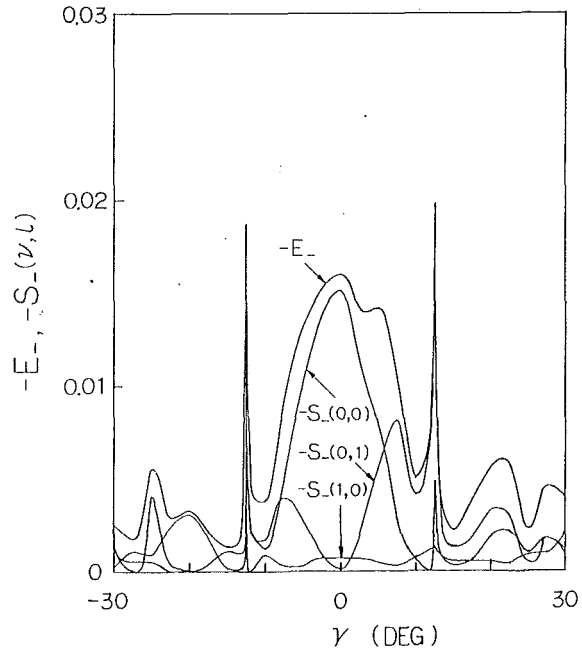

Fig. 8(*b*) Effect of sweep angle on the total and modal acoustic powers

reasons for this phenomenon. One is the reduction of Δp_B itself as the dipole sound source, and another is the reduction of modal acoustic powers of lower radial orders in the cut-on state.

It is worth noting that distinctive increase of the (0, 1) mode power gives rise to sharp peaks of the total acoustic power near $|\gamma| = 12.5$ deg.

Conclusion

The local unsteady blade force due to blade vibration decreases as the sweep angle increases for both forward and backward sweeps. The reduction in the unsteady blade force near the hub is distinctive for large backward sweep angles.

Consequently the total aerodynamic work is reduced considerably at large sweep angles. This can be seen noticeably in the aerodynamic work for the torsional vibration.

Remarkable reduction in the acoustic power generated by interaction with a convected sinusoidal gust is also attained at large sweep angles for both forward and backward sweeps.

It can be said that the adequate blade sweep is a great advantage for both blade flutter suppression and noise reduction.

References

Grieb, H., and Eckardt, D., 1986, "Turbofan and Propfan as Basis for Future Economic Propulsion Concepts," AIAA Paper No. 86-1474.

Hanson, D. B., 1983, "Compressible Helicoidal Surface Theory for Propeller Aerodynamics and Noise," *AIAA Journal*, Vol. 21, pp. 881-889.

Hanson, D. B., 1985, "Compressible Lifting Surface Theory for Propeller Performance Calculation," *AIAA Journal*, Vol. 22, pp. 19-27.

Namba, M., 1977, "Three-Dimensional Analysis of Blade Force and Sound Generation for an Annular Cascade in Distorted Flows," *Journal of Sound and Vibration*, No. 50, No. 4, pp. 479-508.

Namba, M., and Ishikawa, A., 1983, "Three-Dimensional Aerodynamic Characteristics of Oscillating Supersonic and Transonic Annular Cascades," ASME *Journal of Engineering for Power*, Vol. 105, pp. 138-146.

Namba, M., and Abe, T., 1984, "Unsteady Aerodynamic Forces on Supersonic and Transonic Annular Cascades Interacting With Distorted Inlet Flows," *Proceedings of Symposium on Unsteady Aerodynamics of Turbomachines and Propellers*, pp. 205-216.

Namba, M., 1987, "Three-Dimensional Flows," in: *Aero-elasticity in Axial-Flow Turbomachines, Vol. 1, Unsteady Turbomachinery Aerodynamics*, M. F. Platzer and F. O. Carta, eds., AGARD-AG-298, Vol. 1.

Downloaded 01 Jun 2010 to 171.66.16.66. Redistribution subject to ASME license or copyright; see http://www.asme.org/terms/Terms_Use.cfm

Surface Injection Effect on Mass Transfer From a Cylinder in Crossflow: A Simulation of Film Cooling in the Leading Edge Region of a Turbine Blade

J. Karni[1]

R. J. Goldstein

Department of Mechanical Engineering,
University of Minnesota,
Minneapolis, MN 55455

A naphthalene sublimation technique is used to study the effect of surface injection on the mass (heat) transfer from a circular cylinder in crossflow. Using a heat/mass transfer analogy the results can be used to predict film cooling effects in the leading edge region of a turbine blade. Air injection through one row of circular holes is employed in the stagnation region of the cylinder. Streamwise and spanwise injection inclinations are studied separately, and the effects of blowing rate and injection location relative to the cylinder front stagnation line are investigated. Streamwise injection produces significant mass transfer increases downstream of the injection holes, but a relatively small increase is observed between holes, normal to the injection direction. The mass transfer distribution, measured with spanwise injection through holes located near the cylinder front stagnation line, is extremely sensitive to small changes in the injection hole location relative to stagnation. When the centers of the spanwise injection holes are located 5 deg or more from the stagnation line, the holes lie entirely on one side of the stagnation line and the injection affects the mass transfer only on that side of the cylinder, approaching the pattern observed with streamwise injection.

Introduction

Application of film cooling through a single row or multiple rows of circular holes is common in gas turbine systems. The need to improve performance by increasing turbine inlet temperature, without shortening the components' lifespan, has prompted a large number of studies aimed at a better understanding of the complex flow and heat transfer mechanisms involved in film cooling (see Metzger, 1983). Advanced materials such as nickel superalloys and various ceramics, which are used in modern turbines (Kear, 1986), have, in general, relatively low thermal conductivity and diffusivity. Thus, large local variations of the heat transfer coefficient can produce significant temperature gradients in the wall of a turbine blade. These gradients may cause high thermal stresses and ultimately could lead to blade failure. An effective film cooling design must reduce the temperature gradients over the surface, as well as the mean wall temperature. Therefore, knowledge of the heat transfer distribution over the blade surface, with various coolant injection configurations, is necessary for a successful turbine design.

Two methods have been developed to predict film cooling effects on heat transfer. The first method (Eckert, 1983; Goldstein, 1971) defines the heat transfer coefficient with an adiabatic wall temperature

$$q_w = h_H (T_w - T_{aw}) \tag{1}$$

For a constant property flow, the heat transfer coefficient h_H is independent of the temperature difference $T_w - T_{aw}$. A dimensionless adiabatic wall temperature, known as the film cooling effectiveness η is given by

$$\eta = \frac{T_{aw} - T_r}{T_2 - T_r}$$

For low-speed constant property flows $T_r = T_\infty$, and

$$\eta = \frac{T_{aw} - T_\infty}{T_2 - T_\infty} \tag{2}$$

In this method, the heat transfer coefficient and the effectiveness are determined separately. Then, for any given mainstream and coolant temperatures and a prescribed wall heat flux, the wall temperature distribution can be obtained using equation (1).

[1] Present address: The Weizmann Institute of Science, Rehovot 76100, Israel.

Contributed by the International Gas Turbine Institute and presented at the 34th International Gas Turbine and Aeroengine Congres and Exhibition, Toronto, Ontario, Canada, June 4–8, 1989. Manuscript recived at ASME Headquarters February 14, 1989. Paper No. 89-GT-276.

Copyright © 1990 by ASME
Downloaded 01 Jun 2010 to 171.66.16.66. Redistribution subject to ASME license or copyright; see http://www.asme.org/terms/Terms_Use.cfm

In the second method (Metzger et al., 1968; Choe et al., 1974) the heat transfer coefficient is defined by the equation

$$q_w = h'(T_w - T_\infty) \tag{3}$$

This approach provides a direct means of determining heat transfer coefficients for film cooling on an isothermal surface. Here, the heat transfer coefficient h' is not independent of the temperature difference $T_w - T_\infty$; but as shown by Metzger et al. (1968), Metzger and Fletcher (1971), and Eckert et al. (1971), for a constant property flow, h' varies linearly with the dimensionless temperature

$$\theta^* = \frac{T_2 - T_\infty}{T_w - T_\infty} \tag{4}$$

Note that unlike h_H, the coefficient h', defined by equation (3), can take on unusual (e.g., negative) values, especially close to an injection location. The coefficients h_o' and h_1' obtained on an isothermal surface for $\theta^* = 0$ and 1, respectively, can be used to approximate heat transfer coefficients on a surface where gradual temperature variations take place (Eckert, 1983). In that case

$$h_o' \approx h_H \tag{5}$$

and the relation between h' and θ^* is given by

$$\frac{h'}{h_H} = 1 - \eta\theta^* \tag{6}$$

In various studies (Metzger and Fletcher, 1971; Miller and Crawford, 1984; Ligrani and Camci, 1985) values of h_H and η were approximated from h' and θ^* data using a linear extrapolation based on equation (6).

Values of the heat transfer coefficient h_H for two-dimensional slot injection across the span of a flat plate are presented by Hartnett et al. (1961a, 1961b). Their data show relatively large coefficients near the injection slot; as the downstream distance from the slot increases, h_H quickly declines, approaching the coefficient obtained without injection. Measurements of heat transfer coefficients averaged across the test surface are reported in some studies of three-dimensional film cooling from a single row and multiple rows of circular holes (Metzger and Fletcher, 1971; Mayle and Camarata, 1975; Liess, 1975; Metzger et al., 1976; Lander et al., 1972; Ligrani and Breugelmans, 1981). Effects of parameters such as injection geometry, blowing rate, pressure gradient, and boundary layer transition on variation of spanwise-averaged coefficients in the mainflow direction were investigated in these studies.

Local heat transfer coefficients (h_H) over a film-cooled plate with one and two rows of injection holes were measured by Eriksen and Goldstein (1974) and Jabbari and Goldstein (1978). Mick and Mayle (1988) measured local h_H values using two rows of spanwise injection holes located 15 and 44 deg from the stagnation line of a blunt body with a circular leading edge, followed by a flat section. Local measurements near the leading edge of a turbine vane and on the front portion of a cylinder were conducted at Purdue University by Hanus and L'Ecuyer (1977), Luckey et al. (1977), Luckey and L'Ecuyer (1981), and Bonnice and L'Ecuyer (1983). In these studies h' values were obtained near the center of the wind tunnel (cylinder midspan). Spanwise injection through one to five rows of holes was employed.

In an experimental setup where significant temperature differences exist (Ericksen et al., 1974; Jabbari et al., 1978; Mick et al., 1988; Hanus et al., 1977; Luckey et al., 1977, 1981; Bonnice et al., 1983) wall conduction makes it difficult to maintain the imposed boundary condition ($T_w = \text{const}$ or $q_w = \text{const}$) near the injection holes and close to the edges of the test surface. Consequently, in several studies the analysis between heat and mass transfer was utilized to obtain transfer coefficients on flat surfaces (Hay et al., 1985a, 1985b; Goldstein and Taylor, 1982; Kumada et al., 1981). The last two studies demonstrated how mass transfer using naphthalene sublimation can provide contours of local transfer coefficients on a flat plate near the holes of single-row and multiple-row injection geometries.

When naphthalene sublimation is used, a direct analogy to the adiabatic wall heat transfer coefficient (h_H) defined by

Nomenclature

- d = diameter of the test cylinder = 63.5 mm in present study
- D = injection tube inner diameter = 5.95 mm
- D_f = mass diffusion coefficient for naphthalene vapor in air; taking Sc = 2.5 (Sogin, 1958), $D_f = \nu/2.5$. [Note more recent studies by Chen (1987) and Cho (1989) indicate a smaller value of Sc and D_f. This would not affect the relative values of the mass transfer coefficient and Sherwood number with and without blowing.]
- h = local convective heat transfer coefficient
- h_o = reference mass transfer coefficient = h_m without surface injection
- h_H = adiabatic wall heat transfer coefficient for film cooling applications = $q_w/(T_w - T_{aw})$
- h_m = local mass transfer coefficient = $\dot{m}/\bar{\rho}_{v,w}$
- h' = isothermal wall heat transfer coefficient for film cooling applications = $q_w/(T_w - T_\infty)$
- h_o' = isothermal wall heat transfer coefficient for a situation where $\theta^* = 0$ (i.e., $T_2 = T_\infty$)
- h_1' = isothermal wall heat transfer coefficient for a situation where $\theta^* = 1$ (i.e., $T_2 = T_w$)
- H = shape factor = δ^*/δ_2
- k = conductivity
- L = length of test cylinder (also, height of the wind tunnel) = 305 mm in the present study
- $\dot{m}$ = local naphthalene mass transfer rate per unit area of the cylinder surface
- M = blowing rate = $\rho_2 U_2/\rho_\infty U_\infty$
- P_v = vapor pressure of naphthalene determined using the method by Ambrose et al. (1975)
- $\bar{P}_v$ = local vapor pressure of naphthalene at the cylinder surface averaged over the time of exposure in the wind tunnel
- q_w = wall heat flux
- R_n = gas constant for naphthalene (universal gas constant divided by molecular weight of naphthalene = 128.19)
- s = spanwise distance between centers of injection holes
- t = thickness of naphthalene layer
- T = temperature
- T_o = reference temperature
- T_{aw} = adiabatic wall temperature
- T_r = free-stream recovery temperature
- T_w = wall temperature
- T_2 = film coolant temperature at the point of injection
- T_∞ = mainstream temperature
- $\bar{T}$ = local temperature of naphthalene surface averaged over exposure time in the wind tunnel

Downloaded 01 Jun 2010 to 171.66.16.66. Redistribution subject to ASME license or copyright; see http://www.asme.org/terms/Terms_Use.cfm

equation (1) leads to the following definition of a mass transfer coefficient:

$$h_m = \frac{\dot{m}}{(\bar{\rho}_{v,w} - \rho_{v,i})} \tag{7}$$

Alternatively, a relation equivalent to equation (3) gives

$$h_m = \frac{\dot{m}}{(\bar{\rho}_{v,w} - \rho_{v,\infty})} \tag{8}$$

In the naphthalene sublimation technique used in the present study a nearly uniform vapor density is maintained over the entire cylinder surface, and the naphthalene vapor concentration in the mainstream and in the injected gas is zero. This is equivalent to isothermal boundary conditions with $T_2 = T_\infty$ (or $\theta^* = 0$). Thus, equations (7) and (8) both reduce to

$$h_m = \frac{\dot{m}}{\bar{\rho}_{v,w}} \tag{9a}$$

In the present study local mass transfer coefficients are obtained around the entire circumference of a circular cylinder and along a span containing five injection holes (in a single row). Spanwise and streamwise inclined injections are employed at blowing rates of 0.5, 1.0, and 2.0. The injection location is varied relative to the cylinder's front stagnation line. In each test run, measurements are taken at about 3800 local points over the cylinder surface. Thus, exact details of the mass transfer distribution pattern are revealed. Injection geometry and blowing rate effects in the region away from the base of the cylinder, where endwall effects on the flow are relatively small, are reported here. The injection effects near the endwall will be reported later.

Experimental Apparatus and Measurement Techniques

The primary objective of the experimental apparatus is to provide a means of determining the local rate of naphthalene sublimation from the cylinder surface during exposure to an air flow. This local mass transfer rate is then expressed in terms of the coefficients h_m and the Sherwood number. Detailed descriptions of the experimental apparatus and the measurement procedure are given by Karni (1985). The maximum measurement error in obtaining h_m is 6 percent.

The test cylinder ($d = 63.5$ mm) is shown in Fig. 1; a portion extending over about 60 deg of the cylinder circumference and along its entire naphthalene-covered span is removed [see Fig. 1(*a*)] and two sections with different injection inclinations are made to fit in that region [Figs. 1(*b*) and 1(*c*)]. During tests the cast naphthalene layer covers the outer surface of the section used as if it were an integral part of the cylinder. Teflon (Polytetra-Fluoro-Ethylene) injection tubes are installed in these sections; in one section, the tubes are inclined such that the injected air enters the mainstream at a spanwise angle of 20 deg to the cylinder surface [Fig. 1(*b*)]; in the other section, the tubes are angled 37 deg to the surface in the streamwise direction [Fig. 1(*c*)]. All injection tubes have an inside diameter of 5.95 mm and a wall thickness of 0.35 mm. They extend 1.0 mm out of the section surface and thus are flush with the naphthalene layer outer surface. The injection holes extend over an angular range of 18 and 10.5 deg of the cylinder circumference for streamwise and spanwise injection, respectively. If the injection tube's wall thickness is included, these angles become 20 to 12 deg, respectively. The ratio of cylinder diameter to injection hole diameter ($d/D = 10.67$) is similar to that used in the leading edge of many turbine vanes. The hole diameter is of the same order of magnitude as the cylinder boundary layer (see Karni, 1985).

During its exposure to the air stream, the test cylinder is positioned vertically in the middle of the tunnel's cross section, about 450 mm downstream of the test section inlet; the blockage ratio is 0.104. The naphthalene-covered portion of the cylinder extends from about 6.7 mm below the tunnel's bottom wall to 260 mm above it (about 45 mm below the top wall). The secondary (injected) air flow is supplied by a compressor. To insure a steady flow of dry air in the injection system, the secondary air is filtered and passes through two

Nomenclature (cont.)

Tu = turbulence intensity
U_2 = mean velocity in injection tube
$\bar{U}_\infty$ = mean velocity of mainstream
W = width of test section
x = direction along the tunnel test section
x' = downstream distance from downstream edge of injection holes
y = direction along the cylinder center line; $y = 0$ on the tunnel bottom wall
y' = upward distance along the span of the cylinder measured from center of injection holes
z = direction across the tunnel test section; $z = 0$ on the cylinder centerline
α_i = streamwise angle between the injection hole centerline and loal cylinder surface, either 37 or 90 deg in this study
β_i = spanwise angle between the injection hole centerline surface, either 20 or 90 deg in this study
δ^* = displacement thickness of endwall boundary layer just upstream of the cylinder
Δt = change in local naphthalene thickness due to exposure in the wind tunnel
$\Delta\tau$ = time of cylinder exposure in wind tunnel
η = film cooling effectiveness for an adiabatic wall, $\eta = (T_{aw} - T_\infty)/(T_2 - T_\infty)$
θ = angle around the cylinder measured from the front stagnation point, degrees
θ_{inj} = angular location of injection hole center relative to cylinder front stagnation point, degrees
θ^* = dimensionless temperature $= (T_2 - T_\infty)/(T_w - T_\infty)$
μ = dynamic viscosity of air
ν = kinematic viscosity of air $= \mu/\rho$
ρ = density of air
ρ_s = density of solid naphthalene = 1.145 g/cm^3 (Karni, 1985)
$\rho_{v,i}$ = density of naphthalene vapor at an inactive (nonsubliming) surface, zero in this study
$\bar{\rho}_{v,w}$ = local naphthalene vapor density on the cylinder surface averaged over exposure time in the wind tunnel
$\rho_{v,\infty}$ = density of naphthalene vapor in the mainstream, zero in this study

Dimensionless Parameters

Nu = local Nusselt number $= hd/k$
Re = Reynolds number based on cylinder diameter $= U_\infty d/\nu$
Sc = Schmidt number $= \nu/D_f$
Sh = local Sherwood number $= h_m d/D_f$
$\overline{\text{Sh}}_{sp}$ = spanwise-averaged Sherwood number at a given angle

Downloaded 01 Jun 2010 to 171.66.16.66. Redistribution subject to ASME license or copyright; see http://www.asme.org/terms/Terms_Use.cfm

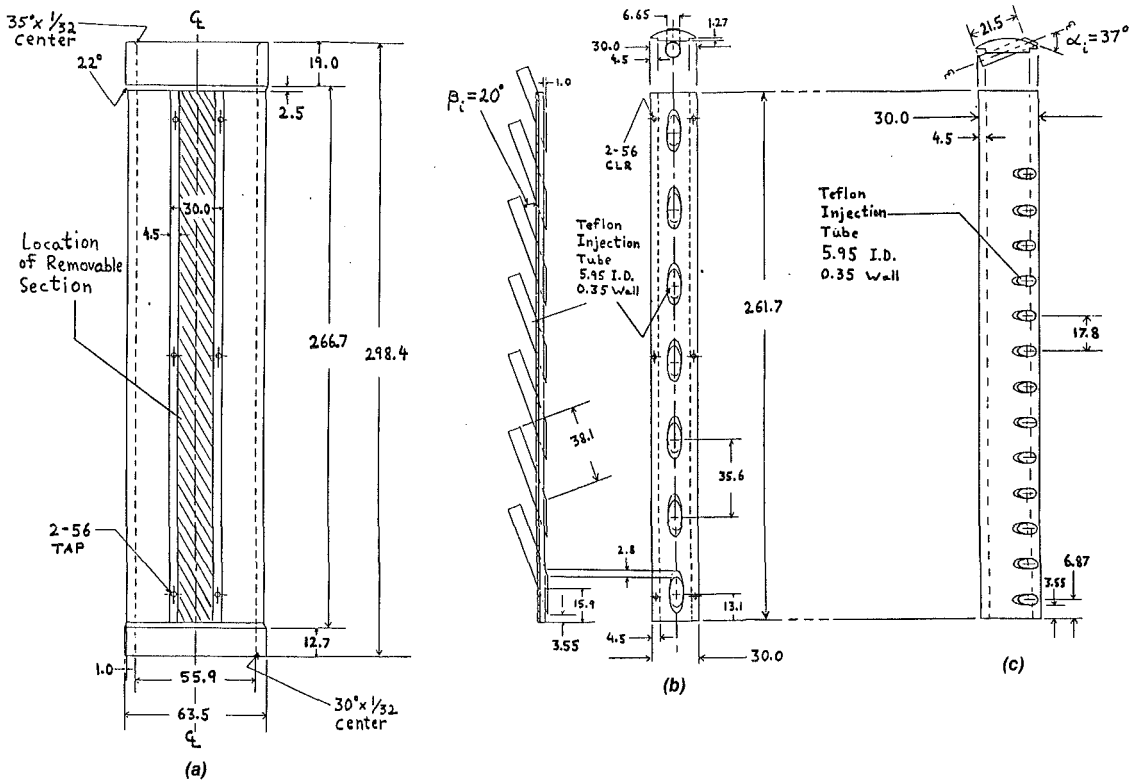

Fig. 1 *(a)* **Test cylinder without removable section; *(b)* removable section with spanwise injection holes; *(c)* removable section with spanwise injection holes (all dimensions in mm)**

flow regulators. It then flows through a calibrated orifice and a temperature-control device. The difference between the mainstream and secondary air temperatures is within 0.25°C in all test runs. To prevent flow rate variations from one injection hole to another, the secondary air enters the test cylinder (d=63.5 mm) through a long narrow slit cut along the span of 25.4 mm o.d. aluminum tube. This tube is attached to the secondary air line on one end and is sealed on the other. It is mounted inside the test cylinder, extending over most of its span. The uniformity of the injected air flow rate was verified experimentally (Karni, 1985).

The time of exposure in the wind tunnel ($\Delta\tau$) is between 35 and 70 min (depending on operating conditions). During tests 0.020–0.13 mm of naphthalene sublime from the cylinder surface. Since the mainstream and the injected air contain no naphthalene vapor, the local mass transfer coefficient is

$$h_m = \frac{\dot{m}}{\bar{\rho}_{v,w}} = \frac{\rho_s \Delta t/\Delta\tau}{\bar{\rho}_{v,w}} \tag{9b}$$

where

$$\bar{\rho}_{v,w} = \frac{\bar{P}_v}{R_n \bar{T}} \tag{10}$$

The results can be expressed in terms of the local Sherwood number

$$\mathrm{Sh} = \frac{h_m d}{D_f} \tag{11}$$

Table 1 Operating conditions

Free stream	Endwall boundary layer
$\mathrm{Re}_d \cong 76{,}000$	$\delta^* \cong 2.23$ mm
$U_\infty \cong 19.16$ m/s	$\delta_2 \cong 1.56$ mm
$\mathrm{Tu} \cong 0.45$ percent	$H \cong 1.43$

Cylinder diameter, d=63.5 mm
Injection hole diameter, D=5.95 mm
Blockage ratio, d/W=0.104
Aspect ratio, L/d=4.8

Streamwise injection		Spanwise injection	
α_i=37 deg	β_i=90 deg s/D=3	α_i=90 deg	β_i=20 deg s/D=6
M	θ_{inj}(deg)	M	θ_{inj}(deg)
0.50	10	0.50	1
0.50	20	0.51	3
0.50	30	0.50	5
1.01	10	0.99	2
1.02	10[1]	1.00	3
1.01	20	1.01	3[1]
1.00	30	0.99	7
1.99	10	2.00	0
2.01	20	2.01	1
1.99	30	1.99	5

[1]Test runs where the lower edge of the first injection hole is located 1.0 hole diameter above the endwall. In all the other tests, the lower side of the first injection hole is adjacent to the tunnel bottom wall.

Operating Conditions

The various operating conditions are specified in Table 1. In all the test runs, the free-stream velocity and the Reynolds number are within 2 percent of the values given in the table. The mainstream turbulence intensity is measured while the cylinder is out of the wind tunnel.

In all the tests, measurements are conducted over a span containing five injection holes (including the region immediately above the endwall) and around the entire cylinder circumference. Spanwise injection is directed toward the endwall.

Downloaded 01 Jun 2010 to 171.66.16.66. Redistribution subject to ASME license or copyright; see http://www.asme.org/terms/Terms_Use.cfm

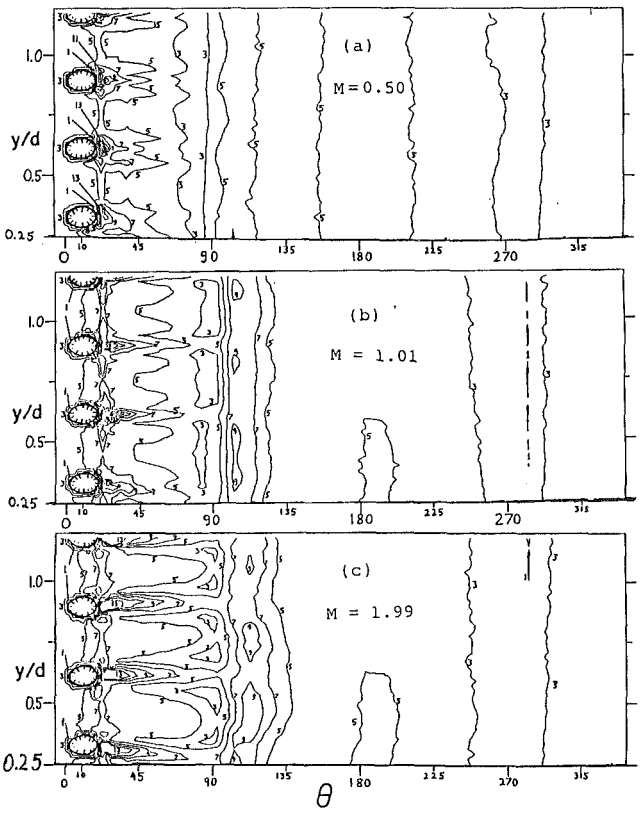

Fig. 2 Sh distribution for streamwise injection: contours of Sh × 10^{-2}, $\alpha_i = 37$ deg; $\beta_i = 90$ deg; $\theta_{inj} = 10$ deg; $s/D = 3$

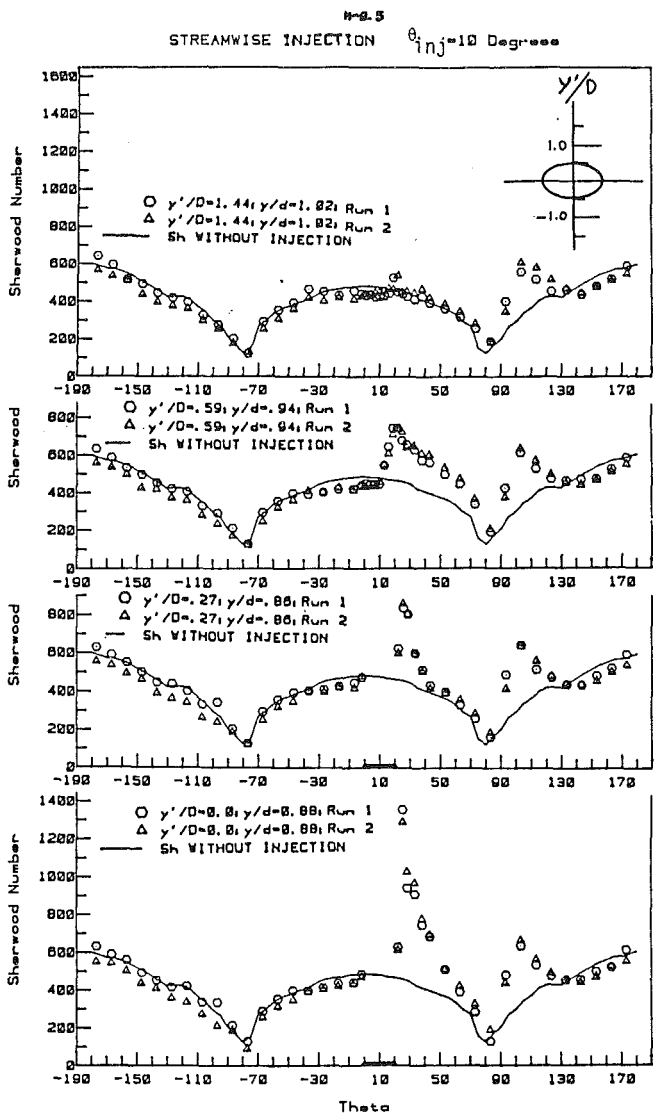

Fig. 3 Angular variations of Sh at slected spanwise distances from the center of an injection hole $M = 0.50$; $\alpha_i = 37$ deg; $\theta_{inj} = 10$ deg

Results

I Streamwise Injection. The Sherwood number distributions for a streamwise injection angle, α_i, of 37 deg, an injection location θ_{inj} of 10 deg, and blowing rate M of 0.50, 1.0, and 2.0, are shown in Figs. 2(*a*), 2(*b*), and 2(*c*), respectively. These (and all other) computer-drawn contour plots are obtained from the actual measurements around the entire cylinder circumference and over part of its span. The difference between adjacent contour lines corresponds to a Sh change of 200. The injection holes are shown by the shaded regions in the left-hand side of each figure. Since the measurement points located nearest each hole are not evenly distributed around its periphery, the contour lines very near the holes are somewhat distorted during the computer drawing process and do not follow the exact shape of the hole where Sh = 0.

Figure 2 demonstrates that the injected air jets produce large Sh values and steep local gradients downstream of the injection holes while a relatively small increase in Sh is seen between the holes. The contours clearly indicate the flow pattern near the injection holes. Somewhat similar mass transfer trends were reported in studies of streamwise injection over flat plates by Hay et al. (1985a), Kumada et al. (1981), and Goldstein et al. (1982). Goldstein et al. (1982) observed larger increases of Sh between injection holes on a flat plate. The present data show that the region downstream of each hole, where the injected flow has a relatively large effect, increases with increasing blowing rate, but is generally limited to the front portion of the cylinder. At $y/d < 0.5$, the spanwise pressure gradients, created by the endwall boundary layer in the cylinder's front stagnation region, divert the jets of the lower injection hole toward the tunnel wall.

Figure 3 shows angular variations of Sh at selected spanwise distances from the center of an injection hole located far from the endwall for $\alpha_i = 37$ deg, $M = 0.50$, and $\theta_{inj} = 10$ deg. The circumferential Sh distribution measured over a cylinder with no injection holes is also shown in this figure. The spanwise distance from the hole's center is denoted by y'. The location of a given y' with respect to the injection hole is shown in the inset at the top right corner of Fig. 3. Immediately downstream of the hole's centerline ($y'/D = 0$), Sh is more than three times its value without injection. As y'/D and/or θ increase, Sh decreases sharply. Figures 2 and 3 show that Sherwood number values measured upstream of an injection hole's centerline and on the opposite side of the cylinder symmetry line are nearly unaffected by the injection jets; the mass transfer pattern in these regions is similar to that measured by Karni (1985) over a cylinder with no injection holes.

Variations of spanwise average Sherwood number, $\overline{Sh}_{sp}$, around the cylinder for $\alpha_i = 37$ deg are presented in Fig. 4. The Sh distribution obtained far from the endwall on a cylinder with no injection holes is also shown in this figure. The spanwise-averaged coefficients confirm the trends seen in Figs. 2 and 3 (local Sh distributions). Maximum Sh values showing an increase of 2–3 times over the mass transfer without injection are observed immediately downstream of the injection holes. In the region most influenced by injection

Downloaded 01 Jun 2010 to 171.66.16.66. Redistribution subject to ASME license or copyright; see http://www.asme.org/terms/Terms_Use.cfm

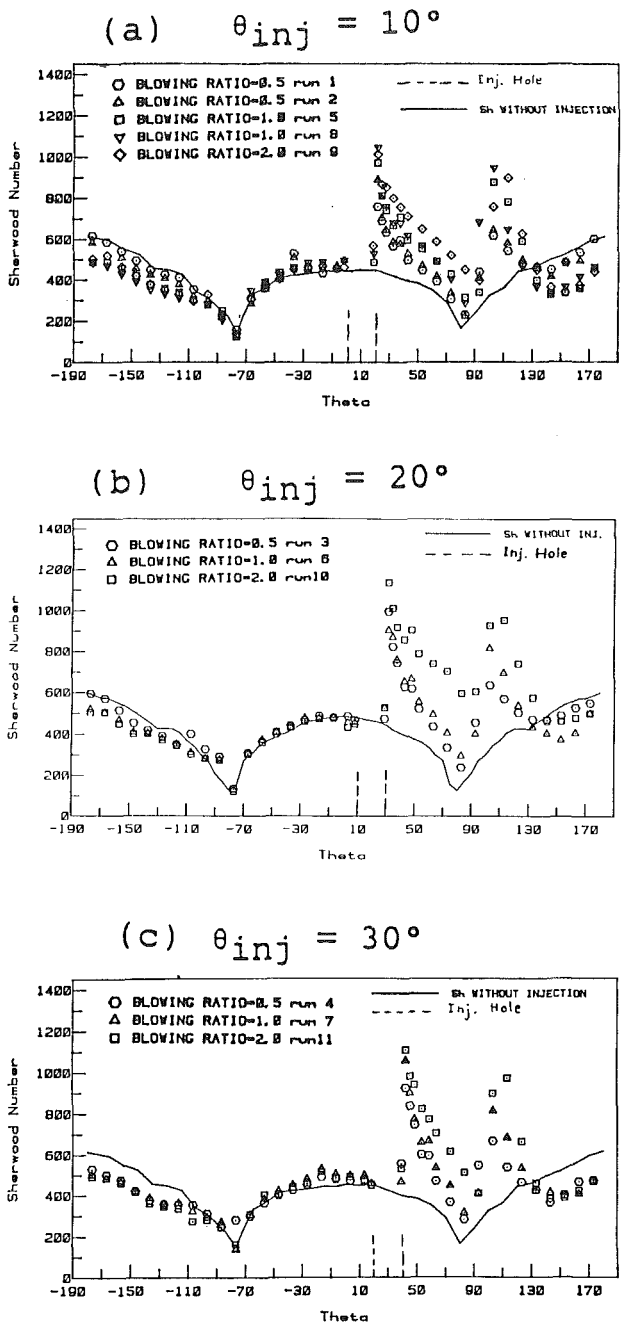

Fig. 4 Spanwise-averaged Sherwood number ($\overline{Sh}_{sp}$) distribution for streamwise injection: $\alpha_i = 37$ deg; $\beta_i = 90$ deg; s/D = 3

($\theta_{inj} < \theta < 120$ deg), $\overline{Sh}_{sp}$ values located immediately downstream of injection fall sharply as θ increases, reaching a minimum near the laminar boundary layer separation angle ($\theta \approx 80$–90 deg); a second peak is observed at $\theta = 110$–120 deg. At 80 deg $< \theta <$ 180 deg, $\overline{Sh}_{sp}$ has a pattern similar to a Nu (Sh) distribution over an impermeable circular cylinder at critical and supercritical Re_d (Schmidt and Wenner, 1941; Giedt, 1949; Achenbach, 1975; Sogin and Subramanian, 1961). At high Reynolds numbers ($Re_d > 2 \times 10^5$), the downstream portion of the cylinder boundary layer becomes turbulent, producing a sharp increase of heat (mass) transfer, and the separation angle is between 110 and 150 deg. It is possible that the additional momentum supplied by the jets causes a delay in the boundary layer separation, and over some portions of the cylinder span a transitional or turbulent boundary layer exists at $\theta \approx 90$–130 deg.

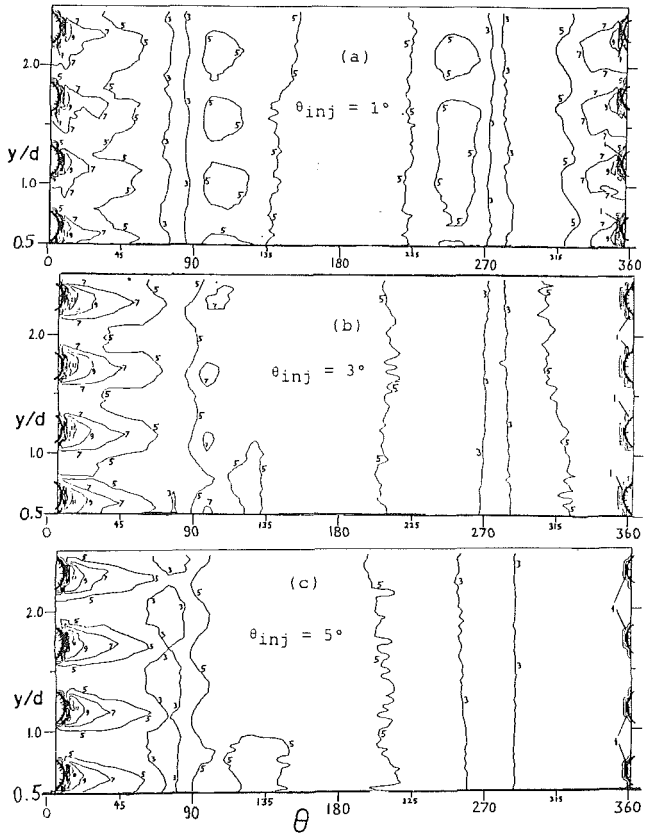

Fig. 5 Sh distribution for spanwise injection; contours of Sh × 10^{-2}, $M = 0.50$; $\alpha_i = 90$; $\beta_i = 20$ deg; s/D = 6

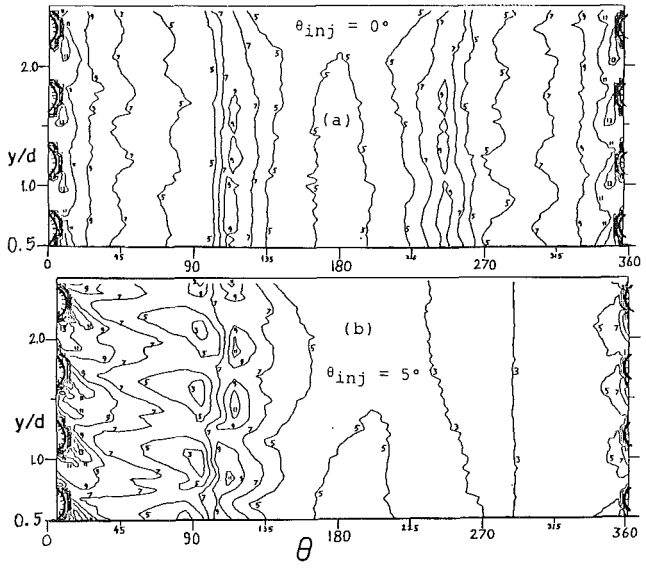

Fig. 6 Sh distribution for spanwise injection; contours of Sh × 10^{-2}, $M = 2.00$; $\alpha_i = 90$; $\beta_i = 20$ deg; s/D = 6

Figure 4 shows that on the side of the cylinder where no injection is employed ($\theta < 0$ deg) $\overline{Sh}_{sp}$ is similar to the impermeable wall coefficient over the front of the cylinder; but, for $M = 1.0$ and 2.0, $\overline{Sh}_{sp}$ is somewhat lower than this coefficient in the wake region. At $\theta_{inj} = 30$ deg, relatively low $\overline{Sh}_{sp}$ values are obtained in the wake for $M = 0.5$ as well. This may be caused by the jets' interference with the characteristic wake pattern of alternating vortex shedding. Note that similar reductions of heat (and mass) transfer were measured in the

Downloaded 01 Jun 2010 to 171.66.16.66. Redistribution subject to ASME license or copyright; see http://www.asme.org/terms/Terms_Use.cfm

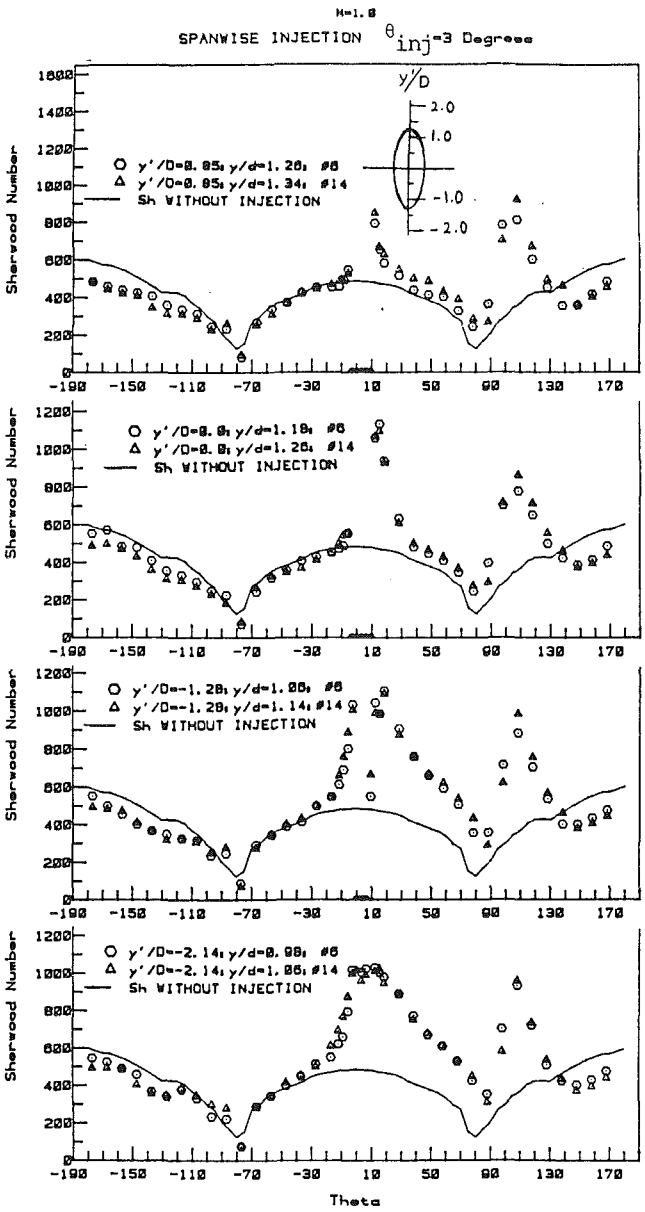

Fig. 7 Angular variatons of Sh at selected spanwise distance from the center of an injection hole; $M = 0.99$; $\beta_i = 20$ deg; $\theta_{inj} = 3$ deg

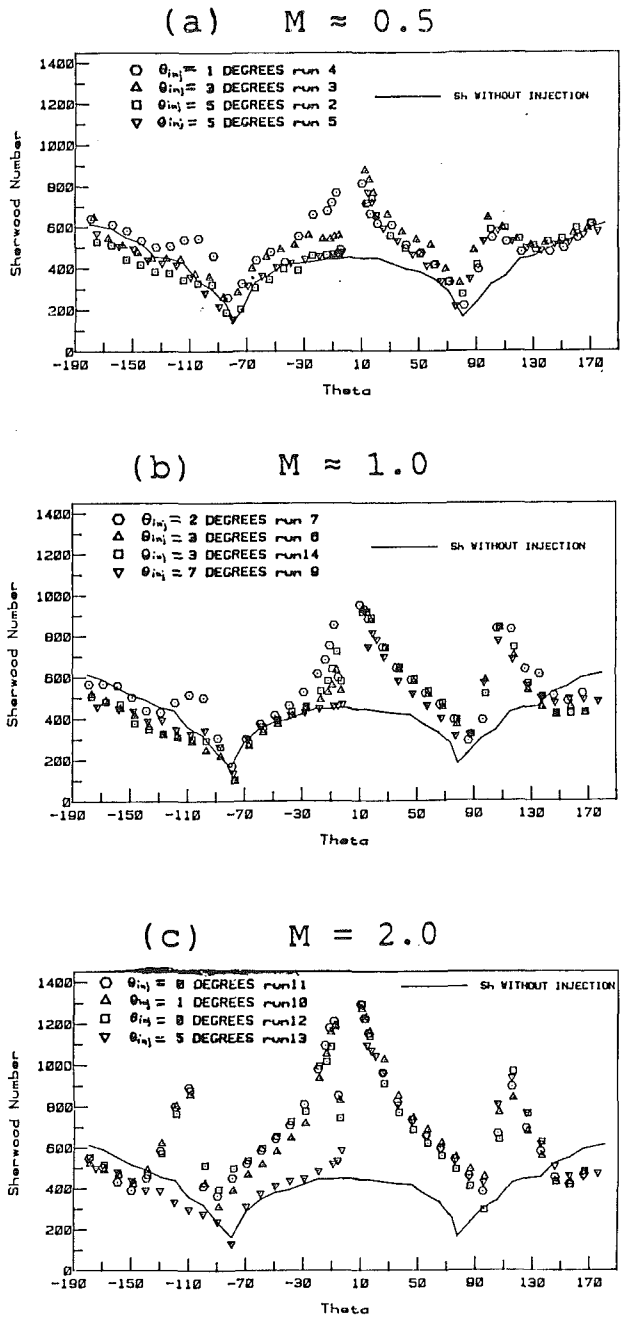

Fig. 8 Spanwise average Sherwood number distribution for spanwise injection; $\alpha_i = 90$ deg; $\beta_i = 20$ deg; $s/D = 6$

wake of a smooth impermeable cylinder exposed to a mainstream with high turbulent intensity (Kestin and Wood, 1971; Lowery and Vachon, 1975), and when a splitter plate was installed at $\theta = 180$ deg (Hiwada et al., 1979).

II Spanwise Injection. The investigation of spanwise injection focuses on the influence of small variations in θ_{inj} near the cylinder front stagnation line at different blowing rates. As in Fig. 2 all computer-drawn contour plots (Figs. 5 and 6) are prepared via interpolations of the actual measurements. The injection holes (which, in these figures, are divided into two parts) are indicated by the shaded regions near the left and right boundaries of the figures. Note that the injected jets are directed toward the endwall.

Sherwood number distributions for an injection angle β_i of 20 deg, a blowing rate M of about 0.5, and injection locations θ_{inj} of 1, 3, and 5 deg are presented in Figs. 5(a), 5(b), and 5(c), respectively. Note that based on their inner diameter, the maximum angular range of the holes is about 10 deg ($\theta_{inj} \pm 5$ deg); thus, at $\theta_{inj} = 5$ deg, the injection holes are entirely on one side of the cylinder stagnation line. A nearly symmetric (around $\theta = 0$) Sh distribution is seen in Fig. 5(a) ($\theta_{inj} = 1$); as θ_{inj} increases to 3 deg [Fig. 5(b)] and to 5 deg [Fig 5(c)], the injection effects become skewed. Although the jets are injected with a relatively large spanwise velocity component ($\beta_i = 20$ deg) and a zero streamwise component ($\alpha_i = 90$ deg), they appear to be turned downstream by the main flow immediately upon their entry when $\theta_{inj} = 3$ or 5 deg [Figs. 5(b) and 5(c)]. Consequently the mass transfer pattern approaches somewhat that observed with streamwise injection (Fig. 2). Mick and Mayle (1988) observed a similar pattern while employing two rows of injection holes at $\beta_i = 30$ deg and $\theta_{inj} = 15$ and 44 deg. In Figs. 5(a, b, c) low transfer coefficients are seen along the cylinder span at $\theta \approx 80$ deg, and local Sh peaks are detected at $\theta \approx 100$ to 110 deg.

Sherwood number distributions for $\beta_i = 20$ deg, $M \approx 2.0$, and $\theta_{inj} = 0$ and 5 deg are presented in Figs. 6(a) and 6(b),

Downloaded 01 Jun 2010 to 171.66.16.66. Redistribution subject to ASME license or copyright; see http://www.asme.org/terms/Terms_Use.cfm

respectively. A symmettric Sh distribution is seen over both sides of the cylinder stagnation line for $\theta_{inj} = 0$ deg [Fig. 6(*a*)], but the Sh distribution is quite skewed at $\theta_{inj} = 5$ deg [Fig. 6(*b*)]. However, at $M = 2.0$ and $\theta_{inj} = 5$ deg [Fig. 6(*b*)] the jet trajectories retain a larger downward spanwise component after entering the main flow than do their counterparts at $M = 0.5$ [Fig. 5(*c*)]. The skewed distribution obtained at all blowing rates when $\theta_{inj} \geq 5$ deg probably result from the entire hole cross section being located on one side of the cylinder front stagnation line. Thus, the other side of this line is unaffected by injection at $M = 0.5$ and 1.0, and only modest increases over a small region are seen at $M = 2.0$. For $M \approx 2.0$ (Fig. 6), relatively low Sh values are detected at $\theta = 90$–100 deg, and local highs are seen at $\theta = 100$–115 deg. Especially large Sh variations occur at 80 deg $< \theta <$ 120 deg when $\theta_{inj} = 5$ deg is employed [Fig. 6(*b*)].

Figure 7 shows angular variations of Sh at selected spanwise distances from the center of an injection hole located far from the endwall for $M \approx 1.0$, $\beta_i = 20$ deg, and $\theta_{inj} = 3$ deg. The relation between the distance from the hole's center (y') and the injection hole is shown in the inset at the top of the figure. These data show that as the downward distance from the hole's center increases, the injection effect increases on both sides of the hole. Maximum Sh values of about 2.5 times that without injection are observed adjacent to the holes and just below them.

Spanwise average Sherwood number ($\overline{Sh}_{sp}$) values are presented in Fig. 8. The circumferential Sh distribution obtained far from the endwall on a cylinder with no injection holes is also shown in these figures. The spanwise-averaged coefficients show some of the trends seen in Figs. 5–7 (local Sh distributions). The Sh peaks near the injection holes increase with the blowing rate and are 2–3 times the Sh value without injection. For a given blowing rate, $\overline{Sh}_{sp}$ on the side of the cylinder's stagnation line opposite to injection (in the angular range -130 deg $< \theta < 0$ deg) drops sharply as θ_{inj} increases (approaching the distribution on a cylinder without injection), whereas $\overline{Sh}_{sp}$ values on the injection side (at $\theta_{inj} < \theta < 130$ deg) are nearly unaffected by changes in the injection location. The last observation is surprising, considering the great influence of small θ_{inj} variations on local Sh distribution (Figs. 5 and 6) and the fact that the bulk mass flow over the injection side increases as θ_{inj} increases while the bulk flow over the other side decreases. For $\theta_{inj} = 5$–7 deg, the $\overline{Sh}_{sp}$ values on the side opposite to injection closely follow the impermeable wall distribution in the angular range -90 deg $< \theta < 0$ deg (Fig. 8). The average coefficients on the injection side (or both sides for 0 deg $\leq \theta_{inj} \leq 3$ deg) peak immediately downstream of injection and fall sharply as θ increases. A minimum $\overline{Sh}_{sp}$ is reached between $\theta = 80$ deg and $\theta = 100$ deg, depending on blowing rate. A second peak is observed at $\theta = 100$–120 deg, and farther downstream, $\overline{Sh}_{sp}$ decreases, approaching values comparable to those obtained without injection. Similar to average coefficients for streamwise injection (Fig. 4), the Sh_{sp} distribution at 90 deg $< \theta <$ 180 deg for spanwise injection (Fig. 8) resembles a circumferential distribution over the rear portion of an impermeable cylinder at critical and supercritical Re_d (Schmidt et al., 1941; Giedt, 1949; Achenbach, 1975; Sogin et al., 1961). For all injection locations, at $M = 2.0$, $\overline{Sh}_{sp}$ values in the downstream portion of the wake ($\theta = 180 \pm 50$ deg) are lower than the Sh measurements without injection [Fig. 8(*c*)]. This is also true at lower blowing ratios when $\theta_{inj} \geq 3$ deg [Figs. 8(*a*) and 8(*b*)]. Local Sh data in Fig. 7 show the same trend in the wake as that mentioned above; it may result from the fact that the injected jets interfere with the symmetric vortex shedding pattern, which is characteristic of a cylinder in crossflow.

III Comparison of Results. Figure 9 presents spanwise-averaged Sherwood number ($\overline{Sh}_{sp}$) distributions for streamwise and spanwise injection at $M \approx 1.0$ and $\theta_{inj} = 10$ and 7 deg,

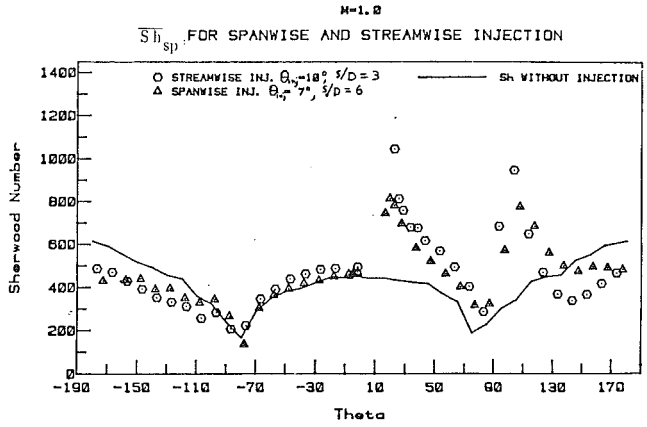

Fig. 9 Comparison of $\overline{Sh}_{sp}$ for streamwise and spanwise injection; $M \approx 1.0$; $\theta_{inj} = 7$–10 deg

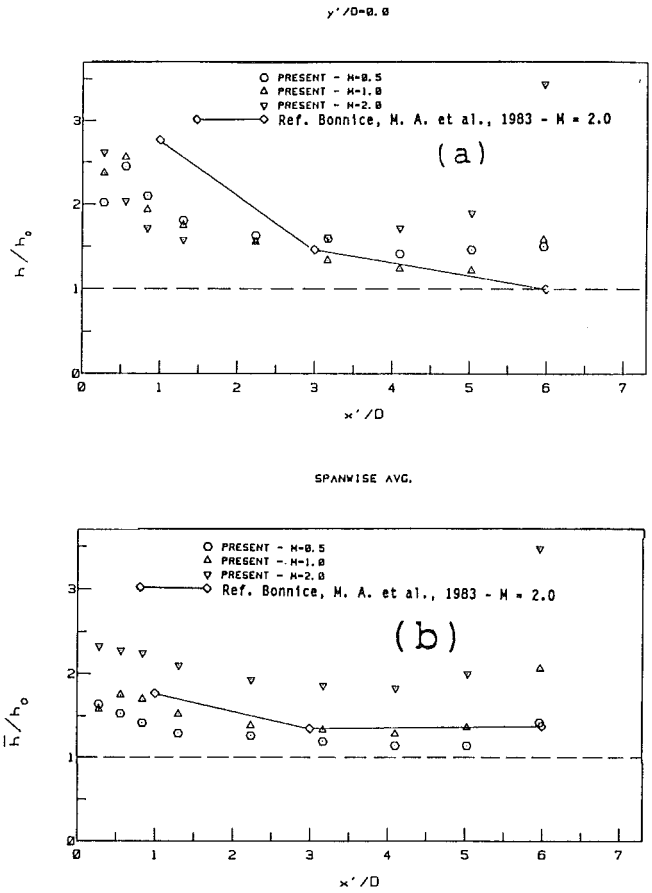

Fig. 10 (*a*) Comparison of local mass transfer downstream of a spanwise injection hole with extrapolated data from Bonnice et al. (1983); $y'D = 0.0$; $\theta_{inj} = 5$–7 deg; (*b*) comparison of $\overline{Sh}_{sp}$ for spanwise injection with extrapolated data from Bonnice et al. (1983); $\theta_{inj} = 5$–7 deg

respectively. The $\overline{Sh}_{sp}$ distributions obtained with the two injection geometries are similar despite the fact that at a given blowing rate, the total injected mass flow for streamwise injection ($s/D = 3$; 13 holes) is nearly twice that of spanwise injection ($s/D = 6$; 7 holes).

Heat transfer measurements over a film-cooled circular cylinder were conducted by Bonnice and L'Ecuyer (1983). A comparison between their data and present results for spanwise injection at similar geometry is given in Figs. 10(*a*) and 10(*b*). Figure 10(*a*) shows local h/h_o values directly downstream of an injection hole ($y'/D = 0$). Figure 10(*b*)

Downloaded 01 Jun 2010 to 171.66.16.66. Redistribution subject to ASME license or copyright; see http://www.asme.org/terms/Terms_Use.cfm

Table 2 Spanwise injection geometry for data shown in Fig. 12

	Cylinder diameter, mm	Injection tube diameter, mm	s/D	s/D	β_i, deg	θ_{inj}, deg	θ^*
Present	63.5	5.95	10.67	6	20	5, 7	0
Bonnice and L'Ecuyer (1983)	150	4.76	31.5	5	25	5	1.03 1.29

shows spanwise-averaged h/h_o values. Table 2 details the geometry used in both studies to obtain the data shown in these figures.

The linear extrapolation approach, commonly used to approximate h_o' ($=h_H$) values from h' measurements at θ^* larger than zero (Choe et al., 1974; Metzger et al., 1971; Miller et al., 1984; Ligrani et al., 1985), is used to obtain h_o'/h' from the data of Bonnice and L'Ecuyer (1983). Note that only the two (relatively close) θ^* values of 1.03 and 1.29 were used by Bonnice and L'Ecuyer (1983). Thus, the extrapolated h_o'/h' values may be inaccurate. (Any error in the measurements or the calculations is magnified by a factor of about 4.0 when h' values at $\theta^* = 1.03$ and 1.29 are extrapolated to give h_o'.)

As shown in Table 2, the main difference between the present injection geometry and that of Bonnice and L'Ecuyer (1983) is the ratio of cylinder to injection hole diameter, d/D. Thus, for a given x'/D, their data points are, in fact, at a much smaller angular distance θ_{inj} than present data. This may account for the somewhat different h/h_o patterns obtained in the two studies at $y'/D=0.0$ [Fig. 10(a)]. The fact that larger injection holes are used in the present study implies that, at a given blowing rate, the total injected mass flow in present tests is higher than that of Bonnice and L'Ecuyer (1983). Thus, their average values $\bar{h}/h_o$ at $M=2.0$ agree better with present data at $M=1.0$ than at $M=2.0$ [Fig. 10(b)].

Conclusions

Several surface injection parameters affecting mass transfer from a circular cylinder (or a turbine vane leading edge) have been investigated. The following conclusions may be drawn from the results obtained with spanwise and streamwise injection holes at angular locations of 0 to 7 deg and 10 to 30 deg from stagnation, respectively, and at blowing rates of 0.5 to 2.0.

(a) The injected jets produce large Sh values and steep local gradients downstream of the *streamwise* injection holes while a relatively small increase in Sh is detected between the holes. A somewhat similar periodic pattern, corresponding to individual jet trajectories, is also observed for *spanwise* injection when the holes are located entirely on one side of the cylinder stagnation line (i.e., $\theta_{inj} \geq 5$ deg). For such geometries, the injection effects on the opposite side of the stagnation line are relatively very small.

(b) For *streamwise* injection, the size of the region directly downstream of each hole, where high Sh values are found, increases with M and decreases as the injection is shifted downstream (i.e., as θ_{inj} increases).

(c) The local mass transfer distribution for *spanwise* injection near the stagnation line is extremely sensitive to small variations in θ_{inj}. Nearly symmetric Sh distributions are obtained for $\theta_{inj}=0$–1 deg, but for θ_{inj} of 3 deg or higher, the injection effects become very skewed. Despite that, the spanwise-averaged coefficients over the side of the stagnation line where injection is employed vary little with θ_{inj}. $\overline{Sh}_{sp}$ does, however, approach values measured over a cylinder without injection on the other side of the symmetry line as θ_{inj} increases.

(d) For both streamwise and spanwise injections, Sh values generally decrease with downstream distance from injection, reaching a minimum at $\theta=80$–100 deg. Farther downstream, local peaks are observed at $\theta=100$–120 deg. This trend could result from a boundary layer transition to turbulence, which may occur over portions of the cylinder span at $\theta=80$–90 deg.

(e) Mass transfer values lower than those obtained with a uniform cylinder are observed in the downstream portion of the wake ($\theta=180\pm50$ deg) for 50 deg) for *streamwise* injection at $M=1.0$ and 2.0. A similar pattern is seen with *spanwise* injection at $M=2.0$ and, if θ_{inj} is between 3 and 7 deg, at $M=1.0$, also. This trend is probably due to the injected jets interfering with the characteristic wake pattern of alternate vortex shedding.

(f) Downstream of injection, the spanwise-averaged Sherwood number generally increases with blowing rate.

References

Achenbach, E., 1975, "Total and Local Heat Transfer From a Smooth Circular Cylinder in Cross-flow at High Reynolds Number," *Int. J. Heat Mass Transfer*, Vol. 18, pp. 1387–1396.

Ambrose, D., Lawrenson, I. J., and Sprake, C. H. S., 1975, "The Vapor Pressure of Naphthalene," *J. Chemical Thermodynamics*, Vol. 7, pp. 1173–1176.

Bonnice, M. A., and L'Ecuyer, M. R., 1983, "Stagnation Region Gas Film Cooling—Effects of Dimensionless Coolant Temperature," NASA CR-168197.

Chen, P. H., 1988, "Measurement of Local Mass Transfer From a Gas Turbine Blade," Ph.D. Thesis, University of Minnesota, Jan.

Cho, K., 1989, "Measurement of the Diffusion Coefficient of Naphthalene Into Air," Ph.D. Thesis, State University of New York at Stony Brook.

Choe, H., Kays, W. M., and Moffat, R. J., 1974, "The Superposition Approach to Film Cooling," ASME Paper No. 74-WA/HT-27.

Eckert, E. R. G., 1983, "Analysis of Film Cooling and Full Coverage Film Cooling of Gas Turbine Blades," ASME Paper No. 83-GTJ-2.

Eckert, E. R. G., Goldstein, R. J., and Pedersen, D. R., 1971, "Comment on 'Evaluation of Heat Transfer for Film-Cooled Turbine Components,' " *J. Aircraft*, Vol. 8, pp. 63–64.

Eriksen, V. L., and Goldstein, R. J., 1974, "Heat Transfer and Film Cooling Following Injection Through Inclined Circular Tubes," ASME *Journal of Heat Transfer*, Vol. 86, pp. XX–XX.

Giedt, W. H., 1949, "Investigation of Variation of Point Unit Heat Transfer Coefficient Around a Cylinder Normal to an Air Stream," *Trans. ASME*, Vol. 71, pp. 375–381.

Goldstein, R. J., 1971, "Film Cooling," in: *Advances in Heat Transfer*, Vol. 7, pp. 321–379.

Goldstein, R. J., and Taylor, J. R., 1982, "Mass Transfer in the Neighborhood of Jets Entering a Crossflow," ASME *Journal of Heat Transfer*, Vol. 104, pp. 715–721.

Hanus, G. J., and L'Ecuyer, M. R., 1977, "Leading-Edge Injection for Film Cooling of Turbine Vanes," *AIAA Journal of Energy*, Vol. 1, No. 1, pp. 44–49.

Hartnett, J. P., Birkebak, R. C., and Eckert, E. R. G., 1961a, "Effectiveness and Heat Transfer in Cooling of a Surface With a Pressure Gradient," in: *International Developments in Heat Transfer*, ASME, New York, Part IV, pp. 682–689.

Hartnett, J. P., Birkebak, R. C., and Eckert, E. R. G., 1961b, "Velocity Distributions, Temperature Distributions, Effectiveness and Heat Transfer for Air Injected Through a Tangential Slot Into a Turbulent Boundary Layer," ASME *Journal of Heat Transfer*, Vol. 83, pp. 293–306.

Hay, N., Lampard D., and Saluja, C. L., 1985a, "Effects of Cooling Fluids on the Heat Transfer Coefficient on a Flat Plate With Zero Mainstream Pressure Gradient," ASME *Journal of Engineering for Gas Turbines and Power*, Vol. 107, pp. 105–110.

Hay, N., Lampard, D., and Saluja, C. L., 1985b, "Effects of the Condition of the Approach Boundary Layer and of Mainstream Pressure Gradients on the Heat Transfer Coefficient on Film-Cooled Surfaces," ASME *Journal of Engineering for Gas Turbines and Power*, Vol. 107, pp. 99–104.

Hiwada, M., Niwa, K., Kumada, M., and Mabuchi, I., 1979, "Effects of Tunnel Blockage on Local Mass Transfer From a Circular Cylinder in Cross Flow," *Heat Transfer—Japanese Research*, Vol. 8, No. 3, pp. 37–51.

Downloaded 01 Jun 2010 to 171.66.16.66. Redistribution subject to ASME license or copyright; see http://www.asme.org/terms/Terms_Use.cfm

Jabbari, M. Y., and Goldstein, R. J., 1978, "Adiabatic Wall Temperature and Heat Transfer Downstream of Injection Through Two Rows of Holes," ASME *Journal of Engineering for Power*, Vol. 100, pp. 303–307.

Karni, J., 1985, "Endwall Boundary Layer, Cylinder Diameter, Reynolds Number and Surface Injection Effects on Local Mass Transfer From a Cylinder in Crossflow," Ph.D. Thesis, University of Minnesota.

Kear, B. H., 1986, "Advanced Metals," *Scientific American*, Vol. 255, No. 4, pp. 158–167.

Kestin, J., and Wood, R. T., 1971, "The Influence of Turbulence on Mass Transfer From Cylinders," ASME *Journal of Heat Transfer*, Vol. 93, pp. 321–327.

Kumada, M., Hirata, M., and Kasagi, N., 1981, "Studies of Full-Coverage Film Cooling, Part 2: Measurement of Local Heat Transfer Coefficient," ASME Paper No. 81-GT-38.

Lander, R. D., Fish, R. W., and Suo, M., 1972, "External Heat Transfer Distribution on Film Cooled Turbine Vanes," *J. Aircraft*, Vol. 9, No. 10, pp. 707–714.

Liess, C., 1975, "Experimental Investigation of Film Cooling With Ejection From a Row of Holes for the Application to Gas Turbine Blades," ASME *Journal of Engineering for Power*, Vol. 97, pp. 21–27.

Ligrani, P. M., and Camci, C., 1985, "Adiabatic Film Cooling Effectiveness From Heat Transfer Measurements in Compressible, Variable-Properties Flow," ASME *Journal of Heat Transfer*, Vol. 107, pp. 313–320.

Ligrani, P. M., and Breugelmans, F. A. E., 1981, "Turbine Blade Cooling Research at the von Karman Institute for Fluid Dynamics," presented at the Fifth International Symposium on Air Breathing Engines, Bangalore, India, Feb.

Lowery, G. W., and Vachon, R. I., 1975, "The Effect of Turbulence on Heat Transfer From Heated Cylinders," *Int. J. Heat Mass Transfer*, Vol. 18, pp. 1229–1242.

Luckey, D. W., Winstanley, D. K., Hanus, G. J., and L'Ecuyer, M. R., 1977, "Stagnation Region Gas Film Cooling for Turbine Blade Leading-Edge Applications," *AIAA Journal of Aircraft*, Vol. 14, No. 5, pp. 494–501.

Luckey, D. W., and L'Ecuyer, M. R., 1981, "Stagnation Region Gas Film Cooling—Spanwise Angled Injection From Multiple Rows of Holes," NASA CR-165333.

Mayle, R. E., and Camarata, F. J., 1975, "Multihole Cooling Film Effectiveness and Heat Transfer," ASME *Journal of Heat Transfer*, Vol. 97, pp. 534–538.

Metzger, D. E., 1983, "Developments in Air Cooling of Gas Turbine Vanes and Blades," ASME Paper No. 83-GT-160.

Metzger, D. E., Carper, H. J., and Swank, L. R., 1968, "Heat Transfer With Film Cooling Near Nontangential Injection Slots," ASME *Journal of Engineering for Power*, Vol. 90, pp. 157–163.

Metzger, D. E., and Fletcher, D. D., 1971, "Evaluation of Heat Transfer for Film-Cooled Turbine Components," *J. Aircraft*, Vol. 8, pp. 33–38.

Metzger, D. E., Kuenstler, P. A., and Takeuchi, D. I., 1976, "Heat Transfer With Film Cooling Within and Downstream of One to Four Rows of Normal Injection Holes," ASME Paper No. 76-GT-83.

Mick, W. J., and Mayle, R. E., 1988, "Stagnation Film Cooling and Heat Transfer, Including Its Effect Within the Hole Pattern," ASME JOURNAL OF TURBOMACHINERY, Vol. 110, pp. 66–72.

Miller, K. L., and Crawford, M. E., 1984, "Numerical Simulation of Single, Double and Multiple Row Film Cooling Effectiveness and Heat Transfer," ASME Paper No. 84-GT-112.

Schmidt, E., and Wenner, K., 1941, "Warmeabgabe uber den Umfang eines angeblasenen geheizten Zylinders," *Forschung. Geb. Ingwes.*, Vol. 12, No. 12, pp. 65–73.

Sogin, H. H., 1958, "Sublimation From Disks to Air Streams Flowing Normal to Their Surfaces," *Trans. ASME*, Vol. 80, pp. 61–71.

Sogin, H., and Subramanian, V. S., 1961, "Local Mass Transfer From Circular Cylinders in Cross Flow," ASME *Journal of Heat Transfer*, Vol. 83, pp. 483–493.

Downloaded 01 Jun 2010 to 171.66.16.66. Redistribution subject to ASME license or copyright; see http://www.asme.org/terms/Terms_Use.cfm

Effects of an Embedded Vortex on Injectant From a Single Film-Cooling Hole in a Turbulent Boundary Layer

P. M. Ligrani
Associate Professor.

W. Williams
Graduate Student.

Department of Mechanical Engineering,
Naval Postgraduate School,
Monterey, CA 93943-5000

Effects of embedded longitudinal vortices on heat transfer in turbulent boundary layers with injection from a single film-cooling hole are described. These results were obtained at a free-stream velocity of 10 m/s, with a film-cooling hole inclined 30 deg to the horizontal and a blowing ratio of about 0.50. The ratio of vortex core diameter to injection hole diameter was 1.58, and the ratio of circulation to injection velocity time hole diameter was about 3.16. Coolant distributions and spatially resolved heat transfer measurements indicate that injection hole centerlines must be at least 2.9–3.4 vortex core diameters away from the vortex center in the lateral direction to avoid significant alterations to wall heat transfer and distributions of film coolant. Under these circumstances, protection from film cooling is evident at least up to 55 hole diameters downstream of injection. When the injection hole is closer to the vortex center, secondary flows convect most injectant into the vortex upwash and thermal protection from film cooling is destroyed for streamwise locations from the injection hole greater than 17.5 hole diameters.

Introduction

Film cooling is used as a means to protect surfaces from the thermal loading that results from exposure to hot gases. However, distributions of coolant and the resulting thermal protection are often disturbed by secondary flows. This is especially true for turbine passages. Here embedded vortices, in particular, cause perturbations that often lead to local hot spots at locations where film cooling would ordinarily be expected to provide adequate protection, and where protection is most needed. Such vortices originate from the centrifugal instability resulting from concave curvature, as well as from local pressure gradients, which exist at locations such as the intersection between the blade and endwall.

Studies of the interactions between embedded vortices and wall injection for gas turbine application are relatively scarce. One of the earliest is reported by Blair (1974), who measured heat transfer on an endwall film cooled using a slot inclined at a 30-deg angle. The large vortex located in the corner between the endwall and the suction surface of their cascade was believed to cause significant variations of measured heat transfer and film cooling effectiveness. Experimental studies on the influence of the endwall on film cooling from blades using one and two rows of injection holes were performed by Goldstein and Chen (1985, 1987). These investigators found a triangular region on the convex side of the blade where coolant is swept away from the surface by the passage vortex. In contrast, the concave side was not significantly affected by secondary flows originating near the endwall. Additional heat transfer and film cooling effectiveness results from an endwall and airfoil within an annular low aspect ratio cascade are presented by Sato et al. (1987).

Of work near concave surfaces with injection, Kobayashi (1972, 1975) examined the effects of blowing and suction and how they affected the onset of longitudinal vortices in laminar boundary layers. Results showed that suction increases the stability of laminar boundary layers to centrifugal instabilities, whereas blowing had little influence on the instability. El-Hady and Verma (1984) showed that the overall effect of suction or cooling was to stabilize boundary layers by reducing the amplitude ratio of the vortices. Honami and Fukagawa (1987) present velocity, temperature, and film effectiveness measured downstream of rows of holes in turbulent flow near flat and concave surfaces. For a blowing ratio of 0.47, concave curvature causes little change in film effectiveness when lateral injection is employed and a significant decrease with streamwise injection. Schwarz and Goldstein (1989) measured local film effectiveness from a row of film cooling jets in turbulent flows near concave surfaces. The authors found that lateral mixing between jets is enhanced as a result of Taylor–Görtler cells at a blowing ratio of 0.4. For m values of 0.8 and 1.6, this mixing and the lateral sway of jets becomes less.

Ligrani et al. (1989) examined the influences of embedded longitudinal vortices on film cooling from a row of holes in

Contributed by the International Gas Turbine Institute and presented at the 34th International Gas Turbine and Aeroengine Congress and Exhibition, Toronto, Ontario, Canada, June 4–8, 1989. Manuscript received at ASME Headquarters January 27, 1989. Paper No. 89-GT-189.

Copyright © 1990 by ASME
Downloaded 01 Jun 2010 to 171.66.16.66. Redistribution subject to ASME license or copyright; see http://www.asme.org/terms/Terms_Use.cfm

turbulent boundary layers. The investigators present surface heat transfer distributions, mean velocities, and mean temperatures, which show that film coolant is greatly disturbed and local Stanton numbers are altered significantly by the secondary flows within the vortices. Because the character of these secondary flows changes around the vortex, the spanwise position of the vortex with respect to film-cooling holes is very important. In addition, secondary heat transfer peaks associated with regions of high streamwise velocity exist, which become higher in magnitude and more persistent with downstream distance as the blowing ratio increases from 0.47 to 1.26.

The present study is intended to provide additional understanding of the complex events that occur when longitudinal vortices disturb injectant from film cooling holes. The study is different from other ones where one or two rows of holes are used (Goldstein and Chen, 1985, 1987; Ligrani et al., 1988, 1989; Schwarz and Goldstein, 1989), since only one film-cooling hole is employed. Consequently, the interaction between the vortex and injection is clearer because interactions with injectant from neighboring injection holes are not present. Attention is focused on heat transfer and film-coolant distributions. In particular, the influence of spanwise vortex position with respect to the injection location is investigated for a constant blowing ratio of approximately 0.50. In order to isolate the influence of the vortex only, tests are conducted on a flat plate in a zero pressure gradient. Because prediction of these complex flow interactions is not yet possible, experimental results such as the ones presented here offer designers the best insight into the complex interactions between wall jets and vortices. Understanding such interactions is needed as improved cooling schemes for turbine passages are designed that allow for maximum inlet temperatures and higher efficiencies.

Experimental Apparatus and Approach

The experiments were conducted in an open-circuit, subsonic wind tunnel located in the laboratories of the Department of Mechanical Engineering at the Naval Postgraduate School. This facility is the same one employed and described by Ligrani et al. (1988, 1989). A centrifugal blower is located at the upstream end, followed by a diffuser, a header containing a honeycomb and three screens, and then a 16-to-1 contraction ratio nozzle. The nozzle leads to the test section, which is a rectangular duct 3.05 m long and 0.61 m wide, with a topwall having adjustable height to permit changes in the streamwise pressure gradient.

A schematic is presented in Fig. 1 showing the locations of the vortex generator, injection hole, and heat transfer surface along the test section. The coordinate system is also included. Here, z is measured from the tunnel centerline. The leading edge of the vortex generator delta wing is 0.48 m downstream of the boundary layer trip. The injection hole is located on the centerline and inclined 30 deg with respect to the horizontal test surface. Its downstream edge is 0.60 m from the delta wing and 0.02 m upstream of the constant heat flux test surface. With the heat transfer surface at elevated temperature, an unheated starting length of 1.10 m exists. Free-stream air is maintained at ambient temperature, and thus, the direction of heat transfer is from the wall to the gas. Also labeled in Fig. 1 are the locations of thermocouple rows along the heat transfer surface.

The vortex generator consists of a half-delta wing attached to the wind tunnel floor at an angle of 18 deg with respect to the tunnel centerline. The height of the wing is 3.0 cm and the base is 7.5 cm. The design is described by Williams (1988) and Ligrani et al. (1989). This configuration produces a vortex at $x/d = 41.9$ with a circulation to free-stream velocity ratio of about -1.10 cm.

The diameter of the centerline injection hole is 0.952 cm, scaled such that δ_1/d is approximately 0.38. Nondimensional coolant temperature θ was maintained at approximately 1.5 for all tests. The injection system is described by Ligrani et al. (1989). Air originates in a 10-hp, two-stage, 150 psig Ingersoll-Rand air compressor. From a plenum chamber beneath the test surface, the injectant enters film cooling tubes, which extend to the floor of the test section. For the present study, an injection tube on the centerline was used in addition to two other tubes on each side. These two peripheral holes are required to maintain steady flow in the injection system at measurable flow rates. The vortex affects injectant only from

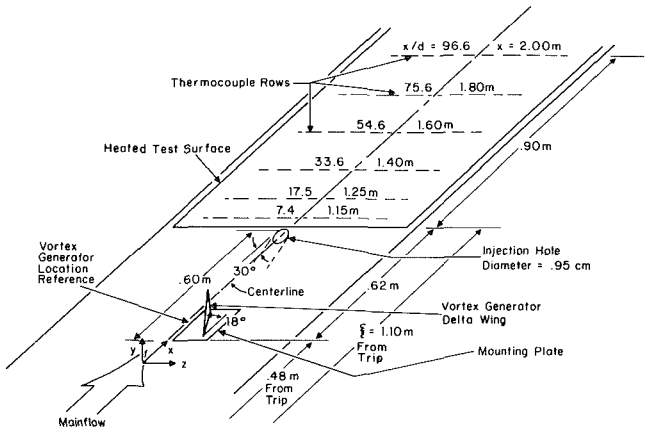

Fig. 1 Schematic of test surface including coordinate system

Nomenclature

- c = average vortex core radius in spanwise direction
- d = injection hole diameter
- h = heat transfer coefficient $= \dot{q}_w''/(T_w - T_{r\infty})$
- m = blowing ratio $= \rho_c U_c/\rho_\infty U_\infty$
- $\dot{q}''$ = heat flux
- St = Stanton number
- St_0 = baseline Stanton number, no film cooling, no vortex
- St_f = Stanton number with film cooling only
- T = temperature
- U = mean velocity
- x = downstream distance as measured from the leading edge of the boundary layer trip or from the downstream edges of injection holes when used as x/d
- y = vertical distance from the test surface upward
- z = spanwise distance from the test section centerline
- Γ = circulation of streamwise vorticity
- δ_1 = boundary layer displacement thickness
- θ = nondimensional coolant temperature $= (T_{rc} - T_{r\infty})/(T_w - T_{r\infty})$
- ξ = unheated starting length
- ρ = density

Subscripts

- c = coolant at exit of injection holes
- o = total condition
- r = recovery condition
- w = wall
- y = normal direction
- z = spanwise direction
- ∞ = free stream

Downloaded 01 Jun 2010 to 171.66.16.66. Redistribution subject to ASME license or copyright; see http://www.asme.org/terms/Terms_Use.cfm

the centerline tube; injectant from the two peripheral holes does not touch the heat transfer surface or affect the heat transfer measurements. The experimental uncertainty of the blowing ratio m, based on a 95 percent confidence level, is about 5.0 percent.

The heat transfer surface was designed and developed to provide a constant heat flux over its area. The plate is constructed so that its upward-facing part is adjacent to the wind tunnel air stream, with a thin stainless steel foil surface, 1.3 m × 0.467 m × 0.20 mm, painted flat black. Attached to the underside of the foil are 126 copper-constantan thermocouples in six rows. In each of the six rows, 21 thermocouples are located 1.27 cm apart to provide adequate spanwise resolution of temperature distributions. A thin foil heater is used to provide power to the surface. The foil within this heater is custom designed with adjacent braces sufficiently close together to maintain a uniform heat flux boundary condition. For all tests, power levels are adjusted to maintain overall temperature differences less than 30°C to minimize the influences of variable properties.

To determine the heat loss by conduction from the heat transfer test surface, an energy balance was performed. Radiation losses from the top of the test plate were estimated analytically. The thermal contact resistance between thermocouples and the foil top surface was estimated based on the outputs of the thermocouples and measurements from calibrated liquid crystals on the surface of the foil. Calibrations of the Chameleon encapsulated liquid crystals (manufactured by Appleton Papers Division of the National Cash Register Company) were made to allow foil surface temperatures to be measured within ±0.3°C by visual comparison. This uncertainty is included in the determination of overall experimental uncertainties of the Stanton number and Stanton number ratio, which are typically about 4.4 and 5.5 percent, respectively.

Calibrated copper-constantan thermocouples were used to measure the free-stream temperature and injection plenum temperature. For plate temperatures, one calibration was used for all thermocouples of similar manufacture, since their outputs were the same within one or two microvolts at any given temperature. Temperature surveys of $(T_o - T_\infty)$ were performed using two individually calibrated thermocouples, and a two-component automated traversing device. Here, T_o is the local boundary layer total temperature. As the traverse was made, one thermocouple was placed to measure the free-stream temperature as the other was traversed through the boundary layer. Two electric motors manufactured by Superior Electric Co. drove the traverse. These were controlled by a microprocessor operated by a Hewlett-Packard 9836S computer. Each survey consisted of 800 probe locations, covering an area of 12 cm × 22 cm. Free-stream and wall temperature experimental uncertainties are typically 0.13 and 0.41°C, respectively.

Measurements without a vortex and without film cooling were used to qualify the heat transfer plate and measurement procedures employed. Spanwise-averaged Stanton numbers show agreement with the empirical equation from Kays and Crawford (1980) within ±6 percent. Comparison is made for a turbulent boundary layer on a flat plate at constant free-stream velocity, constant heat flux, and an unheated starting length of 1.10 m. Additional details regarding qualification tests and measuring details are given by Ortiz (1987) and Williams (1988).

The three mean velocity components were measured using a five-hole pressure probe manufactured by United Sensors and Control Corporation. The probe was a conical-type with a diameter of 6.35 mm. Calibration results are given by Williams (1988). The probe was connected to five Celesco model LCVR differential pressure transducers, each with a range of 2.0 cm of water differential pressure. Transducer outputs were converted to d-c signals by Celesco CD-10D carrier demodulators. Voltages from the carrier demodulators and thermocouples were read by an HP-3497A Data Acquisition/Control Unit with an HP-3498A Extender. These units were controlled by a Hewlett-Packard Series 300, Model 9836S computer.

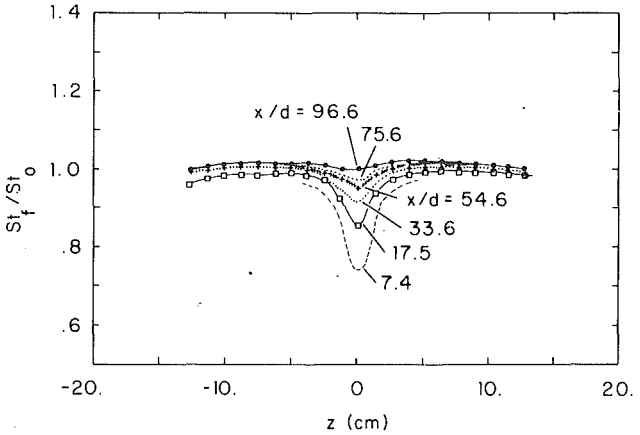

Fig. 2 Local Stanton number ratios with film cooling from a single injection hole and no vortex, $m = 0.53$

The injectant was visualized by contaminating it with atomized liquid droplets in the injecton plenum, produced by a Model 1500 Rosco Fog Machine. For these tests, plenum pressure was maintained entirely by the fog machine. Free-stream wind tunnel conditions were then set to achieve desired blowing ratios.

Boundary Layers With Film Cooling Only

Local Stanton number ratios measured with film injectant from the centerline injection hole at $m = 0.53$ are presented in Fig. 2. These are presented as a function of spanwise coordinate z at different x/d. The influence of the coolant is evident where St_f/St_0 values are non-unity. This is particularly evident for $x/d = 7.4$ where ratio values are as low as 0.75. With downstream distance, the Stanton ratios then increase, the protection provided by film cooling becomes less, and the injectant spreads in the lateral direction. These trends are consistent with Goldstein et al. (1968), who studied the behavior of film cooling from a single injection hole inclined at 35 deg. In that study, adiabatic wall temperatures and adiabatic film cooling effectiveness are used to describe local heat transfer behavior.

The results in Fig. 2 thus further qualify the experimental procedures and apparatus used to produce injection from a single hole and to measure spatially resolved heat transfer distributions.

Vortex Position With Respect to the Injection Hole

In order to investigate the effect of spanwise position of the vortex, the spanwise location of the vortex generator was changed. The four different spanwise locations used are designated b, e, h, and k, and summarized in Table 1. Figure 3 is also presented in order to illustrate the locations of centerline injection with respect to different portions of the vortex.

The secondary flow vectors shown were actually measured just downstream of the injection hole with the vortex at position e. The horizontal axis is then shifted in the figure so that injection centerline location $z = 0$ is appropriately oriented with respect to the vortex center for each of the four vortex positions. The vortex center is located at the peak of the streamwise vorticity.

Downloaded 01 Jun 2010 to 171.66.16.66. Redistribution subject to ASME license or copyright; see http://www.asme.org/terms/Terms_Use.cfm

Table 1 Spanwise locations of the vortex generator, and the vortex at the injection location

VORTEX POSITION DESIGNATION	VORTEX CENTER Z-LOCATION AT INJECTION LOCATION x/d = 0	INJECTION LOCATION WITH RESPECT TO VORTEX	VORTEX GENERATOR MOUNT Z-LOCATION
b	-6.3 cm	BENEATH DOWNWASH	-3.8
e	-2.5 cm	BENEATH DOWNWASH	0.0
h	1.3 cm	BENEATH CORE AND UPWASH	3.8
k	5.1 cm	TO SIDE OF UPWASH	7.6

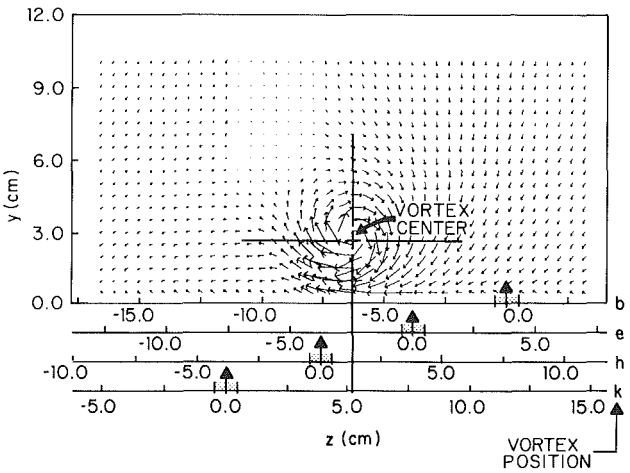

Fig. 3 Film-cooing injection locations with respect to vortex center and secondary flow vectors for vortex positions *b*, *e*, *h*, and *k*. Each horizontal scale corresponds to a different vortex position where $z = 0$ corresponds to centerlines of injection holes.

Of importance here is the location of different positions of the vortex with respect to the injection hole exit. For vortex positions *b* and *e*, the vortex center is estimated to be at $z = -6.3$ cm and $z = -2.5$ cm, respectively, at the injection location, $x/d = 0$. In both cases, injectant exits the hole beneath the vortex downwash, but each at a different part of the downwash. For vortex position *h*, the center of the vortex is located at $z = 1.3$ cm as it passes over the injection location. In this case, injectant issues just to the side of the vortex center, beneath the core and upwash. For position *k*, the coolant exits to the side of the vortex upwash when the vortex center is located at a z coordinate value of 5.1 cm.

Boundary Layers With Film Cooling and Vortex

The effects of an embedded vortex on the film-cooled boundary layer are now discussed. This presentation is made in three parts. First, vortex characteristics are discussed. Second, data are presented showing how the vortex alters and redistributes the injectant from the film cooling hole. Third, heat transfer measurements are presented and discussed. For all tests, the free-stream velocity is maintained at approximately 10 m/s and spanwise vortex locations *b*, *e*, *h*, and *k* are

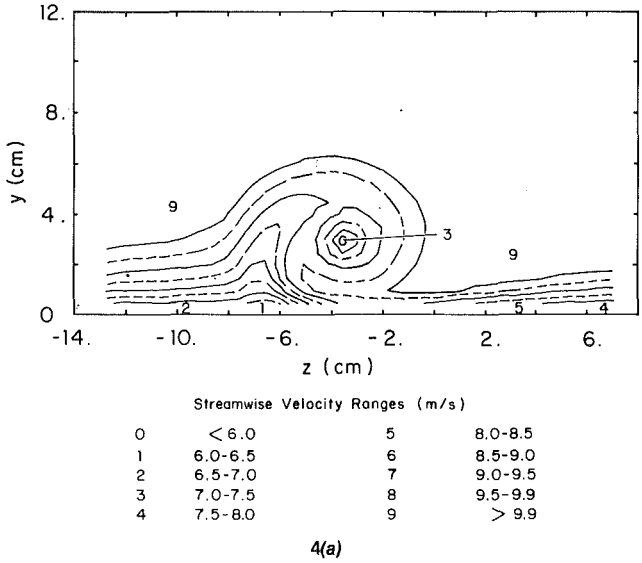

4(a)

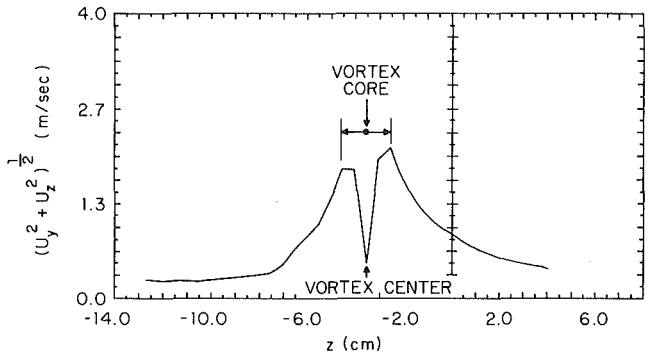

4(b)

Fig. 4 Embedded vortex characteristics at $x/d = 41.9$, $m = 0.5$, and vortex at position *e*: *(a)* streamwise velocity contours, *(b)* secondary flow velocity magnitudes at *y* location of vortex center

employed. The blowing ratio is maintained at 0.50–0.53. According to Goldstein et al. (1968), these values of m are optimal in regard to the protection provided for injection into a turbulent boundary layer from a single hole inclined at 35 deg.

Vortex Characteristics. Streamwise velocity contours measured at $x/d = 41.9$ with an embedded vortex at position *e* and injection from the centerline hole ($z = 0$ cm) are shown in Fig. 4(*a*). The vortex shows typical characteristics. For z equal to -8 cm to -5 cm a secondary flow upwash region is present, which results in the convection of low-momentum fluid away from the wall. Local boundary layer thickness is greater than its nominal two-dimensional value. The downwash region exists for a z range from -2 cm to 2 cm. Here, high-velocity free-stream fluid is brought very close to the wall, as evidenced by a very thin boundary layer. These perturbations to local boundary layer behavior by the secondary flow vectors are more responsible than any other effect for heat transfer differences from those measured in a turbulent boundary layer with a two-dimensional mean flow field. A velocity deficit is also present surrounding the vortex center, which is located at $z = -3.56$ cm and $y = 2.98$ cm. The circulation Γ of this vortex is 0.151 m^2/s, a value calculated assuming that all vorticity magnitudes less than 10 percent of the peak vorticity are zero. The ratio Γ/U_∞ is then 1.51 cm. In order to characterize vortex strength relative to injection rate and jet size, the parameter Γ/dU_c is used. For the vortex at $x/d = 41.9$, the value of this parameter is 3.16.

Downloaded 01 Jun 2010 to 171.66.16.66. Redistribution subject to ASME license or copyright; see http://www.asme.org/terms/Terms_Use.cfm

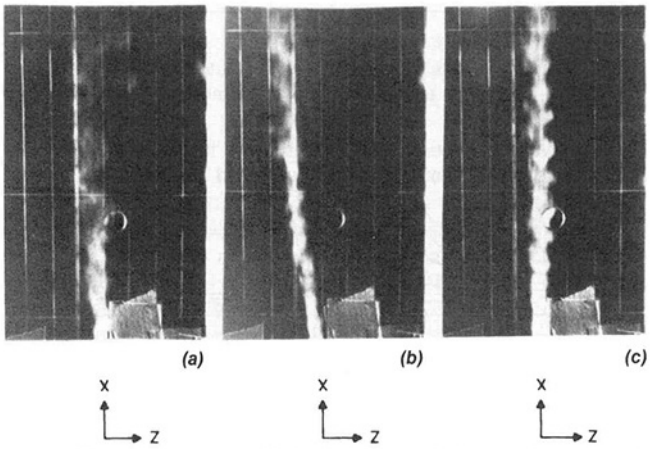

Fig. 5 Flow visualization of injectant for $m = 0.5$; free-stream flow is from top to bottom: *(c)* no vortex, *(b)* vortex at position *e*, *(a)* vortex at position *h*

The magnitudes of the secondary flow vectors $(U_y^2 + U_z^2)^{1/2}$ are plotted in Fig. 4(*b*). These are given for different z locations at a constant y of 2.98 cm, the distance from the wall of the vortex center. The z location of the center is also indicated along with the region corresponding to the vortex core if the vortex were an ideal Rankine vortex. In the present study, the core is the region bounded by vorticity levels which are 40 percent of the maximum vorticity. This boundary level is chosen because it shows a good match to locations corresponding to secondary flow vector maxima. In Rankine vortices, the region bounded by secondary flow vector maxima is where all vorticity is located. 40 percent threshold levels instead of maxima locations are used in the present study because they can be determined with greater accuracy. For the vortex whose characteristics are shown in Figs. 4(*a*) and 4(*b*), the core is approximately circular and axisymmetric with an average spanwise extent of 1.50 cm, or an average radial extent from the vortex center of 0.75 cm. This average core radius in the lateral direction is designated c. $2c/d$, the ratio of spanwise core diameter to hole diameter, is then used to quantify the size of the vortex relative to the injection hole. For the vortex at $x/d = 41.9$, $2c/d$ equals 1.58.

When the vortex of Fig. 4(*a*) passes $x/d = 0$, the center is located at a spanwise position of -2.5 cm (see Table 1). The injection location is then beneath the vortex downwash. At $x/d = 41.9$ Figs. 4(*a*) and 4(*b*) show the center to be further to the left as a result of spanwise motion of the vortex core in the negative z direction. This is caused by the secondary flows between the core and the wall, which are also directed in the negative z direction. Spanwise core motion is also evident from surface Stanton number contours in other studies, particularly those measured downstream of a row of injection holes by Ligrani et al. (1989).

Effects of the Vortex on the Distributions of Film Coolant. Information on the disruption imposed to the injectant is evident from flow visualization results presented in Fig. 5. Horizontal lines in this figure correspond to thermocouple row locations. Vertical lines are 2.54 cm apart starting at the centerline. The longitudinal and spanwise extents of each photograph are approximately 34 and 20 injection hole diameters, respectively. Figure 5(*c*) shows the path and behavior of injectant when no vortex is present. Coolant is convected in the x direction with some spreading with downstream distance. Structures having scales with sizes of the order of the injectant width are present that clearly indicate the turbulent nature of the flow. Results in Fig. 5(*b*) are for vortex position *e* when the cooling hole is initially beneath the downwash. Here, considerable deflection from the nominal x direction is apparent. This results from the rearrangement and distortion imposed by the vortex secondary flow in addition to the spanwise motion of the vortex as it convects downstream. Considerably greater distortion and spreading are apparent in Fig. 5(*a*). Here, the vortex is located at position *h* and the injection hole is initially just beside the vortex core beneath the upwash. Some deflection with downstream distance is apparent as coolant is swirled and spread across the vortex by secondary flows. Because much of this spreading is in the positive z direction, coolant seems to be convected into the area away from the wall above the vortex core where secondary flow vectors are also in the positive z direction. This is discussed in more detail shortly.

Figure 6 provides quantitative information regarding the distortion and redistribution of injectant by the vortex. The figure is presented in four parts, one for each spanwise vortex position. Measured secondary flow vectors are superimposed on each part to illustrate their significance and influence in regard to redistribution of injectant. Mean temperature fields for each vortex position at $x/d = 41.9$ are also included in Fig. 6. These data were obtained using an experimental approach introduced by Ligrani et al. (1989), in which injectant is heated to about 50°C without providing any heat to the test plate. The temperature field is given as $(T_o - T_\infty)$ in °C and thus shows how fluid from the injection hole is convected and distorted by the vortex, where higher temperature differences generally indicate greater amounts of injectant. In cases where higher temperature differences are not from accumulation of injectant by convective processes, they are a result of diffusion of heat from fluid that was initially injectant. However, this is of secondary importance. Thus, the temperature variations in Fig. 6 result from film injection and its interaction with the surrounding flow, since the injectant is the only source of thermal energy (relative to the free stream) for these tests.

A qualitative comparison of Figs. 6(*a–d*) for vortex positions *b*, *e*, *h*, and *k* shows vastly different injectant distributions with spanwise vortex location. Referring to Table 1 and Fig. 6(*a*) for vortex position *b*, the downwash part passes over the film-cooling hole such that the vortex center is -6.3 cm away in the z direction. This distance is equivalent to 8.4 core radii or 8.4*c*. Keeping in mind that the centerline of the injection hole is located at $z = 0$, Fig. 6(*a*) indicates that the bulk of the coolant at $x/d = 41.9$ is at z locations from $z = 0$ to $z = -4.0$ cm. This evidences some skewing of coolant from the nominal streamwise direction. Because of the secondary flow, additional coolant is convected along the wall in the negative z direction. Some is then distributed away from the wall by the vortex upwash to eventually be swirled around the vortex core. The most significant conclusion from Fig. 6(*a*) is that the coolant, although skewed from the nominal streamwise direction and partially depleted from secondary flow convection, remains in sufficient quantity to protect the surface locally and minimize heat transfer.

When the vortex is in position *e*, the injection hole is again beneath the downwash as the vortex passes, but the vortex center is only -2.5 cm or -3.33 *c* away (Table 1). Figure 6(*b*), again for $x/d = 41.9$, shows that the coolant is totally redistributed by vortex secondary flows with little local protection remaining near the wall at any spanwise location. Most coolant is located in the vortex upwash region near $z = -6$ cm, with some above the vortex core. Corresponding streamwise velocity contours in Fig. 4(*a*) show injectant is present at the location of a significant velocity deficit. Such a deficit is typical of the upwash where low-momentum fluid is convected away from the wall; however, here the deficit may be slightly augmented due to accumulation of injectant. Thus, with position *e*, a significant portion of injectant seems to be initially spread along the wall beneath the vortex center, and then convected in the direction of secondary flows, an observation also consistent with the flow visualization results in Fig. 5(*b*).

Downloaded 01 Jun 2010 to 171.66.16.66. Redistribution subject to ASME license or copyright; see http://www.asme.org/terms/Terms_Use.cfm

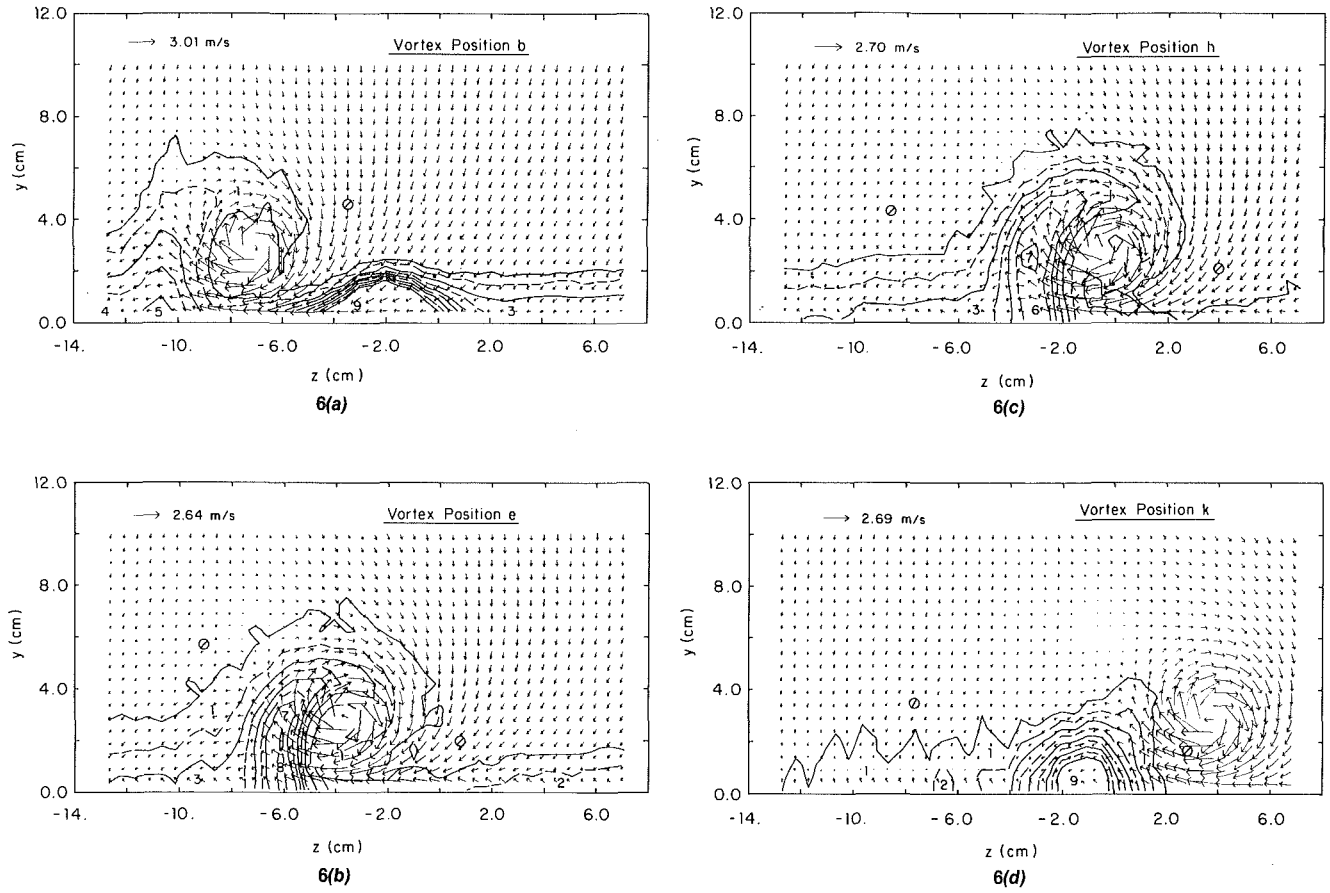

$T_o - T_\infty$ (Degrees Celcius) Ranges

0	$< 0.10^*$	5	1.00-1.25
1	0.10*-0.25	6	1.25-1.50
2	0.25-0.50	7	1.50-1.75
3	0.50-0.75	8	1.75-2.00
4	0.75-1.00	9	> 2.00

*In 6a, this limit is 0.05.

Fig. 6 Mean temperature field showing distributions of film coolant with secondary flow vectors at $x/d = 41.9$, $m = 0.5$: *(a)* vortex at position *b*, *(b)* vortex at position *e*, *(c)* vortex at position *h*, *(d)* vortex at position *k*

Figure 6(c) presents coolant distributions and secondary flow vectors at $x/d = 41.9$ for vortex position h. For this situation, the vortex center was located $+1.3$ cm or about 1.73 c away from the centerline at $x/d = 0$ and the injection hole is beneath the vortex core and upwash (Table 1 and Fig. 3). As for position e, most of the coolant is redistributed into the upwash region and above the vortex core at this streamwise location. There is little evidence of any significant accumulation of coolant near the wall indicating that most all protection is decimated. A comparison of 6(b) and 6(c) shows more significant spanwise spreading for the latter case, a result also seen in the flow visualization photographs in Figs. 5(b) and 5(a). Such behavior is the likely explanation for the high Stanton number regions observed for some vortex positions by Ligrani et al. (1989) as well as the lateral mixing occasionally noted by Schwarz and Goldstein (1989).

Results in Fig. 6(d) are given when the vortex center is located at $z = +5.1$ cm (or about $+6.8$ c) as it passes the injection hole. Coolant thus exits the hole to the side of the vortex upwash region. Although some distortion of the coolant distribution seems to result from the vortex upwash, most of it remains intact. Another interesting feature is the spreading of the injectant along the wall, which occurred upstream of the $x/d = 41.9$ location. This seems to have been significant in the negative z direction; however, secondary flow vectors beneath the vortex core seem to have prevented significant spreading in the positive z direction.

Heat Transfer Results. Spanwise variations of local Stanton numbers for $x/d = 33.6$ are presented in Fig. 7. These are presented for comparison with the injectant distributions of Figs. 6 for all four spanwise vortex positions b, e, h, and k. In this figure and the discussion that follows, St_0 refers to baseline Stanton numbers without a vortex and without film cooling, St_f are measured with film cooling only, and St are obtained with vortex and film cooling.

The most important features of Fig. 7 are the differences between the St/St_0 distributions and the St_f/St_0 curve for no vortex. This illustrates the significance of the perturbation caused by the vortex to the film cooled boundary layer. Also of importance are the changes of the St/St_0 distributions and magnitudes, which occur as the spanwise position of the vortex is changed. Such alterations evidence the complexity of the interactions between the injectant, the vortex, and the boundary layer.

Without the vortex present, St_f/St_0 shows a deficit of ap-

Downloaded 01 Jun 2010 to 171.66.16.66. Redistribution subject to ASME license or copyright; see http://www.asme.org/terms/Terms_Use.cfm

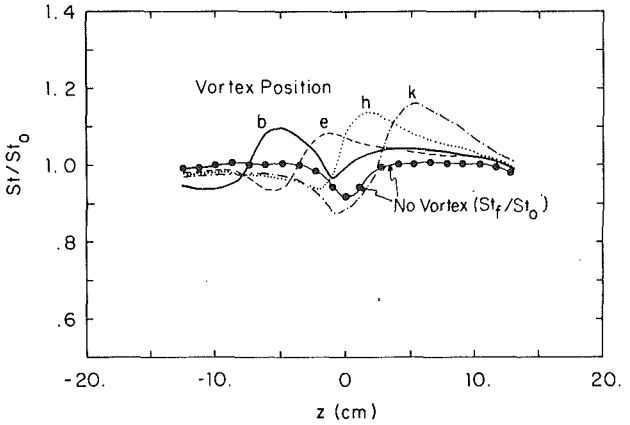

Fig. 7 Local Stanton number ratios at $x/d = 33.6$, $x = 1.4$ m, $m = 0.51$-0.53; boundary layer with film cooling, with and without an embedded vortex at positions *b*, *e*, *h*, and *k*

proximately 0.92 at $z = 0$ resulting from the injectant. Similar deficits, when vortices are present, evidence presence of injectant and the amount of protection that is provided. Ordinarily, without an external perturbation, an embedded vortex produces spanwise Stanton numbers that are augmented near the downwash side and diminished near the upwash side. In the Fig. 7 view looking downstream, the downwash is on the right and the upwash is on the left for each vortex position. With injectant present, upwash and downwash St/St_0 are further altered depending upon the location of the injectant with respect to these regions.

With vortex position *b*, Fig. 6(*a*) shows the presence of injectant near the wall at the exact location that a local deficit exits on Fig. 7 for vortex position *b*: -4.0 cm $< z < 0.0$ cm. Similar deficits are not present near $z = 0$ in Fig. 7 for vortex positions *e* and *h*. For both cases, coolant is swept away from the wall into the upwash and above the vortex core by secondary motion. Consequently, little evidence of lowered St/St_0 from the presence of injectant is seen for these vortex positions, except that the St/St_0 peak for position *e* is slightly lower than for other vortex positions. For vortex position *k*, St/St_0 values are lower than St_f/St_0 data with film cooling only. Thus, the protection provided by the injectant seems to be locally augmented by the vortex for -5 cm $< z < 3$ cm. This protection also appears to be spread over a larger portion of the wall as a result of near-wall secondary motion in the negative *z* direction.

The streamwise development of St/St_0 and St_f/St_0 distributions for vortex positions *b*, *e*, *h*, and *k* are given in Figs. 8, 9, 10, and 11, respectively. Close inspection of these figures, as well as Figs. 6 and 7, reveals vortex positions to be slightly different from the ones produced by the repositioning of the vortex generator alone. This is because of interactions with injection jets, which produce small alterations to the *y* and *z* locations of the vortex center as well as the vortex path as it convects downstream.

Referring to Fig. 8 for vortex position *b* for $x/d = 7.4$, significant influence of the injectant is indicated by St/St_0 values, which are as low as ones without a vortex present. For smaller values of *z*, regions where $St/St_0 > St_f/St_0$ and $St/St_0 < St_f/St_0$ correspond to the downwash and upwash portions of the vortex, respectively. At $x/d = 7.4$, high St/St_0 from the vortex downwash are just to the left of St/St_0 deficits from the film injectant. With downstream development, the influence of injectant on the St/St_0 data is evident for x/d up to 54.6. As x/d increases over this range, Stanton number ratio deficits associated with film cooling near $z/d = 0$ become less apparent. Corresponding St/St_0 are also higher than those obtained without the vortex. This occurs as increasing amounts of injectant are swept away from the wall into the upwash and less coolant is available near the wall to reduce heat transfer. Such behavior is consistent with high St/St_0 attributable to the downwash, which persist to the end of the test plate, as well as the secondary flow motion and injectant distributions presented in Fig. 6(*a*). Because of the coherence of the vortices, their perturbations to heat transfer persist at least 97 injection hole diameters downstream, a result also observed by Ligrani et al. (1989).

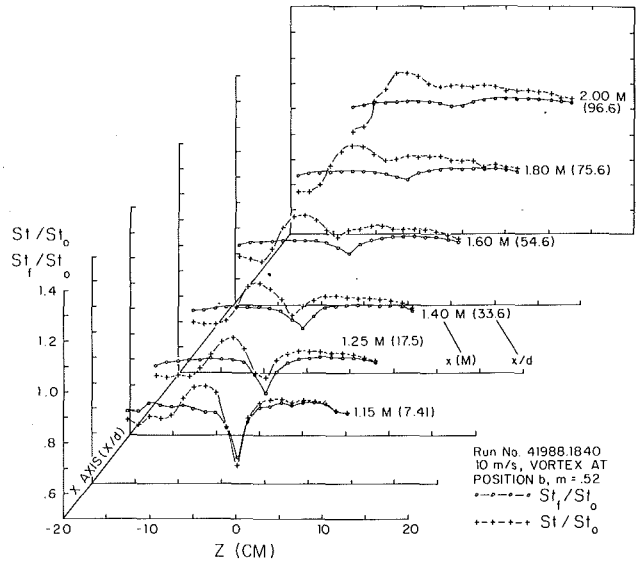

Fig. 8 Local Stanton number ratios; boundary layer with film cooling, with and without embedded vortex

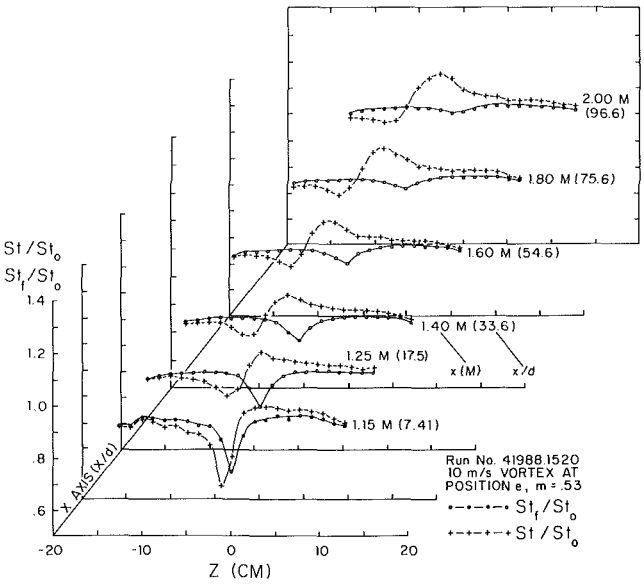

Fig. 9 Local Stanton number ratios; boundary layer with film cooling, with and without an embedded vortex

With vortex position *e* in Fig. 9, a significant St/St_0 valley attributable to film injection exists at $x/d = 7.4$. Here the vortex is probably just lifted off the surface by the injectant. With further downstream development ($x/d \geq 17.5$), the direct application of the vortex downwash begins to take its toll on the region containing the injectant. High St/St_0 from the vortex downwash are at the same spanwise locations as St_f/St_0 minima from film cooling. Consequently, little evidence of injectant is evident except that maximum and minimum St/St_0 at each streamwise location are both slightly less than if no film cooling is present. The protective influence of the film

Downloaded 01 Jun 2010 to 171.66.16.66. Redistribution subject to ASME license or copyright; see http://www.asme.org/terms/Terms_Use.cfm

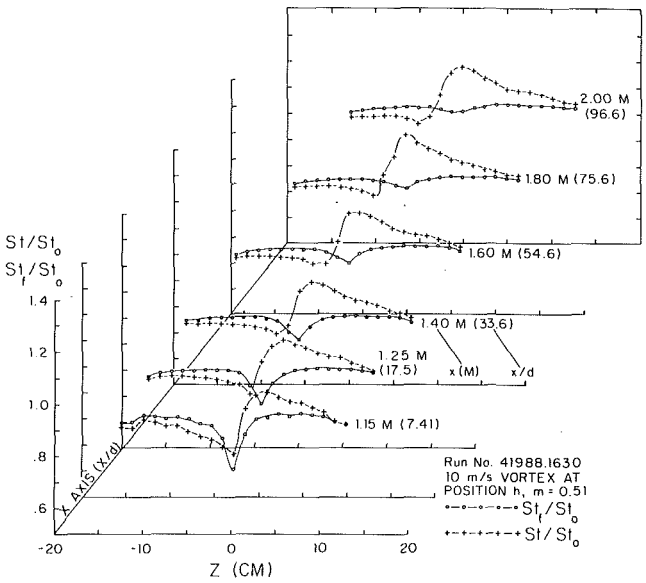

Fig. 10 Local Stanton number ratios; boundary layer with film cooling, with and without an embedded vortex

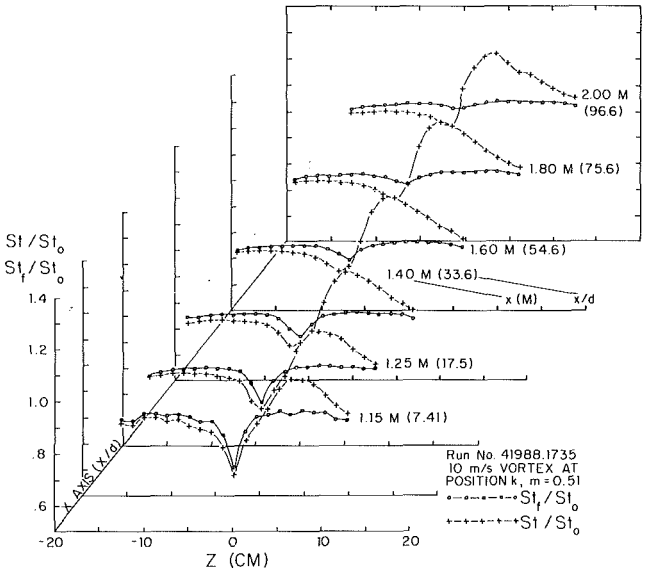

Fig. 11 Local Stanton number ratios; boundary layer with film cooling, with and without an embedded vortex

cooling thus appears to be almost totally decimated, as evidenced by the St/St_0 peak near $z/d=0$ which persists to the end of the test plate.

Similar conclusions may be drawn regarding the St/St_0 data for vortex position h in Fig. 10. Only when x/d equals 7.4 and 17.5 are local minima St/St_0 slightly modified by the injectant. Here, St/St_0 maxima corresponding to the vortex downwash are just to the right of St/St_0 deficits from film injection. At other locations, the spanwise variations of St/St_0 primarily reflect the influence of the vortex only.

With vortex position k, injectant emerges from the cooling hole to the side of the upwash. Consequently, St/St_0 deficits from film injection are at smaller z than St/St_0 peaks from vortex downwash regions. This is evident in Fig. 11, which also shows that evidence of injectant is seen for x/d at least up to 54.6. In addition, minima St/St_0 are lower than St_f/St_0 with cooling only. This results from the combined influence of the downwash and the injection, as well as interactions between the two. Thus, over considerable downstream distances, the protection provided by film cooling is locally augmented and spread over a larger area than if no vortex is present. Similar observations were made by Ligrani et al. (1989) for vortex upwash near a row of holes.

Summary and Conclusions

The interaction and effect of a single embedded vortex on injectant from a single film cooling hole inclined at 30 deg was investigated. All measurements were made with a blowing ratio of approximately 0.50 and a free-stream velocity of 10 m/s. At $x/d=41.9$, the circulation and core diameter of the vortices employed were about 0.151 m^2/s and 1.50 cm, respectively. These give a ratio of core diameter to injection hole diameter $2c/d$ of 1.58, and ratio of circulation to injection velocity times hole diameter $\Gamma/U_c d$ of about 3.1.

Four spanwise vortex positions with respect to the film cooling hole were used to examine the interactions of different parts of the vortex on the injectant. The most important general conclusion is that injectant continues to provide near-wall protection if it is located at least 2.9–3.4 core diameters away from the vortex center in the spanwise direction as the vortex passes. However, regardless of the vortex position with respect to injection location, the vortices produce perturbations to local heat transfer distributions, including local maxima, which persist as far as 97 hole diameters downstream of the injection location. When injectant issues directly beneath the vortex downwash, magnitudes of these maxima are somewhat reduced compared to other vortex positions.

More specific conclusions follow.

1 When the vortex center passes the injection hole within 1.67 diameters ($3.33c$) on the downwash side and within 0.87 core diameters ($1.73c$) on the upwash side (vortex positions e and h, respectively), most injectant is swept beneath the core and into the upwash away from the wall by secondary flows. In these cases, little protection from film cooling remains since local Stanton number deficits are present for x/d of 7.4 but not for $x/d \geq 17.5$. When the vortex downwash passes immediately above the injection location (vortex position e), Stanton number peaks are slightly lower than if no injectant were present.

2 When the injectant emerges beneath the downwash 4.2 core diameters ($8.4c$) from the center (vortex position b), Stanton numbers are influenced by the coolant for x/d up to 76. Even though injectant is skewed from the streamwise direction and is partially depleted by secondary flow convection, it remains in sufficient quantity to minimize heat transfer locally.

3 When injectant leaves the cooling hole on the upwash side 3.4 core diameters ($6.8c$) from the vortex center (vortex position k), local Stanton number distributions show local deficits from film cooling for x/d at least up to 54.6. In this case, the local protection provided by film cooling seems to be augmented by the presence of the vortex. In addition, the area of protection is increased as the injectant is spread over the surface in the direction of near wall secondary flows.

Acknowledgments

This study was supported by the Aero-Propulsion Laboratory of Wright Patterson Air Force Base, MIPR Number FY 1455-88-N0608. Dr. Dick Rivir was program monitor. Some of the facilities used were purchased using funds from the Naval Postgraduate School Foundation Research Program.

References

Blair, M. F., 1974, "An Experimental Study of Heat Transfer and Film Cooling on Large-Scale Turbine Endwalls," ASME *Journal of Heat Transfer*, Vol. 96, pp. 524–529.

El-Hady, N. M., and Verma, A. K., 1984, "Instability of Compressible

Downloaded 01 Jun 2010 to 171.66.16.66. Redistribution subject to ASME license or copyright; see http://www.asme.org/terms/Terms_Use.cfm

Boundary Layers Along Curved Walls With Suction or Cooling," *AIAA Journal*, Vol. 22, No. 2, pp. 206–213.

Goldstein, R. J., and Chen, H. P., 1985, "Film Cooling on a Gas Turbine Blade Near the Endwall," ASME *Journal of Engineering for Gas Turbines and Power*, Vol. 107, pp. 117–122.

Goldstein, R. J., and Chen, H. P., 1987, "Film Cooling of a Turbine Blade With Injection Through Two Rows of Holes in the Near-Endwall Region," ASME JOURNAL OF TURBOMACHINERY, Vol. 109, pp. 588–593.

Goldstein, R. J., Eckert, E. R. G., and Ramsey, J. W., 1968, "Film Cooling With Injection Through Holes: Adiabatic Wall Temperatures Downstream of a Circular Hole," ASME *Journal of Engineering for Power*, Vol. 90, No. 4, pp. 384–395.

Honami, S., and Fukagawa, M., 1987, "A Study on Film Cooling Behavior of a Cooling Jet Over a Concave Surface," Tokyo International Gas Turbine Congress, Tokyo, Japan, Paper No. 87-Tokyo-IGTC-72.

Kays, W. M., and Crawford, M. E., 1980, *Convective Heat and Mass Transfer*, 2nd ed., McGraw-Hill, New York.

Kobayashi, R., 1972, "Note on the Stability of a Boundary Layer on a Concave Wall With Suction," *Journal of Fluid Mechanics*, Vol. 52, pp. 269–272.

Kobayashi, R., 1984, "Taylor–Görtler Instability of a Boundary Layer With Suction or Blowing," *Report Institute of High Speed Mechanics*, Vol. 32, Series B, pp. 129–148.

Ligrani, P. M., Joseph, S. L., Ortiz, A., and Evans, L. D., 1988, "Heat Transfer in Film-Cooled Turbulent Boundary Layers at Different Blowing Ratios as Affected by Longitudinal Vortices," *Experimental Thermal and Fluid Science*, Vol. 1, pp. 347–362.

Ligrani, P. M., Ortiz, A., Joseph, S. L., and Evans, D. L., 1989, "Effects of Embedded Vortices on Film-Cooled Turbulent Boundary Layers," ASME JOURNAL OF TURBOMACHINERY, Vol. 111, pp. 71–77.

Ortiz, A., 1987, "The Thermal Behavior of Film Cooled Turbulent Boundary Layers as Affected by Longitudinal Vortices," M.E. Thesis, U. S. Naval Postgraduate School, Monterey, CA.

Sato, T., Aoki, S., Takeishi, K., and Matsuura, M., 1987, "Effect of Three-Dimensional Flow Field on Heat Transfer Problems of a Low Aspect Ratio Turbine Nozzle," Takasago Research and Development Center, Mitsubishi Heavy Industries, Ltd.

Schwarz, S. G., and Goldstein, R. J., 1989, "The Two-Dimensional Behavior of Film Cooling Jets on Concave Surfaces," ASME JOURNAL OF TURBOMACHINERY, Vol. 111, pp. 124–130.

Williams, W. W., 1988, "Effects of an Embedded Vortex on a Single Film-Cooling Jet in a Turbulent Boundary Layer," M.S. Thesis, Department of Mechanical Engineering, Naval Postgraduate School, Monterey, CA.

Downloaded 01 Jun 2010 to 171.66.16.66. Redistribution subject to ASME license or copyright; see http://www.asme.org/terms/Terms_Use.cfm

J. R. Pietrzyk

D. G. Bogard

M. E. Crawford

Mechanical Engineering Department,
The University of Texas at Austin,
Austin, TX 78712

Effects of Density Ratio on the Hydrodynamics of Film Cooling

This paper presents the results of a detailed hydrodynamic study of a row of inclined jets issuing into a crossflow with a density ratio of injectant to free stream of 2. Laser-Doppler anemometry was used to measure the vertical and streamwise components of velocity for a jet-to-free stream mass flux ratio of 0.5. Mean velocity components and turbulent Reynolds normal and shear stress components were measured at locations in a vertical plane along the centerline of the jet from 1 diameter upstream to 30 diameters downstream of the jet. The results, which have application to film cooling, give a quantitative picture of the entire flow field, from the approaching flow upstream of the jet, through the interaction region of the jet and free stream, to the relaxation region downstream where the flow field approaches that of a standard turbulent boundary layer.

Introduction

This research is part of an ongoing effort to understand film cooling better in its application to help control surface temperature distributions of blades and vanes in the turbine section of propulsion gas turbines. In the blade (or vane) cooling process, compressor bleed air is introduced into the hollow core of a blade and is channeled through then dumped through the blade surface via rows of holes located in the vicinity of the leading edge of the blade, as well as locations on the blade's suction and pressure surfaces. The dumped coolant is intended to cool the surfaces convectively, especially in regions of high heat flux loading, and the external convective process is called film cooling. To be effective, film cooling must result in acceptable blade surface temperature and/or thermal stress distributions in the presence of potentially blade-melting high-enthalpy combustion gases to prolong the life of the blade.

Film cooling research generally focuses on the variables that control heat transfer as the combustion gases form a boundary layer flow over the surface, and the boundary layer, or cross stream, interacts with the jets of coolant emerging at various locations along the surface. Parameters that govern the hydrodynamics of the jet–cross stream interaction and the associated heat transfer include cooling hole geometry and coolant-to-free stream ratios of density, velocity, mass flux, and momentum flux. The mass flux ratio of the coolant to freestream, M, often called the blowing ratio, and the momentum flux ratio, I, are defined as

$$M = \frac{\rho_j U_j}{\rho_\infty U_\infty} \qquad I = \frac{\rho_j U_j^2}{\rho_\infty U_\infty^2}$$

where the numerator represents the density–velocity mass or momentum flux of the coolant, and the denominator is the corresponding mass or momentum flux of the free stream above the boundary layer. Note that with density ratio and blowing ratio as independent variables, the momentum flux ratio for a given test is fixed. Additional parameters that govern film cooling can be identified, such as free-stream turbulence, curvature, and rotation.

Studies of film cooling have varying degrees of compromise because of the difficulty in matching experimental conditions to values of the various parameters that are in the range found in gas turbine engines. This paper focuses on the effects of density ratio on the hydrodynamics of the film cooling process. The density ratio parameter can be matched in three ways: hot free-stream flow, cryogenically cooled injectant flow, and foreign gas injection. The flow diagnostics tools to document the flow field created by the jet–cross stream interaction must be valid in the near-hole vicinity where the flow is strongly three dimensional. This limits the diagnostics to either hot-wire anemometry with multiple-wire probes or laser-Doppler anemometry with multiple beams. Experiments using a hot free-stream flow and using foreign gas injection do not lend themselves to hot-wire investigations.

To date, there have been no studies reported in the open literature that have been devoted to measurement of the film cooling hydrodynamic flow field for blowing ratios applicable to gas turbines, with the effects of density ratio included. There have been several journal articles that document the downstream region of film cooling flow fields, but the major emphasis of these articles has been film cooling effectiveness data. Pitot probe mapping of the streamwise development of mean velocity profiles were reported by Le Brocq et al. (1973). The test surface was comprised of multiple rows of staggered holes at 45 deg inclination, and the emphasis of the research was on hole geometry and density ratio effects. Freon was used to create a density ratio of 4.23. Launder and York (1974) reported data for continuation of the tests using carbon dioxide as the injectant to obtain a more realistic density ratio of 1.5. Pressure gradient and free-stream turbulence effects were the primary emphasis of the study. Foster and Lampard (1980) reported pitot probe mapping of the streamwise

Contributed by the International Gas Turbine Institute and presented at the 34th International Gas Turbine and Aeroengine Congress and Exhibition, Toronto, Ontario, Canada, June 4–8, 1989. Manuscript received at ASME Headquarters January 27, 1989. Paper No. 89-GT-175.

Copyright © 1990 by ASME
Downloaded 01 Jun 2010 to 171.66.16.66. Redistribution subject to ASME license or copyright; see http://www.asme.org/terms/Terms_Use.cfm

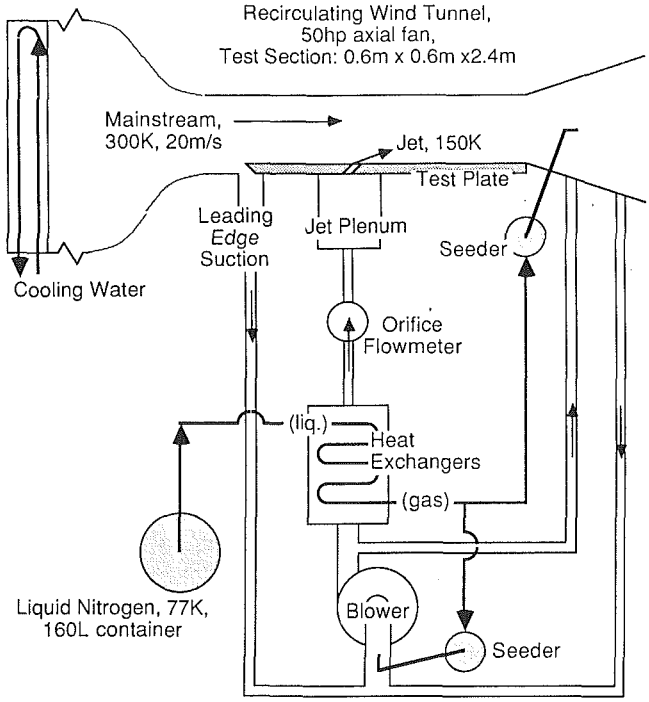

Fig. 1 Arrangement of experimental film cooling facility

development of mean velocity profiles at locations 4, 11, 24, and 61 diameters downstream of a row of holes with $M = 1.4$. The holes were inclined 35, 55, and 90 deg from the surface and a mixture of freon and air was used as the injectant.

In the present study, detailed measurements have been made of the mean and turbulence characteristics of jets in crossflow for injection from a single row of 35 deg holes, laterally spaced 3 diameters apart, on a flat test surface. The data were acquired with a density ratio of 2 and $M = 0.5$. Hydrodynamic conditions for the tests were typical of film-cooled turbine blades, and a short entrance of $L/D = 3.5$ was used for the injected fluid, with the flow approaching the entrance to the holes without a crossflow component. An LDV was used to measure the distributions of streamwise and normal components of the mean and fluctuating velocity along with the uv shear stress over a range extending from one diameter upstream of the hole to 30 diameters downstream. Particular emphasis was placed on acquiring data over the hole and in the region immediately downstream of the hole. The work reported here represents a companion study to a previous paper by Pietrzyk et al. (1989) that presented data for the case of unit density ratio. The effects of the density ratio are presented by contrasting the new data with unit density cases at $M = 0.25$ and 0.5. This allows comparison with tests whose momentum flux ratios bracket the momentum flux of the new data.

Experimental Facility and Instrumentation

The film cooling test facility consisted of a low-speed, recirculating wind tunnel and a cryogenically cooled secondary flow loop, which provided flow for the inclined jets into the test section. The flat, adiabatic wall test plate mounted on the bottom wall of the test section had a row of holes inclined downstream for the simulated film cooling jets. A schematic of this facility is shown in Fig. 1. Measurements of the flowfield were made with a laser-Doppler velocimeter (LDV).

Table 1 Streamwise development of the turbulent boundary layer

x/D	δ_{99}/D	δ_1/D	δ_2/D	H	Re_{δ_2}	$C_f \times 10^3$
-2	0.52	0.089	0.059	1.50	946	4.20
6.5	0.65	0.120	0.083	1.47	1296	3.83
15	0.81	0.143	0.098	1.46	1567	3.64
23	0.91	0.167	0.115	1.44	1842	3.49
30	0.99	0.178	0.124	1.43	1984	3.46

Documentation of the Free-Stream and Turbulent Boundary Layer Quality. The wind tunnel test section, with dimensions $61 \times 61 \times 244$ cm long, was preceded by a 6.25:1 contraction section with a bank of three graduated screens and honeycomb upstream of the contraction. Suction was used to remove the boundary layer preceding the sharp leading edge of the bottom wall test plate. By monitoring pressure measurements made with surface taps located before and after the leading edge, the suction was adjusted to ensure parallel flow at the leading edge. For all experiments, the free-stream velocity was set at 20 m/s and the free-stream turbulence intensity was less than 0.2 percent. The variation of the free-stream velocity was ± 0.5 percent in both the spanwise and streamwise directions. A water-cooled heat exchanger, present in the wind tunnel, maintained the free-stream temperature at 302 K to within ± 0.5 K.

Measurements of the streamwise development and the spanwise uniformity of the turbulent boundary layer on the test plate with no blowing, i.e., $M = 0$, were made to document the two dimensionality of the flow. Quantities related to the streamwise development of the boundary layer were measured at five locations across the region of interest and are presented in Table 1.

All three measures of the boundary layer thickness have been normalized by the hole diameter. The friction coefficients, which were determined from Clauser plots using Spalding's law of the wall (Spalding, 1961), are within 5 percent of the Ludweig and Tillman correlation (White, 1974). Profiles of mean velocities at five streamwise locations are compared in Fig. 2. The profiles collapse together in the inner region of the boundary layer and are well represented by Spalding's law of the wall. Spanwise variation of the momentum thickness and displacement thickness were both ± 5 percent, variation of the shape factor was ± 1 percent, and variation of the friction coefficient was ± 2.5 percent.

Secondary Flow Loop: Dense Jet Flow. Air was used as the working fluid for both the jets and the free stream. A typical jet-to-free stream density ratio of 2.0 was achieved by decreasing the temperature of the jets using the cryogenically cooled secondary flow loop (Fig. 1). A centrifugal fan circulated air through a bank of finned-tube heat exchangers

Nomenclature

D = hole diameter
I = momentum flux ratio, jet-to-free stream
L = hole length
M = mass flux ratio, jet-to-free stream
TL = turbulence level, two-dimensional
U = mean velocity, x direction
u_{rms} = rms velocity, x direction
uv = Reynolds uv shear stress
U_∞ = free-stream velocity
V = mean velocity, y direction
v_{rms} = rms velocity, y direction
x = streamwise distance
y = distance from wall
δ = boundary layer thickness, 99 percent velocity point
δ_1 = boundary layer displacement thickness
δ_2 = boundary layer momentum thickness

Downloaded 01 Jun 2010 to 171.66.16.66. Redistribution subject to ASME license or copyright; see http://www.asme.org/terms/Terms_Use.cfm

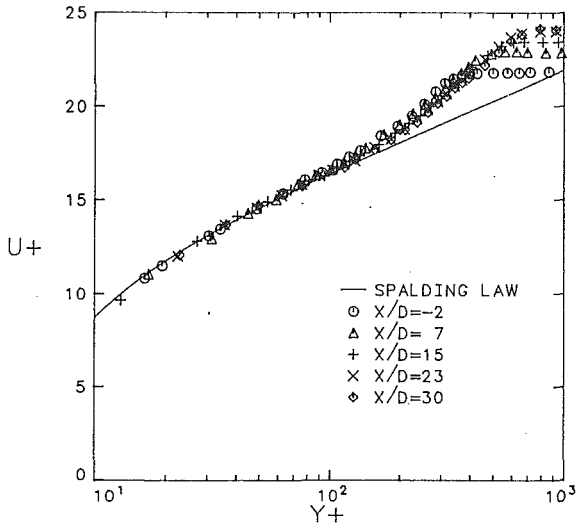

Fig. 2 Mean velocity profiles for turbulent boundary layer on test plate, $M=0$

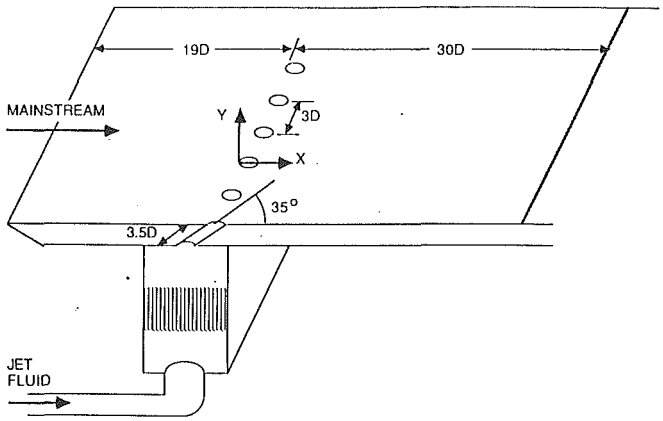

Fig. 3 Geometry of film cooling test plate and coordinate system

where it was cooled using liquid nitrogen supplied by a pressurized 160 liter dewar. The jet temperature (measured in the plenum from which the jets issue) was controlled and maintained at 153 K to within ±3 K by varying the flow rate of liquid nitrogen through the tube side of the heat exchangers. The exhausted nitrogen gas was used to operate two dry particle generators necessary for the operation of the LDV. Different blowing ratios were obtained by varying the flow rate through the secondary flow loop.

The total flow rate passing through the jets was measured with an orifice flow meter installed in the insulated duct leading to a common plenum from which the jets issue. Using laminar flow meters, the orifice flow meter was calibrated in-line and the flow coefficient was determined with a precision uncertainty of ±0.6 percent. The pressure transducer used to measure the pressure difference across the orifice flow meter was calibrated with a micromanometer and had a precision uncertainty less than ±0.7 percent. The temperatures throughout the secondary flow loop and plenum were measured with constantan-chromel thermocouples. The accuracy of these thermocouples, ±0.5 K, was verified at 77.4 K (liquid nitrogen), 273.2 K (ice), and 373.2 K (steam). Using the orifice flow meter, pressure transducer, and thermocouples, the mass flow rate of the jets was determined with a precision of ±0.7 percent. Due to the accumulation of frost in the secondary flow loop, the mass flow rate decreased by a maximum of 5 percent during the experiment.

The test section geometry and coordinate system used are shown in Fig. 3. Air was injected into the free stream through a row of eleven holes, 12.7 mm in diameter, in the flat test plate. The holes are inclined at 35 deg, laterally spaced three diameters apart, and are located 19 diameters downstream of the leading edge of the plate. The length of the hole was made short relative to the diameter ($L/D=3.5$) to better simulate a typical film-cooled turbine blade geometry. The test plate and plenum chamber were constructed of glass-reinforced plastic (EXTREN) because of the low thermal conductivity ($k=0.58$ W/m/K), low thermal contraction coefficient ($\alpha=9\times10^{-6}$/K), and high strength of this material at low temperatures. With no crossflow, the variation of the mean velocity among the jets, checked at three locations 0.1 diameters above each jet exit, was ±2.6 percent. With the crossflow present, similar spanwise uniformity checks were performed five diameters downstream of the jets at two vertical locations (0.1 diameters above the wall and at the location where the peak turbulence level occurred) for blowing ratios of $M=1.0$ and $M=0.25$. The variation of the mean velocity at analogous points in the flow field was ±0.024 U_∞. The variation of the exit temperature among the dense jets was ±0.8 K. The jet exit temperature was less than 3 K greater than the temperature of the air within the plenum.

The low temperature of the dense jets caused water and CO_2 to solidify from the air within the wind tunnel and accumulate on the test plate and in the secondary flow loop. This frosting problem was aggravated by infiltration of room air into the wind tunnel and the addition of two streams of moist aerosol generated by atomizer type seeders used in initial operation of the LDV. Frost accumulation was reduced by sealing the wind tunnel (although an air-tight seal could not be obtained), drying the air within the wind tunnel with 45 kg of molecular sieve dessicant prior to each experiment, and developing a dry particle seed generator. Prior to implementing the above facility modifications and procedures for minimizing moisture, significant accumulation of frost would occur on the test plate within five minutes of operation at a density ratio of 2; following the implementation of these modifications and procedures, no significant accumulation of frost occurred over the measured time of a complete velocity profile (~20 min). Between measurements of each velocity profile a retractable wiper was used to remove any frost present on the test plate.

Laser-Doppler Velocimeter System. Two-component velocity measurements were made with a modified version of the TSI Inc model 9100-10 LDV system described by Pietrzyk et al. (1989). The V component of velocity reported in this paper is composed primarily of the true vertical velocity, but also contains a small lateral velocity component because the entire LDV was tilted 8 deg downward to prevent the lower beam from intersecting the floor of the wind tunnel. The probe volume was 80 μm in diameter and 160 μm long. TSI counters were used for signal processing and a HP-1000 microcomputer system was used for data acquisition and analysis. The microcomputer also controlled the movement of the LDV traverse table, which had a precision of ±0.01 mm. Complete computer control of the LDV was necessary in order to map out the flowfield in sufficient detail in the limited amount of time allowed by the liquid nitrogen supply. The operation of the LDV was not significantly hampered by variations in the index of refraction due to the row of cold jets. To obtain accurate measurements of the turbulence shear stress, essentially coincident measurement of the instantaneous streamwise and vertical components of velocity is necessary. A coincidence time window of 10 μs was used for these measurements, which allowed accurate measurements for flow fluctuations up to 50 kHz.

The free stream and jets were independently seeded with 1-μm TiO_2 particles. To avoid bias errors, flow rates were adjusted to obtain equal seed concentrations in the free stream and the jets. A dry particle generator was designed and con-

Downloaded 01 Jun 2010 to 171.66.16.66. Redistribution subject to ASME license or copyright; see http://www.asme.org/terms/Terms_Use.cfm

structed for this purpose, because the atomizers used in an earlier study (Pietrzyk et al., 1989) introduced large amounts of moisture into the tunnel air (~1/4 liter/h) causing unacceptable frost accumulation. The dry particle generator consisted of a large fluidized bed, composed of steel beads (~0.13 mm diameter) mixed with 1-μm TiO_2 particles, and an eductor. Dry nitrogen gas was passed through the fluidized bed to generate a steady stream of aerosol containing partially deagglomerated particles. The particles in this aerosol were completely deagglomerated by passing the aerosol through the throat of the eductor, where the aerosol interacts with a much higher speed flow of dry nitrogen gas. A sample of seed deposited on a microscope slide was examined using a 400× microscope to verify that the particles contained in the exiting aerosol were completely deagglomerated and small enough to follow flow fluctuations up to 10 kHz.

The time-averaged measurements presented in this paper were obtained using sample sizes of 1024 discrete coincident measurements. Measurement time for these samples varied from 10 s to 100 s. Precision uncertainties for these measurements were determined from repeatability tests carried out in the jet/crossflow interaction region near the wall and found to be ±1 percent for U and V, ±3 percent for u_{rms} and v_{rms}, and ±8 percent for uv, where percentages are based on the free-stream velocity for U and V, and in terms of the maximum level for u_{rms}, v_{rms}, and uv. LDV's have several sources of bias errors. The steps taken to avoid bias errors associated with varying seed concentrations were discussed previously. The LDV was equipped with frequency shifting, which was necessary to distinguish reverse flow and to avoid fringe bias errors. Statistical velocity bias errors were corrected using residence time weighting of the velocity measurements as recommended by Edwards (1987) for low data density measurements. The LDV velocity measurements are directly proportional to the angles between the laser beams forming the probe volume. The bias errors due to the uncertainty of measurements of these angles were estimated to be less than 0.2 percent.

Results and Discussion

Experiments were conducted to obtain a two-dimensional cross section of the mean and turbulent hydrodynamics along the centerline for a high density jet with a density ratio of $\rho_j/\rho_o = 2$ and a mass flux ratio of $M = 0.5$. Results from these experiments are compared with previous unit density experiments (Pietrzyk et al., 1989) with mass flux ratios of $M = 0.5$ and $M = 0.25$. These two unit density cases provide a basis of comparison of the differences and similarities between high density and unit density jets with respect to two fundamental scalings: equal mass flux ratio and equal velocity ratio. The momentum flux ratio for the two unit density cases, $I = 0.062$ and $I = 0.25$, bracketed the momentum flux ratio, $I = 0.125$, for the high-density injectant.

The hydrodynamics of the injection process were evaluated in terms of mean velocity vector profiles and contours of turbulence intensity, Reynolds shear stress, and correlation coefficient. Measurements were made along the centerline of the injectant hole from $x/D = -1$ to $x/D = 30$, where the origin of the coordinate system is located at the point where the leading edge of the jet intersects the test surface. The trailing edge is therefore located at $x/D = 1.74$ for the 35 deg angled injection as shown in Fig. 3. Hydrodynamic characteristics were analyzed with particular attention paid to the quality of the flow exiting the hole, the interaction of the jet with the free stream at the hole exit, the wake region immediately behind the jet, and the relaxation farther downstream.

Mean Velocity Characteristics. Measurements of $M = 0.5$, dense jet mean velocity vector profiles in the near-hole vicinity

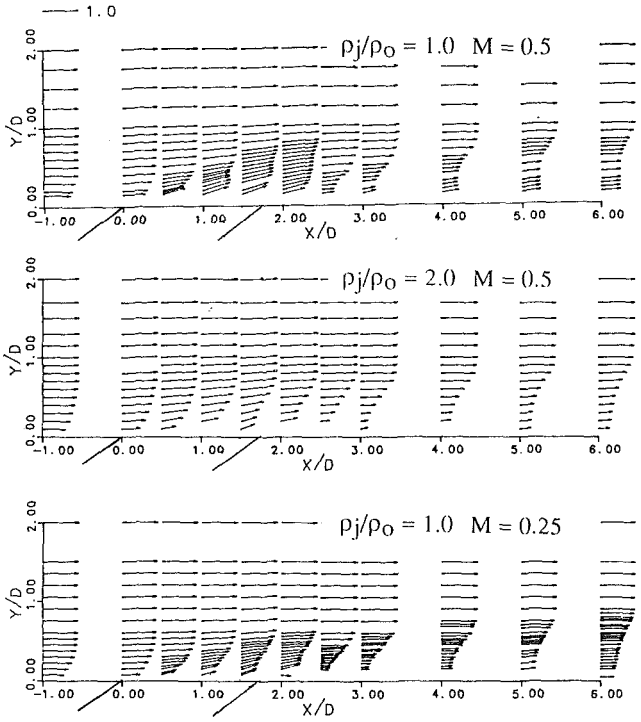

Fig. 4 Near-field mean velocity vectors

are shown in Fig. 4. For comparison, mean velocity vector profiles are also shown for the $M = 0.5$ and $M = 0.25$ unit density jet cases. The distribution of the mean velocity at the hole exit for the dense jet is seen to be similar in magnitude to the $M = 0.25$ unit density jet. The jet-to-free stream velocity ratio for both of these cases equals 0.25. However, above the hole the velocity vectors of the high-density jet are inclined slightly more away from the wall than the $M = 0.25$ unit density jet. Furthermore, downstream of the hole the velocity defect for the high-density case extends a greater distance above the wall. These results are consistent with a higher penetration expected for the high-density jet because of the higher momentum flux than the $M = 0.25$ unit density ratio jet.

The mean velocity vectors for the $M = 0.5$ unit density ratio jet were found to be uniformly larger than those of the $M = 0.5$ high-density jet, consistent with the larger velocity ratio. The velocity vectors immediately above the hole are inclined slightly more away from the wall for the $M = 0.5$ unit density jet than for the high-density jet, which suggests a greater penetration, consistent with the higher momentum flux for the $M = 0.5$ unit density jet.

Of particular interest is the near-wall region immediately behind the jet where the minimum velocity occurs for all three cases. In this region the high-density jet was found to have a lower mean velocity than either unit density cases. This suggests less influx of high-velocity mainstream fluid in this region for the high-density case, which would account for the greater film-cooling effectiveness measured by Foster and Lampard (1975) and Pedersen et al. (1977).

As the dense jet flow develops downstream, the mean velocity profiles transform from being more similar to the unit density case with equal velocity ratio to greater similarity with the unit density case with equal mass flux ratio. Figure 5 shows that beyond $x/D = 15$ the dense jet velocity profiles are essentially equivalent to the $M = 0.5$ unit density profiles. These results suggest that the dense jet flow has increased in temperature and expanded to essentially the same volume flow rate as the $M = 0.5$ unit density jet flow. The similarity of the $M = 0.5$ dense jet and the $M = 0.5$ unit density jet downstream of $x/D = 15$ is somewhat surprising since the initial development of these two flows is so different.

Downloaded 01 Jun 2010 to 171.66.16.66. Redistribution subject to ASME license or copyright; see http://www.asme.org/terms/Terms_Use.cfm

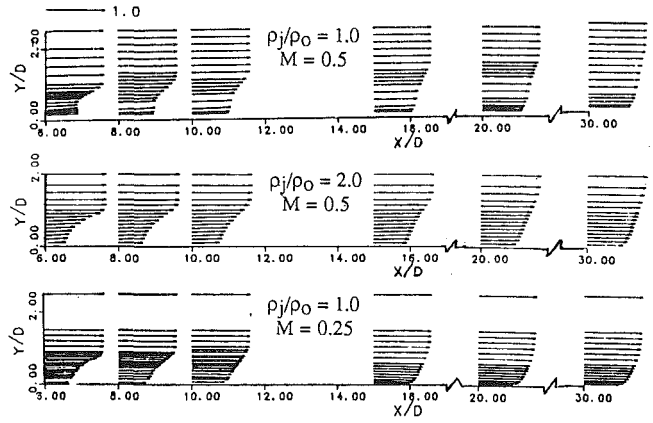

Fig. 5 Far-field mean velocity vectors

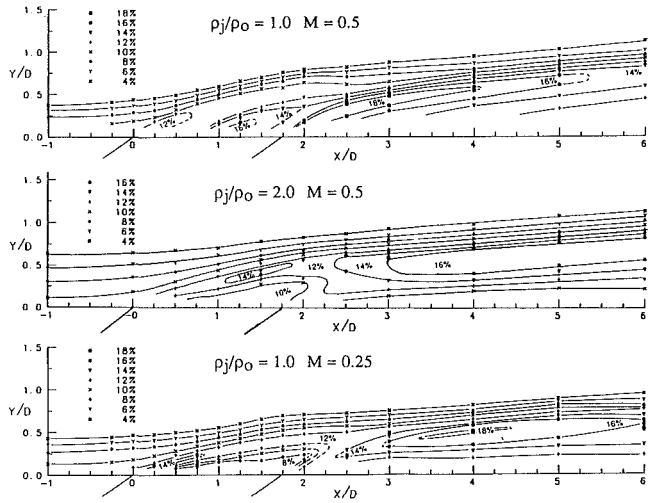

Fig. 6 Near-field turbulence level contours

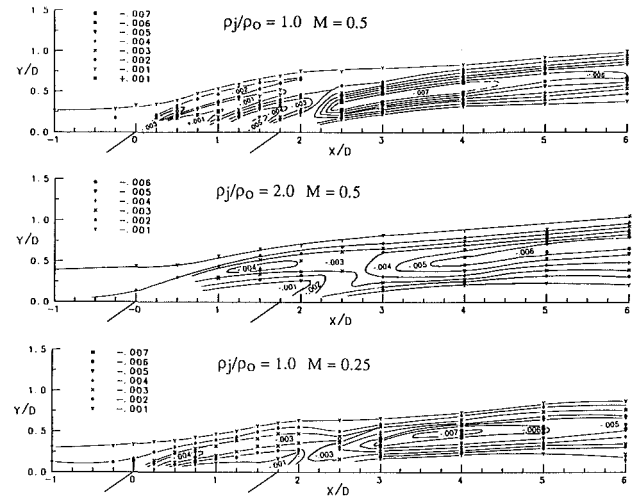

Fig. 7 Near-field turbulent shear stress ($\overline{uv}/U_\infty^2$) contours

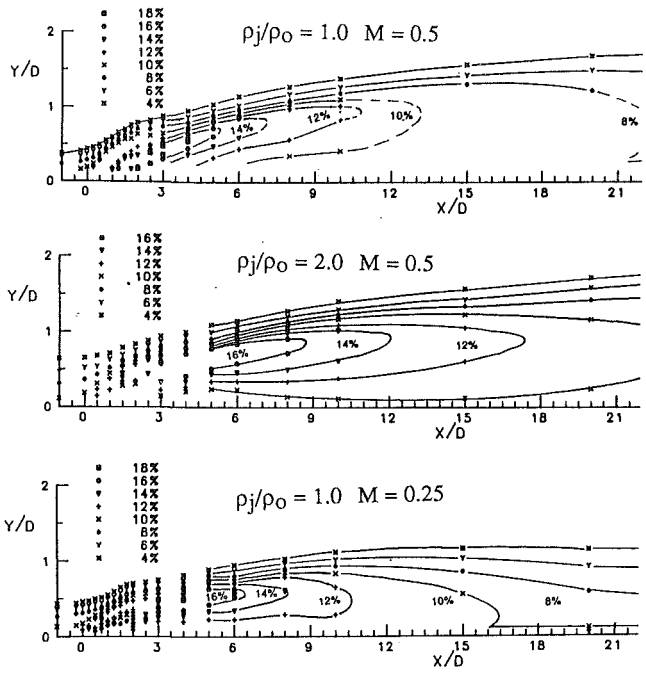

Fig. 8 Far-field turbulence level contours

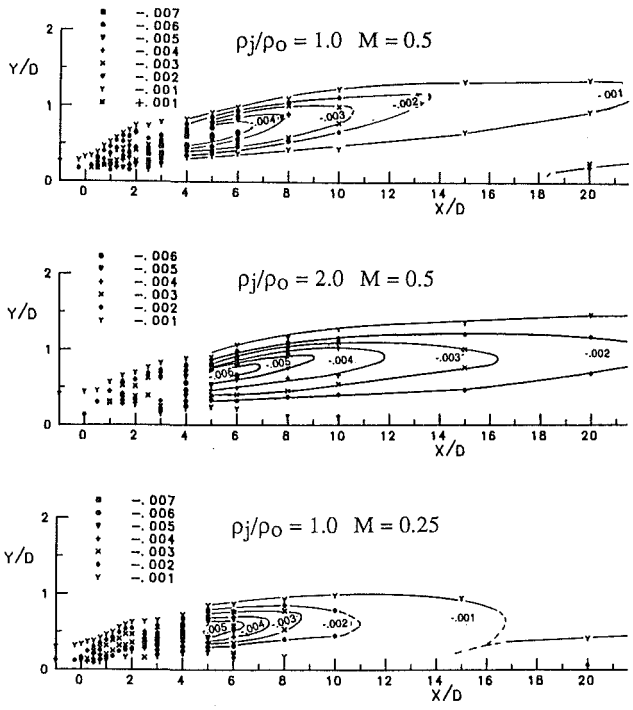

Fig. 9 Far-field turbulent shear stress ($\overline{uv}/U_\infty^2$) contours

Turbulence Characteristics. Because only two-component velocity measurements were made, turbulence levels were defined as $(u_{rms}^2 + v_{rms}^2)^{1/2}/U_\infty$. Although the total turbulence level would require measurement of the third velocity component, the following results based on two velocity components probably represent the essential effects of the film-cooling jets on turbulence levels. Figure 6 presents the near-hole turbulence level contours for the $M = 0.5$, dense jet flow along with the $M = 0.5$ and $M = 0.25$ unit density cases. Although the mean velocity distribution at the hole exit was similar for the dense jet and the $M = 0.25$ unit density jet, turbulence levels immediately above the hole (see Fig. 6) were found to be larger for the dense jet case. Pietrzyk et al. (1989) postulated that the high turbulence levels in the flow exiting the hole were due to a separation region at the hole entrance. The extent of this separation region would be similar to that of the unit density flow with equal velocity ratio, but the higher Reynolds number for the high-density flow apparently causes a slower decay of this turbulence. The turbulence levels at the exit of the dense jet are less than that for the $M = 0.5$ unit density jet.

Corresponding near-hole turbulent shear stresses are shown in Fig. 7. The turbulent shear stresses at the hole exit were uniformly low ($-\overline{uv}/U_\infty^2 < 0.001$) for both the high density jet

Downloaded 01 Jun 2010 to 171.66.16.66. Redistribution subject to ASME license or copyright; see http://www.asme.org/terms/Terms_Use.cfm

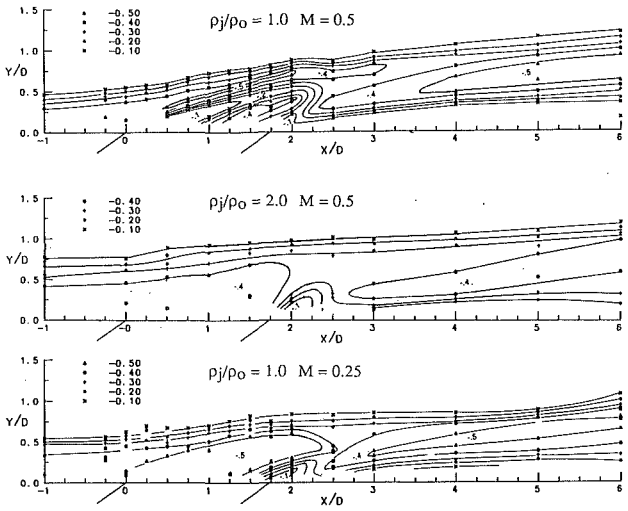

Fig. 10 Near-field correlation coefficient ($-\overline{uv}/(u_{rms} * v_{rms})$) contours

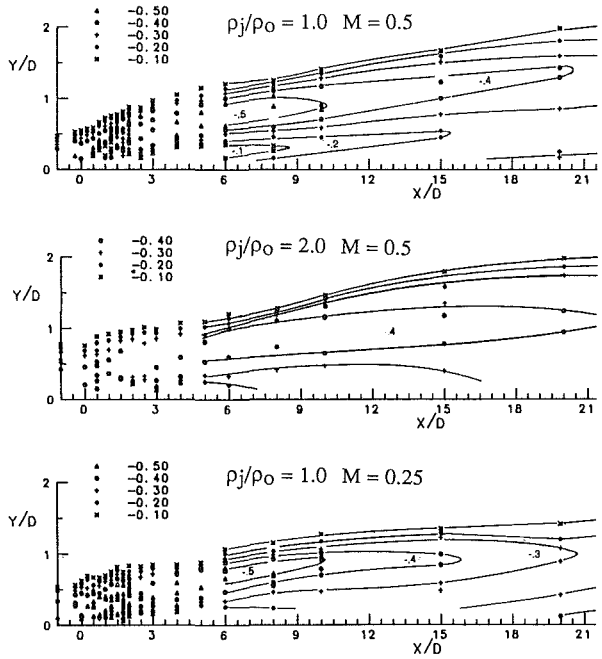

Fig. 11 Far field correlation coefficient ($-\overline{uv}/(u_{rms} * v_{rms})$) contours

and the $M = 0.25$ unit density jet. Turbulent shear stresses exiting the hole for the $M = 0.5$ unit density jet were much different with a strong variation ranging from $\overline{uv}/U_\infty^2 = +0.001$ to $\overline{uv}/U_\infty^2 = -0.005$. These results indicate that, in contrast to the turbulence levels, which appeared to be generated in the upstream part of the hole, the turbulent shear stresses are due more to the local mean velocity gradients at the hole exit. The correspondence between the turbulent shear stress and the local mean velocity gradient is discussed in a later section.

For all three cases, large turbulence levels and uv stresses were generated immediately downstream of the jets in the shear region on the lower part of the jets. The downstream relaxation of the turbulence levels and turbulent shear stresses are presented in Figs. 8 and 9, respectively. Although the magnitudes of the turbulence levels and uv stresses were found to be comparable in all cases, the figures show high levels persisted for greater distances downstream for the dense jet. These results show that the distributions of the mean velocity for the dense jet and the unit density jet with the same mass flux become similar at an earlier point than the turbulence quantities.

Shear Stress Correlation Coefficient. The correlation coefficient, $-uv/(u_{rms} * v_{rms})$, indicates the extent of correlation between fluctuations of the u and v velocity components and is a measure of the structural content of the turbulence. Figure 10 shows the near-hole correlation contours. In the region over the hole, the contours of the correlation coefficient for the dense jet and the $M = 0.25$ unit density jet are similar. The entire region over the hole was found to have a high correlation coefficient (-0.4 to -0.5). Both the uv shear stress and the turbulence level are small in this region (much of the scatter in the correlation coefficient results was caused by

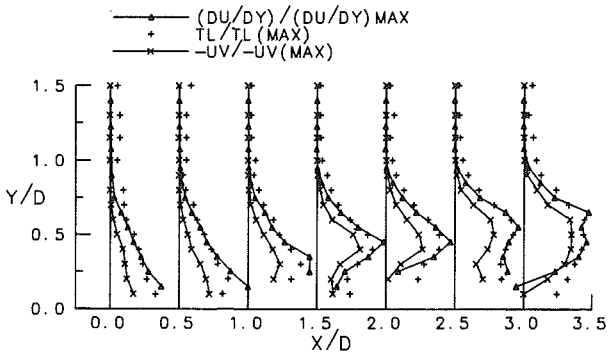

Fig. 12 Correspondence between the normalized turbulence quantities and the normalized mean velocity gradient for the near-hole region of the $M = 0.5$ dense jet

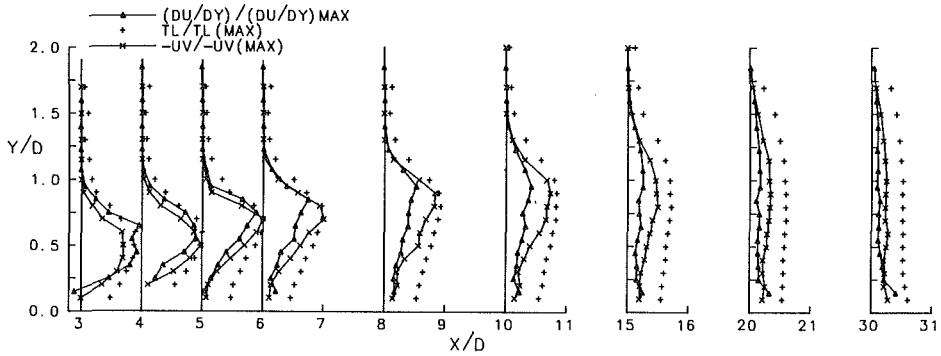

Fig. 13 Downstream development of the correspondence between the normalized turbulence quantities and the normalized mean velocity gradient for the $M = 0.5$ dense jet

Downloaded 01 Jun 2010 to 171.66.16.66. Redistribution subject to ASME license or copyright; see http://www.asme.org/terms/Terms_Use.cfm

taking the ratio of these two small numbers). For the $M=0.5$ unit density jet, the contours of the correlation coefficient correspond well with the contours of the uv shear stress, i.e., the magnitude of the correlation coefficient is low (<0.1) over the upstream portion of the hole and high (>0.4) over the downstream part.

For all three cases, the magnitude of the correlation coefficient is large (>0.4) in the shear layer at the upper leading edge of the jet. For the dense jet and the $M=0.25$ unit density jet, the high levels of correlation coefficient associated with this shear layer have merged into the region with high correlation coefficient existing directly over the hole exit.

The development of the correlation coefficient downstream of the hole is shown in Fig. 11. The data follow the same general trends for all three cases. High values of the correlation coefficient (-0.4 to -0.5) were found in the shear layer, at the lower part of the jet, downstream of the hole up to $x/D=10$. Beyond $x/D=10$ the magnitude of the correlation coefficient associated with the jet decreases until this region merges with the region of increasing correlation coefficient associated with the flow adjacent to the wall. Far downstream, $x/D>20$ for the $M=0.25$ unit density ratio case, the presence of the jet is no longer distinguishable in the correlation coefficient contours. At $x/D=30$ the magnitude of the correlation coefficient is ~ 0.45 over a large portion of the flow near the wall and monotonically decreases, moving away from the wall, indicating that the flow is relaxing back to a standard boundary layer. For the two higher mass flux ratio cases this relaxation process takes place further downstream.

Correlation coefficients of the magnitudes (-0.1 to -0.5) found in the flowfield studied here have been measured in turbulent flows containing separation due to an adverse pressure gradient (Simpson et al., 1981) and downstream of a backward facing step (Etheridge and Kemp, 1978).

Correspondence Between Turbulence Parameters and Mean Velocity Gradients. An important consideration from the standpoint of modeling is the degree of correspondence between turbulence parameters and mean velocity gradients. The near-hole and downstream distributions of uv, the turbulence level, and $\partial U/\partial y$ (normalized by their maximum values) are compared in Figs. 12 and 13 for the high-density jet. Good agreement exists between the distributions of uv and $\partial U/\partial y$ both near the hole and downstream. The same good agreement was also found for the unit density jet cases (Pietrzyk et al., 1989). The agreement found between the distribution of the vertical gradient of the mean streamwise velocity and the distribution of uv shear stress implies that the production of this Reynolds stress is primarily due to this velocity gradient.

The shear layer at the top of the jet is evident from the large values in the velocity gradient profiles between $x/D=0.5$ and 4.0. Good correspondence with uv and the turbulence level was found in this shear layer. Beginning at $x/D=2.5$ (see Fig. 12), a second peak in the velocity gradient profile, located below the previous peak, is apparent. This second peak is due to the large shear layer that exists at the lower part of the jet downstream of the hole. Beyond $x/D=10$ this shear layer is no longer distinguishable. The correspondence with uv and the turbulence level is good in this shear layer, although the magnitude of the velocity gradient decays faster than both uv and the turbulence level, indicating that the elevated levels of these turbulence quantities existing far downstream of the hole are due to the convection of turbulence produced upstream nearer the hole.

Conclusions

Data have been presented to document the film cooling flowfield for $M=0.5$ and a density ratio of 2, and the data were compared to two unit density cases with momentum flux ratios that bracketed the high-density case. Although no unique flow patterns were generated by the higher density jets, significant differences between the dense jets and the unit density jets were apparent. In the dense jet, the velocity field at the hole exit corresponds well with the unit density jet of the same velocity ratio. The penetration of the dense jet into the mainstream was bracketed by the two unit density jets. Downstream of the hole, the dense jet had lower velocities in the near wall region than either of the unit density jets. Farther downstream the velocity field of the dense jet compared well with the unit density case with the same mass flux ratio. Although the turbulence levels and uv shear stresses attained similar maximum values behind the hole for the high-density jet and the unit density jets, there was a significantly lower relaxation rate for these quantities for the high-density jet.

Acknowledgments

The authors gratefully acknowledge Garrett Engine Division of the Allied-Signal Aerospace Corporation for support of this research. We would also like to thank Mr. Alok Sinha and Mr. Robert McAndrews for their assistance in parts of this work.

References

Etheridge, D., and Kemp, P., 1978, "Measurements of Turbulent Flow Downstream of a Rearward-Facing Step," *Journal of Fluid Mechanics*, Vol. 86, pp. 545–566.

Edwards, R. W., 1987, "Report of the Special Panel on Statistical Particle Bias Problems in Laser Anemometry," ASME *Journal of Fluids Engineering*, Vol. 109, pp. 89–93.

Foster, N. W., and Lampard, D., 1975, "Effects of Density and Velocity Ratio on Discrete Hole Film Cooling," *AIAA Journal*, Vol. 13, pp. 1112–1114.

Foster, N. W., and Lampard, D., 1980, "The Flow and Film Cooling Effectiveness Following Injection through a Row of Holes," ASME *Journal of Engineering for Power*, Vol. 102, pp. 584–588.

Launder, B. E., and York, J., 1974, "Discrete-Hole Cooling in the Presence of Free Stream Turbulence and Strong Favourable Pressure Gradient," *International Journal of Heat and Mass Transfer*, Vol. 17, pp. 1403–1409.

Le Brocq, P. V., Launder, B. E., and Priddin, C. H., 1973, "Discrete Hole Injection as a Means of Transpiration Cooling; An Experimental Study," *Proceedings of the Institution of Mechanical Engineers*, Vol. 187, pp. 149–157.

Pedersen, D. R., Eckert, E. R. G., and Goldstein, R. J., 1977, "Film Cooling With Large Density Differences Between the Mainstream and the Secondary Fluid Measured by the Heat-Mass Transfer Analogy," ASME *Journal of Heat Transfer*, Vol. 99, pp. 620–627.

Pietrzyk, J. R., Bogard, D. G., and Crawford, M. E., 1989, "Hydrodynamic Measurements of Jets in Crossflow for Gas Turbine Film Cooling Application," ASME JOURNAL OF TURBOMACHINERY, Vol. 111, pp. 139–145.

Simpson, R., Chew, Y., and Shivaprasad, B., 1981, "The Structure of a Separating Turbulent Boundary Layer. Part 1. Mean Flow and Reynolds Stresses," *Journal of Fluid Mechanics*, Vol. 113, pp. 23–51.

Spalding, D. B., 1961, "A Single Formula for the Law of the Wall," *Journal of Applied Mechanics*, Vol. 83, pp. 455–458.

White, F. M., 1974, *Viscous Fluid Flow*, McGraw-Hill, New York.

Downloaded 01 Jun 2010 to 171.66.16.66. Redistribution subject to ASME license or copyright; see http://www.asme.org/terms/Terms_Use.cfm

The Effect of Density Ratio on the Heat Transfer Coefficient From a Film-Cooled Flat Plate

H. D. Ammari

N. Hay

D. Lampard

Department of Mechanical Engineering,
University of Nottingham,
Nottingham, United Kingdom

The effect of density ratio of cooling films on the heat transfer coefficient on a flat plate is investigated using a heat–mass transfer analogy. The experimental technique employed uses a swollen polymer surface and laser holographic interferometry. A density ratio of 1.0 was achieved using air as the injectant. Density ratios of 1.38 and 1.52, representative of turbine operating conditions, were obtained by using foreign gases. The coolant fluids were injected at various blowing rates through a single normal hole or through a row of holes spaced at three-diameter intervals, and inclined at 35 or 95 deg to the mainstream direction. The experiments were conducted under isothermal conditions in a subsonic, zero mainstream pressure gradient turbulent boundary layer. The results indicated large differences in behavior between the two injection angles. For normal injection, the heat transfer coefficient at a fixed blowing parameter was insensitive to the variation of density ratio, whereas for 35 deg injection strong dependence was observed. Scaling parameters for the heat transfer data have been proposed so that use can be made of data obtained at density ratios not representative of gas turbine practice. In addition, a correlation for normal injection data has been formulated.

Introduction

In film cooling, air bled from the compressor passes through ducts, and is injected onto the component's surface through a single row of holes or multiple staggered rows of holes. Cooling films so produced protect the surfaces of turbine nozzle vanes and rotor blades from the hot combustion gases, which are at temperatures well in excess of material oxidation and creep temperature limits.

To optimize cooling, accurate determination of the heat load to the blade surface is required at flow conditions typical of gas turbine practice. Despite recent advances, more heat transfer data produced by experimental investigations are still required, the complex nature of the cooling process having so far precluded theoretical analyses of acceptable accuracy.

Cost considerations have resulted in many fundamental investigations being carried out at low temperatures, with coolant-to-mainstream density ratios near unity. For example, Eriksen and Goldstein (1974) and Liess (1975) conducted heat transfer measurements for injection of slightly heated jets through a row of holes, while Hay et al. (1985a) used a mass transfer analogue with air-into-air injection. Their results show the order of increase in heat transfer coefficient produced by injection, and give some insight into the flow mechanisms, but do not yield data directly applicable in the design process.

Turbine inlet temperatures of up to 1700 K and coolant air temperatures in the range of 700 to 1000 K are common in modern jet engines. This results in coolant-to-mainstream density ratios well in excess of unity. Previous three-dimensional film cooling studies on density ratio effects, for example Pedersen et al. (1977), Foster and Lampard (1975), and Ito et al. (1978), have mainly been limited to adiabatic wall effectiveness data derived by injecting foreign gases and measuring their concentration at an impermeable wall. Such studies have indicated significant dependence of the film cooling process on density gradients.

Effectiveness data are often presented in terms of the mass flux ratio for constant-property flows, while the momentum flux ratio or the velocity ratio have been used to correlate results in the presence of density gradients (Pedersen et al., 1977; Goldstein et al., 1974) for single rows of holes.

Similarly, cooling film heat transfer coefficients for injection through slots have been shown by Foster and Haji-Sheikh (1975) and by Metzger et al. (1968) to correlate reasonably well with the mass flux ratio at constant density. Again, these data cannot be used at turbine operating density ratios unless the proper scaling can be established and applied.

Recently, Forth and Jones (1985, 1986) have reported considerable progress in determining scaling parameters for two- and three-dimensional film cooling data over a wide range of density and mass flux ratios. They have identified two broad and distinct flow regimes: the weak injection regime, in which the injection flow remains essentially attached to the surface, as for an angled slot or a double row of holes at 30 deg, and the strong injection regime, in which the injected flow lifts off

Contributed by the International Gas Turbine Institute and presented at the 34th International Gas Turbine and Aeroengine Congress and Exhibition, Toronto, Ontario, Canada, June 4–8, 1989. Manuscript received at ASME Headquarters January 27, 1989. Paper No. 89-GT-176.

Copyright © 1990 by ASME
Downloaded 01 Jun 2010 to 171.66.16.66. Redistribution subject to ASME license or copyright; see http://www.asme.org/terms/Terms_Use.cfm

the surface and penetrates some distance into the mainstream, as for a 30 deg inclined single row of holes. For the weak injection regime, the heat transfer data with variable density and velocity ratios collapsed well with the momentum flux ratio, whereas for the strong injection regime, satisfactory scaling was achieved with the velocity ratio. These are the correlating parameters for effectiveness from single row injection reported by Pedersen et al. (1977). Further correlating parameters incorporating the distance downstream are developed by Forth and Jones (1986).

Despite this, there remains a pressing need for further heat transfer coefficient data for density ratios around those of gas turbines, and for further development of correlations to allow the application to design of data from unity density ratio tests.

The work presented in this paper springs from these considerations. Using foreign gas injection with a mass transfer analogue technique, as validated in a companion paper (Ammari et al., 1989), high resolution heat transfer coefficient data have been collected. Density ratio of 1.0 and 1.38 have been used with normal injection through a single hole and 1.0 and 1.52 with injection through single rows of holes of 35 and 90 deg inclination.

Experimental Approach

The heat transfer to a film-cooled wall can be written (Goldstein, 1971)

$$q_f'' = h_f(T_{aw} - T_w)$$

where h_f is the heat transfer coefficient in the presence of film cooling, T_w is the wall temperature, and T_{aw} is the adiabatic wall temperature, usually given in nondimensional form as effectiveness

$$\eta_{aw} = \frac{T_\infty - T_{aw}}{T_\infty - T_c}$$

T_∞ and T_c are the mainstream and coolant temperatures, respectively. Defining a dimensionless coolant-to-mainstream temperature difference as

$$\theta = \frac{T_\infty - T_c}{T_\infty - T_w}$$

the heat flux equation can be rewritten

$$q_f'' = h_f(T_\infty - T_w)(1 - \eta_{aw}\theta)$$

In the absence of cooling, the heat transfer is

$$q_o'' = h(T_\infty - T_w)$$

In the present work, h_0 is determined in the absence of both blowing and injection holes, so that no roughness effects occur.

Thus, if the wall and mainstream temperature are the same in the two cases

$$\frac{q_f''}{q_0''} = \frac{h_f}{h_0}(1 - \eta_{aw}\theta)$$

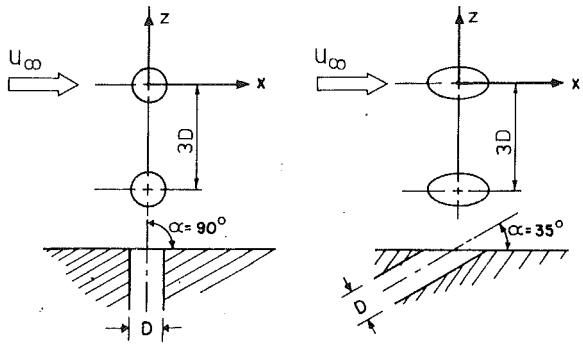

Fig. 1 Injection geometry

For the particular case of $\theta = 0$, the heat flux ratio is equal to the heat transfer coefficient ratio. An identical result is obtained using the "superposition" concept for calculation of heat transfer on film-cooled surfaces (Choe et al., 1974). Here, all influence of injection is absorbed in a heat transfer coefficient, h, such that

$$q'' = h(T_\infty - T_w)$$

Measurements of h performed on an isothermal wall varying θ, such as those of Ville and Richards (1978) should also yield h_f by extrapolation to $\theta = 0$. This is the condition modeled in the experiments reported here. The measured heat transfer coefficient corresponds, therefore, to h_f.

In the present work, h is measured by an analogous mass transfer technique. A constant and uniform wall concentration simulates a fixed temperature, and isothermal wall, and absence of the mass-transferring agent from both the mainstream and the coolant flows gives an equivalent condition to $\theta = 0$. This is the approach used by Hay et al. (1985a) in measurements of heat transfer coefficient under uniform density conditions. It is used here at coolant-to-mainstream density ratios close to those occurring in practice.

Mass transfer techniques are well suited to studies employing large coolant-to-mainstream density ratios, which may be simply obtained by use of foreign gas injection. The problem of wall conduction inherent in thermal techniques using large temperature differences is thus avoided. Concentrations are analogous to temperature, and mass flux to heat flux.

In the mass transfer method used, the thickness changes of a swollen polymer surface (Macleod and Todd, 1973) are measured with laser holographic interferometry (Hildebrand and Haines, 1966). The relative merits of this method over the commonly used naphthalene sublimation technique are discussed by Saluja et al. (1984).

The mass-transferring system incorporates a test surface coated by a silicone rubber polymer swollen to equilibrium in an organic agent. Exposure of the swollen coating to the film cooling flows causes a transfer of the organic agent, so that

Nomenclature

D = injection hole diameter
h = heat transfer coefficient
$\bar{h}$ = lateral average heat transfer coefficient
I = momentum flux ratio
M = blowing rate (mass flux ratio)
P = pressure
q'' = heat flux
Re = Reynolds number
s = distance between injection hole centers
T = temperature
u = velocity
x = downstream distance from injection hole origin
z = lateral distance from injection hole origin
α = injection inclination to the streamwise direction
δ^* = boundary layer displacement thickness
η = effectiveness
θ = temperature difference parameter
ρ = density

Subscripts

aw = adiabatic wall
c = coolant
D = injection hole diameter
f = injection
w = wall
0 = zero injection
∞ = mainstream

Downloaded 01 Jun 2010 to 171.66.16.66. Redistribution subject to ASME license or copyright; see http://www.asme.org/terms/Terms_Use.cfm

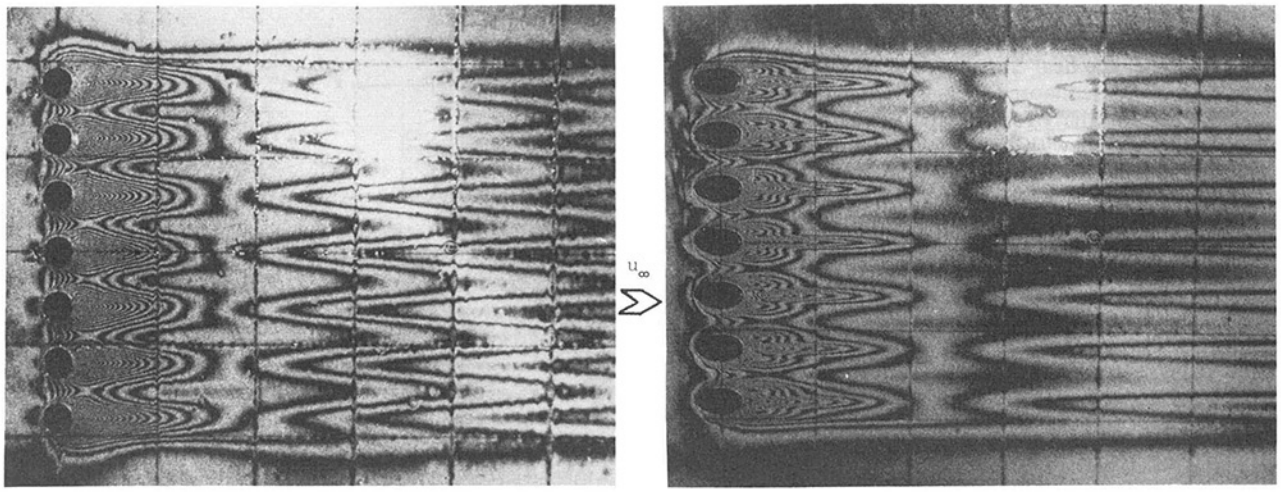

Fig. 2(*a*) 90 deg injection

Fig. 2(*b*) 35 deg injection

Fig. 2 Interference fringes depicting contours of constant heat (mass) transfer ($u_\infty = 25$ m/s, $M = 1$, $\rho_c/\rho_\infty = 1.0$)

the rate of change of the coating thickness is proportional to the local mass (heat) transfer coefficient (Macleod and Todd, 1973). Use of laser interferometry produces a hologram with a fringe pattern from which the coating recession, and therefore h, can be deduced at all points on the surface. For a more comprehensive description of the technique and its applicability to the study of heat transfer on film-cooled surfaces see Hay et al. (1982).

Apparatus

The subsonic, low-turbulence, open-circuit wind tunnel described in the companion paper (Ammari et al., 1989) was also used in the present study. Some changes were needed to the test section and the injection system to suit the present work. Two additional polymer-coated test plates were used. Each new plate contained a single row of seven stainless steel hypodermic injection tubes of 2.3-mm i.d., spaced at three hole diameters in the lateral direction. On one plate the row was normal to the streamwise direction while on the other it was inclined at 35 deg, as shown in Fig. 1.

Three injection fluids were used; air drawn from the same supply as the mainstream, argon, used in the single-tube normal injection experiments only, and carbon dioxide. The foreign gas injectants were fed from pressurized bottles. The injection gases were regulated, controlled, and metered, then passed through a plenum chamber containing a straightener and gauze screens before entering to the injection tubes. Long injection tubes were used to ensure fully developed flow at their exists.

Operating Conditions and Procedures

Steady-state, isothermal conditions prevailed during all tests, with a fully developed, two-dimensional turbulent boundary layer existing over the entire test surface. The maximum tube-to-tube variation of injected flow was less than one percent. The data collection area extended from 5 tube diameters upstream of the injection location to 60 diameters downstream.

The experimental operating conditions were:

Mainstream velocity, $u_\infty = 25$ m/s
Boundary layer displacement thickness at injection location, $\delta^* = 0.40\ D$
Mainstream Reynolds number, $\mathrm{Re}_D = 3.8 \times 10^3$
Mainstream pressure gradient, $dP/dx = 0$

The ranges of the main parameters varied were

Coolant to mainstream density ratio, $\rho_c/\rho_\infty = 1.0$, 1.38, and 1.52
Blowing parameter (mass flux ratio), $\rho_c u_c/\rho_\infty u_\infty = 0.5$–$2.0$
Injection angle, $\alpha = 90$ and 35 deg

The boundary layer displacement thickness ratio, δ^*/D, is rather larger than that typical of blades and vanes. However, Hay et al. (1985b) show that this should have little effect upon the heat transfer coefficient.

The number of holes used in a row was 7. This was found to give a central region representative of an infinitely long row of holes over the full streamwise extent of the test surface. Edge effects of the mainstream on the cooling film heat transfer coefficient were confined to the holes situated at either end of the row. A similar observation was reported by Pedersen et al. (1977) for effectiveness measurements.

Qualification of the present technique for the measurement of heat transfer coefficient by measuring the Stanton number distribution without injection has been described by Ammari et al. (1989). Good agreement was obtained with an established correlation. The measurement of cooling film heat transfer coefficients at non-unity density ratios using a mass transfer technique with foreign gas injection was also shown to be valid.

Typical holograms of 90 and 35 deg injection at similar test conditions are shown in Figs. 2(*a*) and 2(*b*), respectively. Each fringe depicts a contour of equi-recession of the swollen coating or of constant mass (heat) transfer coefficient. Notice the different structure of the contours downstream of injection location, especially immediately after the holes. The differences are attributable to the difference in nature of the jet–mainstream interaction.

Repeatability was excellent. In similar tests the number of contours in the holograms increased or decreased depending on the operating temperature and test duration. However, the values of the local heat transfer coefficient ratio did not differ by more than ± 3 percent, which corresponds to the uncertainty of the measurement, estimated according to the method of Kline and McClintock (1953).

Results and Discussion

As in the companion paper (Ammari et al., 1989) results are presented as ratios of heat transfer coefficients with and without injection, h/h_0, where h_0 is determined in the absence of injection holes. Some are presented as contour plots derived from large numbers of data points read from the holograms. Individual fringes could not be properly resolved in the first

Downloaded 01 Jun 2010 to 171.66.16.66. Redistribution subject to ASME license or copyright; see http://www.asme.org/terms/Terms_Use.cfm

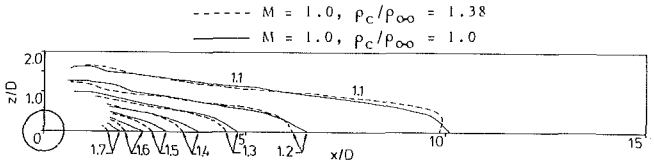

Fig. 3 h/h_0 **contours following normal injection through a single hole**

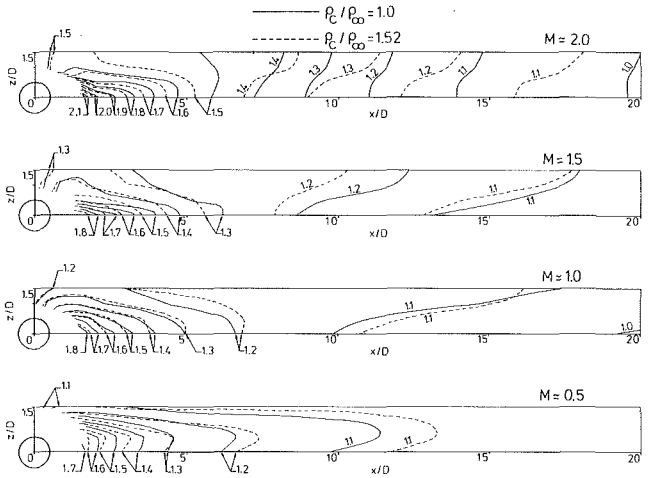

Fig. 4 h/h_0 **contours following normal injection through a row of holes**

one or two diameters downstream of the holes so contours are not shown there. The plots terminate at 20 diameters since, beyond this point, h/h_0 changes very slowly, and is close to unity anyway, for all but the highest blowing rate.

Single Normal Hole. Contours of the heat transfer ratio h/h_0 for two density ratios 1.0 and 1.38 at a blowing rate of unity are plotted in Fig. 3. Increases in the heat transfer coefficient exceeding 10 percent are confined to the first 10 diameters downstream of the holes, and are greatest on the centerlines immediately after the hole.

Although the momentum flux is reduced by approximately 28 percent for the denser injectant, the contours for the two densities hardly differ from one another. The fast mixing and high turbulence levels associated with normal injection diminish the influence of jet density as well as momentum variation on the heat transfer coefficient.

One further result to be extracted from the figure is that the blowing rate M seems to be a promising correlating parameter in this case.

Single Row of 90 deg Holes. It seems logical that the result obtained here, regarding the effect of density ratio on h/h_0, should be similar to that obtained for a single normal hole since the jet–mainstream mixing is essentially identical in nature. This is confirmed by Fig. 4 where the influence of varying the density ratio from 1.0 to 1.52 on the normalized heat transfer coefficient at four blowing rates is shown. Only small differences occur between the contour shapes and levels for the two densities at any position. For most blowing rates, differences do not exceed 3 percent, although they rise to 5 percent at large downstream distances at the highest blowing rate. The density ratio thus has no distinct effect on the normalized heat transfer coefficient at a constant blowing rate.

Figure 4 also shows the effect of jet–mainstream mixing on the heat transfer coefficient. Generally, the contour plots for both density ratios indicate that injection causes large increases in the heat transfer coefficient. For $M=2.0$, this increase exceeds 100 percent just downstream of a hole.

There is also a significant lateral variation in the heat transfer

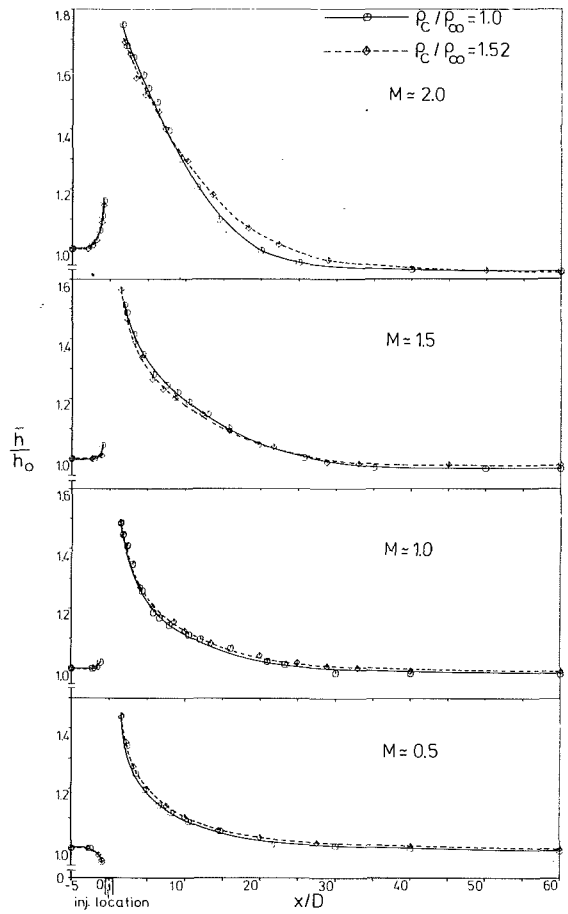

Fig. 5 Effect of density ratio on $\bar{h}/h_0$ **for normal injection through a row of holes**

coefficient. At a blowing rate of 0.5, the maximum heat transfer coefficient occurs near the edge of the jets where they interact with the mainstream. Due to the low jet trajectory, the jets behave like multiple single jets until far downstream. However, for M of 1 to greater, the maximum is initially on the jet centerline, while beyond about $x/D=7$, the maximum h/h_0 occurs at midpitch positions. This behavior may be due to the fact that, at elevated blowing rates, the jets mix quickly with the mainstream, spread rapidly, and coalesce close to the injection location. As a consequence, the lateral distribution of h/h_0 at x/D greater than 7 becomes progressively flatter, and is almost two dimensional at the highest blowing rate.

Comparison of data from Figs. 3 and 4 for the particular case of M of unity shows that the heat transfer coefficient following injection through a row of holes is little higher than that for injection through a single hole at centerline positions, whereas it is appreciably higher at locations between the holes. Mixing between neighboring jets therefore enhances the heat transfer coefficient.

The insensitivity to density ratio of the detailed normalized heat transfer coefficient distribution at a fixed blowing rate naturally implies that the spanwise-average distributions will also correlate with M. This is verified in Fig. 5, where the laterally averaged normalized heat transfer coefficient $\bar{h}/h_0$ is presented for density ratios of 1.0 and 1.52 as a function of x/D. The averages were obtained by numerically integrating the local mass (heat) transfer coefficient distribution.

Upstream of the injection holes, the injection-affected regions is at most 3 hole diameters in extent at high M. At these high blowing rates, the jets are seen as solid bars by the mainstream and the interaction gives rise to an increase in h/h_0 just upstream of up to 16 percent at $M=2$. As the blowing rate

Downloaded 01 Jun 2010 to 171.66.16.66. Redistribution subject to ASME license or copyright; see http://www.asme.org/terms/Terms_Use.cfm

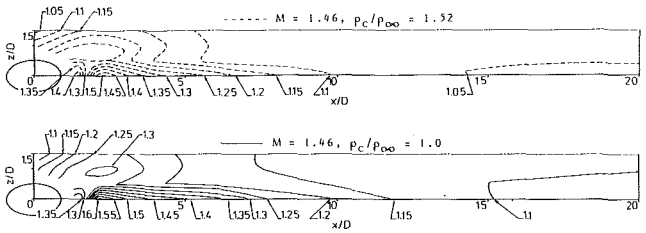

Fig. 6 h/h_0 **contours following injection at 35 deg through a row of holes**

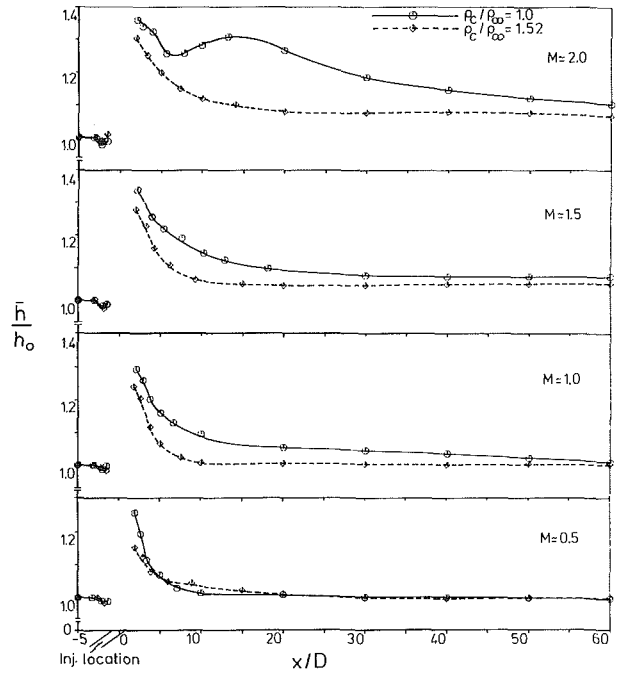

Fig. 7 Effect of density ratio on $\bar{h}/h_0$ **for 35 deg injection through a row of holes**

reduces, so also does the strength of the interaction, until at $M = 0.5$ there is a slight decrease in the heat transfer, probably caused by the slowing down of the mainstream by the jets.

Downstream of the injection location, $\bar{h}/h_0$ increases with M, and decreases monotonically with x/D. Maximum values vary from 1.45 at $M = 0.5$ to 1.75 at $M = 2.0$.

Single Row of 35 deg Holes. Blowing rate does not correlate data from 35 deg tests, as seen from Fig. 6, a contour plot of h/h_0 for $M = 1.5$ at density ratios of 1.0 and 1.52. Differences of the order of 10 percent occur in h/h_0 when the density ratio changes, lower density leading to increased heat transfer. Similar behavior to that in Fig. 6 was seen at the other blowing rates used in this study.

At any given blowing rate, the lower density injectant has the higher momentum. Because the inclined jets do not mix rapidly with the mainstream, this increased momentum is reflected in the cooling film, and hence the Reynolds analogy leads to the expectation of an increased heat transfer coefficient.

Regions of high h/h_0 close to the holes were observed for all blowing rates examined. The heat transfer coefficient in these regions increased in magnitude with increased M, as did their streamwise extent. This is understandable since, at sufficiently high injection momentum ratios, jet lift-off immediately downstream of the holes permits the mainstream to flow beneath the jets creating intense eddies, and increasing the heat transfer. Farther downstream, reattachment of the

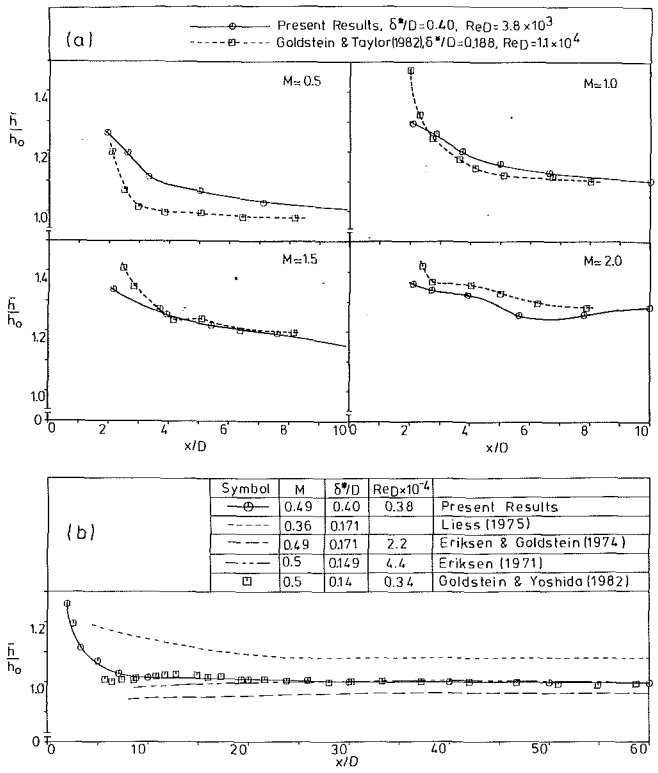

Fig. 8 Comparison of $\bar{h}/h_0$ **results with those of others for 35 deg injection**

streamwise vortices has apparently enhanced the heat transfer coefficient at midpitch positions.

To clarify the influence of density ratio variation on the heat transfer coefficient, the normalized heat transfer coefficient data averaged in the spanwise direction are plotted in Fig. 7 with the density ratio as parameter. Downstream of the holes, an increase in density ratio is seen to result in a considerable decrease in $\bar{h}/h_0$ at all M. As M increases, the difference in momentum between the heavier and lighter gas injectants increases, and this is reflected in a corresponding increase in the difference in $\bar{h}/h_0$ between the two sets of results. Differences in $\bar{h}/h_0$ as high as 8 percent at $M = 0.5$ and 18 percent at $M = 2.0$ are observed. These results are consistent with those obtained using a heat transfer method by Eriksen and Goldstein (1974).

A comparison of part of the present results for a 35 deg injection with those of other experimenters for a density ratio of unity using a similar injection geometry is shown in Figs. 8(*a*) and 8(*b*). The operating conditions for each data set are shown on the figures. In Fig. 8(*a*) the $\bar{h}/h_0$ data for x/D less than 10 and for all M covered are compared with those of Goldstein and Taylor (1982) obtained using the naphthalene sublimation technique. The agreement is generally good, although their results show a much steeper initial fall in h/h_0. This may be due to the differing boundary layer displacement thicknesses and Reynolds numbers.

The results of Eriksen and Goldstein (1974), Liess (1975), Eriksen (1971), and Goldstein and Yoshida (1982) were obtained by thermal methods at different test conditions, and are compared with the present results in Fig. 8(*b*). Very close agreement is seen between the present results and those of Eriksen (1971) and Goldstein and Yoshida (1982). Generally, the difference between the present results and the results of the other experimenters is less than the difference between their results.

The 90 and 35 deg results differ markedly in their response to changes in blowing rate and in density ratio. For 90 deg

Downloaded 01 Jun 2010 to 171.66.16.66. Redistribution subject to ASME license or copyright; see http://www.asme.org/terms/Terms_Use.cfm

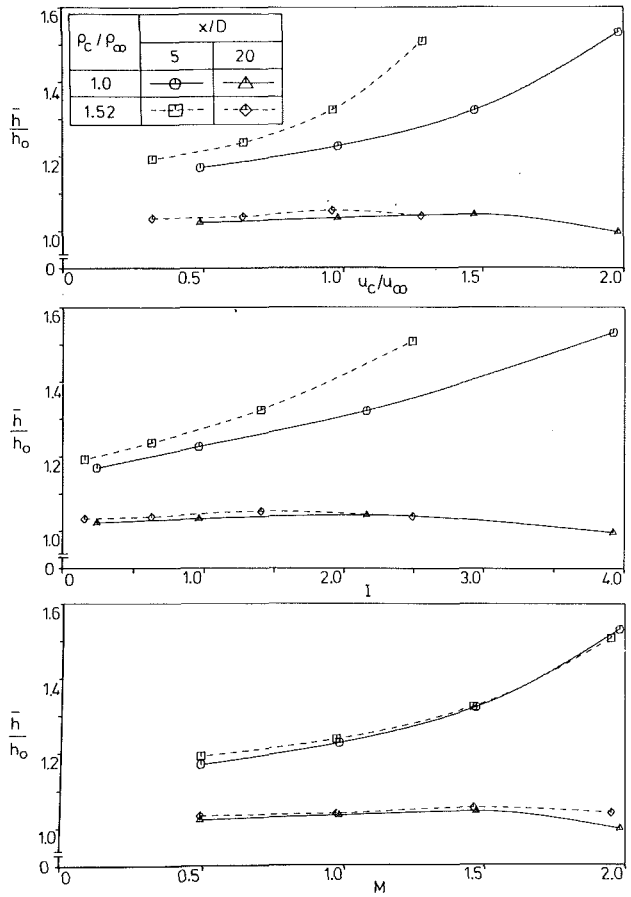

Fig. 9 Effect of injection parameters on $\bar{h}/h_0$ for normal injection

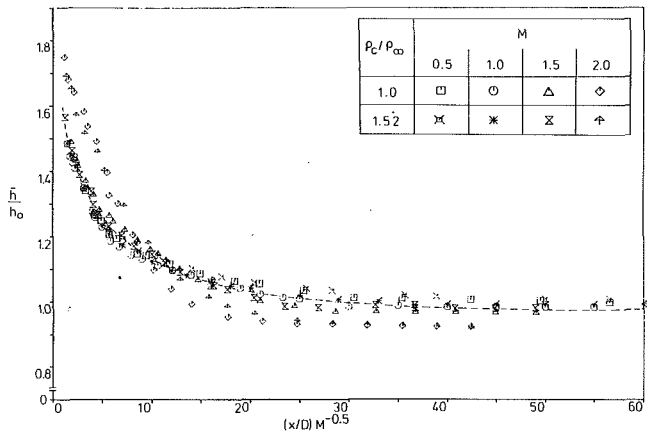

Fig. 10 Correlation of $\bar{h}/h_0$ for normal injection

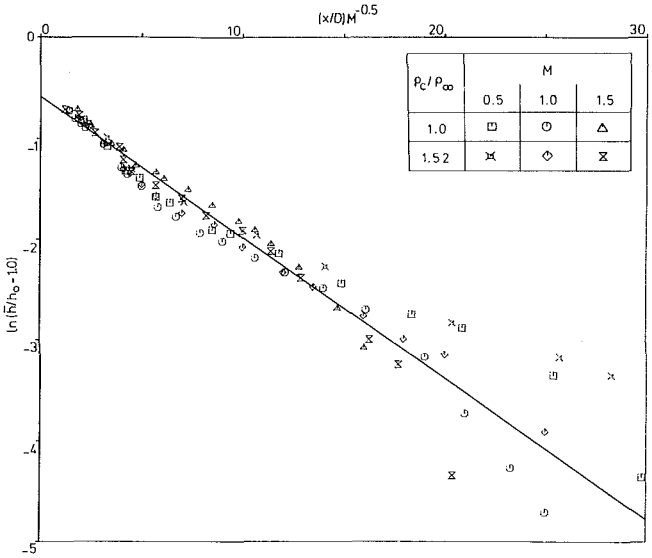

Fig. 11 Correlated $\bar{h}/h_0$ results for $D<25$ and $0.5<M<1.5$ for normal injection

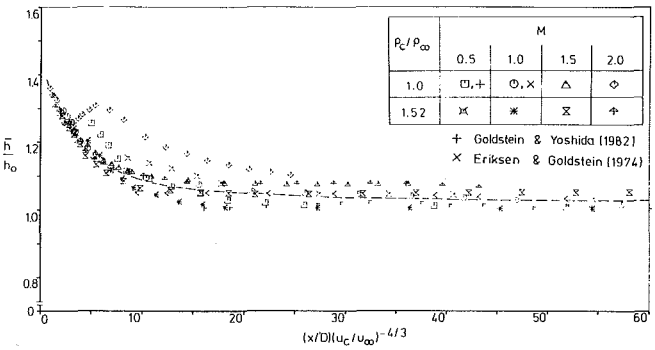

Fig. 12 Correlation of $\bar{h}/h_0$ for 35 deg injection

injection the variation with blowing rate was quite weak at both density ratios. Further, there was little difference between 1.0 and 1.52 density ratio results. By contrast, for 35 deg injection the heat transfer coefficient rose when the blowing rate increased or the density ratio decreased, indicating a dependence on jet-to-mainstream velocity or momentum ratio.

The retention of the jet structure within the cooling film for the shallow angled injection was noted earlier. This is much less pronounced for the normal injection case. The normal jets penetrate deeper into the mainstream, and strong mixing occurs as they are turned parallel to the wall. This mixing results in a film from which the jet structure is almost completely absent, approaching two dimensionality within the first 15 diameters. A velocity distribution similar to a turbulent boundary layer would therefore be expected, with the heat transfer coefficient ratio quickly tending to unity as observed. The enhanced heat transfer immediately downstream of the jets arises from their strong interaction with the mainstream, which gives high turbulence intensities. The inclined jets disturb the mainstream less, and initially show a smaller increase in heat transfer, but the decay is slower because of the reduced mixing.

Correlating Parameters

The parameter correlating film cooling heat transfer coefficient ratio for normal hole injection appeared to be the mass flux ratio M. Confirmation of this is seen in Fig. 9 in which $\bar{h}/h_0$ is plotted against M, I, and u_c/u_∞ for $x/D=5$ and 20, with the density ratio as the varying parameter. For $x/D=20$, data collapse at the two density ratios is achieved in all three plots, but for $x/D=5$, only M gives a satisfactory correlation.

Data correlation is taken a stage further in Fig. 10 where $\bar{h}/h_0$ is plotted against $(x/D)M^{-0.5}$. Significant deviation from a mean curve occurs only for the highest blowing rate. The decay in $\bar{h}/h_0$ looks exponential, and this is confirmed by the log-linear plotting of Fig. 11, from which $M=2$ data are omitted. A best-fit line yields a correlation for single row 90 deg injection as

$$\bar{h}/h_0 = 1.0 + 0.555 \exp\{-0.14(x/D)(M)^{-0.5}\}$$

This correlation is applicable to variable coolant-to-mainstream density ratios, a blowing rate range from 0.5 to 1.5,

Downloaded 01 Jun 2010 to 171.66.16.66. Redistribution subject to ASME license or copyright; see http://www.asme.org/terms/Terms_Use.cfm

and for the important dimensionless downstream distances in film cooling of $x/D<25$. The uncertainty associated with h/h_0 using this correlation is of the order ± 5 percent.

As has been previously noted, M is not a good correlating parameter for 35 deg data. When data at fixed x/D were plotted against the injection parameters, u_c/u_∞ was found to give a better data collapse than either M or I.

Forth and Jones (1986) have correlated some single row, inclined-hole heat transfer data using $x/D(u_c/u_\infty)^{-4/3}$ for the "strong injection" regime. This they associate with jet lift-off, which they state will occur above about $I=0.1$. Below this limit, data were found to correlate on I.

For the tests reported here, a minimum blowing parameter of 0.5 was used, so that $I>0.15$, and strong injection conditions prevailed throughout. A correlation similar to that of Forth and Jones (1986) would therefore be expected to apply, and this is verified in Fig. 12. This figure also includes results from Eriksen and Goldstein (1974) and Goldstein and Yoshida (1982), which corroborate the use of the velocity ratio as a correlating parameter. The correlation is seen to work best for low values of the parameter, with significant deviation only for the highest blowing rate, low-density condition.

The success of blowing rate, rather than velocity ratio, as a correlating parameter for 90 deg injection data seems to indicate that a subdivision of the strong injection regime may be needed.

Conclusions

1 The heat transfer coefficient is increased by injection, and increases with injection rate, for both 35 and 90 deg injection. The 90 deg injection gives higher heat transfer coefficients in regions just downstream of the holes than 35 deg injection, but far downstream, the persistence of the structure of the 35 deg jets yields higher heat transfer coefficients. Upstream of the holes, there is little influence.

2 The blowing rate M satisfactorily correlates heat transfer coefficient data under varying density ratio for normal injection through a single hole or a row of holes. As a consequence, previous normal injection heat transfer studies at density ratios not representative of gas turbine conditions can be applied without correction provided only that blowing parameters are matched. The normalized spanwise averaged heat transfer coefficient, $\bar{h}/h_0$, is well correlated by

$$\bar{h}/h_0 = 1.0 + 0.555 \exp\{-0.14(x/D)M^{-0.5}\}$$

in the range

$$0.5 <= M <= 1.5, \text{ and } 1.5 <= x/D <= 25$$

3 For 35 deg injection, the heat transfer coefficient at a fixed blowing parameter is strongly dependent on the density ratio, decreasing as the density ratio increases. Accordingly, previous studies using inclined injection at density ratio of unity need scaling for application in gas turbine design.

For the range studied here, coolant-to-mainstream velocity ratio is the key parameter in correlating data at differing density ratios. Plotting the normalized spanwise average heat transfer coefficient against $(x/D)(u_c/u_\infty)^{-4/3}$ collapses data for a range of velocity and density ratios.

References

Ammari, H. D., Hay, N., and Lampard, D., 1989, "Simulation of Cooling Film Density Ratios in a Mass Transfer Technique," ASME Paper No. 89-GT-200.

Choe, H., Kays, W. M., and Moffat, R. J., 1974, "The Superposition Approach to Film Cooling," ASME Paper No. 74-WA/HT-27.

Eriksen, V. L., 1971, "Film Cooling Effectiveness and Heat Transfer With Injection Through Holes," NACA CR 72991, University of Minnesota HTL TR No. 102.

Eriksen, V. L., and Goldstein, R. J., 1974, "Heat Transfer and Film Cooling Following Injection Through Inclined Circular Holes," ASME *Journal of Heat Transfer*, Vol. 96, pp. 239-245.

Forth, C. J. P., and Jones, T. V., 1986, "Scaling Parameters in Film-Cooling," *8th Int. Heat Transfer Conference*, pp. 1271-1276.

Forth, C. J. P., Loftus, P. J., and Jones, T. V., 1985, "The Effect of Density Ratio on the Film-Cooling of a Flat Plate," AGARD CP 390, Paper No. 10.

Foster, N. W., and Lampard, D., 1975, "Effects of Density and Velocity Ratio on Discrete Hole Film Cooling," *AIAA J.*, Vol. 13, No. 8, pp. 1112-1114.

Foster, R. C., and Haji-Sheikh, A., 1975, "An Experimental Investigation of Boundary Layer and Heat Transfer in the Region of Separated Flow Downstream of Normal Injection Slots," ASME *Journal of Heat Transfer*, Vol. 97, pp. 260-266.

Goldstein, R. J., 1971, "Film Cooling," *Advances in Heat Transfer*, Vol. 7, pp. 321-379.

Goldstein, R. J., Eckert, E. R. G., and Burggraf, F., 1974, "Effects of Hole Geometry and Density on Three-Dimensional Film Cooling," *Int. J. Heat Mass Transfer*, Vol. 17, pp. 595-607.

Goldstein, R. J., and Taylor, J. R., 1982, "Mass Transfer in the Neighborhood of Jets Entering a Crossflow," ASME *Journal of Heat Transfer*, Vol. 104, pp. 715-721.

Goldstein, R. J., and Yoshida, T., 1982, "The Influence of a Laminar Boundary Layer and Laminar Injection in Film Cooling Performance," ASME *Journal of Heat Transfer*, Vol. 104, pp. 355-362.

Hay, N., Lampard, D., and Saluja, C. L., 1982, "Application of the Swollen Polymer Technique to the Study of Heat Transfer on Film Cooled Surfaces," *7th Int. Heat Transfer Conf.*, Munich, Vol. 4, pp. 503-508.

Hay, N., Lampard, D., and Saluja, C. L., 1985a, "Effects of the Condition of the Approach Boundary Layer and of Mainstream Pressure Gradients on the Heat Transfer Coefficient on Film-Cooled Surfaces," ASME *Journal of Engineering for Gas Turbines and Power*, Vol. 107, pp. 99-104.

Hay, N., Lampard, D., and Saluja, C. L., 1985b, "Effect of Cooling Films on Heat Transfer Coefficient on a Flat Plate With Zero Mainstream Pressure Gradient," ASME *Journal of Engineering for Gas Turbines and Power*, Vol. 107, pp. 105-110.

Hildebrand, B. P., and Haines, K. A., 1966, "Interferometric Measurements Using the Wavefront Reconstruction Technique," *Appl. Opt.*, Vol. 5, pp. 172-173.

Ito, S., Goldstein, R. J., and Eckert, E. R. G., 1978, "Film Cooling of a Gas Turbine Blade," ASME *Journal of Engineering for Power*, Vol. 100, pp. 476-481.

Kline, S. J., and McClintock, F. A., 1953, "Describing Uncertainties in Single Sample Experiments," *Mechanical Engineering*, pp. 3-8.

Liess, C., 1975, "Experimental Investigation of Film Cooling With Injection From a Row of Holes for the Application to Gas Turbine Blades," ASME *Journal of Engineering for Power*, Vol. 97, pp. 21-27.

Macleod, N., and Todd, R. B., 1973, "The Experimental Determination of Wall-Fluid Mass-Transfer Coefficients Using Plasticised Polymer Surface Coatings," *Int. J. Heat Mass Transfer*, Vol. 16, pp. 485-503.

Metzger, D. E., Carper, H. J., and Swank, L. R., 1968, "Heat Transfer With Film Cooling Near Nontangential Injection Slots," ASME *Journal of Engineering for Power*, Vol. 80, pp. 157-163.

Pedersen, D. R., Eckert, E. R., and Goldstein, R. J., 1977, "Film Cooling With Large Density Differences Between the Mainstream and the Secondary Fluid Measured by the Heat Mass Transfer Analogy," ASME *Journal of Heat Transfer*, Vol. 99, pp. 620-627.

Saluja, C. L., Lampard, D., Hay, N., and Burns, I., 1984, "The Determination of Heat Transfer Coefficients on Film Cooled Surfaces Using the Swollen Polymer Technique," *Ist U.K. National Heat Transfer Conference*, Leeds.

Ville, J. P., and Richards, B. E., 1978, "The Measurement of Film Cooling Effectiveness on Turbine Components in Short Duration Wind Tunnels," AGARD CP 229, Paper 34.

Downloaded 01 Jun 2010 to 171.66.16.66. Redistribution subject to ASME license or copyright; see http://www.asme.org/terms/Terms_Use.cfm

Local Heat Transfer in Internally Cooled Turbine Airfoil Leading Edge Regions: Part I—Impingement Cooling Without Film Coolant Extraction

R. S. Bunker

D. E. Metzger

Mechanical and Aerospace Engineering Department,
Arizona State University,
Tempe, AZ 85287

An experimental study has been designed and performed to measure very localized internal heat transfer characteristics in large-scale models of turbine blade impingement-cooled leading edge regions. Cooling is provided by a single line of equally spaced multiple jets, aimed at the leading edge apex and exiting the leading edge region in the opposite or chordwise direction. Detailed two-dimensional local surface Nusselt number distributions have been obtained through the use of aerodynamically steady but thermally transient tests employing temperature-indicating coatings. The thin coatings are sprayed directly on the test surface and are observed during the transient with automated computer vision and data acquisition systems. A wide range of parameter combinations of interest in cooled airfoil practice are covered in the test matrix, including combinations of variations in jet Reynolds number, airfoil leading edge sharpness, jet pitch-to-diameter ratio, and jet nozzle-to-apex travel distance. Measured local Nusselt numbers at each chordwise location back from the stagnation line have been used to calculate both the spanwise average Nusselt number and spanwise Nusselt number gradient as functions of chordwise position. Results indicate general increases in heat transfer with approximately the 0.6 power of jet Reynolds number, increases in heat transfer with decreasing leading edge sharpness as well as with decreasing nozzle-to-apex distance, and increases in spanwise average heat transfer with decreasing jet pitch-to-diameter ratio. The latter increases are accompanied by increases in the spanwise gradient of the heat transfer coefficient. Comparison with available prior results of much coarser spatial resolution shows good agreement and establishes confidence in the use of the results for design purposes and as baseline results for comparison with subsequent experiments involving film cooling bleed.

Introduction

High turbine inlet temperatures are desired to achieve better turbine performance. Current inlet temperatures far exceed the ability of metal alloys or ceramics to perform over desired service lives. The turbine components are maintained hundreds of degrees below the hot gas temperatures by the use of cooling fluid. The vast majority of turbine cooling is accomplished with air drawn from the engine's compressor section. While this air is readily available, its use inflicts additional penalties on turbine performance due to the power required for compression and also usually causes aerodynamic losses when the coolant re-enters the hot gas stream.

The use of various cooling schemes in gas turbine airfoils has been investigated to ascertain more effective ways of providing cooling while minimizing the amount of coolant required. A typical airfoil may utilize both jet impingement cooling and film cooling in the leading edge region, while the midchord and trailing edge regions may be convection cooled with augmentation via roughness elements and/or pin fins. The prediction of airfoil surface temperatures and temperature gradients through three-dimensional conduction heat transfer solutions requires knowledge of convective heat transfer coefficients both between the airfoil and the external hot gas and between the airfoil and the cooling air. At present, experimental methods are the only means to attain detailed and reliable convective heat transfer information for the turbulent, highly three-dimensional flows in the complex cooling flows.

Heat transfer in the leading edge region of a turbine airfoil is necessarily dependent upon the interacting effects of jet impingement, film coolant extraction, and the convection over those portions of the surface not directly impacted by the jets. The parameters that may affect the flow and heat transfer in-

Contributed by the International Gas Turbine Division and presented at the ASME Winter Annual Meeting, Chicago, Illinois, November 27–December 2, 1988. Manuscript received at ASME Headquarters July 1989.

Copyright © 1990 by ASME
Downloaded 01 Jun 2010 to 171.66.16.66. Redistribution subject to ASME license or copyright; see http://www.asme.org/terms/Terms_Use.cfm

clude impinging jet Reynolds number, jet size and distribution, sharpness of the leading edge concave surface, spacing of the leading edge from the jet nozzles, film cooling hole distribution (number, location, angle), and distribution of the total cooling flow among the available flow paths. The possible effects of these parameters are compounded by their interaction. The beneficial effect of a particular jet size and distribution, for example, may be offset by the leading edge sharpness or the film cooling hole locations. Certain parameters may also be limited in range due to other design considerations, e.g., the leading edge sharpness may be dictated by the external aerodynamic design of the airfoil.

In the past several years, there has been a great amount of effort by many researchers to examine the heat transfer performance of such complex flows as are found in turbine airfoil cooling applications. Virtually all of this work has focused on a particular aspect of convective heat transfer, i.e., jet impingement, film cooling, or passages with roughening elements. Much of the earlier work in these areas involved experimental methods, which typically determined regional average values of heat transfer coefficients, e.g., segmented surface heaters. More recently, experimental methods have been developed that provide much finer resolution of local heat transfer coefficients. These include mass transfer methods, the use of melting point surface coatings, and liquid crystal techniques.

Jet impingement deals with multiple jets in a three-dimensional flow field in the airfoil leading edge. While numerical methods are available for the computation of turbulent flows (Launder and Spalding, 1974), and such methods have been applied to an impinging jet (Polat et al., 1985), these are generally restricted to axisymmetric and two-dimensional configurations. The fully three-dimensional cases of jet impingement have only been handled experimentally. Most jet impingement research has dealt with the impingement of a single jet or an array of jets onto a flat plate. An early investigation (Gardon and Cobonpue, 1962) used a heat flux gage to determine local heat transfer coefficients between an isothermal hot surface and jets of cooling air. Further work (Gardon and Akfirat, 1965) dealt with the particular role of turbulence in the heat transfer of impinging jets. Effects due to jet Reynolds number, jet size, and target spacing were examined. Later work (Chupp et al., 1968; Kercher and Tabakoff, 1970; Metzger and Korstad, 1972; Tabakoff and Clevenger, 1972) extended correlations for impingement heat transfer into concave surfaces and impingement in the presence of cross-flow. Recent work (Hollworth and Gero, 1985) has focused on the entrainment effects on impingement heat transfer. Of particular applicability to the airfoil leading edge region have been studies (Metzger et al., 1969, 1972) that have dealt with the impingement cooling of concave surfaces by lines of circular air jets. These experiments, although measuring only surface average coefficients, looked at the effects of jet Reynolds number, jet size and pitch, target spacing, and also leading edge sharpness.

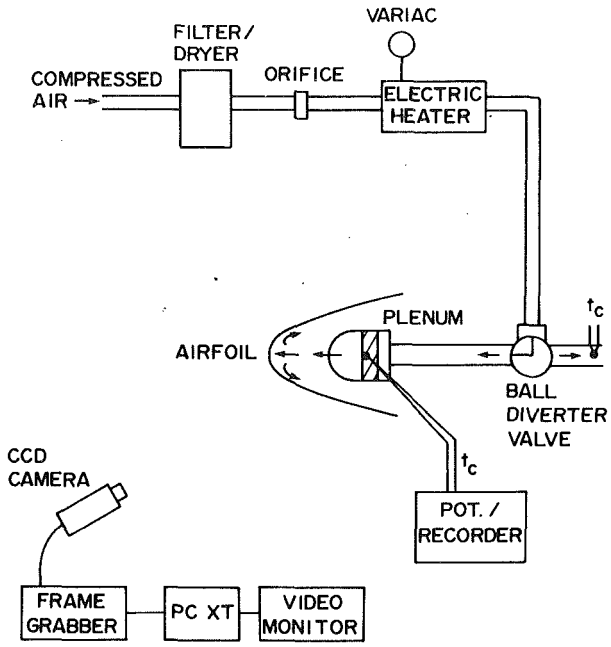

Fig. 1 Schematic of test apparatus

The present study has as its main objective the determination of local heat transfer coefficients in the leading edge region of an airfoil that utilizes impingement cooling and film coolant extraction. The experiments and results reported in this part are restricted to cases involving impingement without film coolant extraction, and provide a basis upon which the effects of film coolant extraction may be examined (Part II).

This research is distinguished from past studies in that the present experiments were conducted with the use of large-scale test surfaces that, together with a thermal transient test technique and optical sensing of local surface temperatures, permitted localized heat transfer measurements. A wide range of parameter combinations of interest was investigated, including combinations of variations in jet Reynolds number, airfoil leading edge sharpness, jet pitch-to-diameter ratio, and jet nozzle-to-apex travel distance.

Experimental Apparatus and Procedures

A schematic of the test apparatus is shown in Fig. 1. The test surface consists of the half of the airfoil viewed by the camera, as measured from the leading edge apex. The entire test section, composed of airfoil, plenum, and containing plates, is fabricated from acrylic plastic. The experiments utilized combinations of four airfoils and three plenums. Figure 2 shows the cross-sectional view of a plenum and airfoil with pertinent dimensions. Also shown is the semicylindrical portion of the plenum with a typical airfoil model, which

Nomenclature

A = heat transfer surface area
B = width of equivalent two-dimensional slot jet
C = jet nozzle pitch
D = jet nozzle diameter
h = convection heat transfer coefficient $= q/A\,(t_p - t)$
k = test surface thermal conductivity
k_f = fluid thermal conductivity
Nu_{2B} = local Nusselt number $= h2B/k_f$
r = airfoil leading edge radius of curvature
R = radius of semicylindrical airfoil
r^* = radius ratio $= r/R$
Re_{2B} = Reynolds number $= \rho V2B/\mu$
s = airfoil arc length measured from apex
t = local test surface temperature
t_i = initial test surface temperature
t_p = plenum temperature
z = jet nozzle-to-airfoil apex distance
α = test surface thermal diffusivity
θ = time
μ = fluid dynamic viscosity
ρ = fluid density
τ = time step

Downloaded 01 Jun 2010 to 171.66.16.66. Redistribution subject to ASME license or copyright; see http://www.asme.org/terms/Terms_Use.cfm

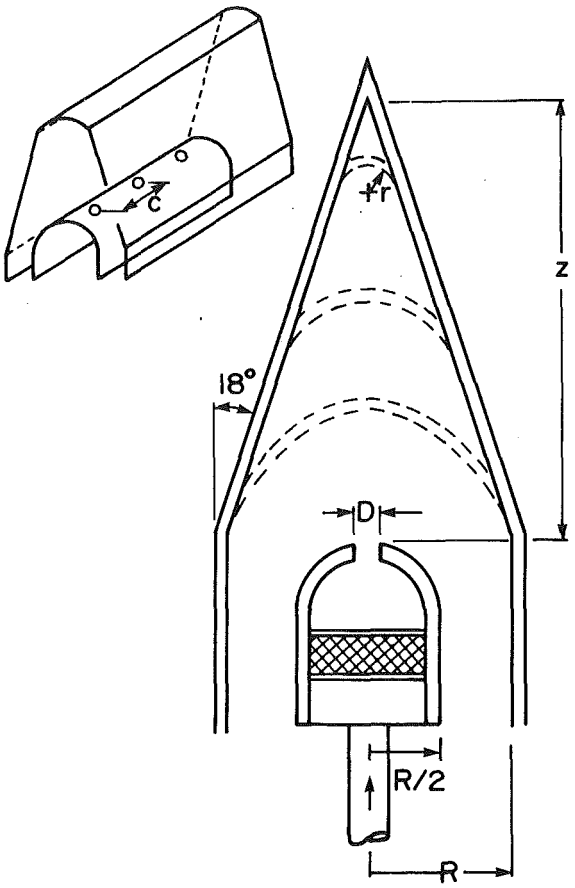

Fig. 2 Test section geometries

together represent a typical segment, at greatly enlarged scale, of a turbine airfoil leading edge.

Each plenum chamber has a diameter R of 7.62 cm, a wall thickness of 0.95 cm, and a height of 40.64 cm. The plenum contains a region of 3M Scotch-Brite material sandwiched between two plates containing regularly spaced holes for the purpose of distributing the incoming air supply evenly throughout the plenum. The impinging jets issue through nozzles of diameter D, which are placed symmetrically along the plenum apex at a uniform spacing (pitch) C between jet centerlines. The present experiments utilized plenums with pitch-to-jet diameter ratios of $C/D = 4.67$, 3.33, and 0. The latter plenum has a continuous, uniform-width slot as the jet orifice rather than individual holes. All plenums have the same total jet flow area. The equivalent two-dimensional slot jet width B is thus the same for each plenum, 0.49 cm.

The four airfoils used, shown approximately in Fig. 2 as one in solid lines and three in dashed lines, each have a different radius of curvature r at the leading edge. The radius ratios $r^* = r/R$ used in the present experiments are 0, 0.2, 0.4, and 1.0. Ratio $r^* = 0$ represents the "sharp" leading edge limit, and $r^* = 1.0$ represents the other limit of a totally rounded or semicircular leading edge. The apparatus also allows continuous variation of the target spacing z, jet nozzle-to-airfoil apex distance, within limits imposed by geometry and fluid dynamic effects.

Laboratory compressed air, filtered and dried, is metered through an ASME standard orifice and supplied to a heating section followed by a diverter ball valve. Local surface heat transfer is determined from melting patterns of coatings sprayed onto the test surfaces prior to each test run. Each test run is a thermal transient, initiated by the sudden introduction of heated air to the test section, resulting in the sequential melting of the surface coating. The experimental method and the procedures used have been previously given in detail (Metzger and Larson, 1986), so only a brief description will be repeated here.

A test run begins with heated air first diverted away from the test section so that the test channel walls remain uniformly at the laboratory ambient temperature. The valve remains in the diverted position until steady flow and a steady-state temperature (above the melting point of the coating applied to the test surfaces) have been achieved in the diversion channel. At that time the valve is used suddenly to route the heated air flow through the test section. The data acquisition program in the IBM PC is initiated simultaneously with the change of valve position.

A thin layer of the coating (approximately 5×10^{-3} cm) is sprayed evenly on the surface to be investigated. The coating material is a commercially available product (Tempil Industries, S. Plainfield, NJ) with a nominal melting point of 43°C. Melting is determined visually from the property of the coating to change from opaque white to transparent upon melting. A black background is used, which becomes visible as melting occurs at any point on the channel wall, facilitating accurate acquisition of melting times by processing of the images captured by the CCD camera.

For the acrylic plastic test surface material used, the depth of heating into the wall over the time duration needed to complete the test is less than the wall thickness, 0.64 cm for the present airfoils. In addition, lateral conduction on the wall has a negligible effect on the local surface temperature response (Metzger and Larson, 1986). At any surface point, the wall temperature is thus represented by the classical one-dimensional response of a semi-infinite medium to the sudden step application of a convecting fluid at temperature t_p:

$$(t - t_i)/(t_p - t_i) = 1 - \exp(h^2\alpha\theta/k^2)\operatorname{erfc}(h\sqrt{\alpha\theta}/k) \qquad (1)$$

If each surface point of interest were subjected to a true step increase in t_p, then measurement of the required times to reach the known phase change temperature allows solution of equation (1) for the heat transfer coefficients. This is the essence of the method, with the thin coating of phase-change material providing a means of acquiring an array of temperature–time pairs over the surface.

However, in actual internal flow experiments, the wall surfaces will not experience a pure step change in the driving air temperature because of the transient heating of the upstream plenum chamber and duct walls. Nevertheless, equation (1) is a fundamental solution that can be used to represent the response to a superposed set of elemental steps in t_p arranged to represent the actual air temperature rise

$$t - t_i = \sum_{i=1}^{N} U(\Theta - \tau_i)\Delta t_p \qquad (2)$$

where

$$U(\Theta - \tau_i) = 1 - \exp\left[\frac{h^2\alpha(\Theta - \tau_i)}{K_2}\right] \cdot \operatorname{erfc}\left[\frac{h\sqrt{\alpha(\Theta - \tau_i)}}{k}\right] \qquad (3)$$

In the present experiments, the air temperature t_p is determined by thermocouple measurement in the plenum just prior to the jet nozzles. The t_p variation with time is recorded and approximated by steps, and the resulting superposed solution, equations (2) and (3), is solved for the local surface heat transfer coefficients, using observed local melting times. The experimental uncertainty for the present study is estimated to be ±10 percent using methods for single-sample experiments (Kline and McKlintock, 1953).

The CCD camera was positioned for each different r^* airfoil so that it viewed the airfoil surface starting at the apex. The relative positioning of airfoil and camera was such that data acquired both on the curved surface and on the straight portion of the surface were free from significant distortion due to angle and thickness of the acrylic plastic.

Downloaded 01 Jun 2010 to 171.66.16.66. Redistribution subject to ASME license or copyright; see http://www.asme.org/terms/Terms_Use.cfm

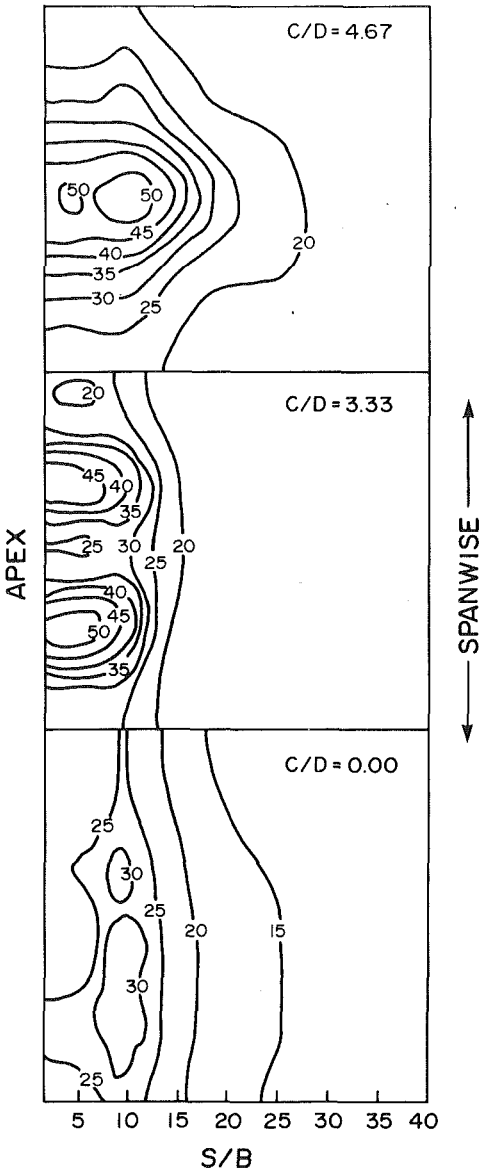

Fig. 3 Nusselt number contour maps for $Re_{2B} = 8450$, $r^* = 0.4$, and $z/B = 18$

Results and Discussion

As previously mentioned, the present experimental system is capable of obtaining the local heat transfer results at any point (or grid) on the surface of interest. By use of computer-graphic processing on the measured data, a two-dimensional, color-coded contour map of surface heat transfer can be produced to show the variation in local heat transfer coefficient on the surface if desired. Each combination of leading edge sharpness r^*, jet pitch-to-diameter ratio C/D, and nondimensional target spacing z/B used in the present study was found to have its own signature of local heat transfer coefficients, or Nusselt number. Figure 3 shows a typical set of three of these local color maps, here represented in black and white by contour lines giving values of Nu_{2B}, the Nusselt number based upon twice the width of an equivalent two-dimensional slot jet. These contour maps depict the results for $C/D = 0$, 3.33, and 4.67 using the common parameters of $r^* = 0.4$, $Re_{2B} = 8450$, and $z/B = 18$. The left side of these maps represents the airfoil apex, while the abscissa is shown as arc length s normalized by B. The arc length s is the airfoil surface coordinate measured from the apex and orthogonal to the span of the airfoil. The spanwise segments shown in Fig. 3 correspond to the middle pitch of the $C/D = 4.67$ plenum shown in Fig. 2.

The variation of C/D used in the present experiments changes the jet diameter and number of jets, while at the same time keeping the jets equally spaced and maintaining the same total flow area. Some of the local effects of C/D upon heat transfer are shown quite clearly in Fig. 3. For $C/D = 3.33$ the number of jets is doubled while the area of each is halved, as compared with $C/D = 4.67$. The result for the conditions shown is a locally higher heat transfer very near the airfoil apex with a more rapidly declining heat transfer away from the leading edge. However, the overall heat transfer for the entire surface is approximately the same for both C/D values. Additionally, it is clear that a significant decline in both local and overall heat transfer results from the use of a slot jet, $C/D = 0$. These results are typical of all the present experiments at $r^* = 0.4$ with respect to the effects of jet pitch-to-diameter ratio.

For other values of r^*, however, the effect of C/D is somewhat different. Experiments using $C/D = 3.3$ and $C/D = 4.67$ with the $r^* = 0$ airfoil show locally higher heat transfer in the immediate impingement area of the airfoil surface for $C/D = 3.33$. The overall heat transfer for the entire surface is also increased. $C/D = 3.33$ results in a more pronounced off-apex peaking for $r^* = 0$, over that of $C/D = 4.67$, due to the smaller jet area at impingement. This off-axis peaking, as will be seen in subsequent figures, results in a double-peaked internal cooling distribution for the entire airfoil leading edge region, including both suction and pressure sides. This off-axis peaking diminishes as r^* is increased, and is essentially eliminated at $r^* = 1.0$. At $r^* = 1.0$, the overall heat transfer for the surface is about the same for both $C/D = 3.33$ and $C/D = 4.67$. For intermediate r^* values, there is a trade-off of effects such as shown in Fig. 3. The higher heat transfer near the airfoil apex attained with $C/D = 3.33$ indicates that this jet configuration may be better for leading edge heat transfer in airfoils of moderate r^* geometry.

The effects of both jet Reynolds number, Re_{2B}, and target spacing, z/B, are depicted in Figs. 4 and 5. Figure 4 shows variations in the spanwise-averaged Nu_{2B} with z/B for each of the Re_{2B} used in the present experiments, for the configuration of $C/D = 4.67$ and $r^* = 0.4$. Similar results are shown in Fig. 5 for $C/D = 3.33$ and $r^* = 0.2$. The spanwise-averaged Nu_{2B} is shown as a function of normalized arc length s/B. Each of the curves shown in Figs. 4 and 5 is a spanwise-averaged version of the surface local results as shown in the contour plots of Fig. 3.

The primary effect of increasing Re_{2B} is to increase both local and overall heat transfer monotonically. Such behavior is indicative of a constancy of flow pattern as flow rate is increased. This is typical of all configurations, not just the two shown. Thus, no flow regime changes, which could result in relative redistribution of Nusselt numbers as flow rate is changed, were observed during the testing. For all points on the surfaces the effect of Nu_{2B} generally follows a proportionality of Re_{2B}^n with $n = 0.6$ to 0.7.

There are two main effects, which are the results of variations in the jet travel distance. All of the experimental results consistently show that as z/B is decreased the local heat transfer performance in the impingement region increases. This is associated with changes in the jet characteristics as the travel distance is varied. As z/B increases, the jet upon reaching the target will have spread through entrainment and interaction with the surrounding air. Heat transfer will also be spread over a larger region with lower local magnitudes. The jet will also cool with increasing z/B due to heat exchange with the surrounding air in the leading edge region, much of which will be traveling in opposite directions to that of the jet (e.g., recirculation regions, spanwise mixing, rearward exhaust). The dependence of Nu_{2B} upon z/B in the impingement area

Downloaded 01 Jun 2010 to 171.66.16.66. Redistribution subject to ASME license or copyright; see http://www.asme.org/terms/Terms_Use.cfm

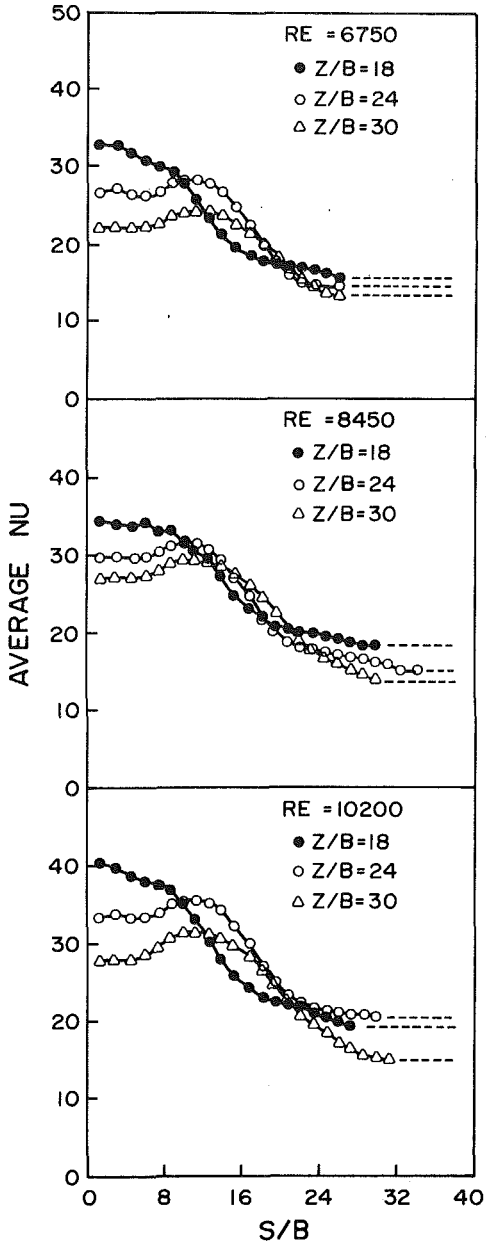

Fig. 4 Effects of Re_{2B} and z/B for $C/D = 4.67$ and $r^* = 0.4$

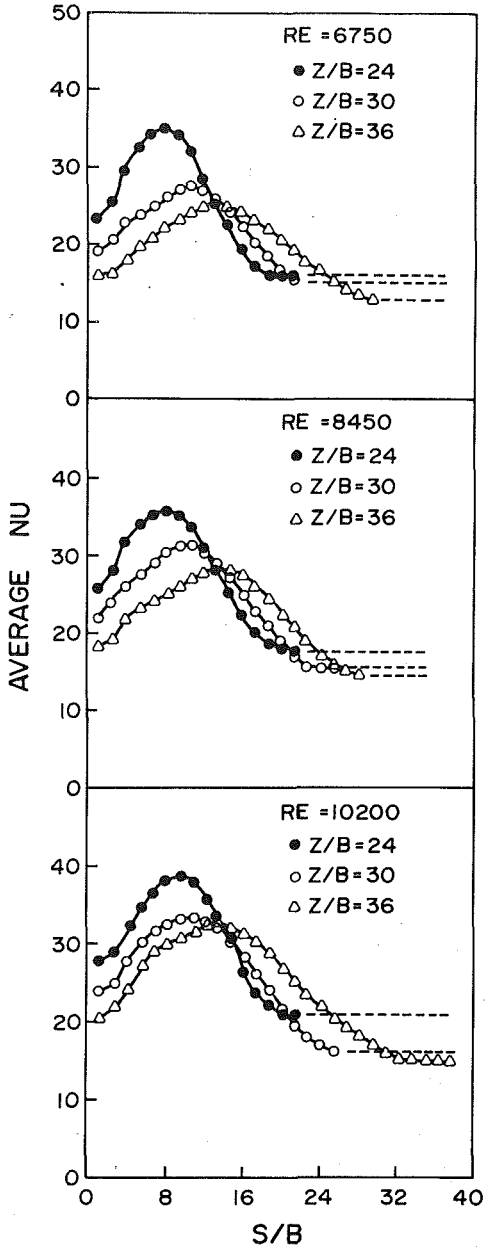

Fig. 5 Effects of Re_{2B} and z/B for $C/D = 3.33$ and $r^* = 0.2$

appears to be proportional to $(z/B)^{-m}$, where m is also in the range 0.6 to 0.7.

Another clear effect of jet travel distance is the movement of the impingement area toward the airfoil apex as z/B is decreased. All experiments with $r^* < 1.0$ exhibit this effect to a smaller or larger degree. AT $r^* = 1.0$, the heat transfer distribution indicates that impingement occurs at the apex regardless of target spacing, at least for the range of z/B used in the present study.

Variation of the leading edge sharpness quite markedly affects the shape of the average Nu_{2B} distribution as well as the apparent location of impingement on the airfoil. Figures 6 and 7 show typically the effect of r^* for $C/D = 3.33$ and $C/D = 4.67$, respectively, at $Re_{2B} = 6750$. As previously noted, the apparent impingement location moves to the leading edge apex as r^* is increased to 1.0. The shape of the average Nu_{2B} distribution with s/B is very similar to a normal distribution for $r^* = 0$, regardless of C/D, Re_{2B}, or z/B. As r^* is increased, the skewness of this distribution increases until it is lost altogether at $r^* = 1.0$. Here the distribution becomes monotonically decreasing with distance from the leading edge. It is evident that heat transfer at the airfoil apex is improved as r^* is increased.

Prior experimental results (Metzger et al., 1969) dealt with the impingement cooling of concave surfaces with $r^* = 1.0$. The methodology employed the transient response of a single-lumped capacitance leading edge model to determine average heat transfer coefficients (averaging done physically in the high-conductivity test surfaces, not averaging of local data as in the present experiments). While the Re_{2B} of the present study are at the upper edge of and outside of the Re_{2B} range for the prior correlated results (Metzger et al., 1969), the correlation should provide some indication of comparison between the two studies. Furthermore, the correlation is for a target spacing of approximately one jet diameter, $z/D = 1$. Present data utilized a minimum of $z/B = 12$, or $z/B = 2.9$, for the jet configuration of $C/D = 3.33$. A target spacing effect factor of 0.9 (Metzger et al., 1969) is used here to compare present data for $C/D = 3.33$, $r^* = 1.0$, and $z/B = 12$ to the correlation

$$Nu_{max} = 0.109\, Re^{0.73}(s/B)^{-0.52} \qquad (4)$$

Figure 8 shows this comparison to be quite good for all Re_{2B}

Downloaded 01 Jun 2010 to 171.66.16.66. Redistribution subject to ASME license or copyright; see http://www.asme.org/terms/Terms_Use.cfm

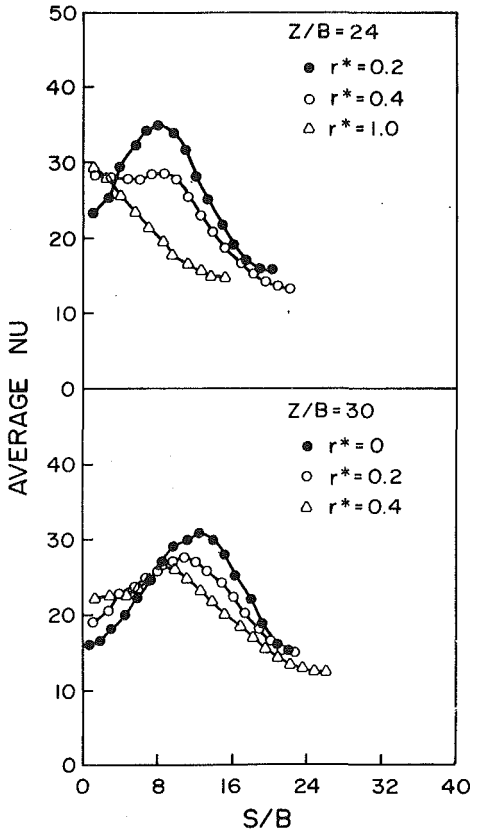

Fig. 6 Effect of r^* for $C/D = 3.33$ and $Re_{2B} = 6750$

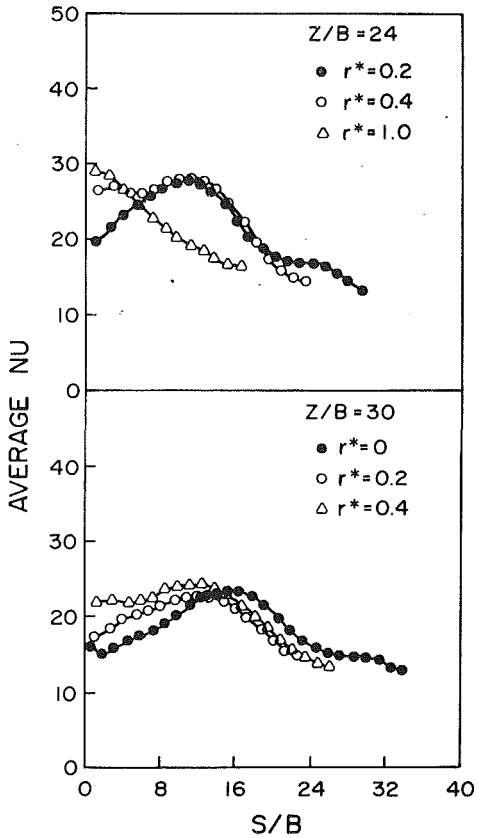

Fig. 7 Effect of r^* for $C/D = 4.67$ and $Re_{2B} = 6750$

values, especially if the derivation range of equation (4) is considered. The point at which the curves cross roughly corresponds to the lower s/B limit for the Nu_{max} correlation of equation (4).

Subsequent work (Metzger et al., 1972) used the same technique to explore the effects of leading edge sharpness r^*. Again, the Re_{2B} range of the present study is above that of the prior work (Metzger et al., 1972) and, in addition, that work covered only cases with $C/D = 1.67$ and $C/D = 6.67$. Figure 9 compares the present results for $Re_{2B} = 6750$ with the results of the highest Re used in the prior work, which is nominally the same. The three sets of present data (solid circles) shown are those that correspond most closely in C/D and z/B to the prior experiments, for $r^* = 0$, 0.2, and 0.4. Considering the differences in test section size and experimental method, and the normalized nature of the prior results, the comparisons are quite good for $r^* = 0.2$ and 0.4. It is only at the sharpest condition, $r^* = 0$, and then only at small s/B close to the leading edge apex, that agreement breaks down. At these conditions, the sharp rise in relative heat transfer very near the apex (Metzger et al., 1972) is not observed in the present study. Considering that $r^* = 0$ is included in the experiments as a limiting case that is much sharper than airfoils used in practice, the overall agreement between present results (averaged from local data) and those of both prior studies is good and lends credence to the present data acquisition and reduction methods.

Another feature that may be observed in contour maps like those of Fig. 3 is the spanwise Nusselt number gradient. Figures 10 and 11 show such gradients as a function of s/B for $C/D = 4.67$ and $C/D = 3.33$, respectively, with $Re_{2B} = 6750$. Variations with z/B are shown for each value of r^*. Each plot presents points that are the difference between Nu_{max} and Nu_{min} occuring along the airfoil span at a given s/B location, divided by the distance between their occurrence, $C/2$. The results have a superficial similarity to the spanwise-averaged Nu_{2B} results, since the largest Nu_{2B} gradients occur at

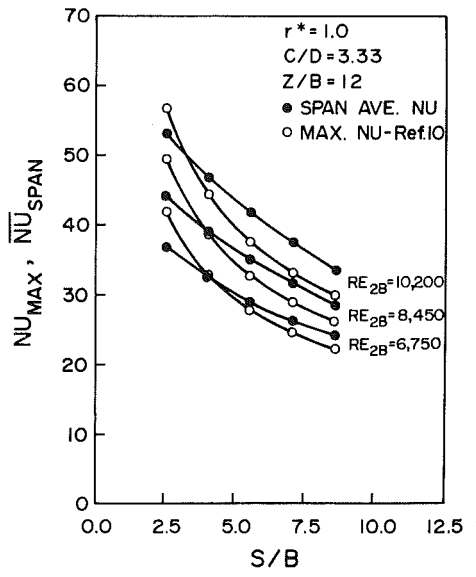

Fig. 8 Comparison with data of Metzger et al. (1969) for $C/D = 3.33$, $r^* = 1.0$, and $z/B = 12$

nominally the same s/B locations where the largest spanwise-averaged Nu_{2B} values occur. Thus, the off-axis peaking and z/B effects seen in the spanwise averaged Nu_{2B} are also present in the spanwise gradients. So, while the largest spanwise-averaged Nu_{2B} occur at the apex for $r^* = 1.0$ and the smallest z/B, the largest spanwise gradients also occur under these conditions.

Of particular interest is the fact that despite the much closer spanwise spacing of the jets at $C/D = 3.33$, as compared with $C/D = 4.67$, and the more slot jet-like appearance of the two-dimensional Nu_{2B} patterns for $C/D = 3.33$ (such as Fig. 3), the spanwise Nu_{2B} gradients for $C/D = 3.33$ are in general much

Downloaded 01 Jun 2010 to 171.66.16.66. Redistribution subject to ASME license or copyright; see http://www.asme.org/terms/Terms_Use.cfm

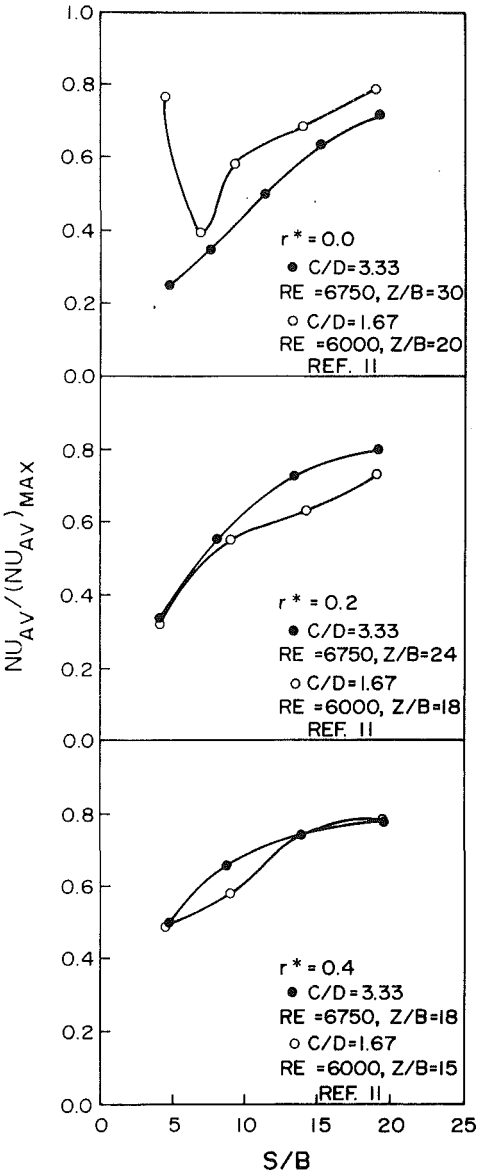

Fig. 9 Comparison with data of Metzger et al. (1972) for various r^*

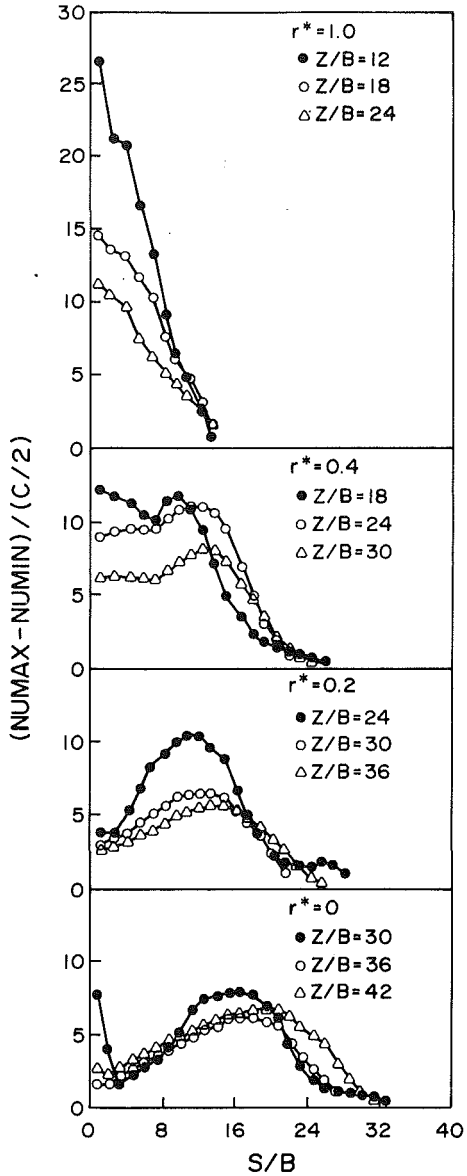

Fig. 10 Spanwise Nu_{2B} gradients for $C/D = 4.67$ and $Re_{2B} = 6750$

larger than those for the same flow rates through the $C/D = 4.67$ configuration. Depending on the thickness and thermal conductivity of the airfoil shell, this could have durability implications for the leading edge region of impingement cooled airfoils. In many cases, the present results indicate that spanwise-averaged Nu_{2B} levels for $C/D = 4.67$ are nearly the same as those for $C/D = 3.33$, but the local Nu_{2B} gradients are significantly smaller. This could indicate that, considering both performance and durability, the larger C/D may be a better, or more optimal, choice in design.

All the present results shown to this point have dealt with symmetric flow division, that is an equal chordwise flow on the pressure and suction sides of the airfoil. Some additional tests were performed with asymmetric flow divisions. To achieve asymmetry, a manifold chamber was constructed to allow each of the two rear exhaust flows to pass through nonstandard orifices. The manifold slowly contracted the air flow from each exhaust area of 1.75 cm^2 to tubes of area 11.4 cm^2. Nonstandard orifices fitted into these tubes allowed variation of the chordwise flows. Figure 12 shows the spanwise averaged Nu_{2B} results for chordwise flows of 30, 40, 60, and 70 percent of the total flow rate, for the configuration of $C/D = 3.33$, $Re_{2B} = 6750$, and $z/B = 27.4$. The asymmetry in flow division is seen to have essentially no discernible effect upon the heat transfer in the leading edge of the airfoil. Indeed, the heat transfer appears to be primarily driven by the jet Reynolds number, not the chordwise flow.

Summary

In the present study, local two-dimensional surface Nusselt number distributions have been obtained over the airfoil interior surface in the leading edge region of various gas turbine airfoil models. This investigation provides a database for jet impingement heat transfer without film coolant extraction, from which further experimentation may determine the heat transfer effects due to the presence of leading edge film coolant extraction.

The geometries tested incorporate features and encompass parameter ranges found in impingement-cooled airfoils in both current and expected future gas turbine engines. The principal conclusions of the present study can be summarized as follows:

1 Overall leading edge heat transfer is increased as the jet nozzle pitch-to-diameter ratio, C/D, is decreased from 4.67 to 3.33.

Downloaded 01 Jun 2010 to 171.66.16.66. Redistribution subject to ASME license or copyright; see http://www.asme.org/terms/Terms_Use.cfm

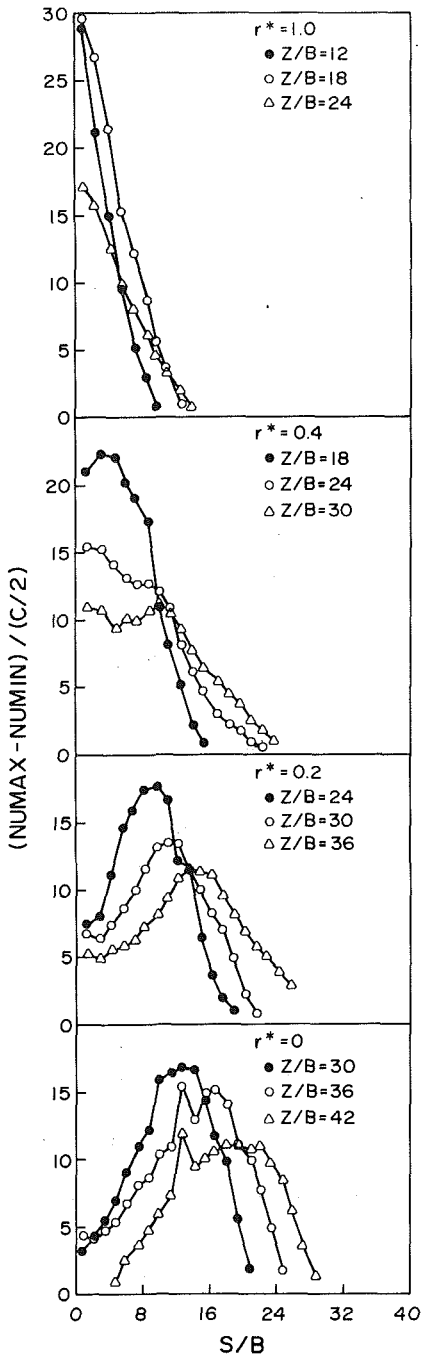

Fig. 11 Spanwise Nu_{2B} gradients for $C/D = 3.33$ and $Re_{2B} = 6750$

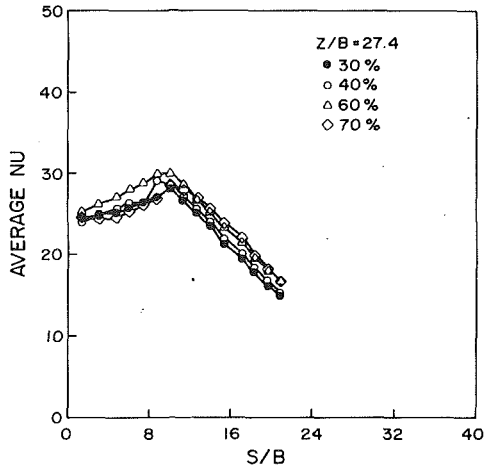

Fig. 12 Effect of asymmetric flow division upon Nu_{2B} for $C/D = 3.33$, $Re_{2B} = 6750$, and $r^* = 0.4$

2 Heat transfer performance in the leading edge region is severely degraded for the slot jet, $C/D = 0$.

3 The effect of jet Reynolds number upon both local and overall heat transfer proceeds as Re_{2B}^n, where $n = 0.6$ to 0.7.

4 Close nozzle-to-apex spacings are desirable for improved leading edge heat transfer.

5 Heat transfer at the airfoil apex is increased as r^* is increased from 0 to 1.

6 Impingement region heat transfer for $C/D = 3.33$ is higher than that for $C/D = 4.67$, but the spanwise Nusselt number gradients for $C/D = 3.33$ are much larger than those for $C/D = 4.67$.

7 Leading edge internal impingement heat transfer appears to be primarily driven by the jet Reynolds number, as opposed to a chordwise Reynolds number developed from flow division asymmetries.

As an extension of the optimal configuration idea, it should be recognized that the availability of the detailed two-dimensional local Nu data acquired in the present study makes it possible to consider optimal leading edge shape, leading edge shell thickness and conductivity, and imposed hot gas thermal loading. The performance, or cost function, could include a number of measures such as local airfoil temperatures and temperature gradients, weighed suitably to bias the optimal configuration toward performance, durability, or a combination of both.

References

Chupp, R. E., Helms, H. E., McFadden, P. W., and Brown, T. R., 1969, "Evaluation of Internal Heat Transfer Coefficients for Impingement Cooled Turbine Airfoils," *Journal of Aircraft*, Vol. 6, pp. 203–208.

Gardon, R., and Akfirat, J. C., 1965, "The Role of Turbulence in Determining the Heat Transfer Characteristics of Impinging Jets," *International Journal of Heat and Mass Transfer*, Vol. 8, pp. 1261–1272.

Gardon, R., and Cobonpue, J., 1962, "Heat Transfer Between a Flat Plate and Jets of Air Impinging on It," *International Developments in Heat Transfer*, Proceedings 2nd International Heat Transfer Conference, ASME, New York, pp. 454–460.

Hollworth, B. R., and Gero, L. R., 1985, "Entrainment Effects on Impingement Heat Transfer: Part II—Local Heat Transfer Measurements," ASME *Journal of Heat Transfer*, Vol. 107, pp. 910–915.

Kercher, D. M., and Tabakoff, W., 1970, "Heat Transfer by a Square Array of Round Air Jets Impinging Perpendicular to a Flat Surface Including the Effects of Spent Air," ASME *Journal of Engineering for Power*, Vol. 92, No. 1, pp. 73–82.

Kline, S. J., and McKlintock, F. A., 1953, "Describing Uncertainties in Single Sample Experiments," *Mechanical Engineering*, Vol. 75, pp. 3–8.

Launder, B. E., and Spalding, D. B., 1974, "The Numerical Computation of Turbulent Flows," *Computer Methods in Applied Mechanics and Engineering*, Vol. 3, pp. 269–289.

Metzger, D. E., Baltzer, R. T., and Jenkins, C. W., 1972, "Impingement Cooling Performance in Gas Turbine Airfoils Including Effects of Leading Edge Sharpness," ASME *Journal of Engineering for Power*, Vol. 94, No. 3, pp. 219–225.

Metzger, D. E., and Korstad, R. J., 1972, "Effects of Crossflow on Impingement Heat Transfer," ASME *Journal of Engineering for Power*, Vol. 94, No. 1, pp. 35–41.

Metzger, D. E., and Larson, D. E., 1986, "Use of Melting Point Surface Coatings for Local Convection Heat Transfer Measurements in Rectangular Channel Flows With 90-deg Turns," ASME *Journal of Heat Transfer*, Vol. 108, pp. 48–54.

Metzger, D. E., Yamashita, T., and Jenkins, C. W., 1969, "Impingement Cooling of Concave Surfaces With Lines of Circular Air Jets," ASME *Journal of Engineering for Power*, Vol. 91, No. 3, pp. 149–158.

Polat, S., Mujumdar, A. S., and Douglas, W. J. M., 1985, "Heat Transfer Distribution Under a Turbulent Impinging Jet—A Numerical Study," *Drying Technology*, Vol. 3, No. 1, pp. 15–38.

Tabakoff, W., and Clevenger, W., 1972, "Gas Turbine Blade Heat Transfer Augmentation by Impingement of Air Jets Having Various Configuration," ASME *Journal of Engineering for Power*, Vol. 94, No. 1, pp. 51–60.

Downloaded 01 Jun 2010 to 171.66.16.66. Redistribution subject to ASME license or copyright; see http://www.asme.org/terms/Terms_Use.cfm

Local Heat Transfer in Internally Cooled Turbine Airfoil Leading Edge Regions: Part II—Impingement Cooling With Film Coolant Extraction

D. E. Metzger

R. S. Bunker

Mechanical and Aerospace Engineering Department,
Arizona State University,
Tempe, AZ 85287

An experimental study has been designed and performed to measure very localized internal heat transfer characteristics in large-scale models of turbine blade impingement-cooled leading edge regions that allow extraction, or bleed-off, of a portion of the internal cooling flow to provide leading edge film cooling along the blade external surface. The internal impingement air is provided by a single line of equally spaced multiple jets, aimed at the leading edge apex and generally exiting, minus the bleed-off flow, in the opposite or chordwise direction. The film coolant flow extraction takes place through two lines of holes, one each on the blade suction side and the blade pressure side, both fairly close to the airfoil leading edge. Detailed two-dimensional local surface Nusselt number distributions have been obtained through the use of aerodynamically steady but thermally transient tests employing temperature-indicating coatings. The thin coatings are sprayed directly on the test surfaces, and are observed during a test transient with automated computer vision and data acquisition systems. A wide range of parameter combinations of interest in cooled airfoil practice is covered in the test matrix, including combinations of variations in jet Reynolds number, airfoil leading edge sharpness, jet pitch-to-diameter ratio, and jet nozzle-to-apex travel distance. Measured local Nusselt numbers at each chordwise location back from the stagnation line have been used to calculate both the spanwise-average Nusselt numbers and spanwise Nusselt number gradients as functions of chordwise position. The results without film coolant extraction, presented in the Part I companion paper, are used as a basis of comparison to determine the additional effects of the film cooling bleed. Results indicate that heat transfer is primarily dependent on jet Reynolds number with smaller influences from the flow extraction rate. The results also suggest that changes in the spanwise alignment of the impingement nozzles relative to the position of the film cooling holes can cause significant variations in leading edge metal temperatures.

Introduction

Various cooling schemes in gas turbine airfoils have been investigated in recent years to develop more effective ways of providing cooling while minimizing the amount of coolant required. A typical airfoil may utilize both jet impingement cooling and film cooling in the leading edge region, while the midchord and trailing edge regions may be convection cooled with augmentation via roughness elements and/or pin fins. At present, experimental methods are the only means to attain detailed and reliable convective heat transfer information for the turbulent, highly three-dimensional flow fields involved in gas turbine airfoil cooling. This paper reports on an extensive experimental study designed to investigate the effects of film coolant extraction on internal impingement heat transfer in airfoil leading edge regions.

Heat transfer in the leading edge region of a turbine airfoil is necessarily dependent upon the interacting effects of jet impingement, film coolant extraction, and the convection over those portions of the surface not directly impacted by the jets. The parameters that may affect the flow and heat transfer include impinging jet Reynolds number, jet size and distribution, leading edge sharpness, travel distance from the jet nozzles to the leading edge surface, film cooling hole distribution (number, location, angle), and distribution of the total

Contributed by the International Gas Turbine Division and presented at the ASME Winter Annual Meeting, Chicago, Illinois, November 27–December 2, 1988. Manuscript received at ASME Headquarters July 1989.

Copyright © 1990 by ASME
Downloaded 01 Jun 2010 to 171.66.16.66. Redistribution subject to ASME license or copyright; see http://www.asme.org/terms/Terms_Use.cfm

cooling flow among the available flow paths. The possible effects of these and other parameters are compounded by their interaction. The beneficial effect of a certain jet size and distribution, for example, may be offset or enhanced to some degree by the film cooling hole distribution.

The addition of film cooling to an airfoil reduces the heat transfer from the hot gas to the external airfoil surface by providing a protective film of cooler air between the two. This is in contrast to jet impingement and convection, which both remove heat from the inner surface of the airfoil. The very addition of film cooling is expected to impact the heat transfer in the internal region of the leading edge. The film cooling holes will necessarily modify the flow field in the leading edge, over that without film coolant extraction, by providing new flow paths for the cooling fluid. It is conceivable that such modified flow could lead to improved or retarded heat transfer performance. Extraction of coolant means less available cooling potential for the airfoil inner surface, but also involves a compensating addition of heat transfer within the airfoil wall. Setting aside for now the question of the effect of heat transfer within the film cooling holes, there remains to be determined the independent effect of film cooling extraction upon internal heat transfer characteristics.

In the past several years, there has been a great amount of effort by many researchers to examine the heat transfer performance of such complex flows as are found in turbine airfoil cooling applications. Virtually all of this work has focused on a particular aspect of convective heat transfer, i.e., jet impingement, film cooling, or passages with roughening elements. Much of the earlier work in these areas involved experimental methods that typically determined regional average values of heat transfer coefficients, e.g., segmented surface heaters. More recently, experimental methods have been developed that provide much finer resolution of local heat transfer coefficients. These include mass transfer methods, the use of melting point surface coatings, and liquid crystal techniques.

Jet impingement deals with multiple jets in a three-dimensional flow field in the airfoil leading edge. Part I of the present study (Bunker and Metzger, 1990) describes the investigation of jet impingement alone in the leading edge region. A wide range of parameter combinations of interest in cooled airfoil practice was examined, including variations in jet Reynolds number, airfoil leading edge sharpness, jet pitch-to-diameter ratio, and jet nozzle-to-apex travel distance. The results compared favorably with prior studies (Metzger et al.., 1972, 1969) dealing with the impingement cooling of concave surfaces by lines of circular air jets, which measured only surface average coefficients. The results reported in Part I, derived from local Nusselt number measurements, are used here as a basis of comparison to determine the independent effect of film cooling extraction.

Airfoil film cooling has been quite extensively investigated, but primarily with application to flow and heat transfer on the airfoil external surfaces (Hartnett et al., 1961). Apparently

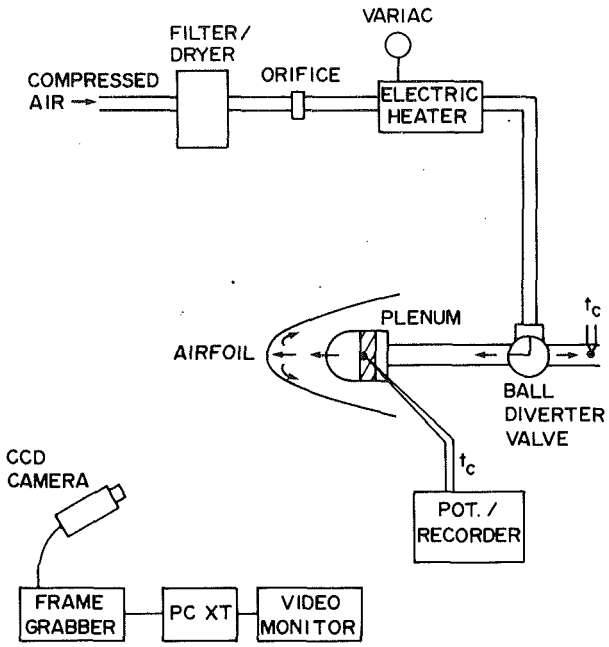

Fig. 1 Schematic of test apparatus

no work has been published that indicates the effects the presence of the film coolant extraction have on the internal cooling of the airfoil. This part of the present study has as its main objective the determination of local heat transfer coefficients in the leading edge region of an airfoil, which utilizes both impingement cooling and film coolant extraction. Experiments were conducted with the use of large-scale test surfaces that, together with a thermal transient test technique and optical acquisition of local surface temperatures, permitted localized heat transfer measurements. A single leading edge sharpness, which closely resembles a geometry used frequently in current gas turbine practice, was used to determine the effects of film coolant extraction under the variation of parameters including jet Reynolds number, jet nozzle-to-airfoil apex travel distance, jet pitch-to-diameter ratio, total amount of film flow bled from the leading edge, and pressure side-to-suction side flow divisions.

Experimental Apparatus and Procedures

A schematic of the test apparatus, without film coolant extraction provision, is shown in Fig. 1. The test surface consists of the half of the airfoil that is viewed by the camera, as measured from the leading edge apex. The entire test section, composed of airfoil, plenum, and containing plates, is fabricated from acrylic plastic. The present experiments involving bleed-off of air used three plenums and a single airfoil with acrylic plastic tubes set in the leading edge for air extraction. Figure 2 shows the cross-sectional view of a plenum and the

Nomenclature

A = heat transfer surface area
B = width of equivalent two-dimensional slot jet
C = jet nozzle pitch
D = jet nozzle diameter
h = convection heat transfer coefficient $= q/A(t_p - t)$
k = test surface thermal conductivity
k_f = fluid thermal conductivity
Nu_{2B} = local Nusselt number $= h2B/k_f$
r = airfoil leading edge radius of curvature
R = radius of semicylindrical airfoil
r^* = radius ratio $= r/R$
Re_{2B} = Reynolds number $= \rho V2B/\mu$
s = airfoil arc length measured from apex
t = local test surface temperature
t_i = initial test surface temperature
t_p = plenum temperature
z = jet nozzle-to-airfoil apex distance
α = test surface thermal diffusivity
θ = time
μ = fluid dynamic viscosity
ρ = fluid density
τ = time step

Downloaded 01 Jun 2010 to 171.66.16.66. Redistribution subject to ASME license or copyright; see http://www.asme.org/terms/Terms_Use.cfm

airfoil with pertinent dimensions. Also shown is the semicylindrical portion of the plenum with the airfoil model, which together represent a typical segment, at greatly enlarged scale, of a turbine airfoil leading edge.

The basic apparatus and procedures have been described by Bunker and Metzger (1990) and will be only briefly reviewed here. The impinging jets issue through nozzles of diameter D placed symmetrically along the plenum apex at a uniform spacing (pitch) C between jet centerlines. The present experiments utilized plenums with pitch-to-jet diameter ratios of C/D = 4.67, 3.33, and 0. The latter plenum has a continuous, uniform-width slot as the jet orifice rather than individual holes. All plenums have the same total jet flow area. The equivalent two-dimensional slot jet width B is thus the same for each plenum, 0.49 cm.

The airfoil used in this part of the present study has a radius ratio $r^* = r/R$ of 0.4. The airfoil has two rows of bleed tubes set at an angle of 45 deg to the line of symmetry (apex). The pitch of the bleed tubes in each row corresponds to the jet nozzle pitch of C/D = 4.67. The bleed tubes issue perpendicularly from the airfoil surface. Each tube has a nominal inside diameter of 1.27 cm, and outside diameter of 1.91 cm. Acrylic plastic manifold chambers were used to route various portions of the air to rotameters for flow measurement, one each for pressure side and suction side, front and rear air flows, as shown in Fig. 2. The rear manifold chambers were sealed to the rear exhaust areas of the airfoil, with extension walls provided to adjust the nozzle-to-apex distance z. The air passing through these manifolds is slowly contracted from each exhaust area of 175 cm^2 to tubes of area 11.4 cm^2. The rear rotameters (Brooks Instrument Division, Model 1307, Size 12) are connected with flexible hoses. Each row of bleed tubes is connected to a front manifold chamber by Tygon tubing, and each manifold is connected to a separate front rotameter (Brooks, 1307, Size 9). Control of the air flow passing through each rotameter was accomplished by use of a viselike clamp on the flexible hoses prior to the rotameter inlet.

Laboratory compressed air, filtered and dried, is metered through an ASME standard orifice and supplied to a heating section followed by a diverter ball valve. Local surface heat transfer is determined from melting patterns of coatings sprayed onto the test surfaces prior to each test run. Each test run is a thermal transient, initiated by the sudden introduction of heated air to the test section, resulting in the sequential melting of the surface coating.

A test run begins with heated air first diverted away from the test section so that the test channel walls remain uniformly at the laboratory ambient temperature. The valve remains in the diverted position until steady flow and a steady-state temperature (above the melting point of the coating applied to the test surfaces) have been achieved in the diversion channel. At that time the valve is used suddenly to route the heated air flow through the test section. The data acquisition program in the IBM PC is initiated simultaneously with the change of valve position.

A thin layer of the coating (approximately 5×10^{-3} cm) is sprayed evenly on the surface to be investigated. The coating material is a commercially available product (Tempil Industries, S. Plainfield, NJ) with a nominal melting point of 43°C. Melting is determined visually from the property of the coating to change from opaque white to transparent upon melting. A black background is used, which becomes visible as melting occurs at any point on the channel wall, facilitating accurate acquisition of melting times by processing of the images captured by the CCD camera.

For the acrylic plastic test surface material used, the depth of heating into the wall over the time duration needed to complete the test is less than the wall thickness, or 0.64 cm. In addition, lateral conduction in the wall has a negligible effect on the local surface temperature response (Metzger and Larson, 1986). At any surface point, the wall temperature is thus represented by the classical one-dimensional response of a semi-infinite medium to the sudden step application of a convecting fluid at temperature t_p:

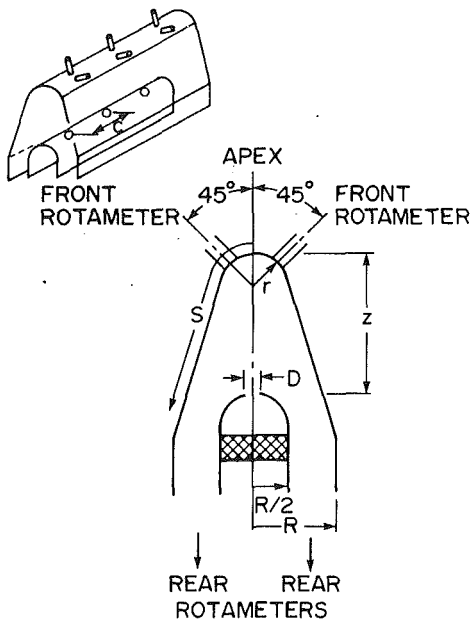

Fig. 2 Test section geometry

$$(t - t_i)/(t_p - t_i) = 1 - \exp(h^2\alpha\theta/k^2)\,\mathrm{erfc}(h\sqrt{\alpha\theta}/k) \quad (1)$$

If each surface point of interest were subjected to a true step increase in t_p, then measurement of the required times to reach the known phase-change temperature allows solution of equation (1) for the heat transfer coefficients. This is the essence of the method, with the thin coating of phase-change material providing a means of acquiring an array of temperature–time pairs over the surface.

However, in actual internal flow experiments, the wall surfaces will not experience a pure step change in the driving air temperature because of the transient heating of the upstream plenum chamber and duct walls. Nevertheless, equation (1) is a fundamental solution that can be used to represent the response to a superposed set of elemental steps in t_p arranged to represent the actual air temperature rise

$$t - t_i = \sum_{i=1}^{N} U(\Theta - \tau_i)\Delta t_p \quad (2)$$

where

$$U(\Theta - \tau_i) = 1 - \exp\left[\frac{h^2\alpha(\Theta - \tau_i)}{k_2}\right]\mathrm{erfc}\left[\frac{h\sqrt{\alpha(\Theta - \tau_i)}}{k}\right] \quad (3)$$

In the present experiments, air temperature t_p is determined from thermocouple measurement in the plenum just before the jet nozzles. The t_p variation with time is recorded and approximated by steps, and the resulting superposed solution, equations (2) and (3), is solved for the local surface heat transfer coefficients, using observed local melting times.

A CCD camera was positioned so that it viewed the airfoil surface starting at the apex. The relative positioning of airfoil and camera was such that data acquired both on the curved surface and on the straight portion of the surface were free from significant distortion due to angle and thickness of the acrylic plastic. The existence of bleed tubes at the leading edge does however cause a small area associated with each tube to be photographically opaque. Since no data were collected in

Downloaded 01 Jun 2010 to 171.66.16.66. Redistribution subject to ASME license or copyright; see http://www.asme.org/terms/Terms_Use.cfm

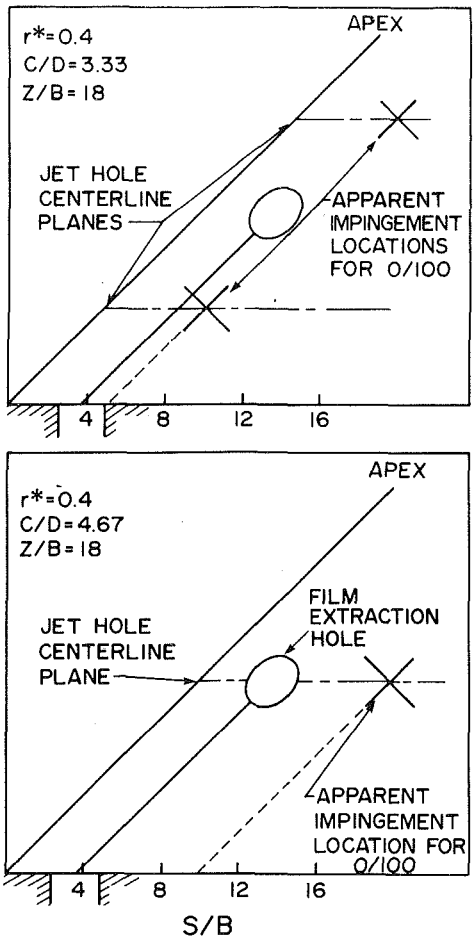

Fig. 3 Relative position sketches at $z/B = 18$

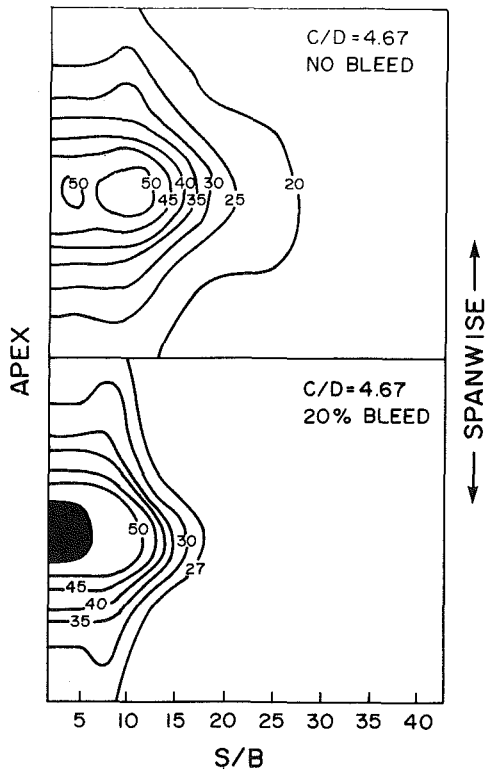

Fig. 4 Comparison of local Nu_{2B} with and without film bleed for $C/D = 4.67$, $Re_{2B} = 8450$, and $z/B = 18$

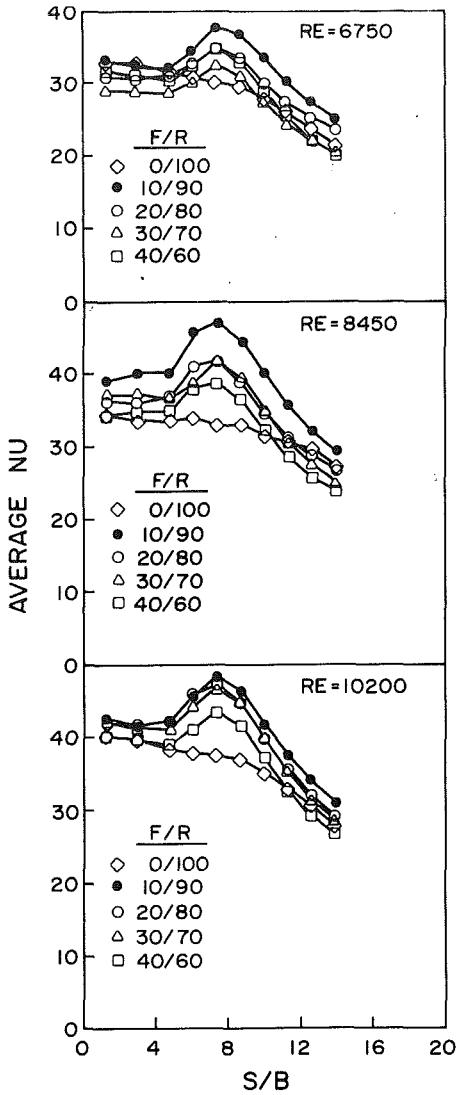

Fig. 5 Average Nu_{2B} with film extraction for $C/D = 4.67$ and $z/B = 18$

this area, the corresponding spanwise results do not include this area. The obscured area roughly corresponds to the bleed-off air flow area where no airfoil inner surface exists.

Results and Discussion

The results presented in Part I, without film coolant extraction (Bunker and Metzger, 1990), showed that the apparent impingement location on the airfoil surface, despite the test section symmetry, is not necessarily at the apex. Rather, the location depends upon the airfoil geometry, jet configuration, and target spacing. For those cases in which impingement is located off-axis, a recirculating flow region is indicated in the leading edge. Without film extraction the only path available to the air is to flow out the rear, around the impingement jets. The addition of film extraction in the leading edge should be expected to modify this recirculating flow zone by providing new flow paths for the air. This effect may also depend upon such factors as geometry, jet configuration, etc. Figure 3 shows the relative positions of the bleed tube, the jet centerline, and the apparent impingement location without film extraction (labeled as a front/rear flow division of 0/100) for both $C/D = 4.67$ and $C/D = 3.33$ at $z/B = 18$.

The effect of film extraction is most apparent for $C/D = 4.67$ where the jet nozzle and bleed tube are coplanar. Figure 4 shows two typical local color-mapped results, here represented in black and white by contour lines, giving values of

Downloaded 01 Jun 2010 to 171.66.16.66. Redistribution subject to ASME license or copyright; see http://www.asme.org/terms/Terms_Use.cfm

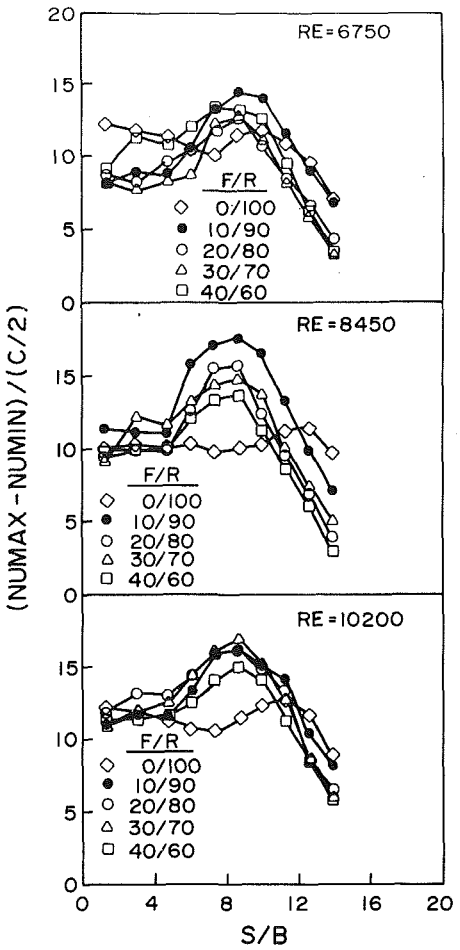

Fig. 6 Nu_{2B} gradient with film extraction for C/D = 4.67 and z/B = 18

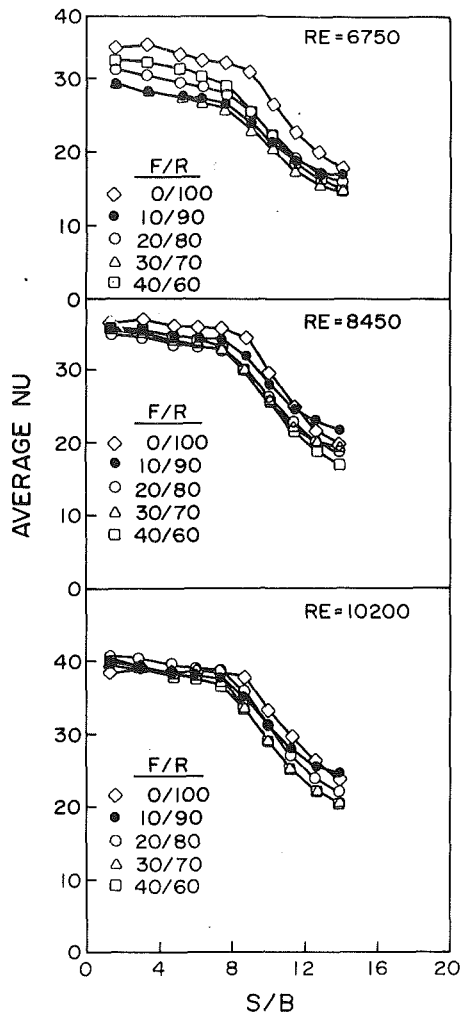

Fig. 8 Average Nu_{2B} with film extraction for C/D = 3.33 and z/B = 18

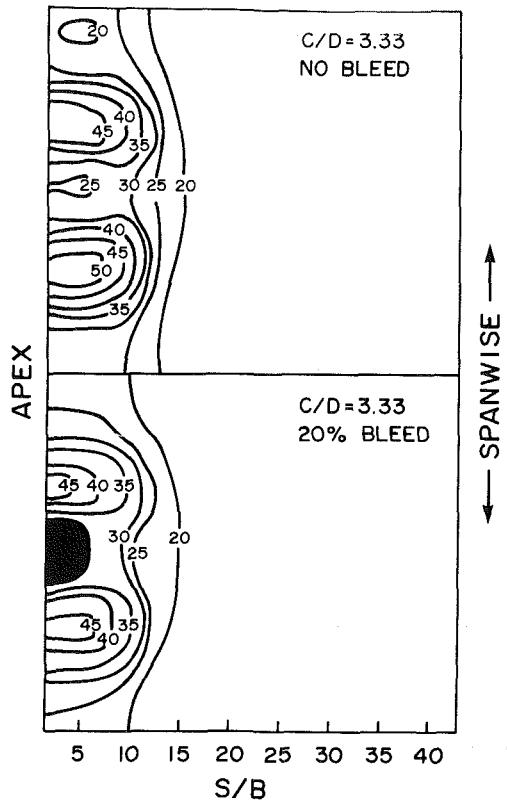

Fig. 7 Comparison of local Nu_{2B} with and without film bleed for C/D = 3.33, Re_{2B} = 8450, and z/B = 18

Nu_{2B}, the Nusselt number based upon twice the width of an equivalent two-dimensional slot jet. The contour maps are a comparison of the local heat transfer results for a case of no film bleed to those of a case with film bleed. The film bleed is 20 percent of the total flow issuing from the jet nozzles, and both maps are for C/D = 4.67, Re_{2B} = 8450, and z/B = 18. The darkened region in the plots represents the film bleed tube as seen by the camera. The contours show that film extraction produces higher spanwise average Nu over most of the leading edge. In addition, the apparent impingement location moves forward from that without film extraction. Both of these effects are plausibly attributed to a modification of the recirculation region in the leading edge. Figure 5 shows spanwise average Nu_{2B} comparisons at each of three Re_{2B}, with four different bleed percentages. The effect of film extraction is seen to be an increase in spanwise average Nu_{2B} over most of the leading edge for all bleed percentages, with some modifications due to the amount of bleed. Figure 6, however, shows that the increase in average Nu is accompanied by a corresponding rise in the spanwise Nu gradient in the impingement portion of the leading edge. The flow divisions in these figures are indicated as front/rear percentages of the total flow rate, e.g., 10/90 refers to the sum of all film coolant extraction flow as being 10 percent of the total flow. These experiments all utilize symmetric flow division between the airfoil pressure side and suction side. In addition to the flow out each row of bleed tubes being equal, the flow out each individual bleed tube is essentially the same. Asymmetries with respect to the flow division of bleed flow, rear flow, or both will be discussed later.

Downloaded 01 Jun 2010 to 171.66.16.66. Redistribution subject to ASME license or copyright; see http://www.asme.org/terms/Terms_Use.cfm

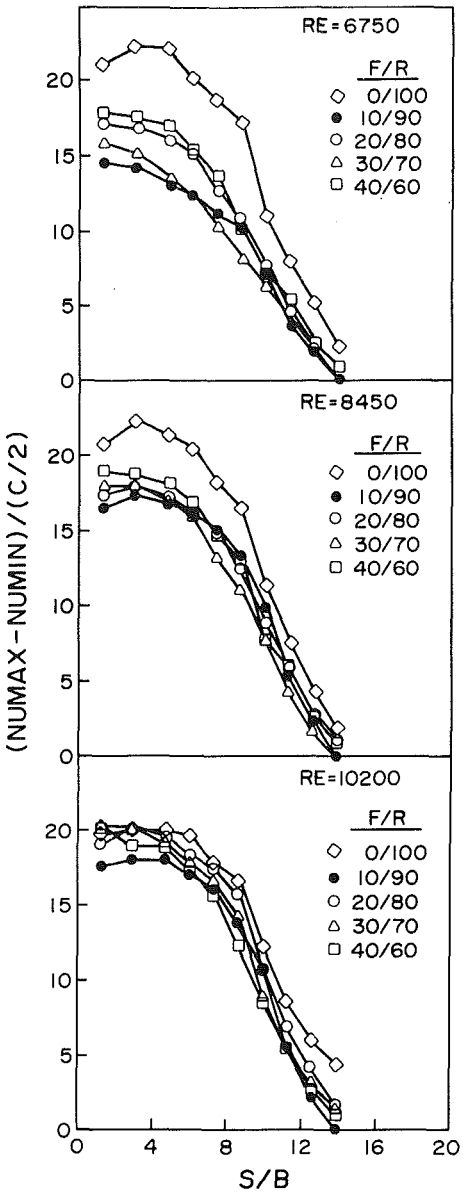

Fig. 9 Nu_{2B} gradient with film extraction for C/D = 3.33 and z/B = 18

In contrast, for C/D = 3.33, Fig. 3 shows that the jets are not coplanar with the bleed tubes. The contour maps of Fig. 7 show again the typical local Nusselt number results for cases with and without bleed, for C/D = 3.33, Re_{2B} = 8450, and z/B = 18. Contrary to the comparison of Fig. 4, these contour maps indicate that a small decrease in leading edge heat transfer results from the film coolant bleed. Figure 8 shows that the spanwise-averaged Nu is generally reduced by the addition of film extraction. Apparently, the relative positioning of the jets and bleed tubes is such that the recirculation region is little modified in the leading edge. The bleed tubes do add an additional flow path, but it is along the flow path that existed without showerhead bleed. The effect of bleeding off air in this instance is apparently to reduce the spanwise average Nu by removing some convecting fluid without causing a compensating reduction in recirculation. In addition, the apparent impingement locations move forward only slightly compared to those without bleed. Figure 9 shows a clear decrease in the spanwise Nu gradient, indicating that the addition of bleed helps to make the Nu variations a little more uniform for C/D = 3.33.

The effect of film extraction for the two-dimensional slot

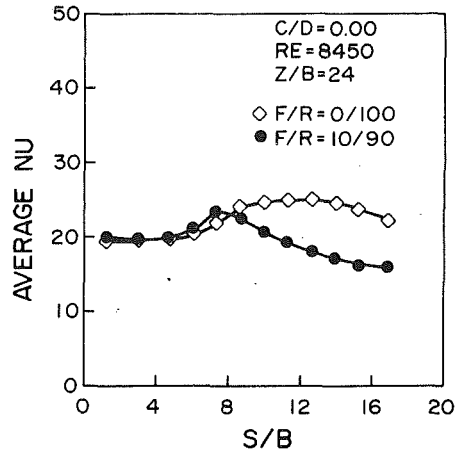

Fig. 10 Average Nu_{2B} with film extraction for C/D = 0 and z/B = 18

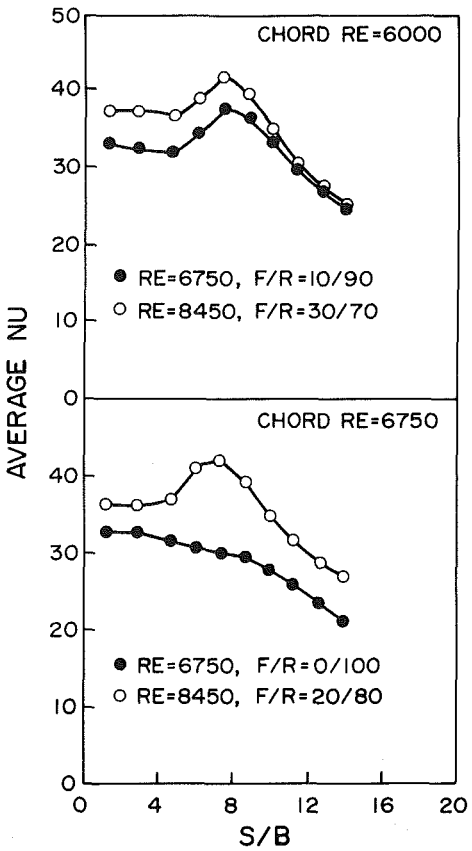

Fig. 11 Comparison of average Nu_{2B} configurations of like net chordwise Re with C/D = 4.67, and z/B = 18

jet, C/D = 0, is seen in Fig. 10 to be a large reduction of average Nu in the region behind the impingement location. In this case, the addition of film extraction apparently aids the reduction of leading edge recirculation, and the indicated impingement location moves forward. However, this also eliminates the effective barrier, which gave higher average Nu values to the rear of the recirculation region. This C/D = 0 jet configuration is of relatively low current interest, and no further results for this configuration have been obtained at this time.

The effect of varying the front-to-rear flow division is again most apparent for C/D = 4.67. Figure 5 shows that of the four bleed ratios tested, that of 10/90 generally yields the highest spanwise-averaged Nu. From this figure also, the spanwise-averaged Nu declines as more air is routed through the bleed tubes. This might suggest that the surface heat transfer

Downloaded 01 Jun 2010 to 171.66.16.66. Redistribution subject to ASME license or copyright; see http://www.asme.org/terms/Terms_Use.cfm

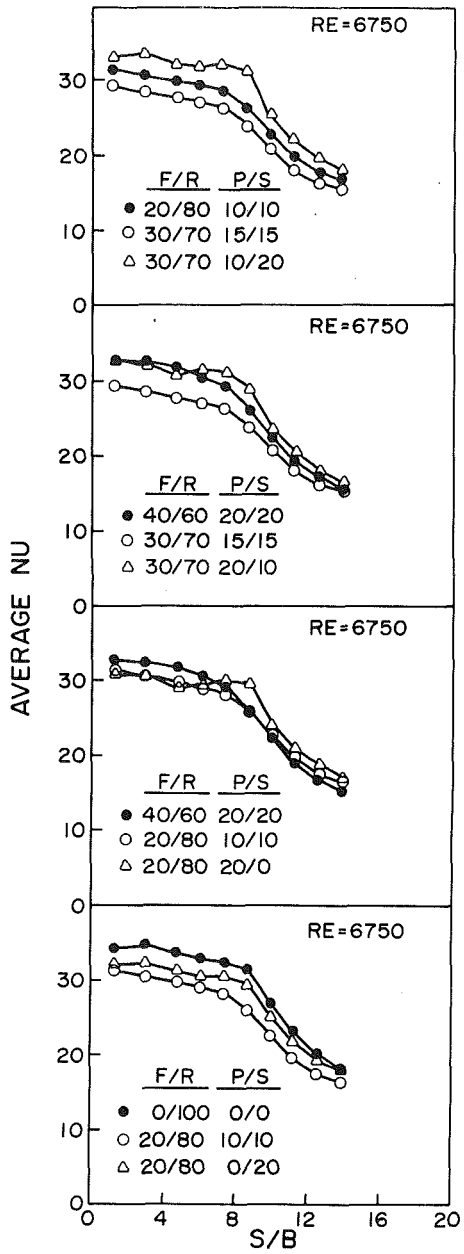

Fig. 12 Average Nu_{2B} with asymmetric bleed flow for $C/D = 3.33$, $Re_{2B} = 6750$, and $z/B = 18$

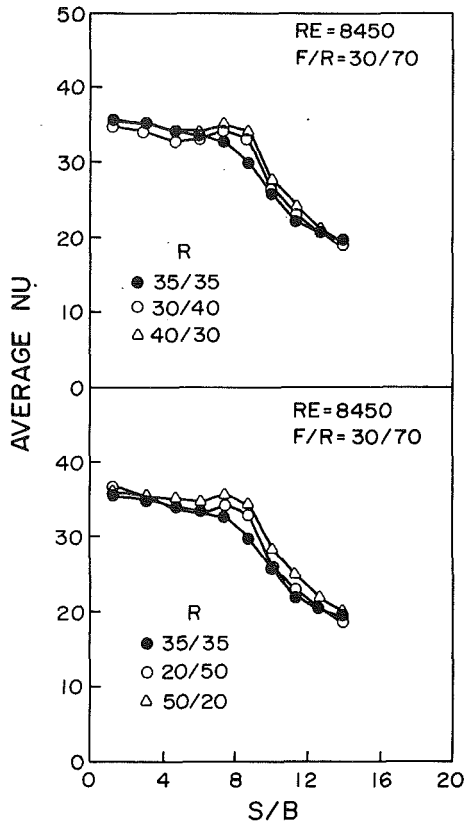

Fig. 13 Average Nu_{2B} with asymmetric rear flow for $C/D = 3.33$, $Re_{2B} = 8450$, and $z/B = 18$

is driven by the net chordwise Re. However, this supposition was tested in the present study and was found to be false. Experimental configurations having nearly the same net chordwise flow, as shown in Fig. 11, indicate the higher spanwise average Nu to be associated with the higher jet Re_{2B}. This implies that the chordwise Nu number levels with leading edge bleed are established primarily by the total amount of jet flow, with only a small adjustment due to the amount of bleed flow. In addition, Fig. 6 shows some variation in Nu gradient with the amount of bleed, again typically peaking for the case of 10/90.

In the configurations using $C/D = 3.33$, the effect of varying the flow division is less apparent. In most of the results shown in Fig. 8, the spanwise-averaged Nu for all four bleed ratios are within experimental uncertainty of each other: generally ± 10 percent as determined by methods for single-sample experiments (Kline and McKlintock, 1953). There is no clear pattern to be discerned. These results lend even stronger evidence to the conclusion that the total jet flow is the primary driver. Figure 9 shows that the same conclusions may be reached with respect to spanwise Nu gradients.

The effect of varying the jet Reynolds number, Re_{2B}, may be seen clearly in both Figs. 5 and 8. The Re_{2B} effect upon Nu_{2B} is essentially the same with or without bleed for both $C/D = 4.67$ and $C/D = 3.33$. Similarly, the effect of varying the jet travel distance, z/B, is also essentially the same with or without bleed. Variations with these parameters are detailed in Part I.

While experiments with symmetric flow division help to establish the apparent effects of the film coolant extraction on leading edge heat transfer, the conditions of pressure, temperature, and temperature gradients involved in practice will normally differ from the pressure side of the airfoil to the suction side. It is expected therefore that asymmetric flow divisions will be necessary to cool the airfoil leading edge region properly. It is important then to determine the effects that such asymmetries have upon local heat transfer, and a variety of these cases were investigated in the present study.

The asymmetric experimental cases covered include (*a*) asymmetric division of bleed flow with symmetric rear flow, and (*b*) asymmetric division of rear flow with symmetric bleed flow. The bleed-to-rear flow division is again referred to as a front-to-rear (F/R) division given as percentages of the total flow. Each pressure-to-suction side flow division is given a different designation depending upon its application to bleed flow or rear flow. The asymmetric division of bleed flow is denoted a pressure-to-suction (P/S) division. The side designated as pressure P is always the side presented in the figures. The asymmetric division of rear flow is called simply rear (R) division (e.g., $R = 20/50$), where the first number always refers to the side presented. Testing of any particular flow division requires two tests, one for each side of the airfoil, with the rotameter control settings reversed between tests.

In all of the results presented, fully symmetric tests used for

Downloaded 01 Jun 2010 to 171.66.16.66. Redistribution subject to ASME license or copyright; see http://www.asme.org/terms/Terms_Use.cfm

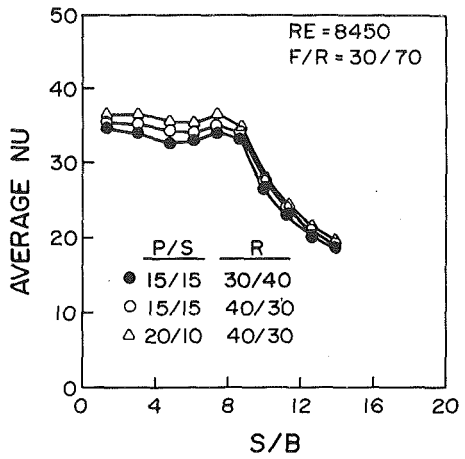

Fig. 14 Average Nu_{2B} and gradient with asymmetric bleed and rear flows for $C/D = 3.33$, $Re_{2B} = 8450$, and $z/B = 18$

comparisons have been designated in a manner similar to the asymmetric tests for consistency and clarity (e.g., $P/S = 10/10$ for $R = 35/35$ are symmetric tests). All division numbers refer to percentages of the total flow.

Figures 12 shows the results of asymmetric bleed flow with symmetric rear flow for $C/D = 3.33$, $Re_{2B} = 6750$, and $z/B = 18$. For each asymmetric case, three curves are shown. One curve depicts the asymmetric result, another shows the corresponding fully symmetric result with bleed flow rate equal to that of the asymmetric test for the side presented, and the third shows the corresponding fully symmetric result with rear flow rate equal to that of the asymmetric test.

In general the spanwise average Nu for all asymmetric cases is equal to or slightly greater than each fully symmetric case (to within experimental uncertainty). The only exception is that of comparison to the zero bleed flow case (0/100). For this case there were no bleed tubes present at all, which might cause the average Nu to be higher in the leading edge due to the increased surface area available for data acquisition. Results presented for fully symmetric cases showed that for $C/D = 3.33$, leading edge heat transfer with bleed flow is generally slightly lower than that without bleed flow. This effect is confirmed in the present data.

The increase in spanwise average Nu observed with the asymmetric bleed flow division, if present, is in all cases less than 5 percent over the bounds of experimental uncertainty. It may be concluded from this that no significant increase or decrease in spanwise-averaged Nu is associated with asymmetric bleed flow.

The results of asymmetric rear flow with symmetric bleed flow are shown in Fig. 13, compared with fully symmetric data for spanwise average Nu, for $C/D = 3.33$, $Re_{2B} = 8450$, and $z/B = 18$. In all cases the asymmetric flows give nearly the same spanwise average Nu, regardless of whether the side tested had 20, 30, 40, or even 50 percent of the total flow going through the rear rotameter. The major effect evident is that of increased jet Re. For a given Re, all asymmetric results are equal within experimental uncertainty. Also, as with the asymmetric bleed flow, some data would tend to indicate that the asymmetric rear flow division leads to a small increase in spanwise average Nu over that with fully symmetric flow division. But again, such an increase is always less than 5 percent over the bounds of experimental uncertainty.

The asymmetric bleed and asymmetric rear flow data all lead to the conclusion that, at least for $C/D = 3.33$, asymmetry in flow division has very little effect on the spanwise average Nu and spanwise Nu gradient. To confirm this for a general configuration with asymmetry present in both the bleed and rear flows, one test was performed with a front-to-rear division of 30/70, a bleed flow division of 20/10, and a rear flow division of 40/30. Figure 14 shows the spanwise average Nu compared to other asymmetric test data for $C/D = 3.33$, $Re_{2B} = 8450$, and $z/B = 18$. As expected, the results are the same to within experimental uncertainty.

Finally, the spanwise Nu gradients that correspond to the spanwise average Nu data of Figs. 12–14 exhibit the same characteristics as described and discussed above for the average Nu results.

Summary

Local two-dimensional surface Nusselt number distributions have been obtained over the entire airfoil interior surface through use of transient experiments employing melting point coatings applied directly on the test surface together with automated computer vision and data acquisition systems. The present study has investigated heat transfer in the airfoil leading edge region involving impingement cooling with film coolant extraction. Fully symmetric flow divisions, where equal partitioning of flow between pressure and suction sides is imposed both in the chordwise exhaust flow and in the film extraction bleed flow, have been examined and compared to results obtained without film coolant extraction (Part I). Asymmetric bleed and/or chordwise exhaust flow cases have also been examined and compared to fully symmetric flow results. The principal conclusions of the present study can be summarized as follows:

1 In general, the level of heat transfer appears to be driven primarily by the impinging jets, secondarily modified by the amount of the jet flow bled off in the leading edge region.

2 With jet holes and bleed holes in line, bleed flow leads to generally increased heat transfer. This effect can be significant, with some local measured heat transfer coefficient increases approaching 50 percent.

3 With jet holes and bleed holes 180 deg out of phase in their alignment, bleed flow generally leads to decreased heat transfer.

4 In the leading edge region of an impingement cooled airfoil with asymmetric film extraction bleed and/or asymmetric chordwise exhaust, heat transfer can be predicted accurately from fully symmetric data. While this conclusion strictly applies only to the jet configuration used in the present asymmetric experiments, that of $C/D = 3.33$, it is anticipated that this will not be significantly altered for $C/D = 4.67$.

Based upon the configurations used in the present experiments, these observations suggest that changes in the spanwise alignment of the impingement nozzles relative to the position of the film cooling holes can act to cause significant variations in leading edge metal temperatures.

References

Bunker, R. S., and Metzger, D. E., 1990, "Local Heat Transfer in Internally Cooled Turbine Airfoil Leading Edge Regions: Part I—Impingement Cooling Without Film Coolant Extraction," ASME JOURNAL OF TURBOMACHINERY, Vol. 112, this issue.

Hartnett, J. P., "Birkebak, R. C., and Eckert, E. R. G., 1961, "Velocity Distributions, Temperature Distributions, Effectiveness and Heat Transfer for Air Injected Through a Tangential Slot Into a Turbulent Boundary Layer," ASME *Journal of Heat Transfer*, Vol. 83, pp. 293–306.

Kline, S. J., and McKlintock, F. A., 1953, "Describing Uncertainties in Single Sample Experiments," *Mechanical Engineering*, Vol. 75, pp. 3–8.

Metzger, D. E., and Baltzer, R. T., and Jenkins, C. W., 1972, "Impingement Cooling Performance in Gas Turbine Airfoils Including Effects of Leading Edge Sharpness," ASME *Journal of Engineering for Power*, Vol. 94, No. 3, pp. 219–225.

Metzger, D. E., and Larson, D. E., 1986, "Use of Melting Point Surface Coatings for Local Convection Heat Transfer Measurements in Rectangular Channel Flows With 90-deg Turns," ASME *Journal of Heat Transfer*, Vol. 108, pp. 48–54.

Metzger, D. E., Yamashita, T., and Jenkins, C. W., 1969, "Impingement Cooling of Concave Surfaces With Lines of Circular Air Jets," ASME *Journal of Engineering for Power*, Vol. 91, No. 3, pp. 149–158.

Downloaded 01 Jun 2010 to 171.66.16.66. Redistribution subject to ASME license or copyright; see http://www.asme.org/terms/Terms_Use.cfm

Impingement/Effusion Cooling: The Influence of the Number of Impingement Holes and Pressure Loss on the Heat Transfer Coefficient

A. M. Al Dabagh

G. E. Andrews

R. A. A. Abdul Husain

C. I. Husain

A. Nazari

J. Wu

Department of Fuel and Energy,
The University of Leeds,
Leeds, United Kingdom

Measurements of the overall heat transfer coefficient within an impingement/effusion cooled wall are presented. The FLUENT CFD computer code has been applied to the internal aerodynamics to demonstrate the importance of internal recirculation in the impingement gap. This generates a convective heat transfer to the impingement jet. Measurements of this heat transfer plate coefficient are presented that show it to be approximately half of the impingement/effusion heat transfer coefficient. The influence of the relative pressure loss or X/D between the impingement and effusion walls was investigated, for an effusion X/D of 4.67 and a Z of 8 mm, and shown to be only significant at high G where a reduction in h of 20 percent occurred. Increasing the number of holes N in the impingement/effusion array at a constant Z of 8 mm reduced h by 20 percent, mainly due to the higher Z/D for the smaller holes at high N. Reduced numbers of impingement holes relative to the effusion holes, in a ratio of 1 to 4, were shown to have a small influence on h with a maximum reduction in h of 20 percent at high G and a negligible effect at low G.

Introduction

Impingement/effusion cooling of gas turbine combustor and turbine blade walls offers very efficient cooling with minimal coolant mass flow. The double-skin wall design is easily manufactured using conventional techniques, and thermal stresses are reduced by the double-skin design. This allows the outer impingement jet wall to operate at a lower temperature than the inner effusion jet wall. The presence of the effusion holes gives additional heat transfer at the effusion hole inlet and within the short hole (Andrews et al., 1986, 1987). The overall heat transfer coefficient is thus usually higher for impingement/effusion than it is for impingement alone. Hollworth et al. (1980, 1981) for an X/D of 10 and effusion/impingement jet area ratio of 3.07 found an increase of 30 percent due to the addition of effusion holes offset from the impingement holes. Andrews et al. (1988) found similar increases with values of 30 percent for an X/D of 10 with an effusion/impingement jet area ratio of 5.6 and 45 percent for an area ratio of 2.4.

The objective of the present work was to extend the range of impingement/effusion geometries for which overall heat transfer data are available. The influence of the number of holes N, the relative number of impingement/effusion holes, and the area ratio between the impingement and effusion holes were investigated to determine their relative importance. Andrews et al. (1985a) showed that impingement and impingement/effusion heat transfer gave rise to convective heat transfer from the target or effusion wall to the impingement jet wall. This indicated that there was recirculation within the impingement gap and this was investigated using an isothermal model and the FLUENT CFD computer code (Creare, 1985). Heat transfer data are also presented for one geometry for the recirculated convective heat transfer to the impingement jet plate.

Andrews et al. (1988) showed that the dominant heat transfer mode in impingement/effusion internal wall heat transfer was that due to the impingement jets. Far more heat transfer data exist for impingement heat transfer than for the combined impingement/effusion heat transfer. There have been many investigations of impingement heat transfer for multijet arrays, with much of the work aimed at gas turbine cooling applications (Tabakoff and Clevenger, 1972; Kercher and Tabakoff, 1970; Florschuetz et al., 1981; Hollworth and Berry, 1978; Andrews and Hussain, 1984a, 1984b, 1986, 1987; Andrews et al., 1987b). In the present work the pressure loss of the impingement wall was important and this is determined by the X/D (Andrews and Hussain, 1984a, 1984b). Few general heat transfer correlations for impingement heat transfer include the influence of the main variables, X, D, Z, N, and G, over a practical range of values. For a range of X/D from 1.9 to 21.5, Z/D from 0.5 to 35, N from 1000 to 10,000

Contributed by the International Gas Turbine Institute and presented at the 34th International Gas Turbine and Aeroengine Congress and Exhibition, Toronto, Ontario, Canada, June 4–8, 1989. Manuscript received at ASME Headquarters January 27, 1989. Paper No. 89-GT-188.

Copyright © 1990 by ASME
Downloaded 01 Jun 2010 to 171.66.16.66. Redistribution subject to ASME license or copyright; see http://www.asme.org/terms/Terms_Use.cfm

Table 1 Experimental impingement/effusion configurations

Configuration No.	1	2	3	4	5
A_e/A_i	1	1	5.6	1	5.3
Z/D_i	0.5–5	1.0	5.8	6.1	2.8
Impingement wall					
N, m^{-2}	4306	4306	4306	26,910	1076
X, mm	15.2	15.2	15.2	6.1	30.4
D_i, mm	3.24	8.2	1.38	1.32	2.86
X/D	4.7	1.8	11.0	4.7	10.6
152 mm square hole array	10×10	25×25	10×10	25×25	5×5
Effusion wall					
N, m^{-2}	4306	4306	4306	26,910	4306
X, mm	15.2	15.2	15.2	6.1	15.2
D_e, mm	3.27	8.2	3.27	1.32	3.27
X/D_e	4.7	1.8	4.7	4.7	4.7

m^{-2}, G from 0.1 to 2 kg/sm^2, and Re from 300 to 50,000, Andrews and Hussain (1984a, 1984b) and Andrews et al. (1985d, 1987b) have established the correlation in equation (1), which has been shown to be in reasonable agreement with the data of other workers

$$\frac{\mathrm{Nu}}{\mathrm{Pr}^{0.33}} = 1.05\ \mathrm{Re}^{0.72} \left(\frac{X}{D}\right)^{-0.72} \left(\frac{Z}{D}\right)^{-0.14} D^{0.28} \quad (1)$$

which in terms of h and G for air for a typical Z/D of 4.5 reduces to

$$h = 61(G\ X/D)^{0.72} \quad (2)$$

Andrews et al. (1985a) showed that for a practical range of Z from 2 to 12 mm there was little influence of Z on the impingement heat transfer for X/D from 1.9 to 21.5. For this range of Z the correlation in equations (3) and (4) applied

$$\mathrm{Nu} = 0.29 \left(\frac{X}{D}\right)^{-1.08} \mathrm{Re}^{0.72} \quad (3)$$

$$h = 75 \left(\frac{X}{D}\right)^{0.64} G^{0.72} \quad (4)$$

In the present work a constant Z of 8 mm was used, well inside the above range of Z for which equations (3) and (4) applied.

In association with the present work there has been a parallel program on the determination of the overall film cooling effectiveness. This was measured by placing the impingement/effusion test geometry in the wall of a duct with a high-temperature crossflow. Andrews et al. (1988) showed typical results for impingement/effusion geometries and demonstrated a significant improvement in the cooling effectiveness of effusion film cooling due to the addition of impingement cooling. The present heat transfer coefficient measurements will be used in a heat balance model of the cooling effectiveness data so as to yield film heat transfer coefficients.

Impingement/Effusion Design

The combustor design requirements are that the bulk of the pressure loss occurs at the impingement plate and the pressure loss across the effusion wall is small, as this ensures good film cooling characteristics (Andrews et al., 1985b). For turbine blades the relative pressure loss between the impingement and effusion surfaces is more complex than for combustor applications due to large static pressure variations around the blade surfaces. In regions such as the stator vane leading edge, the static pressure at the film cooling hole outlet is very high and a low-pressure loss would be necessary at the impingement holes and at the effusion holes. The present work investigates this situation, where the effusion and impingement hole pressure loss are low. Further data are also presented for the situation of a high impingement wall pressure loss with low effusion wall pressure loss. The influence of the number of holes per unit surface area was investigated and the range of geometries is given in Table 1.

In the present work, square arrays of impingement/effusion holes were used with equal numbers of holes offset half a pitch relative to each plate so that an impingement jet was located on the center of each four effusion holes. All the impingement air was discharged through the effusion holes and hence there was no net crossflow in the impingement gap. This test configuration is shown in Fig. 1. For geometries with the main pressure loss at the impingement wall the hole sizes are small and the manufacturing costs relatively high and a minimum number of holes should be used. Effusion film cooling requires a large number of holes, N, for optimum film cooling effectiveness. Andrews et al. (1987b) showed that for impingement heat transfer N could be varied over a wide range without any major reduction in the heat transfer. Thus, there may be no requirement to have equal numbers of impingement and effusion holes and the variation of their ratio forms part of the present investigations using the geometries detailed in Table 1. Hollworth et al. (1980, 1981) used one impingement hole for every four effusion holes and their data were very similar to those of Andrews et al. (1988) for equal numbers of holes.

Experimental Techniques

The experimental equipment is shown in Fig. 2. A 152-mm-square Nimonic 75 test wall was used with a PTFE (Teflon)

Nomenclature

A = total hole approach surface area per hole $= A^2 - \pi/4\ D^2$, m^2
A_h = hole internal surface area per hole $= \pi DL$, m^2
A_e = total effusion hole flow area per hole
A_i = total impingement hole flow area per hole
C_p = specific heat of the wall material
D = hole internal diameter, m
G = coolant mass flow per unit wall area, kg/sm^2
h = surface-averaged convective heat transfer coefficient based on the surface area per hole A, W/m^{2}K
k = thermal conductivity of the coolant, W/mK
L = hole length, m
m = mass of the test plate heat transfer section, kg
N = number of holes per unit surface area, m^{-2}
Nu = Nusselt number based on h and the impingement hole diameter $D = hD/k$
Pr = Prandtl number
Re = hole Reynolds number based on the impingement hole diameter D and the coolant velocity in the hole
T_c = coolant temperature, K
T_g = hot gas temperature, K
T_I = impingement jet wall temperature, K
T_m = mean wall temperature in central 76 mm of the 152-mm test wall
T_w = local wall temperature, K
T_{wi} = initial local wall temperature, K
X = hole pitch, m
Z = impingement gap, m
τ = time constant, equation (6)

Downloaded 01 Jun 2010 to 171.66.16.66. Redistribution subject to ASME license or copyright; see http://www.asme.org/terms/Terms_Use.cfm

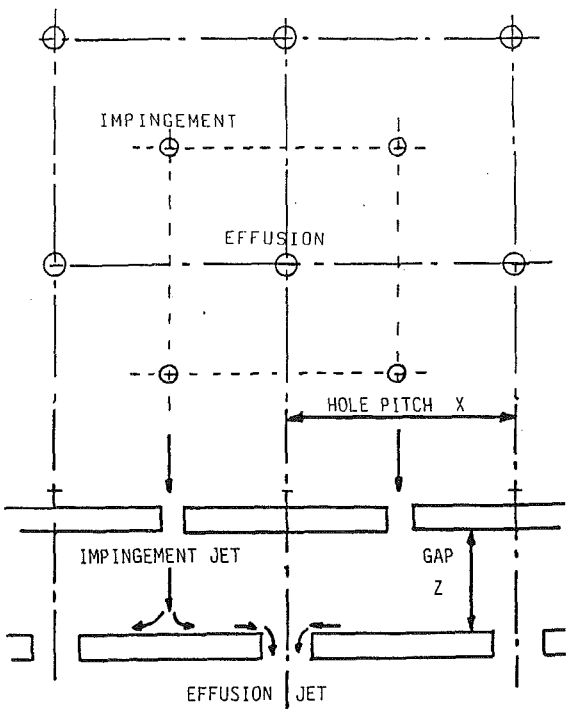

Fig. 1 Impingement/effusion configuration

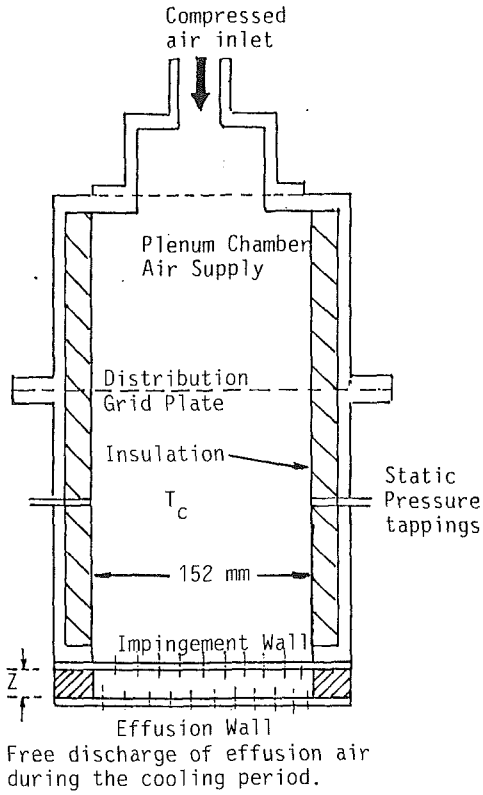

Fig. 2 Experimental equipment

separation flange forming the impingement gap, which also minimized thermal conduction between the impingement and effusion test geometries. A range of impingement gap flanges was used to achieve different impingement gap (Z) to hole diameter (D) ratios, Z/D. The impingement/effusion geometry and PTFE separation gaps were all bolted to an internally insulated air supply plenum chamber. Each test plate, both impingement and effusion, was instrumented with at least five Type K mineral insulated grounded junction thermocouples, vacuum brazed to the exit side of the test plates on the centerline of the plate midway between the holes. In addition, the effusion test plate had thermocouples brazed to the feed side of the plate to investigate temperature gradients. There was no significant difference in the temperature across the effusion plate metal thickness. Previous work using steady-state heat transfer techniques showed that temperature gradients, both axially between the jets and through the wall thickness, were less than 2 percent of the mean wall temperature (Andrews and Hussain, 1984b). This was in agreement with the findings of the more complex film cooling situation where even at high temperatures the test plate was at a uniform temperature with maximum temperature differences of less than 3 percent of the mean temperature (Andrews et al., 1985c). The test plate centerline thermocouples were used for the heat transfer measurements, rather than the mean plate temperature, as this avoided any slight edge effects. By comparing h determined from different thermocouples, the experimental uncertainty was evaluated.

The heat transfer coefficient was determined by using a transient cooling technique. This was the same as that used for single wall effusion cooling short hole heat transfer (Andrews et al., 1986a, 1987a). The impingement/effusion test wall was heated in the absence of any coolant air flow by placing the wall and plenum chamber assembly on an insulated uniform heat flux electrical mat heater. Prior to heating the wall, the air flow controls were set to give the desired air flow by opening a single valve. The test wall was heated to approximately 80°C and then rapidly hoisted free of the heater and the coolant flow established. The test plate was then cooled by the air flow and the temperatures of all the thermocouples were recorded as a function of time using a 32-channel data acquisition system interfaced to a microcomputer.

The transient cooling of the impingement/effusion assembly is governed by the classical first-order differential equation with a solution for a step change in heat input that gives an exponential fall in temperature with time. These equations are valid provided the wall was at a uniform temperature. For convective heat transfer to a slab, a uniform wall temperature is achieved if the Biot number is low. For the present work, the Biot number was always less than 0.2 and temperature differences of less than 10 percent of the mean would be expected from classical heat conduction analysis. For most of the test conditions, the Biot number was less than 0.1 and temperature gradients less than 5 percent of the mean would be expected. The experimental measurements of the maximum temperature gradients, discussed above, were all less than 5 percent. Successive temperature data points were used to determine the time constant τ from equations (5) and (6).

$$T_w = T_c - \tau \frac{\Delta T_w}{\Delta t} \tag{5}$$

$$\tau = \frac{m\, c_p}{h\, A} \tag{6}$$

Each pair of successive temperatures was used to calculate $\Delta T_w/\Delta t$ and this was associated with the mean of the two temperatures. This mean temperature T_w was then plotted against $\Delta T_w/\Delta t$ and a least-square fit was made to the data to yield the gradient, which was τ. Equation (6) shows that h may be calculated directly from τ as the other parameters are all known constants for a particular plate material and geometry. This technique was used in the present work to determine the heat transfer coefficient for both the effusion wall and the recirculated heat transfer to the impingement jet wall.

Downloaded 01 Jun 2010 to 171.66.16.66. Redistribution subject to ASME license or copyright; see http://www.asme.org/terms/Terms_Use.cfm

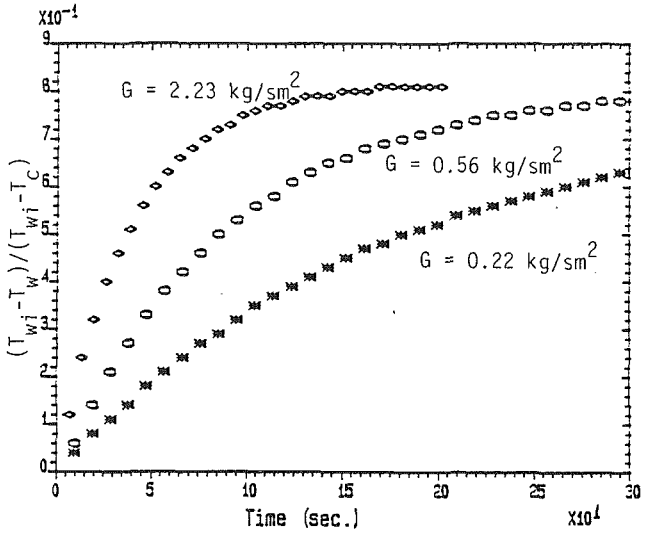

Fig. 3 Transient cooling response of the effusion wall for configuration No. 1, $X/D = 4.7$, $Z = 8$ mm, for three flow rates G of 0.22, 0.56, and 2.23 kg/sm^2

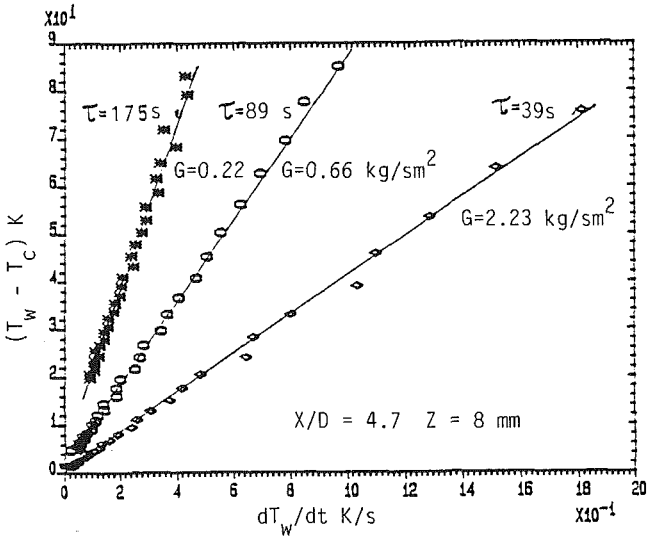

Fig. 4 Determination of the time constant from the transient cooling response for configuration 1

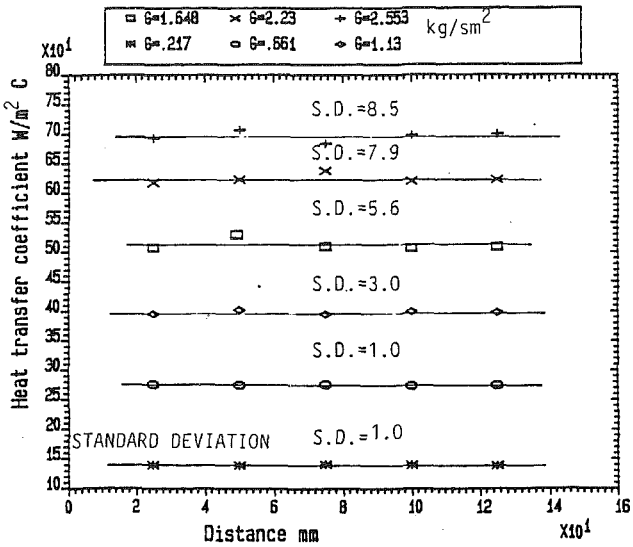

Fig. 5 Axial variation of h on the effusion wall for configuration 1, $X/D = 4.7$, $Z/D = 3$, for a range of G from 0.22 to 2.55 kg/sm^2

The choice of the dominant heat transfer surface area A to use in equation (6) is crucial to the establishment of a viable heat transfer correlation. In an impingement/effusion situation, the choice of area is uncertain as the impingement heat transfer acts over the effusion plate surface area, whereas conventionally the effusion plate heat transfer is ascribed to the internal hole surface area A_h. However, Andrews et al. (1986, 1987a) have shown that the effusion plate cooling was dominated by the hole approach surface heat transfer and that the effusion plate surface area A was the most appropriate area to use in the correlation. As this is the same area as used for the impingement heat transfer coefficient, the comparison between impingement, effusion, and impingement/effusion systems is easily made.

The heat transfer coefficient was evaluated for each thermocouple on the test walls, so that the variations in h over the test surface could be determined. Typical transient test results for a single thermocouple are shown in Figs. 3 and 4 for a range of G. Other heat losses from the test section, such as convection from the bottom side of the wall, were small and do not influence the transient response as the heat transfer coefficients were much smaller than those being measured. The transient response analysis was confined to the rapid cooling part of the results, where any temperature change due to other lower convective heat transfer events would be negligible. Edge conduction losses were also small during the transient and heat losses were much less of a problem than during steady-state heat balance tests. The least-squares fit to the data in Fig. 4 gave a maximum uncertainty in an individual measurement of τ and hence in h of ± 5 percent. The uniformity of h with axial distance on the centerline of the test wall is shown in Fig. 5 for a range of G. Taking the 95 percent confidence limits as twice the standard deviation, then Fig. 5 shows h to be constant on the test wall centerline to ± 1 percent of h at low G and ± 3 percent of h at high G. This small deterioration in the confidence limits at high G was due to the small increase in Biot number.

Aerodynamics in the Impingement/Effusion Gap

The aerodynamics in the gap between the impingement and effusion walls is complex with recirculation between the impingement jets. This was investigated initially in a simplified two-dimensional form using both water flow visualization and the FLUENT CFD code (Creare, 1985). Typical predicted flow patterns are shown in Fig. 6 for a range of geometries of relevance to the present work. These were very close to the flow visualization flow patterns. They show that on the centerline between the impingement jets there was a strong reverse flow jet between two counterrotating vortices. In the two-dimensional simulation, the reverse flow jet was directly in line with the effusion jet, which would reduce the reverse flow velocity compared with the three-dimensional situation of offset impingement and effusion hole centerlines.

Figure 6 shows that high velocities were induced in opposite directions on the jet and effusion target walls. These wall velocities are shown in Figs. 7 and 8 as a ratio of the inlet jet velocity, for a range of jet velocities for one impingement/effusion configuration. Figure 7 shows that the peak velocities on the jet plate surface were as high as 25 percent of those of the jet velocity. This was the main cause of the convective heat transfer to the jet plate from the effusion plate that is detailed later.

Figure 7 shows the velocity variation along the effusion plate surface as a ratio of the impingement jet velocity. This shows that at the edge of the effusion hole the velocity was 30 percent higher than the jet velocity. This was the source of the

Downloaded 01 Jun 2010 to 171.66.16.66. Redistribution subject to ASME license or copyright; see http://www.asme.org/terms/Terms_Use.cfm

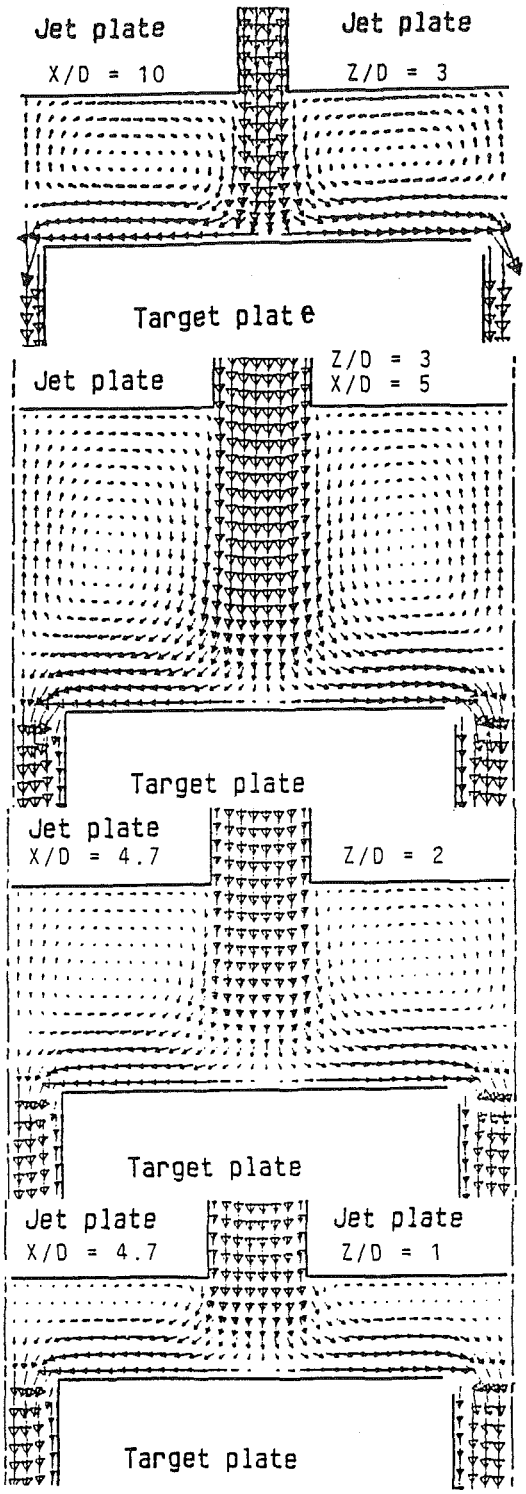

Fig. 6 Impingement/effusion gap aerodynamics predicted using the FLUENT CFD code in two dimensions (Creare, 1985)

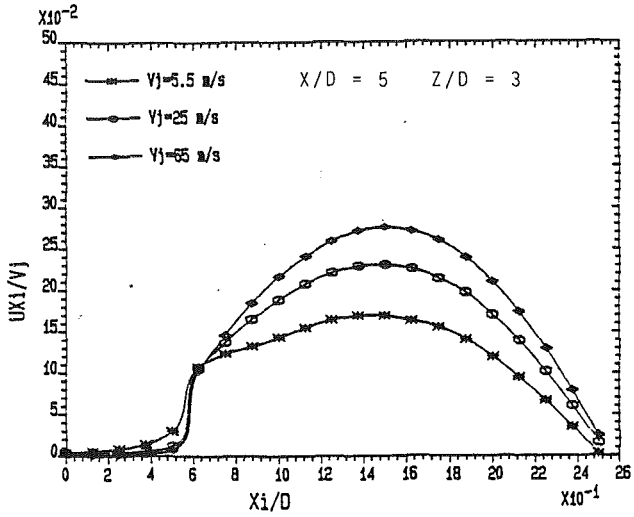

Fig. 7 FLUENT 2D computations of the horizontal velocity distribution on the impingement wall due to recirculation in the gap; horizontal velocity expressed as a ratio to the impingement jet velocity

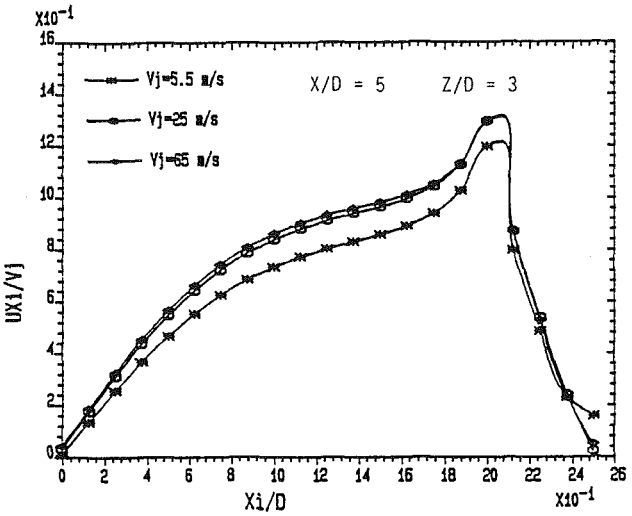

Fig. 8 Horizontal surface velocity distribution on the effusion wall gap side, velocities expressed as a ratio to the impingement jet velocity, two-dimensional predictions using the FLUENT CFD code (Creare)

enhanced heat transfer due to the presence of the effusion holes. Andrews et al. (1988) showed that the impingement/effusion heat transfer was mainly due to the addition of the impingement and effusion heat transfer. However, there was a 15–20 percent overprediction of the measured impingement/effusion heat transfer coefficient using the summation of the separately measured impingement and effusion heat transfer coefficients. This overprediction was considered to be partially due to aerodynamic interaction effects in the combined geometry, as shown in Fig. 6.

Impingement Jet Wall Heat Transfer

The heating of the impingement jet wall due to the recirculation of heat by the aerodynamics shown in Fig. 6 was first measured experimentally by Andrews et al. (1985a). The heating of the impingement jet plate was expressed by the dimensionless temperature T_z, defined by

$$T_z = \frac{T_I - T_c}{T_m - T_c} \tag{7}$$

A comparison of the steady-state T_z results for impingement/effusion cooling with those for impingement only is made in Fig. 9. At low coolant flow rates G, the impingement jet plate was heated quite appreciably. This would transfer heat to the impingement air raising its temperature above the supply coolant temperature T_c. The impingement results were obtained on the present equipment during steady-state operation. Reliable steady-state results could not be established with impingement/effusion cooling due to the flow of coolant through the heater. The results in Fig. 9 were obtained from high-temperature tests with the impingement/effusion wall mounted flush in the wall of a 76×152 mm duct with high-velocity propane combustion products at 750 K as the heat

Downloaded 01 Jun 2010 to 171.66.16.66. Redistribution subject to ASME license or copyright; see http://www.asme.org/terms/Terms_Use.cfm

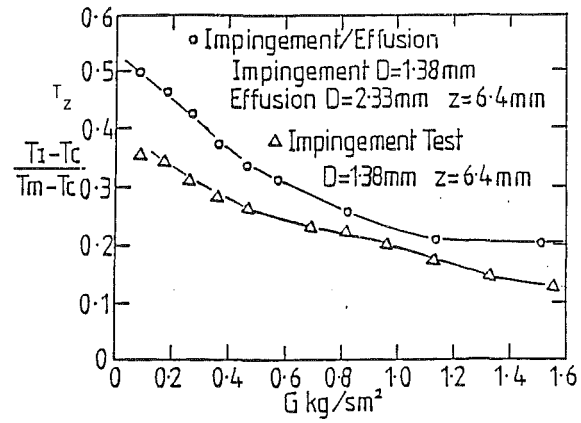

Fig. 9 T_Z versus G for impingement/effusion and impingement alone

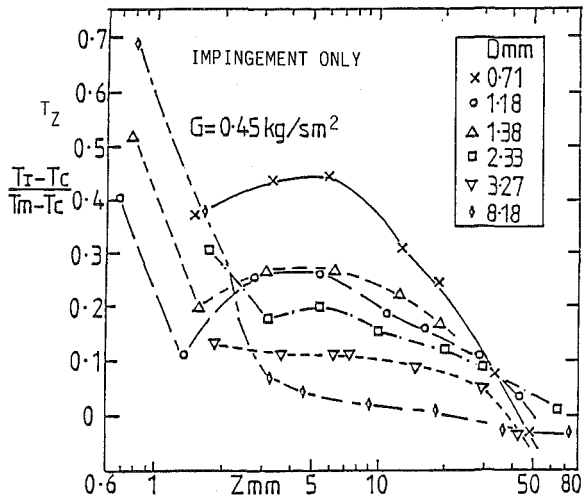

Fig. 10 T_Z as a function of Z for G = 0.45 kg/sm²

source. The effusion jets provided film cooling and the results were presented by Andrews et al. (1988). Considering the major differences between the two test facilities, the agreement in the values of T_z in Fig. 9 is quite good. The higher values for impingement/effusion may be due to the acceleration of the reverse flow jet, shown in Fig. 6, by the heating received during the impingement heat transfer.

Values of T_z as a function of the impingement gap Z for a coolant flow rate G of 0.45 kg/sm² are shown in Fig. 10 for a range of impingement jet diameters. At low Z values the interwall heating was very significant. In this region the Z/D was less than unity and the flow aerodynamics did not exhibit recirculation but high-velocity flow from wall to wall across the impingement gap. The transition to this type of flow can be seen for a Z/D of 1 in Fig. 6. At low Z this effect is greater the higher the impingement hole diameter and the smaller the X/D. For larger Z, where the counterrotating vortices shown in Fig. 6 exist, T_z increases with reduced hole size or increased X/D. This was because the reverse flow jet velocity was greater due to the higher impingement jet velocity with consequently greater reverse flow heat transfer.

The transient cooling technique was used simultaneously to determine the impingement jet wall and target effusion wall heat transfer coefficients. The impingement/effusion configuration 1 in Table 1 was used. This had equal impingement and effusion hole sizes and was designed for a low overall pressure difference application. Figure 10 showed that the impingement gap was an important parameter in determining the magnitude of T_z. Consequently, the impingement gap was varied for configuration 1 giving a range of Z/D from 0.5 to 5.

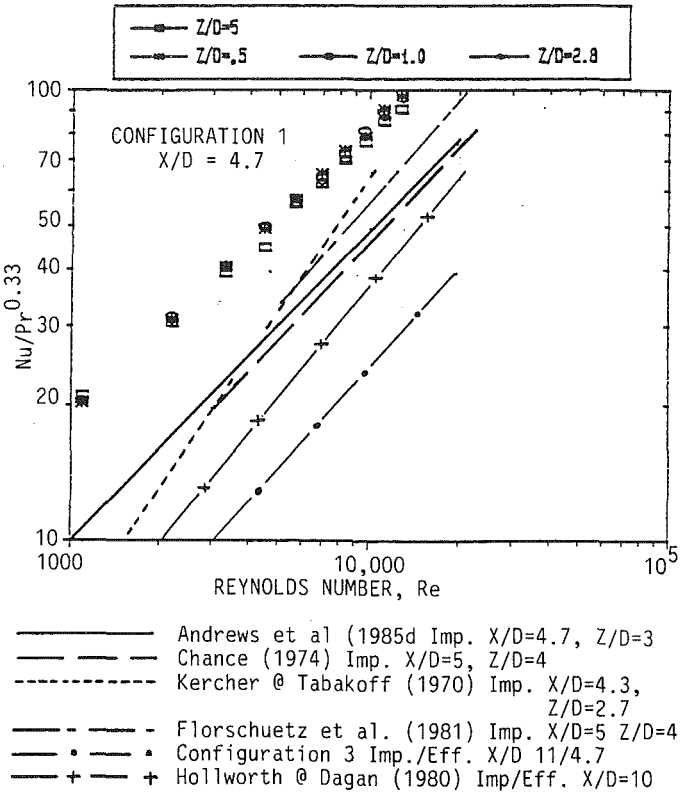

Fig. 11 Influence of Re on heat transfer for configuration 1 at various Z/D and configuration 3 at Z = 8 mm, with a comparison with previous data for similar geometries for impingement and impingement/effusion

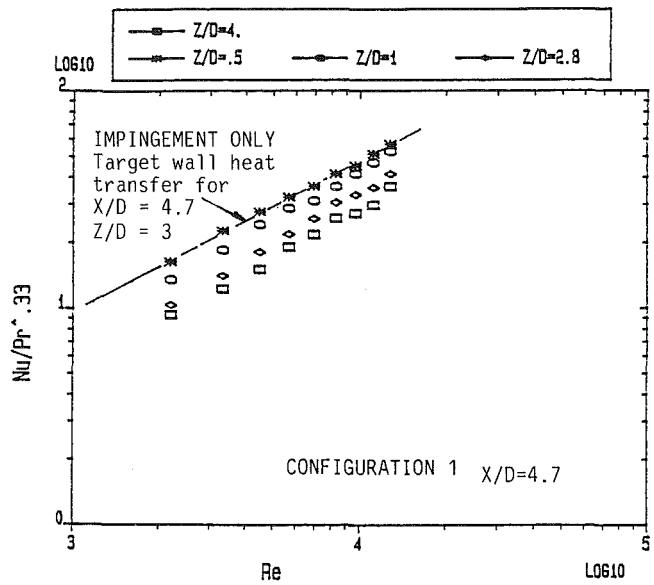

Fig. 12 Heat transfer to the impingement wall due to recirculation within the impingement gap

The results as $Nu/Pr^{0.33}$ as a function of the impingement jet Re are shown in Figs. 11 and 12 for the effusion and impingement jet walls, respectively.

Figure 11 shows that there was a negligible influence of Z/D on the heat transfer to the effusion wall. Z/D cannot influence the heat transfer due to the effusion hole and hence any influence of Z/D must be due to the impingement heat transfer. Andrews et al. (1985d) showed, for the 3.2-mm-dia impingement jet plate of configuration 1 in Table 1, that there was only a small influence of Z/D on the impingement heat transfer over the range of Z/D from 0.5 to 5 for a constant G. The prediction of the aerodynamics in the impingement/effu-

Downloaded 01 Jun 2010 to 171.66.16.66. Redistribution subject to ASME license or copyright; see http://www.asme.org/terms/Terms_Use.cfm

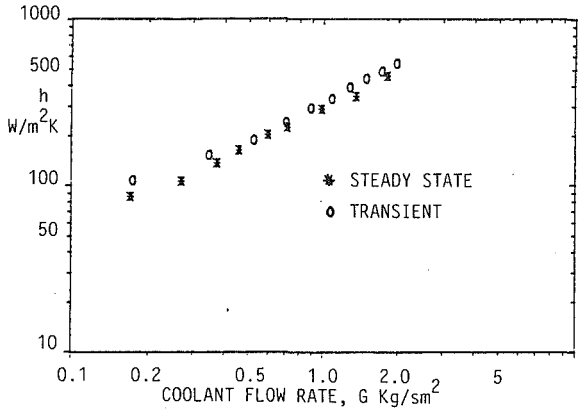

Fig. 13 Comparison of steady-state and transient techniques for the determination of h for impingement heat transfer with X/D = 6.8, Z = 8 mm

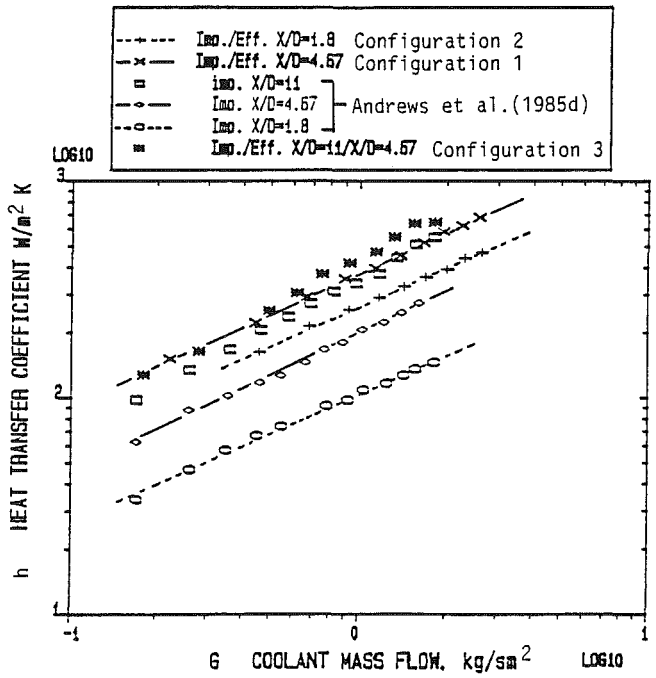

Fig. 14 Heat transfer coefficient as a function of G for impingement alone and impingement/effusion at Z/D = 3, with different X/D

sion gap using the FLUENT CFD program showed that the flow along the effusion wall had no strong dependence on Z/D, as shown in Fig. 6. However, the interjet recirculation zone aerodynamics were significantly influenced by Z/D.

Figure 12 shows that Z/D had a strong influence on the heat transfer due to the internal flow recirculation from the effusion wall to the impingement jet wall, as was found for T_z in Fig. 10. Heat transfer increased as Z/D was reduced due to the more compact recirculation and the full gap width flow at $Z/D < 1$. Comparison of the heat transfer data in Figs. 11 and 12 shows that at low Z/D the impingement jet plate heat transfer was approximately half that of the combined impingement/effusion heat transfer. However, if the impingement jet plate heat transfer data are compared with the impingement target plate data of Andrews et al. (1984) for the 3.2 mm impingement jet array, then these two heat transfer results are quite similar as shown in Fig. 12. This indicates that this reverse flow heat transfer was of a very significant magnitude and was an important feature of both impingement and impingement/effusion cooling systems.

Comparison With Previous Impingement Heat Transfer Results

The present results are compared with a range of previous heat transfer data in Fig. 11. For impingement/effusion heat transfer, the results for configuration 3 in Table 1 (Andrews et al., 1988) are compared with those of Hollworth and Dagan (1980) for an X/D of 10. They used a steady-state heat balance technique with a very low N and large D. In spite of these differences there was reasonable agreement with the present results.

For impingement heat transfer only, the steady-state impingement heat transfer results for configuration 1 with an X/D of 4.7 and a Z/D of 4 (Andrews and Hussain, 1984b) are shown in Fig. 11. These results are in excellent agreement with those of Chance (1974) for an X/D of 5.3 and a Z/D of 4. They are also in reasonable agreement with the results of Florschuetz et al. (1981) for an X/D of 5 and Z/D of 3, and with the results of Kercher and Tabakoff (1970) for an X/D of 4.3 and a Z/D of 2.7.

The present transient techniques for determining h have also been applied to impingement heat transfer alone. The results are compared in Fig. 13 with the steady-state results of Andrews et al. (1985a) for $N = 4306\ \text{m}^{-2}$ and an X/D of 6.83 ($D = 2.33$ mm). The agreement between the two quite different techniques for determining h was good, with a maximum difference of 20 percent between the results for the same G. The transient results were slightly higher than for the steady-state results and this may have been due to the lower influence of heat losses in the transient tests. These results indicate that valid comparisons may be made between the present impingement/effusion transient results in Fig. 14, and the previously published steady-state results.

Low-Pressure Loss Impingement/Effusion Heat Transfer

For some turbine blade cooling applications a low overall wall pressure loss is required across the impingement/effusion wall. The pressure loss is directly controlled, at a fixed flow rate G, by the hole pitch-to-diameter ratio as shown by equation (8) (Andrews et al., 1985d).

$$\frac{X}{D} = \text{const}\ \frac{(\Delta P/P)^{0.25}}{G^{0.5}} \tag{8}$$

Equation (8) shows that a low-pressure loss requires a small value of X/D. In the present work values of X/D of 4.7 and 1.8 were used, which are typical of the X/D used in some turbine blade cooling designs. Previous work for combustion chamber applications (Andrews et al., 1988) used a high-pressure loss impingement jet wall ($X/D = 11$) with low-pressure loss effusion walls ($X/D = 4.7$) and these results will be used for comparison. The same hole size and X/D were used for the impingement and effusion walls to achieve the desired low overall pressure loss. The design details of all these three configurations are given in Table 1.

The influence of Z/D for configuration 1 was shown above to be small for a wide range of Z/D. A small Z/D of unity was used for configuration 2, which gave a practical impingement gap size for the relatively large hole diameter. The 8-mm gap used for configuration 3 in Table 1 resulted in a Z/D of 5.8 compared with 1.0 for configuration 2 for the same gap width. Figure 11 shows that the effusion wall heat transfer was insensitive to Z/D over this range and hence a valid comparison between the present and previous work at different Z/D can be made.

The results for impingement/effusion configurations 1, 2, and 3 are shown as the heat transfer coefficient as a function of coolant flow rate G in Fig. 14. The heat transfer coefficient data for the impingement jet wall are also included for com-

Downloaded 01 Jun 2010 to 171.66.16.66. Redistribution subject to ASME license or copyright; see http://www.asme.org/terms/Terms_Use.cfm

parison in Fig. 14, taken from the work of Andrews et al. (1985d), which used a steady-state heat balance technique to determine h.

Figure 13 shows that for impingement/effusion heat transfer with the same effusion wall X/D of 4.7, the effect of decreasing the impingement X/D from 11 to 4.7 was to decrease h by approximately 20 percent at high G. However, at low G the influence of impingement X/D was negligible. This effect was much less than the equivalent difference in the two impingement heat transfer coefficients, which Fig. 13 shows to have decreased by approximately 40 percent at all G. This shows that the influence of the effusion wall jets on the increase in the impingement heat transfer was greater for low X/D impingement geometries than for the high-pressure loss and high X/D geometries. The increase in the heat transfer coefficient due to the addition of the effusion holes was a factor of 1.8 for an impingement X/D of 4.7 compared with 1.3 for an X/D of 11 (Andrews et al., 1988). Hollworth and Dagan (1980) also found an increase in heat transfer of 1.3 for an X/D of 11.

For configuration 2 with an X/D of 1.8 at both the impingement and effusion walls, there was a decrease in h compared with configuration 1 of approximately 30 percent compared with a difference of 50 percent in the two impingement heat transfer coefficients. However, the combined impingement/effusion heat transfer coefficient for an X/D of 1.8 was approximately 25 percent higher than the impingement h for an X/D of 4.7. The relatively large reduction in h, for impingement/effusion heat transfer with an X/D of 1.8 compared with that for an X/D of 4.7, was contributed to by a reduction in the effusion wall h as well as the impingement wall h. Hence, where possible the X/D should be at least 4.7 for both the impingement and effusion walls if the heat transfer coefficient is to be maximized for a given G for a low overall pressure loss.

The increase in the heat transfer coefficient due to the addition of the effusion holes was a factor of 2.3 for an $X/D = 1.8$ compared with 1.8 for an X/D of 4.7 and 1.3 for configuration 3 with an impingement X/D of 11. The reason for the greater relative influence of the effusion wall at low X/D was the additive effect of the impingement and the effusion hole entry heat transfer. Reducing the impingement X/D at constant effusion X/D simply reduces the proportion of the overall heat transfer due to impingement, as the effusion hole entry heat transfer remained unchanged.

For an X/D of 4.7, configuration 1, the value of h at a G of 1 kg/sm^2 was 200 W/m^{2}K for the impingement jets (Andrews et al., 1985d) and also 200 W/m^{2}K for the effusion wall (Andrews et al., 1987a). With no interaction between the two heat transfer modes, the combined heat transfer should be 400 compared with the measured 360 W/m^{2}K. This was only a 10 percent reduction in heat transfer due to interaction effects compared with 19 percent for an impingement X/D of 11 (Andrews et al., 1988). For the X/D of 1.8 configuration, the combined impingement and effusion heat transfer coefficient was the same as the present measured impingement/effusion heat transfer and there was thus no significant interaction. The reason for this was the more rapid decay of the impingement jet velocities on the surface of the effusion wall for low X/D. For an X/D of 11 but the same X as the lower X/D results, this surface velocity was high and would dominate the effusion hole entry velocities. Thus the enhancement of the velocities at the effusion hole lip, as shown for an X/D of 5 in Fig. 8, was considerably reduced for an X/D of 11.

Influence of the Number of Holes

Andrews et al. (1987b) showed that for the impingement heat transfer there was little major influence of the number of holes per unit surface area N over a wide range of N. Reduced

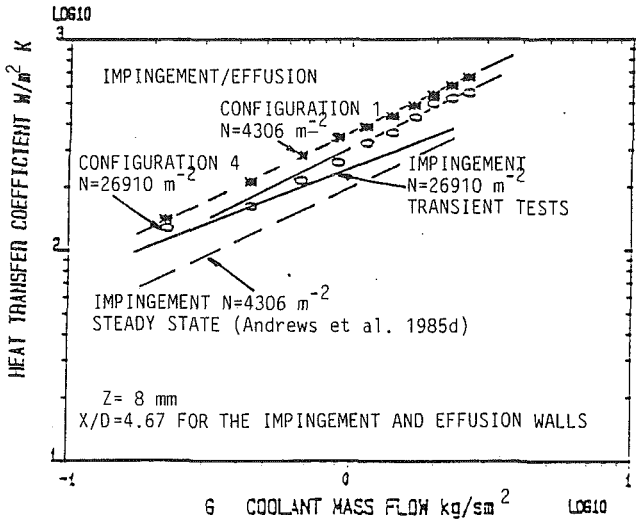

Fig. 15 Impingement/effusion and impingement heat transfer coefficients as a function of G for different numbers of holes, $N = 4306$ and 26,910 m^{-2}, for an X/D of 4.7 for the impingement and effusion walls

heat transfer was found at very low values and very high values of N. This was due to lack of adequate surface coverage of the enhanced heat transfer regions at low N and crossflow effects at high N. The aim of the present work was to investigate whether there was any advantage in using a high N for impingement/effusion cooling.

Configurations 1–3 in Table 1 were for an N of 4306 m^{-2} and for an X/D of 4.7; these results were compared at a Z of 8 mm with those for an N of 26,910/m^2, configuration 4. This comparison is shown in Fig. 15 as h versus G, which shows that there was a small reduction in the heat transfer coefficient with increased N in the impingement/effusion array and hence that there was no advantage in using the much higher number of holes of configuration 4.

The decrease in heat transfer with the increase in N shown in Fig. 15 was approximately 20 percent at all G. Part of the reason for this decreased heat transfer was the use of an 8-mm impingement gap for both tests. This involved different Z/D, as shown in Table 1, with a Z/D of 2.5 for an N of 4306 m^{-2} and 6.1 for an N of 26,910 m^{-2}. The Z/D exponent of 0.14 in equation (1) is sufficient to account for the 20 percent lower heat transfer at the larger Z/D. An impingement gap of approximately 3 mm would be required for the same Z/D as at an N of 4306 m^{-2}. This is feasible for turbine blade applications but too small for large surface area combustor applications.

The results for impingement heat transfer (Andrews et al., 1987b) also showed that there was a deterioration in heat transfer at Z of 10 mm and N of 26,910/m^2 compared with an N of 4306/m^2. The reason for this difference was the influence of crossflow in the impingement gap with impingement cooling alone. Crossflow in the impingement gap decreases the heat transfer and this effect increased with the number of rows of upstream holes and with a decrease in Z/D (Andrews and Hussain, 1986, 1987).

The impingement results in Fig. 13 were obtained for a flow discharge on all edges of the impingement gap and this minimized the impingement crossflow influence, compared with the more usual single-sided flow exit. However, in impingement/effusion cooling with equal numbers of impingement and effusion jets there can be no crossflow and hence there should be no deterioration in the impingement heat transfer at any value of N. Under these circumstances, a minimum value of N can be used to minimize manufacturing costs and the only limit is that of adequate surface coverage of the high impingement heat transfer. For this minimum N, a

Downloaded 01 Jun 2010 to 171.66.16.66. Redistribution subject to ASME license or copyright; see http://www.asme.org/terms/Terms_Use.cfm

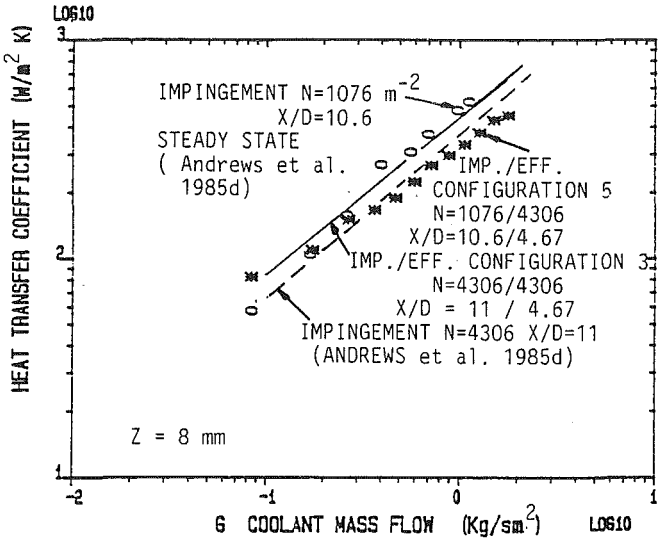

Fig. 16 Comparison of *h* as a function of *G* for impingement/effusion configurations 3 and 5 with different numbers of impingement holes but the same impingement *X/D*

small Z/D should be used to achieve practical impingement gaps.

Reduced Number of Impingement Jets Relative to the Effusion Jets

Hollworth and Dagan (1980) have emphasized that design features that maximize the heat transfer of the coolant as it passes through the impingement effusion wall will be different from those that maximize the film cooling effectiveness of the effusion jets. Andrews et al. (1985b, 1985c) have investigated the film cooling performance of some of the present effusion designs. They showed that the film cooling effectiveness and the overall cooling effectiveness increased as the X/D was reduced for a fixed number of holes. This was achieved by increasing the hole diameter, which reduced the effusion wall pressure loss. In subsequent unpublished work, the authors have also shown that there was a very strong influence of the number of effusion holes on the film and overall cooling effectiveness. Thus the requirements for optimum effusion cooling in impingement/effusion cooling are different from those for optimum impingement cooling. A major difference is in the influence of the number of holes N.

For optimum effusion film cooling a large N was required, but this was not necessary for the impingement cooling. Also the impingement hole size becomes very small and manufacturing costs increase if a large N is used, together with a high impingement wall pressure loss. Consequently, there are advantages in using different numbers of impingement and effusion holes. Hollworth and Dagan (1980) used one impingement hole for every four effusion holes with both sets of holes of similar diameter. This gave an area ratio of 3.07 between the effusion and impingement jets. Andrews et al. (1988) investigated area ratios of 2.4 and 5.6 using equal numbers of holes but larger effusion hole diameters. Their results were shown to be in good agreement with those of Hollworth and Dagan (1980) for the same impingement jet X/D.

In the present work the number of impingement jets was reduced and the same effusion wall was used as for the equal number of jets situation. However, the diameters of the impingement jets were increased so that the same area ratio of 5.6 was used for both configurations. One impingement hole was used for four effusion holes and the design, configuration 5, is detailed in Table 1. The heat transfer results are compared with the results for an equal number of holes in Fig. 16, and this also includes the impingement heat transfer results for Andrews et al. (1987b) for the reduced number of impingement jets without any effusion jets. The reduced number of impingement jets has a small influence on the impingement/effusion heat transfer. Figure 16 shows that at a high G of 1–2 kg/sm^2 the reduction in heat transfer was approximately 20 percent, but at a low G of below 0.3 kg/sm^2 there was a negligible difference between the results.

It is considered that the decrease in the impingement/effusion heat transfer coefficient at high G, with a reduced number of impingement holes, was due to an increase in the interaction between the two heat transfer modes. The impingement jets will set up at very similar double vortex aerodynamics to those shown in Fig. 6, but the effusion jets will no longer be in the plane of the reverse flow jet. They will be exposed to a potentially high velocity crossflow across the hole entrance. There will thus be a much reduced enhanced heat transfer due to the flow acceleration into the hole. The combined heat transfer will thus be dominated by the impingement jets with little additive heat transfer.

Comparison of the impingement/effusion results with those for impingement alone in Fig. 16 shows a deterioration in heat transfer with the addition of effusion jets, of approximately 30 percent at high G (0.3 kg/sm^2), but negligible at low G (0.3 kg/sm^2). This was possible due to the reduction in impingement heat transfer due to the removal of impingement mass flow in the high velocity near the impingement jet region with a consequent reduction in surface velocities and gap recirculation rates. However, the addition of the impingement heat transfer to the effusion wall resulted in a 65 percent increase in the heat transfer coefficient, as shown in Fig. 16. Thus, even though the interaction between the impingement and effusion aerodynamics resulted in a deterioration in both modes of heat transfer, the combined effect was still a substantial increase on that for the effusion wall alone.

Conclusions

1 The internal aerodynamics in the gap between the impingement and effusion walls are complex and are dominated by the counterrotating vortices between the impingement jets, with a reverse flowing jet in-line with the effusion hole. This causes significant heat transfer to the impingement jet plate.

2 For equal numbers of impingement and effusion holes the interaction between the two heat transfer components is small and the effusion wall gives an additive heat transfer to the impingement jets and the overall heat transfer for impingement/effusion is much higher than for impingement alone. However, if the number of impingement jets is lower than the number of effusion jets then the interaction between the two heat transfer components is larger and little additional heat transfer due to the effusion holes then occurs.

3 The area ratio between the effusion and impingement holes influences the heat transfer coefficient with larger values for large area ratios. However, the effect is not large and systems with equal hole size and equal numbers of holes have a high heat transfer coefficient with less impingement and effusion heat transfer interaction.

4 Increasing the number of impingement and effusion holes at constant Z caused a small decrease in the impingement/effusion wall heat transfer coefficient, due to the increased Z/D at constant N and X/D.

Acknowledgments

We would like to thank the U.K. Science and Engineering Research Council for a research grant, GR/D/53029, in support of this work. Some of the test geometries were manufactured by GEC/Ruston Gas Turbines and we would like to thank M.F. Cannon for technical advice. A. M. Al Dabagh and R. A. A. Abdul Husain received research scholarships from the Iraqi Government.

Downloaded 01 Jun 2010 to 171.66.16.66. Redistribution subject to ASME license or copyright; see http://www.asme.org/terms/Terms_Use.cfm

References

Andrews, G. E., and Hussain, C. I., 1984a, "Impingement Cooling of Gas Turbine Components," *1983 Tokyo International Gas Turbine Conference*, pp. 67–74; *High Temperature Technology*, Vol. 2, p. 99–106.

Andrews, G. E., and Hussain, C. I., 1984b, "Full Coverage Impingement Heat Transfer: The Influence of Impingement Jet Size," *1st U.K. National Heat Transfer Conference*, I.Chem.E. Symposium Series No. 86, Vol. 2, pp. 115–1124.

Andrews, G. E., and Hussain, C. I., 1986, "Full Coverage Impingement Heat Transfer: The Influence of Channel Height," *8th International Heat Transfer Conference*, San Francisco, CA, pp. 1205–1211.

Andrews, G. E., and Hussain, C. I., 1987, "Full Coverage Impingement Heat Transfer: The Influence of Crossflow," presented at the AIAA/ASME/SAE/ASEE 23rd Joint Propulsion Conference, AIAA Paper No. 87–2010.

Andrews, G. E., Asere, A. A., Hussain, C. I., and Mkpadi, M. C., 1985a, "Transpiration and Impingement/Effusion Cooling of Gas Turbine Combustion Chambers," *Seventh International Symposium on Air Breathing Engines*, Beijing, China, pp. 794–803, AIAA/ISABE Paper No. 85-7095.

Andrews, G. E., Asere, A. A., Gupta, M. L., and Mkpadi, M. C., 1985b, "Full Coverage Discrete Hole Film Cooling: The Influence of Hole Size," ASME Paper No. 85-GT-53; *International Journal of Turbo and Jet Engines*, Vol. 2, pp. 213–225.

Andrews, G. E., Gupta, M. L., and Mkpadi, M. C., 1985c, "Full Coverage Discrete Hole Wall Cooling: Cooling Effectiveness," ASME Paper No. 84-GT-212; *Int. J. of Turbo and Jet Engines*, Vol. 2, pp. 199–212.

Andrews, G. E., Asere, A. A., Hussain, C. I., and Mkpaki, M. C., 1985d, "Full Coverage Impingement Heat Transfer: The Variation in Pitch to Diameter Ratio at a Constant Gap," AGARD CP-390, Paper No. 26.

Andrews, G. E., Alikhanizadeh, M., Asere, A. A., Hussain, C. I., Koshkbar Azari, M. S., and Mkpadi, M. C., 1986, "Small Diameter Film Cooling Holes: Wall Convective Heat Transfer," ASME JOURNAL OF TURBOMACHINERY, Vol. 108, pp. 283–289.

Andrews, G. E., Alikhanizadeh, M., Bazdidi-Tehrani, F., Hussain, C. I., and Koshkbar Azari, M. S., 1987a, "Small Diameter Film Cooling Holes: The Influence of Hole Size and Pitch," presented at the ASME/AIChE Heat Transfer Conference, ASME Paper No. 87-HT-28.

Andrews, G. E., Durance, J., Hussain, C. I., and Ojobor, S. N., 1987b, "Full Coverage Impingement Heat Transfer: The Influence of the Number of Holes," ASME JOURNAL OF TURBOMACHINERY, Vol. 109, pp. 557–563.

Andrews, G. E., Asere, A. A., Hussain, C. I., Mkpaki, M. C., and Nazari, A., 1988, "Impingement/Effusion Cooling: Overall Wall Heat Transfer," ASME Paper No. 88-GT-290.

Chance, J. L., 1974, "Experimental Investigations of Air Impingement Heat Transfer Under an Array of Round Jets," *Tappi*, Vol. 57, pp. 108–112.

Creare, 1985, "Fluent Manual: Version 2.8," Creare Incorporated, TN-369 Rev. 2.

Florschuetz, L. W., Truman, C. R., and Metzger, D. E., 1981, "Steamwise Flow and Heat Transfer Distribution for Jet Array Impingement With Initial Crossflow," ASME *Journal of Heat Transfer*, Vol. 103, pp. 337–342.

Hollworth, B. R., and Berry, R. D., 1978, "Heat Transfer for Arrays of Impinging Jets With Large Jet-to-Jet Spacing," ASME Paper No. 78-GT-117.

Hollworth, B. R., and Dagan, L., 1980, "Arrays of Impinging Jets With Spent Fluid Removal Through Vent Holes on the Target Surface. Part 1: Average Heat Transfer," ASME *Journal of Engineering for Power*, Vol. 102, pp. 994–999.

Hollworth, B. R., Lehmann, G., and Rosiczkowski, J., 1981, "Arrays of Impinging Jets With Spent Fluid Removal Through Vent Holes on the Target Surface. Part 2: Local Heat Transfer," ASME Paper No. 81-HT-76.

Kercher, D. M., and Tabakoff, W., 1970, "Heat Transfer by a Square Array of Round Air Jets Impinging Perpendicular to a Flat Surface," ASME *Journal of Engineering for Power*, Vol. 92, pp. 73–82.

Tabakoff, W., and Clevenger, W., 1972, "Gas Turbine Blade Heat Transfer Augmentation by Impingement of Air Jets Having Various Configurations," ASME *Journal of Engineering for Power*, Vol. 94, pp. 51–60.

Downloaded 01 Jun 2010 to 171.66.16.66. Redistribution subject to ASME license or copyright; see http://www.asme.org/terms/Terms_Use.cfm

An Experimental Study of Turbine Vane Heat Transfer With Leading Edge and Downstream Film Cooling

N. V. Nirmalan

L. D. Hylton

Allison Gas Turbine Division,
General Motors Corporation,
Indianapolis, IN 46206

This paper presents the effects of downstream film cooling, with and without leading edge showerhead film cooling, on turbine vane external heat transfer. Steady-state experimental measurements were made in a three-vane, linear, two-dimensional cascade. The principal independent parameters—Mach number, Reynolds number, turbulence, wall-to-gas temperature ratio, coolant-to-gas temperature ratio, and coolant-to-gas pressure ratio—were maintained over ranges consistent with actual engine conditions. The test matrix was structured to provide an assessment of the independent influence of parameters of interest, namely, exit Mach number, exit Reynolds number, coolant-to-gas temperature ratio, and coolant-to-gas pressure ratio. The vane external heat transfer data obtained in this program indicate that considerable cooling benefits can be achieved by utilizing downstream film cooling. The downstream film cooling process was shown to be a complex interaction of two competing mechanisms. The thermal dilution effect, associated with the injection of relatively cold fluid, results in a decrease in the heat transfer to the airfoil. Conversely, the turbulence augmentation, produced by the injection process, results in increased heat transfer to the airfoil. The data presented in this paper illustrate the interaction of these variables and should provide the airfoil designer and computational analyst with the information required to improve heat transfer design capabilities for film-cooled turbine airfoils.

Introduction

One of the classical ways to improve the thermal efficiency of a gas turbine engine is to increase the turbine inlet temperature. Today's advanced gas turbine engines operate at temperatures much greater than allowable metal temperatures of turbine airfoils, which in turn necessitates the cooling of airfoils. In addition, uniform airfoil cooling is also required to avoid thermal stresses. Some of the common methods of providing thermal protection to the airfoil are internal convective cooling and impingement cooling, external film cooling, and trailing edge ejection. A typical cooled airfoil incorporating all the above-mentioned cooling techniques is shown in Fig. 1. The degree of internal cooling must be limited because of the thermal stresses resulting from large thermal gradients in the metal wall. However, film cooling has the advantage that it provides thermal protection to the metal wall by the injection of cooler air over the external surface. To achieve uniform film cooling, it is necessary to inject coolant air at the leading edge and at multiple locations on the suction and pressure surfaces. Leading edge film cooling is generally accomplished by using a "showerhead" type of geometry of film cooling holes. Downstream pressure and suction surface film cooling are usually achieved by single or multiple rows of injection holes at locations comparable to the airfoil shown in Fig. 1.

The thermal design of a typical film-cooled blade, similar to the one shown in Fig. 1, represents one of the more difficult engineering tasks. Aerodynamic and thermal procedures currently available to turbine designers have deficiencies that do not permit a priori designs that achieve design goals without expensive development iterations. Improvements in predictive capability of the cooling requirements have significant payoffs in terms of enhanced turbine life, development cost, and turbine engine performance. One of the first steps in the development of a prediction tool is the availability of a relevant data base. The experimental measurements reported in this paper present external heat transfer data with downstream film cooling with and without leading edge showerhead film cooling. The data were obtained at conditions that fully simulate engine conditions of a first-stage vane of an advanced turbine.

A review article on turbine blade cooling by Moffat (1986) indicates that the majority of data on film cooling in the literature have been obtained on flat plates and cylinders, which were intended to simulate engine geometry. Recently, several film cooling studies on turbine airfoils have been con-

Contributed by the International Gas Turbine Institute and presented at the 34th International Gas Turbine and Aeroengine Congress and Exhibition, Toronto, Ontario, Canada, June 4-8, 1989. Manuscript received at ASME Headquarters January 13, 1989. Paper No 89-GT-69.

Copyright © 1990 by ASME
Downloaded 01 Jun 2010 to 171.66.16.66. Redistribution subject to ASME license or copyright; see http://www.asme.org/terms/Terms_Use.cfm

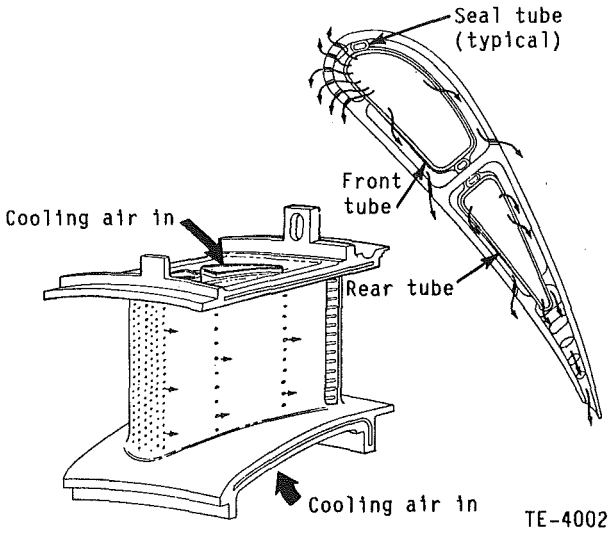

Fig. 1 Typical cooled airfoil

ducted. Camci and Arts (1985a, 1985b) studied the effects of leading edge and suction side film cooling in a six airfoil cascade using the short-duration measurement technique. Camci (1988) measured the heat flux near the film cooling hole on the suction side of a turbine blade previously investigated by Camci and Arts (1985b). Horton et al. (1985), also using the short duration measurement technique, measured heat transfer to turbine blades with suction and pressure side film cooling. Goldstein and Chen (1985) considered the effects of film cooling of a turbine blade near the end wall in a low-speed wind tunnel using the mass/heat transfer analogy. Turner et al. (1985) conducted heat transfer measurements on a leading edge film-cooled airfoil geometry using a three-vane cascade at simulated engine conditions. A five-row simulated common plenum showerhead geometry was tested to determine the differences between film-cooled and non-film-cooled heat transfer coefficient distributions. This investigation is one of very few in the open literature that have been conducted at fully simulated engine conditions represented by the aerothermodynamic parameters such as Mach number, Reynolds number, wall-to-gas temperature ratio (T_w/T_g), coolant-to-gas temperature ratio (T_c/T_g), and turbulence intensity.

The objective of the investigation presented in this paper was to generate an engine representative database of downstream film cooling with and without leading edge film cooling, thus extending the two earlier leading edge film cooling (Turner et al., 1985) and non-film-cooled (Nealy et al., 1984) vane heat transfer studies conducted at Allison Gas Turbine Division. The aerodynamic configuration of the vane profile used in this study is the same as the one used in the leading film cooled experiments reported by Turner et al. (1985) and the same as one of the two airfoils used in the non-film-cooled experiments reported by Nealy et al. (1984). The leading edge showerhead five-row film cooling hole geometry in the present study is identical to the hole geometry of the earlier study (Turner et al., 1985). The airfoil in the current study had film cooling arrays added on the suction and pressure sides, each consisting of two rows of holes. The three film cooling arrays were fed by separate plenums. The experiments were conducted in a moderate-temperature, three-vane, linear, two-dimensional cascade. Heat transfer data were acquired downstream of the pressure and suction surface film cooling arrays under steady-state conditions. The principal independent parameters—Mach number, Reynolds number, turbulence intensity, coolant-to-gas temperature ratio, and coolant-to-gas pressure ratio—were maintained over ranges consistent with actual engine conditions, and the test matrix was structured to provide an assessment of the independent influence of parameters of interest, namely, exit Mach number, true chord exit Reynolds number, coolant-to-gas absolute temperature ratio, and coolant-to-gas pressure ratio.

In the following sections, descriptions of the hardware, instrumentation, and data reduction technique are given and the experimental results for surface pressure and heat transfer distributions are presented and discussed. Because of the large amount of data obtained in this investigation, only a summary of the data can be presented in this paper. More complete details are available in the report by Hylton et al. (1988).

Experimental Apparatus and Procedures

Facility Description. This experimental investigation was performed in the Allison Gas Turbine (AGT) Aerothermodynamic Cascade Facility (ACF). The purpose of this facility is to conduct experimental research in high-temperature turbine component models that embody advanced cooling techniques, aerodynamics, or materials. The experimental approach employs a two-dimensional cascade technique, with full dynamic similarity in free-stream Mach number and boundary layer Reynolds number effects, and provides an experimental method to separate the effects on local heat transfer.

The facility consists of a burner, a convergent section, a free-stream section with instrumentation and optical access, a test section with instrumentation, a quench zone with back pressure regulation, and an exhaust system. The facility is shown schematically in Fig. 2.

The Mach number and Reynolds number modeling considerations necessitate a burner with a large temperature, flow, and pressure range. This burner capability, coupled with back pressure regulating valve, allows experimental separation of free-stream Mach number and boundary layer Reynolds number effects to simulate a wide range of engine designs and operating conditions accurately.

A constant cross section is provided downstream of the burner to establish uniform inlet velocity, temperature, and

Nomenclature

c_p = specific heat at constant pressure
Cr = correction factor for thermal entrance region effects
dT/dn = surface normal temperature gradient
h = heat transfer coefficient
Ma_2 = downstream or vane row exit Mach number
P = plenum pressure
Re_2 = downstream or vane row exit Reynolds number
S = percent surface distance
SNR = Stanton number reduction
St = Stanton number
T = temperature
u = free-stream velocity
ρ = free-stream density

Subscripts

c = coolant plenum conditions
ds = downstream
FC = film-cooled conditions
g = cascade inlet conditions
le = leading edge
NFC = non-film-cooled conditions
o = reference
ps = pressure side
ss = suction side
s = surface static conditions
w = wall

Downloaded 01 Jun 2010 to 171.66.16.66. Redistribution subject to ASME license or copyright; see http://www.asme.org/terms/Terms_Use.cfm

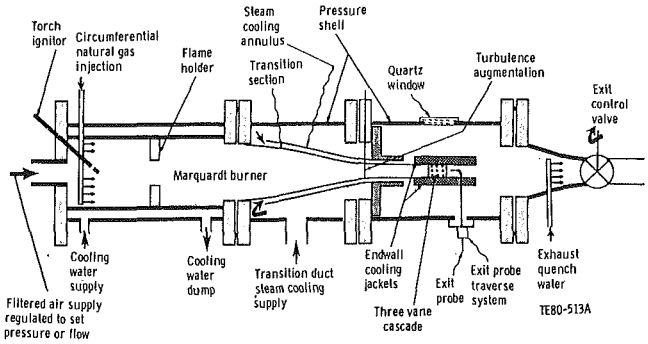

Fig. 2 Schematic of aerothermodynamic cascade facility

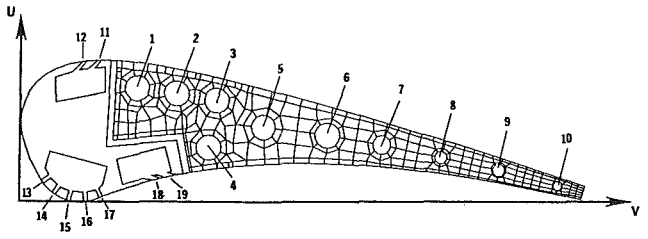

Radial cooling holes					Film cooling holes		
Hole No.	U, mm	V, mm	Diameter, mm	Cr	Hole No.	U, mm	V, mm
1	28.70	29.92	6.30	1.118	11	35.92	20.24
2	27.33	39.98	6.30	1.118	12	35.56	16.31
3	25.55	49.91	6.30	1.118	13	4.98	5.41
4	13.64	47.88	6.30	1.118	14	2.11	8.28
5	18.69	61.82	6.30	1.118	15	0.41	11.96
6	16.66	77.47	6.30	1.118	16	0.05	16.00
7	14.12	92.35	4.70	1.090	17	1.09	19.94
8	10.87	107.59	3.10	1.056	18	5.59	35.05
9	7.37	122.53	3.10	1.056	19	6.43	38.91
10	3.45	137.57	1.98	1.025			

Fig. 3 Film-cooled C3X vane showing internal geometry and finite element grid

turbulence profiles. This section is provided with temperature-controlled cooled walls and isolates the test section from radiant heat transfer from the primary combustion zone. The walls of the test section are cooled with steam to keep them at, or close to, the vane surface temperature to eliminate radiation errors in the data.

The flow path upstream of the cascade in the ACF takes the burner discharge from a 0.315 m diameter through a 0.508 m long transition section to a 0.076 m × 0.279 m rectangular section. The rectangular section upstream of the cascade is 0.368 m long and contains inlet instrumentation. Details of the inlet and exit instrumentation have been reported by Hylton et al. (1988).

Facility operations and data acquisition are handled by a dedicated, state-of-the-art computer-controlled data acquisition system. A multitask, facility-oriented software system that contains general subprograms to do all routine control measurement tasks exists. The system is flexible and provides for real-time facility monitoring and diagnosis of instrumentation or control problems. Software routines developed to meet specific data acquisition requirements of individual experiments are incorporated into the main system as interchangeable program segments.

Cascade Description. The three-vane cascade employed in this test was the C3X cascade previously used in the earlier experimental studies reported by Turner et al. (1985) and Nealy et al. (1984). The center test vane was replaced with a new C3X vane, which had suction side, leading edge, and pressure side film cooling arrays. The test vane, which has a nominal chord of 14.5 cm and span of 7.6 cm, was initially fabricated as a single piece. After all the film cooling holes and plenums and the ten radial cooling holes were machined, the vane was cut into a nose and a tail piece to form a thermal barrier between the film-cooled nose piece and the rest of the vane.

Table 1 Film cooling hole geometry

Leading edge geometric parameters	Values
Rows of holes	5
Hole diameter, mm	0.99
Hole length, mm	3.35
Hole pitch-to-diameter ratio	4.0
Hole spacing-to-diameter	7.5
Hole slant angle, deg	45
Hole skew angle, deg	90

Downstream geometric parameters	Values
Rows of holes (each surface)	2
Hole diameter, mm	0.99
Hole length, mm	3.35
Hole pitch-to-diameter ratio	4.0
Hole spacing-to-diameter	3.0
Hole slant angle, deg	90
Hole skew angle, deg	
Pressure surface	20
Suction surface	35

The test vane was internally cooled by an array of 10 radial cooling holes, the locations of which are shown in Fig. 3. Each hole in the center test vane was supplied from a separate, metered line.

The film cooling geometry for the test vane consists of film cooling arrays on the leading edge, the suction surface, and the pressure surface. The leading edge film cooling geometry employed a showerhead array of five equally spaced rows of holes with the center row located at the predicted aerodynamic stagnation point. The hole array is staggered with the holes in the second row located midway (radially) between the holes in the first and the third rows. The holes are angled at 45 deg to the surface in the radial (spanwise) direction (slant angle). They are normal to the surface in the chordwise direction (skew angle). Coordinates of the film cooling hole rows are also listed in Fig. 3. Geometry information for all film cooling arrays is detailed in Table 1.

Previous leading edge film cooling data of Turner et al. (1985) indicated that the downstream film cooling arrays should be located at 25.2 percent of the surface distance (as measured from the geometric stagnation point, which is defined as the tangency point on the airfoils of the inlet plane to the cascade) on the suction side and 22.5 percent of the surface distance on the pressure side. This is just upstream of the suction and pressure surface pressure recovery region in the non-film-cooled case and thus appear to provide maximum film cooling effectiveness. Two cooling hole rows were centered on each surface at these points. The downstream film cooling hole arrays are also staggered with the holes in the second row located midway (radially) between the holes of the first row. The length-to-diameter ratio of the holes were kept the same as the showerhead hole length-to-diameter ratio. The suction surface holes were inclined at 35 deg to the surface in the chordwise direction while the pressure surface holes were at 20 deg in the chordwise direction. Holes in both downstream arrays were normal to the surface in the spanwise direction.

Three independent supply plenums were designed to feed the three film cooling arrays as shown in Fig. 3. This system was designed to provide the capability of individually controlling the blowing parameters of each array. The relatively large plenum results in a nearly uniform coolant flow distribution in the spanwise direction. The film coolant supply was piped through an electric heating system that provided the capability to vary the coolant supply temperature.

Downloaded 01 Jun 2010 to 171.66.16.66. Redistribution subject to ASME license or copyright; see http://www.asme.org/terms/Terms_Use.cfm

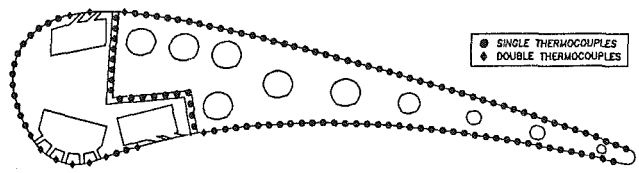

(a) Thermocouple locations

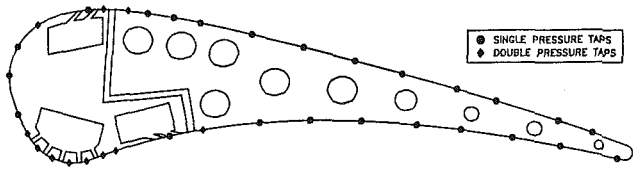

(b) Pressure tap locations

Fig. 4 Instrumentation location for the C3X airfoil

The heat transfer measuring technique used for this test does not make heat transfer measurements in the actual film-cooled nose piece. Consequently, the film-cooled area was thermally isolated from the rest of the airfoil. As mentioned before, the thermal barrier was achieved by cutting the test vane into two segments, with the airfoil profile maintained in its original contour by two retaining bars pinned to the airfoil ends. Prior to testing, a thin, 0.254-mm shim was welded across the thermal barrier gap on both the pressure and suction surfaces. This provided a smooth continuous surface on the airfoil. Also, the gap was sealed at the two ends of the airfoil, thereby creating a sealed air gap between the film-cooled region and the rest of the airfoil. The sealed air gap provided the thermal barrier.

Instrumentation. Figure 4 shows the distribution of the thermocouples and pressure taps for the C3X airfoil. The airfoil surface was instrumented with 123 0.51 mm diameter sheated Chromel-Alumel (CA) thermocouples, while the thermal barrier region was instrumented with 18 1.02 mm CA thermocouples. The thermocouple junctions were located in the fully two-dimensional region of the airfoil in a plane 2.54 mm off midspan, directly downstream of film cooling holes. Since this was an engine-like environment and not an adiabatic test, surface conduction effects resulted in uniform spanwise temperature gradients similar to what occurs in an engine. Thermocouples were brought off the vane in 0.58-mm-deep radial grooves covered with cement, and blended by hand to provide a smooth surface. The vane was fabricated of ASTM type 310 stainless steel, which has a relatively low thermal conductivity, thereby minimizing the error introduced by the grooves.

The test vane surface was also instrumented with surface static pressure taps in addition to the heat transfer instrumentation. Forty-six taps were located around the airfoil outer surface in a plane 5.08 mm from midspan away from the thermocouple instrumentation. The pressure taps were located so that the taps would be downstream of a film cooling hole. The spacing was varied to provide a higher density of instrumentation in high pressure gradient regions. Figure 4(*b*) illustrates the relative locations of the surface pressure taps on the C3X airfoil. Stainless steel tubing, 0.51 mm in diameter, was laid in a radial surface groove, and the end of the tubing was bent 90 deg to achieve surface orientation.

In addition to the thermocouples on the instrumentation

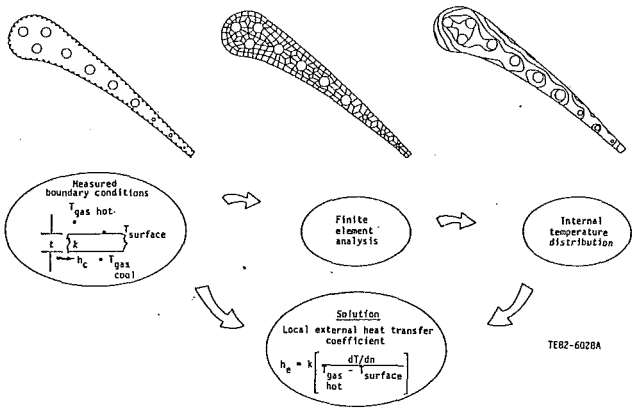

Fig. 5 Heat transfer data reduction technique

plane, twelve extra thermocouples were placed on the suction and pressure surfaces, 19.05 mm on either side of the instrumentation plane at three axial locations. These and the instrumentation plane temperatures at the same axial locations provided a check on the validity of the two dimensionality of the heat transfer solution.

Each of the tubes supplying the radial cooling holes of the test vane was instrumented with two static pressure taps and two thermocouples at both the vane inlet and exit. The static pressure taps were located upstream of the thermocouples in all cases. The flow to each cooling tube was measured using a calibrated orifice meter.

Each film cooling plenum was instrumented with thermocouples and pressure taps at various locations to provide the coolant supply temperature and pressure. The flow rate to each plenum was measured using a calibrated orifice meter.

Data Reduction Procedure. The method used to obtain heat transfer measurements is based on the work of Turner (1971), who employed a two-dimensional plane of a test piece as a fluxmeter. The technique is implemented by measuring the internal and external boundary conditions of the test piece at thermal equilibrium and solving the steady-state heat conduction equation for the internal temperature field of the test piece. The heat transfer coefficient distribution can be directly obtained from the normal temperature gradient at the surface.

For the present study, the heat transfer measurement technique used a finite element solution of two-dimensional Laplacian heat conduction equation as illustrated in Fig. 5. The finite element grid structure actually used for the solution was shown in Fig. 3. The external boundary conditions were measured using the thermocouples installed in grooves on the exterior surface of the test vane and in the thermal barrier on the tail piece of test vane. Average heat transfer coefficients and coolant temperatures for each of the 10 radial cooling holes provided the internal boundary conditions for the finite element solution. The heat transfer coefficient for each cooling hole was calculated, using standard correlations, from the hole diameter, measured coolant flow rate, and coolant temperature with a correction applied for thermal entry region effects.

The accuracy of the external heat transfer coefficient measurement is primarily dependent on the accuracy of the external vane surface and free-stream gas temperature measurements, the geometry description for the finite element program, the calculation of the heat transfer coefficients for the radial cooling holes, and the knowledge of the thermal conductivity of the vane material. Using the uncertainties of the individual measurements, a calculation of the overall uncertainty in the external heat transfer coefficient was made using the methods of Kline and McClintock (1953). Due to variations in the airfoil thickness along the chord, it was

Downloaded 01 Jun 2010 to 171.66.16.66. Redistribution subject to ASME license or copyright; see http://www.asme.org/terms/Terms_Use.cfm

necessary to calculate the uncertainty at several points. The maximum uncertainty, based on minimum wall thickness (distance from cooling hole to exterior surface), was calculated at various regions on the airfoil. The values ranged from ±7.1 to ±22.5 percent. The uncertainties increase significantly beyond midchord due to a decrease in airfoil thickness. The uncertainties presented are intended to provide the analyst with an indication of the uncertainty in absolute levels in using the data for verification purposes. In comparing data runs for a given cascade (i.e., looking for Reynolds number trends, etc.), the uncertainty in the comparisons is considerably less than the values just described. This difference is due to the fact that several of the variables contributing to the uncertainty do not change from run to run. Reproducibility of heat transfer coefficients for a given cascade condition is on the order of ±2 percent.

Results

Range of Experimental Conditions. The experimental results presented in this study were obtained at different test conditions with the variable parameters being exit Reynolds number, exit Mach number, coolant-to-gas absolute temperature ratio, and coolant-to-gas total pressure ratio. The nominal run conditions where heat transfer data were obtained are shown in graphic form in Fig. 6. Each nominal test condition is represented by a five-digit alphanumeric code. Each alphanumeric digit of the code number corresponds to one of the control variables of the experiment as also described in Fig. 6. Exit Reynolds numbers referred to in the figure are based on airfoil true chord (not axial chord), and exit Mach numbers are based on measured inlet total pressure and midpassage-to-midpassage average measured exit plane pressure. All tests were conducted at a nominal gas stream temperature of 700 K, and a burner-generated turbulence intensity level of 6.5 percent, based on LDA mesurements taken previously at the cascade inlet plane as reported by Nealy et al. (1984).

Airfoil Static Pressure Distributions. Prior to obtaining film-cooled data, baseline data (i.e., without film cooling) were obtained at the seven baseline conditions, as shown in Fig. 6. Starting first with the exit Mach number effects, typical baseline measured surface static pressure distributions corresponding to the four cascade expansion ratios tested are shown in Fig. 7. The percent surface distance in Fig. 7 and all figures that follow is measured from the geometric stagnation point. In this figure and in other similar figures, the vertical dashed lines mark the locations of the film cooling hole rows and the vertical solid lines mark the locations of the thermal barrier on the pressure and suction surfaces. As observed by Turner et al. (1985) and Nealy et al. (1984), at transonic exit Mach numbers of 0.9 and 1.05, the primary effect of exit Mach number variation is to alter the suction surface pressure distribution downstream of the throat. However, at the lower Mach numbers of 0.6 and 0.75, larger differences in surface static pressure due to Mach number variations are seen on both surfaces; at surface distances of 60 percent and greater on the pressure surface and at 15 percent and greater on the suction surface.

The effect of downstream blowing on the vane surface static pressure distribution is shown in Fig. 8, where the base flow conditions are at an exit Mach number of 0.9 and an exit Reynolds number of 2.0×10^6. Figure 8 indicates that increasing the downstream blowing strength from a coolant-to-free stream pressure ratio of 1.00 (no blowing) to 1.63 has no measurable effect on the vane surface static pressure distribution.

Heat Transfer Results. The measured baseline heat transfer for different Mach numbers is shown in Fig. 9. On the

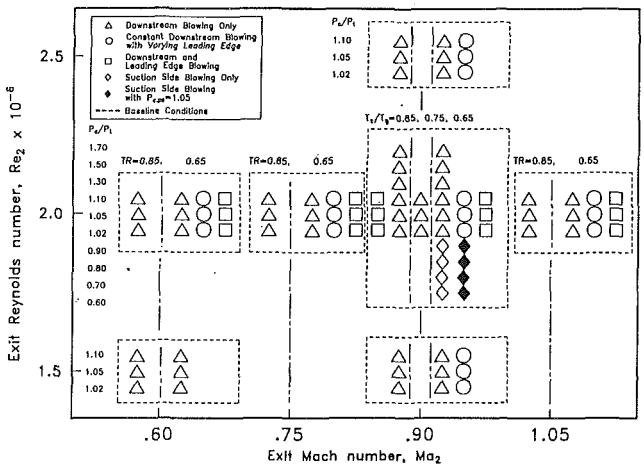

Code No.	Control variable by position					
	Position 1—Ma_2	Position 2—$Re_2 \times 10^{-6}$	Position 3—T_c/T_g	Position 4—$P_{c,le}/P_t$	Position 5—$P_{c,de}/P_t$ ss	ps
0			No coolant flow	1.00	1.00	1.00
1			Min			
2	0.60		Med			
3	0.75	1.5	Max	1.02	1.02	1.02
4	0.90	2.0		1.05	1.05	1.05
5	1.05	2.5		1.10	1.10	1.10
6					1.30	1.30
7					1.50	1.50
8					1.70	1.70
A					0.60	1.00
B					0.70	1.00
C					0.80	1.00
D					0.90	1.00
E					0.60	1.05
F					0.70	1.05
G					0.80	1.05
H					0.90	1.05

Fig. 6 Test matrix and control code description

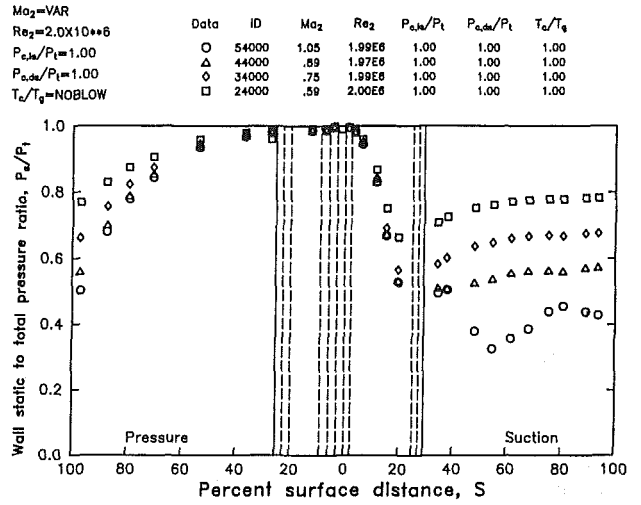

Fig. 7 The effects of exit Mach number variation on baseline static pressure distribution

suction surface, the level of heat transfer coefficient decreases with exit Mach number due to different static pressure distribution. On the pressure surface, much less variation in heat transfer due to variation in Mach number is noticed, again caused by lesser variation in the static pressure distribution. The effect of exit Reynolds number variation on the baseline heat transfer coefficient distribution is shown in Fig. 10. As expected, the overall heat transfer levels systematically increase as the exit Reynolds number increases.

The present baseline heat transfer data match reasonably well with the previously obtained data of Turner et al. (1985) and Nealy et al. (1984) at surface percentage distances greater

Downloaded 01 Jun 2010 to 171.66.16.66. Redistribution subject to ASME license or copyright; see http://www.asme.org/terms/Terms_Use.cfm

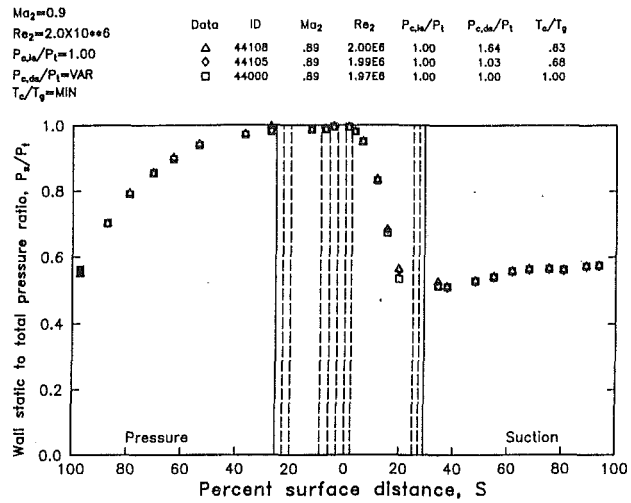

Fig. 8 Effects of downstream blowing on surface static pressure distribution

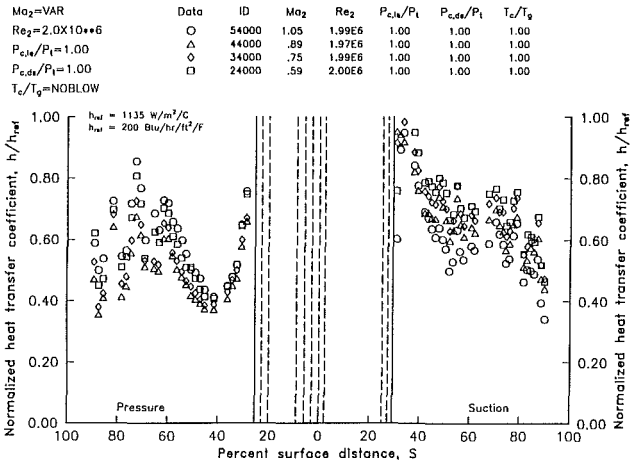

Fig. 9 Effects of exit Mach number variation on baseline heat transfer coefficient distribution

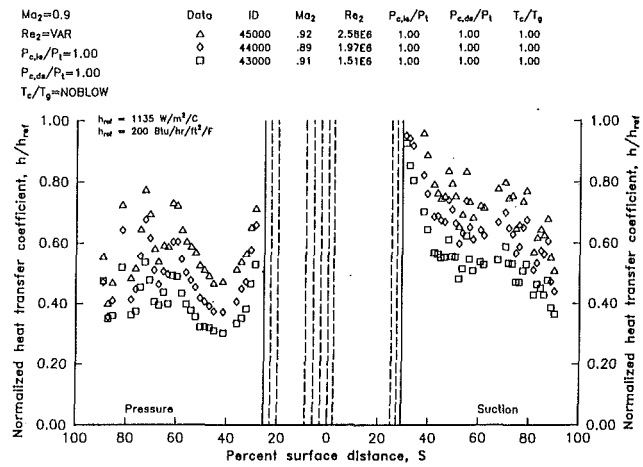

Fig. 10 Effects of exit Reynolds number variation on baseline heat transfer coefficient distribution

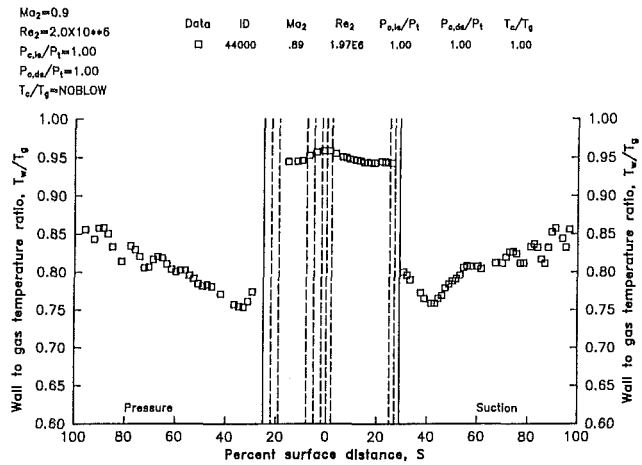

Fig. 11 Surface-to-gas absolute temperature distribution at baseline flow condition of $M_2 = 0.9$ and $Re_2 = 2.0 \times 10^6$

than 50 percent on both suction and pressure surfaces. However, at surface distance less than 50 percent, the differences in film cooling geometry between the vane of the present study and the previous studies causes differences in absolute heat transfer data. In the present study, during baseline runs, there is a developing thermal boundary layer, which begins at the thermal barrier. This occurs on both surfaces at about 20–25 percent surface distance and results in differences in absolute heat transfer levels at surface distances less than 50 percent. In the case of a vane that is uniformly cooled throughout, the hydrodynamic and the thermal boundary layer would originate simultaneously at the leading edge. However, in the present study, under non-film-cooled conditions, the nose piece of the vane is not cooled (radially or otherwise). This results in a step change in vane surface temperature across the thermal barrier on both surfaces as shown in Fig. 11, which gives the vane surface-to-gas absolute temperature ratio (T_w/T_g) distribution at the baseline condition corresponding to an exit Mach number (M_2) of 0.9 and exit Reynolds number (Re_2) of 2.0×10^6. This indicates that the origin of the thermal boundary layer is at the thermal barrier, while the hydrodynamic boundary layer still originates at the leading edge. In Figs. 9 and 10, the decreasing slope of the heat transfer coefficient downstream of the thermal barrier on both surfaces is a result of the developing thermal boundary layer.

Also in Fig. 11, a spatial variation in vane surface temperatures is seen near the trailing edge on both surfaces. These variations are due to coolant air flowing through the internal cooling holes. These variations in surface temperature result in the heat transfer coefficient fluctutations seen earlier in Figs. 9 and 10. Figure 12 repeats the measured heat transfer distribution for the baseline condition of $M_2 = 0.9$ and $Re_2 = 2.0 \times 10^6$, which again shows the fluctuations in heat transfer coefficient over the rear 50 percent of the airfoil. Also in Fig. 12, results predicted (Hylton et al., 1987) for the same conditions using the Allison STANCOOL code developed by Turner et al. (1985) are given. Here, the solid curve is the predicted results with a constant temperature boundary condition. The dashed curve is the prediction made using the actual measured surface temperature boundary condition given in Fig. 11. Figure 12 shows significantly better agreement between the experimental data and the prediction using the measured surface temperature for the boundary condition. Considering the uncertainty in absolute value of the experimentally determined heat transfer coefficient, the agreement is quite good. This comparison illustrates the significance of the actual wall temperature boundary condition on the heat transfer predictions.

The goal of presenting the film-cooled heat transfer results is to isolate the differences between non-film-cooled and film-cooled (in this case, downstream film cooling with and without leading edge injection) heat transfer downstream of

Downloaded 01 Jun 2010 to 171.66.16.66. Redistribution subject to ASME license or copyright; see http://www.asme.org/terms/Terms_Use.cfm

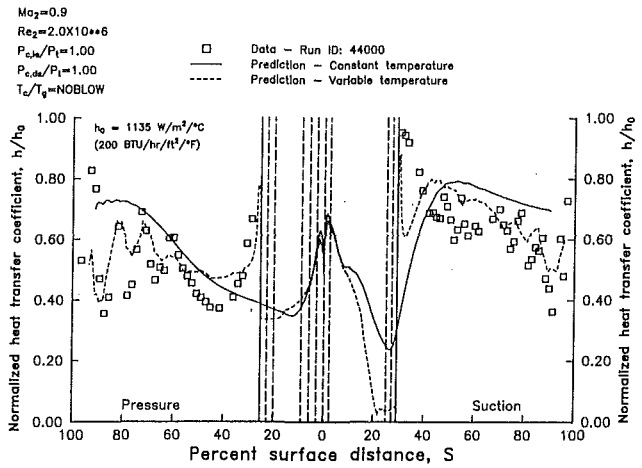

Fig. 12 Surface local heat transfer distribution at baseline flow condition of $M_2 = 0.9$ and $Re_2 = 2.0 \times 10^6$

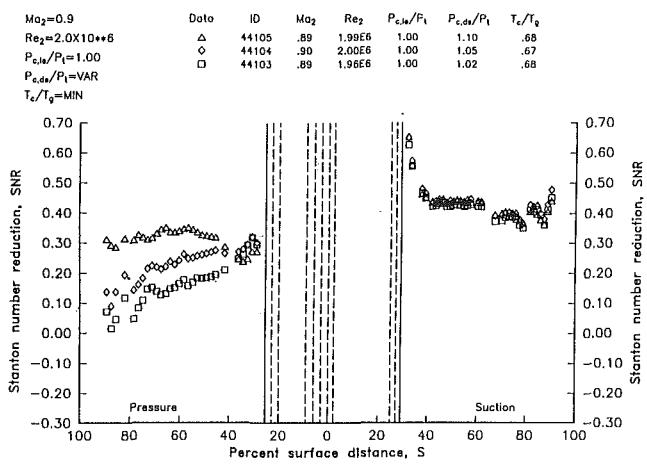

(a) T_c/T_g = MIN

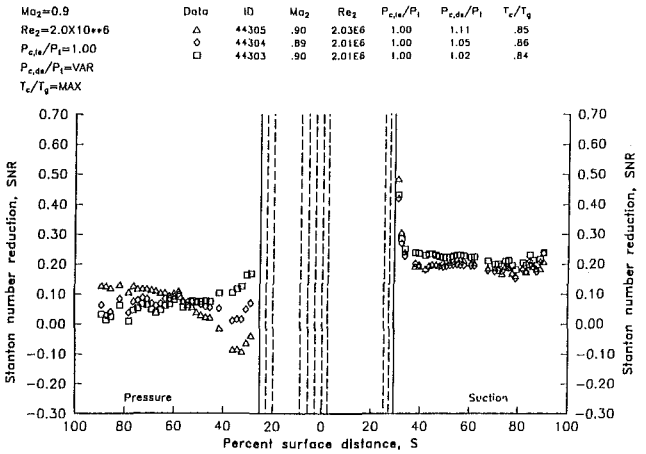

(b) T_c/T_g = MAX

Fig. 13 Effects of downstream blowing on Stanton number reduction

the suction and pressure side film cooling arrays. This goal is achieved, as done previously by Turner et al. (1985), by calculating the ratio of the experimentally determined local Stanton number for cases where coolant is being ejected to the local Stanton number determined for the case where no coolant is added.

Rather than simply form the film-cooled Stanton number to non-film-cooled Stanton number ratio (St_{FC}/St_{NFC}), which would take on values about a "no difference" value of unity, an alternate parameter referred to as Stanton number reduction (SNR) is used. SNR is defined as

$$\text{SNR} = 1 - (\text{St}_{\text{FC}}/\text{St}_{\text{NFC}})$$

When SNR is greater or less than zero, it implies reduced or increased heat transfer levels, respectively. When SNR is equal to zero, it implies no difference in the heat transfer level. Forming SNR values along the entire test surface gives the actual SNR distribution of the airfoil. In addition, if the film-cooled Stanton number to non-film-cooled Stanton number ratio were determined using data obtained at equivalent exit Mach number and exit Reynolds number conditions, SNR would be approximately equal to the actual heat transfer coefficient reduction

$$\text{SNR} = 1 - (h_{\text{FC}}/h_{\text{NFC}})$$

because $(\rho c_p u)_{e,\text{NFC}}/(\rho c_p u)_{e,\text{FC}}$ would be near unity. SNR results shown here were formed by using the above equation. Basic heat transfer coefficient and wall temperature data are available in the final report of Hylton et al. (1988).

Figure 13 shows the effects of varying the blowing strength at two constant thermal dilution (T_c/T_g) levels with only the downstream film cooling arrays active. The base flow conditions are at an exit Mach number of 0.9 and an exit Reynolds number of 2.0×10^6. Figure 13(*a*) shows the effect of varying blowing strength (P_c/P_t) at the lowest coolant-to-gas temperature ratio ($T_c/T_g = 0.65$, MIN). [Film cooling flow rate, absolute pressure, etc., are available in the final report (Hylton et al., 1988). Coolant hole exit temperatures, if desired, can be calculated from heat pickup estimations using the information available in the final report.] A positive SNR is seen on both surfaces at all three blowing strengths, indicating a comparatively large decrease in heat transfer due to downstream film cooling. A pronounced variation in SNR due to different blowing strengths is seen on the pressure surface. Also, on the pressure surface, as the blowing strength is increased, the effect of film cooling is felt further downstream. However, the higher level of turbulence near the film cooling holes, resulting from increased blowing, tends to increase heat transfer (i.e., reduce SNR) in the near hole region. On the other hand, on the suction surface, there is no significant effect due to varying blowing strengths. This is due to the lower free-stream pressure on the suction surface, causing the film coolant flow on the suction surface to be choked over this range of pressure ratios. The choked conditions keep the blowing ratio almost invariant on the suction surface. Figure 13(*b*) shows similar behavior at a higher T_c/T_g ratio of 0.85 (MAX), though, as expected, with lower values of SNR due to the lower level of thermal dilution (warmer air being injected). Also, on the pressure surface at the lower thermal dilution level (high T_c/T_g), the effect of turbulence due to the higher blowing strengths increases heat transfer (i.e., decreases SNR values) just downstream of the film cooling holes to a larger extent than at higher thermal dilution level (i.e., low T_c/T_g). It should also be noted that for the higher blowing strengths, SNR increases over the last 60 percent of the airfoil, whereas, for the lower blowing strengths, the SNR decreases. This is the result of the interaction of the thermal dilution and turbulence augmentation effects. On the SNR data presented above, just downstream of the suction side film cooling holes, SNR attain high values. These high SNR values are caused by the non-film-cooled and the film-cooled tests having different surface temperatures in the leading edge region. In a film-cooled case,

Downloaded 01 Jun 2010 to 171.66.16.66. Redistribution subject to ASME license or copyright; see http://www.asme.org/terms/Terms_Use.cfm

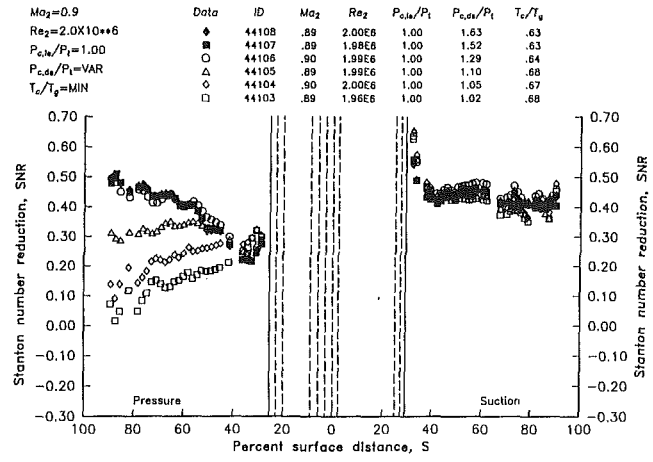

(a)T_c/T_g = MIN

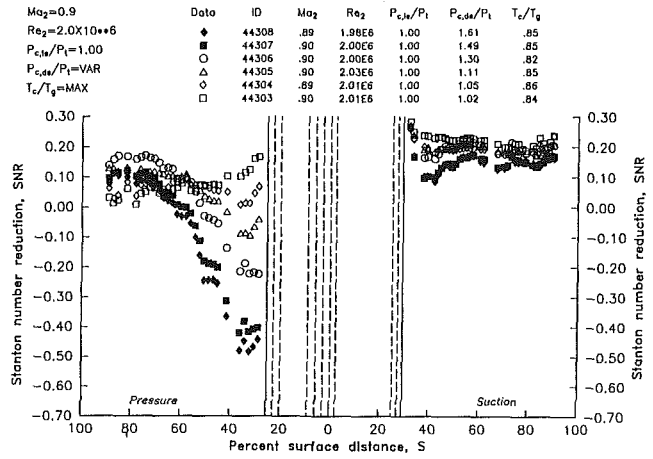

(b)T_c/T_g = MAX

Fig. 14 Effects of high downstream blowing on Stanton number reduction

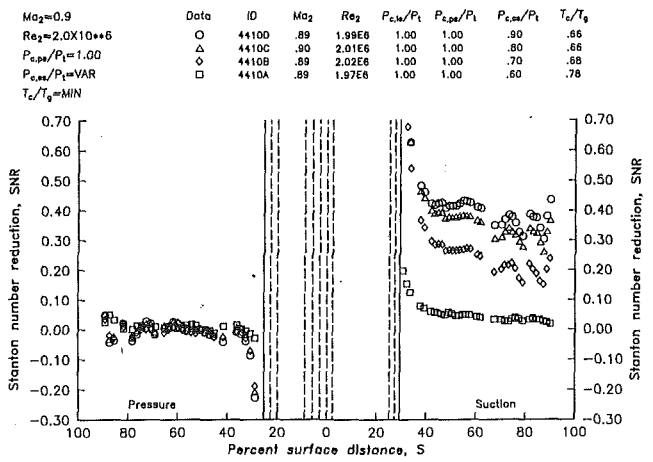

(a)$P_{c,ps}/P_t$ = 1.00

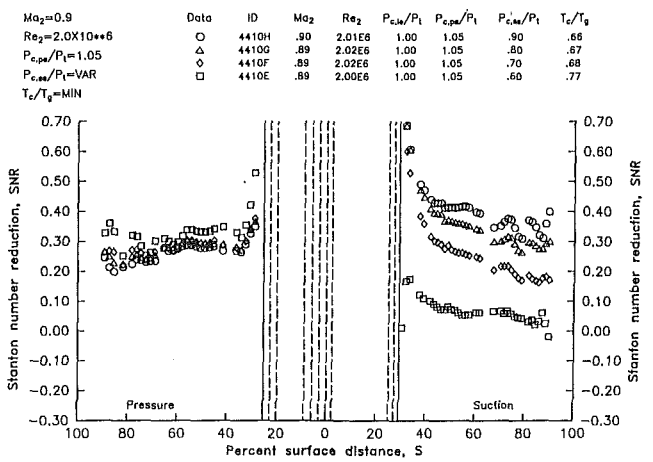

(b)$P_{c,ps}/P_t \approx 1.05$

Fig. 15 Effects on Stanton number reduction of variable suction side blowing at reduced pressure ratio

the surface temperature in the leading edge region, in contrast to the surface temperature shown in Fig. 11, would be much lower and nearly at the same levels as the rest of vane surface. Therefore when comparing film-cooled data to non-film-cooled data there are apparent high SNR values just downstream of the thermal barrier.

The same trends noticed above are further brought out by Fig. 14, which shows data with downstream film cooling holes active for blowing strengths at levels up to 1.7 at MIN and MAX levels of thermal dilution. On the pressure surface, at both coolant-to-gas temperature ratios, the turbulence due to high blowing strengths decreases the SNR near the film cooling holes. At the lower coolant-to-gas temperature ratio, as shown in Fig. 14(*a*), a positive value of SNR is seen, even at the highest blowing strength. However, in Fig. 14(*b*), at the higher coolant-to-gas temperature ratio, almost all the data on the pressure surface at high blowing strengths ($P_c/P_t > 1.3$) show negative SNR values. (Note that in Fig. 14(*b*), the SNR scales are offset.) On the other hand, there is hardly any effect of coolant pressure on the suction surface due to the fact that the film coolant flow is choked and no significant variation in blowing ratio occurred. Nevertheless, at the higher coolant-to-gas temperature ratio, on the suction surface, there is a slight decrease in SNR near the film cooling holes at the high blowing strengths. Although the flow is choked, increasing coolant supply pressure increases the coolant mass supply, causing an increase in turbulence level near the coolant holes, which in turn reduces SNR at very high blowing strengths. This also may be due to the damping of turbulence at increased velocity levels.

Figure 15 shows the effects of varying only the suction side blowing strength ($P_{c,ss}/P_t$) from 0.6 to 0.9, with the pressure side blowing strength ($P_{c,ps}/P_t$) kept constant at two levels of 1.00 (no blowing) and 1.05, respectively. These data are at flow conditions of $M_2 = 0.9$ and $Re_2 = 2.0 \times 10^6$ and the coolant-to-gas temperature ratio at MIN level. Figure 15 shows that the SNR on the suction side increases with increasing blowing strength until the coolant flow chokes. Also, these data indicate, as expected, that the performance of the two downstream film cooling arrays are independent of each other.

To illustrate the effects of thermal dilution, data shown earlier in Fig. 13 were replotted with additional data as a function of T_c/T_g at two blowing strengths of 1.02 and 1.10 and are shown in Fig. 16. On the suction surface, in both cases, there is a significant effect due to different coolant-to-gas temperature ratios. Conversely, on pressure side, at the lower blowing strength, as shown in Fig. 16(*a*), only a small effect is

Downloaded 01 Jun 2010 to 171.66.16.66. Redistribution subject to ASME license or copyright; see http://www.asme.org/terms/Terms_Use.cfm

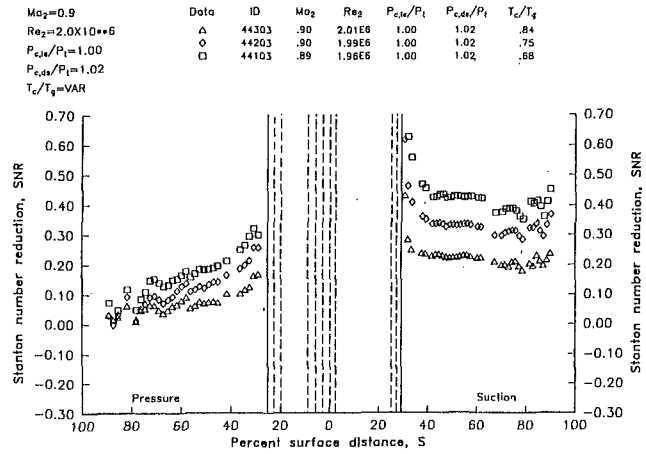

(a)P_c/P_t = 1.02

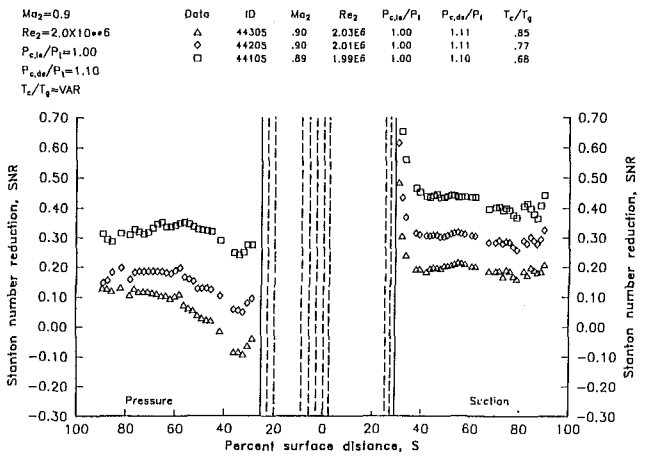

(b)P_c/P_t = 1.10

Fig. 16 Effects of downstream film cooling thermal dilution on Stanton number reduction

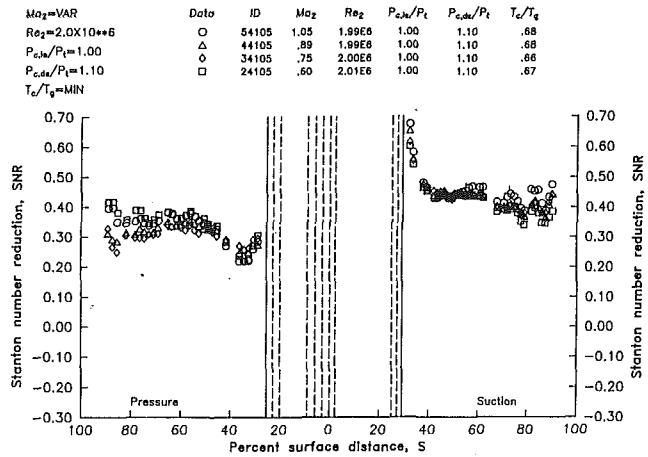

(a)T_c/T_g = MIN

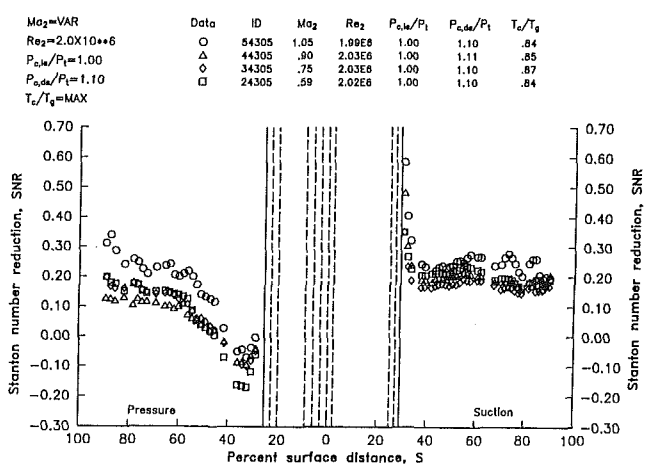

(b)T_c/T_g = MAX

Fig. 17 Effects of exit Mach number on Stanton number reduction

noticed. However, as seen in Fig. 16(*b*), there is a larger effect on the pressure surface due to varying thermal dilution at the higher blowing strength of $P_c/P_t = 1.10$. Also in Fig. 16(*b*), at higher coolant-to-gas temperature ratio, SNR is negative on the pressure surface at surface distances less than 50 percent. As mentioned before, this increase in heat transfer is due to the high blowing strength causing a higher level of turbulence augmentation, which offsets the thermal dilution effects in the vicinity of the film cooling holes.

Figure 17 illustrates the effects of varying the exit Mach number from 0.6 to 1.05 while keeping other flow and film cooling conditions constant. In these instances, the downstream film cooling hole arrays are at blowing strengths, $P_{c,ds}/P_t$, of 1.10 and the coolant-to-gas temperature ratios, T_c/T_g, are at MIN (Fig. 17(*a*)) and MAX (Fig. 17(*b*)) levels. In these cases, each film cooling data point is compared with the baseline at that flow condition. In other words, these SNR data show the increase or decrease of the heat transfer over the particular baseline case. Figure 17 shows that there is no significant effect of SNR due to variations in Mach number on either the suction surface or pressure surfaces at the lower coolant-to-gas temperature ratio. However, on the pressure surface at the higher coolant-to-gas temperature ratio, Fig. 17(*b*) shows that there is a Mach number effect. As pointed out earlier, at the higher coolant-to-gas temperature ratio, on the pressure surface, the favorable thermal dilution effects are offset by the adverse turbulence augmentation effects, thereby increasing heat transfer near the vicinity of the film cooling holes. For regions where this phenomenon occurs, the change in heat transfer due to film cooling seems to depend on the Mach number, suggesting that the turbulent augmentation effect may be Mach number dependent.

The effects of three different exit Reynolds numbers of 1.5×10^6, 2.0×10^6, and 2.5×10^6 on downstream film cooling are shown in Fig. 18. As in Fig. 17, the SNR data show the change in heat transfer due to film cooling above the particular baseline. Figure 18(*a*) presents data at the MIN level of coolant-to-gas temperature ratio and coolant pressure ratio of 1.10. On both surfaces, SNR increases with increasing Reynolds number, indicating that a more favorable effect of film cooling is attainable at a higher Reynolds number, though the trends are more pronounced on the pressure surface than on the suction surface. In Fig. 18(*b*), where the coolant-to-gas temperature is a MAX level, the effect of Reynolds number variation is not as marked as in the case of the lower coolant-to-gas temperature ratio.

Figure 19 shows the effects of both the downstream and the leading edge film cooling arrays being active with the varying blowing strengths at the MIN and MAX levels of thermal dilution, respectively. The flow conditions are at an exit Mach number of 0.9 and exit Reynolds number of 2.0×10^6. In comparison to Fig. 13, the trends and levels of SNR are very

Downloaded 01 Jun 2010 to 171.66.16.66. Redistribution subject to ASME license or copyright; see http://www.asme.org/terms/Terms_Use.cfm

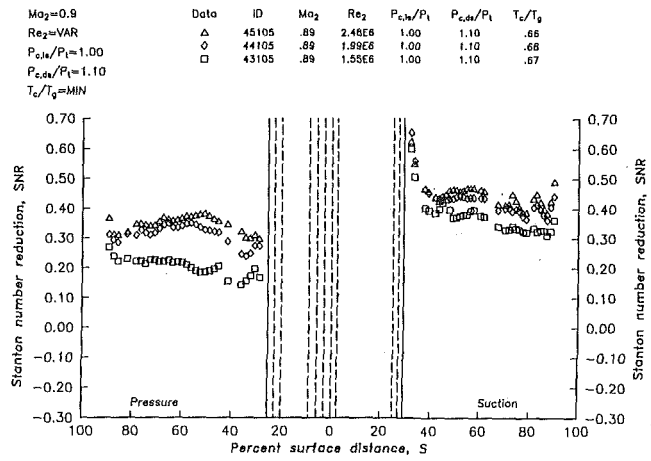

(a)T_c/T_g = MIN

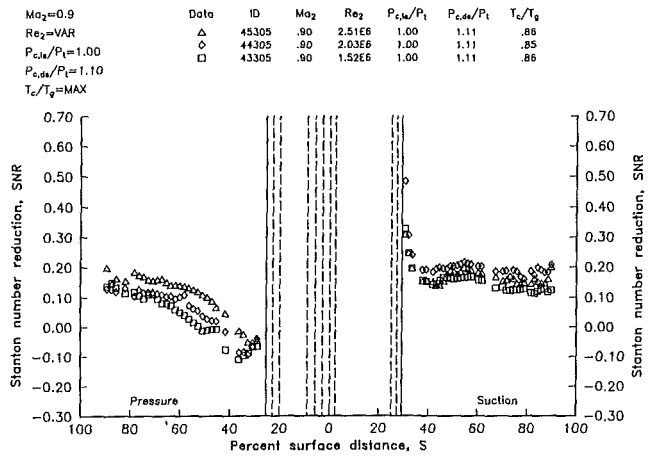

(b)T_c/T_g = MAX

Fig. 18 Effects of exit Reynolds number on Stanton number reduction

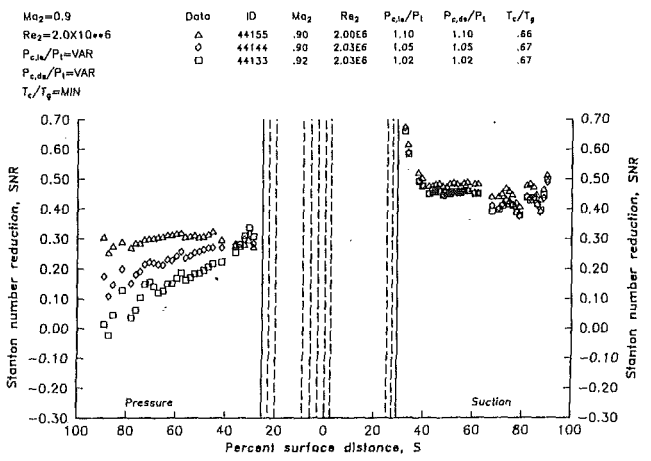

(a)T_c/T_g = MIN

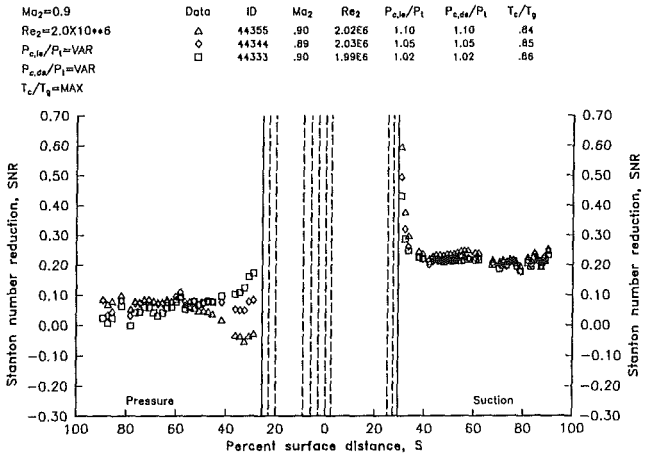

(b)T_c/T_g = MAX

Fig. 19 Effects of leading edge and downstream blowing on Stanton number reduction

similar to the case where only the downstream film cooling holes are active. However, comparing Figs. 13 and 19, on the pressure surface just downstream of the film cooling holes, slightly higher values of SNR are seen due to the leading edge film cooling holes being active.

The SNR data for the case where downstream film cooling hole arrays are at a constant blowing strength of 1.10 while the leading edge film cooling blowing strength is varied from 1.00 (no leading edge blowing) to 1.10 are shown in Fig. 20. These data are at the flow conditions corresponding to an exit Mach number of 0.6 and an exit Reynolds number of 2.0×10^6. On the pressure surface, SNR is increased by low leading edge blowing values ($P_{c,le}/P_t = 1.02$). However, at higher leading edge blowing values, SNR values drop off, to the extent that SNR is lower than without any leading edge blowing. This indicates that high leading edge blowing rates can actually increase heat transfer over the entire pressure surface of the airfoil due to increased turbulence levels. On the other hand, very little effect of leading edge blowing is seen on the suction surface.

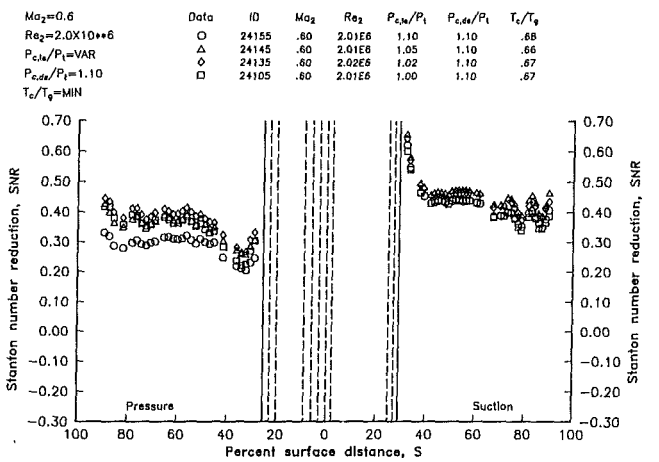

Fig. 20 Effects of variable leading edge blowing with constant downstream blowing on Stanton number reduction

Conclusions

The results from this experiment have provided a database for characterizing the effects of downstream film cooling with and without leading edge (showerhead) film cooling on external heat transfer of the C3X airfoil.

Static pressure data indicate that vane surface static pressure is independent of downstream and leading edge blowing over the range investigated.

The external heat transfer data indicate that considerable

Downloaded 01 Jun 2010 to 171.66.16.66. Redistribution subject to ASME license or copyright; see http://www.asme.org/terms/Terms_Use.cfm

cooling can be attained by downstream film cooling. The downstream film cooling process is shown to be a complex function of mainly two competing mechanisms: (*i*) the thermal dilution, due to the injection of relatively cold fluid, which decreases heat transfer to the airfoil, and (*ii*) turbulence augmentation, due to the injection process, which increases heat transfer to the airfoil. It is also observed that favorable cooling effects actually reverse as the coolant-to-gas temperature ratio is varied.

The pressure surface of the airfoil is shown to exhibit a considerably higher degree of sensitivity to the combined effect of turbulence augmentation and thermal dilution. At moderate blowing strengths ($P_c/P_t > 1.0$), the pressure surface shows considerable dependence on blowing strength, while the suction surface is insensitive to variations in blowing strength, due to the coolant flow being choked and causing no significant change in blowing ratio. However, at low blowing strengths ($P_c/P_t < 1.00$), the suction surface also shows a dependence on blowing strength. Also, the heat transfer levels are significantly dependent on thermal dilution, to the extent that at high levels of thermal dilution, the adverse turbulence augmentation effect is negligible. The data also indicate that, at high thermal dilution levels (i.e., low coolant-to-gas temperature ratio), the film cooling effects are relatively insensitive to exit Mach numbers; and higher favorable film cooling effects are seen at higher exit Reynolds numbers. Conversely, at low thermal dilution levels (i.e., high coolant-to-gas temperature ratio), film cooling effects are dependent on exit Mach number; and lesser effects due to exit Reynolds number are seen.

Acknowledgments

The investigation reported herein was performed by Allison Gas Turbine Division with portions of the funding provided by NASA-Lewis Research Center under contract NAS 3-24619. The authors gratefully acknowledge the technical assistance of the NASA program manager, Mr. H. J. Gladden, and his cooperation in allowing the publication of this paper.

In addition, the authors wish to acknowledge the contributions made by Mr. R. M. Kaufman and Dr. B. K. Sultanian toward acquiring and analyzing the results reported herein.

References

Camci, C., 1989, "An Experimental and Numerical Investigation of Near Cooling Hole Heat Fluxes on a Film-Cooled Turbine Blade," ASME JOURNAL OF TURBOMACHINERY, Vol. 111, pp. 63–70.

Camci, C., and Arts, T., 1985a, "Experimental Heat Transfer Investigation Around the Film Cooled Leading Edge of a High Pressure Gas Turbine Rotor Blade," *ASME Journal of Engineering for Gas Turbines and Power*, Vol. 107, pp. 1016–1021.

Camci, C., and Arts, T., 1985b, "Short-Duration Measurements and Numerical Simulation of Heat Transfer Along the Suction Side of a Film-Cooled Gas Turbines Blade," ASME *Journal of Engineering for Gas Turbines and Power*, Vol. 107, pp. 991–997.

Goldstein, R. J., and Chen, H. P., 1985, "Film Cooling on a Gas Turbine Blade Near the End Wall," ASME *Journal of Engineering for Gas Turbines and Power*, Vol. 107, pp. 117–122.

Horton, F. G., Schultz, D. L., and Forest, A. E., 1985, "Heat Transfer Measurements With Film Cooling on Turbine Blade Profile in Cascade," ASME Paper No. 85-GT-117.

Hylton, L. D., Nirmalan, V., Sultanian, B. K., and Kaufman, R. M., 1987, "Turbine Airfoil Film Cooling," *Turbine Engine Hot Section Technology—1987*, NASA CP-2493.

Hylton, L. D., Nirmalan, V., Sultanian, B. K., and Kaufman, R. M., 1988, "The Effects of Leading Edge and Downstream Film Cooling on Turbine Vane Heat Transfer," NASA CR-182133.

Kline, S. J., and McClintock, F. A., 1953, "Describing Uncertainties in Single-Sample Experiments," *Mechanical Engineering*, Jan.

Moffat, R. J., 1986, "Turbine Blade Cooling," in: *Heat Transfer and Fluid Flow in Rotating Machinery*, W.-J. Yang, ed., Hemisphere Publishing Corporation, Washington, DC, pp. 1–26.

Nealy, D. A., Mihelc, M. S., Hylton, L. D., and Gladden, H. J., 1984, "Measurements of Heat Transfer Distribution Over the Surfaces of Highly Loaded Turbine Nozzle Guide Vanes," *ASME Journal of Engineering for Gas Turbines and Power*, Vol. 106, pp. 149–158.

Turner, A. B., 1971, "Local Heat Transfer Measurements on a Gas Turbine Blade," *Journal of Mechanical Engineering Sciences*, Vol. 13, pp. 1–12.

Turner, E. R., Wilson, M. D., Hylton, L. D., and Kaufman, R. M., 1985, "Turbine Vane External Heat Transfer, Vol. 1, Analytical and Experimental Evaluation of Surface Heat Transfer Distributions With Leading Edge Showerhead Film Cooling," NASA CR-174827.

Downloaded 01 Jun 2010 to 171.66.16.66. Redistribution subject to ASME license or copyright; see http://www.asme.org/terms/Terms_Use.cfm

K. Takeishi
Senior Research Engineer.

M. Matsuura
Research Engineer.

S. Aoki
Assistant Chief Research Engineer.

T. Sato
Deputy General Manager.

Takasago R&D Center,
Mitsubishi Heavy Industries, Ltd.,
Takasago, Japan

An Experimental Study of Heat Transfer and Film Cooling on Low Aspect Ratio Turbine Nozzles

The effects of the three-dimensional flow field on the heat transfer and the film cooling on the endwall, suction, and pressure surface of an airfoil were studied using a low speed, fully annular, low aspect $h/c = 0.5$ vane cascade. The predominant effects on the horseshoe vortex, secondary flow, and nozzle wake of increases in the heat transfer and decreases in the film cooling on the suction vane surface and the endwall were clearly demonstrated. In addition, it was demonstrated that secondary flow has little effect on the pressure surface. Pertinent flow visualization of the flow passage was also carried out for better understanding of these complex phenomena. Heat transfer and film cooling on the fully annular vane passage surface are discussed.

Introduction

Large, LNG burning gas-steam combined cycle power plants with about 10 percent higher efficiency than the latest turbine thermal plants have been commercially operating in Japan with much success (Sudo et al., 1986). A high-temperature heavy-duty gas turbine with a 1150°C level turbine inlet temperature has been adopted to such combined cycle power plants. To achieve higher efficiency, high-temperature heavy-duty gas turbines have been actively developed (Scalzo et al., 1989; Brandt, 1988) and the turbine inlet gas temperature of the latest one will reach a level of 1300°C.

By increasing the turbine inlet temperature, the turbine vane and blade will be exposed to a high gas stream and subjected to a more and more severe environment (Sato et al., 1986). As there is a temperature gradient in the combustion exhaust gas, the first stationary vanes are put in the most severe thermal condition. Therefore, the first stationary vane for such high-temperature gas turbines should adopt a cooling system using an effective convection cooling and film cooling method for not only the vane surface but also the endwall. As the first stationary vane needs such an elaborate cooling system, the turbine airfoil design reaches a low aspect ratio and low solidity because of the optimization of performance and manufacturing cost by reducing the number of vanes. In such a low aspect ratio guide vane, three-dimensional flow field strongly affects the vane and endwall surface heat transfer and film cooling. Therefore, the usual cooling design data based on the two-dimensional cascade test are insufficient to develop a highly reliable and high-performance first vane.

The complicated aerodynamic nature of turbine secondary flows has been studied by a number of investigators. A comprehensive review of such investigations through 1984 is given by Sieverding (1985). However, only minimal investigations of the passage secondary flow effect on the heat transfer and film cooling are available. Blair (1974) investigated the film cooling effectiveness and convective heat transfer coefficient distributions on the endwall of a large-scale turbine passage. Graziani et al. (1980) studied the endwall and blade surface heat transfer in a large scale linear cascade of blades and observed that the inlet boundary layer flows greatly influenced the heat transfer. York et al. (1984) measured the endwall heat transfer coefficient using a double layer grid of thermocouples by hot cascade. Gaugler and Russell (1984) compared the heat transfer distribution and the visualized secondary flows on an enlarged replica of York's turbine endwall, and compared secondary flow directly with heat transfer distributions. Georgiou et al. (1979) and Dunn et al. (1979) measured the film cooling effectiveness on a turbine endwall and the heat transfer coefficient on a turbine airfoil and endwall, respectively, by the short duration method. Goldstein et al. (1984, 1987a) investigated the film cooling effectiveness on the turbine blade near the endwall and in the literature (1987b) measured the detailed distribution of mass transfer Stanton number on the turbine endwall by using the mass transfer analogy.

Those were the experimental approaches to the investigation of turbine secondary flow effects on heat transfer. Recently, some numerical predictions of three-dimensional heat transfer field have been developed (Sharma et al., 1987).

The heat transfer and film cooling influenced by the passage secondary flow are extremely complex; thus further understanding and measurement is necessary.

The present experimental work has been done to study the influence of the passage secondary flow on heat transfer and film cooling of the airfoil and the endwall for further understanding and utilization of the cooling design. The tests

Contributed by the International Gas Turbine Institute and presented at the 34th International Gas Turbine and Aeroengine Congress and Exhibition, Toronto, Ontario, Canada, June 4-8, 1989. Manuscript received at ASME Headquarters January 27, 1989. Paper No. 89-GT-187.

Copyright © 1990 by ASME
Downloaded 01 Jun 2010 to 171.66.16.66. Redistribution subject to ASME license or copyright; see http://www.asme.org/terms/Terms_Use.cfm

were carried out using a fully annular, three-dimensional cascade for identifying the radial pressure gradient effects with low aspect ratio model vanes ($h/c = 0.5$).

Flow Field

It is very significant to review briefly the flow field in the turbine passage to understand the effect of the passage secondary flow on the heat transfer and film cooling of the airfoil and the endwall before the discussion of our test results. The fluid mechanism in the passage has been studied by a number of investigators with flow visualization and direct measurements. Here the essential results will be reviewed.

Figure 1 shows the conception of the three-dimensional flow field inside a first-stage turbine vane passage (Breugelmans).

A fluid particle in the inlet boundary layer is forced downward by pressure variation at the leading edge–endwall intersection. It then rolls up to generate the so-called horseshoe vortex. The pressure-side leg of the horseshoe vortex combines with the low-momentum flow near the endwall to form what is known collectively as the passage vortex. The other leg is convected around the leading edge to the suction surface and remains close to the suction surface until it comes to the separation line of the endwall boundary layer. At the separation line, the suction-side leg of the horseshoe vortex lifts off the endwall and grows rapidly downstream along the suction surface adjacent to the passage vortex, the so-called countervortex. The relative positions of the countervortex and passage vortex depend on the cascade geometry and overall flow conditions. The passages of both legs of the horseshoe vortex and the low-momentum flow (crossflow B) adjacent to the endwall were strongly influenced by the strong pressure gradient across the passage determined by the cascade geometry and the aerodynamic loading.

The separation line, which was formed as the endwall boundary layer approached the turbine vane, and the attachment line, which divides the incoming boundary layer flow entering a vane passage from the flow entering the adjacent passage, are shown in Fig. 1. The intersection of these two lines is a so-called saddle point.

The final region to be noticed is the wake region just downstream of the turbine vane trailing edge. The intensity of the nozzle wake of the air-cooled turbine vane is stronger compared with that of the noncooled vane because of the thick trailing edge.

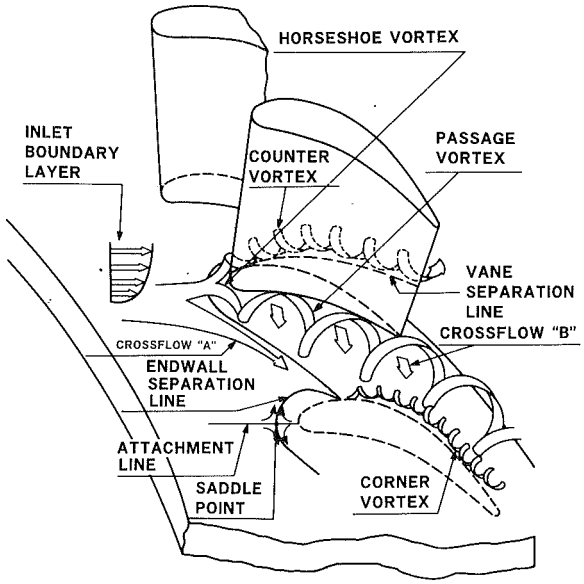

Fig. 1 Endwall secondary flow model

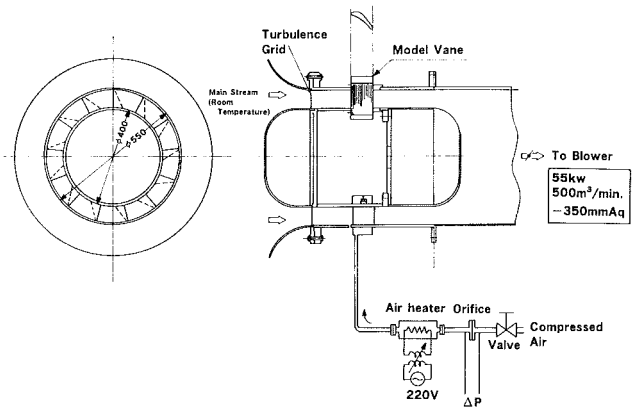

Fig. 2 Cross section of low speed annular cascade test equipment

Experimental Apparatus

The experiment was conducted with a low-speed open-circuit, fully annular cascade wind tunnel facility of 400 mm i.d. and 550 o.d. Figure 2 shows a schematic diagram of the test apparatus. The inlet velocity was measured by the Pitot tube mounted 35 mm in front of the leading edge of the vane. The inlet velocity was 15 m/s and the exit velocity was 64 m/s under typical test conditions. The boundary layer thickness measured at a point 35 mm in front of the leading edge of the vane was $\delta^*_{99} = 1.9$ mm on the inner and outer endwall and the ratio to the vane height was 2.5 percent. The turbulence intensity of the mainsteam was $\tau = 2.7$ percent at the leading edge in the middle channel of the model vane.

The annular cascade was constructed with 13 vanes with an aspect ratio of $h/c = 0.5$. The vane chord length and height are 150.25 mm and 75.0 mm, respectively. The Reynolds number based on chord length is 6.1×10^5. This valve is about one tenth of the actual engine condition. The Reynolds and Mach numbers are low compared with the actual engine condition,

Nomenclature

C = vane chord
D = film cooling hole diameter
h = vane height
M = blowing rate $= \dfrac{\rho_2 U_2}{\rho_\infty U_\infty}$
P = film cooling hole pitch
P = circumference pitch of the vane
Re = Reynolds number
r = radius
s = equivalent film cooling slot width $= D^2/4p$
s = vane throat width
T = temperature
U = velocity
x = distance downstream of film cooling holes or leading edge
α = heat transfer coefficient
$\delta_{.99}$ = boundary layer thickness
η_f = film cooling effectiveness
ρ = specific density
τ = meanstream turbulence intensity

Subscripts

aw = adiabatic wall
ex = exit
in = inlet
L.E. = leading edge
T.E. = trailing edge
w = wall
2 = injected air
∞ = mainstream

Downloaded 01 Jun 2010 to 171.66.16.66. Redistribution subject to ASME license or copyright; see http://www.asme.org/terms/Terms_Use.cfm

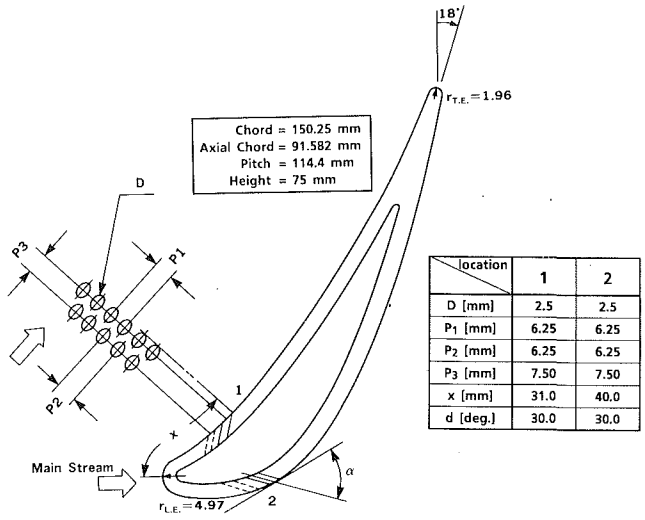

location	1	2
D [mm]	2.5	2.5
P_1 [mm]	6.25	6.25
P_2 [mm]	6.25	6.25
P_3 [mm]	7.50	7.50
x [mm]	31.0	40.0
d [deg.]	30.0	30.0

Fig. 3 Film cooling hole geometry on model vane

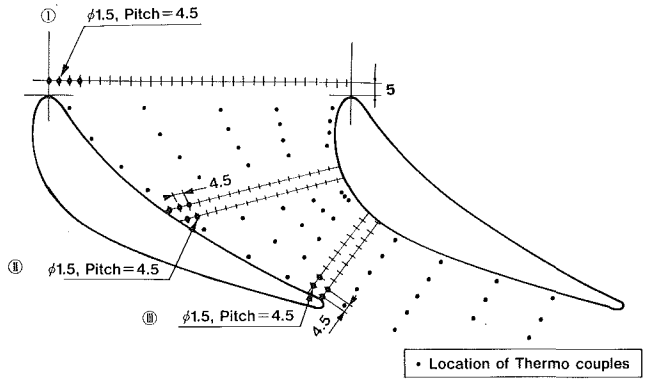

Fig. 4 Film cooling geometry on outer endwall

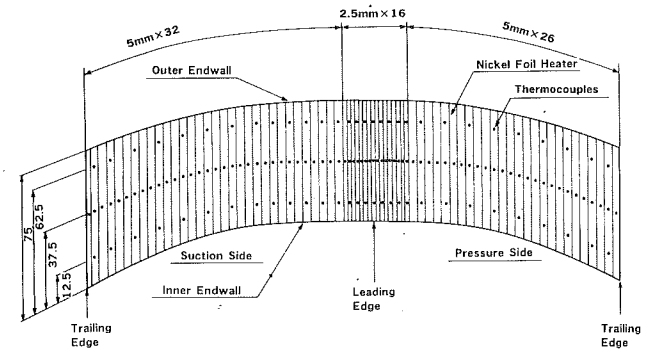

Fig. 5 Diagram of vane instrumentation

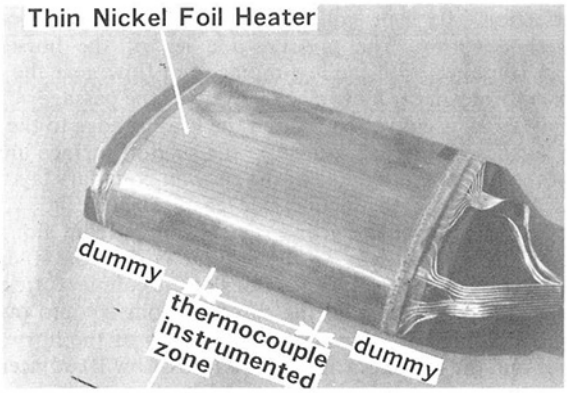

Fig. 6 Photographs of vane heat transfer model

but sufficient to understand the three-dimensional flow effect on heat transfer and film cooling. These data are important for verification of the three-dimensional viscous flow code. The vane profile shown in Fig. 3 is the typical first-stage vane for a heavy-duty gas turbine and is the same as the previous two-dimensional film cooling test (Nakahara et al., 1981). The model vane simulates the air-cooled turbine vane blowing through the trailing edge, so the trailing edge is thicker than that of the noncooled vane. The pitch-chord ratio (p/c) and the trailing edge radius-slot width ratio (r/s) vary from 0.644 to 0.885 and 0.0784 to 0.0456 from inner side to outer side, respectively.

Six of the thirteen vanes were made of the low thermal conductivity material, Bakelite, to measure the heat transfer and film cooling. The remaining seven vanes were made of metal to measure the aerodynamic conditions. The two flow passages were made of acrylate for visibility into the passage.

The double rows of film cooling holes, whose configuration and dimensions are shown in Fig. 3, were positioned at the suction surface and pressure surface on the airfoil, and inclined at a 30 deg angle to the surface. The configuration and dimensions of the film cooling were also the same as those of the previous two-dimensional cascade test (Nakahara et al., 1981).

On the inner and outer endwalls, the film cooling holes were placed at three locations between the leading edge and the nozzle throat as shown in Fig. 4 and each location was labeled from I to III. A single row of holes was located near the leading edge and double rows of holes were located at the remaining two positions. The diameter of the injection holes is 1.5 mm; they are inclined at a 30 deg angle to the endwall surface and spaced three diameters apart.

Measuring Method

The local heat transfer coefficient on the airfoil and on the endwall was measured using the airfoil and the endwall without film cooling holes with electrically heated, instrumented, isothermal models. 5-μm-thick nickel foil was pressed on a 0.3-mm-thick epoxy sheet, and rectangular shaped heaters were made by photoetching the nickel foil. The width of the foil heater used near the leading edge on the airfoil is 2.5 mm and that used on the suction and pressure surface is 5.0 mm. The narrow gap between each of the heaters was 50 μm. To measure the wall temperature, the airfoil test region was instrumented with 134 0.1-mm-dia chromel-alumel thermocouples at the location shown in Fig. 5.

The embedded surface was polished and the foil heater sheet was attached with a thin epoxy adhesive. The photograph of the vane heat transfer model is shown in Fig. 6. The model vane can be moved radially through slots in the endwalls, so the necessary wall temperature can be measured. In this study the wall temperatures of seven sections at heights of 16.7, 33.3, 50.0, 58.3, 66.7, 83.7, and 91.7 mm were measured.

The endwall heat transfer foil heater was constructed with 47 5.0-mm-wide stripes. The 235 0.1-mm-dia chromel-alumel thermocouples were instrumented in the inner and outer endwalls.

The accuracy of the heat transfer measurements by using this foil heater attached to the Bakelite was confirmed by the flat plate model under a mainstream velocity of 15 m/s. The results were compared with the well-known flat plate heat transfer equation and they fall within ±10 percent.

The film cooling test was conducted using a different airfoil and endwall with film cooling holes from the heat transfer test

Downloaded 01 Jun 2010 to 171.66.16.66. Redistribution subject to ASME license or copyright; see http://www.asme.org/terms/Terms_Use.cfm

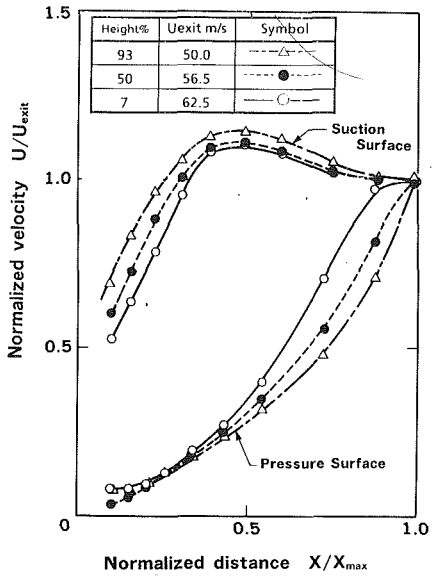

Fig. 7 Surface velocity distribution on vane surface calculated by the measured static pressure distribution

under the conditions in which the mainstream was kept at an ambient temperature and heated air was blown through the film cooling holes.

To get an ideal adiabatic wall, rigid urethane foam was embedded in the Bakelite airfoil and endwall and the adiabatic wall temperature was measured by the embedded 0.1-mm-dia chromel-alumel thermocouples in the airfoil and the endwall to derive the following film cooling effectiveness:

$$\eta_f = \frac{T_\infty - T_w}{T_\infty - T_2} \tag{1}$$

The total number of embedded thermocouples on the airfoil is 192, and 102 on each endwall.

The infrared pyrometer was also used to measure the wall temperature of the region where the temperature gradient is steep. The surface of the vane and the endwall was painted with thin carbon black paint to obtain a surface with an emissivity approximately equal to one, and the measured temperature by the infrared pyrometer was calibrated by the embedded thermocouples.

Experimental Results and Discussion

Velocity Distribution on the Airfoil. The velocity distribution around the airfoil was calculated by the static pressure distribution measured by using static taps on the airfoil with an inlet velocity of 13.3 m/s as shown in Fig. 7. It is apparent that the aerodynamic loading is increasing toward the outer side because of the high P/C ratio. The authors checked the velocity distribution at the mean section of the annular cascade with the previous two-dimensional cascade test results (Nakahara et al., 1981) and it was confirmed that the two dimensionality was maintained.

Flow Visualization. Flow visualization on the airfoil and the inner and outer endwalls was performed. The surface-streamline flow-visualization technique, which is suitable for use in low-speed wind tunnels, was developed by Langston and Boyle (1982) and applied as per Gangler and Russell (1984). In this test, a matrix of ink dots was not applied, but polyester drafting film was painted uniformly with a felt-tipped pen (Pentel OPM4W) containing water-insoluble blue ink and sprayed with wintergreen.

The flow visualization results of the vane and endwall surfaces ink trace by the abovementioned method are shown in Figs. 8–10. The intent of these results is to point out the predominant aerodynamic characteristics of the flow field on the airfoil and on the endwall, which can help to interpret the heat transfer and film cooling. It is clearly evident in Fig. 8 that the limiting streamlines converge toward the midspan of the airfoil suction surface. The separation line intrusion is longer on the outer side than the inner side because of high aerodynamic loading on the outer side.

The reason that stagnation of paint occurred at $x/x_{MAX} \simeq 0.5$ is a laminar bubble, which seemed to be generated at the de-acceleration region on the suction airfoil surface. On the contrary, airfoil pressure surface limiting streamlines exhibit the same apparent two-dimensional pressure surface flow field.

The horseshoe vortex, endwall crossflow A, separation line B, and nozzle wake on the inner and outer endwall are clearly indicated in Figs. 9 and 10. When these figures were combined with Fig. 8 and the streamline was carefully investigated, we could understand the three-dimensional flow field of the low aspect ratio turbine vane passage. The characteristic separation lines on the endwalls reached the highest velocity point on the suction surface of the vane. The convergent separation line on the suction surface started just from this point and from here, the passage vortex lifted up the endwall and continued downward along the suction surface of the vane. It is clear by comparing Figs. 9 and 10 that crossflow B is stronger on the outer endwall and the nozzle wake is stronger on the inner endwall, which is attributed to the aerodynamic loading and the r/s effect.

Airfoil Heat Transfer and Film Cooling. The heat transfer distributions measured on the suction and pressure surfaces are shown in Figs. 11 and 12, respectively. The lines in Figs. 11 and 12 were plotted using computer graphics according to the measured data; therefore, measured locations did not fit exactly along the lines. By looking at the heat transfer coefficient on the suction surface shown in Fig. 11, it can be seen that the heat transfer coefficient of the leading edge and the region between the leading edge until $x/x_{MAX} \simeq 0.3$, are constant in the height direction. However, after $x/x_{max} \simeq 0.3$, the heat transfer coefficient on the airfoil near the outer endwall increases rapidly compared with that of the mean section. The rapid increase of the heat transfer coefficient in this region is attributed to the passage secondary flow developed along the suction surface near the endwall; this is clear with the flow visualization test result of the suction surface shown in Fig. 8.

The heat transfer coefficient of the suction surface near the inner endwall increased rapidly at $x/x_{MAX} \simeq 0.6$, but the rate of increase is not as strong as that near the outer endwall.

It is considered that near the inner endwall the passage vortex is not as strong as that near the outer endwall, and the intersection point of measuring section with separation line on the suction surface of the inner endwall is situated downstream of the trailing edge compared with that of the outer endwall.

Contrary to the suction surface, the heat transfer coefficient distribution on the pressure surface is constant in the height direction from the leading edge to the trailing edge except near the leading edge. A separation bubble might occur near the leading edge and influence the heat transfer coefficient. From the endwall secondary flow model, it is expected that the three-dimensional flow field has little effect on pressure surface. These heat transfer test results support the evidence.

In this test, the effect of the horseshoe vortex did not appear clearly on the leading edge heat transfer near the endwall.

Next, we will discuss the film cooling test results on the airfoil. The typical film cooling effectiveness distributions associated with coolant injection through the film cooling holes on the suction surface with blowing parameter of $M = 0.426$, the typical actual vane condition, are shown in Fig.

Downloaded 01 Jun 2010 to 171.66.16.66. Redistribution subject to ASME license or copyright; see http://www.asme.org/terms/Terms_Use.cfm

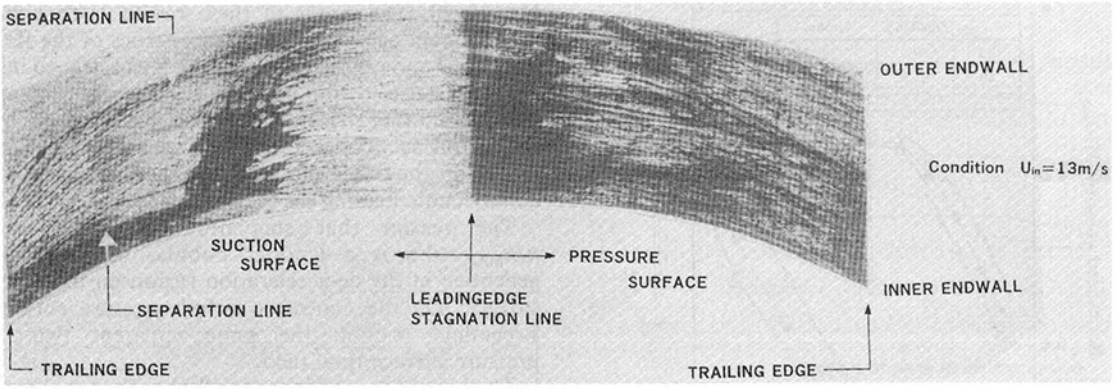

Fig. 8 Streaklike pattern on the vane surface of a low aspect ratio turbine vane

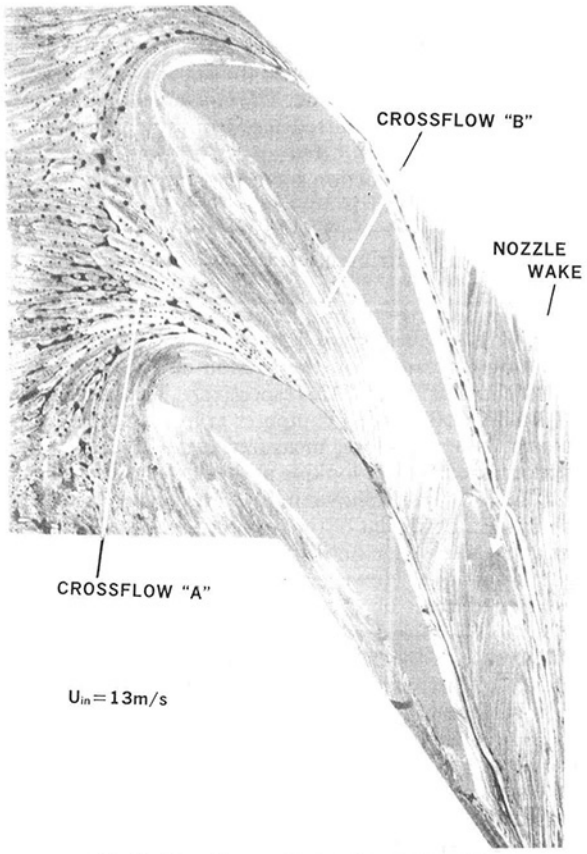

Fig. 9 Streakline pattern on inner endwall

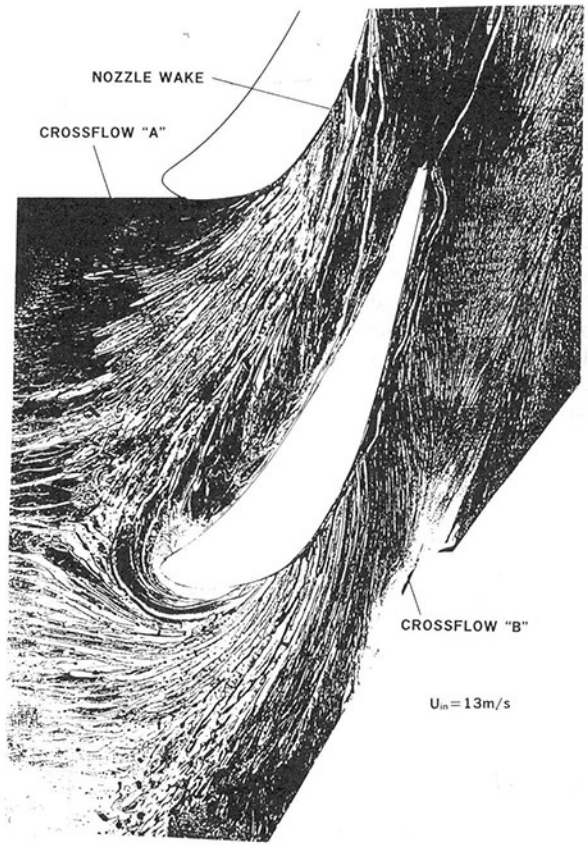

Fig. 10 Streakline pattern on outer endwall

13. It is clear from this figure that the film cooling effectiveness decreases rapidly toward the endwall. Especially, a triangular region, where the coolant is swept from the convex surface by the passage vortex system and the film cooling effectiveness decreases to 0, exists near each endwall.

To evaluate these test results quantitatively, the film cooling effectiveness of a typical suction and pressure surface was plotted against x/MS, where S is an equivalent film cooling slot width defined by $\pi D^2/4p$ and shown in Figs. 14 and 15. The film cooling test was carried out by varying the blowing parameter M over a wide range. However, only two test results of M were shown in Figs. 14 and 15 because the film cooling effectiveness changed linearly between these two M values. On the suction surface, the film cooling effectiveness decreased more rapidly at 83 percent height compared with 23 percent and midheight, as shown in Fig. 14. Another characteristic shown in Fig. 14 is that the film cooling effectiveness decreased more rapidly with the higher blowing parameter M near the outer endwall. It was considered that in the triangular region, there is a screwed flow and the film cooling air was swept easily when the coolant penetrated the main flow with the high blowing parameter M.

The same plots were made for the pressure surface and shown in Fig. 15. Contrary to the results of the suction surface, the rate of the decrease of the film cooling effectiveness on the pressure surface was not so rapid as that on the suction surface, and that near the endwall was the same as that at midheight. The secondary flow effects on the film cooling effectiveness on the pressure surface are weak, as expected from the flow visualization test results shown in Fig. 8. These film cooling effectiveness test values were compared with the results of the previous two-dimensional film cooling study to obtain the film cooling effectiveness value without the influence of the three-dimensional flow field. The authors de-

Downloaded 01 Jun 2010 to 171.66.16.66. Redistribution subject to ASME license or copyright; see http://www.asme.org/terms/Terms_Use.cfm

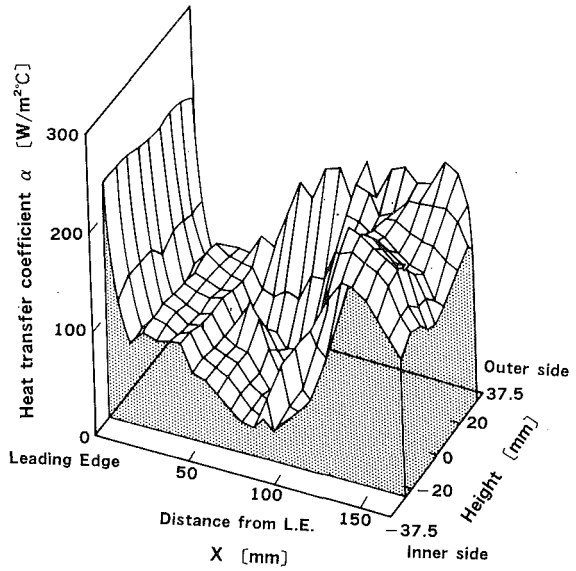

Fig. 11 Distribution of heat transfer coefficient on vane suction surface without film cooling holes

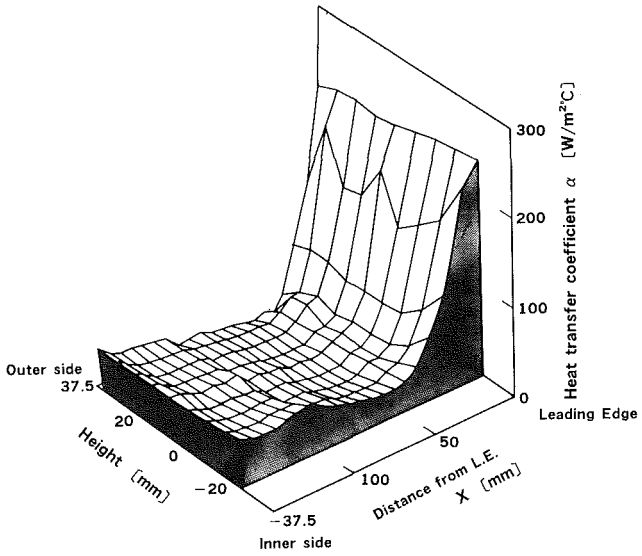

Fig. 12 Distribution of heat transfer coefficient on vane pressure surface without film cooling holes

rived the following experimental equations from the two-dimensional film cooling test (Sato and Takeishi, 1987a, 1987b):

Suction surface:

$$\eta_f = \frac{C}{2.8 + 0.027(x/MS)} \tag{2}$$

where

$$C = 1.5/M^{0.3} \quad M < 1$$

$$C = 1.5/M^{0.8} \quad M \geq 1$$

Pressure surface:

$$\eta_f = \frac{1}{1.67 + 0.00456\ (x/MS)^{1.6}} \tag{3}$$

The film cooling effectiveness values recorded midheight on the suction and pressure surface of the full annular cascade fit well with equation (2) and (3).

These airfoil heat transfer and film cooling test results

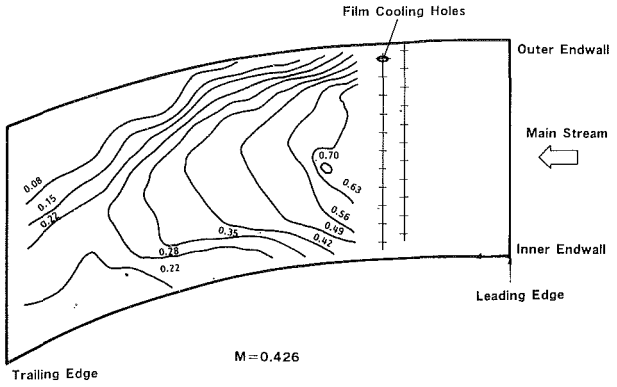

Fig. 13 Film cooling effectiveness on vane suction surface

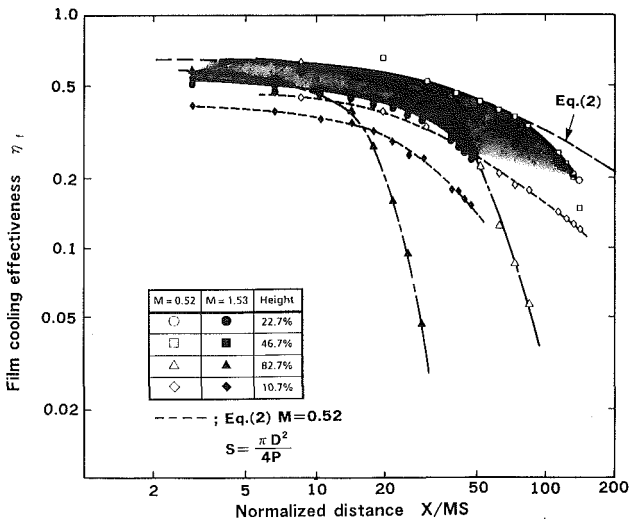

Fig. 14 Variation of film cooling effectiveness on vane suction surface

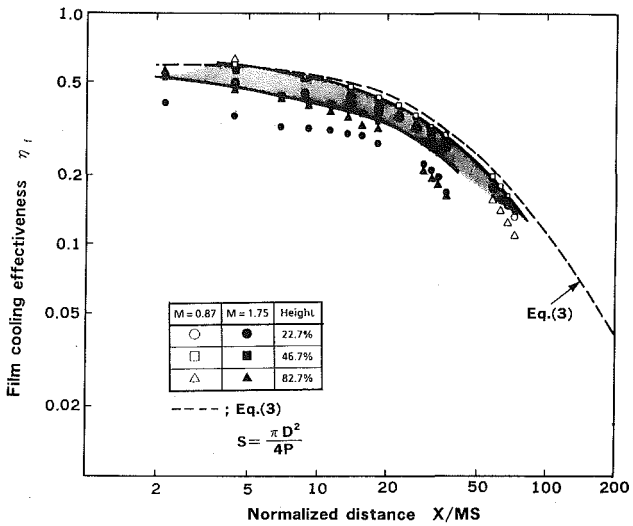

Fig. 15 Variation of film cooling effectiveness on vane pressure surface

showed that the two-dimensional test data were applicable for cooling design except for the triangular zone near the endwall even in such a low aspect ratio turbine vane.

Endwall Heat Transfer and Film Cooling. Typical heat transfer contours of the inner and outer endwall without film cooling holes are shown in Figs. 16 and 17. These contour plots show complex and remarkable shapes. On the inner endwall, the heat transfer coefficient increases concentrically

Downloaded 01 Jun 2010 to 171.66.16.66. Redistribution subject to ASME license or copyright; see http://www.asme.org/terms/Terms_Use.cfm

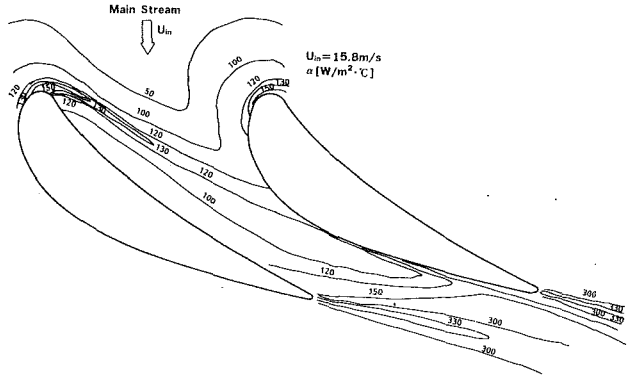

Fig. 16 Iso-heat transfer distribution on inner endwall without film cooling holes

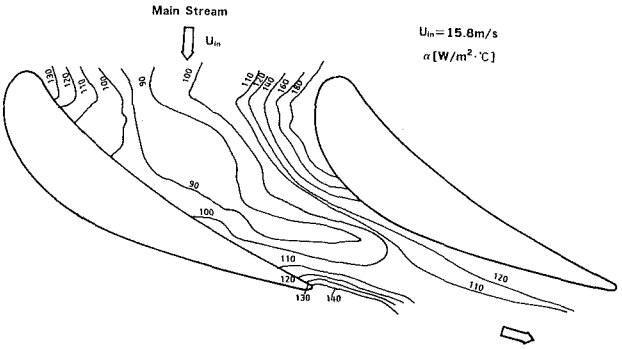

Fig. 17 Iso-heat transfer distribution on outer endwall without film cooling holes

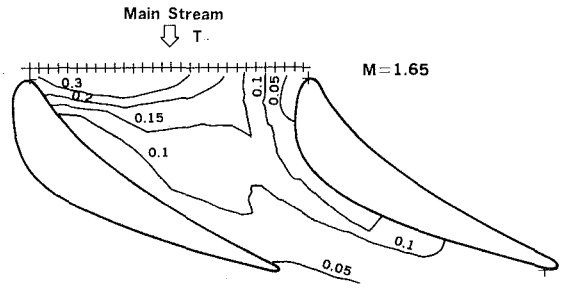

Fig. 18 Film cooling effectiveness distribution on outer endwall

around the leading edge. This increase results from the horseshoe vortex formed at the endwall near the vane leading edge. The iso-heat transfer coefficient line of $\alpha = 130$ W/m^{2}K travels around the leading edge to the suction surface of the opposite vane. This high heat transfer region was caused by the passage vortex traveled along the separation line; a footprint of the passage vortex was shown in the flow visualization test results in Fig. 9. It is noticed that the passage vortex affects a much larger area. In the throat region near the suction surface, the heat transfer increases strongly as a result of the suction side corner vortices. Another significant heat transfer increase can be found at the trailing edge region, a result of a strong wake that is clear from Fig. 9.

On the other hand, there is a high heat transfer region near the leading edge on the outer endwall caused by the same reason as the inner endwall. However, a high heat transfer zone appears on the suction surface near the leading edge. This is the result of a highly turbulent flow caused by the transverse pressure gradient turning the upstream boundary layer flow and forcing it to flow toward the suction surface. When Fig. 17 was contrasted with Fig. 10, we recognized that crossflow B occupies a much larger area and the heat transfer coefficient of the wake region in the trailing edge region is weaker than that on the inner endwall.

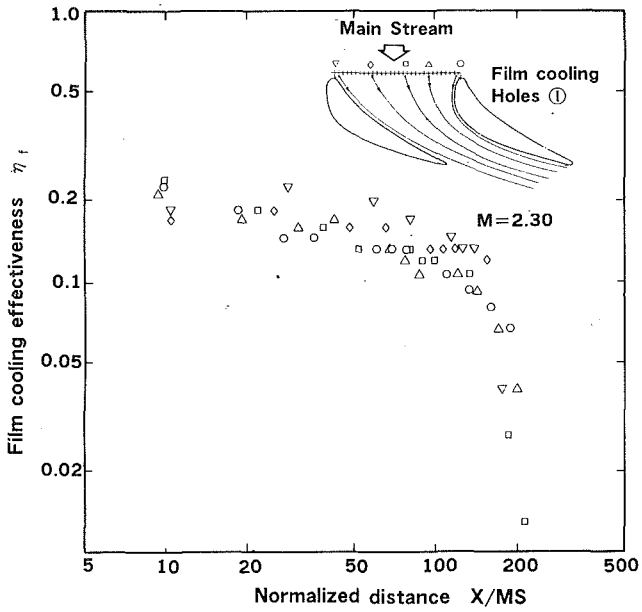

Fig. 19 Film cooling effectiveness variation along potential streamlines on the inner endwall blowing through film cooling hole I

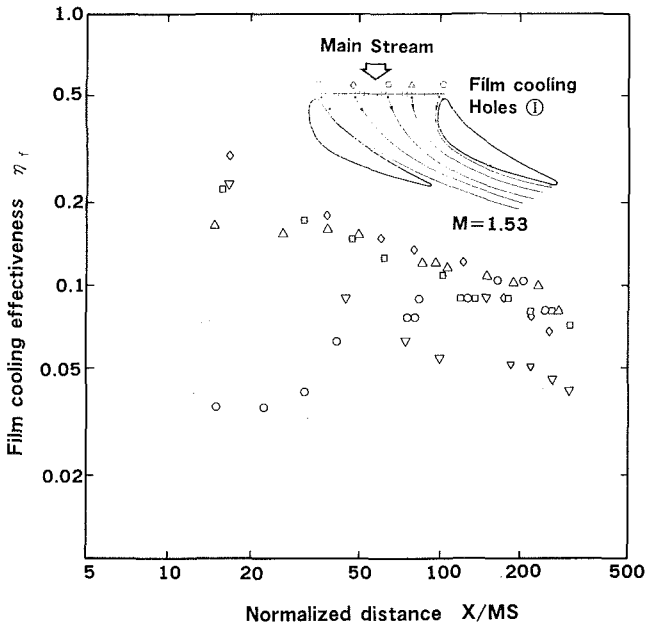

Fig. 20 Film cooling effectiveness variation along potential streamlines on the outer endwall blowing through film cooling hole I

Endwall film cooling effectiveness distributions were measured at the coolant flow rates of $M = 0.5$ to 2.5. Typical iso-film cooling effectiveness contour blowing through the film cooling holes I (holes II and III exist without blowing) of the outer endwall is shown in Fig. 18. The film cooling effectiveness value is very low near the leading edge of the suction surface. The reason for this is that the horseshoe vortex strongly rolls up the inlet boundary layer flow and the coolant could not remain near the endwall. In the region of crossflow A, shown in Fig. 1, the film cooling effectiveness decreases when the downstream distance from the film cooling hole edge increases. The contour line of $\eta_f = 0.1$ near the pressure surface is expected to exist close to the separation line of the passage vortex when Fig. 18 was contrasted with the flow visualization test results of Fig. 10. The serpentine contour line $\eta_f = 0.1$ is also the effect of the passage vortex. The coolant was sent from the pressure surface across the passage to the adjacent suction surface in the crossflow B region. The

Downloaded 01 Jun 2010 to 171.66.16.66. Redistribution subject to ASME license or copyright; see http://www.asme.org/terms/Terms_Use.cfm

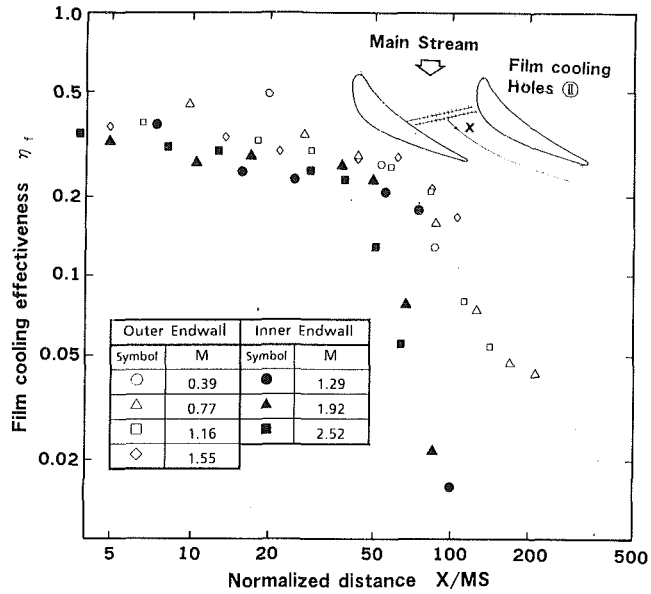

Fig. 21 Film cooling effectiveness variation along potential streamlines on the outer endwall blowing through film cooling hole II

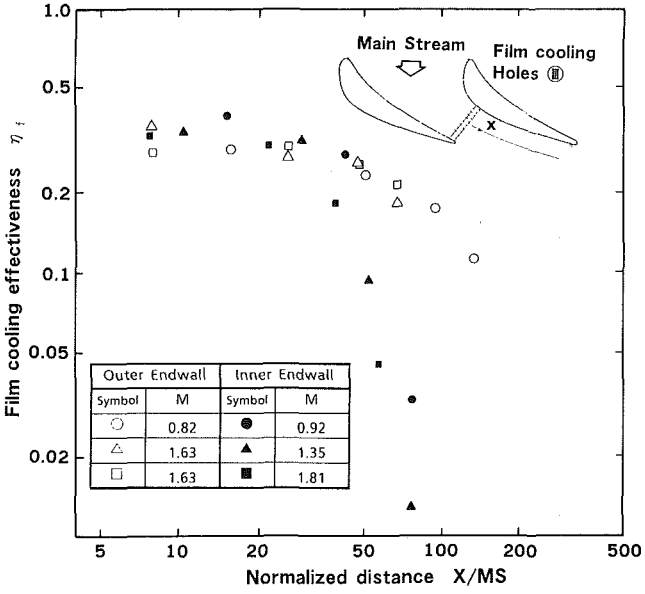

Fig. 22 Film cooling effectiveness variation along potential streamlines on the outer endwall blowing through film cooling hole III

low film cooling effectiveness in the trailing region was caused by the nozzle wake flow.

To evaluate the film cooling effectiveness on the endwall qualitatively, film cooling effectiveness blowing through each of the holes I and III was plotted against the normalized distance from the hole edge along the potential flow lines and shown in Figs. 19–22. The test was conducted with the wide blowing parameter M, but only typical test results of M were shown in Figs. 19 and 20 to know the effect of location.

Interesting characteristics appear from the film cooling effectiveness when Fig. 19 is contrasted with Fig. 20. On the outer endwall the film cooling effectiveness along the potential flow line near the suction surface is 0.035 near the leading edge. It increases to a maximum value of 0.1 when the distance increases because of the supply of coolant by the crossflow B. The film cooling effectiveness along the potential flow linear near the pressure surface decreases rapidly when the distance increases. The reason for this is that the coolant is swept by the crossflow B and little coolant remains along the potential flow line. The film cooling effectiveness between these two lines decreases gradually, but slightly wavily, when the distance increases.

In comparison with the film cooling on the outer endwall, the same characteristics did not appear in the film cooling effectiveness on the inner endwall as shown in Fig. 19. The secondary flow effect on film cooling effectiveness is weaker on the inner endwall than on the outer endwall because of the difference of the aerodynamic loading. The characteristic evidence in Fig. 19 is a rapid decrease of the film cooling effectiveness downstream of the nozzle wake region. However, on the outer endwall, such rapid decrease did not appear in the nozzle wake region. This is caused by the generation of strong nozzle wake as trailing edge radius versus throat width; r/s is larger on the inner side. A thick trailing edge must take into account such film cooling results.

The measured film cooling effectiveness blowing through the film cooling holes II and III was plotted along the centerline of the passage potential flow and shown in Figs. 21 and 22, respectively. The coolant blowing through the film cooling holes II and III was governed by the crossflow B. The film cooling effectiveness decreased at the same rate as when increasing the distance until the nozzle wake region. The rapid decrease of the film cooling effectiveness on the inner endwall in Fig. 21 and Fig. 22 was the effect of the strong nozzle wake in the trailing edge region.

Figures 21 and 22 also show that the film cooling effectiveness could be arranged by using the nondimensional parameter x/MS. This evidence is very useful for film cooling design of the endwall.

Conclusions

Measurements of local heat transfer coefficient and film cooling effectiveness were made on the endwall and airfoil surfaces of a fully annular guide vane cascade with an aspect ratio of $h/C=0.5$. A surface streamline flow-visualization technique was also adopted to understand the secondary effect on heat transfer phenomena in three-dimensional flow passages. The following conclusions were obtained through these results:

1 Passage secondary flows strongly affect heat transfer and film cooling on the suction surface of the vane and the endwalls.

2 The secondary flow has little influence on the heat transfer and film cooling on the pressure surface of the vane.

3 The horseshoe vortex increases the heat transfer and decreases the film cooling effectiveness near the leading edge on the endwall.

4 The heat transfer and film cooling distribution on the endwall shows a very complex pattern dependent on the passage vortex, crossflows A and B, and nozzle wake.

5 The demonstrated influence of the passage secondary flow on heat transfer and film cooling is stronger near the outer endwall than near the inner endwall because the aerodynamic loading on the outer side was greater than that on the inner side.

6 Two-dimensional heat transfer and film cooling cascade data were applicable for cooling design of the low aspect ratio vane except for the triangular zone near the endwall.

Acknowledgments

The authors wish to express their indebtedness to Mitsubishi Heavy Industries, Ltd. for permission to publish this paper.

References

Blair, M. F., 1974, "An Experimental Study of Heat Transfer and Film Cooling on Large-Scale Turbine Endwalls," ASME *Journal of Heat Transfer*, Vol. 96, pp. 524–529.

Downloaded 01 Jun 2010 to 171.66.16.66. Redistribution subject to ASME license or copyright; see http://www.asme.org/terms/Terms_Use.cfm

Breugelmans, F., VKI Lecture Series.

Brandt, D. E., 1988, "The Design and Development of an Advanced Heavy-Duty Gas Turbine," ASME *Journal of Engineering for Gas Turbines and Power*, Vol. 110, pp. 243–250.

Dunn, M. G., and Stoddard, F. J., 1979, "Measurement of Heat Transfer Rate to a Gas Turbine Stator," ASME *Journal of Engineering for Power*, Vol. 101, pp. 275–280.

Gaugler, R. E., and Russell, L. M., 1984, "Comparison of Visualized Turbine Endwall Secondary Flows and Measured Heat Transfer Patterns," ASME *Journal of Engineering for Gas Turbines and Power*, Vol. 106, pp. 168–172.

Georgiou, D. P., Godard, M., and Richards, B. E., 1979, "Experimental Study of the Iso-Heat-Transfer-Rate Lines on the End-Wall of a Turbine Cascade," ASME Paper No. 79-GT-20.

Goldstein, R. J., and Chen, H. P., 1984, "Film Cooling on a Gas Turbine Blade Near the Endwall," ASME *Journal of Engineering for Gas Turbines and Power*, Vol. 107, pp. 117–122.

Goldstein, R. J., and Chen, P. H., 1987a, "Film Cooling of a Turbine Blade With Injection Through Two Rows of Holes in the Near-Endwall Region," ASME JOURNAL OF TURBOMACHINERY, Vol. 109, pp. 588–593.

Goldstein, R. J., and Spores, R. A., 1987b, "Turbulent Transport on the Endwall in the Region Between Adjacent Turbine Blades," *Heat Transfer in Gas Turbines*, D. E. Metzger, ed., ASME HTD-Vol. 87, pp. 75–83.

Graziani, R. A., Blair, M. F., Taylor, J. R., and Mayle, R. E., 1980, "An Experimental Study of Endwall and Airfoil Surface Heat Transfer in a Large-Scale Turbine Blade Cascade," ASME *Journal of Engineering for Power*, Vol. 102, pp. 257–267.

Langston, L. S., and Boyle, M. T., 1982, "A New Surface Streamline Flow-Visualization Technique," *Journal of Fluid Mechanics*, Vol. 125, pp. 53–57.

Nakahara, T., Aoki, S., and Takeishi, K., 1981, "Effect of Surface Pressure Distribution of Gas Turbine Vane on Film Cooling," presented at the 14th International Congress of Combustion Engine (CIMAC), GT6, Helsinki.

Sato, T., Takeishi, K., and Sakon, T., 1986, "Thermal Fatigue Life Predictions of Air-Cooled Gas Turbine Vanes," ASME *Journal of Engineering for Gas Turbines and Power*, Vol. 108, pp. 414–420.

Sato, T., and Takeishi, K., 1987a, "Investigation of Heat Transfer in High Temperature Gas Turbine Vanes," ASME Paper No. 87-GT-137.

Sato, T., Aoki, S., Takeishi, K., and Matsuura, M., 1987b, "Effect of Three-Dimensional Flow Field on Heat Transfer Problems of a Low Aspect Ratio Turbine Nozzle," presented at the 1987 Tokyo Int. Gas Turbine Congress, Paper No. 87-TOKYO-IGTC-59.

Scalzo, A. J., et al., 1989, "A New 150-MW High Efficiency Heavy-Duty Combustion Turbine," ASME *Journal of Engineering for Gas Turbines and Power*, Vol. 111, pp. 211–217.

Sharma, O. P., Nguyen, P., Ni, R. H., Rhie, C. M., White, J. A., and Finke, A. K., 1987, "Aerodynamic and Heat Transfer Analysis of a Low Aspect Ratio Turbine," AIAA Paper No. AIAA-87-1916.

Sudo, Y., Sato, M., and Kobayashi, Y., 1986, "Construction and Operation of Gas–Steam Combined Cycle Plant for Higashi Niigata Thermal Power Station No. 3," ASME Paper No. 86-GT-236.

Sieverding, C. H., 1985, "Recent Progress in the Understanding of Basic Aspects of Secondary Flows in Turbine Blade Passages," ASME *Journal of Engineering for Gas and Turbines and Power*, Vol. 107, pp. 248–257.

York, R. E., Hylton, L. D., and Mihelc, M. S., 1984, "An Experimental Investigation of Endwall Heat Transfer and Aerodynamics in a Linear Vane Cascade," ASME *Journal of Engineering for Gas Turbines and Power*, Vol. 106, pp. 159–167.

Downloaded 01 Jun 2010 to 171.66.16.66. Redistribution subject to ASME license or copyright; see http://www.asme.org/terms/Terms_Use.cfm

An Experimental Convective Heat Transfer Investigation Around a Film-Cooled Gas Turbine Blade

C. Camci[1]
Aerospace Engineering Department,
The Pennsylvania State University,
University Park, PA 16802

T. Arts
von Karman Institute for Fluid Dynamics,
Rhode Saint Genèse, Belgium

The present paper deals with an experimental convective heat transfer investigation around a film-cooled, high-pressure gas turbine rotor blade mounted in a stationary, linear cascade arrangement. The measurements were performed in the von Karman Institute Isentropic Light Piston Compression Tube facility. The test blade was made of Macor glass ceramic and was instrumented with thin film gages. The coolant flow was ejected simultaneously through the leading edge (three rows of holes), the suction side (two rows of holes), and the pressure side (one row of holes). The effects of overall mass weight ratio. coolant to free-stream temperature ratio, and free-stream turbulence were successively investigated.

1 Introduction

A classical way to improve the thermal efficiency of a Joule/Brayton cycle is to increase the turbine entry temperature and pressure ratio. As a result, the specific fuel consumption, size, and weight of aero-engines have been significantly reduced during the two last decades. A 25/1 pressure ratio and an 1800 K turbine entry temperature are typical values observed in high-performance jet engines (Olsson, 1982). For such temperatures, efficient blade cooling is most often required to ensure acceptable lifetimes. Over the last few years, a popular method to solve this problem has been discrete hole film cooling.

In the severe engine environment of a film-cooled turbine blade, the large temperature differences existing between the mainstream and the blade surface induce a wall temperature pattern quite different from an adiabatic distribution. Considering, moreover, the important spatial temperature variations due to internal cooling passages and the strongly varying heat flux distribution downstream of a film-cooling hole or slot, the most representative heat transfer parameter seems to be the convective heat transfer coefficient h, defined from the local wall heat flux, the mainstream total or recovery temperature, and the local wall temperature, for given values of the blowing rate m and the coolant temperature. As a matter of fact, either an experimental or a numerical determination of h is essential to perform any detailed heat conduction or thermal stress analysis.

Some of the representative available measurements on film-cooled turbine cascade models were presented by Lander et al. (1972), Nicolas and Le Meur (1974), Ito et al. (1978), Daniels (1979), Dring et al. (1980), Horton et al. (1985), and Camci and Arts (1985a, 1985b). A large number of these heat transfer data, presented either in terms of adiabatic effectiveness or in terms of heat transfer coefficient, are however difficult to use as such for modern cooled gas turbine designs because of the limited range of Reynolds and Mach numbers, as well as gas-to-wall and gas-to-coolant temperature ratios considered in some of these investigations.

The aim of the present experimental heat transfer investigation was to look at the multilocation, discrete hole film cooling of a high-pressure rotor blade mounted in a six-profile, stationary, linear cascade arrangement and subjected to correctly simulated flow conditions, i.e., Mach and Reynolds numbers, as well as free-stream/wall/coolant temperature ratios. The mainstream flow was generated in the von Karman Institute Isentropic Light Piston Compression Tube facility and the coolant flow was ejected simultaneously through the leading edge, the suction side, and the pressure side. The heat transfer distributions were measured over a wide range of coolant to free-stream mass weight and temperature ratios; the influence of free-stream turbulence was also considered.

2 Experimental Apparatus

2.1 Test Facility. A short-duration measurement technique was applied and use was made of the VKI Isentropic Compression Tube facility. The operating principles of this type of wind tunnel were developed about 15 years ago by Jones et al. (1973) and Schultz et al. (1977). A detailed description of the VKI CT-2 facility and of its capabilities was provided by Richards (1980), and Consigny and Richards (1982).

2.2 Model Description. All measurements reported in this paper were carried out along the same rotor blade section as tested by Consigny and Richards (1982). The blade and cascade geometry are described in detail in this reference. The main characteristics are listed as follows:

Chord length: 80 mm
Blade height: 100 mm
Stagger angle: 38.5 deg
Pitch-to-chord ratio: 0.670

[1]Previous address: the Von Karman Institute for Fluid Dynamics, Rhode Saint Genèse, Belgium.

Contributed by the International Gas Turbine Institute for publication in the JOURNAL OF TURBOMACHINERY. Manuscript received at ASME Headquarters May 1989.

Copyright © 1990 by ASME
Downloaded 01 Jun 2010 to 171.66.16.66. Redistribution subject to ASME license or copyright; see http://www.asme.org/terms/Terms_Use.cfm

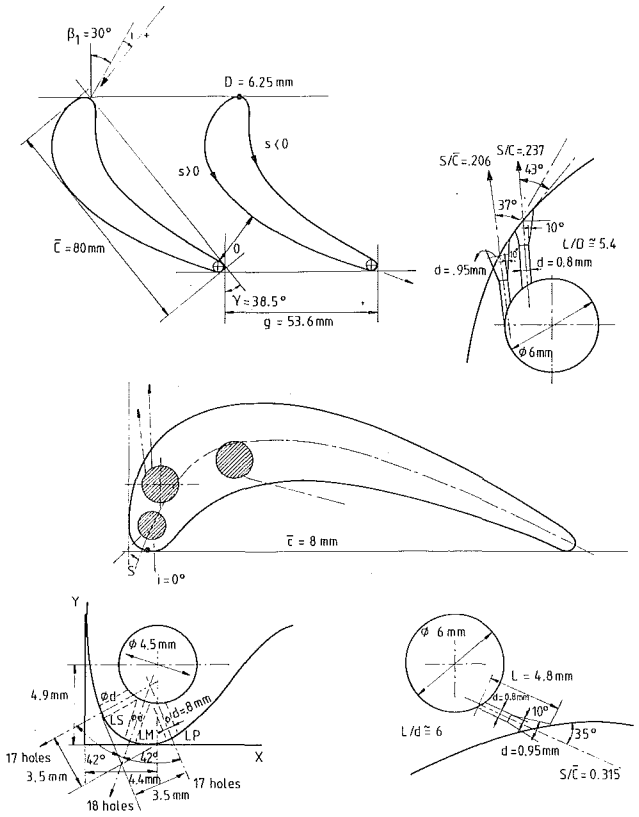

Fig. 1 Cascade geometry and cooling configuration

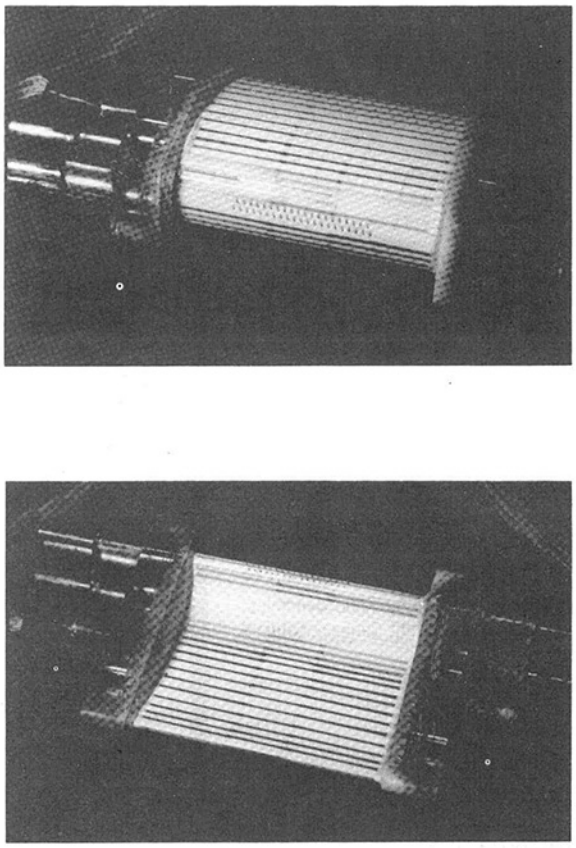

Fig. 2 Heat transfer apparatus

Arcsin (throat/pitch): 21 deg
Design inlet flow angle: 30 deg (referred to axial direction)
Leading edge diameter: 6.25 mm
Trailing edge diameter: 3.0 mm

The cascade consisted of one ceramic and five aluminum airfoils.

The cooling configuration is summarized in Fig. 1. Three rows of cylindrical cooling holes ($d=0.8$ mm; $s/c=-0.031$, 0, 0.031) were located around the leading edge (rows *LP*, *LM*, *LS*). The row and hole spacing were both 2.5 mm. These holes were spanwise angled at 30 deg from the tangential direction and drilled in a plane perpendicular to the blade surface. Two staggered rows of conical holes ($d=0.8$ mm; $s/c=0.206$, 0.237) were located on the suction side (row *S*). The row and hole spacings were respectively 2.5 and 2.6 mm. These holes were inclined at 37 and 43 deg with respect to the local blade surface and drilled in a plane perpendicular to the blade height. One row of conical holes ($d=0.8$ mm; $s/c=-0.315$) was located along the pressure side (row *P*). The hole spacing was 2.6 mm. These holes were inclined at 35 deg with respect to the local blade surface and drilled in a plane perpendicular to the blade height.

The blade instrumented for heat flux measurements was milled from "Macor" glass ceramic and 45 platinum thin films were applied on its surface (Fig. 2). Three independent cavities were drilled along the blade height to act as plenum chambers. The coolant flow was supplied by a regenerative cryogenic heat exchanger. Pressure tappings and ther-

Nomenclature

c = blade chord
$\overline{C_D}$ = mean value of the discharge coefficient
d = film cooling hole diameter
h = convective heat transfer coefficient
LP, *LM*, *LS* = leading edge film cooling rows of holes (three rows)
M = Mach number
m = blowing rate
$\dot{m}$ = mass flow rate
P = pressure side film cooling row of holes (one row)
p = pressure
Re = Reynolds number
S = suction side film cooling rows of holes (two rows)
s = curvilinear coordinate measured from row *LM* along the blade surface (+ along the suction surface, − along the pressure surface)
T = temperature
T_{ref} = reference temperature (290 K)
Tu = free-stream turbulence intensity $=((\overline{u'^2})^{1/2}/\bar{u})$
u = instantaneous velocity
u' = fluctuating component of velocity
ρ = density

Subscripts

c = related to the cooling flow
is = isentropic
∞ = related to the free-stream flow
0 = related to a stagnation condition
1 = related to the free-stream upstream conditions

Downloaded 01 Jun 2010 to 171.66.16.66. Redistribution subject to ASME license or copyright; see http://www.asme.org/terms/Terms_Use.cfm

mocouples continuously provided the coolant characteristics at the entrance and exit of each plenum.

2.3 Measurement Technique. The local wall convective heat flux was deduced from the corresponding time-dependent surface temperature evolution, provided by the platinum thin-film gages. The wall temperature/wall heat flux conversion was obtained from an electrical analogy, simulating a one-dimensional semi-infinite body configuration. A detailed description of this transient technique was given by Schultz and Jones (1973). The convective heat transfer coefficient is defined as the ratio of the measured wall heat flux and the difference between the free-stream recovery and wall temperatures. A recovery factor equal to 0.896 was used, as if the boundary layer on the blade surface was turbulent everywhere. The uncertainty on the different measured quantities has been estimated as follows, based on a 20:1 confidence interval:

$h = 1000\ \text{W/m}^2\text{K} \pm 50\ \text{W/m}^2\text{K}$
$p = 10^5\ \text{N/m}^2 \pm 750\ \text{N/m}^2$
$T = 100°\text{C} \mp 1°\text{C}$
$\dot{m}_c = 0.020\ \text{kg/s} \pm 0.0005\ \text{kg/s}$
$\Sigma \dot{m}_{ci}/\dot{m}_\infty = 2 \pm 0.1$ percent

It should also be realized that the uncertainty associated with the heat transfer measurements obtained from the two gages located between rows LS, LM, and LP was quite high (~10 . . . 15 percent) as these thin films were affected by undesirable conduction phenomena was well as strong deviations from the assumed one-dimensional heat transfer.

All pressure, temperature, and heat flux measurements were directly acquired by means of a PDP 11/34 computer through one of the VKI data acquisition systems. For the present investigation, the sampling rate was selected to be 1 kHz; the flow duration was about 500 ms. The free-stream total temperature was chosen to be 415 K.

2.4 Free-Stream Turbulence Generation. The free-stream turbulence was generated by a grid of parallel, spanwise-oriented bars. The turbulence intensity was varied by displacing the grid upstream of the cascade; a maximum of 5.2 percent was obtained. The natural turbulence of the facility was about 0.8 percent. The turbulence level, defined in the present paper as $(\overline{u'^2})^{1/2}/\bar{u}$, was measured by means of a VKI constant temperature hot-wire anemometer. The definition of turbulence spectrum could not be carried out for practical reasons. These measurements are currently underway and will be reported in a later paper.

3 Free-Stream Flow Characteristics

The isentropic Mach number distribution measured along the blade profile at zero incidence and without film cooling is shown in Fig. 3. The isentropic outlet Mach number selected for this investigation was chosen equal to 0.925. The flow accelerated quite regularly along the suction side up to transonic conditions close to the trailing edge. Along the pressure side, a velocity peak was predicted at $s/c = -0.08$. Farther downstream, the favorable pressure gradient accelerated the flow up to the trailing edge. Because of the small leading edge radius, detailed static pressure measurements could unfortunately not be carried out around the stagnation point position.

A two-dimensional inviscid time-marching program (Arts, 1982) provided a valuable prediction of this velocity distribution (Fig. 3). Because of the weakness of this type of approach in accurately determining the stagnation point position, a singularity method (Van den Braembussche, 1973) was also used around the leading edge. Both calculation methods were inviscid and no attempt was made to simulate the effect of film cooling. At zero incidence, the stagnation point position

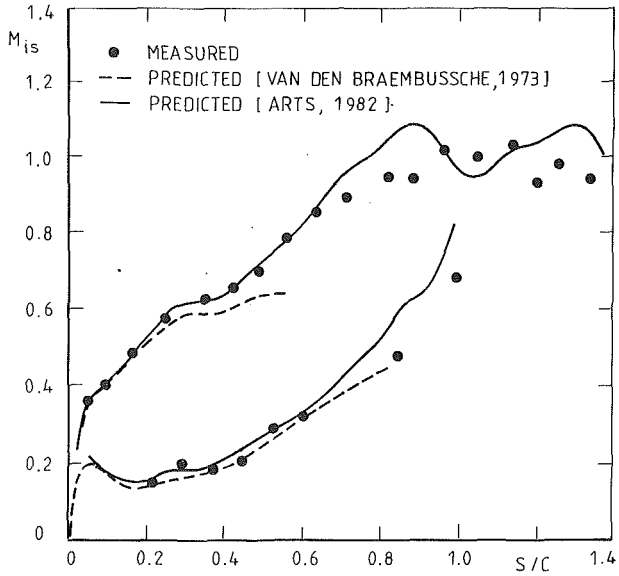

Fig. 3 Blade velocity distribution

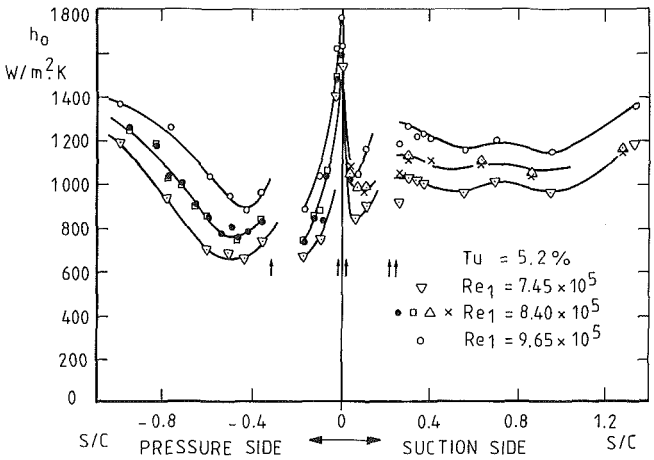

Fig. 4 Heat transfer distribution without film cooling: effect of Reynolds number

was calculated to be at $s/c = -0.019$ (on the pressure side), between rows *LM* and *LP*. This result suggested that the suction side boundary layer would be affected by rows *LM* and *LS* whereas the pressure side boundary layer would only be affected by row *LP*. This behavior was confirmed from the detailed heat transfer measurements conducted by Camci and Arts (1985a) around the leading edge.

4 Heat Transfer Without Film Cooling

The convective heat transfer coefficient distributions measured at zero incidence, and without any coolant emission, are shown in Fig. 4 for three free-stream Reynolds number (based on chord length and upstream conditions) values. Possible undesirable free-stream air recirculation was avoided by filling the three plenum chambers with flexible inserts. In the absence of the inserts, as was demonstrated from oil flow visualizations (Camci, 1985), free-stream air entered into the leading edge plenum through row *LM* and was ejected through rows *LS* and *LP*, influencing the local heat transfer rates. The same phenomenon was observed across the two suction side rows (*S*).

The highest wall heating rates were measured in the leading edge region; a detailed investigation of this area, without and with film cooling, was presented by Camci and Arts (1985a).

Downloaded 01 Jun 2010 to 171.66.16.66. Redistribution subject to ASME license or copyright; see http://www.asme.org/terms/Terms_Use.cfm

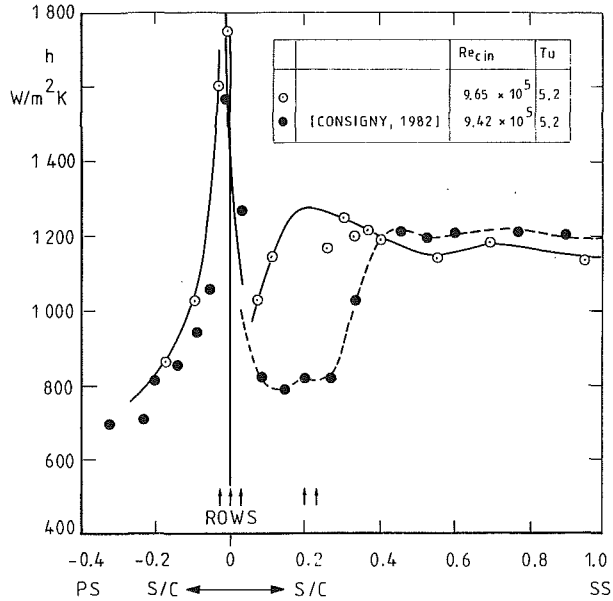

Fig. 5 Heat transfer distribution without film cooling: effect of cooling holes

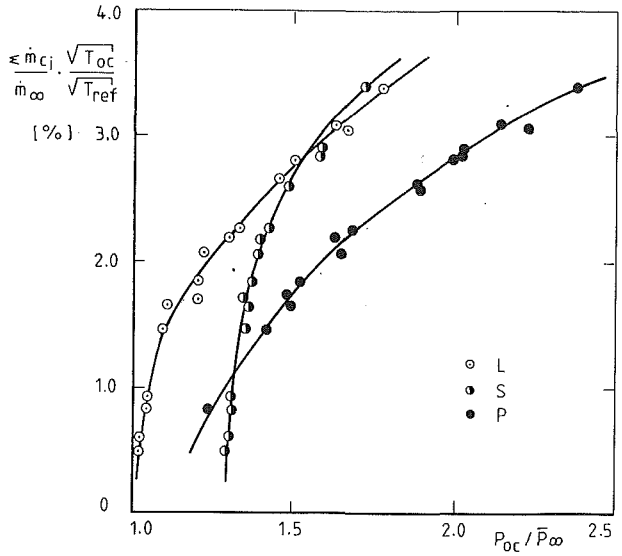

Fig. 6 Normalized total coolant mass flow rate

Figure 5 demonstrates a definite influence of the existence of rows *LM* and *LS* on the suction side boundary layer behavior between $s/c = 0.0$ and 0.22. The results from the present model (open symbols) were obtained without any coolant flow emission, the plenum cavities being filled with the inserts previously mentioned; the free-stream turbulence intensity was equal to 5.2 percent. The comparison between the present data and those obtained by Consigny and Richards (1982) (solid symbols) for the same turbulence intensity around an identical but smooth, undrilled blade, reveals indeed an earlier transition. Along the pressure side, an eventual tripping effect of row *LP* is not as obvious; similar heat transfer distributions were measured along the present blade and that of Consigny and Richards. As a matter of fact, the early pressure side boundary layer transition is principally due to the existence of the velocity peak and the curvature inversion.

The boundary layers developing along the suction and pressure surfaces are much thinner than the diameter of the emission holes. The boundary layer thickness, computed at the location of row *S* by means of a two-dimensional boundary layer program (Crawford et al., 1980) is about five times smaller than the hole diameter; this corresponds to a local value of the hole diameter to momentum thickness ratio equal to 43, representative of a real configuration. One direct consequence of this situation is that such a boundary layer most probably undergoes a local separation and reattachment over the rows of emission. This behavior is exemplified by the data scatter observed in Fig. 4 over rows *S* and *P*.

5 Coolant Flow Characteristics

5.1 Total Coolant Mass Flow Rate. The coolant flow across rows *S*, *L*(*S*, *M*, *P*), and *P* originated from a single reservoir through a heat exchanger providing the required coolant to free-stream temperature ratios. This implied that the total coolant mass flow rate $\Sigma\dot{m}_{ci}$, measured across a single choked orifice, was shared among the suction side, leading edge, and pressure side plenum chambers. The amount of coolant passing through each of these cavities had therefore to be calculated in order to evaluate local values of coolant to free-stream mass weight ratio and blowing rate. The first step was to establish a unique dependency between $\Sigma\dot{m}_{ci}$ and the local coolant to free-stream static pressure ratio (Fig. 6). A normalized overall mass weight ratio $(\Sigma\dot{m}_{ci}/\dot{m}_\infty)\,(T_{oc}/T_{\text{ref}})^{1/2}$ was therefore defined from $\Sigma\dot{m}_{ci}$, pressure and temperature measurements in each plenum, and free-stream static pressure at each row of emission; $\dot{m}_\infty$ is the free-stream mass flow through one blade passage. All the measurements were taken for three different values of the coolant to free-stream temperature ratio ($T_{oc}/T_{o_\infty} = 0.7$, 0.6, 0.5).

5.2 Discharge Coefficient. The second step was to determine local values of the discharge coefficient. Averaged values of this parameter were obtained (Fig. 7) at the location of rows *S*, *L* (*S*, *M*, *P*), and *P* from independent film cooling investigations performed by Camci and Arts (1985a, 1985b). Significant losses were observed across the leading edge holes compared to the two other emission sites. These values showed, nevertheless, qualitative agreement with data presented by Tillman et al. (1984), obtained in an incompressible flow (water tunnel) situation. The relatively low C_D values measured in the leading edge region were expected to occur because of the highly complicated nature of the coolant flow, with compound angle emission. Across the pressure and suction side rows, C_D values varied between 0.4 and 0.5.

5.3 Coolant Flow Distribution Among the Emission Rows. The third and final step was the quantitative determination of the coolant mass flow rate through each ejection site. It was obtained by combining data from Figs. 6 and 7. The coolant to free-stream static pressure ratio for each plenum was obtained from Fig. 6, knowing the measured total mass flow rate $\Sigma\dot{m}_{ci}$. The isentropic mass flow rate across the corresponding film cooling rows was then calculated. The application of the corresponding discharge coefficient values (Fig. 7) finally provided the three real mass flow rates, characterized by the parameter $\dot{m}_{ci}/\Sigma\dot{m}_{ci}$ (Fig. 8). For very low pressure ratios, the flow conditions were not well defined in the leading edge plenum and very low C_D values were responsible for quite low local mass flow rates. The cooling rows *S* and *P* then performed the largest percentage of the emission. However, for a typical value of the overall mass weight ratio ($\Sigma\dot{m}_{ci}/\dot{m}_\infty = 3$ percent), the coolant split was found to be 40 percent/35 percent/25 percent, respectively, through the leading edge, suction, and pressure side emission rows.

5.4 Local Blowing Rate Evolution. The local blowing rate variations (Fig. 9) were determined from the three emission mass flow rate distributions (Fig. 8), the corresponding emission surfaces (Fig. 1), and the local free-stream conditions

Downloaded 01 Jun 2010 to 171.66.16.66. Redistribution subject to ASME license or copyright; see http://www.asme.org/terms/Terms_Use.cfm

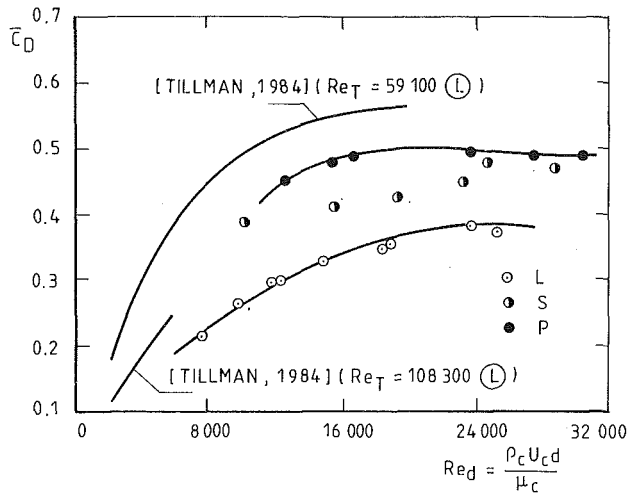

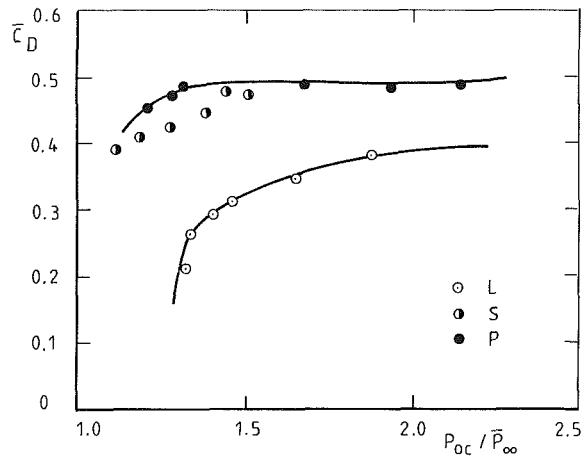

Fig. 7 Discharge coefficient distribution

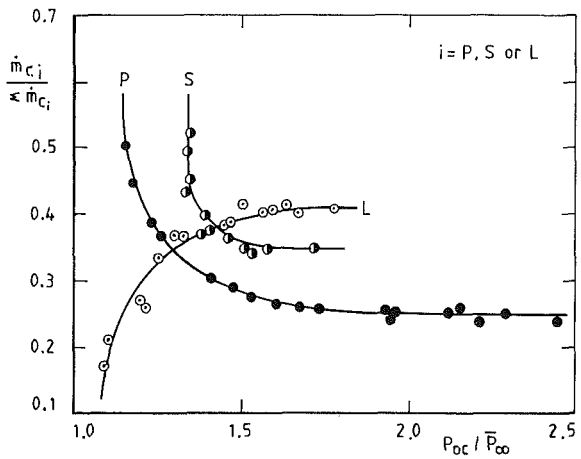

Fig. 8 Coolant flow distribution

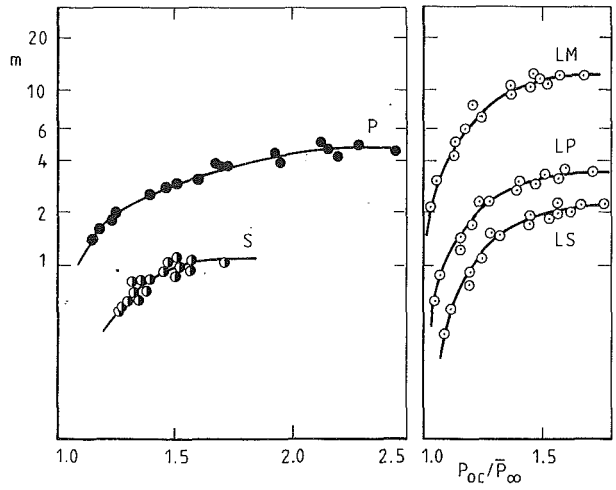

Fig. 9 Local blowing rate evolution

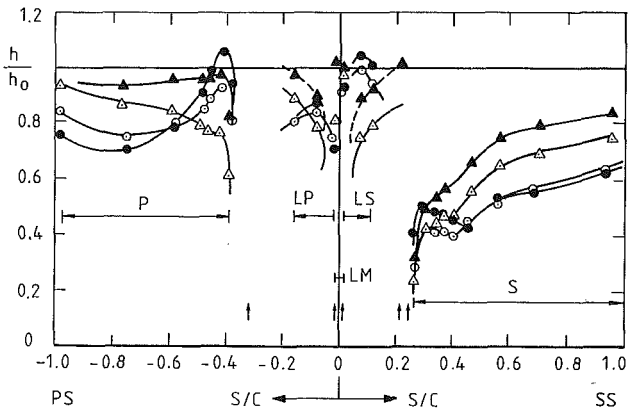

	$\Sigma \dot{m}_{ci}/\dot{m}_\infty$	$T_{oc}/T_{o\infty}$	m_p	m_{LP} / P^*	m_{LM} / P^*	m_{LS} / P^*	m_s
▲	0.50%	0.71	1.42	1.004	0.984	1.038	0.59
△	0.93%	0.71	1.94	1.022	1.002	1.056	0.62
⊙	2.07%	0.70	3.03	1.74 / 1.21	5.98 / 1.19	1.11 / 1.25	0.72
●	3.09%	0.70	4.17	3.20 / 1.58	11.0 / 1.55	2.05 / 1.63	0.93

$P^* = P_{oc}/\bar{P}_\infty$

Fig. 10 Heat transfer distribution with film cooling: effect of overall mass weight ratio

(Fig. 3). The data of Fig. 9 are representative for three different coolant to free-stream total temperature ratios ($T_{oc}/T_{c_\infty} = 0.7$, 0.6, and 0.5). The scatter is mainly due to the measurement difficulties associated with the lowest temperature ratio ($T_{oc}/T_{o_\infty} = 0.5$; $T_{oc} \cong 200$ K).

6 Heat Transfer With Film Cooling

The heat transfer measurement with film cooling were performed for constant values of the downstream Reynolds (2.32×10^6; based on chord length and downstream isentropic conditions) and isentropic Mach (0.92) numbers. The overall mass weight ratio ($\Sigma \dot{m}_{ci}/\dot{m}_\infty$) was varied between 0.5 and 3.3 percent and coolant to free-stream temperature ratios (T_{oc}/T_{o_∞}) ranging between 0.51 and 0.70 were considered.

6.1 Effect of Overall Mass Weight Ratio. The results presented in this section were obtained for a coolant to free-stream temperature ratio equal to 0.70. The effect of overall mass weight ratio variations is demonstrated in Fig. 10. Downstream of row *LS*, the heat transfer coefficient distribution was observed to be quite smooth for low values of $\Sigma \dot{m}_{ci}/\dot{m}_\infty$ (0.50, . . . , 0.93 percent). As expected, increasing values of the mass weight ratio resulted in lower wall convective heat fluxes. For higher values (2.07, . . . , 3.09 percent) however, a continuously increasing heat transfer coefficient was measured around $s/c = 0.08$. This behavior was explained by the higher blowing rate values (up to 2.05) observed along this highly curved surface; the effect of the coolant film was

Downloaded 01 Jun 2010 to 171.66.16.66. Redistribution subject to ASME license or copyright; see http://www.asme.org/terms/Terms_Use.cfm

more to augment the local free-stream turbulence, and hence heat transfer in this not yet fully turbulent region, than to protect the surface efficiently.

Downstream of row *LP*, similar behavior was observed for the different values of the overall mass weight ratio. An additional effect might be due to the existence of the pressure side curvature inversion; the latter induced the reattachment ($s/c = -0.16$) of the coolant layers, separated from the wall at the high blowing rate values.

Downstream of row *S*, different phenomena were identified. For low values of $\Sigma\dot{m}_{ci}/\dot{m}_\infty$ (0.5, . . . , 0.93 percent), significant difference was observed in heat flux levels, although the row *S* blowing rate variation was rather limited (0.59, . . . , 0.62). This behavior was explained by a cumulative effect, due to the additional contribution of the leading edge films (rows *LM*+*LS*), more effective for the highest value of the overall mass weight ratio (0.93 percent). For even higher values (2.07, . . . , 3.09 percent), a more and more significant heat transfer coefficient increase was measured downstream of row *S*. This phenomenon, due to the strong jet/mainstream interaction, was spread over a length equal to almost 30 film-cooling hole diameters. No significant differences were observed farther downstream.

Downstream of row *P*, two regions had to be considered. Just downstream of the cooling holes, the heat transfer coefficient first decreased with increasing overall mass weight ratio (0.5, . . . , 0.93 percent). For higher values (2.07, . . . , 3.09 percent) the classical heat transfer augmentation took place. Farther downstream, on the contrary, the lowest heat transfer coefficient values were observed for the highest values of $\Sigma\dot{m}_{ci}/\dot{m}_\infty$. This was most probably due to the concave nature of the wall; the free-stream pressed the separated jets back to the wall.

6.2 Effect of Coolant to Free-Stream Temperature Ratio. Values of the coolant to free-stream temperature ratio as low as 0.5 are most usually observed in advanced aero-engines. In order to identify the effect of this important parameter, measurements were taken for three different values (0.7, 0.56, and 0.51), while $\Sigma\dot{m}_{ci}/\dot{m}_\infty$ was maintained at a constant value of about 3.1 percent. The results presented in Fig. 11 were obtained.

As obviously expected, significant heat transfer coefficient reductions were obtained when lowering the coolant temperature. The only exception was observed along the suction side front part, just downstream of row *LS*. This phenomenon was explained by the very high local blowing rate value, causing a separation of the coolant film. Just downstream of rows *P*, *LP*, and *S*, although local blowing rates were maintained at constant values, the importance of the wall heat flux augmentation identified in the preceding paragraph decreased with T_{oc}. As a matter of fact, a decrease of the temperature ratio (T_{oc}/T_{o_∞}) results in an increase of the density ratio (ρ_c/ρ_∞) and hence, for a constant blowing rate, a decrease of the velocity ratio (u_c/u_∞) and moreover of the momentum ratio ($\rho_c u_c^2/\rho_\infty u_\infty^2$). The penetration of a "colder" film in the boundary layer was thus less severe; in other words, the turbulence augmentation just downstream of these film cooling rows was less important.

6.3 Effect of Free-Stream Turbulence Intensity. The effect of free-stream turbulence was also investigated in the presence of film cooling (Fig. 12). The turbulence level was varied from 0.8 to 5.2 percent while maintaining almost constant values of $\Sigma\dot{m}_{ci}/\dot{m}_\infty$ (~2.5 percent) and T_{oc}/T_{o_∞} (~0.5). The values of h and h_o plotted in Fig. 12 were obtained for equal values of the turbulence intensity. No significant changes in the wall heat flux were observed when varying *Tu*. As a matter of fact, this behavior was expected because of the dominant effect of the coolant flow (almost a new boundary layer) just downstream of the emission rows and of the turbulent nature of the boundary layers developing along the suction and pressure surfaces.

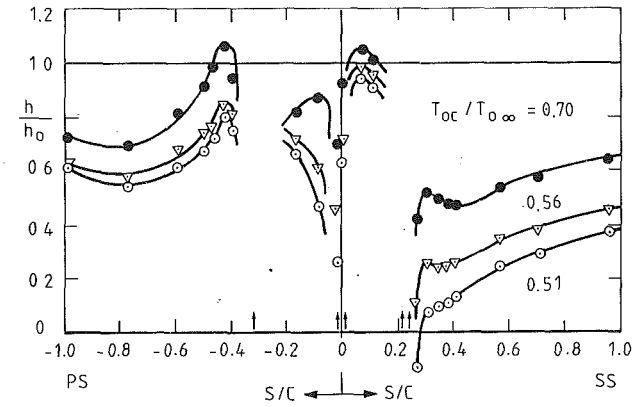

	$\frac{\Sigma\dot{m}_{ci}}{\dot{m}_\infty}$	T_{oc}/T_{o_∞}	m_p	m_{LP} / p^*	m_{LM} / p^*	m_{LM} / p^*	m_s
●	3.09%	0.70	4.17	3.20 / 1.58	11.0 / 1.55	2.05 / 1.63	0.93
▽	3.32%	0.56	4.67	3.36 / 1.53	11.5 / 4.50	2.15 / 1.58	0.99
⊙	3.12%	0.51	4.37	3.02 / 1.41	10.4 / 1.38	1.93 / 1.46	0.98

$P^* = P_{oc}/\bar{P}_\infty$

Fig. 11 Heat transfer distribution with film cooling: effect of temperature ratio

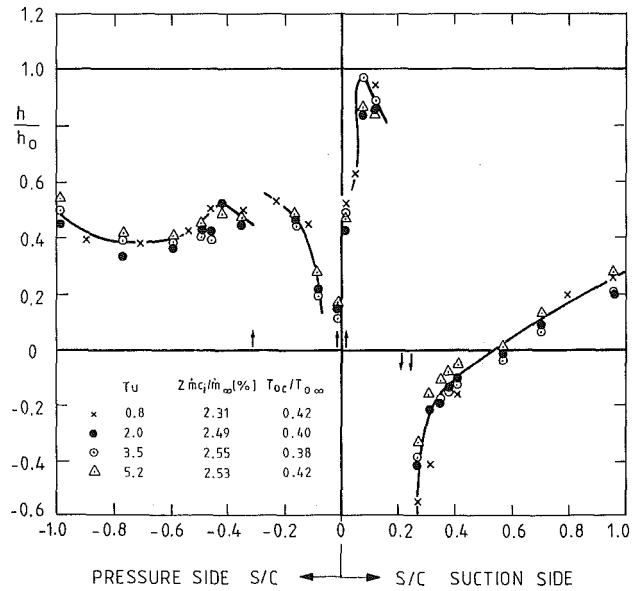

Fig. 12 Heat transfer distribution with film cooling: effect of turbulence intensity

7 Conclusions

Detailed convective heat transfer measurements were obtained for a high-pressure, film-cooled rotor blade mounted in a stationary cascade arrangement and submitted to correctly simulated aero-engine conditions (Mach and Reynolds numbers as well as temperature ratios). The effects of overall mass weight ratio, coolant to free-stream temperature ratio, and free-stream turbulence intensity were successively investigated.

Downloaded 01 Jun 2010 to 171.66.16.66. Redistribution subject to ASME license or copyright; see http://www.asme.org/terms/Terms_Use.cfm

The main conclusions of this investigation are:

- In the absence of coolant emission, the suction side boundary layer was dominated by the existence of the leading edge film cooling holes, while the pressure side boundary layer behavior was dominated by the free-stream pressure gradient. Moreover, the influence of free-stream turbulence on the heat transfer coefficient distribution was extremely limited;
- film cooling around the leading edge proved to be quite effective for low overall mass weight ratio values. The same conclustion was drawn downstream of rows S and P. For higher values of $\Sigma \dot{m}_{ci}/\dot{m}_{\infty}$, increases in local heat transfer were measured just downstream of the various film cooling rows;
- the convective heat transfer coefficient distribution proved to be strongly dependent on the coolant to free-stream temperature ratio; no significant effect of free-stream turbulence was identified.

References

Arts, T., 1982, "Cascade Flow Calculation Using a Finite Volume Method," in: *Numerical Methods for Flow in Turbomachinery*, von Karman Institute Lecture Series, 1982-05.

Camci, C., and Arts, T., 1985, "Experimental Heat Transfer Investigation Around the Film-Cooled Leading Edge of a High-Pressure Gas Turbine Rotor Blade," ASME *Journal of Engineering for Gas Turbines and Power*, Vol. 107, No. 4, pp. 1016–1021.

Camci, C., and Arts, T., 1985, "Short Duration Measurements and Numerical Simulation of Heat Transfer Along the Suction Side of a Film-Cooled Turbine Blade," ASME *Journal of Engineering for Gas Turbines and Power*, Vol. 107, No. 4, pp. 991–997.

Camci, C., 1985, "An Experimental and Theoretical Heat Transfer Investigation of Film Cooling on a High Pressure Gas Turbine Blade," Ph.D. Thesis, Katholieke Universiteit Leuven, Belgium.

Consigny, H., and Richards, B. E., 1982, "Short Duration Measurements of Heat Transfer Rate to a Gas Turbine Blade," ASME *Journal of Engineering for Power*, Vol. 104, No. 3, pp. 542–551.

Crawford, M. E., Kays, W. M., and Moffat, R. J., 1980, "Full Coverage Film Cooling. Part II: Heat Transfer Data and Numerical Simulation," ASME *Journal of Engineering for Power*, Vol. 102, No. 4, pp. 1006–1012.

Daniels, L. C., 1979, "Film Cooling of Gas Turbine Blades," Ph.D. Thesis, University of Oxford, United Kingdom.

Dring, R. P., Blair, M. F., and Joslyn, H. D., 1980, "An Experimental Investigation of Film Cooling on a Turbine Rotor Blade," ASME *Journal of Engineering for Power*, Vol. 102, No. 1, pp. 81–87.

Horton, F. G., Schultz, D. L., and Forest, A. E., 1985, "Heat Transfer Measurements With Film Cooling on a Turbine Blade Profile in Cascade," ASME Paper No. 85-GT-117.

Ito, S., Goldstein, R. J., and Eckert, E. R. G., 1978, "Film Cooling of a Gas Turbine Blade," ASME *Journal of Engineering for Power*, Vol. 100, pp. 476–481.

Jones, T. V., Schultz, D. L., and Hendley, A. D., 1973, "On the Flow in an Isentropic Free Piston Tunnel," ARC R&M 3731.

Lander, R. D., Fish, R. W., and Suo, M., 1972, "External Heat Transfer Distribution of Film Cooled Turbine Vanes," *Journal of Aircraft*, Vol. 9, No. 10, pp. 707–714.

Nicolas, J., and Le Meur, A., 1974, "Curvature Effects on a Turbine Blade Cooling Film," ASME Paper No. 74-GT-156.

Olsson, U., 1982, "Advanced Engine Technology and Its Influence on Aircraft Performance," *Journal of Aircraft*, Vol. 19, No. 5, pp. 380–384.

Richards, B. E., 1980, "Heat Transfer Measurements Related to Hot Turbine Components in the von Karman Institute Hot Cascade Tunnel," in: *Testing and Measurement Techniques in Heat Transfer and Combustion*, AGARD CP 281, Paper 6.

Schultz, D. L., and Jones, T. V., 1973, "Heat Transfer Measurements in Short Duration Hypersonic Facilities," AGARDograph 165.

Schultz, D. L., Jones, T. V., Oldfield, M. L. G., and Daniels, L. C., 1977, "A New Transient Facility for the Measurement of Heat Transfer Rates," in: *High Temperature Problems in Gas Turbine Engines*," AGARD CP 229, Paper 31.

Tillman, E. S., Hartel, E. L., and Jen, H. F., 1984, "The Prediction of Flow Through Leading Edge Holes in a Film Cooled Airfoil With and Without Inserts," ASME Paper No. 84-GT-4.

Van Den Braembussche, R., 1973, "Calculation of Compressible Subsonic Flow in Cascades With Varying Blade Height," ASME *Journal of Engineering for Power*, Vol. 95, No. 4, pp. 345–351.

Downloaded 01 Jun 2010 to 171.66.16.66. Redistribution subject to ASME license or copyright; see http://www.asme.org/terms/Terms_Use.cfm

Prediction of Heat Transfer Characteristics for Discrete Hole Film Cooling for Turbine Blade Applications

D. K. Tafti
Assistant Professor,
Department of Mechanical Engineering,
West Virginia Institute of Technology,
Montgomery, WV 25136

S. Yavuzkurt
Associate Professor,
Mechanical Engineering Department,
The Pennsylvania State University,
University Park, PA 16802
Mem. ASME

A two-dimensional injection model is used with a two-dimensional low Reynolds number k–ϵ model boundary layer code. The three-dimensional effects of the discrete hole injection process are introduced in the two-dimensional prediction scheme through an "entrainment fraction" (ϒ). An established correlation between ϒ and the injection parameters obtained in a previous paper is used to predict the film cooling effectiveness ($\bar{\eta}$) and heat transfer coefficients for multirow injection, injection into a laminar boundary layer, and finally injection on convex curved surfaces. Predictions of $\bar{\eta}$ are in good agreement with experimental data for most of the cases tested. Predictions of Stanton numbers defined by St(0) and St(1) are good for low injection ratios (M) but as M increases the values are underpredicted. In spite of some shortcomings, in the authors' opinion the present two-dimensional prediction scheme is one of the most comprehensive developed so far. It is seen that the entrainment fraction ϒ is quite universal in its application to two-dimensional predictions of the discrete hole film cooling process.

Introduction

Discrete hole film cooling is used extensively on turbine blades to protect the blade surface from high combustor gas temperatures. Jets of cooler compressor air are injected into the external boundary layer to form a blanket between the hot mainstream gases and the blade surface. The injected fluid mixes with the boundary layer fluid and lowers the temperature near the blade surface. A typical three-dimensional injection geometry is shown in Fig. 1.

To measure the overall effectiveness of the film cooling process, two approaches are used, both of which are based on the linearity of the energy equation. In one (Goldstein, 1971), the wall heat flux is defined and the film cooling process is characterized by

$$\bar{\eta} = \frac{T_{aw} - T_e}{T_j - T_e} \tag{1}$$

$$h_f = \frac{q_w}{T_w - T_{aw}} \tag{2}$$

where $\bar{\eta}$ is the spanwise-averaged effectiveness and h_f is the heat transfer coefficient. By definition h_f and $\bar{\eta}$ are functions of the flow field and independent of T_j. In the other method (Choe et al., 1976), T_w is defined along with a nondimensional jet temperature $\theta = (T_j - T_e)/(T_w - T_e)$. Using the linearity of the energy equation the Stanton number (St) for an arbitrary θ can be written as

$$\mathrm{St}(\theta) = \mathrm{St}(\theta = 0) + \theta \{\mathrm{St}(\theta = 1) - \mathrm{St}(\theta = 0)\} \tag{3}$$

and the effectiveness can be obtained as follows:

$$\bar{\eta} = \frac{\mathrm{St}(0) - \mathrm{St}(1)}{\mathrm{St}(0)} \tag{4}$$

The process of film cooling, besides being affected by the injection geometry (α_0, β, p, s, d) and the injection ratio (M), is also affected by (*a*) the state of the approach boundary layer, i.e., whether the boundary layer is laminar or turbulent; (*b*) the hydrodynamic state of the injected fluid; (*c*) free-stream pressure gradients and turbulent intensity; (*d*) surface curvature; and (*e*) rotational effects. Typically, in flow over a turbine blade all these effects are present and the three-dimensional flow field is quite complex.

The effects of injection geometry and injection ratio have been experimentally investigated by a number of workers. Ramsey and Goldstein (1971), and Eriksen and Goldstein (1971, 1974), investigated the effect of M and α_o on jet trajectory and spread. Kruse and Metzinger (1984) did a systematic study on the effect of M, α_o, and p/d on the spanwise-averaged effectiveness ($\bar{\eta}$). In general an increase in M and α_o increased the jet penetration into the boundary layer and lowered $\bar{\eta}$. Goldstein et al. (1974) studied the effect of hole geometry, density ratio (ρ_j/ρ_e), and boundary layer thickness on $\bar{\eta}$. Again,

Contributed by the International Gas Turbine Institute and presented at the 34th International Gas Turbine and Aeroengine Congress and Exhibition, Toronto, Ontario, Canada, June 4–8, 1989. Manuscript received at ASME Headquarters January 23, 1989. Paper No. 89-GT-139.

Copyright © 1990 by ASME
Downloaded 01 Jun 2010 to 171.66.16.66. Redistribution subject to ASME license or copyright; see http://www.asme.org/terms/Terms_Use.cfm

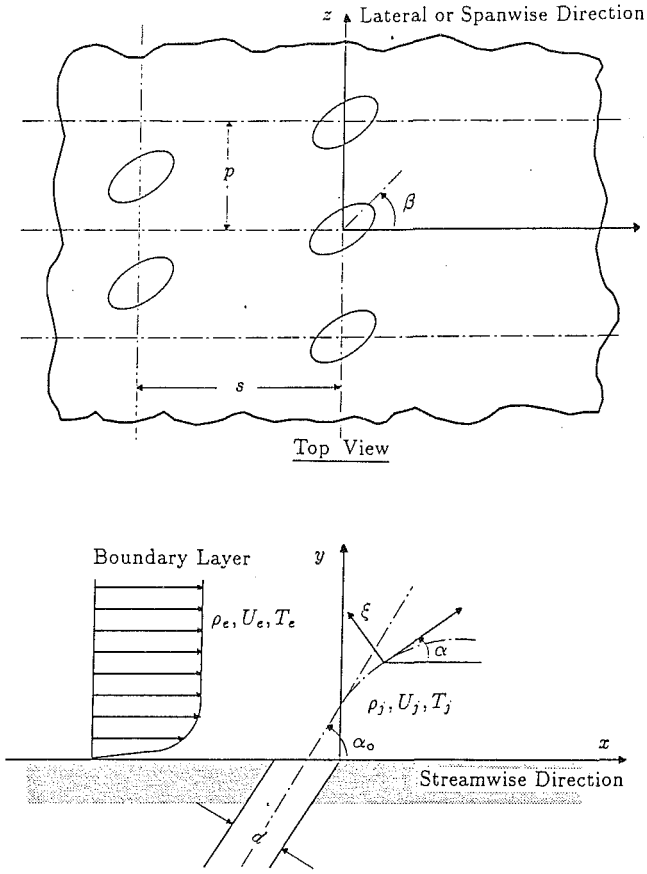

Fig. 1 Three-dimensional discrete hole injection geometry

all three factors directly influenced the jet penetration and $\bar{\eta}$. Goldstein and Yoshida (1981) investigated the effect of laminar and turbulent injection into a laminar and turbulent approach boundary layer on $\bar{\eta}$ and h_f. They found that laminar jets detached from the surface earlier than turbulent jets and a maximum in $\bar{\eta}$ occurred at a lower M.

Jubran and Brown (1985) measured $\bar{\eta}$ for two rows of injection with and without free-stream turbulence. The increased turbulence did not have any effect on $\bar{\eta}$ near the injection location but considerably decreased $\bar{\eta}$ downstream of injection. Kadotani (1975) and Jabbari (1973) investigated the effect of free-stream pressure gradient ($K=(\nu/U_e^2)\ dU_e/dx=0,\ 0.4\times10^{-6},\ 1.0\times10^{-6}$) on $\bar{\eta}$ and h_f for one and two rows of injection, respectively. The pressure gradient affected the lateral distribution of effectiveness but it did not affect the spanwise-averaged effectiveness ($\bar{\eta}$) to a large extent.

Ito (1976) investigated the effect of convex and concave surface curvature on $\bar{\eta}$. Furuhama et al. (1983) did an experimental study of injection into a turbulent boundary layer on a convex curved surface for 2, 4, 6, and 13 rows of injection. They measured the Stanton numbers St(0) and St(1). Liess (1974) investigated the effect of Mach number, displacement thickness (∂^*), and pressure gradient on $\bar{\eta}$. The Mach number ($M=0.3$–0.9) did not affect $\bar{\eta}$, although a favorable pressure gradient considerably reduced $\bar{\eta}$. For $\partial_o^*/d>0.2$ there was a considerable decrease in $\bar{\eta}$.

In the computational field most of the three-dimensional prediction schemes have used the k–ϵ model of turbulence. Bergeles et al. (1978) used a partially parabolic three-dimensional Navier–Stokes solver to predict the velocity and temperature field for a single jet in crossflow. They obtained good predictions for relative low M and α_o. Demuren et al. (1985) employed a three-dimensional locally elliptic solver for a wide range of injection geometries. The predictions of $\bar{\eta}$ were not very good in the near field ($x/d\leq5\sim10$) and for large p/d ratios ($p/d=0.5$). Although three-dimensional prediction schemes have been relatively successful in capturing the overall features of the flow field, the mapping of the computational domain requires 20,000 to 40,000 grid nodes and takes 30 to 90 min of computer time (Demuren et al., 1985). If we consider the number of independent parameters in film cooling studies a considerable amount of time and effort have to be spent in doing an optimization study.

On the other hand a two-dimensional boundary layer code

Nomenclature

C_n = aerodynamic drag coefficient on jet
d = diameter of injection hole
h_o = heat transfer coefficient without injection $=q_w/(T_w-T_e)$
h_f = film cooling heat transfer coefficient $=q_w/(T_w-T_{aw})$
I^* = total enthalpy
k = turbulent kinetic energy $=(\bar{u}^2+\bar{v}^2+\bar{w}^2)/2$
L = momentum ratio $=\rho_j U_j^2/\rho_e U_e^2$
M = injection ratio $=\rho_j U_j/\rho_e U_e$
$\dot{m}$ = rate of mass flow
p = pitch = distance between injection holes in z direction
R = radius of curvature of wall
q = heat flux
s = distance between injection rows in x direction
St = Stanton number $=h/(\rho_e U_e C_p)$
T = temperature
U, V, W = mean velocities in x, y, and z directions
u, v, w = fluctuating velocities in x, y, and z directions
$\overline{uv}$ = Reynolds shear stress
U_j = mean velocity of discrete jet
x, y, z = streamwise, cross-stream, and lateral coordinates; origin of x is at downstream edge of injection row
α = inclination of jet axis with horizontal
α_o = angle made by injection hole axis with horizontal
β = angle made by horizontal projection of the injection hole axis with x direction
∂ = boundary layer thickness (defined at $U=0.99\ U_e$)
∂^* = boundary layer displacement thickness
ϵ = rate of dissipation of turbulent kinetic energy
$\bar{\eta}$ = spanwise-averaged film cooling effectiveness $=(T_{aw}-T_e)/(T_j-T_e)$
θ = nondimensional jet temperature $=(T_j-T_e)/(T_w-T_e)$
ξ = jet coordinate orthogonal to jet trajectory
ρ = density
Υ = entrainment fraction

Subscripts

aw = adiabatic wall
$c.l.$ = two-dimensional equivalent jet centerline
e = pertaining to local free-stream condition
j = pertaining to injected jet
jet = pertaining to two-dimensional equivalent jet
o = at injection location
w = at wall

Downloaded 01 Jun 2010 to 171.66.16.66. Redistribution subject to ASME license or copyright; see http://www.asme.org/terms/Terms_Use.cfm

can give a relatively quick and accurate estimate of performance parameters like $\bar{\eta}$ and heat transfer coefficients. A two-dimensional prediction scheme is particularly advantageous when dealing with shaped holes and multirow injection where the implementation of a three-dimensional prediction scheme would be quite tedious. Until recently the only two-dimensional prediction scheme available was that developed by Crawford et al. (1976). This method has evolved over a period of time and it is based on the use of an "augmented mixing length" to simulate the injection process. Although this method has been fairly successful in predicting St numbers for full coverage film cooling and $\bar{\eta}$ (Miller and Crawford, 1984) for one and two-row injection, two constants have to be tuned for each prediction run. Recently Schonung and Rodi (1987) developed a prediction scheme using the low Reynolds number version of the k–ϵ model of turbulence. The effects of injection are introduced through an "injection model," and additional "dispersion terms" in the governing equations account for the effects of three-dimensional entrainment. The method uses 15 empirical constants derived from three-dimensional predictions (Demuren et al., 1985) and is quite successful in predicting $\bar{\eta}$ for one row of injection.

The present authors (Tafti and Yavuzkurt, 1988) developed an injection model and used it with a low Reynolds number k–ϵ model boundary layer code. The effect of three-dimensional entrainment is introduced in the two-dimensional prediction scheme by using an "entrainment fraction" and an "entrainment enthalpy." The entrainment fraction is correlated to the injection parameters (M, p/d, s/d, etc.) by comparing predictions of $\bar{\eta}$ to experimental data for one row of injection into a turbulent boundary layer (Tafti and Yavuzkurt, 1987). It was found that this relatively simple model (compared to other prediction schemes) worked very well for a wide range of injection geometries and injection ratios.

The objective of the present paper is to extend the prediction scheme developed by Tafti and Yavuzkurt (1988) to (1) multirow injection geometries; (2) injection into a laminar boundary layer; (3) injection on convex curved surfaces; and (4) injection on a turbine blade. Predictions of $\bar{\eta}$, St(0), and St(1) are compared with experimental data. In the following section a brief outline of the prediction scheme developed by Tafti and Yavuzkurt (1988) is given. The results and discussion section discuss the results obtained for each case outlined in the objectives. This is followed by concluding remarks about the overall effectiveness of the prediction scheme. In most of the test that follows mathematical symbols are used to conserve space.

Theory

Conversation Equations. The governing boundary layer equations are outlined by Wang et al. (1984) along with the initial and boundary conditions. The Reynolds stress terms in the x-momentum equation and the turbulent heat transfer term in the energy equation are modeled using the Jones and Launder (1973), low Reynolds number k–ϵ model. In the absence of a given initial experimental velocity profile, a 1/7th power law is used for a turbulent boundary layer and the Blasius profile for a laminar boundary layer. At the surface ($y=0$) the boundary conditions are $U=k=\epsilon=0$. For $\bar{\eta}$ calculations the wall heat flux (q_w) is set equal to zero. For calculating St(0) and St(1) the wall temperature (T_w) is specified. For most of the calculations made, 100–120 grid nodes are used across the calculation domain with a grid expansion ratio of 1.03 to 1.02. The injected jet mass is resolved within 2 percent of its total mass. For multirow injection the boundary layer thickness increases substantially at each injection location, and the number of nodes in the region where the jet is injected decrease. To overcome this problem the boundary layer code is provided with the capability to increase the number of grid nodes in the region the jet is injected, if the number of nodes in this region falls below 21.

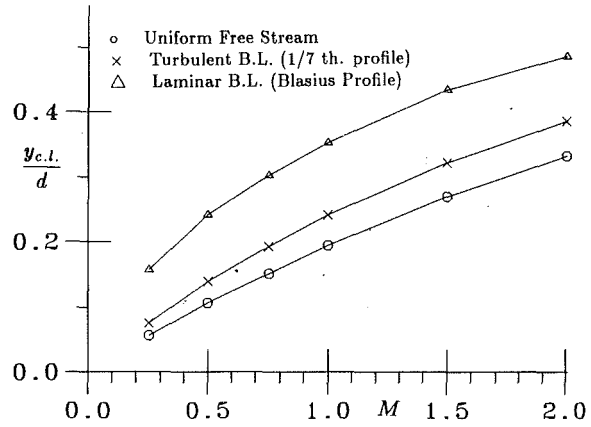

Fig. 2 Relative variation of jet centerline with injection ratio for injection into a uniform external flow, a turbulent boundary layer and a laminar boundary layer ($\alpha_o = 45$ deg, $p/d = 3$, $C_n = 10$)

Injection Model. The injection model approximates the three-dimensional process in a two-dimensional framework (Tafti and Yavuzkurt, 1988). Each time an injection row is encountered the two-dimensional equivalent jet is placed at the downstream edge of the injection row. The jet velocity profile is of the form

$$\frac{U_{\text{jet}}}{U_{c.l.}} = \left\{1 - \left(\frac{9}{10}\frac{\xi}{\xi^*}\right)^{3/2}\right\}^2 \tag{5}$$

where $U_{c.l.} = 1.43\ U_j$ and $\xi^* = 0.7\pi d/(4p/d)$. The two-dimensional jet temperature profile is assumed to be uniform and equal to the jet temperature ($T_{\text{jet}} = T_j$). The equation describing the jet trajectory is of the form

$$\frac{y_{c.l.}}{d} = \frac{2}{k_n}\left\{\left(k_n\frac{x}{d} + \cot^2\alpha_o\right)^{1/2} - \cot\ \alpha_o\right\} \tag{6}$$

where k_n is a function of the injection geometry and is given by

$$k_n = \frac{4C_n\dfrac{p}{d}\rho_j}{\pi M_{\text{eff}}^2\ \rho_e \sin\ \alpha_o} \tag{7}$$

In equation (6), x is measured from the center of the injection row.

A value for the aerodynamic drag coefficient $C_n = 10$ is obtained by computer optimization of $\bar{\eta}$ predictions for one row of injection. M_{eff} is defined as an effective injection ratio and is given by

$$M_{\text{eff}} = M\frac{(\rho U)_e}{(\rho U)_{ej}} \tag{8}$$

where $(\rho U)_{ej}$ is the mass-averaged velocity as seen by the jet. M_{eff} accounts for the shape of the boundary layer velocity profile (momentum defect) near the wall where the jet is injected. The experimental evidence of Goldstein and Yoshida (1981) suggests that the greater the momentum defect near the wall compared to a uniform flow, the further the jet penetrates into the boundary layer. Figure 2 based on equation (6) shows the relative penetration of the jet into a uniform flow, a turbulent and a laminar boundary layer. The jet penetrates much more into the laminar boundary layer due to the larger momentum defect near the wall. Also the presence of the density ratio (ρ_j/ρ_e) in equations (7) and (8) accounts for its effect on jet penetration. After determining the velocity and temperature profile of the two-dimensional equivalent jet, the jet centerline is placed at a distance $y_{c.l.}$, from the wall at the downstream

Downloaded 01 Jun 2010 to 171.66.16.66. Redistribution subject to ASME license or copyright; see http://www.asme.org/terms/Terms_Use.cfm

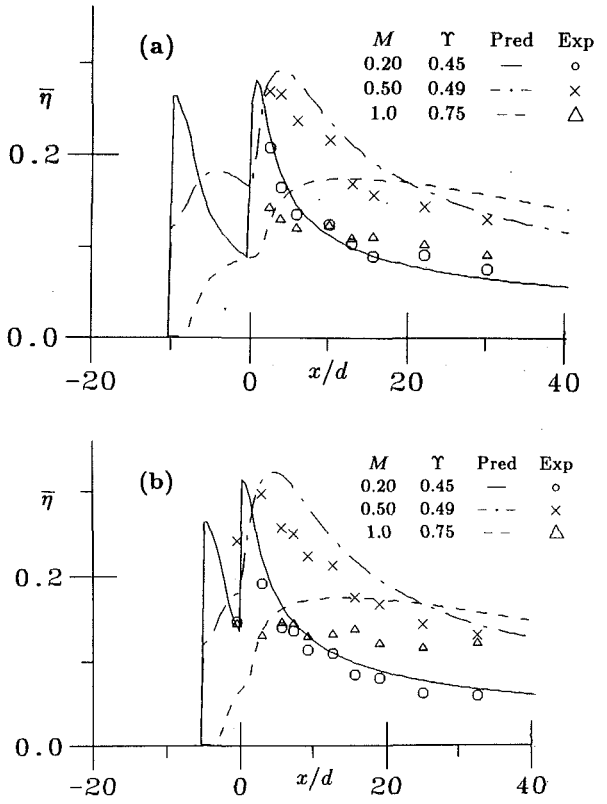

Fig. 3 Predictions of $\bar{\eta}$ for two-row injection into a turbulent boundary layer for the experiments of Jubran and Brown (1985): $\rho_j/\rho_e = 1.10$, $\alpha_o = 30$ deg, $p/d = 5.4$, $C_n = 10$; (*a*) $s/d = 10.0$ (*b*) $s/d = 5.0$

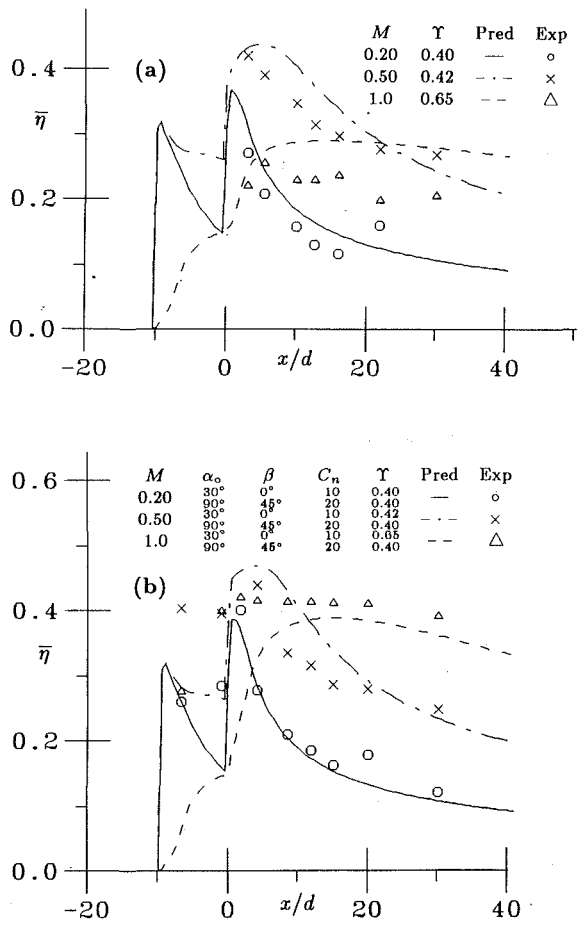

Fig. 4 Predictions of $\bar{\eta}$ for two-row injection into a turbulent boundary-layer for the experiments of Jubran and Brown (1985); (*a*) streamwise injection, $\rho_j/\rho_e = 1.10$, $\alpha_o = 30$ deg, $p/d = 3.0$, $s/d = 10.0$, $C_n = 10$; (*b*) compound angle injection, $\rho_j/\rho_e = 1.10$, $p/d = 3.0$, $s/d = 10.0$

edge of the injection row. The effect of injection on the boundary layer is introduced by conserving mass, momentum, and energy of the jet and the boundary layer in each streamtube, after each row of injection. In order to account for the effect of three-dimensional entrainment on the temperature profile, the energy conservation equation takes the form

$$\dot{m}_{\text{new}_i} I^*_{\text{new}_i} = \dot{m}_{\text{old}_i} I^*_{\text{old}_i} + \dot{m}_{\text{jet}_i} I^*_{\text{jet}_i} + \Upsilon \dot{m}_{\text{jet}_i} (I^*_{\text{ent}} - I^*_{\text{jet}_i}) \qquad (9)$$

where Υ is defined as the "entrainment fraction" and I^*_{ent} is the entrainment enthalpy." Υ is correlated to injection parameters (Tafti and Yavuzkurt, 1987). The resultant functional dependence is obtained from data for one row of injection into a turbulent boundary layer. For low injection ratios the injected jet is attached to the surface and Υ is nearly a constant (entrainment is mostly due to turbulent diffusion in the lateral direction). For high injection ratios the jet detaches from the surface and a low-pressure zone is formed in the wake of the jet. This causes boundary layer fluid to rush into this region and some of it is entrained by the jet. The p/d ratio determines the degree of three dimensionality of the injection geometry. For $p/d = 1.5$ (small distance between jets) the jets merge into each other immediately after injection, and the three-dimensional entrainment is more dependent on the two dimensionality of the flow field than the injection ratio. I^*_{ent} is calculated by averaging the enthalpy of the approach boundary layer from the wall to the outer edge of the jet (Tafti and Yavuzkurt, 1988). This method of calculating the entrainment enthalpy takes into account the effects of injection from previous rows.

Results and Discussion

Two Rows of Injection Into a Turbulent Boundary Layer. The data sets of Jubran and Brown (1985), and Jabbari (1973) are chosen and compared with the predictions of $\bar{\eta}$. The fundamental difference between these two data sets is the proximity of the two rows (s/d ratio). Jubran and Brown use $s/d \geqq 5$; in Jabbari's experimental setup, $s/d = 2.6$. The experimental conditions of Jubran and Brown (1985) are: $d = 0.0194$ m, $\alpha_o = 30$ deg, $p/d = 3.0$ and 5.4, $s/d = 5$ and 10, $U_e = 10.0$ m/s, $\delta^*_o/d = 0.077$, and $\rho_j/\rho_e = 1.10$. Predictions of $\bar{\eta}$ for different geometries are shown in Figs. 3 and 4 for $M = 0.2$, 0.5, and 1.0. For $M = 0.2$ and 0.5 the predictions are in very good agreement with the experimental values. For $M = 1.0$ the predicted values of $\bar{\eta}$ are overpredicted, particularly for $p/d = 5.4$ in Fig. 3. This could be because the values of Υ used for these predictions were derived from three-dimensional predictions of Demuren et al. (1985). Due to inaccuracies present in the three-dimensional prediction scheme for high p/d ratios (Demuren et al., 1985) the values of Υ may not be very accurate representations of the actual entrainment process.

Figure 4(*b*) shows the effect of compound angle injection where the second row is injected at an angle to the free-stream direction ($\beta = 45$ deg). When the jet is injected in such a manner, more of the jet areas is exposed to the oncoming stream, resulting in a higher aerodynamic force. This results in lower jet penetration and faster lateral dispersion when compared to streamwise injection, particularly at high injection ratios. The effect of compound injection on $\bar{\eta}$ is not so pronounced at low injection ratios but has a very positive effect on $\bar{\eta}$ as injection ratio increases. Unfortunately, not many data sets are available in the literature for a systematic study of this process. In the prediction scheme $C_n = 20$ is used to simulate the lower jet penetration and $\Upsilon = 0.40$ gives good agreement

Downloaded 01 Jun 2010 to 171.66.16.66. Redistribution subject to ASME license or copyright; see http://www.asme.org/terms/Terms_Use.cfm

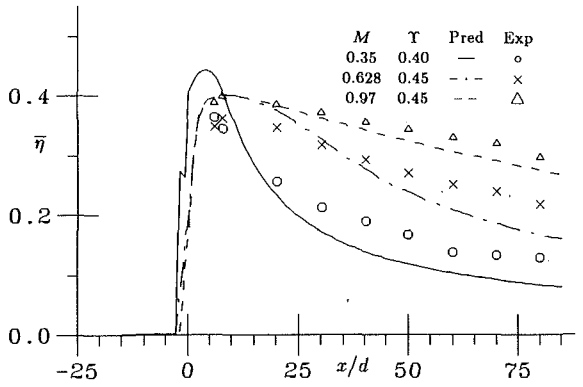

Fig. 5 Predictions of $\bar{\eta}$ for two row injection into a turbulent boundary layer for the experiments of Jabbari (1973): $\rho_j/\rho_e = 0.84$, $\alpha_o = 35$ deg, $p/d = 3.0$, $s/d = 2.6$, $C_n = 10$

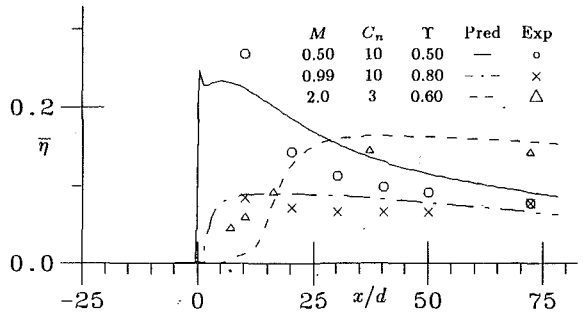

Fig. 6 Predictions of $\bar{\eta}$ for one row injection into a laminar boundary layer for the experiments of Goldstein and Yoshida (1981): $\rho_j/\rho_e = 0.85$, $\alpha_o = 35$ deg, $p/d = 3.0$

with the experimental results. By comparing Figs. 4(*a*) and 4(*b*), it is interesting to note that $\bar{\eta}$ for $M = 1.0$ nearly doubles with compound angle injection, while the increase in $\bar{\eta}$ for $M = 0.2$ and 0.5 is not so noticeable. This is due to the fact that at $M = 1.0$, the jet detaches from the surface for streamwise injection, whereas for compound injection it does not.

Jabbari's experimental conditions are $d = 0.0109$ *m*, $\alpha_o = 35$ deg, $p/d = 3.0$, $s/d = 2.6$, $U_e = 16.5$ m/s, $\delta_o^*/d = 0.231$, and $\rho_j/\rho_e = 0.84$. The initial experimental velocity profile is given by the 1/6th power law, and the temperature profile is uniform. For this injection geometry, because of the close proximity of the two rows, the value of Υ for $p/d = 3.0$ will not represent the entrainment process accurately. In this case the three-dimensional entrainment of each row will be mutually affected by the presence of the other row. If we consider the limiting case of $s/d \to 0$ then the two rows merge into one with an effective $p/d \to 1.5$. Based on this viewpoint we would expect the values of Υ to have values between those for $p/d = 1.5$ and $p/d = 3.0$. For low injection ratios the interference between the rows is not so strong due to the weak effects of injection, but as the injection ratio increases the effect on Υ is quite pronounced. The predictions of $\bar{\eta}$ and the values of Υ used are shown in Fig. 5 for $M = 0.35$, 0.628, and 0.970. For $M = 0.35$ the values of Υ are close to that for $p/d = 3.0$, but as M increases, Υ takes on a constant value of 0.45. This behavior of Υ is very similar to that for $p/d = 1.5$.

We can relate the results obtained for the two data sets to the superposition approach of Sellers (1963). The superposition is based on the premise that if the $\bar{\eta}$ distribution of each individual row acting alone is known, then the $\bar{\eta}$ distribution of all the rows acting together can be found by superposing the distribution of $\bar{\eta}$ of each individual row. The superposition is done by replacing T_e for the second row by T_{aw} of the first row and so on. In the present prediction scheme the method of calculating I^*_{ent} is very similar in principle. Another implicit assumption in the superposition approach is that there is no mutual interference between injection rows. This condition is violated in the experiments of Jabbari ($s/d = 2.6$) and the simple additive nature of the entrainment fraction Υ is no longer valid. The limiting value of s/d above which the additive nature of film cooling is valid depends on the injection ratio.

Injection Into a Laminar Boundary Layer. Injection into a laminar boundary layer differs from injection into a turbulent boundary layer in two respects: one, the turbulence characteristic of the boundary layer is different, which could affect the entrainment; and the other is the larger velocity defect near the wall, which results in greater jet penetration. The experiments of Goldstein and Yoshida (1981) are used for comparison with the predictions. The experimental conditions are: $d = 0.0118$ m, $\alpha_o = 35$ deg, $p/d = 3.0$, $U_e = 4.5$ m/s, $\delta_o^*/d = 0.160$, $\rho_j/\rho_e = 0.85$, and the turbulent intensity $\text{Tu}_e = 1.0$ percent. At the injection row $\text{Re}_\delta^* \approx 500$ and $\text{Re}_\delta \approx 1360$. The initial conditions of velocity are approximated by the Blasius profile. The predictions of $\bar{\eta}$ are shown in Fig. 6 for $M = 0.50$, 0.99, and 2.0. For $M = 0.50$ there are some discrepancies in the slope in the near field. The experiments indicate a steeper slope than the predictions. This can be explained in the following way: The "point of instability" as defined by Schlichting (1979) for transition to a turbulent boundary layer is $\text{Re}_\delta^* \approx 520$. On the basis of this value we would expect the boundary layer to become turbulent immediately after the strong disturbance caused by the injection. However, in the prediction scheme transition to turbulence does not take place until after $M > 1.0$. This is due to the inability of the prediction scheme to simulate the full extent of turbulence augmentation caused by the three-dimensional interaction of the jet and the boundary layer. In spite of this deficiency, the predicted values of $\bar{\eta}$ are in good agreement with experimental values. These results strengthen the assumption made by Tafti and Yavuzkurt (1987) that Υ is a very weak function of the external flow conditions, namely the turbulent structure of the boundary layer. For $M = 2.0$, $C_n = 3$ is used. It is found that a value of $C_n = 3$ is more appropriate in defining the jet trajectory for high injection ratios ($M \approx 2$).

Multirow Injection Into a Turbulent Boundary Layer on a Convex Surface. Convex streamwise curvature in boundary layers tends to reduce the turbulent length scales in the outer half of the boundary layer due to negative production of the primary shear stress $\overline{uv}$ (Gillis et al., 1980). The modified forms of the boundary layer equations for curved boundary layers used in the present work are those developed by Jen and Wang (1986). Jen and Wang have extensively tested the prediction capability of a non-film-cooled version of the present code with the hydrodynamic and heat transfer data of Gillis et al. (1980) and Simon et al. (1980). In the present case the experimental data of Furuhama et al. (1983) are used to compare predictions of St(0), St(1), and $\bar{\eta}$. The experimental conditions are: $d = 0.01$ m, $\alpha_o = 30$ deg, $p/d = 5.0$, $s/d = 5.0$, $U_e = 14.5$ m/s, $\delta_o/d \approx 4.0$, and $\rho_j/\rho_e \approx 1.0$. The curved region ($R = 0.45$ m) extends 7.6 cm upstream from the center of the first row of injection to 62.4 cm downstream. The δ/R ratio at the beginning of the curved section is ≈ 0.1. The initial conditions are obtained from experimental data at the beginning of the curved section. $\bar{\eta}$ predictions are made using the adiabatic wall method outlined in the introduction. The predictions of St(0), St(1), and $\bar{\eta}$ are made for two, four, and six rows of injection with $M = 0.20$, 0.40, and 0.60. Calculated $\bar{\eta}$ for two, four, and six rows are shown in Fig. 7 for $M = 0.4$ and 0.6. The predictions are in good agreement with the experimental data. Calculated values of St(0) and St(1) are shown in Fig. 8 for $M = 0.20$ and $M = 0.60$ for six rows of injection. The two cases represent the

Downloaded 01 Jun 2010 to 171.66.16.66. Redistribution subject to ASME license or copyright; see http://www.asme.org/terms/Terms_Use.cfm

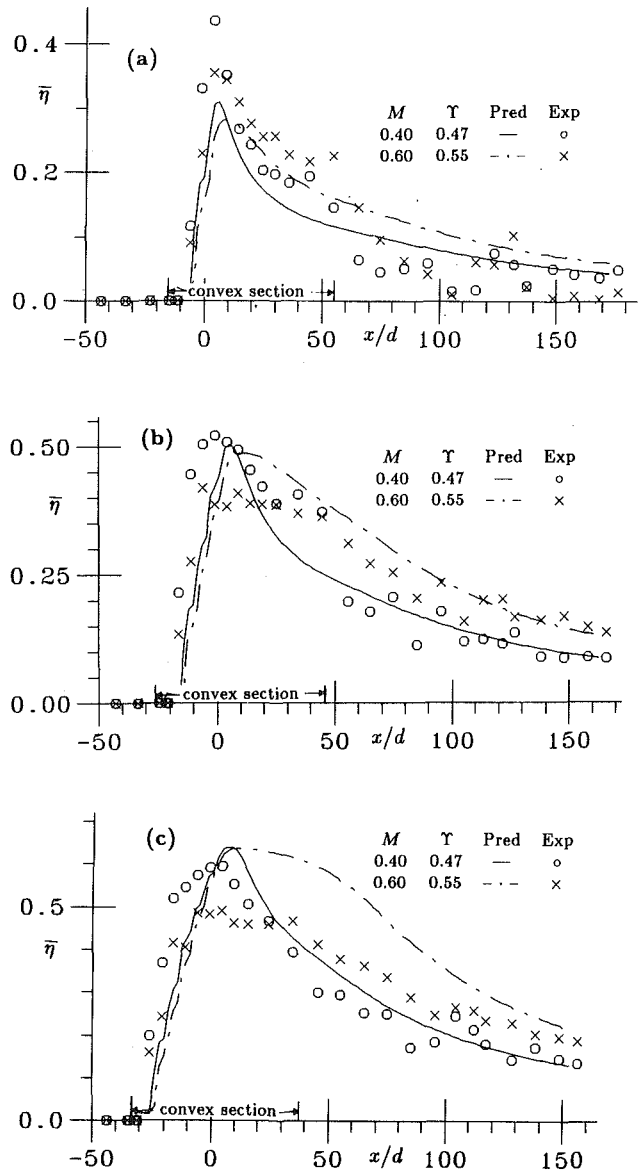

Fig. 7 Predictions of $\bar{\eta}$ with injection into a turbulent boundary layer on a convex surface for the experiments of Furuhma et al. (1983): $\rho_j/\rho_e = 1.0$, $\alpha_o = 30$ deg, $p/d = 5.0$, $s/d = 5.0$, $C_n = 10$; (*a*) two rows, (*b*) four rows, (*c*) six rows

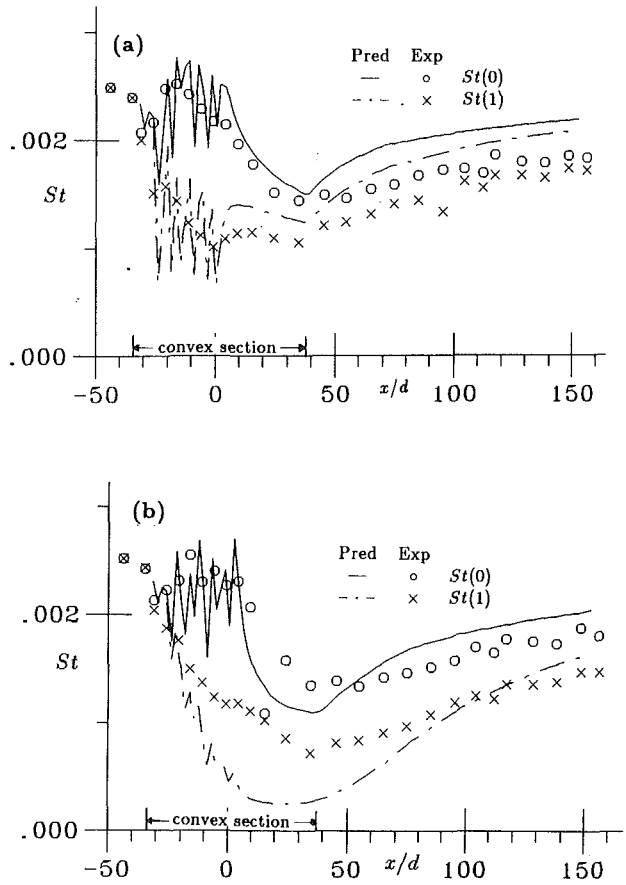

Fig. 8 Predictions of St(0) and St(1) for six rows of injection into a turbulent boundary layer on a convex surface for the experiments of Furuhama et al. (1983): $\rho_j/\rho_e = 1.0$, $\alpha_o = 30$ deg, $p/d = 5.0$, $s/d = 5.0$, $C_n = 10$; (*a*) $M = 0.20$, $\Upsilon = 0.45$; (*b*) $M = 0.60$, $\Upsilon = 0.55$

typical trends in the prediction of St(0) and St(1) very well. In Fig. 8(*a*), for $M = 0.20$ the predicted results are good. For this case the jet is attached to the surface. In Fig. 8(*b*) for $M = 0.60$, predictions of St(0) are good; however, predictions of St(1) are much lower than the experimental values. In this case the jet is detached from the surface and there is three-dimensional entrainment of boundary layer fluid between the jet and the wall. Unlike h_f, which is only a function of the flow field, both St(0) and St(1) are functions of the jet temperature and the effects of three-dimensional entrainment on the temperature profile after injection. Although $\bar{\eta}$ is also dependent on the effect of three-dimensional entrainment on the temperature profile, the value of $\bar{\eta}$ is determined by the wall temperature (T_{aw}). T_{aw} is less sensitive to the temperature profile than $dT/dy|_{y=0}$, which determines the St numbers. The entrainment fraction Υ accounts for three-dimensional entrainment in an averaged way but cannot accurately represent the temperature gradients at the wall. For $M = 0.2$ the predictions of both St(0) and St(1) are relatively good even for six rows of injection. Low predictions of St(1) for $M = 0.6$ (Fig. 8(*b*)) suggest that fluid at or near T_e is entrained between the jet and the wall as the jet lifts off the surface.

Injection Into a Boundary Layer on the Suction Side of a Turbine Blade. Ito (1976) measured $\bar{\eta}$ for one row of injection on the suction side (convex surface) and the pressure side of a turbine blade in a cascade. He determined analytically that for a convex surface if $L \cos^2\alpha_o < 1$ (L is the momentum ration $= \rho_j U_j^2/\rho_e U_e^2$) then $\bar{\eta}$ is higher than for injection on a flat plate, and the opposite is true if $L \cos^2\alpha_o > 1$. The experimental conditions are: $d = 0.00238$ m, $\alpha_o = 35$ deg, $p/d = 3.0$, $U_e \approx 25.7$ m/s, $\delta_o^*/d = 0.09$, and $\rho_j/\rho_e = 0.95$. In the prediction scheme the initial conditions are specified at 15 percent of the suction arc. Although U_e accelerates from the stagnation point, a laminar Blasius profile is used with $\delta = 0.00053$ m for the initial conditions in order to obtain $\delta_o^*/d \approx 0.09$ at injection. For this case the ratio $\delta_o/d \approx 0.2$, so the shape of the boundary layer velocity profile near the wall does not have much effect on the jet centerline. Predictions of $\bar{\eta}$ are shown in Fig. 9. In Fig. 9(*a*), for $M = 0.198$ the predicted $\bar{\eta}$ is in good agreement with the experiments, though there is a slight discrepancy in the slope in the near field. For $M = 0.50$ the error in the slope increases. This can again be attributed to the inability of the prediction scheme to generate enough turbulence to facilitate a faster decay of $\bar{\eta}$ in the streamwise direction. In spite of this the entrainment fraction still does a reasonable job in predicting $\bar{\eta}$. However, for $M = 0.74$ in Fig. 9(*a*) and for $M = 0.984$ in Fig. 9(*b*) the slope of the $\bar{\eta}$ curves are well represented, but the values of $\bar{\eta}$ are underpredicted. As the injection ratio increases further to $M = 1.49$ and $M = 1.99$ the predictions of $\bar{\eta}$ start getting better again. These results can be explained by

Downloaded 01 Jun 2010 to 171.66.16.66. Redistribution subject to ASME license or copyright; see http://www.asme.org/terms/Terms_Use.cfm

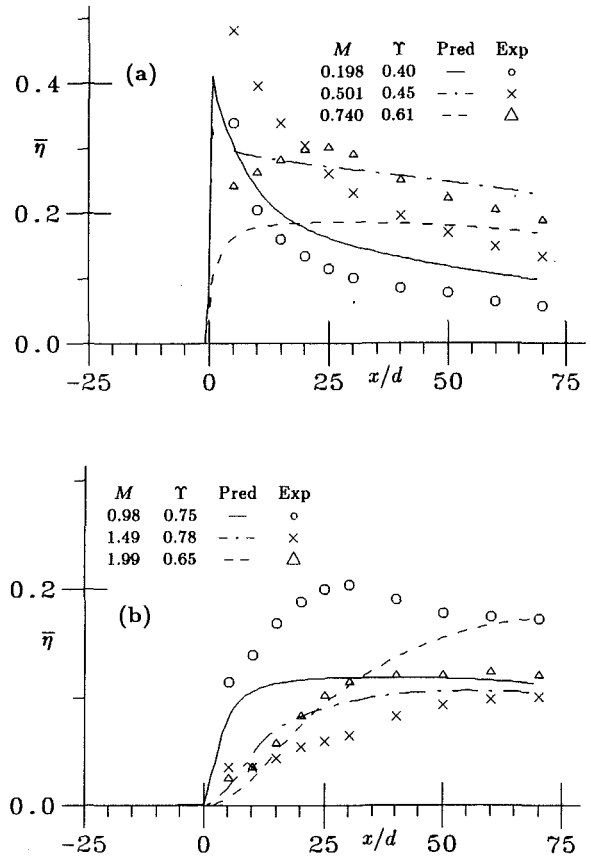

Fig. 9 Predictions of $\bar{\eta}$ for injection on the convex surface of a turbine blade for the experiments of Ito (1976): $\rho_j/\rho_e = 0.95$, $\alpha_o = 35$ deg, $p/d = 3.0$, $C_n = 10$

considering the effects of curvature on the jet trajectory, and the inability of equation (6) to simulate these effects.

On a convex wall the radial static pressure force tends to push the jet toward the wall, while due to the curvature, the wall moves away from the jet. Both of these effects have an opposite influence on the effectiveness. For $M = 0.198$ and 0.50 the jet has still not completely detached from the surface, and the effect of curvature, which tends to push the jet toward the surface, does not have a large effect on Υ and $\bar{\eta}$. For $M = 0.74$ and $M = 0.984$, $L \cos^2\alpha_o < 1.0$ and based on equation (6) the jets are detached from the surface. The effect of curvature tends to push the jet toward the wall. This decreases jet penetration and decreases the effective value of Υ. For $M = 1.5$ and 1.99, $L \cos^2\alpha_o > 1.0$. In this case the jet is injected far from the wall and the effects of curvature tend to push it farther away. Because the jets are already far from the wall, curvature does not have a dramatic effect on Υ as in the previous case.

A very fundamental difference between this flow and all the other experimental data is the ∂_o/d ratio. In all the prediction runs made so far $\partial_o/d \geq 1$ and the jet is injected within the domain of the boundary layer. In this case, which is typical of almost all turbine blade applications, the jet falls outside the boundary layer. The two resulting flow fields are quite different and it is encouraging to note that the established values of Υ do a relatively good job in predicting $\bar{\eta}$.

Conclusions

The two-dimensional scheme developed by Tafti and Yavuzkurt (1988) is applied to different flow conditions applicable to film cooling over turbine blades. The previously developed correlation between the entrainment fraction Υ and the injection parameters is applied to multirow injection, injection into laminar boundary layers, injection on curved surfaces, and injection on a turbine blade. The predictions of spanwise-averaged effectiveness compare well with experimental data for most of the cases tested. Predictions of Stanton numbers St(0) and St(1) are not as well predicted due to the inability of the entrainment fraction Υ to reproduce the shape of the temperature profile accurately near the wall after injection.

The present prediction scheme is simple and comprehensive and can accurately predict the spanwise averaged effectiveness for a wide range of injection geometries and external flow fields. The accuracy obtained is better than or the same when compared to other two-dimensional prediction schemes. The present scheme is based on strong physical reasoning and can easily be extended to other injection geometries not covered in this paper. The entrainment fraction is quite universal in its application and plays a very important role in determining the heat transfer characteristics of an injected boundary layer.

Acknowledgments

The authors wish to thank the Heat Transfer Department of Textron Lycoming for their financial support and permission of publication of material contained in this paper. We would also like to express our thanks to Drs. H. Jen and K. Poon for their assistance during the course of this research.

References

Bergeles, G., Gosman, A. D., and Launder, B. E., 1978, "The Turbulent Jet in a Cross Stream at Low Injection Rates: A Three-Dimensional Numerical Treatment," *Numerical Heat Transfer*, Vol. 1, pp. 217–242.

Choe, H., Kays, W. M., and Moffat, R. J., 1976, "Turbulent Boundary Layer on a Full-Coverage Film-Cooled Surface—An Experimental Heat Transfer Study With Normal Injection," NASA CR-2642; also Stanford Report No. HMT-22.

Crawford, M. E., Kays, W. M., and Moffat, R. J., 1976, "Heat Transfer to a Full-Coverage Film-Cooled Surface With 30 Degree Slant Hole Injection," NASA CR-2786; also Stanford Report No. HMT-25.

Demuren, A. O., Rodi, W., and Schonung, B., 1985, "Systematic Study of Film Cooling With a Three-Dimensional Calculation Procedure," ASME Paper No. 85-IGT-2.

Eriksen, V. L., and Goldstein, R. J., 1974, "Heat Transfer and Film Cooling Following Normal Injection Through a Round Hole," ASME Paper No. 74-GT-6.

Furuhama, K., Moffat, R. J., Johnston, J. P., and Kays, W. M., 1983, "Film Cooling on a Convex Wall: Heat Transfer and Hydrodynamic Measurements for Full and Partial Coverage," NASA CR-174964; also Stanford Report No. HMT-37.

Gillis, J. C., Johnston, J. P., Kays, W. M., and Moffat, R. J., 1980, "Turbulent Boundary Layer on a Convex Curved Surface," NASA CR-3391; also Stanford Univ. Rep. No. HMT-31.

Goldstein, R. J., 1971, "Film Cooling," *Advances in Heat Transfer*, Vol. 7, pp. 321–379.

Goldstein, R. J., Eckert, E. R. G., and Burggraf, F., 1974, "Effects of Hole Geometry and Density on Three-Dimensional Film Cooling," *International Journal of Heat Mass Transfer*, Vol. 17, pp. 595–607.

Goldstein, R. J., and Yoshida, T., 1981, "The Influence of a Laminar Boundary Layer and Laminar Injection on Film Cooling Performance," ASME Paper No. 81-HT-38.

Ito, S., 1976, "Film Cooling and Aerodynamic Loss in a Gas Turbine Cascade," Ph.D. Thesis, University of Minnesota, Minneapolis, MN.

Jabbari, M. Y., 1973, "Film Cooling and Heat Transfer With Air Injection Through a Staggered Row of Holes Into an Accelerating Flow," Ph.D. Thesis, University of Minnesota, Minneapolis, MN.

Jen, H. F., and Wang, J. H., 1986, "Applications of a k–ϵ Two-Equation Turbulence Model for Predicting Thin Shear Flows Over a Curved Wall and a Turbine Airfoil," Textron Lycoming, Heat Transfer Dept., Tech. Rep. Memo No. K3-H-126-86.

Jones, W. P., and Launder, B. E., 1973, "The Calculation of Low-Reynolds-Number Phenomenon With a Two-Equation Model of Turbulence," *International Journal of Heat Mass Transfer*, Vol. 16, pp. 1119–1130.

Jubran, B., and Brown, A., 1985, "Film Cooling From Two Rows of Holes Inclined in the Streamwise and Spanwise Directions," ASME *Journal of Engineering for Gas Turbines and Power*, Vol. 107, pp. 84–91.

Kadotani, K., 1975, "Effect of Mainstream Variables on Heated and Unheated

Downloaded 01 Jun 2010 to 171.66.16.66. Redistribution subject to ASME license or copyright; see http://www.asme.org/terms/Terms_Use.cfm

Jets Issuing From a Row of Inclined Round Holes," Ph.D. Thesis, University of Minnesota, Minneapolis, MN.

Kruse, H., and Metzinger, H., 1984, "Der Einfluss der Belochungsgeometrie auf die Filmkuhlwirkung einer Lochreihe," *Deutsche Forschungs- und Versuchsanstalt fur Luft- und Raumfahrt*, Koln, Interner Bericht IB 325-9-84.

Liess, C., 1974, "Experimental Investigation of Film Cooling With Ejection From a Row of Holes for the Application to Gas Turbine Blades," ASME Paper No. 74-GT-5.

Miller, K. L., and Crawford, M. E., 1984, "Numerical Simulation of Single, Double and Multiple Row Film Cooling Effectiveness and Heat Transfer," ASME Paper No. 84-GT-112.

Ramsey, J. W., and Goldstein, R. J., 1971, "Interaction of a Heated Jet With a Deflecting Stream," ASME *Journal of Heat Transfer*, Vol. 93.

Schlicting, H., 1979, *Boundary Layer Theory*, 7th ed., McGraw-Hill, New York.

Schonung, B., and Rodi, W., 1987, "Prediction of Film Cooling by a Row of Holes With a Two-Dimensional Boundary Layer Procedure," ASME JOURNAL OF TURBOMACHINERY, Vol. 109, pp. 579–587.

Sellers, J. P., 1963, "Gaseous Film Cooling With Multiple Injection Stations," *AIAA J.*, Vol. 1, No. 9, pp. 2154–2156.

Simon, T. W., Moffat, R. J., Johnston, J. P., and Kays, W. M., 1980, "Turbulent Boundary Layer Heat Transfer Experiments: Convex Curvature Effects Including Introduction and Recovery," NASA CR-3510; also Stanford Univ. Rep. No. HMT-32.

Tafti, D. K., and Yavuzkurt, S., 1987, "Two-Dimensional Turbulence Modeling for Flat Plate and Turbine Airfoil With Discrete Film Cooling," RFQ: YC69359, Final Report submitted to: Heat Transfer Department, Textron, Lycoming.

Tafti, D. K., and Yavuzkurt, S., 1988, "Prediction of Heat Transfer Characteristics for Discrete Hole Film Cooling—One Row Injection Into a Turbulent Boundary Layer," presented at the ASME Winter Annual Meeting, Chicago, IL, HTD-Vol. 103, pp. 45–52.

Wang, J. H., Jen, H. F., and Hartel, E. O., 1985, "Airfoil Heat Transfer Calculation Using a Low Reynolds Number Version of a Two-Equation Turbulence Model," ASME *Journal of Engineering for Gas Turbines and Power*, Vol. 107, pp. 60–67.

Downloaded 01 Jun 2010 to 171.66.16.66. Redistribution subject to ASME license or copyright; see http://www.asme.org/terms/Terms_Use.cfm

Behavior of a Coolant Film With Two Rows of Holes Along the Pressure Side of a High-Pressure Nozzle Guide Vane

T. Arts
von Karman Institute for Fluid Dynamics,
B-1640 Rhode Saint Genèse, Belgium

A. E. Bourguignon
SNECMA-Centre de Villaroche,
F-77550 Moissy Cramayel, France

The purpose of this paper is to quantify the influence on external convective heat transfer of a coolant film whose position varies along the pressure side of a high-pressure turbine nozzle guide vane. The measurements were performed in the short-duration Isentropic Light Piston Compression Tube facility of the von Karman Institute. The effects of external and internal flow are considered in terms of Mach number, Reynolds number, free-stream turbulence intensity, blowing rate, and coolant to free-stream temperature ratio. The way to evaluate these results in terms of film cooling efficiency and heat transfer coefficient is finally discussed.

Introduction

A continuous improvement in the performance of modern aero-engines requires more and more detailed optimization of each of their components. Especially in the field of high-pressure turbine cooling, methods allowing a very accurate prediction of the airfoil temperature are essential to guarantee the lifetime of that component. A large number of research projects have therefore been addressed over the two last decades to various film cooling techniques. The numerous parameters to be investigated in this field concern both the main (or free-stream) and the secondary (or coolant) flow; they can be listed in a nonexhaustive way as follows:

- airfoil geometry: curvature distribution, coolant emission location;
- coolant emission geometry: hole shape, diameter, and spacing, inclination and/or sweep angle of the hole, number of rows of holes;
- blade loading: transition location, boundary layer status, shock/boundary layer interaction;
- free-stream Reynolds number;
- free-stream turbulence intensity;
- blowing ratio or coolant to free-stream mass weight ratio;
- coolant to free-stream temperature ratio;
- etc.

In the area of film cooling, a large number of basic experimental investigations have been presented, typically on flat plates, with the objective of identifying and understanding the thermal and aerodynamic behavior of the coolant film; typical examples of this type of research can be found from Goldstein (1971), Forth and Jones (1986), and Pietrzyk et al. (1989). The effect of streamwise, and especially concave, curvature on film cooling however has received much less attention from the engineering community. Basic experiments on concave film cooled walls were recently reported by Ko et al. (1986) and by Schwarz and Goldstein (1989). Both experiments were performed at low speed and all results were only presented in terms of adiabatic wall temperature and adiabatic effectiveness. As a matter of fact, in the severe engine environment of a film-cooled turbine blade, the large temperature differences existing between the mainstream and the blade surface induce a wall temperature pattern quite different from an adiabatic distribution. Considering, moreover, the important spatial temperature variations due to internal cooling passages and the strongly varying heat flux distributions downstream of a film cooling hole or slot, the most representative heat transfer parameter seems to be the convective heat transfer coefficient h. Either an experimental or a numerical determination of h is essential to perform any detailed heat conduction or thermal stress analysis.

Most of the available measurements on film-cooled turbine cascade models were presented by Landon et al. (1972), Nicolas and LeMeur (1974), Ito et al. (1978), Daniels (1979), Dring et al. (1980), Horton et al. (1985), Camci and Arts (1985), and Camci et al. (1985). A large number of these heat transfer data, presented either in terms of adiabatic effectiveness or in terms of heat transfer coefficient, are however difficult to use as such for modern cooled gas turbine design, because of the limited range of Reynolds and Mach numbers, as well as gas to wall and gas to coolant temperature ratios considered in some of these investigations.

Over the last five years, SNECMA and the von Karman Institute have been conducting a systematic research program on leading edge, suction side, and pressure side film-cooled turbine vanes and blades. The global objective of this investigation is twofold: on one hand to develop and verify accurate

Contributed by the International Gas Turbine Institute and presented at the 34th International Gas Turbine and Aeroengine Congress and Exhibition, Toronto, Ontario, Canada, June 4–8, 1989. Manuscript received at ASME Headquarters January 27, 1989. Paper No. 89-GT-186.

Copyright © 1990 by ASME
Downloaded 01 Jun 2010 to 171.66.16.66. Redistribution subject to ASME license or copyright; see http://www.asme.org/terms/Terms_Use.cfm

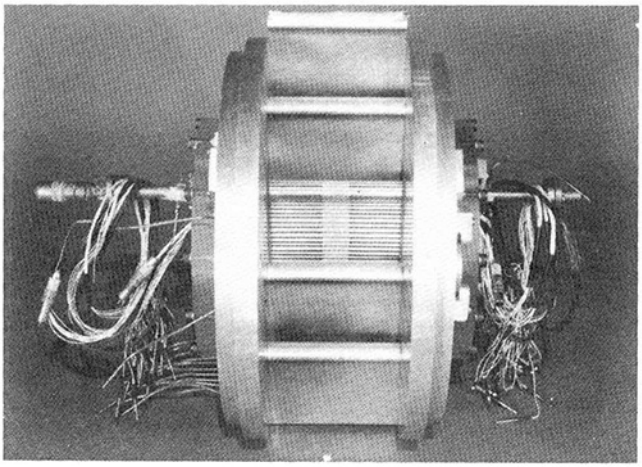

Fig. 1 Cascade configuration

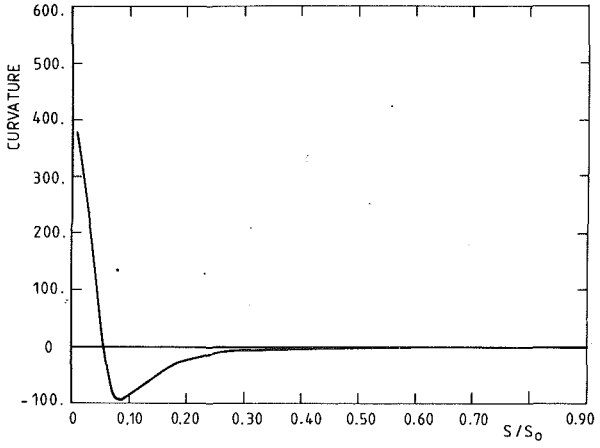

Fig. 2 Pressure side curvature distribution

and reliable boundary layer calculation methods with the presence of film cooling at different locations around the vane or the blade, and on the other hand possibly to identify relatively simple correlations, accounting for the different main and coolant flow parameters, to be used during the different design steps of cooled turbines. The selection of the different airfoil geometries and cooling configurations did not especially depend upon the fact that these profiles eventually were or were not used in an existing engine, rather, the tested models were considered as general demonstrator test cases, representative of modern aerodynamic designs.

The more specific objective of the present contribution is to address one of the investigated topics, namely to quantify the influence on convective heat transfer of a coolant film whose position varies along the pressure surface of a high-pressure turbine nozzle guide vane. The effects of both external and internal flows are considered in terms of Mach and Reynolds number, free-stream turbulence intensity, blowing ratio, and coolant to free-stream temperature ratio.

Experimental Apparatus

Wind Tunnel. The facility used for this experimental investigation is the VKI Isentropic Light Piston Compression Tube facility. The operating principles of this type of wind tunnel were developed about 15 years ago by Jones et al. (1973). This short-duration facility is based on an isentropic compression of the test gas by means of a lightweight piston until the desired free-stream total pressure and total temperature are obtained. The flow is then initiated in the test section by a fast opening valve and constant free-stream conditions are maintained for about 0.5 s. Further details about this particular wind tunnel were presented by Richards (1980), Consigny and Richards (1982), and Camci (1985). Its definite advantage is to provide at moderate cost an exact similitude in terms of Mach and Reynolds numbers as well as gas to wall and gas to coolant temperature ratio with respect to the values actually observed in an engine.

Model Description. The measurements presented in this paper were carried out along the film-cooled pressure side of a nozzle guide vane mounted in a linear cascade configuration. This cascade, which consisted of one ceramic and four aluminum airfoils (four passages) is shown in Fig. 1. The pressure surface curvature distribution of the blade is plotted in Fig. 2, as a function of a nondimensional wetted length (s/s_0). Four different cooling locations were considered on four different models. Each of these emission sites consisted of two staggered rows of 30 cylindrical holes ($d=0.5$ mm). As in many other investigations, the row and hole spacing were both equal to 3 hole diameters and the upstream row was angled at 50 deg with respect to the blade surface; the downstream row was drilled parallel to the first one. The four different sites were respectively located at 6.6 percent (I1), 15 percent (I2), 22 percent (I3), and 28.6 percent (I4) of the pressure side length. These locations were selected to obtain a maximum of information on a well-known (and very popular in the literature) coolant film. They do not duplicate the exact cooling configurations observed on a real nozzle guide vane. The four different models, made of Macor glass ceramic and instrumented by means of 20 platinum thin-film gages, are shown in Fig. 3. Results will be reported in this paper for configurations I2 and I3. The coolant flow was provided through a cavity ($d=4.5$ mm), drilled inside the blade along its height, by means of a regenerative type cryogenic heat exchanger allowing the simulation of different coolant to free-stream temperature ratios.

Nomenclature

c = chord
C_D = discharge coefficient
d = diameter
h = convective heat transfer coefficient
h_0 = convective heat transfer coefficient without film cooling
k = thermal conductivity
m = blowing rate
$\dot{m}$ = coolant mass flow rate
M = Mach number
Nu = Nusselt number $= hs/k$
Nu_0 = Nusselt number without film cooling
p = pressure
q = heat flux
q_0 = heat flux without film cooling
Re = Reynolds number (based on chord length)
s = coordinate along the pressure side length
s_0 = pressure side length
T = temperature
Tu = free-stream turbulence intensity
x = coordinate along the blade chord

Subscripts

0 = stagnation condition
1 = upstream condition
2 = downstream condition
c = coolant condition
is = isentropic
w = condition at the wall
∞ = free-stream condition

Downloaded 01 Jun 2010 to 171.66.16.66. Redistribution subject to ASME license or copyright; see http://www.asme.org/terms/Terms_Use.cfm

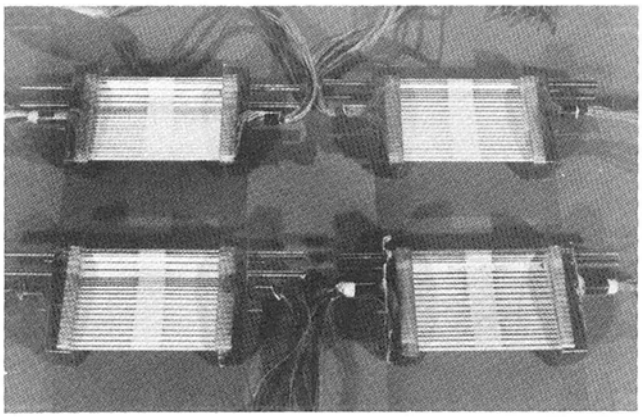

Fig. 3 Tested vanes

Measurement Technique. The local wall heat flux was deduced from the corresponding time-dependent surface temperature evolution, provided by the thin-film gages. The wall temperature/wall heat flux conversion was obtained from an electrical analogy, simulating a one-dimensional semi-infinite body configuration. A detailed description of this transient measurement technique was presented by Schultz and Jones (1973). The convective heat transfer coefficient h used in this paper is defined as the ratio of the measured wall heat flux and the difference between the total free stream and the local wall temperatures. It is worthwhile to mention that the heat transfer measurements discussed in the present contribution describe a spanwise-averaged behavior as the different thin films were about 20 mm long.

The coolant mass flow was measured by means of a choked orifice and miniature total pressure and total temperature probes continuously provided the coolant characteristics at the inlet and the exit of the plenum cavity. Valydine and National Semi-Conductor transducers were used for pressure measurements whereas type K (chromel/alumel) thermocouples ($\phi = 0.2$ mm) were selected for temperature measurements. The free-stream turbulence was generated by a grid of spanwise oriented cylindrical bars, displaced upstream of the model. The turbulence intensity was measured using a VKI manufactured constant temperature hot-wire probe. The data acquisition was made by a 48-channel, 12-bit resolution, on-line acquisition system designed and built at the VKI and connected to a VAX 11/780 computer. The sampling rate was set at 1 kHz for heat transfer, pressure, and temperature measurements and at 25 kHz for turbulence intensity measurements.

The uncertainty on the different measured quantities has been estimated as follows, based on a 20:1 confidence interval:

$h = 1000\ \text{W/m}^2\text{K} \pm 50\ \text{W/m}^2\text{K}$
$p = 10^5\ \text{N/m}^2 \pm 750\ \text{N/m}^2$
$T = 100\ \text{K} \pm 1\ \text{K}$
$m_c = 0.020\ \text{kg/s} \pm 0.0005\ \text{kg/s}$

Repeatability was found to be very good, as well for repeated measurements on a given model as for similar measurements repeated on different models.

Test Conditions. The test program was built up by varying the free-stream conditions according to the following matrix:

Re_2	M_2	Tu_∞, percent
2.25×10^6	1.10	1, 4, 6
2.25×10^6	0.85, 1.25	4
1.50×10^6	1.10	4
3.00×10^6	1.10	4

For each of these test conditions, three values of the coolant to free-stream temperature ratio were considered (0.8, 0.7, 0.6) as well as five to seven values of the blowing rate m (0.2–3.0). All these tests were performed for both configurations I2 and I3.

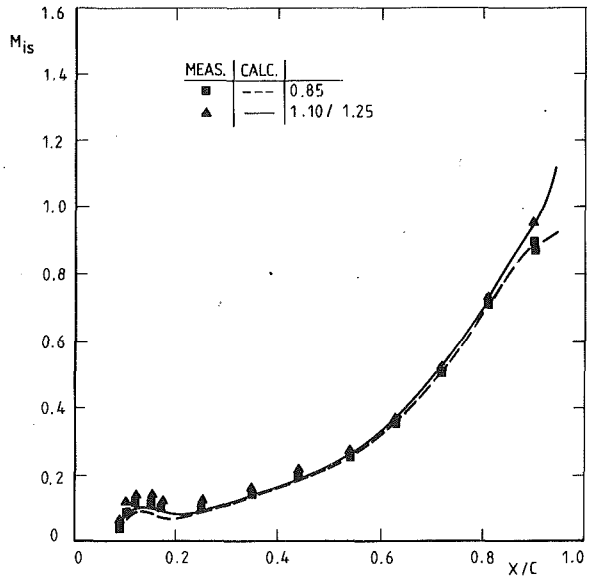

Fig. 4 Pressure side velocity distribution

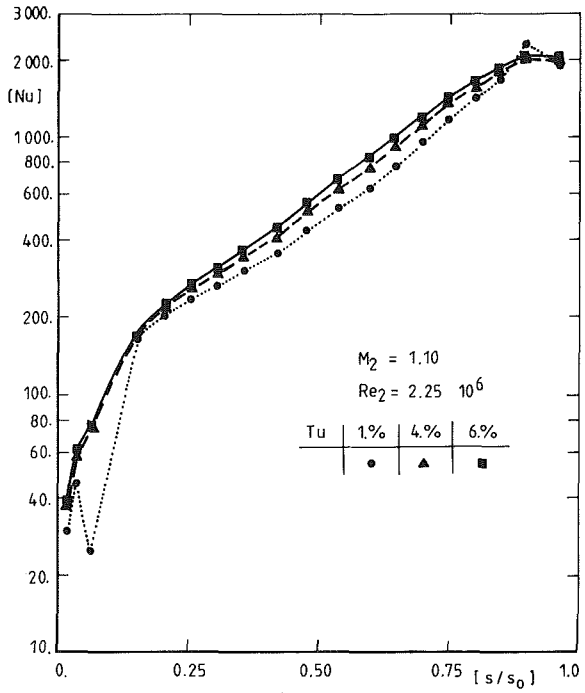

Fig. 5 Influence of Tu (no cooling)

Velocity Distribution

Blade isentropic Mach number distributions were obtained for different loadings from local static pressure measurements, referred to the upstream total pressure. The measured values along the pressure side are presented in Fig. 4 and compared to the results obtained from an inviscid time marching program (Arts, 1982). A velocity peak, followed by a small deceleration, is clearly observed between 15 and 20 percent of the wetted length. The flow then regularly reaccelerates up to the trailing edge. The influence on the pressure surface velocity distribution of a downstream Mach number variation is, as expected, very small.

Downloaded 01 Jun 2010 to 171.66.16.66. Redistribution subject to ASME license or copyright; see http://www.asme.org/terms/Terms_Use.cfm

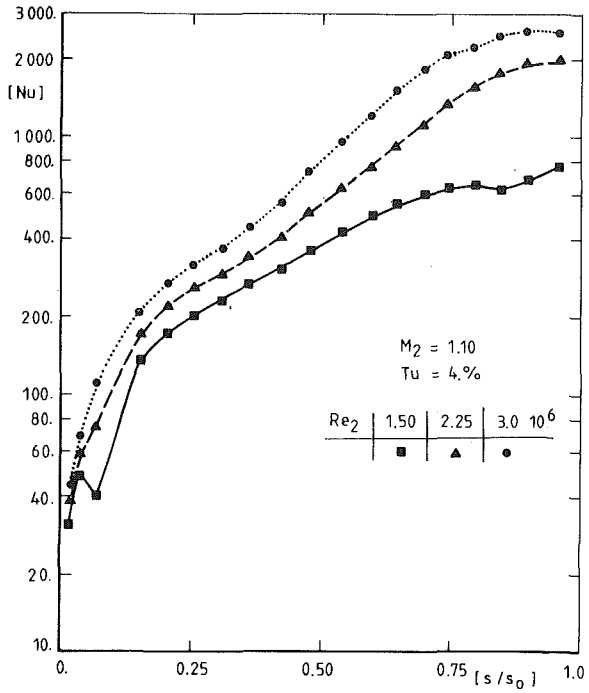

Fig. 6 Influence of Re (no cooling)

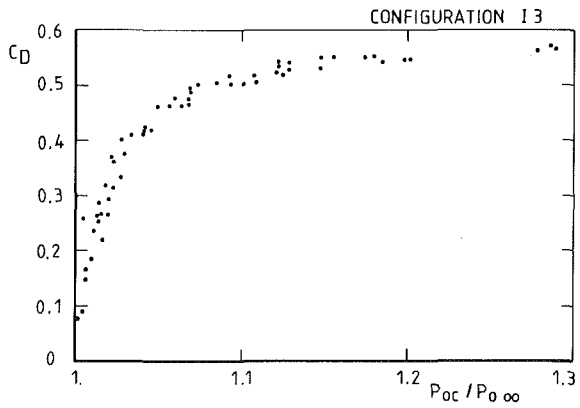

Fig. 7 Discharge coefficient (I3)

Heat Transfer Without Film Cooling

In order to identify the effects of Mach and Reynolds numbers as well as of free-stream turbulence intensity on the convective heat transfer distribution along the pressure side, a first series of heat transfer measurements was performed on an uncooled, smooth profile without any film cooling holes present.

As expected from the velocity distribution measurements, no significant effects were noticed on the heat transfer distribution from a variation of the downstream Mach number ($M_2 = 0.85$–1.25). Varying the free-stream turbulence (1–6 percent), however, led to the Nusselt number distributions presented in Fig. 5. The previously identified deceleration of the flow induces a small laminar separation downstream of the stagnation point, resulting in a very low heat transfer level followed by the expected high heating rate due to a reattaching turbulent boundary layer. The influence of free-stream turbulence on the magnitude of this heat transfer jump is illustrated by the near disappearance of the recirculation bubble at the highest turbulence intensities. The effect of a Reynolds number (based on downstream conditions) variation is illustrated in Fig. 6. For a low value of Re_2 (1.5×10^6) the flow appears to remain transitional all along the pressure surface.

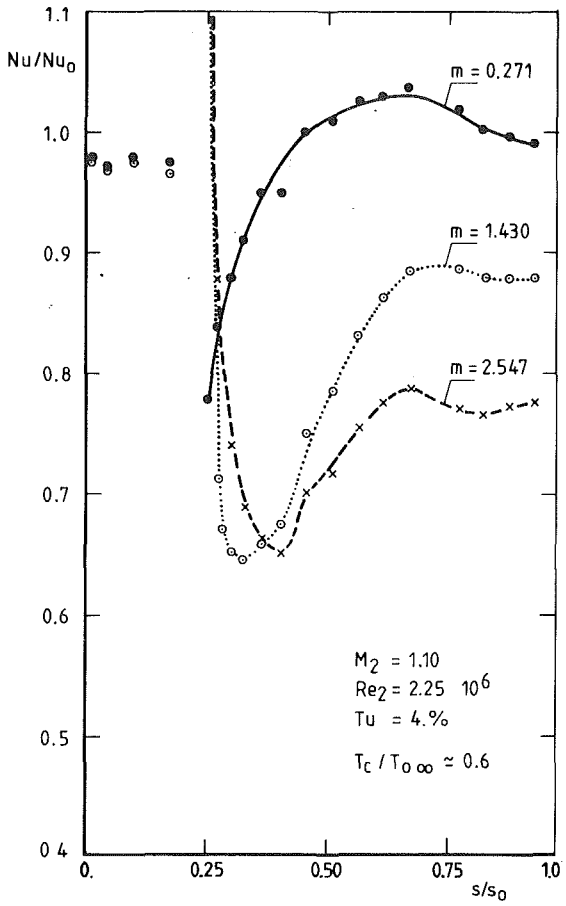

Fig. 8(*a*) Influence of *m* (nominal Re-I3)

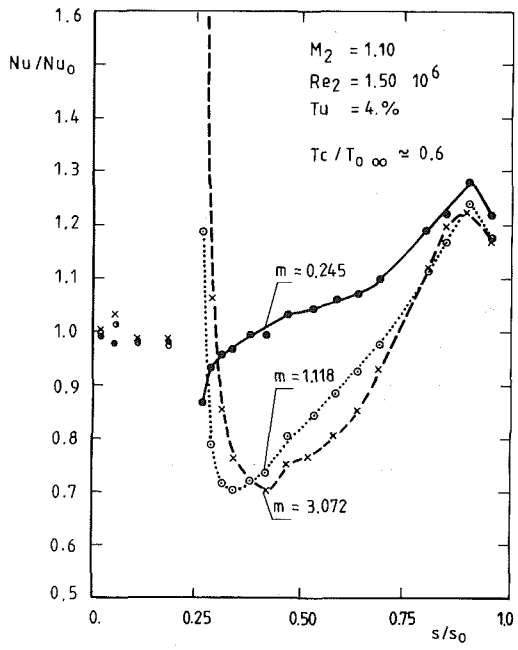

Fig. 8(*b*) Influence of *m* (low Re-I3)

At higher values (2.25–3.0×10^6), the heat fluxes increase as expected and the boundary layer is definitely in a turbulent state. It is also clear from the different tests that the importance of the separation bubble is not at all a function of the Reynolds number level, but only, for a given velocity distribution, of the free-stream turbulence intensity.

Downloaded 01 Jun 2010 to 171.66.16.66. Redistribution subject to ASME license or copyright; see http://www.asme.org/terms/Terms_Use.cfm

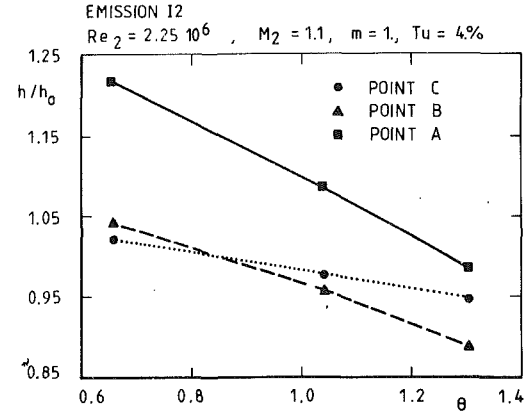

Fig. 9(*a*) Typical h/h_0 versus θ evolution (I2)

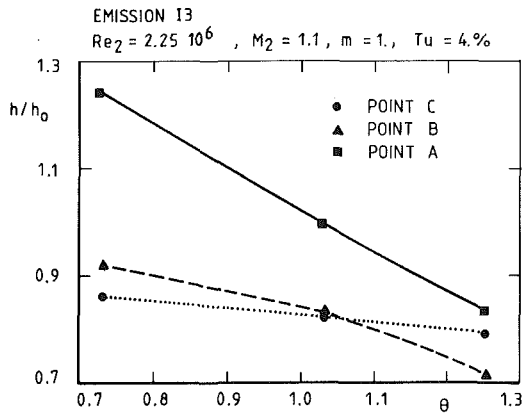

Fig. 9(*b*) Typical h/h_0 versus θ evolution (I3)

Heat Transfer With Film Cooling

More than 200 heat transfer distributions were obtained for cooling configurations I2 and I3 by varying both free-stream and coolant conditions in the range previously mentioned. The information extracted from most of these will be combined and discussed synthetically in the next section. Some typical examples of isolated effects will be presented in the present section in terms of Nu/Nu_0 distributions.

As a representative example, the discharge coefficient evolution corresponding to configuration I3 is presented in Fig. 7 as a function of coolant to free-stream pressure ratio. The tests were performed for different coolant to gas temperature ratios and different free-stream Reynolds numbers.

Figure 8(*a*) presents the heat transfer distribution for the nominal test conditions ($M_2 = 1.10$, $Re_2 = 2.25 \times 10^6$, $Tu = 4$ percent, and $T_c/T_{0\infty} \approx 0.6$) and demonstrates the effect of blowing rate, again for configuration I3. For a low value of the blowing rate ($m = 0.271$), the best protection is obtained just downstream of the cooling holes; the effect of the coolant then regularly decreases and disappears at about 0.5 s_0. When the value of m is increased, higher heating rates are observed just downstream (about three diameters) of the holes. These heat transfer augmentations, previously observed by other authors, can go up to about 1.5 times that heat transfer coefficient value corresponding to the noncooled case for the highest value of the blowing rate (2.5–3.). Farther downstream, the heat transfer rate very rapidly decreases to about 65 percent of the value corresponding to the noncooled situation in a region located between 15 and 50 hole diameters. The heat transfer reduction along the rear part of the blade is proportional to the blowing rate value (at least within the considered range of m values). It is obvious from these results that a compromise must be found in terms of near hole and far downstream heat transfer reduction. The effect of coolant temperature in the near hole region is observed in the magnitude (both in numerical value and spatial extension) of the heat transfer augmentation. Just downstream of the cooling holes, and for a coolant to gas temperature ratio of 0.8, the heat transfer levels were more than doubled for the highest blowing rates; this is a result of an even more severe momentum flux effect (increasing with the coolant temperature and the square of the coolant velocity) of the coolant at a constant blowing rate value. Far downstream, the behavior is similar to that previously described.

The results obtained downstream of configuration I2 for the same free-stream conditions were similar in nature. It should however be mentioned that the heat transfer reductions were less important: 15–17 percent were the maximum reductions observed. This was most probably due to a much closer proximity of the small recirculation bubble. The influence of the latter will be confirmed in the next section.

Some remarkable effects were observed for the low free-stream Reynolds number (1.5×10^6) tests. These results are presented in Fig. 8(*b*) for configuration I3. In the near hole region, the flow and heat transfer levels behave as previously explained for the nominal flow conditions. On the contrary, along the rear part of the blade, heat transfer augmentations up to 25–30 percent were measured, with a rather small effect of blowing rate as well as of coolant to gas temperature ratio. The explanation of this phenomenon is believed to be found in the state of the boundary layer. As seen in the preceding section, the latter is still in a transitional state at this Reynolds number and it is most probable that the perturbation created by the jets has a dominant destabilizing effect along that part of the blade, accelerating the passage of the boundary layer to a turbulent state. The same behavior was observed for cooling configuration I2.

Comparison of Configurations

Superposition Principle. The application of the superposition principle (Metzger et al., 1968) provides a relationship linking the measured heat transfer coefficients to the film cooling effectiveness. The uncooled wall convective heat flux can be expressed as follows:

$$q_0(x) = h_0(x)\ (T_{0\infty} - T_w) \tag{1}$$

When the effect of a coolant film is considered, equation (1) becomes

$$q(x) = h(x)\,(T_{0\infty} - T_w) \tag{2}$$

If $T_{aw}(x)$ is the wall adiabatic temperature with film cooling, an associated heat transfer coefficient can be introduced as follows:

$$q(x) = h_f(x)\,(T_{aw} - T_w) \tag{3}$$

The film cooling effectiveness is defined as

$$\eta(x) = (T_{0\infty} - T_{aw}(x))/(T_{0\infty} - T_{0c}) \tag{4}$$

where T_{0c} is the coolant temperature at the exit of the cooling holes. Combining relations (1)–(4) provides the following equation:

$$h(x)/h_0(x) = (h_f(x)/h_0(x))\,(1 - \eta(x)\theta) \tag{5}$$

$$\theta = (T_{0\infty} - T_{0c})/(T_{0\infty} - T_w) \tag{6}$$

Relation (5) is verified for a constant state of the boundary layer. The two parameters η and h_f can be considered to be independent of θ because of the relatively small coolant to gas temperature ratio variation ($0.6 < T_{0c}/T_{0\infty} < 0.8$). The linearity of relation (5) has been verified experimentally and is illustrated for both configurations I2 and I3 in Figs. 9(*a*) and 9(*b*).

Downloaded 01 Jun 2010 to 171.66.16.66. Redistribution subject to ASME license or copyright; see http://www.asme.org/terms/Terms_Use.cfm

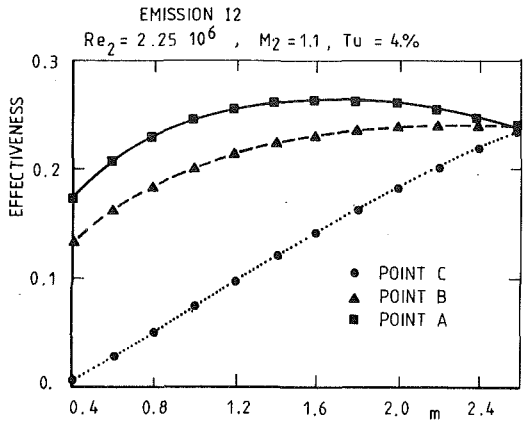

Fig. 10 Influence of m on η (I2)

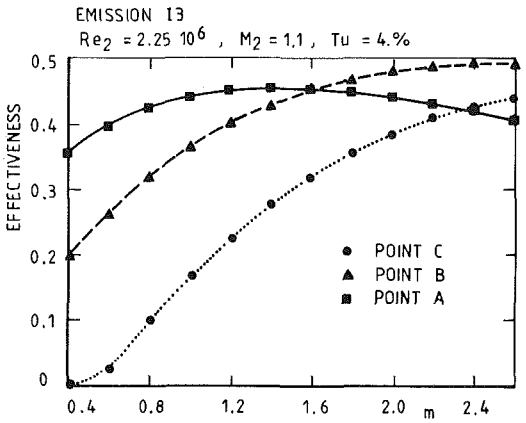

Fig. 11 Influence of m on η (I3)

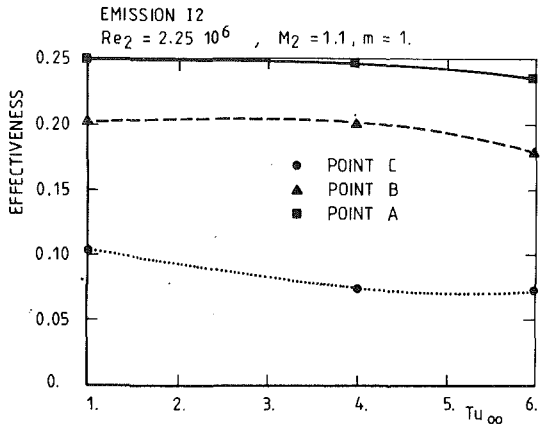

Fig. 12 Influence of Tu on η (I2)

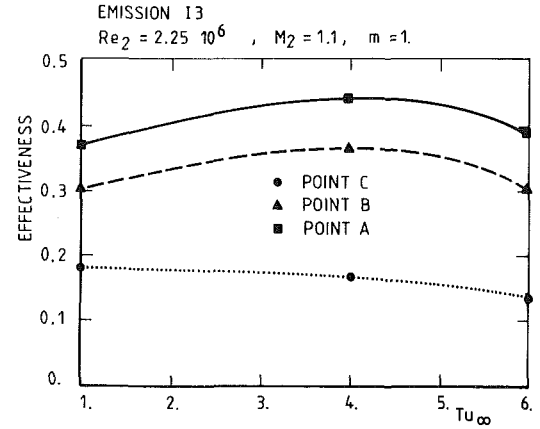

Fig. 13 Influence of Tu on η (I3)

Film Cooling Effectiveness

Influence of Blowing Rate. The influence of blowing rate ($m = 0.4$–2.6) on film cooling effectiveness is respectively presented in Figs. 10 and 11 for configurations I2 and I3. These results are given in three different locations, called A, B, and C on the present and following figures. Point A is located just downstream of the emission holes, point B is just a little farther (next measurement point), and point C is situated downstream of the jet coalescence point and of the film reattachment point.

Just downstream of the emission sites (point A), the film cooling effectiveness reaches a maximum for values of the blowing rate respectively equal to 1.8 (configuration I2) and 1.5 (configuration I3). This evolution is explained by the fact that the relative position of point A changes with respect to the limits of the small recirculation and three-dimensional flow region when the blowing rate varies. This effect appears to be more important for configuration I3 where, above a certain blowing rate value, the film cooling effectiveness at point A becomes lower than the values calculated at points B and even C. Considering point B configuration I2, the film cooling effectiveness increases for blowing rate values lower than 2 and remains nearly constant for higher values. The same phenomenon is observed for configuration I3, but an almost constant film cooling effectiveness is now obtained for a slightly higher blowing rate value of about 2.6. Finally, at point C, the film cooling effectiveness increases more or less regularly with the blowing rate for both configurations.

Influence of Free-Stream Turbulence. The influence of free-stream turbulence intensity ($Tu_\infty = 1$, 4, 6 percent) on film cooling effectiveness is respectively presented in Figs. 12 and 13 for configurations I2 and I3.

Let us first consider configuration I2. At points A and B, the film cooling effectiveness does not seem to be affected by turbulence intensity, up to a value of 4 percent, whereas it decreases for a higher value (6 percent). At point C, the film cooling effectiveness decreases for increasing values of the free-stream turbulence intensity. If configuration I3 is now considered, it appears that the film cooling effectiveness reaches a maximum value for the intermediate turbulence intensity (4 percent) at points A and B. At point C, it has a trend analogous to that observed for configuration I2.

An explanation of this behavior is found in the presence of the small recirculation region, extending more or less between 15 and 20 percent of the pressure side wetted length. As seen before, it is only free-stream turbulence that affects the importance of this bubble. The configuration I3, situated just downstream of the separated region, will therefore be more affected, depending on the size of the bubble.

Influence of Reynolds Number. The influence of free-stream Reynolds number ($Re_2 = 1.50$–3.0×10^6) on the film cooling effectiveness is respectively presented in Figs. 14 and 15 for configurations I2 and I3.

Looking at the results obtained at points A, B, and C for configuration I2, there seems to be a maximum in film cooling effectiveness for a value of Re_2 slightly lower than 2.25×10^6; a decrease is then observed for higher free-stream Reynolds number values. This effect is rather important for point C: For the highest Reynolds number flow, no significant effectiveness is still present in this location. The effect of a maximum film cooling effectiveness is explained by the modification of the boundary layer status, going from highly transitional for the lowest value of Re_2 to fully turbulent for the intermediate and highest values of the same parameter. As seen in Fig. 15,

Downloaded 01 Jun 2010 to 171.66.16.66. Redistribution subject to ASME license or copyright; see http://www.asme.org/terms/Terms_Use.cfm

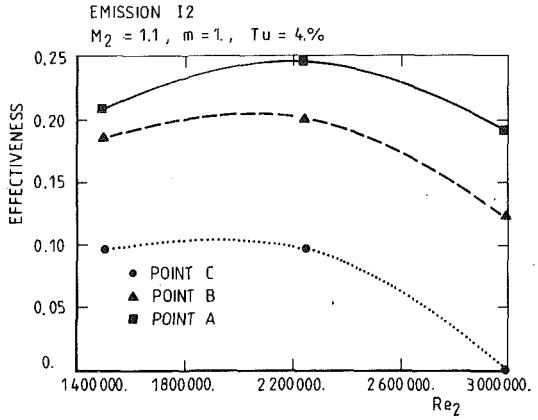

Fig. 14 Influence of Re on η (I2)

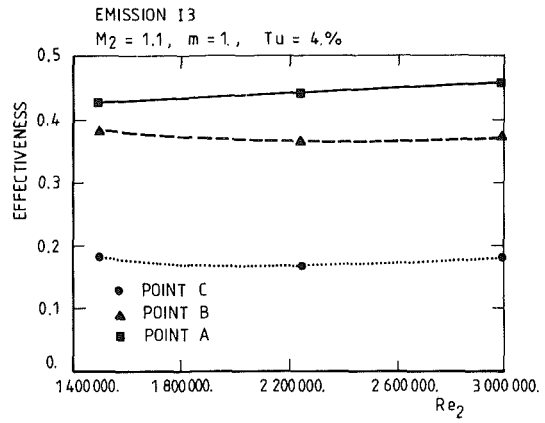

Fig. 15 Influence of Re on η (I3)

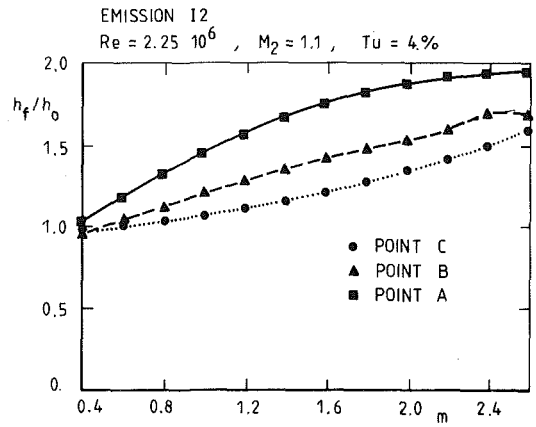

Fig. 16 Influence of m on h_f/h_0 (I2)

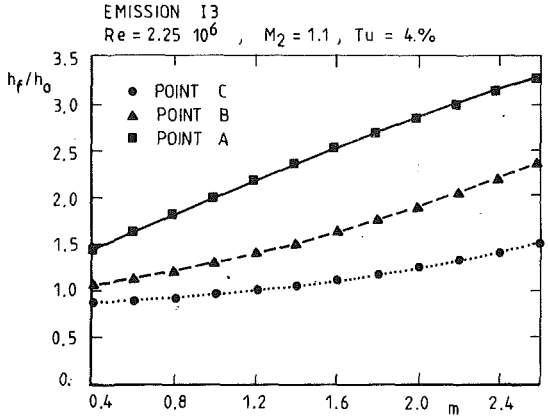

Fig. 17 Influence of m on h_f/h_0 (I3)

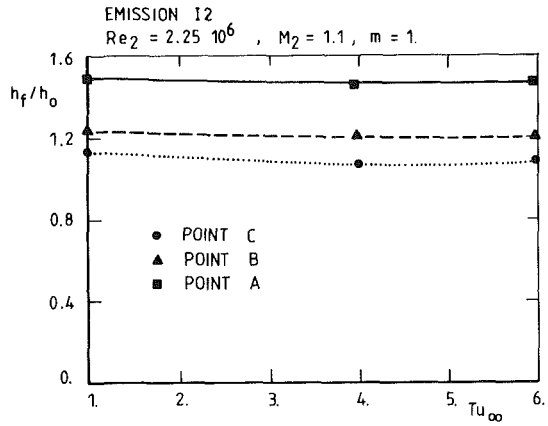

Fig. 18 Influence of Tu on h_f/h_0 (I2)

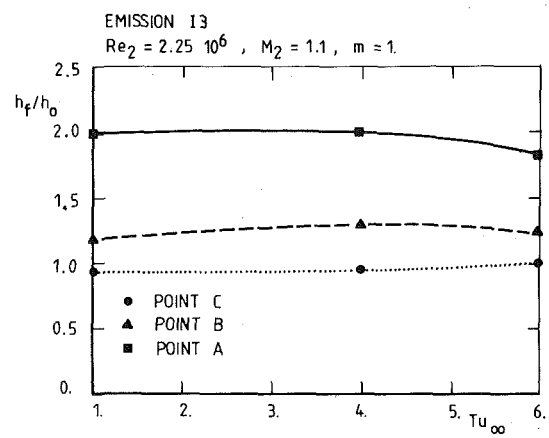

Fig. 19 Influence of Tu on h_f/h_0 (I3)

the effect of free-stream Reynolds number is rather limited for configuration I3.

Performance of Both Configurations. For all free-stream and coolant parametric variations, configuration I3 appears to be more effective than configuration I2. The values of the film cooling effectiveness are nearly doubled and the streamwise decays of both films are rather similar. Moreover, configuration I3 appears less sensitive to all free-stream conditions, and especially Reynolds number, modifications.

Heat Transfer Coefficient

Influence of Blowing Rate. The influence of blowing rate on the external convective heat transfer coefficient distribution is presented in Figs. 16 (configuration I2) and 17 (configuration I3).

For all measurement points considered along the pressure side and for both configurations, the value of the ratio h_f/h_0 increases with the blowing rate. This behavior is, as expected, particularly important in the near vicinity of the cooling holes where, for a blowing rate value equal to 2.6, values of this ratio equal to 2 are observed for configuration I2 and values in excess of 3 for configuration I3. Farther downstream, this ratio tends to a value of 1, i.e., recovering the value of the heat transfer coefficient without film cooling.

Influence of Free-Stream Turbulence. The influence of free-stream turbulence intensity on the external convective heat transfer coefficient distribution is presented in Figs. 18 (configuration I2) and 19 (configuration I3).

Downloaded 01 Jun 2010 to 171.66.16.66. Redistribution subject to ASME license or copyright; see http://www.asme.org/terms/Terms_Use.cfm

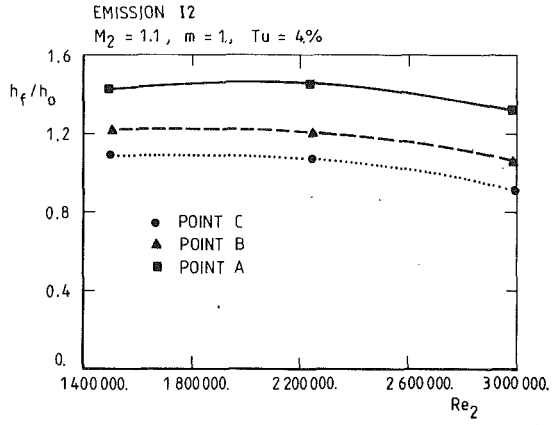

Fig. 20 Influence of Re on h_f/h_0 (I2)

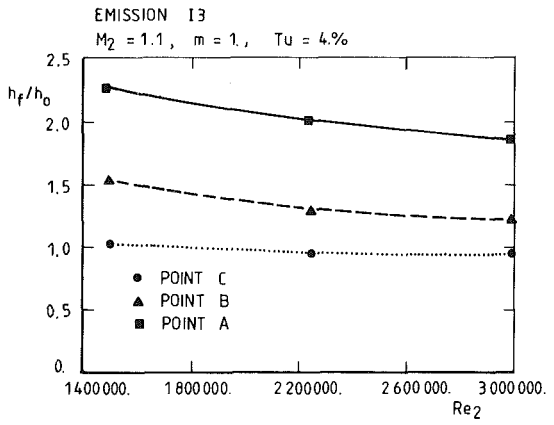

Fig. 21 Influence of Re on h_f/h_0 (I3)

The influence of this parameter is negligible for all measurement points considered on both configurations. The small variations observed in the figures remain well within the measurement uncertainty limits.

Influence of Reynolds Number. The influence of the free-stream Reynolds number on the external convective heat transfer coefficient distribution is presented in Figs. 20 (configuration I2) and 21 (configuration I3).

Looking at configuration I2, the ratio h_f/h_0 looks rather insensitive below a Re_2 value equal to about 2.0×10^6. For higher values the ratio h_f/h_0 decreases. This behavior can be linked to the drop in film cooling efficiency observed for the same conditions. The variation is more sensitive for configuration I3. At point A, the reduction in the ratio h_f/h_0 amounts to about 22 percent between the results obtained for the lowest and highest values of the Reynolds number. Smaller variations are observed when moving farther downstream of the cooling holes.

Performance of Both Configurations. The effects on heat transfer coefficient are again more important for configuration I3. For a given geometry, the most sensible parameter is the blowing rate. Free-stream turbulence intensity and Reynolds number variations induce only small variations in the ratio h_f/h_0.

Conclusions

Results have been obtained from a systematic experimental program on external convective heat transfer measurements with film cooling along the pressure side of a high-pressure turbine nozzle guide vane. The major effects of the different main and coolant flow parameters on film cooling effectiveness and heat transfer coefficient have been identified.

The external convective heat transfer coefficient distributions measured under the presence of film cooling provide an evaluation of the overall performance of the cooling configuration:

- better thermal protection is obtained for both configurations when the blowing rate value is increased, except in the near hole region and especially for higher coolant to gas temperature ratios;
- for the lowest free-stream Reynolds number, a heat transfer augmentation is observed for both configurations along the rear part of the blade. It demonstrates the dominant destabilizing effect of the coolant film on a not yet fully established turbulent boundary layer.

The data reduction in terms of film cooling effectiveness and isothermal heat transfer coefficient allows separate evaluation of the aerodynamic and thermal behavior of the coolant film:

- considered in function of the blowing rate, the film cooling effectiveness exhibits a maximum; the coordinates of the latter depend on the location of the cooling holes;
- free-stream turbulence has a definite effect on film cooling effectiveness. A fundamental explanation of this phenomenon requires however more detailed measurements of the boundary layer structure;
- the observations drawn from the convective heat transfer distributions enforce those drawn from the film cooling effectiveness distributions.

The consideration of the heat transfer coefficient distributions has a major effect on the thermal design of turbine blades. The present investigation not only demonstrates the film cooling effectiveness variations due to geometric and aerothermal modifications, but also points out the boundary layer perturbation due to the film, seen from a convection point of view.

Acknowledgments

The authors wish to thank SNECMA for financial support and the permission to publish the paper and the technical personnel of the VKI Turbomachinery Department for the assistance throughout the testing program.

References

Arts, T., 1982, "Etude de l'écoulement tridimensionnel complet dans un étage de turbine transsonique," Ph.D. Thesis, Université Catholique de Louvain, Belgium.

Camci, C., 1985, "An Experimental and Theoretical Heat Transfer Investigation of Film Cooling on a High Pressure Gas Turbine Blade," Ph.D. Thesis, Katholieke Universiteit Leuven, Belgium.

Camci, C., and Arts, T., 1985, "Short Duration Measurements and Numerical Simulation of Heat Transfer Along the Suction Side of a Film Cooled Gas Turbine Blade," ASME *Journal of Engineering for Gas Turbines and Power*, Vol. 107, No. 4, pp. 991-997.

Camci, C., Arts, T., Breugelmans, F. A., 1985, "Experimental Convective Heat Transfer Investigation Around a Film Cooled High Pressure Turbine Blade," presented at the 7th Int. Symposium on Air Breathing Engines, Beijing, Peoples Republic of China.

Consigny, H., and Richards, B. E., 1982, "Short Duration Measurements of Heat Transfer Rate to a Gas Turbine Rotor Blade," ASME *Journal of Engineering for Power*, Vol. 104, No. 3, pp. 542-551.

Daniels, L. C., 1979, "Film Cooling of Gas Turbine Blades," Ph.D. Thesis, University of Oxford, United Kingdom.

Dring, R. P., Blair, M. F., and Josyln, H. D., 1980, "An Experimental Investigation of Film Cooling on a Turbine Rotor Blade," ASME *Journal of Engineering for Power*, Vol 102, No. 1, pp. 81-87.

Forth, C. J. P., and Jones, T. V., 1986, "Scaling Parameters in Film Cooling," *8th Int. Heat Transfer Conference*, Hemisphere Publishing Corp., New York.

Goldstein, R. J., 1971, "Film Cooling," *Advances in Heat Transfer*, Vol. 7, Academic Press, pp. 321-379.

Horton, F. G., Schultz, D. L., and Forest, A. E., 1985, "Heat Transfer Measurements With Film Cooling on a Turbine Blade Profile in Cascade," ASME Paper No. 85-GT-117.

Ito, S., Goldstein, R. J., and Eckert, E. R. G., 1978, "Film Cooling of a Gas Turbine Blade," ASME *Journal of Engineering for Power*, Vol. 100, pp. 476-481.

Downloaded 01 Jun 2010 to 171.66.16.66. Redistribution subject to ASME license or copyright; see http://www.asme.org/terms/Terms_Use.cfm

Jones, T. V., Schultz, D. L., and Hendley, A. D., 1973, "On the Flow in an Isentropic Free Piston Tunnel," A.R.C. R&M 3731.

Ko, S. Y., Yao, Y. Q., Xia, B., and Tsou, F. K., 1986, "Discrete Hole Film Cooling Characteristics Over Concave and Convex Surfaces," *8th Int. Heat Transfer Conference*, Hemisphere Publishing Corp., New York, Vol. 3, pp. 1297–1301.

Lander, R. D., Fish, R. W., and Suo, M., 1972, "External Heat Transfer Distribution on Film Cooled Turbine Vanes," *J. of Aircraft*, Vol. 9, No. 10, pp. 707–714.

Metzger, D. E., Carper, H. J., and Swank, L. R., 1968, "Heat Transfer With Film Cooling Near Nontangential Injection Slots," ASME *Journal of Engineering for Power*, Vol. 90, No. 2, pp. 157–163.

Nicolas, J., and LeMeur, A., 1974, "Curvature Effects on a Turbine Blade Cooling Film," ASME Paper No. 74-GT-156.

Pietrzyk, J. R., Bogard, D. G., and Crawford, M. E., 1989, "Hydrodynamic Measurements of Jets in Crossflow for Gas Turbine Film Cooling Applications," ASME JOURNAL OF TURBOMACHINERY, Vol. 111, pp. 139–145.

Richards, B. E., 1980, "Heat Transfer Measurements Related to Hot Turbine Components in the von Karman Institute Hot Cascade Tunnel," in: *Testing and Measurement Techniques in Heat Transfer and Combustion*, AGARD CP 281, Paper 6.

Schultz, D. L., and Jones, T. V., 1973, "Heat Transfer Measurements in Short Duration Hypersonic Facilities," AGARDograph 165.

Schwarz, S. G., and Goldstein, R. J., 1989, "The Two-Dimensional Behavior of Film Cooling Jets on Concave Surfaces," ASME JOURNAL OF TURBOMACHINERY, Vol. 111, pp. 124–130.

Downloaded 01 Jun 2010 to 171.66.16.66. Redistribution subject to ASME license or copyright; see http://www.asme.org/terms/Terms_Use.cfm

Jones, T. V., Schultz, D. L., and Hendley, A. D., 1973, "On the Flow in an Isentropic Free Piston Tunnel," A.R.C. R&M 3731.

Ko, S. Y., Yao, Y. Q., Xia, B., and Tsou, F. K., 1986, "Discrete Hole Film Cooling Characteristics Over Concave and Convex Surfaces," *8th Int. Heat Transfer Conference*, Hemisphere Publishing Corp., New York, Vol. 3, pp. 1297–1301.

Lander, R. D., Fish, R. W., and Suo, M., 1972, "External Heat Transfer Distribution on Film Cooled Turbine Vanes," *J. of Aircraft*, Vol. 9, No. 10, pp. 707–714.

Metzger, D. E., Carper, H. J., and Swank, L. R., 1968, "Heat Transfer With Film Cooling Near Nontangential Injection Slots," ASME *Journal of Engineering for Power*, Vol. 90, No. 2, pp. 157–163.

Nicolas, J., and LeMeur, A., 1974, "Curvature Effects on a Turbine Blade Cooling Film," ASME Paper No. 74-GT-156.

Pietrzyk, J. R., Bogard, D. G., and Crawford, M. E., 1989, "Hydrodynamic Measurements of Jets in Crossflow for Gas Turbine Film Cooling Applications," ASME JOURNAL OF TURBOMACHINERY, Vol. 111, pp. 139–145.

Richards, B. E., 1980, "Heat Transfer Measurements Related to Hot Turbine Components in the von Karman Institute Hot Cascade Tunnel," in: *Testing and Measurement Techniques in Heat Transfer and Combustion*, AGARD CP 281, Paper 6.

Schultz, D. L., and Jones, T. V., 1973, "Heat Transfer Measurements in Short Duration Hypersonic Facilities," AGARDograph 165.

Schwarz, S. G., and Goldstein, R. J., 1989, "The Two-Dimensional Behavior of Film Cooling Jets on Concave Surfaces," ASME JOURNAL OF TURBOMACHINERY, Vol. 111, pp. 124–130.

DISCUSSION

P. M. Ligrani[1]

The authors are to be congratulated for a useful and important piece of work. The purpose of this comment is to point out some additional interesting features of the data presented and of other data obtained under similar conditions in compressible, variable property flow (Ligrani and Camci, 1985). Further discussion of the effects of variable properties is also presented.

1 As the authors have indicated, the linear extrapolation procedure given by equation (5) is valid provided that h_f and adiabatic effectiveness η are independent of nondimensional temperature θ for the range of θ considered. This is true for the range of experimental data covered by the authors' study because, as they have pointed out, their coolant to gas temperature ratio variation is small ($0.6 < T_{oc}/T_{0\infty} < 0.8$). However, generally, this is not true if property variations are significant over the range of experimental conditions covered by the data. The properties whose variations are most important in boundary layer flows are density, molecular thermal conductivity, and molecular viscosity. In turbulent film cooling applications, one of the more important variable property parameters is the ratio of coolant density to free-stream density ρ_c/ρ_∞.

Density ratio ρ_c/ρ_∞ varies with θ according to the equation

$$\theta = [1/(\rho_c/\rho_\infty) - 1]/[T_w/T_{r\infty} - 1] \qquad (a)$$

Here, $T_c/T_\infty = T_{oc}/T_{0\infty}$ is assumed, where the subscript 0 denotes stagnation conditions. (It is actually more appropriate to use recovery temperatures instead of stagnation temperatures.) Because the density ratio varies with θ, the effectiveness η will also vary (Pedersen et al., 1977). The amount of h/h_0 data nonlinearity then depends on the extent of the variation of the density ratio over the range of θ (as well as the dependence of η on ρ_c/ρ_∞) from axis to axis for the particular experimental condition.

Such nonlinearity of h/h_0 plots is illustrated by the curve for Point B in Fig. 9(*b*) of the Arts and Bourguignon paper. If other data are extended beyond the range presented in this paper, h/h_0 plots will also likely be nonlinear because of variations of ρ_c/ρ_∞ along the curve. This is further illustrated by data presented by Ligrani and Camci (1985) obtained using the same experimental facility as used by Arts and Bourguignon. The nonlinearity of h/h_0 versus θ data is also tied to the fact that, in variable property flow, the energy equation is *nonlinear* and coupled to the momentum equation.

The main point here is then that the extrapolation procedure represented by equation (5) does not give the same η and h_f/h_0 as given by plots of h/h_0 versus θ experimental data if these data are obtained at the intercepts.

2 This is further illustrated by the results presented in Fig. 22. Here, an empirical fit to experimental data from Ligrani and Camci (1985) is shown to illustrate the nonlinearity of such data. This equation was developed for data obtained downstream of two rows of holes on a flat plate. This empirical equation is given by

$$\hat{h}/h_0 (T_{rc}/T_{r\infty})^n (T_{r\infty}/T_w)^p = h_f'/h_0 (1 - \eta'\theta) \qquad (b)$$

here, $\hat{h}/h_0$ represents variable property h/h_0, and n and p are empirical constants. The intercepts at the two axes are h_f'/h_0 and $1/\eta'$. These are different from the $1/\eta$ and h_f/h_0 values given by a *linear* interpolation to data for θ from 0.75 to 1.2, which is about the same data range employed by Arts and Bourguignon.

3 If the density ratio then varies significantly over the range of θ of the experimental data, it is also important to specify which film cooling parameter—blowing ratio, velocity ratio, or momentum flux ratio—is constant along a collection of h/h_0 versus θ data, as keeping one of these constant will result in variation of the others (Ligrani and Camci, 1985). In the Arts and Bourguignon paper, the blowing ratio is maintained constant along the h/h_0 versus data. In Fig. 1, blowing ratio is maintained constant; however, in the Ligrani and Camci 1985) paper, effectiveness is determined using all three injection parameters.

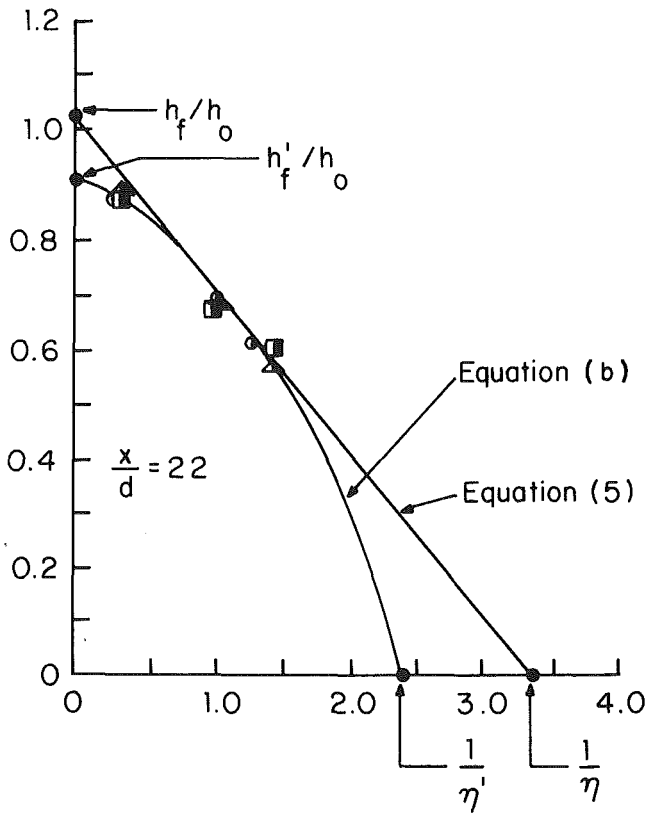

Fig. 22 h/h_0 versus θ plot illustrating axis intercepts from equation (5) and from equation (*b*)

[1]Associate Professor, Department of Mechanical Engineering, Naval Postgraduate School, Monterey, CA, 93943-5000.

Copyright © 1990 by ASME

Downloaded 01 Jun 2010 to 171.66.16.66. Redistribution subject to ASME license or copyright; see http://www.asme.org/terms/Terms_Use.cfm

4 Values of η and h_f/h_0 from equation (5) in the Arts and Bourguignon paper are then the *ones that give* h/h_0 data for a particular downstream location and particular experimental conditions for θ values ranging from about 0.7 to approximately 1.2. From a gas turbine thermal design point of view, resulting η and h_f/h_0 are entirely valid provided the procedures used to obtain them are kept in mind, and provided corresponding θ and ρ_c/ρ_∞ are presented, as the authors have done.

5 In order to obtain h/h_0 versus θ data, which approach linearity over the entire range of θ from axis to axis, one of two situations is needed: (*a*) near-constant property flow wherein the variation of θ does not result in significant variation of the density ratio (Metzger et al., 1968; Choe et al., 1975), or (*b*) a situation where θ is varied without changing the coolant temperature so that ρ_c/ρ_∞ remains constant. This latter situation is accomplished in experiments such as the one described by Loftus and Jones (1983), wherein θ is varied by altering the wall temperature as the coolant temperature and free-stream temperature are maintained constant.

6 Variable property, film-cooled turbulent boundary layers are complex thermal fluid systems. The importance of variable properties cannot be minimized, and it is hoped that this comment will provoke more attention and discussion to this important area.

References

Choe, H., Kays, W. M., and Moffat, R. J., 1975, "The Turbulent Boundary Layer on a Full-Coverage Film-Cooled Surface: An Experimental Heat Transfer Study With Normal Injection," Report No. HMT-22, Thermosciences Division, Department of Mechanical Engineering, Stanford University, Stanford, CA.

Ligrani, P. M., and Camci, C., 1985, "Adiabatic Film Cooling Effectiveness From Heat Transfer Measurements in Compressible, Variable-Property Flow," ASME *Journal of Heat Transfer*, Vol. 107, pp. 313–320.

Loftus, P. J., and Jones, T. V., 1983, "The Effect of Temperature Ratios on the Film-Cooling Process," ASME *Journal of Engineering for Power*, Vol. 105.

Metzger, D. E., Carper, H. J., and Swank, L. R., 1968, "Heat Transfer With Film Cooling Near Nontangential Injection Slots," ASME *Journal of Engineering for Power*, pp. 157–163.

Pedersen, D. R., Eckert, E. R. G., and Goldstein, R. J., 1977, "Film Cooling with Large Density Differences Between the Mainstream and the Secondary Fluid Measured by the Heat Mass Transfer Analogy," ASME *Journal of Heat Transfer*, Vol. 99, pp. 620–627.

Authors' Closure

The authors thank Dr. Ligrani for his interesting comments. It is definitely true that phenomena associated with large variations of the coolant and free-stream parameters deserve considerable attention, not only from a thermal point of view, but also from an aerodynamic point of view. These topics have been addressed by many researchers in recent years. As pointed out by Dr. Ligrani, the particular procedure used in the present paper to calculate effectiveness is valid because of the small range of coolant to gas temperature ratio considered in this investigation

The authors would also like to make an additional comment. The two global objectives of this investigation were to provide accurate data to develop and verify detailed boundary layer calculation methods and to identify simple correlations to be used in the current design procedure of cooled turbines. The first objective was met by considering individual heat transfer coefficient data for different values of the cooling parameters. The second objective introducing the use of effectiveness, was dictated by the fact that the current design procedures still imply the definition of an intermediate temperature, in this case the blade skin temperature, in order to solve the complete problem (external convection, conduction, and internal convection) in successive steps by means of some kind of iterative procedure. A more direct, if not more elegant, way would be to solve this complex design problem in one step, considering the boundary conditions in terms of heat fluxes rather than in terms of temperature or adiabatic effectiveness. However, this approach does not seem to be applicable yet and more attention should be given to it in the future.

Downloaded 01 Jun 2010 to 171.66.16.66. Redistribution subject to ASME license or copyright; see http://www.asme.org/terms/Terms_Use.cfm

4 Values of η and h_f/h_0 from equation (5) in the Arts and Bourguignon paper are then the *ones that give* h/h_0 data for a particular downstream location and particular experimental conditions for θ values ranging from about 0.7 to approximately 1.2. From a gas turbine thermal design point of view, resulting η and h_f/h_0 are entirely valid provided the procedures used to obtain them are kept in mind, and provided corresponding θ and ρ_c/ρ_∞ are presented, as the authors have done.

5 In order to obtain h/h_0 versus θ data, which approach linearity over the entire range of θ from axis to axis, one of two situations is needed: (*a*) near-constant property flow wherein the variation of θ does not result in significant variation of the density ratio (Metzger et al., 1968; Choe et al., 1975), or (*b*) a situation where θ is varied without changing the coolant temperature so that ρ_c/ρ_∞ remains constant. This latter situation is accomplished in experiments such as the one described by Loftus and Jones (1983), wherein θ is varied by altering the wall temperature as the coolant temperature and free-stream temperature are maintained constant.

6 Variable property, film-cooled turbulent boundary layers are complex thermal fluid systems. The importance of variable properties cannot be minimized, and it is hoped that this comment will provoke more attention and discussion to this important area.

References

Choe, H., Kays, W. M., and Moffat, R. J., 1975, "The Turbulent Boundary Layer on a Full-Coverage Film-Cooled Surface: An Experimental Heat Transfer Study With Normal Injection," Report No. HMT-22, Thermosciences Division, Department of Mechanical Engineering, Stanford University, Stanford, CA.

Ligrani, P. M., and Camci, C., 1985, "Adiabatic Film Cooling Effectiveness From Heat Transfer Measurements in Compressible, Variable-Property Flow," ASME *Journal of Heat Transfer*, Vol. 107, pp. 313–320.

Loftus, P. J., and Jones, T. V., 1983, "The Effect of Temperature Ratios on the Film-Cooling Process," ASME *Journal of Engineering for Power*, Vol. 105.

Metzger, D. E., Carper, H. J., and Swank, L. R., 1968, "Heat Transfer With Film Cooling Near Nontangential Injection Slots," ASME *Journal of Engineering for Power*, pp. 157–163.

Pedersen, D. R., Eckert, E. R. G., and Goldstein, R. J., 1977, "Film Cooling with Large Density Differences Between the Mainstream and the Secondary Fluid Measured by the Heat Mass Transfer Analogy," ASME *Journal of Heat Transfer*, Vol. 99, pp. 620–627.

Authors' Closure

The authors thank Dr. Ligrani for his interesting comments. It is definitely true that phenomena associated with large variations of the coolant and free-stream parameters deserve considerable attention, not only from a thermal point of view, but also from an aerodynamic point of view. These topics have been addressed by many researchers in recent years. As pointed out by Dr. Ligrani, the particular procedure used in the present paper to calculate effectiveness is valid because of the small range of coolant to gas temperature ratio considered in this investigation

The authors would also like to make an additional comment. The two global objectives of this investigation were to provide accurate data to develop and verify detailed boundary layer calculation methods and to identify simple correlations to be used in the current design procedure of cooled turbines. The first objective was met by considering individual heat transfer coefficient data for different values of the cooling parameters. The second objective introducing the use of effectiveness, was dictated by the fact that the current design procedures still imply the definition of an intermediate temperature, in this case the blade skin temperature, in order to solve the complete problem (external convection, conduction, and internal convection) in successive steps by means of some kind of iterative procedure. A more direct, if not more elegant, way would be to solve this complex design problem in one step, considering the boundary conditions in terms of heat fluxes rather than in terms of temperature or adiabatic effectiveness. However, this approach does not seem to be applicable yet and more attention should be given to it in the future.

Copyright © 1990 by ASME

Downloaded 01 Jun 2010 to 171.66.16.66. Redistribution subject to ASME license or copyright; see http://www.asme.org/terms/Terms_Use.cfm

Effects of Wake Passing on Stagnation Region Heat Transfer

J. E. O'Brien
NASA Lewis Research Center,
Cleveland, OH 44135

An experimental study is described in which both time-averaged and time-resolved effects of wake passing were measured in a cylinder stagnation region. The experiments were carried out in an annular-flow wind tunnel, which was fitted with a spoked-wheel wake generator. The cylindrical spokes produce wakes that simulate those shed from a turbine inlet guide vane. Time-averaged heat transfer results indicate an asymmetric distribution of heat transfer coefficient about the stagnation line, with higher heat transfer coefficients on the windward side (with respect to the bar-passing direction), which corresponds to the suction side of a turbine blade. This asymmetry is also reflected in the time-resolved heat transfer results, which were obtained using a test cylinder instrumented with platinum thin-film gages. Unsteady heat flux records reveal very large positive excursions (as much as a factor of three) in instantaneous heat flux during wake passing on the windward side of the cylinder and much smaller effects on the leeward side. Hot-film records in the cylinder stagnation region were also obtained by operating the thin-film gages in the constant-temperature mode. Spectra of these hot-film records indicate that vortex shedding is a major contributor to the unsteady buffeting of the test-cylinder boundary layer at circumferential stations located at both +60 deg and −60 deg from the stagnation line, but makes a very small contribution on the stagnation line itself.

Introduction

There has been a great deal of interest in recent years in the unsteady effects of wake passing in turbomachinery. The high levels of unsteadiness present in the wakes give rise to increased stagnation-region heat transfer and early boundary layer transition on downstream blades. The stagnation region is of particular interest for several reasons. First, turbine heat transfer rates are higher by far on the stagnation line than at any position along the blade surface other than the tip region. Consequently, accurate prediction of stagnation line heat transfer coefficients is highly desirable. Second, from an intellectual viewpoint, the nature of a stagnation-region boundary layer in the presence of high disturbance levels is not fully understood. It may be rfeferred to as a buffeted laminar boundary layer. The effect of high free-stream turbulent and the impact of turbulent length scales on the stagnation-region boundary layer have been important research topics in heat transfer for many years (e.g., see O'Brien and Van Fossen, 1985). Wake passing is characterized both by very high levels of unsteadiness and by the presence of coherent vortical structures. In addition, changes in flow incidence angle that occur during wake passing may give rise to instantaneous flow separation on an airfoil pressure surface. All of these effects have been identified in the present study.

For the present study, simulated inlet guide vane (IGV) wakes were produced by means of a rotating spoked wheel wake generator. This type of wake generator, which was developed by Doorly and Oldfield (1985a), has been shown to reproduce very closely the correct relative velocity vector diagram and mean wake velocity profiles associated with the IGV/rotor combination found in an actual turbine stage (Doorly, 1984). Detailed turbulence characteristics of the flow downstream of the wake-generating spokes have recently been documented by O'Brien and Capp (1988).

Several researchers have studied various aspects of unsteady turbine airfoil heat transfer. Experiments on the effects of wake (Doorly et al., 1985) and shock-wave (Doorly and Oldfield, 1985b) passing on unsteady turbine blade heat transfer revealed the importance of these disturbances in forcing transient premature transition on the suction surface. Separate effects due to natural transition and wake passing have been resolved by LaGraff et al. (1989) in the same linear cascade facility. Unsteady and time-averaged heat transfer effects have been documented by Dunn et al. (e.g., 1989) in a shock-tunnel facility that accommodates a full-scale rotating turbine stage. Full-scale rotating-stage experiments aimed at documenting both time-resolved and time-averaged heat transfer have also been performed by Guenette et al. (1989) in a short-duration blowdown facility. Heat transfer results of the Guenette et al. experiments compared favorably to results obtained by Ashworth et al. (1985) on the same blade profiles in a linear cascade behind a rotating spoked wheel wake generator.

This paper presents a detailed account of the unsteady heat transfer processes that occur in a cylinder stagnation region as a result of wake passing. Heat transfer results will be presented in three forms: time-averaged (steady-state), time-resolved (instantaneous), and phase-averaged. From the standpoint of modeling, the phase-averaged results may be

Contributed by the International Gas Turbine Institute and presented at the ASME Winter Annual Meeting, Chicago, Illinois, November 27–December 2, 1988. Manuscript received at ASME Headquarters March 1988.

Copyright © 1990 by ASME
Downloaded 01 Jun 2010 to 171.66.16.66. Redistribution subject to ASME license or copyright; see http://www.asme.org/terms/Terms_Use.cfm

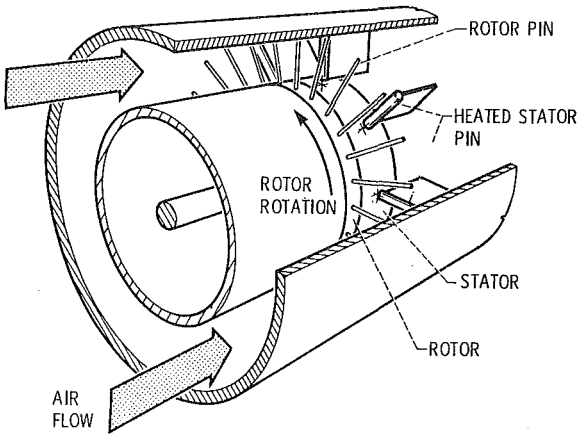

Fig. 1 Schematic of rotor-wake heat transfer facility test section

more useful since these results reveal the mean behavior of the boundary layer during one complete wake-passing cycle for which phase-averaged flowfield (and turbulence) data are also available.

Facility and Instrumentation

Test Facility. The experiments were carried out in an annular-flow open-circuit wind tunnel, which has been described in detail previously (Simoneau et al., 1984). Air flow drawn from the test cell passes through a flow-conditioning section and an 8.3 to 1 contraction before entering the test section, which is shown schematically in Fig. 1. The test-section annulus (40.64 cm o.d., 27.05 cm i.d.) was fitted with a turbulence grid, which produced a background free-stream turbulence intensity of about 1.2 percent at the measurement station.

A special feature of this tunnel was the incorporation of a wake-generating rotor for the production of simulated turbine inlet-guide-vane wakes. Previous work in this facility was aimed at determining the effects of these wakes on steady-state heat transfer in the stagnation region of a downstream circular cylinder (Morehouse and Simoneau, 1986). Preliminary unsteady heat transfer results and comparisons to steady-state results were also obtained (O'Brien et al., 1986). For the present study, there was a total of eight stationary cylinders (two of which were instrumented), located 45 deg apart, mounted downstream of the spoked-wheel rotor. Four of these stators can be seen in Fig. 1.

The wake simulation was accomplished by means of the rotating spoked wheel shown in Fig. 1. The rotor was fitted with 24 equally spaced cylindrical spokes (or bars) 0.3175 cm in diameter. The leading edges of the heat transfer test cylinders were located eight bar diameters downstream of the rotor. Bar-passing frequencies f_b could be set from 200 to 2800 Hz, and were nondimensionalized in terms of the bar-passing Strouhal number S_b, defined as

$$S_b = \frac{2\pi f_b d_b}{\bar{U}}$$

where d_b is the bar diameter and $\bar{U}$ is the overall-average velocity.

A schematic of the unsteady flow situation in the rig test section is shown in Fig. 2. This schematic represents an instan-

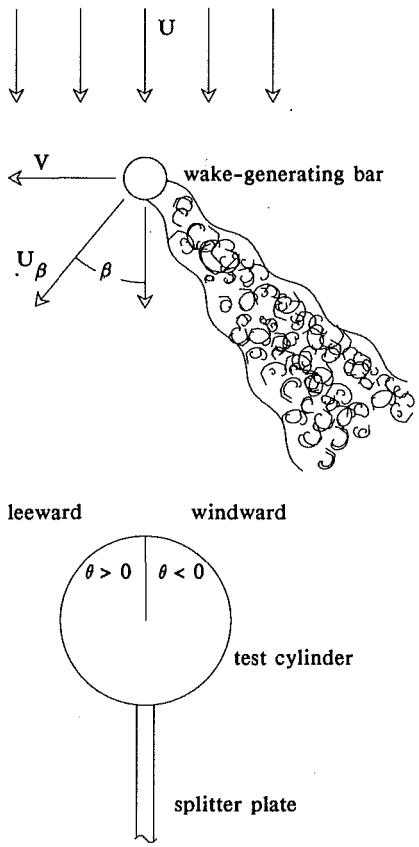

Fig. 2 Wake flow schematic

Nomenclature

c_p = specific heat, J/kg K
d_b = wake-generating bar diameter, m
D = test cylinder diameter, m
e = fluctuating hot-film voltage, V
$e(f)$ = power spectral density of hot-film voltage, V^2/Hz
E = hot-film voltage, V
Ec = Eckert number
f = frequency, Hz
Fr = Frössling number
h = heat transfer coefficient, W/m^2K
M = Mach number
N = total number of samples
Pr = Prandtl number
q'' = heat flux, W/m^2
Re = Reynolds number
s = general quantity to be phase averaged
S = Strouhal number
t = time, s
T = temperature, °C
Tu = turbulence intensity
Tu' = flow unsteadiness parameter
u = fluctuating axial velocity, m/s
U = axial velocity, m/s
v = fluctuating tangential velocity, m/s
V = tangential velocity, m/s
α = rotor phase angle, deg
β = flow incidence angle, deg
θ = angle from stagnation on test cylinder, deg

Subscripts

b = bar or bar-passing
r = recovery
ref = reference
s = static
so = approach static
t = total
w = wall

Superscripts

$\bar{}$ = overall (time) averaged quantity
$\tilde{}$ = phase-averaged quantity

Downloaded 01 Jun 2010 to 171.66.16.66. Redistribution subject to ASME license or copyright; see http://www.asme.org/terms/Terms_Use.cfm

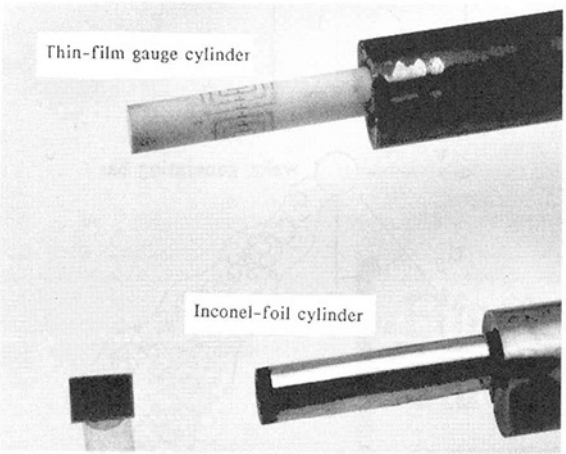

Fig. 3 Heat transfer test cylinders

taneous snapshot of the wake as would be produced, for example, by a spark Schlieren photograph. Upstream of the wake-generating bar, the incident flow velocity is represented by U while the motion of the bar is indicated at velocity V. The motion of the wake-generating bar with respect to the air flow produces a velocity vector U_β in the wake, which has a nonzero flow incidence angle β as shown. Some of the terminology to be used in the paper is also indicated in the figure. The "leeward" side of the test cylinder is the side opposite the direction of rotation of the wake-generating bar for which the angle from stagnation θ is positive. The "windward" side of the test cylinder is as shown.

In order to enable the calculation of phase-averaged data, a fiber-optic sensor was mounted on the outside annulus of the tunnel. This sensor detected the passage of one of the wake-generating bars whose tip had been coated with a silver reflecting paint. The resulting once/rev signal was input to an electronic shaft-angle encoder, which generated a corresponding once/wake signal updated each rotor revolution.

Downstream of the stator row, the air encounters a set of flow straighteners designed to minimize large-scale swirl. Flow velocities in the test section could be set from 10 to 120 m/s, yielding Reynolds numbers based on mass-averaged axial flow velocity and heat transfer cylinder diameter up to 96,000. An ASME standard sharp-edged orifice located downstream of the test section exit was used to establish and monitor tunnel flow rates.

Instrumentation and Models. Steady-state heat transfer data were acquired using the 12.7-mm-dia test cylinder shown in Fig. 3. It was fabricated by wrapping a rectangular section of inconel foil (0.025-mm thickness) around two copper rings, which served as electrical buses to which power lead wires were attached. The inconel foil had nine thermocouples (0.075-mm wire diameter) spot-welded to its inside surface at 20 deg circumferential intervals along the midspan of the cylinder. The entire core of the cylinder was filled with urethane foam in order to minimize extraneous conduction losses. Direct electrical current was passed through the inconel foil, providing a uniform heat flux thermal boundary condition. Inconel is a particularly good choice for this application due to its relatively high electrical resistivity and low temperature coefficient of resistance.

Unsteady heat flux information was obtained using the thin-film gage test cylinder, also shown in Fig. 3. It was fabricated from 12.7-mm-dia machinable ceramic rod (MACOR). Seven platinum thin-film gages (approximately 0.1 μm thick, 0.25 mm wide, and 2.8 mm long) were deposited on the surface of the ceramic rod, also at 20 deg circumferential intervals. The thin films were operated in the constant-current ($\sim$ 8 mA) mode, serving as high-frequency-response surface temperature sensors. Due to their very thin application, the thermal mass of each of the films is negligible. This type of thin-film heat-flux gage, originally developed by Vidal (1956), has been employed extensively in short-duration facilities. Details of thin-film gage measurement and analysis techniques are available from Schultz and Jones (1973) and from Schultz et al. (1978). Unsteady thin-film voltage signals, which correspond to unsteady surface temperature fluctuations, were processed by means of analog circuitry designed by Oldfield et al. (1984). This circuitry performs the conversion from unsteady temperature to a signal proportional to unsteady heat flux based on an electrical analogue (RC transmission line) of one-dimensional semi-infinite heat conduction. The circuit has broadband frequency response characteristics, 0.01 Hz to 100 kHz.

Steady-state rig operating conditions (temperatures, pressures, flow rates, etc.) were sampled and displayed on a control-room CRT by means of a 256-channel multiplexing digitizer and remote minicomputer, which provided data updates in engineering units approximately every two seconds. High-speed multichannel data acquisition was achieved using an eight-channel system that provided simultaneous 12-bit digitization with sampling rates up to 1 MHz and 128K of digital memory per channel. The high-speed data acquisition system was controlled by a dedicated desktop computer system, which was also used for data analysis and graphics. Frequency domain data were acquired using a separate hardware-based FFT analyzer, which was also interfaced to the cell desktop computer.

Experimental Procedure

Steady-State Heat Transfer. Prior to any data acquisition, steady-state rig operating conditions were established and a predetermined electrical power input was supplied to the inconel foil for several minutes to insure steady conditions. Due to a small voltage-tap error resulting from the intimate contact of the thermocouples with the foil, temperature data were acquired twice, with opposite power-supply polarities. Averaging of the two sets of temperature data was then performed. In addition, in order to minimize the effects of any slight misalignment or asymmetry of the cylinder, heat transfer data were acquired with both forward and reverse rotation of the wake-generating rotor. The results for corresponding circumferential locations were averaged.

Unsteady Heat Flux Measurements. In short-duration facilities, thin-film instrumented heat transfer models are essentially at room temperature prior to a test run. Heat transfer occurs upon firing of the tunnel when the model is subjected to a high-enthalpy flow for a short time period. In order to utilize this thin-film technique in a low-speed, steady-flow tunnel, the test cylinder of the present study was uniformly preheated to about 95°C in an oven located on the inside annulus of the tunnel test section and then suddenly injected into the flow by means of a pneumatic actuator. Transient heat transfer then occurs as a result of the temperature difference between the preheated cylinder and the ambient-temperature flow stream. A similar strategy of injecting a test model (in this case an ambient-temperature model) into a steady-flow tunnel has been utilized by Miller (1981) for experiments in a high-enthalpy long-duration hypersonic tunnel. Triggering of the high-speed data acquisition system was accomplished by means of d-c signal wired into the switch used to initiate the actuation of the test cylinder into the flow.

The thin-film gages were also operated in the constant-temperature mode using hot-film anemometer circuitry. In this case the signals are continuous and no injection or preheating of the model is necessary. The hot-film signals may be related to unsteady skin friction. Quantitative calibration

Downloaded 01 Jun 2010 to 171.66.16.66. Redistribution subject to ASME license or copyright; see http://www.asme.org/terms/Terms_Use.cfm

of the films for unsteady skin friction is very difficult, however, due to substrate conduction effects (eg., Cook, 1986). Also, since the hot-film anemometry circuits are feedback devices, the frequency response is not as high as in the case of the heat transfer signals. Nevertheless, the continuous hot-film signals are convenient for qualitative monitoring of the state of the boundary layer and for spectral analysis.

Data Reduction

Heat transfer coefficients were determined from measured heat flux values and wall temperatures as follows:

$$h = q''/(T_w - T_r)$$

where q'' is the local heat flux corrected for radiation and conduction losses (when applicable) and T_r is the local recovery temperature. Use of the local recovery temperature was particularly important in this case since the cylinder models were of relatively small diameter, and consequently, achievement of high Reynolds numbers resulted in fairly high Mach numbers (eg., M $\simeq$ 0.46 for Re = 96,000). Correspondingly large differences therefore existed between the total and static temperatures ($T_t - T_s \simeq 12°C$ for M = 0.46). Local recovery temperatures were calculated from

$$T_r = T_{so} + r(T_t - T_{so})$$

where T_{so} is the approach static temperature and r is the local recovery factor for flow around a cylinder, obtained from Eckert and Drake (1959). The local recovery factor, as defined above, varies from 1.0 on the stagnation line to 0.6 at 80 deg from stagnation. If instead the recovery factor is based on the local static temperature just outside the boundary layer, the value is found to be uniform over the range from 0 to 80 deg from stagnation and equal to 0.84 ($\sqrt{\text{Pr}}$), which is the standard value for air in a laminar boundary layer.

The relevant parameter governing the relative importance of viscous dissipation in the heat transfer process is the Eckert number, Ec = $U^2/c_p\Delta T$. This parameter indicates that even for low-speed flows viscous dissipation may be important if the driving temperature difference is small. Conversely, viscous dissipation may be neglected for high-speed flows if the driving temperature difference is large. For the present study, with Re = 96,000 and an average wall-to-fluid temperature difference of 25°C (typical for the inconel cylinder data), Ec $\simeq$ 0.68.

These considerations are only important if results are to be compared to low-speed results or low-speed analyses. One is free to define experimentally determined heat transfer coefficients as, for example, $h = q''/(T_w - T_t)$ if no such comparison is to be made. This definition of h, however, predicts a nonzero heat flux when $T_w = T_r$. In addition, its value is dependent on flow velocity. Nevertheless, this definition is widely used for flow in complex geometries, such as occurs in gas turbines (e.g., Dunn and Hause, 1982), since it avoids the necessity to know the distribution of local recovery temperature.

Properties were evaluated at the Eckert reference temperature

$$T_{ref} = T_s + 0.5(T_w - T_s) + 0.22(T_r - T_s)$$

where T_s is the local static temperature just outside the boundary layer. Reynolds numbers were based on the diameter of the test cylinder and the mass-averaged flow velocity through the test section just upstream of the test cylinder.

Phase-averaged quantities were formed by dividing each bar-passing cycle into an arbitrary number of bins (typically 50) and entering data from the appropriate portion of the cycle into each bin. The phase-averaged quantity for each bin is then simply the sum of all the entries for that bin divided by the number of entries as follows:

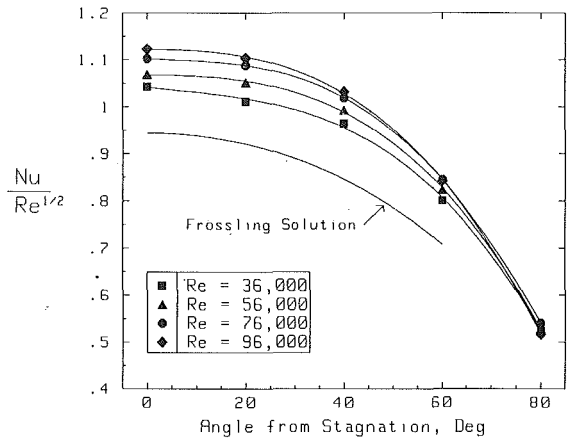

Fig. 4 Steady-state baseline heat transfer results

$$\tilde{s} = \frac{1}{N}\sum_{i=1}^{N} s_i(\alpha)$$

where $\tilde{s}$ represents any phase-averaged quantity and (α) indicates at constant phase. For the present study, digital sampling rates were selected in a range from 50 to 200 kHz, depending on bar-passing frequency, such that approximately 900 bar-passing cycles and 140 samples per cycle were included in each digital record.

Measurements of steady-state rig operating conditions and heat transfer results were subjected to a detailed error analysis, which was performed as an integral part of the data reduction process for each run. The analysis was based on the method outlined by Moffat (1982). Twenty samples were obtained for each steady-state measurement and averaged in order to minimize random errors. Estimates of the random-error standard deviations were also obtained from the twenty samples for each quantity. The results of the error analysis indicated an average uncertainty (95 percent confidence) of ± 2.5 percent for Reynods number, ±4.3 percent for Nusselt number, and ±4.5 percent for Frössling number. An error analysis was also performed for the "steady-state" heat transfer results obtained using the thin-film gage cylinder. This analysis indicated higher average uncertainties of ± 8.5 percent for Nusselt number and ± 9.0 percent for Frössling number. These values should also apply to the phase-averaged heat transfer results.

Results

Baseline steady-state heat transfer results are shown in Fig. 4. These data were obtained with the wake-generating rotor removed from the test rig. The ordinate in the figure is the Frössling number, Nu/$\sqrt{\text{Re}}$. Also shown in the figure is the semi-analytical solution obtained by Frössling (1958) for stagnation region heat transfer with zero free-stream turbulence. The level of heat transfer enhancement of the present data above the Frössling solution is consistent with the test section background free-stream turbulence intensity of approximately 1.2 percent (nearly independent of Reynolds number). For example, using the correlation of Lowery and Vachon (1975), with $Tu\sqrt{\text{Re}}$ = 2.72 (the value corresponding to the present data for Re = 56,000 and Tu = 0.0115) yields an expected stagnation-line Frössling number of 1.079. The measured value for Re = 56,000 is 1.07, as shown in Fig. 4.

Steady-state heat transfer behavior with wake passing is detailed in Fig. 5. In this figure, Frössling number is plotted as a function of angle from the geometric stagnation line, including data from both sides of the cylinder. The negative angles represent locations on the "windward" side of the cylinder with respect to wake passing. These locations corre-

Downloaded 01 Jun 2010 to 171.66.16.66. Redistribution subject to ASME license or copyright; see http://www.asme.org/terms/Terms_Use.cfm

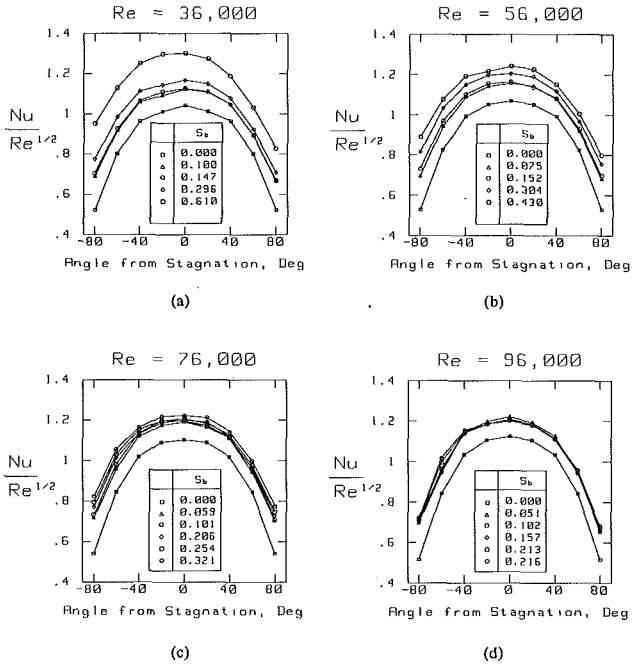

Fig. 5 Effect of wake passing on steady-state heat transfer

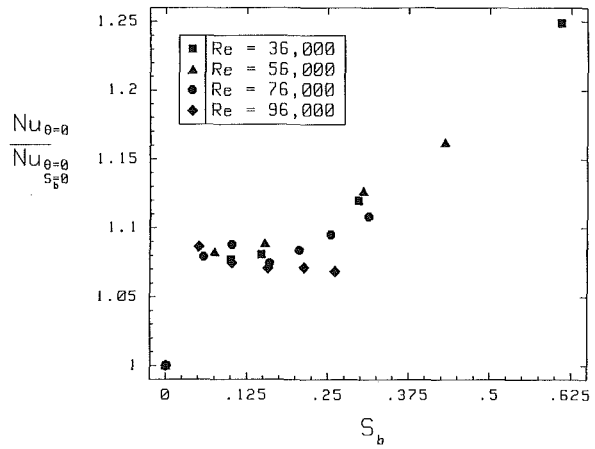

Fig. 6 Stagnation-line wake-induced heat transfer enhancement

spond to the suction side of a turbine blade. Heat transfer data are shown for four Reynolds numbers (Figs. 5*a*-5*d*) and several Strouhal numbers for each Reynolds number, including the rotor-removed ($S_b = 0$) baseline case.

The Frössling number distributions of Fig. 5 reveal the time-averaged heat transfer enhancement associated with wake passing. For low values of bar-passing Strouhal number, this enhancement is nearly uniform circumferentially at about 8 percent above the baseline level. For higher Strouhal numbers, the distributions are asymmetric about the stagnation line, with higher values on the "windward" side. The circumferential asymmetry is most pronounced for the highest Strouhal numbers. For example, in Fig. 5(*a*), a marked asymmetry is evident for $S_b = 0.610$. Achievement of very high Strouhal numbers was limited to the lowest Reynolds number cases due to the maximum rotor rpm constraint.

Stagnation-line time-averaged heat transfer enhancement due to wake passing is shown in Fig. 6 as a direct function of bar-passing Stouhal number. In this figure, the ordinate is the stagnation-line Nusselt number normalized by the baseline stagnation-line Nusselt number of the same Reynolds number. This plot indicates a wake-induced stagnation-line heat transfer enhancement of about 8 percent, nearly independent

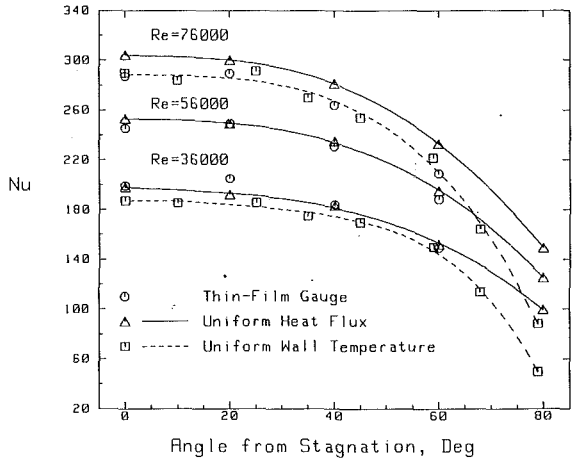

Fig. 7 Comparison of time-averaged thin-film gage and steady-state results

of both Reynolds and Strouhal number, up to $S_b \simeq 0.25$. At higher Strouhal numbers, enhancement levels increase dramatically to about 25 percent for the highest Strouhal number shown. This higher level is consistent with the enhancement level that would be produced by uniform free-stream turbulence with a magnitude equal to the overall-average apparent turbulence intensity behind the wake-generating bars of about 9 percent. The conclusion is that, at high Stouhal numbers, wake interactions cause the unsteadiness produced by the wake-generating bars to resemble uniform free-stream turbulence as might be produced by a grid, for example. At lower Strouhal numbers, the wake-generated unsteadiness is periodic and the flow recovers fully to its background free-stream turbulence level between wakes (see O'Brien and Capp, 1988, for flow unsteadiness details).

One of the main objectives of this research was to document the *unsteady* effects of wake passing on stagnation region heat transfer. To this end, the previously described thin-film gage (TFG) cylinder was fabricated. In order to establish confidence in the results obtained from the TFG cylinder, a series of qualification experiments was carried out. For these experiments, the wake-generating rotor was again removed and the TFG cylinder was injected into the undisturbed free stream. Results of these experiments are shown in Fig. 7 along with baseline results obtained using the inconel-foil uniform heat flux cylinder. Also included in Fig. 7 are results obtained in the same rig by Morehouse and Simoneau (1986) for heat transfer from a segmented copper-strip cylinder in which each strip was individually heated and controlled to produce a uniform wall temperature thermal boundary condition. Two points need to be made in reference to this figure. First, the level of agreement between the thin-film gage results and the steady-state results is excellent. Second, there is a thermal boundary condition effect that causes the uniform-heat-flux results to be higher at circumferential stations away from stagnation. This effect is most pronounced at 80 deg from stagnation.

Representative instantaneous heat flux traces obtained using the TFG cylinder are presented in Fig. 8. These simultaneously acquired traces represent a small excerpt from a much larger digital record. At the top of the figure, the timing pulse used to perform phase-averaging operations is depicted. The high degree of flow unsteadiness present in the wakes is reflected in the instantaneous heat flux traces. Wake-induced heat transfer enhancement is most pronounced on the windward ($\theta \leq 0$ deg) side of the cylinder, with positive heat flux excursions as high as a factor of three above the interwake heat flux level for $\theta = -60$ deg. On the leeward side of the cylinder, the magnitude of the wake-induced heat transfer ef-

Downloaded 01 Jun 2010 to 171.66.16.66. Redistribution subject to ASME license or copyright; see http://www.asme.org/terms/Terms_Use.cfm

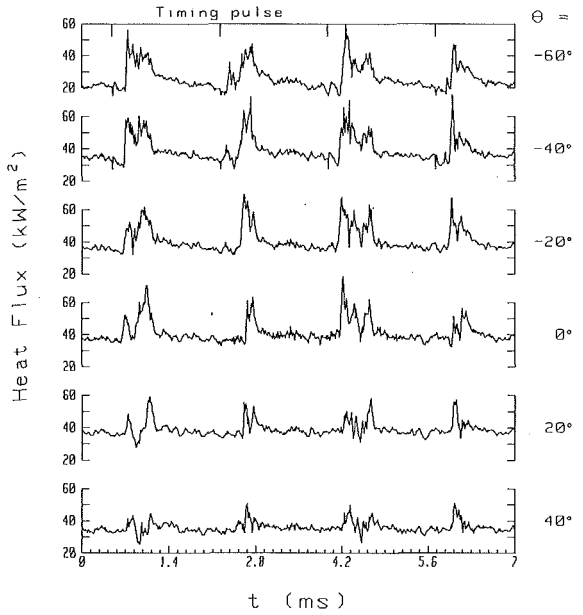

Fig. 8 Instantaneous heat flux records: Re = 76,000; S_b = 0.107

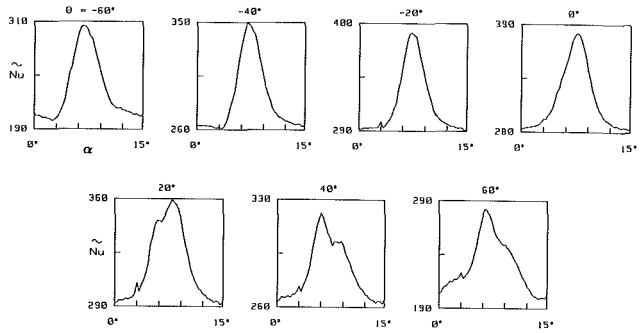

Fig. 9 Phase-averaged Nusselt number profiles: Re = 76,000; S_b = 0.107

fects is much smaller, and instantaneous excursions that fall below the interwake level may be observed. A high degree of correlation is evident from gage to gage, indicating the possible influence of large-scale flow structures.

Phase-averaged heat transfer results corresponding to the instantaneous traces of Fig. 8 are presented in Fig. 9 in the form of Nusselt number versus rotor phase angle. From the viewpoint of the modeler, these phase-averaged profiles may be more useful than the instantaneous results since they could be predicted using a periodic mean description of the flow. The overall-average Nusselt numbers obtained from integration of the phase-averaged results over one complete bar-passing cycle are in good agreement with the steady-state inconel-cylinder results presented in Fig. 5. In addition, interwake Nusselt numbers agree well with the baseline rotor-removed data of Fig. 5 in the range of -40 deg $\leq \theta \leq +20$ deg. Outside this range, interwake Nusselt numbers fall below the baseline data, particularly at $\theta = +40$ deg and $\theta = +60$ deg. Referring to the $\theta = 0$ deg profile, stagnation-line peak heat transfer enhancement is about 35 percent above the interwake level on a phase-averaged basis. At $\theta = -60$ deg, peak phase-averaged enhancement is 50 percent, whereas at $\theta = +40$ deg, it is only about 20 percent. The fraction of time spent in the undisturbed flow is highest on the windward side of the cylinder as indicated by the relative sharpness of the profiles for $\theta \leq 0$ deg. On the leeward side of the cylinder the boundary layer is disturbed by the distorted wake for a larger fraction of

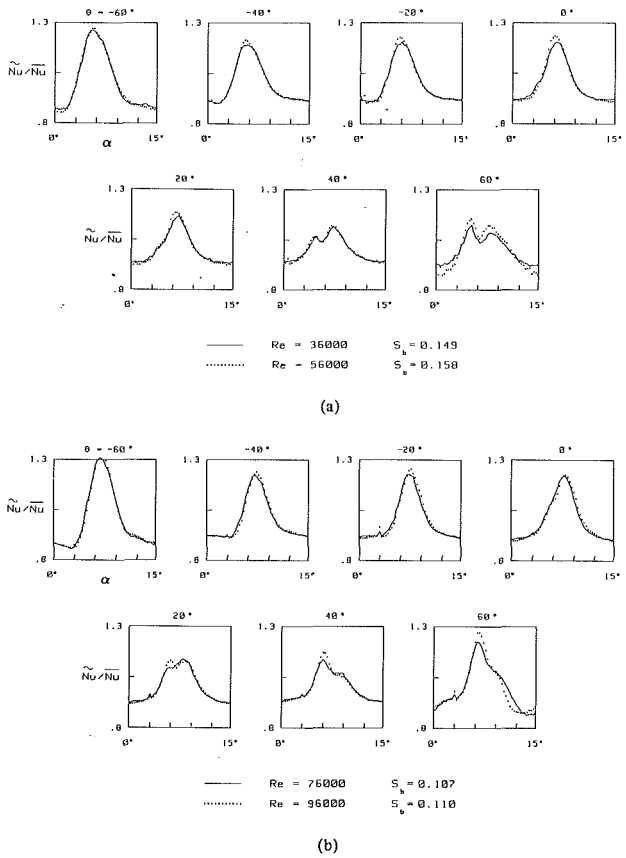

Fig. 10 Phase-averaged Nusselt number profiles: Reynolds number dependence

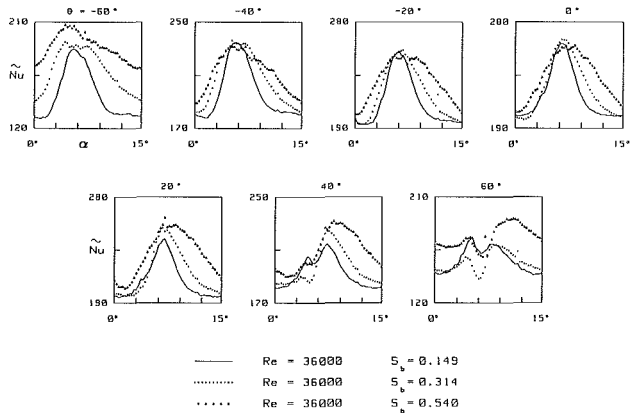

Fig. 11 Phase-averaged Nusselt number profiles: effect of Strouhal number

the bar-passing cycle and consequently the Nusselt number profiles are broader, with very little indication of the undisturbed flow in some cases.

The shapes of the phase-averaged Nusselt number profiles are determined primarily by the value of the Strouhal number, as shown in Figs. 10(*a*) and 10(*b*). In each of these figures, normalized profiles are presented for two different Reynolds numbers, but with nearly equal bar-passing Strouhal number. The normalized profiles are nearly coincident, indicating only minor Reynolds number dependence.

Trends with respect to Strouhal number at a fixed Reynolds number are shown in Fig. 11. The high-Strouhal-number profiles are broader, with incomplete interwake recovery, yielding higher overall-average Nusselt numbers. The most dramatic

Downloaded 01 Jun 2010 to 171.66.16.66. Redistribution subject to ASME license or copyright; see http://www.asme.org/terms/Terms_Use.cfm

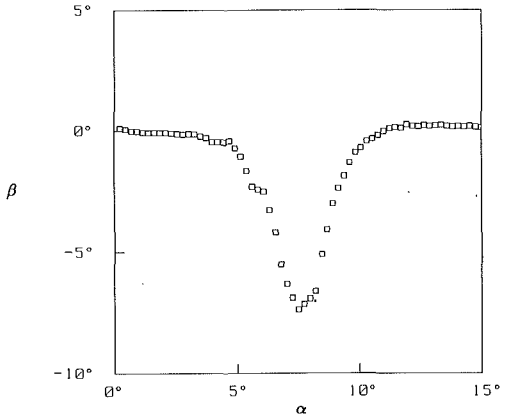

Fig. 12 Phase-averaged flow incidence angle: Re = 36,000; $S_b = 0.314$

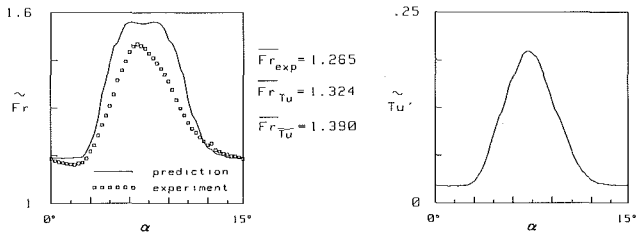

(a) (b)

Fig. 13 Prediction of stagnation-line heat transfer using measured unsteadiness profile and the correlation of Lowery and Vachon (Re = 56,000; $S_b = 0.303$)

effect of increasing Strouhal number is observed in the profiles for $\theta = +40$ deg and $\theta = +60$ deg. At these circumferential locations, instantaneous flow separation occurs during wake passing as a result of the change in flow incidence angle and the resultant shift in the stagnation line toward the windward ($\theta < 0$ deg) side of the cylinder. Separation is reflected in the Nusselt number profiles by the appearance of a pronounced midwake dip at intermediate and high Strouhal numbers.

A profile of phase-averaged flow incidence angle obtained in the freestream away from the heat transfer test cylinder but at the axial location of the cylinder leading edge (O'Brien and Capp, 1988) is shown in Fig. 12. The flow conditions for this profile are the same as for the intermediate Strouhal number case of Fig. 11. The maximum phase-averaged flow incidence angle deviation for this case is -7.5 deg. Of course, on an instantaneous basis, the fluctuations in flow incidence angle are much larger.

As a simple first attempt to predict the wake-induced heat transfer enhancement on the cylinder stagnation line, the correlation of Lowery and Vachon (1975) was used in conjunction with phase-averaged flow unsteadiness data acquired in a related study (O'Brien and Capp, 1988). For the purposes of this calculation, unsteadiness was evaluated as

$$Tu' = (\sqrt{\bar{u}^2} + \sqrt{\bar{v}^2})/2\bar{U}$$

where Tu' is the unsteadiness parameter. This parameter will be substituted into the correlation in place of turbulence intensity. It differs from turbulence intensity since it includes flucatuations associated with organized structures such as those due to vortex shedding along with random turbulent fluctuations. Representative results of these calculations are presented in Fig. 13 alongside the unsteadiness profile used in the calculations. Heat transfer coefficients are nondimensionalized in terms of the Frössling number Fr. Comparison of the predicted values with the measured values reveals surprisingly good agreement considering the simplicity of the approach used. Heat transfer coefficients are generally overpredicted, especially to either side of the wake centerline. Overall cycle-average Fr values are also shown in the figure. The values shown are, respectively: the experimentally measured value obtained from integration of the phase-averaged profile, the predicted result obtained from integration of the Lowery and Vachon correlation-based profile, and a value obtained by substituting the overall cycle-average unsteadiness into the Lowery and Vachon correlation. The value obtained from integration of the predicted profile of Fig. 13(*a*) is 4.6 percent above the experimental value while substitution of the overall-average unsteadiness into the Lowery and Vachon correlation yields a value that is 9.8 percent high.

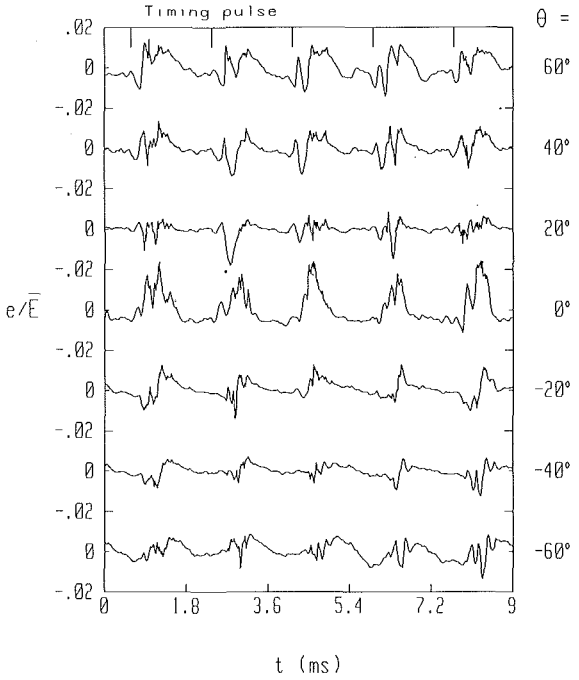

Fig. 14 Instantaneous hot-film records: Re = 56,000; $S_b = 0.15$

Hot-Film Measurements. The thin-film gages of the heat transfer test cylinder were also operated in the constant-temperature mode using hot-film anemometer circuitry. All seven of the gages were operated simultaneously using seven anemometer circuits. A portion of a representative instantaneous hot-film bridge-voltage record is shown in Fig. 14. A major advantage of this mode of operation is that the signals are continuous. This feature was particularly convenient for spectral analysis since averaging could be done in the frequency domain using a digital FFT analyzer.

The hot-film signals clearly indicate each wake-passing event and provide useful qualitative information on the state of the boundary layer during wake passing. On the stagnation line, the hot-film signal resembles the typical stagnation-line unsteady heat flux signal in that the wake-induced voltage excursions are all positive. In contrast to the heat flux signals, however, the hot-film signals off the stagnation line include both positive and negative voltage excursions during wake passing. This behavior is consistent with the idea that the hot films are responding to fluctuations in skin friction. On the stagnation line, skin friction can only increase during wake passing since it is nominally zero during the undisturbed flow. Away from the stagnation line, however, local skin friction is influenced by several factors including the instantaneous flow incidence angle, increased transport of momentum across the boundary layer, and possible flow separation. These factors combine to produce a complex skin friction response.

Downloaded 01 Jun 2010 to 171.66.16.66. Redistribution subject to ASME license or copyright; see http://www.asme.org/terms/Terms_Use.cfm

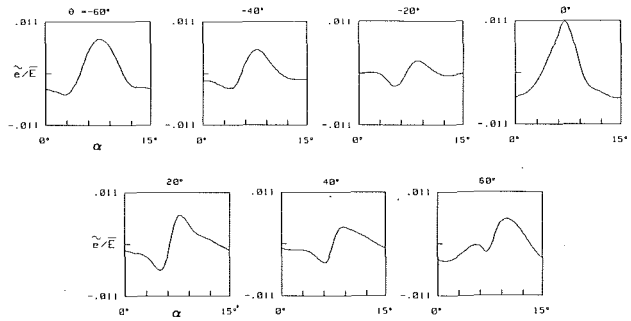

Fig. 15 Phase-averaged hot-film profiles (Re = 56,000; S_b = 0.15)

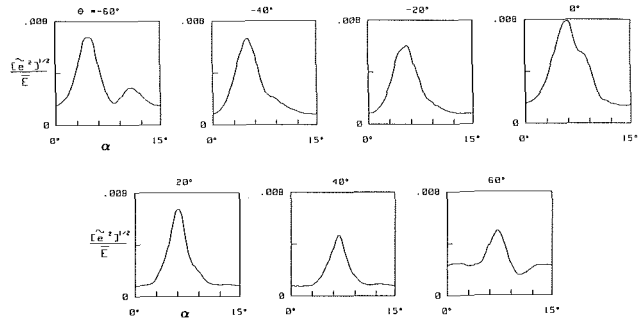

Fig. 16 Phase-averaged hot-film rms profiles (Re = 56,000; S_b = 0.15)

Phase-averaged hot-film profiles corresponding to the instantaneous traces of Fig. 14 are presented in Fig. 15. These profiles are similar in some respects to the phase-averaged Nusselt-number profiles of Fig. 10(*a*) (Re = 56,000), which were obtained under identical flow conditions. Stagnation-line profiles and profiles for $\theta = -60$ deg and $\theta = -40$ deg are qualitatively similar. An indication of probable flow separation during wake passing is present in the profiles for $\theta = 40$ deg and $\theta = 60$ deg at $\alpha \simeq 6$ deg in both the Nusselt number and the hot-film results. However, the hot-film profile for $\theta = -20$ deg also includes a large dip at $\alpha \simeq 4$ deg. No corresponding dip is present in the Nusselt number profile. The heat transfer behavior may be dominated by the increased mixing associated with wake-induced turbulence while the hot-film response could be dominated by the flow incidence shift.

A high level of unsteadiness is present in the boundary layer during wake passing as indicated by the phase-averaged rms hot-film profiles shown in Fig. 16. It is also interesting to note that the peaks in the rms profiles for $\theta = -20$ deg, $\theta = +40$ deg, and $\theta = +60$ deg correspond to the large dips observed in the mean profiles of Fig. 15.

Boundary Layer Spectra. The hot-film signals were also analyzed for spectral information using a digital FFT analyzer. Spectral results are shown in Fig. 17. In the figure, the ordinate variable is a dimensionless power spectral density and the abscissa is a dimensionless frequency. The parameter shown in the upper right of each plot is the bar-passing Strouhal number. The series of spectra shown was acquired using the signal from the thin-film gage located at $\theta = -60$ deg. The topmost spectrum was obtained with the wake-generating rotor held fixed and one of the bars positioned directly in front of the test cylinder stagnation line. In this case, the large peak at $fd/U \simeq 0.17$ is due to vortex shedding from the stationary bar. The peak occurs at a value lower than the standard cylinder vortex-shedding Strouhal number of 0.2 since the vortices are imbedded in the stagnating cylinder-approach flow. Spectra obtained from the stagnation gage show only a very weak indication of the vortex-induced peak. The remaining spectra presented in Fig. 17 were obtained with the wake-generating rotor in motion. The large peaks at the

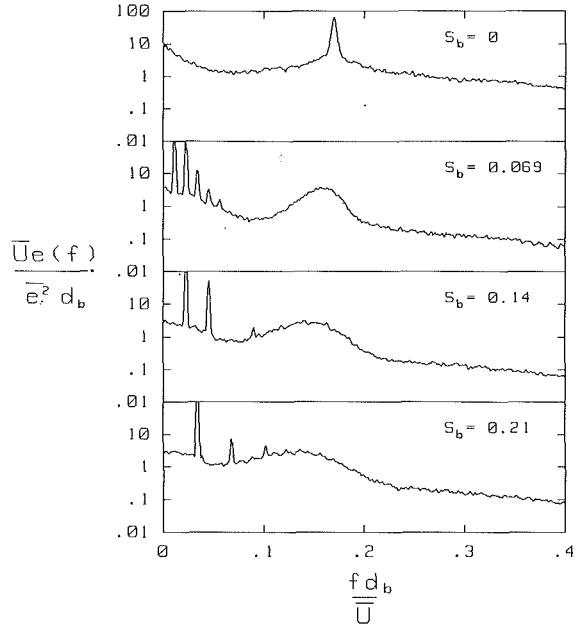

Fig. 17 Hot-film boundary layer spectra (Re = 56,000; $\theta = -60$ deg)

left of each spectrum represent the primary blade-passing frequency and harmonics. As the blade-passing frequency is increased, the peak associated with vortex shedding remains large, but becomes more broadband and is shifted to lower frequencies. This result is consistent with spectra obtained downsteam of the wake-generating rotor away from the test cylinder using a hot wire (O'Brien and Capp, 1988). The spectra indicate that, away from the stagnation line (at both $\theta = -60$ deg and $\theta = +60$ deg), the behavior of the boundary layer is strongly influenced by shed vortices. Surprisingly, on the stagnation line itself, shed vortices do not appear to have much influence.

Shed vortices may also play an important role in actual turbomachines. For example, spark Schlieren flow visualization results obtained by Doorly (1984) and Doorly et al. (1985) clearly show vortex streets shed from the trailing edges of both guide-vane and rotor blades in cascade. Laser velocimetry measurements obtained in a full rotating stage axial compressor by Hathaway et al. (1986) produced double-peaked velocity histograms, which were attributed to the presence of shed vortices.

Concluding Remarks

The experiments described in this paper detail both time-averaged and time-resolved effects of wake passing on cylinder stagnation region heat transfer. Baseline heat transfer results obtained with the wake-generating rotor removed were found to be consistent with the test-section background free-stream turbulence level of 1.2 percent. With wake passing, steady-state heat transfer levels were found to increase uniformly by about 8 percent above the baseline level for low bar-passing Strouhal numbers. For higher Strouhal numbers, heat transfer coefficients were asymmetric about the stagnation line and the enhancement levels increased to as high as 25 percent above the baseline value on the stagnation line. Unsteady heat transfer measurements were obtained using a test cylinder that was instrumented with platinum thin-film gages. Time-averaged heat transfer results obtained from this cylinder were found to be in excellent agreement with results obtained from conventional steady-state measurements. On an instantaneous basis, wake-induced heat transfer enhancement was most pronounced on the windward side of the cylinder, with positive heat flux excursions as high as a factor

Downloaded 01 Jun 2010 to 171.66.16.66. Redistribution subject to ASME license or copyright; see http://www.asme.org/terms/Terms_Use.cfm

of three above the interwake heat flux level. Phase-averaged heat transfer profiles derived from the instantaneous measurements indicate peak stagnation-line wake-induced heat transfer enhancement of about 35 percent. Instantaneous records and phase-averaged profiles obtained from gages located 40 and 60 deg from stagnation on the leeward side of the cylinder were characterized by a drop in heat transfer during wake passing, indicating probable flow separation. The shapes of the phase-averaged Nusselt-number profiles were determined primarily by the value of the Strouhal number, independent of Reynolds number. Stagnation-line phase-averaged profiles were predicted using the correlation of Lowery and Vachon in conjuction with measured wake-induced unsteadiness profiles. Predicted profiles were in surprisingly good agreement with measured profiles, considering the simplicity of the approach used. The thin-film gages were also operated in the constant-temperature hot-film mode. Hot-film signals from gages off the stagnation line included both positive and negative wake-induced voltage excursions. This behavior is consistent with the idea that the hot films are responding to skin friction fluctuations. Phase-averaged hot-film profiles also indicate probable flow separation at 40 and 60 deg from stagnation on the leeward side. Hot-film spectra obtained at +60 deg and −60 deg exhibited large peaks associated with vortex shedding from the wake-generating bars. On the stagnation line, shed vortices did not appear to have much influence.

References

Ashworth, D. A., LaGraff, J. E., Schultz, D. L., and Grindrod, K. J., 1985, "Unsteady Aerodynamic and Heat Transfer Processes in a Transonic Turbine Stage," ASME *Journal of Engineering for Gas Turbines and Power*, Vol. 107, pp. 1022–1030.

Cook, W. J., Giddings, T. A., and Murphy, J. D., 1986, "Response of Hot-Element Wall Shear-Stress Gauges in Laminar Oscillating Flows," AIAA Paper No. AIAA-86-1100.

Doorly, D. J., 1984, "A Study of the Effect of Wake-Passing on Turbine Blades," OEUL Report No. 1515/84, Oxford University, Oxford, United Kingdom.

Doorly, D. J., and Oldfield, M. L. G., 1985a, "Simulation of Wake-Passing in a Stationary Turbine Rotor Cascade," AIAA *Journal of Propulsion and Power*, Vol. 1, No. 4, pp. 316–318.

Doorly, D. J., and Oldfield, M. L. G., 1985b, "Simulation of the Effects of Shock-Wave Passing on a Turbine Rotor Blade," ASME *Journal of Engineering for Gas Turbines and Power*, Vol. 107, pp. 998–1006.

Doorly, D. J., Oldfield, M. L. G., and Scrivener, C. T. J., 1985, "Wake-Passing in a Turbine Rotor Cascade," AGARD CP-390 Paper No. 7, AGARD Symposium on Heat Transfer and Cooling in Gas Turbines, Bergen, Norway.

Dunn, M. G., and Hause, A., 1982, "Measurement of Heat Flux and Pressure in a Turbine Stage," ASME *Journal of Engineering for Power*, Vol. 104, pp. 215–223.

Dunn, M. G., Seymour, P. J., Woodward, S. H., George, W. K., and Chupp, R. E., 1989, "Phase-Resolved Heat-Flux Measurements on the Blade of a Full-Scale Rotating Turbine," ASME JOURNAL OF TURBOMACHINERY, Vol. 111, pp. 8–19.

Eckert, E. R. G., and Drake, R. M., 1959, *Heat and Mass Transfer*, 2nd ed., McGraw-Hill, New York, p. 266.

Frössling, N., 1958, "Evaporation, Heat Transfer and Velocity Distribution in Two-Dimensional and Rotationally Symmetric Laminar Boundary Layer Flow," NACA TM-1432.

Guenette, G. R., Epstein, A. H., Giles, M. B., Haimes, R., and Norton, R. J. G., 1989, "Fully Scaled Transonic Turbine Rotor Heat Transfer Measurements," ASME JOURNAL OF TURBOMACHINERY, Vol. 111, pp. 1–7.

Hathaway, M. D., Gertz, J., Epstein, A., and Strazisar, A. J., 1986, "Rotor Wake Characteristics of a Transonic Axial Flow Fan," *AIAA Journal*, Vol. 24, No. 11, pp. 1802–1810.

LaGraff, J. E., Ashworth, D. A., and Schultz, D. L., 1989, "Measurement and Modeling of the Gas Turbine Blade Transition Process as Disturbed by Wakes," ASME JOURNAL OF TURBOMACHINERY, Vol. 111, pp. 315–322.

Lowery, G. W., and Vachon, R. I., 1975, "The Effect of Turbulence on Heat Transfer From Heated Cylinders," *International Journal of Heat and Mass Transfer*, Vol. 18, No. 11, pp. 1229–1242.

Miller, C. G., 1981, "Comparison of Thin-Film Resistance Heat Transfer Gages With Thin-Skin Transient Calorimeter Gages in Conventional Hypersonic Wind Tunnels," NASA TM 83197.

Moffat, R. J., 1982, "Contributions to the Theory of Single-Sample Uncertainty Analysis," ASME *Journal of Fluids Engineering*, Vol. 104, pp. 250–260.

Morehouse, K. A., and Simoneau, R. J., 1986, "Effect of a Rotor Wake on the Local Heat Transfer on the Forward Half of a Circular Cylinder," *Proceedings, 8th International Heat Transfer Conference*, C. L. Tien et al., eds., Hemisphere Publishing Corp., Washington, DC, Vol. 3, pp. 1249–1256.

O'Brien, J. E., and Capp, S. P., 1989, "Two-Component Phase-Averaged Turbulence Statistics Downstream of a Rotating Spoked-Wheel Wake Generator," ASME JOURNAL OF TURBOMACHINERY, Vol. 111, pp. 475–482.

O'Brien, J. E., Simoneau, R. J., LaGraff, J. E., and Morehouse, K. A., 1986, "Unsteady Heat Transfer and Direct Comparison to Steady-State Measurements in a Rotor-Wake Experiment," *Proceedings, 8th International Heat Transfer Conference*, C. L. Tien et al., eds., Hemisphere Publishing Corp., Washington, DC, Vol. 3, pp. 1243–1248.

O'Brien, J. E., and VanFossen, G. J., 1985, "The Influence of Jet-Grid Turbulence on Heat Transfer From the Stagnation Region of a Cylinder in Crossflow," ASME Paper No. 85-HT-58.

Oldfield, M. L. G., Burd, H. J., and Doe, M. G., 1984, "Design of Wide-Bandwidth Analog Circuits for Heat Transfer Instrumentation in Transient Tunnels," *Heat and Mass Transfer in Rotating Machinery*, D. E. Metzger and N. H. Afgan, eds., Hemisphere Publishing, Washington, DC, pp. 233–258.

Schultz, D. L., and Jones, T. V., 1973, "Heat Transfer Measurements in Short-Duration Hypersonic Facilities," AGARD-AG-165, AGARD, Paris, France.

Schultz, D. L., Jones, T. V., Oldfield, M. L. G., and Daniels, L. C., 1978, "Measurement of the Heat Transfer Rate to Turbine Blades and NGV's in a Transient Cascade," *Proceedings, 6th International Heat Transfer Conference*, Vol. 2, Hemisphere Publishing, Washington, DC, pp. 73–78.

Simoneau, R. J., Morehouse, K. A., VanFossen, G. J., and Behning, F. P., 1984, "Effect of a Rotor Wake on Heat Transfer From a Circular Cylinder," NASA TM-83613.

Vidal, R. J., 1956, "Modal Instrumentation Techniques for Heat Transfer and Force Measurements in a Hypersonic Shock Tunnel," Report No. AD-917-A-1, Cornell Aeronautical Laboratory, Ithaca, NY.

Downloaded 01 Jun 2010 to 171.66.16.66. Redistribution subject to ASME license or copyright; see http://www.asme.org/terms/Terms_Use.cfm

Phase and Time-Resolved Measurements of Unsteady Heat Transfer and Pressure in a Full-Stage Rotating Turbine

M. G. Dunn
Calspan-UB Research Center,
Buffalo, NY 14225

This paper presents detailed phase-resolved heat-flux data obtained on rotor blades and a comparison of simultaneously obtained time-resolved heat-flux and static pressure data obtained on the stationary shroud of a Garrett TFE 731-2 HP full-stage rotating turbine. A shock tube is used to generate a short-duration source of heated and pressurized air and platinum thin-film gages are used to obtain heat-flux measurements. Blade results are presented at several selected blade locations. Shroud surface pressure and heat-flux time histories are presented for comparable locations relative to the blade position. For these measurements, the turbine was operating at the design flow function, the design stage pressure ratio, and at 100 percent corrected speed.

Introduction

It is well known that turbomachinery flow fields are inherently unsteady because of the disturbances generated when rotating blades transit nozzle vane wakes and exit passages. Years of experience have illustrated that satisfactory flow field and heat transfer predictions can be performed by assuming that the flow is quasi-steady. However, the state of the art has progressed to the point where relevant unsteady-flow calculations can now be performed and supporting measurements of the unsteady flow field become a valuable input to the development of computational codes. Significant current research is directed at determining the influence of flowfield unsteadiness on the blade heat-flux and the surface-pressure distributions, on the inner blade-row gas dynamic parameters, on the state of the blade and vane surface boundary layers, and on the stage efficiency. The results reported in this paper will emphasize phase-resolved[1] heat-flux data on the rotating blade. However, typical time-resolved heat-flux and static pressure data simultaneously obtained on the stationary shroud will also be presented.

Papers relevant to unsteady flow fields in turbomachinery have been present in the literature for at least the past 35 years. Early work by Kemp and Sears (1953, 1955) provided the ground work for much of the research that was to follow. Subsequently, Giesing (1968), Parker (1969), and Kerrebrock and Mikolajczak (1970) made contributions to the understanding of these problems. More recently, Dring et al. (1980, 1981, 1982) have used a large-scale rotating axial turbine stage to obtain experimental data on the nature of the unsteady flow field. Also, Hodson (1984, 1985a, 1985b) has used several different facilities to study wake-generated unsteadiness in vane exit passages and to perform measurements of boundary-layer transition and flow separation. Detailed measurements of the unsteadiness in the rotor incoming flow are presented by Hodson (1985b) that illustrate the change in incidence angle and the change in turbulence associated with the vane wakes.

Another extensive research program concerned with unsteady flow fields was reported by Lakshminarayana et al. (1982). They reported the results of several programs designed to measure the boundary-layer and turbulence characteristics inside turbomachinery rotor passages using a large-scale, slowly rotating rig as the test device. Binder et al. (1985, 1987) reported the results of laser velocimeter measurements in the unsteady rotor flow field. These authors demonstrate very high turbulence levels associated with the vane wakes. Sharma et al. (1985) presented the results of an extensive study conducted to obtain low-speed rig data on the unsteady flow environment associated with axial flow turbines. Doorly and Oldfield (1985) used a piston-driven tunnel and a system of rotating bars to simulate the effects of shock waves and waves shed from a nozzle on the blade. The Schlieren photographs presented by Doorly and Oldfield (1985) are helpful in interpreting the results presented herein because they illustrate the rather exten-

[1]The term "phase" is used here to denote the pitchwise angular displacement of a given rotor blade with respect to the stator vanes. It varies across each stator passage, in a sawtooth fashion, between the limits 0 and 360 deg/B, where B is the number of stators. The term "phase-resolved" denotes time-resolved data, which are presented as a function of phase, rather than as a function of time. The term "phase-averaged" denotes an ensemble average in which phase-resolved data at a given phase, over a succession of stator passages, are taken to be different realizations of the same event. This averaging is referred to by Adamczyk (1985) as passage-to-passage averaging.

Contributed by the International Gas Turbine Institute and presented at the 34th International Gas Turbine and Aeroengine Congress and Exhibition, Toronto, Ontario, Canada, June 4–8, 1989. Manuscript received at ASME Headquarters January 23, 1989. Paper No. 89-GT-135.

Copyright © 1990 by ASME
Downloaded 01 Jun 2010 to 171.66.16.66. Redistribution subject to ASME license or copyright; see http://www.asme.org/terms/Terms_Use.cfm

sive nature of the vane wake, and the manner in which these wakes interact with the blade. More recently, Wittig et al. (1988) have reported the results of a study designed to investigate the influence of upstream generated turbulence, superimposed on the wake flow, on the blade heat-flux distribution. They used the Doorly and Oldfield rotating bar technique to generate the wake behavior, a grid to produce the turbulence, and LDV and heat transfer measurements to characterize the turbulence.

Dunn et al. (1989) presented detailed phase-resolved heat-flux data obtained on the blade of the Teledyne 702 HP full-stage rotating turbine. Results were presented along the midspan at many locations on the blade suction and pressure surfaces from the stagnation point to near the trailing edge. Guenette et al. (1989) presented time-resolved heat-flux data for the rotor of a Rolls-Royce turbine.

The purpose of this paper is to present a detailed set of phase-resolved heat-flux data obtained on the blade of the Garrett TFE 731-2 HP full-stage rotating turbine. An earlier report by Dunn (1984) presented the time resolved heat-flux histories for several locations on the vane, the vane endwall, and the blade of this turbine. These data, however, were not phase resolved. Two more recent papers (Dunn et al., 1986; George et al., 1987) provide a description of the analysis techniques that were previously developed at the Calspan–UB Research Center to obtain instantaneous heat-flux values from the thin-film gages at a sampling frequency consistent with the requirements of this experiment. Several changes have been made to the electronics of the data recording system since the experimental data reported by Dunn et al. (1986) were taken. These changes were incorporated into the data collection system used for this work and they were previously described by Dunn et al. (1989). Previous papers (Dunn and Hause, 1982; Dunn, 1986a; Dunn et al., 1984a, 1986) have described time-resolved rotor shroud pressure and time-resolved blade heat-flux measurements for this turbine, but these blade data were not phase locked as was noted above and the shroud data time resolution was not as good as that presented herein. Epstein et al. (1985) have also reported time-resolved and time-averaged heat-transfer and pressure measurements taken in the stationary shroud over a rotating turbine. The machine used by Epstein was a Rolls-Royce design for which the stage pressure ratio was approximately twice the value of the Garrett TFE 731-2 turbine making quantitative comparison of the two data sets for the stationary shroud heat-transfer distributions difficult. However, the results of the two measurements are qualitatively consistent in that the trend of both is for the heat flux to be maximum near the blade leading edge and then to decrease with axial distance through the stage. This trend in shroud heat flux is anticipated because of the decreasing local enthalpy level as a result of work extraction by the turbine.

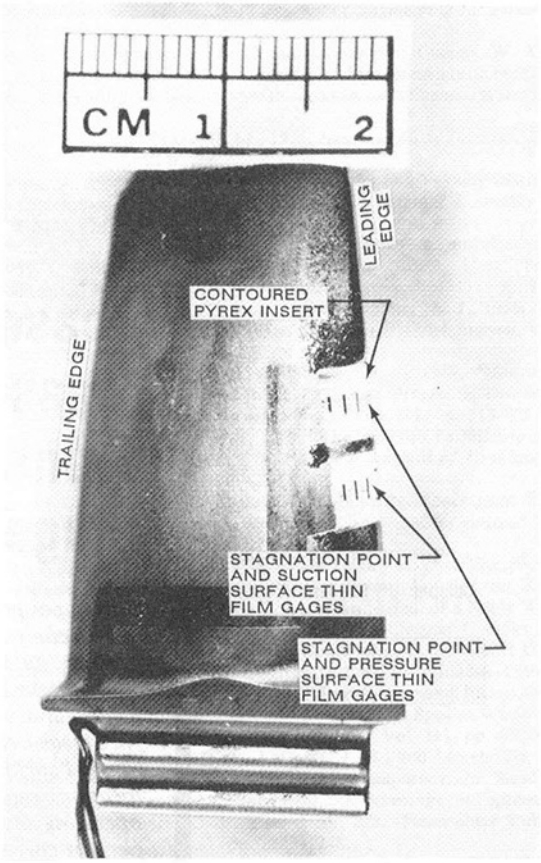

Fig. 1 Photograph of contoured leading-edge inserts for rotor blade

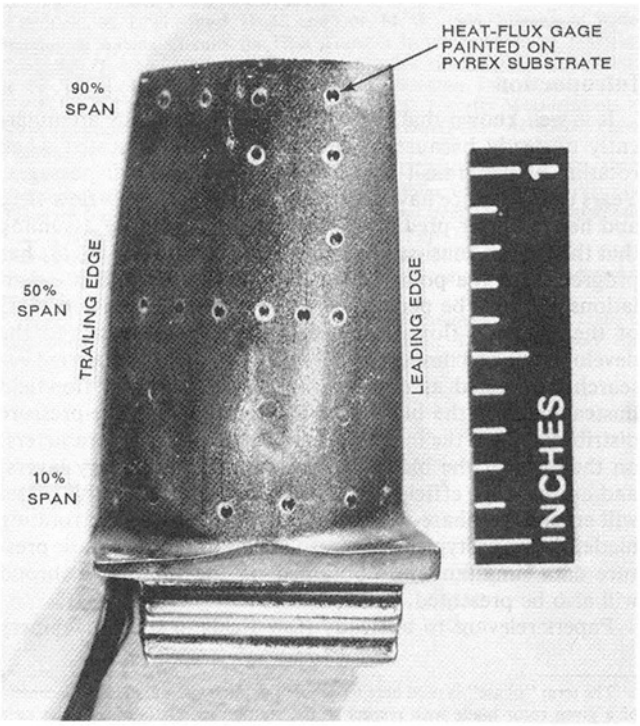

Fig. 2 Photograph of blade suction surface button-type heat-flux gages

Experimental Apparatus

The experimental apparatus used in this work has been described in depth in previous publications noted above and will not be repeated here. Only those portions of the apparatus important to the clarity of this paper will be included.

The thin-film heat-flux gages used in this work were constructed to have a room temperature resistance of 80 to 100 ohms. Each gage is supplied a constant current of 1 mA for the duration of the experiment. Prior to the experiment, the gages are calibrated in a temperature-controlled oil bath over the entire range of anticipated temperatures. The voltage versus time (or phase) histories of the individual gages are transferred to the data recording system using a slip-ring technique. The particular slip ring used here was a Poly Scientific 100-channel gold-on-gold unit that is continuously cooled and lubricated under pressure with a Freon/oil mixture. The slip ring contact noise is generally very low, having a maximum value of 25 μV compared to a thin-film gage output, which is in the tens of millivolts range. Any one of the 100 rings with a noise level in excess of 25 μV was eliminated from the system.

The gage output signals were recorded on a data laboratories 2000 series recorder using a technique described by Dunn et al. (1986). The 2000 series recorder is a 10-bit unit with eight

Downloaded 01 Jun 2010 to 171.66.16.66. Redistribution subject to ASME license or copyright; see http://www.asme.org/terms/Terms_Use.cfm

Table 1 Test conditions and parameters

Reflected-shock pressure	7.43 x 10^3kPa	(1078 psia)
Reflected-shock temperature	559.4°K	(1007°R)
NGV inlet total temperature	559.4°K	(1007°R)
Static pressure at NGV inlet	6.79 x 10^2kPa	(98.5 psia)
Static pressure downstream of rotor	3.56 x 10^2kPa	(51.7 psia)
Area on which Stanton number is based	3.17 x $10^{-2}m^2$	(0.34 ft^2)
Weight flow without coolant	9.31 kg/sec	(20.5 lb/sec)
Weight flow with coolant	9.45 kg/sec	(20.8 lb/sec)
Corrected rotor speed	100%	-
Turbulence intensity upstream of NGV	5.5%	-
Reflected-shock enthalpy	5.6x10^5 J/kg	(240.98 BTU/lb)
Wall enthalpy at 530°R	2.96 x 10^5 J/kg	(127.30 BTU/lb)
T_w/T_o	0.53	

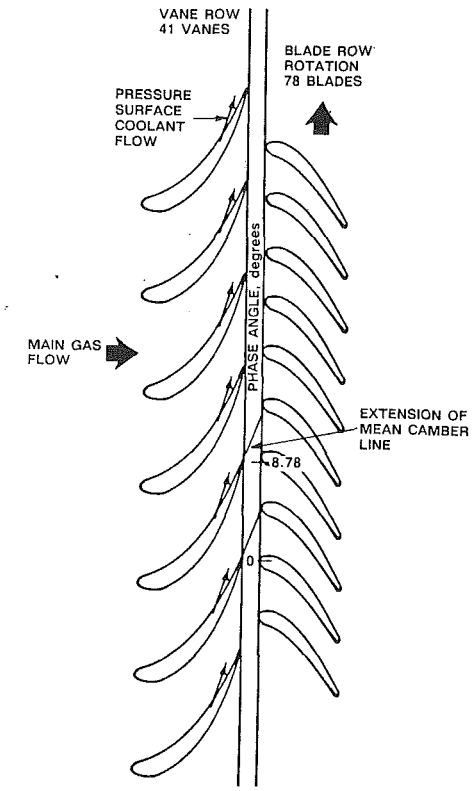

Fig. 3 Sketch of stage and phase angle reference

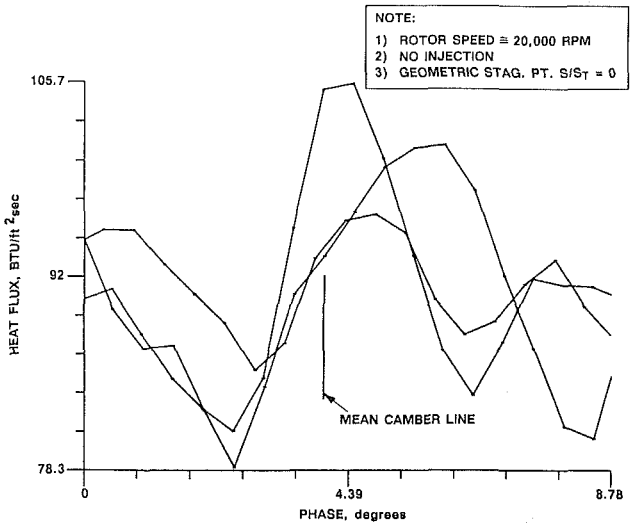

Fig. 4 Phase-resolved heat-flux data at geometric stagnation point on blade for three different vane passages

recording channels, a storage capability of 4K words/channel, and each channel can be sampled at a frequency in the range of 200 kHz to 2 MHz. A shaft encoder that will be described later is used to trigger the recorder. Dunn et al. (1986), note that some of the features of the data reported in that work could not be readily explained by the analysis and that electronic noise combined with frequency splitting due to sampling the data on the slightly accelerating turbine at constant time intervals made it difficult to easily recognize the character of the passage heat flux. Therefore, prior to obtaining the results reported here, the electronic system and the amplifiers used in the thin-film gage temperature recording circuits were redesigned and rebuilt. The amplifiers were constructed to provide capability of wide band (200 kHz), low noise (less than 3 bits out of 1024 bits), single gain data recording and were powered by d-c voltage (batteries). Great care was taken in providing electrical shielding and adequate grounding for all of the equipment. Where possible, batteries were used as the power supply for the electronic equipment. The noise level on each individual heat-flux gage channel was measured through the entire recording system (including the slip ring) with the turbine rotating. For all channels, the prerun system noise measured at the recording device just prior to recording the data (with the turbine at full speed) was less than 5 bits out of 1024 bits. Throughout the measurement program, an attempt was made to use as large a portion of the 1024 bits as possible for data recording.

The thin-film gage instrumentation used to perform the heat-flux measurements consisted of two contoured leading-edge inserts and flush-mounted button-type gages. The shroud pressure gages were piezoelectric-type gages. Figure 1 is a photograph of the two leading-edge inserts. Both inserts have four gages with the distribution such that each has a stagnation point gage and three additional gages spaced on the order of 1 mm (0.040 in.) apart on either the suction or the pressure surface. Figure 2 is a photograph of the suction surface button-type gages. The pressure surface was instrumented in a similar manner and a photograph is shown by Dunn (1986b). Phase-resolved heat-flux data obtained on both the pressure and suction surface will be presented here. The heat-flux gage signals could be time resolved or phase resolved, but we have elected to phase resolve because of an interest in looking at the passage variation of heat flux and because of spatial location difficulties arising because of the slightly accelerating

Downloaded 01 Jun 2010 to 171.66.16.66. Redistribution subject to ASME license or copyright; see http://www.asme.org/terms/Terms_Use.cfm

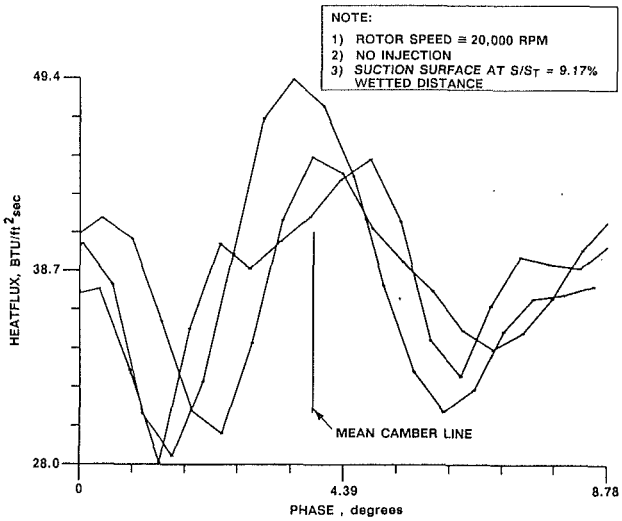

Fig. 5 Phase-resolved heat-flux data on blade at 9.17 percent wetted distance on suction surface for three different vane passages

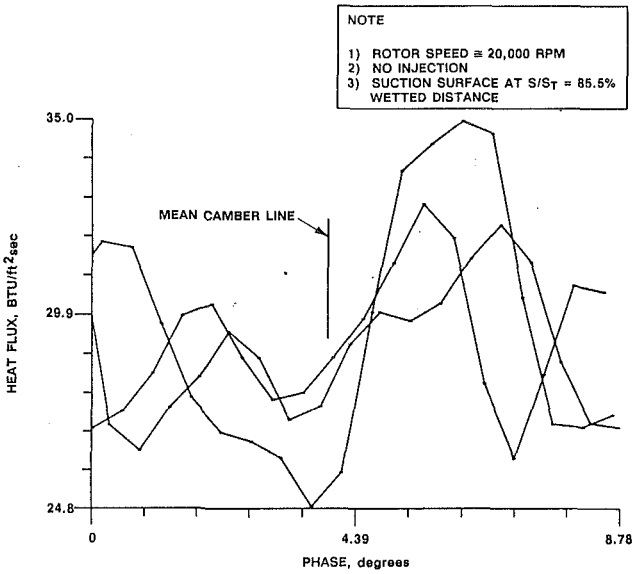

Fig. 6 Phase-resolved heat-flux data on blade at 85.5 percent wetted distance on suction surface for three different vane passages

turbine noted in the previous paragraph. The technique for phase resolving will be described in the next paragraph.

The turbine used here had 41 vanes and 78 blades. At 100 percent corrected speed, a blade traverses a vane exit passage in about 75 μs. The sampling on the heat-flux gages was controlled by a shaft encoder installed on the rotor assembly, which provided 720 pulses per revolution along with an index of one pulse per revolution. At the time of model assembly, the leading edge of the insert was carefully aligned with the trailing edge of a known vane. The shaft encoder was then adjusted so that the one-pulse-per-revolution index pulse always occurred at this alignment point. The vane passages are 8.78 deg or 17.56 pulses apart. The output signal from the shaft encoder was used as an input to the recording equipment in order to sample the blade data at the same angular location within the passage from one revolution to the next, thus phase resolving the data. This technique resulted in a sampling frequency on the order of 240 kHz, a value well above twice the highest frequency present in the data as required by the Nyquist criterion. The technique used to obtain these data and the data processing procedure are explained in detail by Dunn et al. (1986, 1989).

Experimental Conditions

Table 1 gives the experimental conditions at which the measurements reported here were performed. For this turbine, the turbulence intensity just upstream of the vane row was measured (Dunn et al., 1984b; Rivir et al., 1985) to be about 5 percent. The scale of the turbulence was not measured at that time, but an effort to measure the scale is ongoing.

Discussion of Results

A sketch of the physical arrangement of the vane, blade, and the orientation of the blade at 0 and 8.78 deg phase (360 deg/41) is given in Fig. 3. An extension of the vane mean camber line illustrates the approximate location at which the vane wake would intersect the plane of the blade row leading edge, which is about 3.86 deg. The physical location of the vane wake with respect to the blade phase angle in the operating stage is difficult to predict for the unsteady flow environment.

Data were obtained from many more heat-flux gages on the instrumented blades and the stationary shroud than can be discussed here. A few sample results will be presented to illustrate the general characteristic of the data. The heat transfer results are given in the form of heat-flux (Btu/ft^{2}s) history as a function of phase angle instead of the previous format used to present the time-averaged results, which was a nondimensional Stanton number.

Figure 4 presents the passage phase-resolved heat-flux history for the geometric stagnation point. These data were obtained for the rotor at design corrected speed and without cooling air injection from the vane. Data from three separate passages during one revolution have been reproduced in Fig. 4. The individual dots are the heat-flux values calculated from the temperature data points taken from the digitally sampled data recorded at the particular phase angle sampled. Straight lines are drawn between successive data points. The heat-flux signal is sampled every 0.5 deg (or about every 4 μs) and thus turbulent fluctuations, as one might expect to see them, are not obvious but are buried in the data record. The location of the mean camber line is also shown in Fig. 4. Note that the scale of the heat-flux value shown on the ordinate has been expanded to illustrate the unsteady nature and does not begin at 0 but rather at 78. The heat-flux value is lowest in the early portion of the passage, which is felt to correspond to flow outside the vane wake. As the phase angle corresponding to the location of the mean camber line intersection is approached, the heat flux increases rapidly, reaching a peak in the vicinity of 4.4 deg and then begins to fall off. The stagnation-region flow is unsteady as the blade moves from passage to passage, but the general character of the heat-flux history is repeatable. The unsteady nature of the stagnation-region heat-flux data can be attributed to several factors. Among them are: (1) changes in the flow incidence angle as the blade moves through the vane passage exit flow and then through the vane wake flow, (2) differences in the relative turbulence intensity of the passage and wake flows, and (3) differences resulting from manufacturing tolerances associated with the turbine stage. A spectral analysis of the heat-flux data was obtained using Fast Fourier Transform techniques (see typical results given by Dunn et al., 1986a, for this turbine at the present operating condition) and it was demonstrated that the dominant frequency in the data correspond to the 41 vane passages (or wakes). It is difficult (but possible) to distinguish between passages and wakes with the Fourier analysis.

Figures 5 and 6 are phase-resolved heat-flux histories for blade locations of 9.17 and 85.5 percent wetted distance on the blade suction surface, which can be directly compared with the stagnation-point data presented in Fig. 4. The general characteristics of these downstream data are similar to those of the stagnation-region data in that the heat-flux level starts out

Downloaded 01 Jun 2010 to 171.66.16.66. Redistribution subject to ASME license or copyright; see http://www.asme.org/terms/Terms_Use.cfm

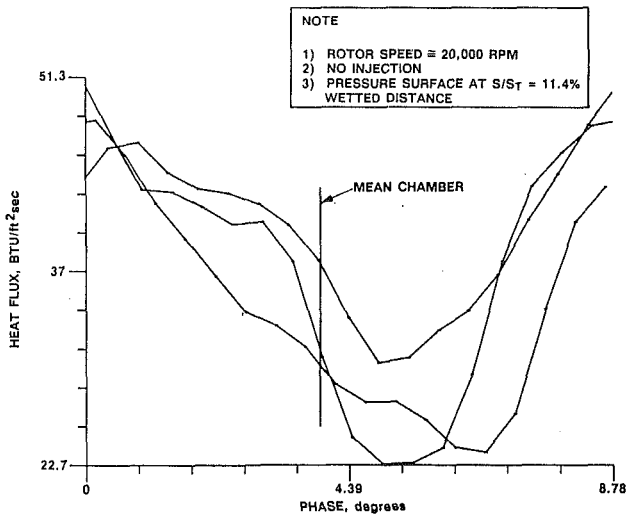

Fig. 7 Phase-resolved heat-flux data on blade at 11.4 percent wetted distance on pressure surface for three different vane passages

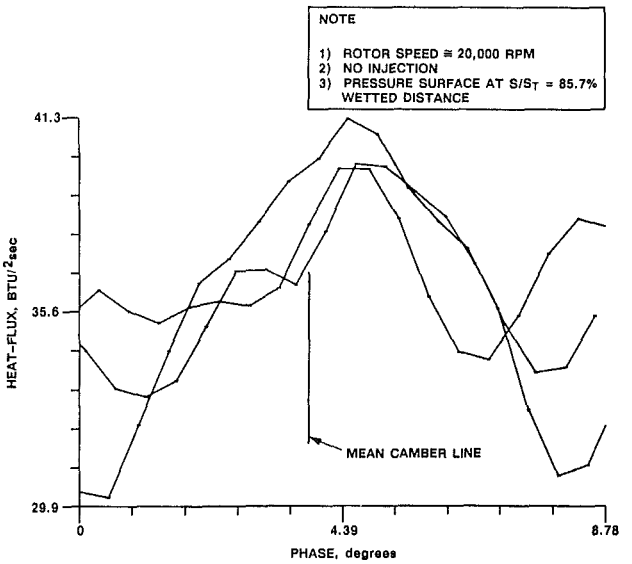

Fig. 8 Phase-resolved heat-flux data on blade at 85.7 percent wetted distance on pressure surface for three different vane passages

relatively low at small phase angles and then increases rapidly to a peak at phase angles in the vicinity of the intersection of the extended mean camber line with the leading-edge plane of the rotor. In the case of the data presented by Dunn et al. (1989) for the Teledyne turbine, it was shown that the peak heat-flux values were in the vicinity of the predicted turbulent boundary-layer level and that the minimum heat-flux values were in the vicinity of the laminar boundary-layer levels. Such was not the case for the Garrett turbine results discussed herein. In general, the quasi-steady turbulent boundary-layer predictions were higher than the peak heat flux, the flat-plate laminar boundary-layer predictions were lower than the minimum heat-flux level. The time-averaged data for this turbine presented by Dunn (1986b) and by Taulbee et al. (1989) are consistent with this observation. The phase-resolved results presented in Figs. 4–6 were not ensemble averaged but multiple passages can be superimposed to get a better picture of the heat-flux signal with a result comparable to that presented in Fig. 12(*c*) from Dunn et al. (1989). An effort was initiated to perform correlations among the signals recorded for several different heat-flux gages on the same surface. This effort is still in progress and results will be reported at a later time.

It is of interest to discuss some of the physical factors that may contribute to the differences observed between the phase-resolved heat-flux histories of the two turbines for which detailed data have been obtained. The Teledyne stage has significantly fewer (23) guide vanes than the Garrett stage (41), and a lower solidity, resulting in angular spacing between vane wakes of 15.65 deg versus 8.78 deg. Further, the Garrett blade rotates slower but transits a guide vane passage in a smaller time interval (73 μs) than the Teledyne blade (97 μs). Both turbines used the same shaft encoder, which provided an external trigger to the data sampling system so that the heat-flux gages were sampled every 1/2 deg of rotation. The vane/blade axial spacing of the two turbines was also comparable, being on the order of 19 percent of the vane axial chord. The vane trailing edge thickness of the Garrett turbine is about 73 percent of the vane trailing edge value of the Teledyne turbine. It should be anticipated that the heat-flux results for the two turbines will be similar, but there is no reason to expect that they will be identical. The rate at which the Garrett blade intercepts guide vane wakes induces a disturbance on the blade boundary layer of higher frequency than was present for the Teledyne turbine. It appears that the blade boundary-layer transition is influenced by the vane wakes, and thus it is argued that the high-frequency disturbance caused by the vane wakes results in the boundary layer being in an unsteady state. However, on the basis of these data the possibility cannot be ruled out that the rapid changes in heat-flux level on the blade observed in transiting the vane wake might be due to differences in turbulence level (and/or turbulence scale) associated with the passage and wake flow regions and that these turbulence parameters would be different for the two turbines considered because of geometric considerations. Traci and Wilcox (1975) and Lowery and Vachon (1975) have both shown that turbulence intensity can have a significant influence on stagnation-point heat transfer. Blair (1983a, 1983b) reported the results of a study designed to determine the influence of free-stream turbulence on the heat transfer to a flat plate in the presence of a fully turbulent boundary layer. Later, O'Brien and Van Fossen (1985) demonstrated the influence of turbulence intensity and turbulence length scale on heat transfer in the stagnation region of a cylinder. Moffat and Maciejewski (1985) demonstrated that flat-plate heat transfer levels can be significantly increased as a result of turbulence. More recently Moffat and Maciejewski (1988) have presented a much more detailed study of the influence of high free-stream turbulence on heat transfer in turbulent boundary layers. Subsequent work by O'Brien (1988) suggests that vortex shedding may be a major contributor to the magnitude of the excursions of heat flux experienced by the blade in passage through the vane wake. It should also be noted that the vane exit Mach number for the Garrett turbine was slightly less than unity, while the vane exit Mach number for the Teledyne turbine was equal to or slightly greater than unity.

Figures 7 and 8 are heat-flux histories for locations of 11.4 and 85.7 percent wetted distance on the blade pressure surface obtained for the same experimental conditions as those of Figs. 4–6. The shape of the pressure surface heat-flux history at 11.4 percent wetted distance is very different from the corresponding result on the suction surface. This is not unexpected since these locations have a very different exposure to the vane exit flow. The three passages shown in Fig. 7 illustrate that the peak heat flux occurs at small phase angles and then decreases, reaching a minimum just beyond the intersection of the mean camber line. This general characteristic is consistent with that found at a corresponding location on the Teledyne blade (see Fig. 10 of Dunn et al., 1989). Figure 8 illustrates the heat-flux history for three passages at a location of 85.7 percent wetted distance on the pressure surface. These data indicate a peak heat-flux value at a phase angle just beyond mid passage. This

Downloaded 01 Jun 2010 to 171.66.16.66. Redistribution subject to ASME license or copyright; see http://www.asme.org/terms/Terms_Use.cfm

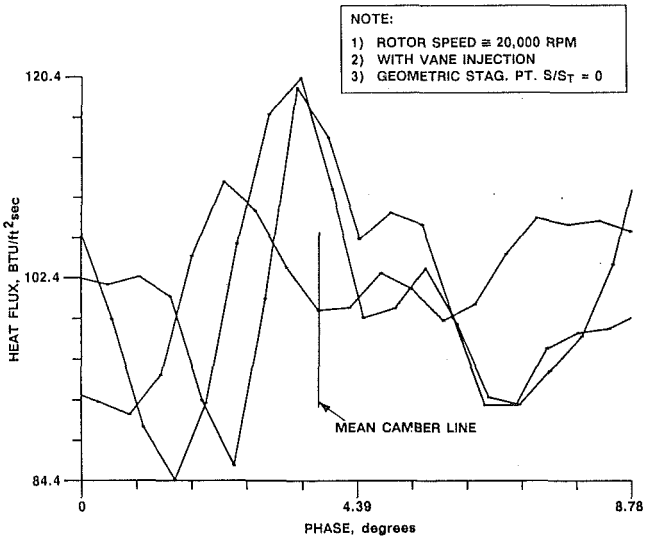

Fig. 9 Phase-resolved heat-flux data at geometric stagnation point on blade with vane injection for three different vane passages

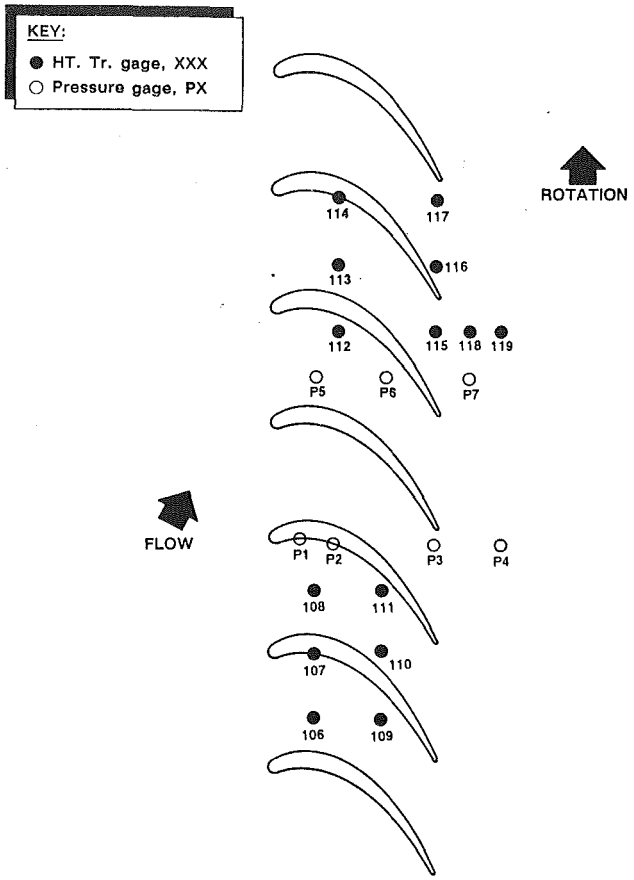

Fig. 10 Sketch of shroud heat-flux and pressure instrumentation relative to blade location

trend is somewhat different from, but not inconsistent with that observed with the Teledyne machine. The contour plots presented by Dunn et al. (1989) (see Fig. 11(*b*) of that paper) illustrate a sharp peak at small phase angle followed by a trend that is completely consistent with that observed here. For Figs. 7 and 8, the predicted heat-flux levels obtained from the turbulent flat-plate prediction and the laminar flat-plate prediction compare to the data in about the same manner as described in the preceding paragraph for the suction surface.

The Garrett TFE 731-2 HP turbine uses slot injection from the vane pressure surface to cool the trailing edge. This cooling system has been used to investigate the influence of cooling gas injection on both vane and blade time-averaged heat-flux levels (Dunn, 1985, 1986b). This previous work indicated that vane injection results in an increase in blade heat-flux level at the geometric stagnation point and at locations on the blade suction surface up to wetted distances of about 15 percent. Figure 9 is a plot of the phase-resolved heat-flux history at the blade geometric stagnation point in the presence of upstream vane injection. The overall heat-flux level is higher than the corresponding no-injection result shown in Fig. 4 as would have been anticipated. The time-averaged results reported by Dunn (1986b) illustrate that at the stagnation point, injection resulted in a 15 to 20 percent increase in heat flux. The slot injection appears to disturb the flow significantly in the stagnation region and on the early portion of the suction surface of the blade. However, the general characteristics of the heat-flux histories for the two cases are similar. There are several possible reasons for this observed increase in heat-flux level, among them being the potential for changes in the local turbulence intensity and scale as a result of the injection. As noted earlier in this paper, several authors have demonstrated the importance of turbulence intensity and/or turbulence scale on the heat transfer in the stagnation region of a cylinder and to the surface of a flat plate.

In looking at the heat-flux data presented in Figs. 4–9, an estimate of the uncertainty in both heat-flux value and phase angle is important. A detailed calibration of voltage output versus temperature at constant current is obtained for each heat-flux gage using an NBS-traceable thermometer and an oil bath system. After the gage is placed in the turbine component and the turbine model installed in the tunnel, a calibration signal is passed from the gage terminals through the data recording system. Immediately prior to initiation of the test-gas flow, the room temperature signal from each of the gages is sampled and recorded with the rotor at design speed. These prerun heat-flux data are a very small percentage of the time-averaged heat-flux signal recorded during the test-gas flow. However, the prerun values provide an estimate of the system noise level. The data obtained from the experiment consist of a heat-flux phase (or time) history with the fluctuating component due to vane passage cutting superimposed on the time-averaged signal (the heat flux averaged over several revolutions). The uncertainty associated with the time-averaged portion of the heat-flux data is estimated to be on the order of ± 1 percent. As noted above, the heat-flux signals associated with blade transit of the vane passages represent fluctuations superimposed on a much larger signal. The magnitude of the heat-flux fluctuations can be relatively large as illustrated by Dunn et al. (1989) and in Figs. 4–9 of this paper. The magnitude of the gage temperature fluctuation is small compared to the temperature corresponding to the time-averaged heat flux, but the rate of change of temperature with respect to phase angle (or time) is very large. The combination of a small gage temperature change and the large temperature gradient increases the uncertainty in the measurement. It is estimated that the uncertainty in the instantaneous heat-flux value is on the order of ± 3 percent. The uncertainty in the phase angle is mainly associated with turbine manufacturing tolerances and not with the shaft encoder. Once the encoder unit is secured to the shaft and aligned with a particular vane trailing edge, there is little uncertainty in where it will provide repeat signals to trigger the data recording system.

The instrumentation package in the stationary shroud for this turbine includes heat-flux gages and pressure transducers. The time-resolved data taken in the shroud region were obtained as part of a larger program intended to determine the detailed behavior of leakage flow in the tip/shroud region.

Downloaded 01 Jun 2010 to 171.66.16.66. Redistribution subject to ASME license or copyright; see http://www.asme.org/terms/Terms_Use.cfm

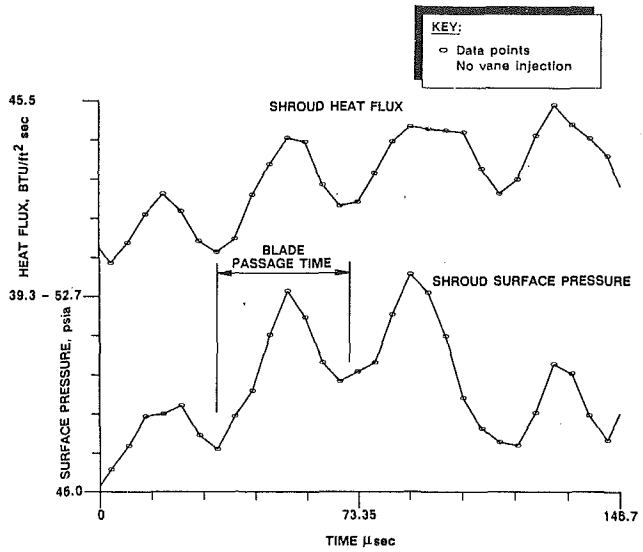

Fig. 11 Time-resolved stationary shroud heat-flux and surface-pressure history

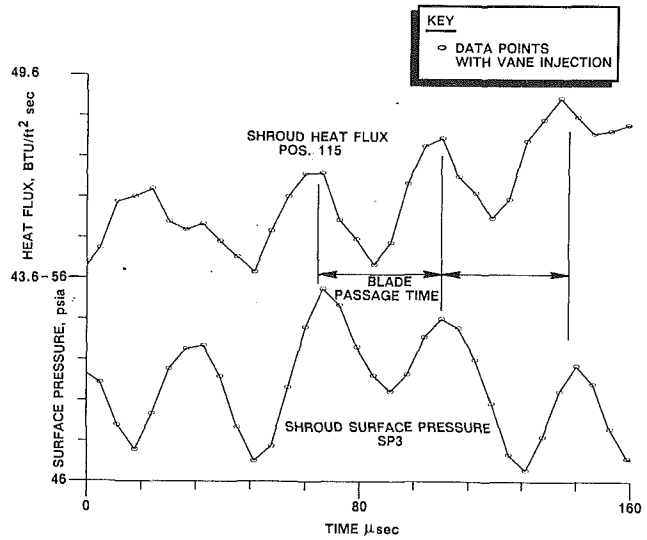

Fig. 12 Time-resolved stationary shroud heat-flux and surface-pressure history

The blade tip as well as the blade surfaces in the immediate vicinity of the tip (90 percent span) were all instrumented with heat-flux gages. The time-averaged heat-flux distributions on the respective surfaces are relatively easy to obtain and these form the basic data for the purposes of the leakage flow study mentioned above. However, the time-resolved heat-flux and surface-pressure data are helpful in understanding the behavior of the leakage flow. Figure 10 is a sketch of the shroud instrumentation relative to the blade location drawn approximately to scale. For the purposes of this discussion, attention will be confined to heat-flux gage position 115 and pressure gage position P3, which are both in about the same location relative to the blade pressure surface and of about the same axial chord. The time elapsed between successive blade passage at a fixed shroud location is on the order of 38.5 μs and the sampling rate is on the order of 4.2 μs/sample, which results in approximately nine data samples per blade passage. This sampling rate is sufficient to define the characteristic of the heat-flux and pressure time history, as will be illustrated in Fig. 11. Here, comparisons are made on the same time base of the heat-flux history at position 115 and the surface pressure history at location SP3. Approximately four blade passages are shown in Fig. 11. The heat-flux data give the appearance of a slightly upward trend with time. If a larger portion of the blade revolution were presented, it would be illustrated that the heat-flux level has a slight waviness but is relatively constant. The agreement between the peaks and valleys of the respective time histories is felt to be reasonably good, suggesting that the heat-flux and surface pressure are tracking each other in phase. The blade passage time is noted on the figure. Figure 12 is a plot comparable to Fig. 11 but for the case of vane slot injection. From previous work with this turbine it is known that the magnitude of the time-averaged heat flux is only slightly influenced by the presence of injection. The with-injection value was found to be on the order of 46 Btu/ft^2 sec and the corresponding value without injection being on the order of 44 Btu/ft^2 sec. The standard deviations of the time-averaged data are such that the influence of vane injection on the shroud heat-flux values is not significant.

Conclusions

Phase-resolved heat-flux data have been presented for several locations on the Garrett TFE 731-2 HP turbine blade. The peak heat-flux value at the geometric stagnation point and on the blade suction surface appears to be associated with the flow coming from the vane trailing edge wake. Whether this increased heat flux is due to enhanced turbulence in the wake whether it is due to the influence of the wake flow on the blade boundary layer cannot be determined from these measurements. The presence of vane slot injection is shown to have an insignificant influence on the level of heat flux in the stationary shroud for this particular turbine. However, at the geometric stagnation point of the blade near midspan, the influence of upstream vane injection has a significant influence on the heat-flux history. Time-resolved stationary shroud heat-flux and surface pressure histories are shown to be in phase with each other for the geometric location investigated in this work.

Acknowledgments

The research reported in this paper was jointly supported by the U.S. Air Force Aero Propulsion Laboratory and the NASA Lewis Research Center. The Air Force Support was covered under Exploratory Development Funds. The NASA portion of the work was supported under NASA Grant NAG3-581. The Air Force technical monitor is Dr. William Troha and the NASA technical monitors are Mr. Kas Civinskas and Dr. Raymond Gaugler.

References

Adamczyk, J. J., 1985, "Model Equation for Simulating Flows in Multistage Turbomachinery," ASME Paper No. 85-GT-226.

Binder, A., Forster, W., Kruse, H., and Rogge, H., 1985, "An Experimental Investigation Into the Effect of Wakes on the Unsteady Turbine Rotor Flow," ASME *Journal of Engineering for Gas Turbines and Power*, Vol. 107, pp. 458–466.

Binder, A., Forster, W., Mach, K., and Rogge, H., 1987, "Unsteady Flow Caused by Stator Secondary Vortices in a Turbine Rotor," ASME JOURNAL OF TURBOMACHINERY, Vol. 109, pp. 251–257.

Blair, M. F., 1983a, "Influence of Free-Stream Turbulence on Turbulent Boundary Layer Heat Transfer and Mean Profile Development, Part I — Experimental Data," ASME *Journal of Heat Transfer*, Vol. 105, pp. 33–40.

Blair, M. F., 1983b, "Influence of Free-Stream Turbulence on Turbulent Boundary Layer Heat Transfer and Mean Profile Development, Part II — Analysis of Results," ASME *Journal of Heat Transfer*, Vol. 105, pp. 41–47.

Carslaw, H. S., and Jaeger, J. C., 1959, *Conduction of Heat in Solids*, 2nd ed., Oxford University Press, New York, p. 72.

Doorly, D. J., and Oldfield, M. L. G., 1985, "Simulation of the Effects of Shock Wave Passing on a Turbine Rotor Blade," ASME *Journal of Engineering for Gas Turbines and Power*, Vol. 107, pp. 998–1006.

Dring, R. P., Blair, M. F., and Joslyn, H. D., 1980, "An Experimental

Downloaded 01 Jun 2010 to 171.66.16.66. Redistribution subject to ASME license or copyright; see http://www.asme.org/terms/Terms_Use.cfm

Investigation of Film Cooling on a Turbine Rotor Blade," ASME *Journal of Engineering for Power*, Vol. 102, pp. 81–87.

Dring, R. P., and Joslyn, H. D., 1981, "Measurement of Turbine Rotor Blade Flows," ASME *Journal of Engineering for Power*, Vol. 103, pp. 400–405.

Dring, R. P., Joslyn, H. D., Hardin, L. W., and Wagner, J. H., 1982, "Turbine Rotor–Stator Interaction," ASME *Journal of Engineering for Power*, Vol. 104, pp. 729–742.

Dunn, M. G., and Hause, A., 1982, "Measurements of Heat Flux and Pressure in a Turbine Stage," ASME *Journal of Engineering for Power*, Vol. 104, pp. 76–82.

Dunn, M. G., 1984, "Time-Resolved Heat-Flux Measurements for a Full-Stage Turbine," AFWAL-TR-84-2025, May.

Dunn, M. G., Lukis, G., Urso, M., Hiemenz, R. J., Orszulak, R. L., and Kay, N. J, 1984a, "Instrumentation for Gas Turbine Research in Short-Duration Facilities," Aerospace Congress and Exposition (SAE), Long Beach, CA, Paper No. 841504.

Dunn, M. G., Rae, W. J., and Holt, J. L., 1984b, "Measurement and Analyses of Heat Flux Data in a Turbine Stage: Part II — Discussion of Results and Comparison With Predictions," ASME *Journal of Engineering for Gas Turbines and Power*, Vol. 106, pp. 234–240.

Dunn, M. G., 1985, "Turbine Heat Flux Measurements: Influence of Slot Injection on Vane Trailing Edge Heat Transfer and Influence of Rotor on Vane Heat Transfer," ASME *Journal of Engineering for Gas Turbines and Power*, Vol. 107, pp. 76–83.

Dunn, M. G., 1986a, "Experimental Measurements of Heat-Flux Distribution in a Turbine Stage With Upstream Disturbances," NASA CP-2436, Vol. I, pp. 614–636.

Dunn, M. G., 1986b, "Heat-Flux Measurements for the Rotor of a Full-Stage Turbine: Part I — Time-Averaged Results," ASME JOURNAL OF TURBOMACHINERY, Vol. 108, pp. 90–97.

Dunn, M. G., George, W. K., Rae, W. J., Woodward, S. H., Moeller, J. C., and Seymour, P. J., 1986, "Heat Flux Measurements for the Rotor of a Full-Stage Turbine: Part II — Technique and Typical Time-Resolved Measurements," ASME JOURNAL OF TURBOMACHINERY, Vol. 108, pp. 98–107.

Dunn, M. G., Seymour, P. J., Woodward, S. H., George, W. K., and Chupp, R. E., 1989, "Phase-Resolved Heat-Flux Measurements on the Blade of a Full-Scale Rotating Turbine," ASME JOURNAL OF TURBOMACHINERY, Vol. 111, pp. 8–19.

Epstein, A. H., Guenette, G. R., Norton. R. J. G., and Cas Yuhang, 1985, "Time Resolved Measurements of a Turbine Rotor Stationary Tip Casing Pressure and Heat Transfer Field," 21st Joint Propulsion Conference, Monterey, CA, Paper No. AIAA-85-1220.

George, W. K., Rae. W. J., Seymour, P. J., and Sonnenmeier, J. K., 1987, "An Evaluation of Analog and Numerical Techniques for Unsteady Heat Transfer Measurements With Thin-Film Gauges in Transient Facilities," *Proc. of the 1987 ASME-JSME Thermal Engineering Joint Conference*, pp. 611–617.

Giesing, J. P., 1968, "Nonlinear Interaction of Two Lifting Bodies in Arbitrary Unsteady Motion," ASME *Journal of Basic Engineering*, Vol. 90, pp. 387–394.

Guenette, G. R., Epstein, A. H., Giles, M. B., Haimes, R., and Norton, R. J. G., 1989, "Fully Scaled Transonic Turbine Rotor Heat Transfer Measurements," ASME JOURNAL OF TURBOMACHINERY, Vol. 111, pp. 1–7.

Hodson, H. P., 1984, "Boundary Layer and Loss Measurements on the Rotor of an Axial-Flow Turbine," ASME *Journal of Engineering for Gas Turbines and Power*, Vol. 106, pp. 391–399.

Hodson, H. P., 1985a, "Boundary-Layer Transition and Separation Near the Leading Edge of a High-Speed Turbine Blade," ASME *Journal of Engineering for Gas Turbines and Power*, Vol. 107, pp. 127–134.

Hodson, H. P., 1985b, "Measurements of Wake-Generated Unsteadiness in the Rotor Passages of Axial Flow Turbines," ASME *Journal of Engineering for Gas Turbines and Power*, Vol. 107, pp. 467–476.

Kemp, N. H., and Sears, W. R., 1953, "Aerodynamic Interference Between Moving Blade Rows," *J. Aero Sci.*, Vol. 20, No. 9, pp. 585–597.

Kemp, N. H., and Sears, W. R., 1955, "The Unsteady Forces Due to Viscous Wakes in Turbomachine," *J. Aero. Sci.*, Vol. 22, No. 7, pp. 478–483.

Kerrebrock, J. L., and Mikolajczak, A. A., 1970, "Intra-stator Transport of Rotor Wakes and Its Effect on Compressor Performance," ASME *Journal of Engineering for Power*, Vol. 92, pp. 359–368.

Lakshminarayana, B., Govindan, T. R., and Reynolds, B., 1982, "Effects of Rotation and Blade Incidence on Properties of Turbomachinery Rotor Wake," *AIAA Journal*, Vol. 20, No. 2, pp. 245–253.

Lowery, G. W., and Vachon, R. I., 1975, "The Effect of Turbulence on Heat Transfer From Heated Cylinders," *International Journal of Heat and Mass Transfer*, Vol. 18, pp. 1229–1242.

Moffat, R. J., and Maciejewski, P. K., 1985, "Heat Transfer With Very High Free Stream Turbulence," *Turbine Engine Hot Section Technology*, NASA Conference Publication 2405, Oct.

Moffat, R. J., and Maciejewski, P. K., 1988, "The Effects of High Free Stream Turbulence on Heat Transfer in Turbulent Boundary Layers," Zoran Zaric Memorial Session, International Seminar on Near Wall Turbulence, International Center for Heat and Mass Transfer, Dubrovnik, Yugoslavia, May.

O'Brien, J. E., and Van Fossen, G. J., 1985, "The Influence of Jet-Grid Turbulence on Heat Transfer From the Stagnation Region of a Cylinder in Crossflow," ASME Paper No. 85-HT-58.

O'Brien, J. E., 1988, "Effects of Wake Passing on Stagnation Region Heat Transfer," presented at the ASME Winter Annual Meeting, Chicago, IL, Dec.

Parker, R., 1969, "Relation Between Blade Row Spacings and Potential Flow Interaction Effects in Turbomechanics," *Proceedings of the Institute of Mechanical Engineering*, Vol. 184, Pt. 3G, No. 11, pp. 1–8.

Rivir, R. B., Elrod, W. C., and Dunn, M. G., 1985, "Two Spot Laser Velocimeter Measurements of Velocity and Turbulence Intensity in Shock Tube Driven Turbine Flows," AGARD Conference Preprint No. 390, Propulsion and Energetics Panel 65th Symposium, Bergen, Norway, 6–10 May.

Sharma, O. P., Butler, T. L., Joslyn, H. D., and Dring, R. P., 1985, "Three-Dimensional Unsteady Flow in an Axial Flow Turbine," *J. of Propulsion*, Vol. 1, No. 1, pp. 28–38.

Taulbee, D. B., Tran, L., and Dunn, M. G., 1989, "Stagnation Point and Surface Heat Transfer for a Turbine Stage: Prediction and Comparison With Data," ASME JOURNAL OF TURBOMACHINERY, Vol. 111, pp. 28–35.

Traci, R. M., and Wilcox, D. C., 1975, "Free Stream Turbulence Effects on Stagnation Point Heat Transfer," *AIAA Journal*, Vol. 13, No. 7, pp. 890–896.

Wittig, S., Schulz, A., Dullenkopf, K., and Fairbanks, J., 1988, "Effects of Free-Stream Turbulence and Wake Characteristics on the Heat Transfer Along Cooled Gas Turbine Blade," ASME Paper No. 88-GT-179.

Downloaded 01 Jun 2010 to 171.66.16.66. Redistribution subject to ASME license or copyright; see http://www.asme.org/terms/Terms_Use.cfm

F. Bario
Research Engineer CNRS.

F. Leboeuf
Professor.

A. Onvani[1]
Research Fellow.

A. Seddini[2]
Research Fellow.

Laboratoire de Mécanique des Fluides et d'Acoustique,
C.N.R.S. U.A. 263-Ecole Centrale de Lyon,
B.P. 163-F69131 Ecully Cedex, France

Aerodynamics of Cooling Jets Introduced in the Secondary Flow of a Low-Speed Turbine Cascade

The aerodynamic behavior of cold discrete jets in a cold secondary flow is investigated. Configurations including single jets and rows of jets are studied. These jets are introduced through the side wall of a low-speed nozzle turbine cascade. The experimental setup and the jet behavior are fully described. The effects of location with respect to the blades, mass flow ratio, yaw, and incidence angles on the aerodynamics of single jets are investigated. The influence of neighboring jets is detailed in the case of multiple jet configurations. The interaction with the secondary flow is presented. The local pressure and velocity fields, trajectories, and visualizations are discussed. The measuring apparatus includes a five-hole probe and a hot wire for intermittency measurements.

Introduction

Nowadays the tendency is to raise the upstream temperature of the turbine, in order to increase the thermal efficiency of the engine. Cooling of blades and side walls is therefore necessary, particularly in the first nozzle, in order to protect the material from the hot flow. Discrete jets have been found to be one of the most efficient ways of cooling. Some attention has to be paid to the aerodynamic interactions between the jet flows and the secondary flow in a turbine. The goal is to minimize the injected mass flow for a given cooling efficiency and to decrease the aerodynamic losses induced by the jet–secondary flow interaction.

Discrete jets have been introduced on the side wall of a turbine cascade. The results emphasize the mixing and diffusion processes of the jet flow in the secondary flow, as well as the mutual interactions of the jets.

Both thermal and aerodynamic aspects of the subject have to be studied. Only the latter is developed in this paper.

Before dealing with that point, we shall give a qualitative description of the phenomena observed in a jet introduced, at given incidence and yaw angles, into a three-dimensional external flow. This description is partly based on previous experimental studies (Moussa et al., 1977).

Three important effects control the dynamic of the jet (Fig. 1): drag, longitudinal vortices, and entrainment effects. In the zone close to the orifice, the jet behaves as a flexible solid body. A wake develops downstream of the jet. The resulting static pressure drag induces a bending of the jet trajectory.

One of the fundamental characteristics of the interaction between the external flow and the jet is the appearance of contrarotating vortices Ω_s within the jet (Fig. 1). According to Moussa et al. (1977), the vortices are located under the jet stream and exhibit a regular structure. We propose the following model for the vortex development. The process lying behind the vortex production is tied to the existence of transverse gradients of the longitudinal velocity component $\partial V_s/\partial n$, $\partial V_s/\partial b$ and jet deflection at $(d\alpha_n, d\alpha_b)$ under the external flow influence. The mechanism for the vortex production is probably very similar to that which controls the generation of the passage vortex in a blade cascade (Lakshminarayana and Horlock, 1973; Bario et al., 1981). By their respective kinetic moments, the vortices will tend to stiffen the jet, thus opposing the deflection that created them.

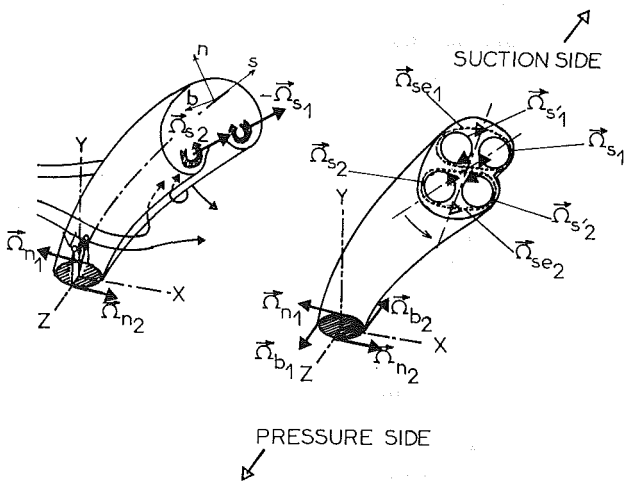

Fig. 1 Aerodynamics of a jet introduced from the side wall in a two-dimensional flow (left) and in a cascade flow (right)

[1]Current address: Assistant Professor, Mechanical Engineering Department, Iranian Open University, and Director of Training Department, Mebarabeh Steel Complex, Ispahan, Iran.

[2]Current address: Assistant Professor, Inst. National d'Enseignement Supérieur d'Hydraulique, Tlemcen, Algeria.

Contributed by the International Gas Turbine Institute and presented at the 34th International Gas Turbine and Aeroengine Congress and Exhibition, Toronto, Ontario, Canada, June 4–8, 1989. Manuscript received at ASME Headquarters January 27, 1989. Paper No. 89-GT-192.

Copyright © 1990 by ASME
Downloaded 01 Jun 2010 to 171.66.16.66. Redistribution subject to ASME license or copyright; see http://www.asme.org/terms/Terms_Use.cfm

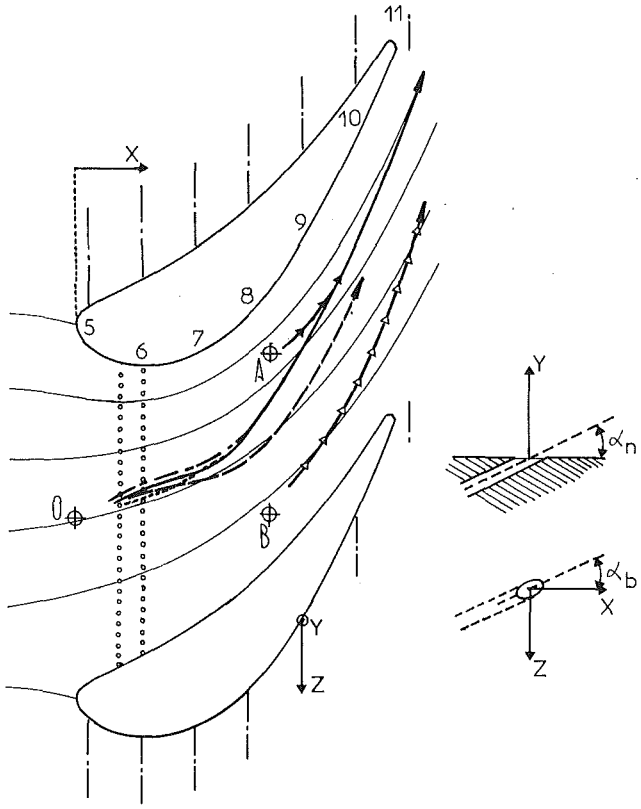

STATION	1	5	6	7	8	9	10	11
X/C$_X$	-1.95	0.041	0.204	0.369	0.532	0.696	0.860	1.016

Fig. 2 Jet orifice location, trajectories of single jets, and inviscid midspan streamlines (see also Table 1)

The behavior of secondary flows in turbines has been widely studied in recent years. Sieverding (1988) gives a good picture of the present knowledge of these phenomena. The strong flow deviation and acceleration in the turbine passage give rise to the growth of secondary vortices inducing a high three-dimensional structure into the flow. We shall investigate the development of cooling jets introduced from the side wall in the secondary flow region.

Pressure and velocity measurements and thermal detection of the jets for different configurations are presented. The experimental equipment and the results are described below.

Experimental Setup

Wind Tunnel and Blade Cascade. The wind tunnel consists of a ventilator, a plenum chamber with honeycombs, and a convergent, which drives the flow on the blade cascade; its convergence ratio is 15. The test section is rectangular and its dimensions are 0.274 m × 1.275 m. The inclinations of the upper and lower walls were adjusted in order to obtain a proper two-dimensional flow along the cascade. The periodicity of the flow downstream is obtained by acting on the upper wall and on a small deflector placed on the lower and upper walls. The periodicity of the flow is checked with the help of a three-hole directional probe, which is introduced downstream of the cascade, and displaced along the Z direction.

The straight cascade consists of nine nontwisted blades of a gas turbine nozzle. The main dimensions of the blades are: span $H = 0.274$ m, cord $c = 0.163$ m, and solidity $c/g = 1.16$. The stagger angle defined with respect to the axial direction is 41°30′. The blade profile is given in Fig. 2. The profiles are numbered from 1 to 9, starting from the lower wall.

Table 1

ORIFICE	α_n	α_b	D(m)	X/Cx	V_o/V_{ex}	FIGS.2,10
O	60°	0°	.0022	0.	2.58	
O	"	"	"	"	0.65	
O	"	-45°	"	"	"	
O	"	45°	"	"	"	
A	60°	-45°	.0022	0.610	0.65	
B	60°	-45°	.0022	0.610	0.65	
1rst ROW	30°	-10°	.002	0.147	1.20	
2nd ROW	30°	-20°	.002	0.213	1.20	

Jet Configurations. For the single-jet configurations, three different locations of the jet have been chosen in the channel (Fig. 2). The first one (0) is at the leading edge in the middle of the channel. The second and third ones are located at the throat level between measurement stations 8 and 9, one at 0.025 m from the suction surface (A), and the other at 0.020 m from the pressure surface (B) of the blade. The orifice diameter is 0.0022 m. The angle α_n between the direction of the jet outlet and the X-Z surface is $\alpha_n = 60$ deg (Fig. 2). The orifice is drilled on a cylinder that can be turned around its axis Y in order to define various angles α_b within the X-Z plane. The different parameters used for each jet are presented in Table 1. Two velocity ratios have been used: $V_o/V_{ex} = 0.65$, and $V_o/V_{ex} = 2.58$, where V_{ex} is the local velocity of the flow external to the viscous layer and V_o is the mass-averaged outlet velocity at the orifice.

Two rows of jet configurations have also been studied. They have, respectively, 28 and 27 holes (Fig. 2), the first one being located at $x/C_x = 0.147$, the second one at $x/C_x = 0.213$. The two rows and the front of the cascade are parallel. The diameter of the jet orifices is $D = 0.002$ m; the distance between two holes in one row is $l = 0.004$ m ($l/D = 2$); the distance between the two rows is $a = 0.008$ m ($a/D = 4$).

Nomenclature

C_D = drag coefficient
C_x = axial chord
D = orifice diameter
g = gravitational acceleration
H = blade span
H_{12} = shape factor = displacement thickness/momentum thickness
P = static pressure
P_T = stagnation pressure
V = velocity
X = axial direction (see Fig. 2)
Y = direction normal to the side wall (see Fig. 2)
Z = tangential direction (see Fig. 2)
α_n = orifice pitch angle (see Fig. 2)
α_b = orifice yaw angle (see Fig. 2)
β = absolute flow angle (with respect to the axial direction)
Γ = intermittence coefficient
ρ = density
Ω = vorticity
$\bar{}$ = mean quantity

Subscripts

ex = midspan reference
b, n = normal to the jet streamline (see Fig. 1)
o = at the jet orifice
ref = reference upstream condition
s = longitudinal to the jet streamline (see Fig. 1)
x, y, z = along X, Y, or Z directions

Downloaded 01 Jun 2010 to 171.66.16.66. Redistribution subject to ASME license or copyright; see http://www.asme.org/terms/Terms_Use.cfm

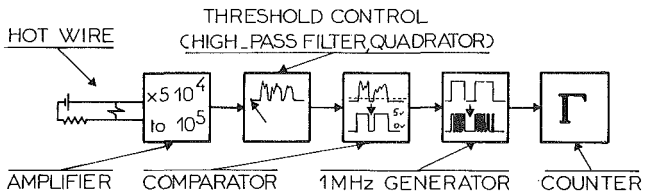

Fig. 3 Electronic detection system; measurement of the intermittence coefficient

The angles that define the injection directions are $\alpha_n = 30$ deg for the two rows, $\alpha_b = -10$ deg for the first row, and $\alpha_b = -20$ deg for the second row. These last two values have been chosen in order to obtain, near the orifices, the alignment of the jet flow with the mean external streamline. All the jets of a row have the same parallel initial direction. Note that the value of the angle α_n ($\alpha_n = 30$ deg) is lower than that used for the single jet cases. The velocity ratio is $V_o/V_{ex} = 1.2$, where V_{ex} is the gap-averaged mean velocity.

Measurement Methods

Pressure and Velocity Measurements. Measurements of the aerodynamic field are carried out with a five-hole directional cobra type probe. Its head has a diameter of 1.5 mm and is located at 30 mm from an 8-mm-dia stem. This probe has been calibrated in the potential core of a square low-speed jet. The calibration has been realized for values of the pitch angle γ_s between +30 and −30 deg, and for five values of the yaw angle $\beta_s = -4, -2, 0, +2$, and +4 deg.

The probe has been introduced into the cascade in sections through slots realized in one side wall (Fig. 2). Special care has been taken in order to avoid any leakage flow through the slot while displacing the probe. The measurements have been obtained near the opposite wall, thus avoiding any disturbing effects of the slots. The probe is fixed on a carrier, which enables the displacement along the Y and Z directions. Rotation of the probe around its axis is also used in order to align its head with the local direction of the flow. Therefore, β_x is nearly zero thus minimizing the use of the calibration map.

The accuracy of the displacements along Y and Z is 0.1 mm. The angle β, after rotation of the probe, is estimated with an accuracy of 0.5 deg. The pressure is obtained with an error of 0.35 mm of water. The relative velocity error is then of the order of 1 percent.

Data Reduction. Most of the pressure values are given in mm H_2O with respect to a reference stagnation pressure P_{ref} taken upstream in the plenum chamber. For these experiments, we have $P_{ref} = 60$ mm H_2O. In the following, space-averaged quantities will also be given; they are obtained from about 30 values, distributed along the Z direction.

Thermal Detection of the Jet. We shall see that it is very difficult to detect the jet using a pressure sensor, in particular for very low velocity ratio, as the pressure and velocity of the jet have the same magnitude as that of the secondary flow. A thermal detection system has been developed. Its principle is simple. The jet is heated up to a temperature of 40–50°C above the temperature of the flow in the cascade. A hot wire with a low heating coefficient is used as a thermometer. The wire signal is processed electronically. As most of the measurements are done outside of the potential core of the jet, the detection (localization) of the jet is thus reduced to a measurement of a turbulent quantity such as an intermittence coefficient Γ, Γ being defined as the ratio between the sum of the time durations during which the wire is within the hot bursts and the total measurement time duration.

A high value of the intermittence coefficient characterizes a region of hot flow. As the centers of the vortices are not easily fed by external flow, the intermittence coefficient will be higher there. The shape and level of iso-intermittence curve can be used to describe the jet evolution.

The technique of thermal sampling has been described by Sunyach (1971). A simpler technique is used here. The output of the hot wire, amplified 50,000 to 100,000 times as shown in Fig. 3, is input to a "threshold control" system, which matches the "cold" signal level to a reference threshold, thus avoiding the problems of low-frequency temperature drift of the wind tunnel air. The second stage of the electronics is used to detect the hot bubbles emitted by the jet. Comparisons are made with a controllable threshold. At the output, a logic signal is obtained (0 V for the cold fluid and 5 V for the hot fluid), which is used to control a 1 MHz generator. Counting the pulses gives a measure of the intermittence coefficient. A simple calculation of the drag force ($F_D \sim \rho_{ex} C_D S V_{ex}^2$ where $C_D \sim 1.8$ (Ramette and Louis, 1984), and ρ and V are the density and velocity of the external flow acting on the surface S of the jet, which can be taken as a solid body $S \sim L^2$, L being a length scale of the jet) and buoyancy force F_B balance ($F_B \sim (\rho_{ex} - \rho) L^3 g$) shows that the effect of buoyancy can be neglected. As a consequence, the necessity of using low jet heating for hot wire detection is not a problem for measurement analysis.

A laser visualization technique has also been used. For that purpose, smoke is mixed with the air injected through the orifice. A laser beam hits a rotating mirror, which creates a laser light sheet parallel to the (Y, Z) plane. A cross section of the jet is then visualized.

Results and Discussion

General Conditions. The cascade has first been adjusted in order to obtain proper uniform conditions upstream and periodic conditions downstream. The periodicity was found to be adequate for the passages between the blades 2 to 7. Variation of the dynamic head less than 1 percent has been observed for homologous points in the blade passage, except for the lowest velocity on the wake, where variations of the order of 4 percent have been reached. In the following, measurements are presented between the blades numbered 5 and 6.

The upstream conditions are two dimensional at station 1. The velocity modulus outside of the wall layer is 15.2 m/s. The Reynolds number based on the chord and the downstream midspan conditions is 330,000. The viscous layer thickness is of the order of 60 mm. Other integral quantities for station 1 are: displacement thickness, $\delta_x^* = 4.33$ mm, shape factor $H_{12} = 1.34$. This last value is typical for a turbulent boundary layer on a flat plate without pressure gradient. The details of the flow are presented in Fig. 4. The axial velocity profile has been described by a logarithmic law for $y^+ = 150$ to 1000, where $Y^+ = YV_W/\nu$ and $V_w = \sqrt{\tau_w/\rho}$. The friction coefficient $C_f = 2\tau_w/\rho V_{ex}^2$ is $C_f = 0.0035$, as determined by Clauser's method, according to the law of the wall $V/V_w = 2.5 \ln y^+ + 4.9$. There exists a small gradient of the velocity angle β, which goes from +1 deg at the wall to −1 deg at midspan. We believe that this is linked to the particular adjustment of the upper and lower walls of the wind tunnel. In connection, a slight static pressure gradient exists in the direction Y normal to the side wall.

Single Jet Configurations

Injection at Point 0 With a Velocity Ratio $V_o/V_{ex} = 2.58$ and Yaw Angle $\alpha_b = 0$ deg. The iso-stagnation pressure curves show that the jet is properly detected by the pressure sensor (Fig. 5). An increase in the stagnation pressure is observed at the center of the jet. There is a modification in the shape of the curves close to the wall, indicating that the wake of the

Downloaded 01 Jun 2010 to 171.66.16.66. Redistribution subject to ASME license or copyright; see http://www.asme.org/terms/Terms_Use.cfm

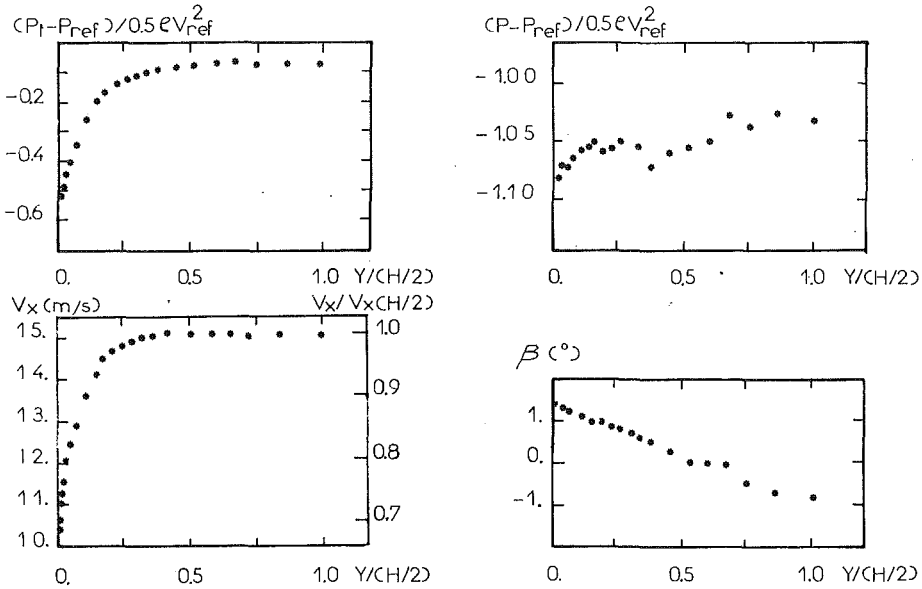

Fig. 4 Upstream flow conditions; station 1

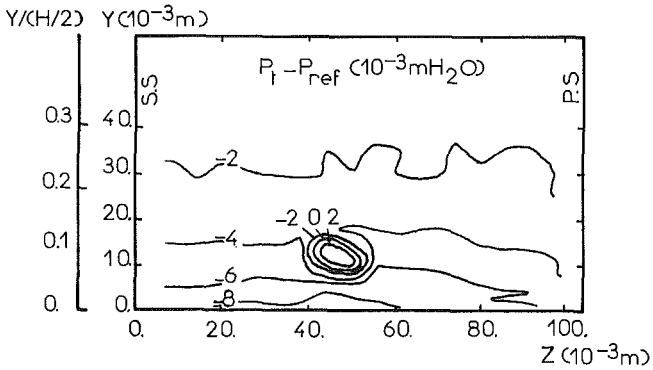

Fig. 5 Iso-stagnation pressure curves, station 6, single jet coming from 0 with $V_o/V_{ex} = 2.58$

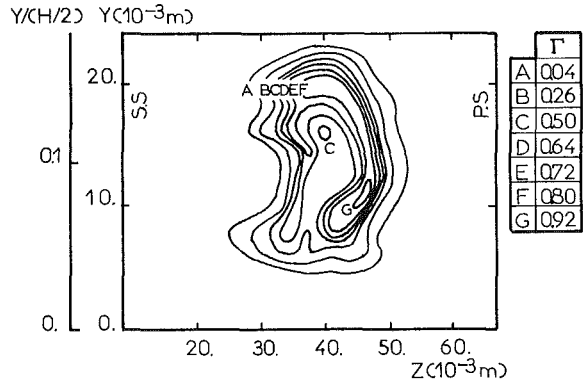

Fig. 7 Iso-intermittence curves, station 6, single jet coming from 0 with $V_o/V_{ex} = 2.58$

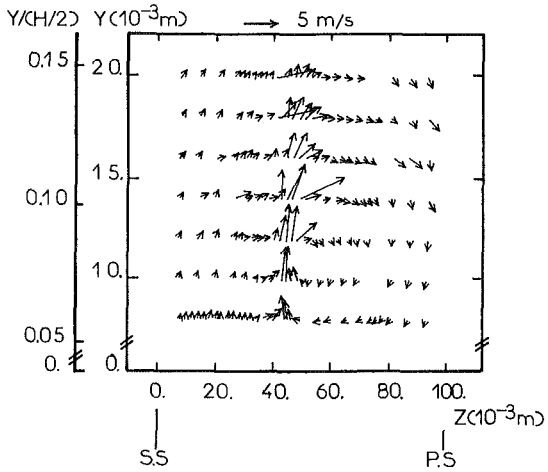

Fig. 6 Secondary velocity vectors, station 7, single jet coming from 0 with $V_o/V_{ex} = 2.58$

first part of the jet is clearly observed at station 6. The static pressure field is only locally disturbed. The minimum of the static pressure in the jet corresponds to the local maximum velocity V_s. The presence of the jet is clearly distinguished by the observation of the secondary velocity vectors (Fig. 6). This velocity is the projection of the measured velocity on a plane normal to the local inviscid computed streamline. Note the overall tendency for the jet to rotate in the same direction as the external secondary flow. The iso-intermittence curves (Fig. 7) show that the jet development occurs with a diffusion practically equivalent in the X and Z directions. There exist two areas with high intermittence coefficients, giving to the jet section a classical kidney shape. They correspond to the nuclei of the hot fluid emitted from the jet. Note that the area located close to the pressure side tends to stay very marked compared with the other. Similarly the rotation of the axis linking these two areas is quite pronounced during the evolution along the path. The rotation of the jet structure can be associated with the vorticity development along the jet path. We have already described how the pair of longitudinal vortices Ω_{s_1}, Ω_{s_2} may be linked to the jet deflection. Similarly, the jet is influenced by a new curvature, which is associated with the blade-to-blade deflection (Fig. 1). The corresponding vortices, which are located on the front and back faces of the jet Ω_{b_1} and Ω_{b_2}, induce longitudinal vortex $\Omega_{s_1'}$ and $\Omega_{s_2'}$. A structure Ω_{se_1} appears, which may be described by one vortex on the upper-suction side resulting from the association of the vortices Ω_{s_1} and $\Omega_{s_1'}$; and similarly there appears Ω_{se_2} on the lower pressure side. The two vortices Ω_{se_1} and the passage vortex Ω_{SF} having an opposite rotation, the shear stresses on the jet boundaries are probably stronger than for Ω_{se_2} and Ω_{SF}. The turbulent

Downloaded 01 Jun 2010 to 171.66.16.66. Redistribution subject to ASME license or copyright; see http://www.asme.org/terms/Terms_Use.cfm

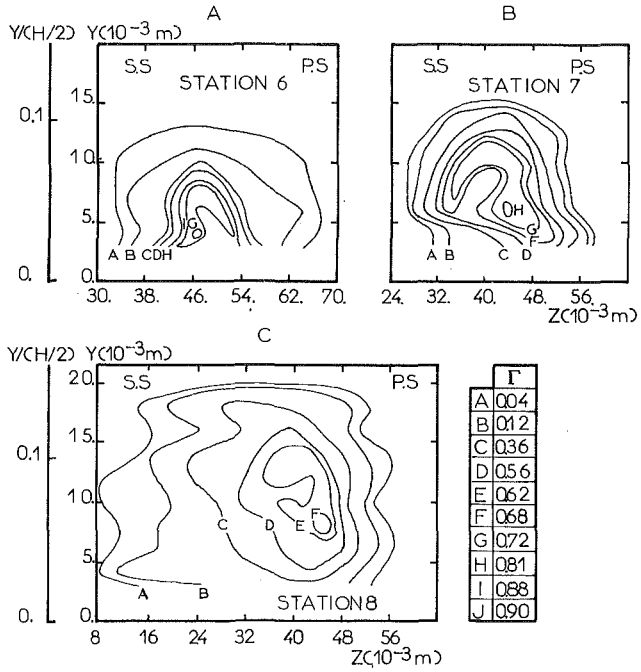

Fig. 8 Iso-intermittence curves, single jet coming from 0 with $V_o/V_{ex} = 0.65$

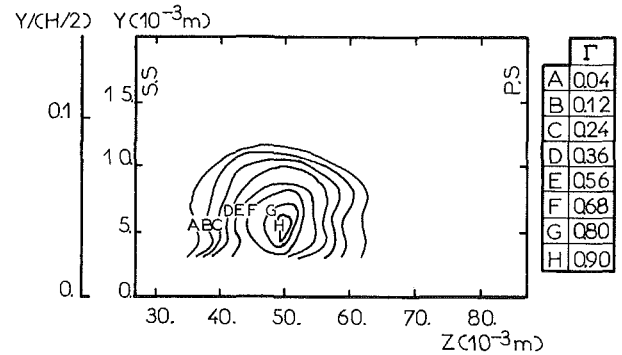

Fig. 9 Iso-intermittence curves, station 6, single jet coming from 0 with $V_o/V_{ex} = 0.65$, $\alpha_b = +45$ deg

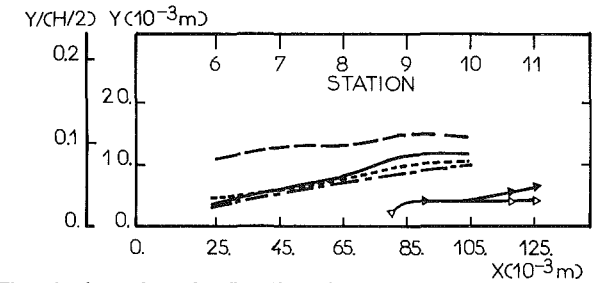

Fig. 10 Jet trajectories (location of the maximum value of the intermittence coefficient); see also Table 1

mixing is increased probably on the suction side vortex Ω_{se_1}. The decay of the suction side vortex Ω_{se_1} may be due then to this higher mixing. Close to the wall there is a zone 0.005 m thick, which is not influenced by the jet; this can be explained by the quite large initial value of the incidence angle α_n and the velocity ratio. Finally, we observed that the development of the secondary flow is not appreciably influenced by the presence of the jet, which can be considered simply as a local perturbation superimposed on the main flow in the cascade in the absence of injection.

Injection at Point 0 With a Velocity Ratio $V_o/V_{ex} = 0.65$ and Yaw Angle $\alpha_b = 0$ deg. The jet does not appreciably modify

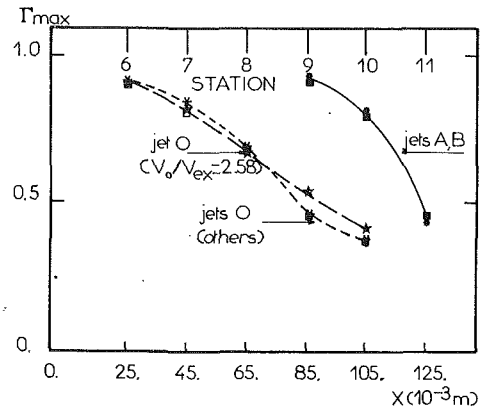

Fig. 11 Mixing of the jets; decrease of the intermittence coefficient maximum value

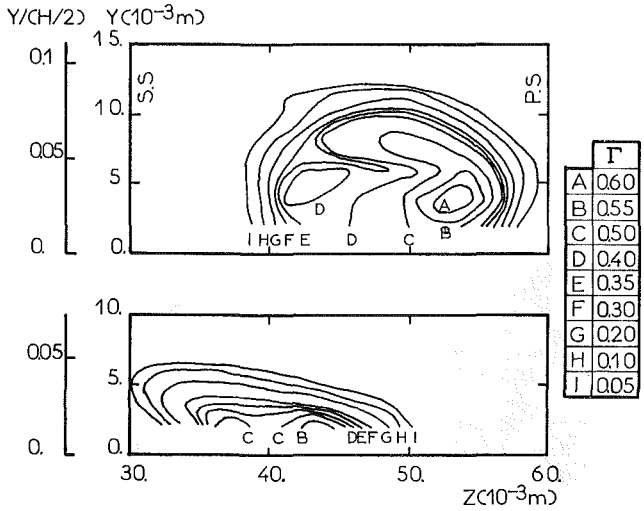

Fig. 12 Iso-intermittence curves, jet No. 15 of first row, $V_o/V_{ex} = 1.2$, Station 8; top: single-jet configuration; bottom: row of jet configuration

the distribution of the stagnation pressure except very close to the wall. The static pressure field is not changed. It is no longer possible to detect the jet except by thermal detection. The iso-intermittence curves still show a "kidney" type structure (Figs. 8*a–c*). The jet is close to the wall. The jet diffusion is stronger in the blade-to-blade direction (Z direction) than in the spanwise direction. The ratio of the jet characteristic transverse length is now about 2.

Injection at Point 0 With a Velocity Ratio $V_o/V_{ex} = 0.65$ and Yaw Angle $\alpha_b = -45$ deg and $\alpha_b = +45$ deg (Fig. 9). When a yaw angle exists with respect to the external flow through the cascade, the "kidney" structure exhibited by the iso-intermittence curves disappears; it seems that only one center of high intermittence Γ remains. The iso-intermittence curves have a shape similar to those found for a two-dimensional round jet, although the diffusion in the Z direction due to blade-to-blade pressure gradient is still clearly dominant compared with the diffusion in the Y direction.

Description of the Jet Trajectories. The locus of the maxima of the intermittence coefficient is indicated in Figs. 2 and 10. In the case of injection at point 0 at high velocity ratio ($V_o/V_{ex} = 2.58$), the jet tends to move away from the platform approaching closer to the pressure side of the guide vane than for the similar case at a low velocity ratio ($V_o/V_{ex} = 0.65$). This can be simply explained by the difference between the kinetic energies of the jet and the fluid flowing through the cascade. The different yaw angles used at point 0 have little influence on the jet trajectory, except very near the orifice. A comparison

Downloaded 01 Jun 2010 to 171.66.16.66. Redistribution subject to ASME license or copyright; see http://www.asme.org/terms/Terms_Use.cfm

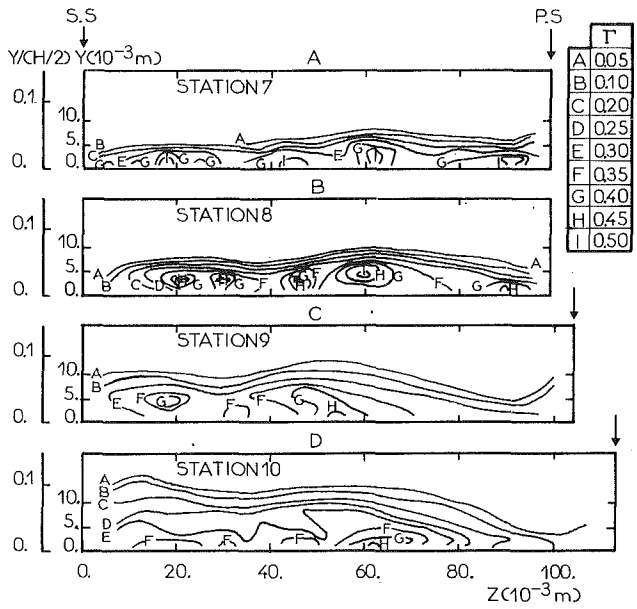

Fig. 13 Iso-intermittence curves, one row of jets, $V_o/V_{ex} = 1.2$

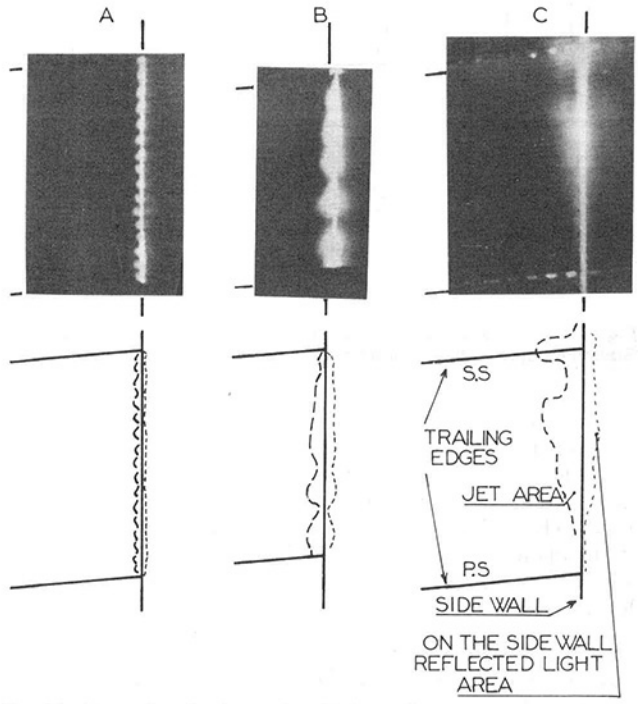

Fig. 14 Laser visualizations of multiple jet flow coming from row No. 1. Left: station 6, center: station 7, right: station 11 (viewed from the exit of the cascade, camera is above and on the left of the photographed channel). For stations 6 and 7, only the upper part (near suction surface S.S.) of the jet area is visualized; the lower part (near pressure surface P.S.) is masked by the lower blade).

of the position of the jet trajectory with that of the streamlines obtained by means of a blade-to-blade inviscid flow calculation is given in Fig. 2. We note an overdeflection of these trajectories, compared with the inviscid streamlines, under the influences of the secondary flow.

Jet Dilution. Two parameters describe the jet dilution in the cascade flow. Firstly, the maximum value of the intermittence coefficient characterizes the jet nucleus mixing with the mean flow. The decay of this maximum is practically identical for all the jets coming from the same orifice (Fig. 11).

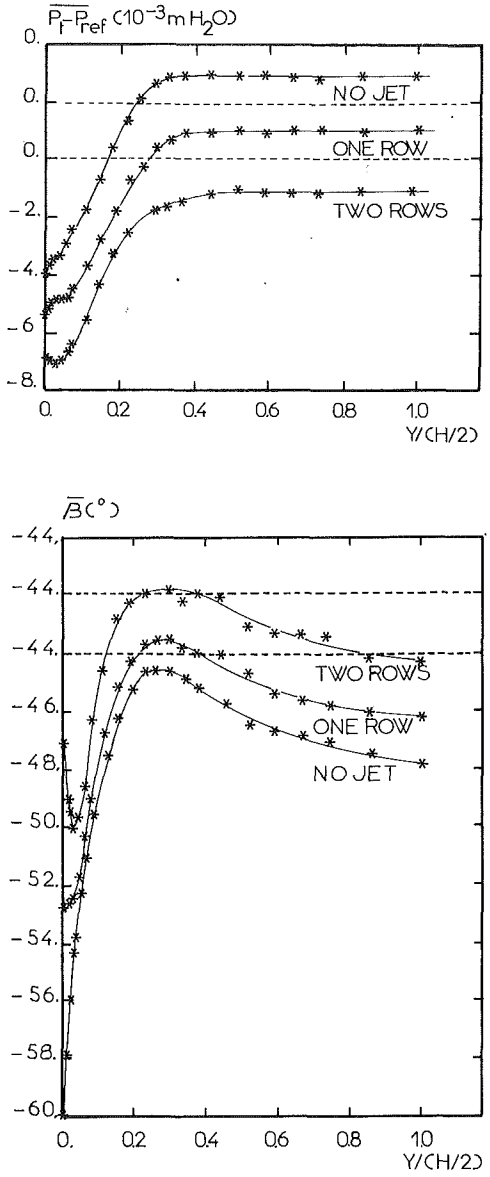

Fig. 15 Station 9: Comparison of the evolution of (*a*) stagnation pressure (bottom) and (*b*) flow angle (top)

Secondly, the development of the jet transverse section in the *Y-Z* plane points out the transverse diffusion of the jet (Fig. 8).

Multiple Jet Configurations

Influence of Adjacent Jets, One Row of Jet Configuration (V_o/V_{ex}) = 1.2. The iso-intermittence coefficient of jet No. 15 (coming from orifice No. 15 of the first row) is compared for the cases of a single injection and multiple injection from the first row (Fig. 12) for measurement station 8. The width of the single jet section is twice as big as that of the same jet in multiple jet configuration. This is because of the interaction of neighboring jet vortices, which prevents the diffusion and the mixing with the external flow.

The streamwise evolution of the flow injected from the first row is presented in Fig. 13. The thickness of the jet flow zone is more important on the suction side as compared to the pressure side. This is an effect of the secondary flow, which moves the jet flow from the pressure to the suction side (Fig. 13*d*). Some high intermittence coefficient zones exist. It is important to notice that their number is less than the number (28) of injection orifices. The laser visualization technique has

Downloaded 01 Jun 2010 to 171.66.16.66. Redistribution subject to ASME license or copyright; see http://www.asme.org/terms/Terms_Use.cfm

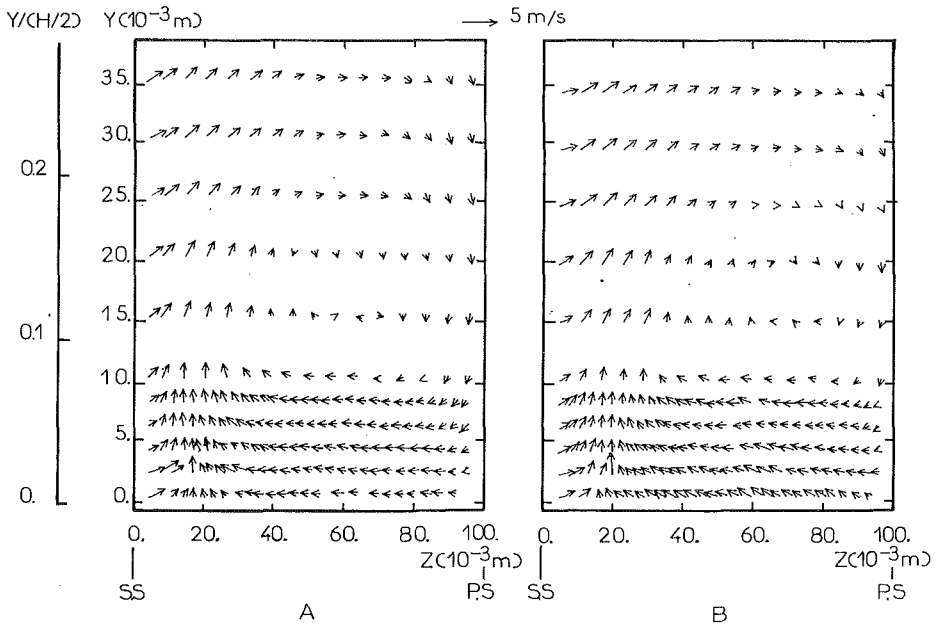

Fig. 16 Secondary velocity vectors, Station 8: (*a*) one row of jets (left); (*b*) two row of jets (right)

confirmed the presence of these structures. The cross section of the jets is visualized. Figures 14(*a*) and 14(*b*) show these sections for the stations 6 and 7. All the shapes and dimensions of the jet sections are still the same in section 6. However, big structures separated by crossflow regions are present in section 7. This is in good agreement with the intermittence measurements. We may suppose that these structures are connected to the coalescence of the jets. At the exit of the cascade (Station 11, Fig. 14*c*), the displacement of the jet area toward the suction side may be clearly observed. Also, a decrease of the jet thickness may be seen near the suction side corner. This means that another vortex effect may exist near the corner. In the wake of the blade the smoke moves away from the wall.

Two Rows of Jets. The influence of the second row of jets on the evolution of the intermittence is not very sensible. The gapwise-averaged quantities such as the stagnation pressure and the deflection angle $\bar{\beta}$ are only slightly modified (Figs. 15*a* and 15*b*). An increase of the stagnation pressure and of the relative flow angle $\bar{\beta}$ is detected near the wall. These are direct consequences of the higher jet momentum compared to the local external flow. The jets add kinetic energy to the wall layer. Simultaneously under the blade-to-blade static pressure difference, the jet layer is less deflected than the outer secondary flow. In particular cases, the use of film cooling can then counterbalance the secondary flow effects locally. As reported by Sieverding and Wilputte (1980), the influence of cooling jets on the selection of the blading must be considered. The secondary velocity vector is presented in Fig. 16(*a*) for the single-row case and Fig. 16(*b*) for the double-row case (station 8). The effect of increasing the number of rows of jets may be observed by a corresponding growth of the normal velocity component V. On these figures, the secondary flow passage vortex is clearly visible. Near the suction surface corner, there is also a contrarotating vortex close to the wall.

Conclusions

Some experimental results on the aerodynamic behavior of discrete jets introduced into the secondary flow of a nozzle turbine cascade have been presented. These materials give some insights into the mechanics of single jets and rows of jets. The main conclusions are:

1 For a single-jet configuration without yaw at high velocity ratio $V_o/V_{ex}=2.58$, the jet section has a "kidney" shape. One of the two centers generated by the normal to the wall deflection keeps high values of the intermittence coefficient and may be observed far downstream of the orifice; the other one disappears probably because of shear stress mixing effects. The axis of these two centers rotates under the blade-to-blade deflection influence. With this high velocity ratio, the jet is lifted away from the wall. The diffusion is similar in the transverse and normal directions.

2 For a single jet without yaw at low velocity ratio $V_o/V_{ex}=0.65$, the jet is closer to the wall. The diffusion occurs in a more pronounced way in the blade-to-blade direction. The shape of the jet is elliptic (length ratio 2).

3 When yaw with respect to the external flow exists at the orifice, the "kidney" shape disappears. The jet section is very similar to the two-dimensional jet.

4 The trajectories of single jets are affected by the secondary flow, but the yaw influence is weak for these velocity ratios, except very near the orifice.

5 The transverse section thickness of a single jet is twice as big as that of the same jet when operating in the same external aerodynamic conditions in a multiple jet configuration. This is a consequence of the neighboring jets, which prevent the external flow from reaching the wall and thus decrease the lateral diffusion.

6 In multiple jet configurations some high intermittence cores of jet flow resulting from jet coalescence exist.

7 The multiple jet layer thickness tends to be more pronounced on the suction side under secondary flow influence.

8 The wall-suction surface corner is weakly influenced by the jet flow. The passage vortex does not seem able to transfer the jet flow in this region.

9 For a velocity ratio of 1.2, the stagnation pressure and the normal to the wall velocity component are increased near the wall. Simultaneously, in the blade-to-blade plane, the velocity angle is decreased near the wall compared to the no-jet case. This suggests that the jet flow may counterbalance the classical secondary flow effect.

Downloaded 01 Jun 2010 to 171.66.16.66. Redistribution subject to ASME license or copyright; see http://www.asme.org/terms/Terms_Use.cfm

Acknowledgments

This work was carried out under the financial support of DRET (Direction des Recherches, Etudes et Techniques) and METRAFLU (Ecully).

References

Bario, F., Leboeuf, F., and Papailiou, K. D., 1982, "Study of Secondary Flows in Blade Cascade of Turbomachines," ASME *Journal of Engineering for Power*, Vol. 104, pp. 491–509.

Lakshminarayana, B., and Horlock, J. H., 1973, "Generalized Expressions for Secondary Vorticity Using Intrinsic Co-ordinates," *J. Fluid Mech.*, Vol. 59, Part I, pp. 97–115.

Moussa, Z. M., Trischka, J. N., and Eskinazi, S., 1977, "The Near Field in the Mixing of a Round Jet With a Cross-Stream," *J. Fluid Mech.*, Vol. 80, Part I, pp. 49–80.

Ramette, Ph., and Louis, J. F., 1984, "Analytical Study of the Thermal and Fluid Mechanical Evolution of a Cooling Film Injected From a Single Line of Inclined Round Holes," *Int. J. of Turbo. and Jet-Engines*, Vol. I (1).

Sieverding, C. H., 1988, "Recent Progress in the Understanding of Basic Aspects of Secondary Flows in Turbine Blade Passage," ASME *Journal of Engineering for Gas Turbines and Power*, Vol. 107, No. 2.

Sieverding, C. H., and Wilputt, Ph., 1981, "Influence of Mach Number and End Wall Cooling on Secondary Flows in a Straight Nozzle Cascade," ASME *Journal of Engineering for Power*, Vol. 103, pp. 257–264.

Sunyach, M., 1971, "Contribution à l'étude des frontières d'écoulements turbulents libres," Thèse de Doctorat-ès-Sciences, Université Claude Bernard de Lyon, France.

Downloaded 01 Jun 2010 to 171.66.16.66. Redistribution subject to ASME license or copyright; see http://www.asme.org/terms/Terms_Use.cfm

Experimental Determination of Stator Endwall Heat Transfer

R. J. Boyle

L. M. Russell

NASA Lewis Research Center,
Cleveland, OH 44135

Local Stanton numbers were experimentally determined for the endwall surface of a turbine vane passage. A six-vane linear cascade having vanes with an axial chord of 13.81 cm was used. Results were obtained for Reynolds numbers based on inlet velocity and axial chord between 73,000 and 495,000. The test section was connected to a low-pressure exhaust system. Ambient air was drawn into the test section; inlet velocity was controlled up to a maximum of 59.4 m/s. The effect of the inlet boundary layer thickness on the endwall heat transfer was determined for a range of test section flow rates. The liquid crystal measurement technique was used to measure heat transfer. Endwall heat transfer was determined by applying electrical power to a foil heater attached to the cascade endwall. The temperature at which the liquid crystal exhibited a specific color was known from a calibration test. Lines showing this specific color were isotherms, and because of uniform heat generation they were also lines of nearly constant heat transfer. Endwall static pressures were measured, along with surveys of total pressure and flow angles at the inlet and exit of the cascade.

Introduction

Gas turbine cycle efficiency can be increased by raising the turbine inlet temperature or by decreasing the amount of coolant air.To take either of these approaches without adversely affecting the structural durability of the machine requires an accurate understanding of the heat transfer in the turbine. The endwall heat transfer is significant, especially for low-aspect-ratio turbines, where the endwall area exposed to the hot gases approaches in size the blade surface area. The concern with knowing the endwall heat transfer characteristics extends over the entire range of machine sizes. Large turbines are very sensitive to improvements in efficiency. Smaller turbines have greater exposed area per unit of flow, and endwall coolant requirements result in larger decrements in efficiency.

Several investigators have studied the heat transfer for stator endwalls employing a variety of different measuring techniques. Transient measurements were made using shock tubes by Dunn and Hause (1982), and by Dunn et al. (1986) to measure stator endwall heat transfer on two different stator designs. Isentropic light piston tunnels were used by Brooks et al. (1985) and Georgiou et al. (1979) to measure endwall heat transfer for two additional stators. The transient measurements were done at transonic flow conditions. Steady-state measurements were made by Hippensteele and Russell (1988) and by Blair (1974) using a moderately heated endwall, but again for different stator geometries. York et al. (1984) made steady-state measurements using heated air and cooled walls to simulate engine gas-to-wall temperature ratios for a stator geometry of their design. The data obtained by the different investigators were for a wide range of Reynolds numbers. The Reynolds number based on inlet flow velocity and axial chord varied from less than 100,000 to 500,000. When results from different investigators were compared, it was found that heat transfer distributions varied greatly. For example, the region of maximum heat transfer within the passage varied from near the suction surface to near the pressure surface. While the stators used by the various investigators had about the same amount of flow turning, the vane shapes differed noticeably. The differences among the experiments make it difficult to determine confidently the reasons for the different endwall heat transfer patterns.

To understand better the factors governing endwall heat transfer, a program was undertaken to determine the endwall heat transfer distribution for a turbine stator. Results were obtained for a range of Reynolds numbers, and for three different inlet boundary layers for a single vane geometry. The passage heat transfer distributions were mapped, and detailed measurements were made for the endwall region adjacent to the vane leading edge. The data were obtained in a linear cascade using a liquid crystal measurement technique to determine the endwall heat transfer. In addition to the heat transfer measurements, a number of pressure measurements were made. Endwall static as well as spanwise surveys of total pressure and flow angle were made upstream and downstream of the cascade. The flow rate was controlled to give Reynolds numbers between 73,000 and 495,000, so as to be in the range of Reynolds numbers used by other investigators.

Experimental Facility

Figure 1 shows an overall view of the test facility. The facility consists of a bellmouth, a constant cross-sectional area inlet

Contributed by the International Gas Turbine Institute and presented at the 34th International Gas Turbine and Aeroengine Congress and Exhibition, Toronto, Ontario, Canada, June 4–8, 1989. Manuscript received at ASME Headquarters February 1, 1989. Paper No. 89-GT-219.

Copyright © 1990 by ASME
Downloaded 01 Jun 2010 to 171.66.16.66. Redistribution subject to ASME license or copyright; see http://www.asme.org/terms/Terms_Use.cfm

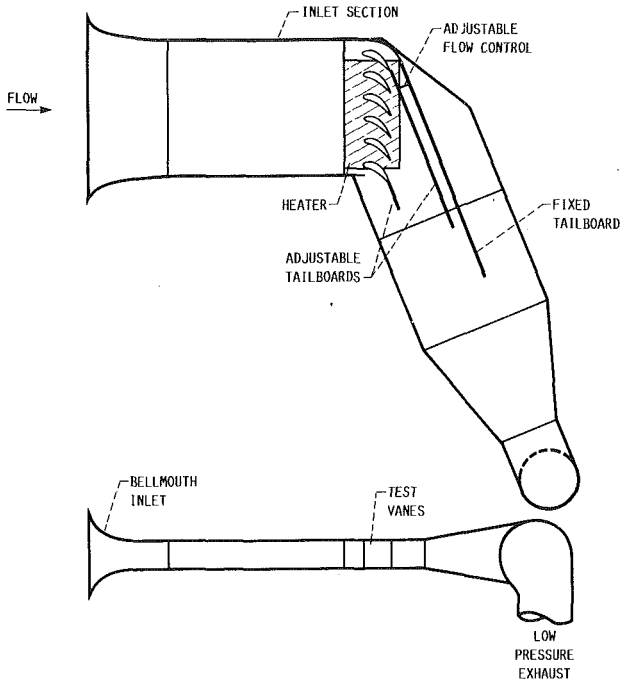

Fig. 1 Test facility

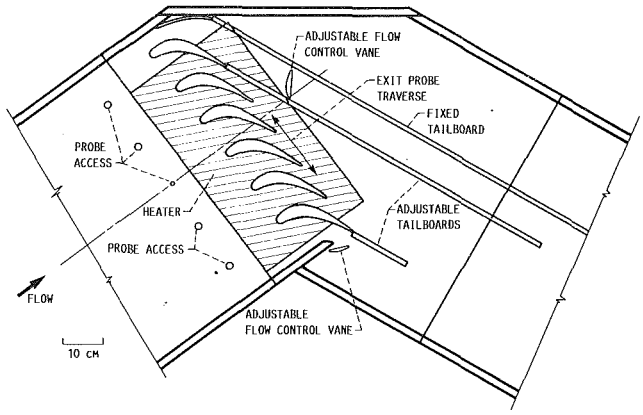

Fig. 2 Endwall heat transfer test configuration

duct, the test section proper with the vanes and heated endwall, and an exhaust section. A series of tests were run for each of three different inlets. In the first series the heated test section was adjacent to the bellmouth inlet. The other two series of tests were done with constant cross-sectional inlet area ducts 0.914 m (3.0 ft), and 1.524 m (5.0 ft) in length between the bellmouth and the heated section. The duct was 15.2 cm (6.0 in.) high and 68.6 cm (27.0 in.) wide. The maximum test velocity in the duct was 59.4 m/s (195 fps).

Figure 2 shows a closeup view of the heated test section. The vanes had an axial chord of 13.81 cm. The ratio of axial to true chord was 0.718. The pitch-to-axial chord ratio was 0.759. The heated area was 30.5 cm (12 in.) long and 51.0 cm (20.1 in.) wide. The heated area began 0.736 axial chords upstream of the test vanes. Three tailboards are shown in Fig. 2. The two tailboards behind the outer vanes were used to obtain periodicity at the exit of each of the passages. Two adjustable flow control vanes are shown in Fig. 2. These two vanes were used to control the flow to ensure upstream periodicity. There were six turbine vanes in the cascade, and the center passage was used as the test passage. Three different lids were used for the test section. One lid had pressure taps, and was used to map the endwall flow field. The second lid was made of clear acrylic, and was used during the heat transfer tests. The third lid had an open area downstream of the cascade, and was used for the exit surveys. During the exit survey tests an actuator table was secured to the top of the lid.

The vane profile shapes were scaled from those used in the heat transfer tests of Blair (1974). The passage flow characteristics of the vanes used by Blair were measured by Bailey (1979). Both of these investigations were done in a single-passage wind tunnel. The vanes used in the present investigation were scaled down from the coordinates given by Bailey. The vanes were made of wood, but the two vanes forming the test passage had brass bases. Cooling passages were formed into the brass bases. This was done to insure that the heat generated underneath the vanes could be removed, so that excessive temperatures underneath the vanes would not damage the liquid crystal sheet. Thermocouples were attached to the bases, and routed out through the top of the vane. No active cooling was necessary, because the fin effect of the base was sufficient to remove the heat generated underneath the vane. After the tests were completed some deterioration of the liquid sheet was noted underneath the all-wood guard vanes.

Nomenclature

A = area
C_p = specific heat
c = chord
c^* = critical velocity
D = diameter of vane leading edge or of cylinder
d = distance in front of vane or of cylinder
F = ratio of heat transfer with vane to that without vane
h = heat transfer coefficient
I = electrical current
K = acceleration parameter = $\nu/V^2 dV/dn$
k = thermal conductivity
L = pressure loss coefficient = $(P'_{in} - P'_{out})/Q_{out}$
l = length of inlet section
M^* = dimensionless speed = V/c^*
n = normal distance
P = pressure
Q = dynamic head = $\rho V^2/2$
q = heat flux
R = electrical resistance of foil
Re = Reynolds number
R_g = gas constant
r = recovery factor
St = Stanton number
T = temperature
t = thickness
V = velocity
x = distance from start of heater
Y = pressure coefficient = $(P'_{in} - P)/Q_{in}$
γ = ratio of specific heats
δ = deadband of yellow color
θ = normalized temperature = $(T_{lc} - T_i) / (T_{lc} - T'_g)$
ν = viscosity
ρ = density
σ = Stefan–Boltzmann constant

Subscripts

a = ambient condition
c = conduction
f = heater foil
g = gas
i = insulation
in = cascade inlet
lc = liquid crystal
$loss$ = sum of conduction and radiation losses
M = Mylar cover sheet
m = measured
out = cascade outlet
r = recovery
uc = uncorrected
x = axial
0 = denotes reference position
1 = based on inlet velocity and axial chord
2 = based on inlet velocity and leading edge diameter

Superscripts

$'$ = total conditions

Downloaded 01 Jun 2010 to 171.66.16.66. Redistribution subject to ASME license or copyright; see http://www.asme.org/terms/Terms_Use.cfm

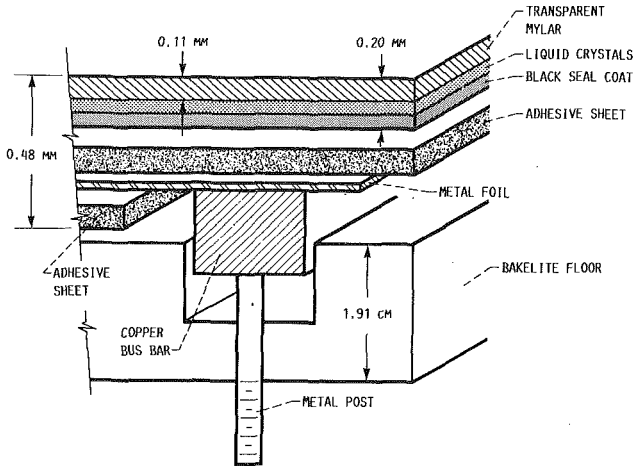

Fig. 3 Heater and liquid crystal sheet assembly

Figure 3 shows the assembly of the liquid crystal/heater composite. A thin sheet of metallic foil, 0.025 mm (1 mil) thick, was electrically heated to provide the heat source. Inconel was used because of its high electrical resistivity and low thermal coefficient of resistivity. The Inconel foil was bonded to copper bus bars. The heat flux was determined from the sheet's resistivity and the electrical current. The voltage drop at the bus bars was measured to assure that there was no significant heat generated at the bus bar–foil junctions. The foil heater was attached to the floor of the test section using double-sided tape. The floor was 1.91 cm thick, and made of Bakelite to minimize heat loss. The composite liquid crystal sheet was attached to the foil heater using double-sided tape. The liquid crystal composite consisted of an opaque seal coat, the sheet of liquid crystal material, and a transparent Mylar outer cover. The thickness of the composite sheet was 0.20 mm, of which 0.11 mm was the Mylar cover sheet. The liquid crystal sheet was the cholesteric type, which changed color with temperature. The highest sensitivity to temperature was obtained at a yellow color. The temperature at which the liquid crystal sheet exhibited this color was 40.9°C (105.6°F). Changes in temperature of ±0.06°C caused the yellow color to disappear. A uniformly spaced grid was inked onto the Mylar surface using black ink.

Instrumentation

The electrical current was measured using the voltage drop across a calibrated shunt. Chromel-constantan (Type E) thermocouples were used to measure inlet gas total temperature, the temperature of the base of the two vanes forming the test passage, and the temperatures on the outer surface of the Bakelite floor.

The top of the inlet section contained access holes into which total pressure probes were inserted. Spanwise traverses were made to insure uniformity of total pressure outside of the endwall boundary layers. The same access holes were subsequently used with drilled plugs to measure static pressures. Having uniformity in the pitchwise direction in static and total pressures resulted in uniform inlet flow.

Endwall static pressures were recorded using a Scanivalve measuring system. Approximately 40 static taps were used to measure the endwall pressure distribution. Boundary layer measurements were made upstream and downstream of the cascade using three-hole total-angle probes. A three-hole probe with a thickness of 0.51 mm (0.020 in.) was used for the boundary layer probe. In order to make accurate pressure surveys over a wide range of flow velocities, parallel measurements were made using transducers with different ranges. The full-range transducers output varied between ±0.6895 and ±34.47 kPa (0.1 to 5.0 psid).

The position of the yellow isotherm was recorded using photographic slides. To obtain full photographic coverage of the passage, as well as both leading edges, photographs were taken with up to three cameras simultaneously. Contour maps of the endwall heat transfer were obtained by plotting the digitized results from a number of different slides. The isotherm was digitized by projecting the slide onto a digitizing tablet. The position on the endwall was determined by digitizing both the yellow line and grid coordinates. In some locations, such as around the leading edge, there were very steep gradients in isotherms. Some photographs did not have good contrast between the grid lines and the background color. The digitizing of these data was more tedious than necessary. In retrospect, it would be better to have inked the grid in a color that contrasted with both the yellow line and with the black background.

All pressure transducer signals, voltage measurements, and thermocouple readings were continuously recorded on a 3-s update cycle. When the photographs were made, a simultaneous record of these signals was also recorded. The photographs were time stamped as part of the recording process.

Analysis of Data

The Stanton number is given by

$$\mathrm{St} = \frac{q_{net}}{(\rho V)_{in} C_p (T_M - T_r)}$$

The heat flux was obtained from

$$q_{net} = \frac{I^2 R}{A_f} - q_{loss}$$

The first term, I^2R/A_f, is the heat flux generated by the electrical power applied to the foil heater. The q_{loss} term represents the corrections to the measured heat transfer due to losses. There were heat losses due to conduction through the Bakelite insulation material, and radiation from the endwall surface. In addition there was a correction to the heat transfer due to the temperature drop across the Mylar cover sheet. The appendix gives a more detailed discussion of the corrections made to the measured heat flux, as well as a discussion of the importance of the individual losses over the range of flow conditions.

In the presentation of the results the recovery factor was taken as 1.0. Therefore, $T_r = T_g'$. When the temperature difference used in the Stanton number definition is the difference between the surface and gas total temperatures, the defined heat transfer coefficient depends on the inlet velocity, and not the local velocity. The effect of a variable recovery temperature on the Stanton number is proportional to the ratio of the temperature difference with the actual recovery temperature, ΔT_1, to the temperature difference with a recovery factor of one, ΔT_2. This ratio is given by

$$\frac{\Delta T_1}{\Delta T_2} = \frac{T_M/T_g' - T_r/T_g'}{T_M/T_g' - 1.0}$$

The ratio T_r/T_g' is given by

$$\frac{T_r}{T_g'} = \frac{T}{T_g'}(1-r) + r$$

The ratio T/T_g' is given by

$$\frac{T}{T_g'} = 1 - \frac{(\gamma-1)}{(\gamma+1)} M^{*2}$$

where $M^* = V/c^*$, and the local velocity can be found from the pressure coefficient Y using the relationship $Y = \rho V^2/$

Downloaded 01 Jun 2010 to 171.66.16.66. Redistribution subject to ASME license or copyright; see http://www.asme.org/terms/Terms_Use.cfm

$\rho_{in}V_{in}^2$. Since the inlet velocities are low, $\rho_{in} = \rho'$. The local density is found from

$$\frac{\rho'}{\rho} \cong 1 + \frac{M^{*2}}{\gamma+1}$$

Since $c^{*2} = 2\gamma R_g T_g'/(\gamma + 1)$, the ratio of the two temperature differences becomes

$$\frac{\Delta T_1}{\Delta T_2} \cong 1 + \frac{(1-r)}{(T_M/T_g' - 1)} \frac{(\gamma-1)}{2\gamma} \frac{YV_{in}^2}{R_g T_g'} \left[1 + \frac{YV_{in}^2}{2\gamma R_g T_g'}\right]$$

The flow is turbulent so that the recovery factor r is 0.89. The second term inside the brackets represents the effect due to compressibility. The two terms were evaluated for the maximum values of Y and V_{in}. The ratio of the two temperature differences was within 15 percent. The actual heat transfer would be less than the presented one by at most this amount. Since the experimental data present a contour plot of the pressure coefficient, the heat transfer results given in this paper can be compared with results using a locally varying recovery temperature, if necessary.

The uncertainty in the Stanton number contours comes from two sources. There is the uncertainty in the individual measurements used to determine the Stanton number, and there is the uncertainty in the position of the Stanton number contour. The uncertainty analysis for the Stanton number measurement is conveniently done for the uncorrected Stanton number. The uncorrected Stanton number is given by

$$\mathrm{St}_{uc} = \frac{I^2 R}{A_f (\rho V)_{in} C_p \Delta T}$$

The temperature difference is $\Delta T = T_{lc} - T_g'$. In terms of measured quantities this becomes

$$\mathrm{St}_{uc} = \frac{I^2 R}{\sqrt{\Delta P \Delta T}} \frac{\sqrt{T/P}}{A_f} \frac{\sqrt{R_g}}{C_p \sqrt{2}}$$

The pressure difference, ΔP, is $P' - P$ at the inlet, and is a single measurement. The absolute quantities T, P, and A can be measured precisely, and do not significantly contribute to the Stanton number uncertainty. For the remaining terms

$$\frac{d\mathrm{St}_{uc}}{\mathrm{St}_{uc}} = \frac{2dI}{I} - \frac{d\Delta P}{2\Delta P} - \frac{d\Delta T}{\Delta T} + \frac{dR}{R}$$

Since the uncertainty is obtained from the square root of the sum of the individual uncertainties squared, for a uniform relative uncertainty, the uncertainty in the electric current I dominates the uncertainty in the Stanton number. Prior to the first of a series of tests, the signal for the current was measured. The zero value was used to adjust each of the heat transfer measurements. In addition, the current signal was integrated over a 10-s interval to average out any high-frequency noise. Based on an analysis of the uncertainty of the individual measurements, the uncertainty in the Stanton number was estimated to be 10 percent or less.

The uncertainty in the location of the Stanton number is largely determined by the gradient of the Stanton number. There is a small, ± 0.06°C, temperature range over which the liquid crystal appears yellow. This temperature range corresponds to a range of Stanton numbers. The variation in the position of the yellow line is given by

$$n - n_0 = \frac{\mathrm{St} - \mathrm{St}_0}{d\mathrm{St}/dn}$$

The subscript uc has been dropped for simplicity. Only T_{lc} is a function of position. At the point n_0

$$\frac{d\mathrm{St}_0}{dn} = \frac{q_{net}}{\rho V_{in} C_p \Delta T_0^2} \frac{dT_0}{dn}$$

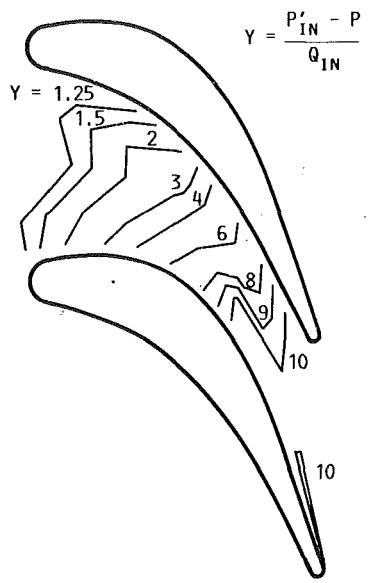

Fig. 4 Endwall pressure coefficients

ΔT_0 is the temperature difference between the liquid crystal sheet and the gas. The variation in position can be expressed in terms of temperatures as

$$n - n_0 = \left(\frac{1}{\Delta T} - \frac{1}{\Delta T_0}\right) \Delta T_0^2 \frac{dn}{dT_0}$$

The uncertainty for the specified (yellow) color is $\delta T = \Delta T - \Delta T_0$ and was estimated to be 0.06°C.

Since $\Delta T_0 dn/dT_0 = \mathrm{St}_0 dn/d\mathrm{St}_0$, the variation in position can be expressed as

$$\frac{n - n_0}{c_x} = \frac{-\sqrt{2}\delta T}{\Delta T} \frac{\mathrm{St}_0}{c_x} \frac{dn}{d\mathrm{St}_0}$$

The $\sqrt{2}$ is included because the reference position, n_0, is also subject to uncertainty. For the test conditions employed, a variation of 10 percent in the Stanton number over a normal distance equal to 10 percent of axial chord results in an uncertainty in position of less than 1 percent.

Experimental Results

Flow Measurements. Inlet boundary layer surveys were made when each of the two constant-area ducts were between the bellmouth and the heated section. At the beginning of the heated section the displacement thickness for the short inlet, $l/c_x = 6.4$, was 2.65 mm, and for the longer inlet, $l/c_x = 11$, the displacement thickness was 3.30 mm when the inlet velocity was 15.2 m/s. These values were approximately consistent with calculated values of boundary layer thickness assuming the boundary layer started at the beginning of the constant area duct. Turbulence intensity measurements were made using hot-wire measurements when the shorter of the two inlets was in place. The midspan turbulence intensity was measured to be about 2 percent at a location just upstream of the heated section.

Figure 4 shows a contour plot of the endwall static pressures. This figure shows the pressure coefficient Y contours. Y is defined so that upstream of the vane row Y is approximately 1.0. The contour plot shows that the exit dynamic head is 10 times that of the inlet dynamic head. The results shown are for an inlet velocity of 53 m/s. There was not definite change in the endwall static pressure distribution as the inlet velocity was decreased. Since the dynamic head increases as the velocity

Downloaded 01 Jun 2010 to 171.66.16.66. Redistribution subject to ASME license or copyright; see http://www.asme.org/terms/Terms_Use.cfm

squared, the precision of the measurements was best at the highest velocity.

Heat Transfer Results. The primary heat transfer results consist of Stanton number contour plots over the entire endwall region at different Reynolds numbers for the three different inlet boundary layers. The liquid crystal measurement technique allows for detailed measurement in regions of high heat transfer gradients. The heat transfer in the leading edge region of the vane is discussed in detail. The heat transfer upstream of the vanes is compared with expected results for flow over a flat plate with an unheated starting length.

Overall Endwall Heat Transfer Results. Figures 5, 6, and 7 show lines of constant Stanton numbers for the endwall region for the three different inlet sections. Each figure has results for a range of Reynolds numbers. The Reynolds number is based on the inlet velocity and axial chord. The trends in the data are very similar for the different inlet boundary layers. The difference in the average endwall Stanton number for the different Reynolds numbers is close to what is expected for turbulent flow. For a flat plate the Stanton number varies as the Reynolds number to the -0.2 power. A factor of 6 increase in Reynolds number would decrease the Stanton number for a flat plate by 43 percent. These figures show similar heat transfer near the leading edges for the two vanes that define the test passage.

There is a marked change in the heat transfer pattern with changes in Reynolds number. At low Reynolds numbers the Stanton number contours tend to follow inviscid streamlines, and then deflect toward the suction surface. For low Reynolds numbers the secondary flow from the pressure surface toward the suction surface occurs to a greater degree. Also, the acceleration parameter K becomes more significant at low Reynolds numbers. When variations in density are neglected, the acceleration parameter is given as

$$K \cong \frac{1}{2\mathrm{Re}_1 Y^{3/2}} \frac{dY}{d(n/c_x)}$$

When the acceleration parameter exceeds 3×10^{-6}, the bound-

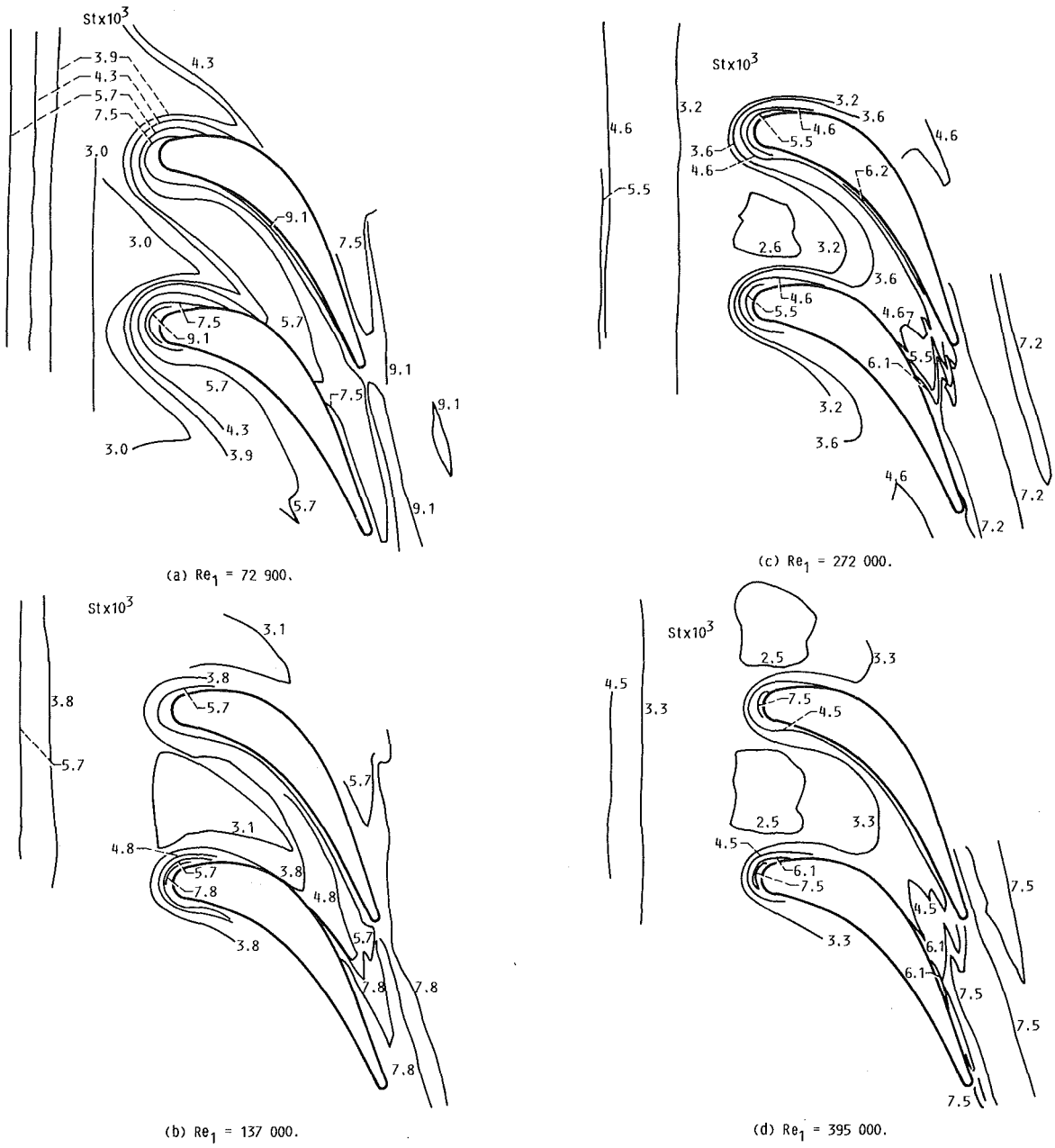

Fig. 5 Endwall Stanton number contours with no inlet section

Downloaded 01 Jun 2010 to 171.66.16.66. Redistribution subject to ASME license or copyright; see http://www.asme.org/terms/Terms_Use.cfm

ary layer relaminarizes, thus lowering the Stanton number. The pressure coefficient Y and its gradient can be determined at different locations within the passage from the data in Fig. 4. For pressure coefficients between 4.0 and 9.0 the term $dY/d(n/c_x)/Y^{3/2}$ has a value of approximately 1.1. Using this value indicates that relaminarization will only occur for Reynolds numbers less than about 165,000. The relaminarization of the endwall flow may be the reason that, at low Reynolds numbers, the Stanton number does not respond to the increased velocity in the throat region to the same extent that it does at high Reynolds numbers. At high Reynolds numbers the acceleration parameter is less, and the Stanton number contours reflect the influence of the free-stream velocity. Consequently, the highest Stanton numbers are in regions of highest free-stream velocity. The Stanton number contours are similar in shape to the pressure contours shown in Fig. 4. The Stanton numbers given in Figs. 5, 6, and 7 are based on an inlet reference velocity. Consequently, changes in Stanton number correspond to changes in heat transfer coefficient. For turbulent flow $h \propto$

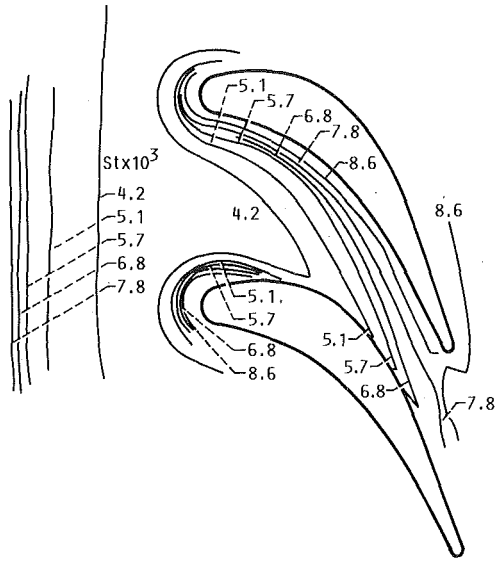

(a) Re_1 = 77 000.

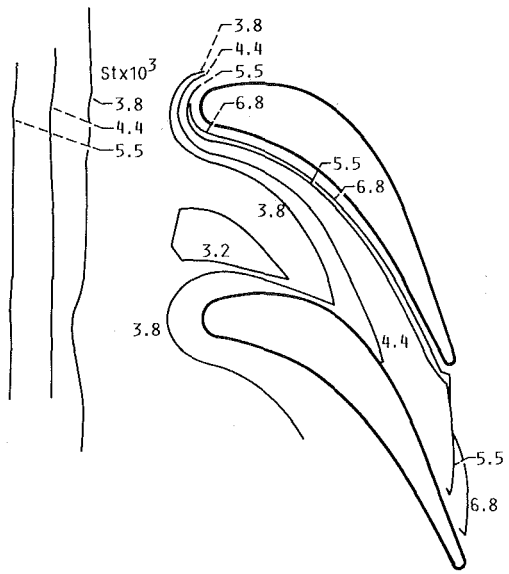

(b) Re_1 = 147 000.

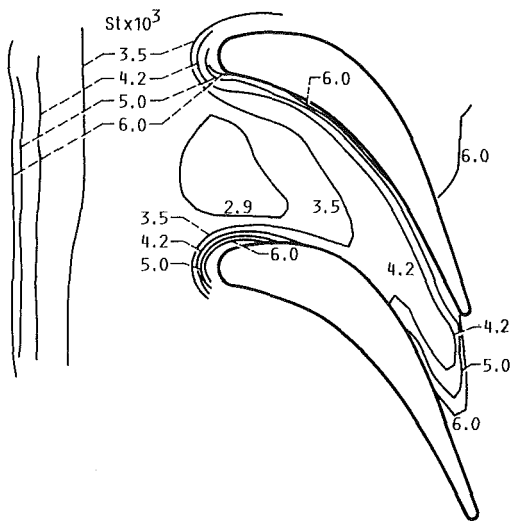

(c) Re_1 = 266 000.

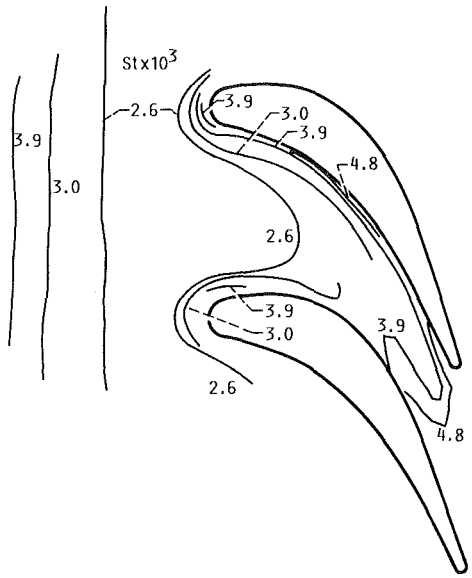

(d) Re_1 = 420 000.

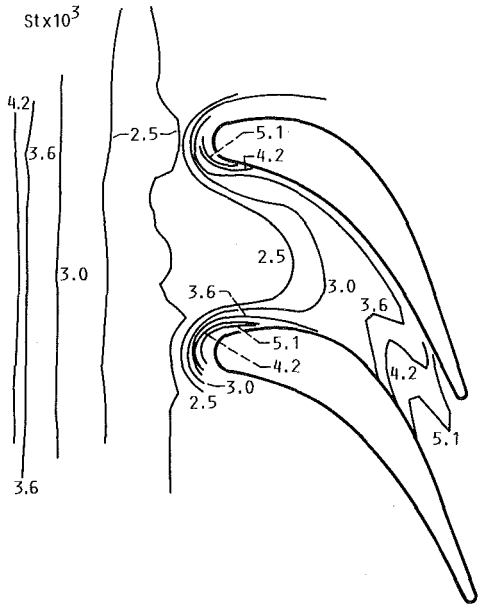

(e) Re_1 = 495 000.

Fig. 6 Endwall Stanton number contours with short inlet

Downloaded 01 Jun 2010 to 171.66.16.66. Redistribution subject to ASME license or copyright; see http://www.asme.org/terms/Terms_Use.cfm

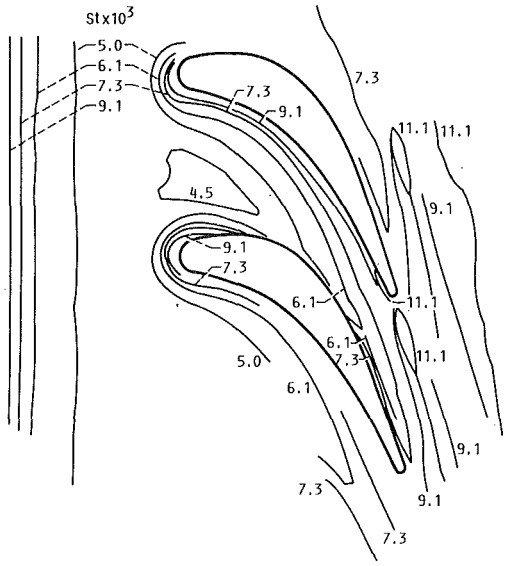

(a) Re_1 = 78 000.

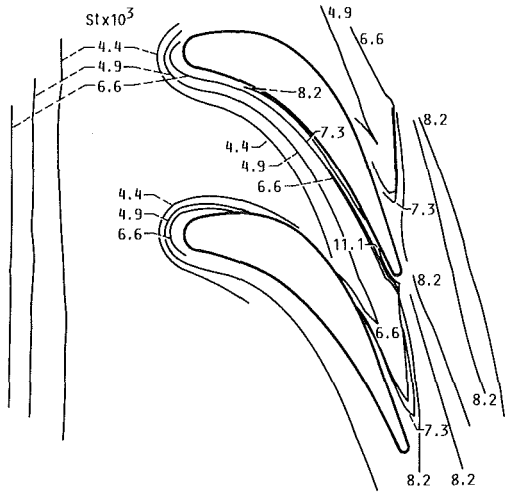

(b) Re_1 = 160 000.

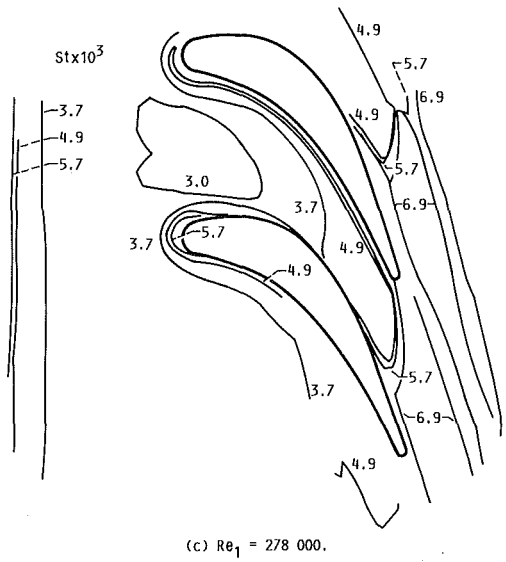

(c) Re_1 = 278 000.

$(\rho V)^{0.8}$. To a first-order approximation $h \propto Y^{0.4}$. At high Reynolds numbers the experimental data show that the ratio of the Stanton number from just upstream of the vane to the local value within the passage correlates reasonably well with the value of $Y^{0.4}$ from Fig. 4.

Leading Edge Region Heat Transfer. Figure 8 shows the endwall heat transfer in the region of the vane leading edge. The augmentation factor F is given as a function of the distance in front of the vane. The augmentation factor is the ratio of the local Stanton number to the local value when there are no vanes. No tests were run without vanes. The denominator used to form the augmentation factor was determined from the experimental heat transfer at the leading edge, but at a pitchwise location midway between the vanes. The results shown in the three parts of Fig. 8 are for the average of the two vanes. To improve spatial resolution near the leading edge one camera's field of view was concentrated in this area. Each part of Fig. 8 is for a different inlet, and each part contains results for different Reynolds numbers. The Reynolds numbers given in the figure are based on the diameter of the vane leading edge circle. The flow conditions are actually the same as for the figures showing the passage Stanton number contours. The augmentation increases as the distance in front of the vane decreases. Figure 9 shows the heat transfer augmentation in front of a cylinder presented by a number of investigators. Hinckel and Nagamatsu (1986) measured heat transfer using

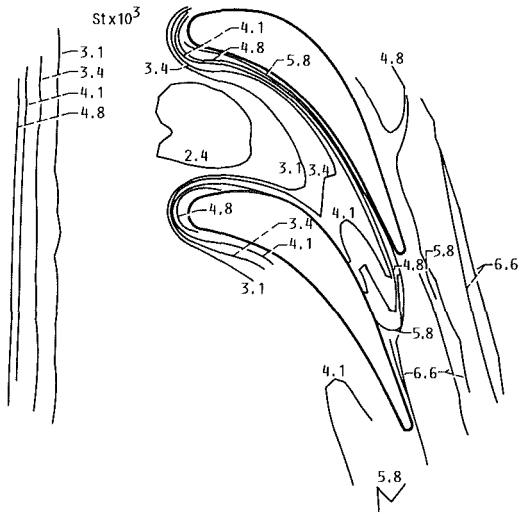

(d) Re_1 = 390 000.

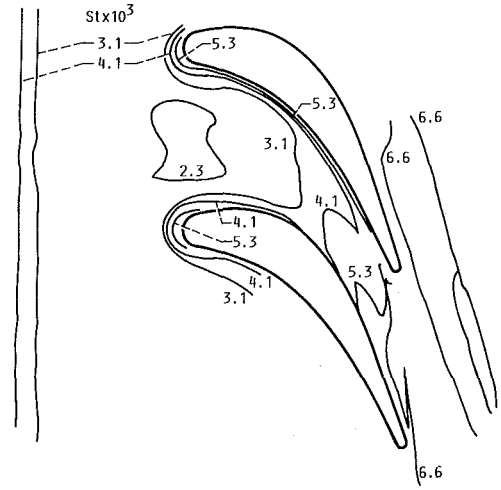

(e) Re_1 = 490 000.

Fig. 7 Endwall Stanton number contours with long inlet

Downloaded 01 Jun 2010 to 171.66.16.66. Redistribution subject to ASME license or copyright; see http://www.asme.org/terms/Terms_Use.cfm

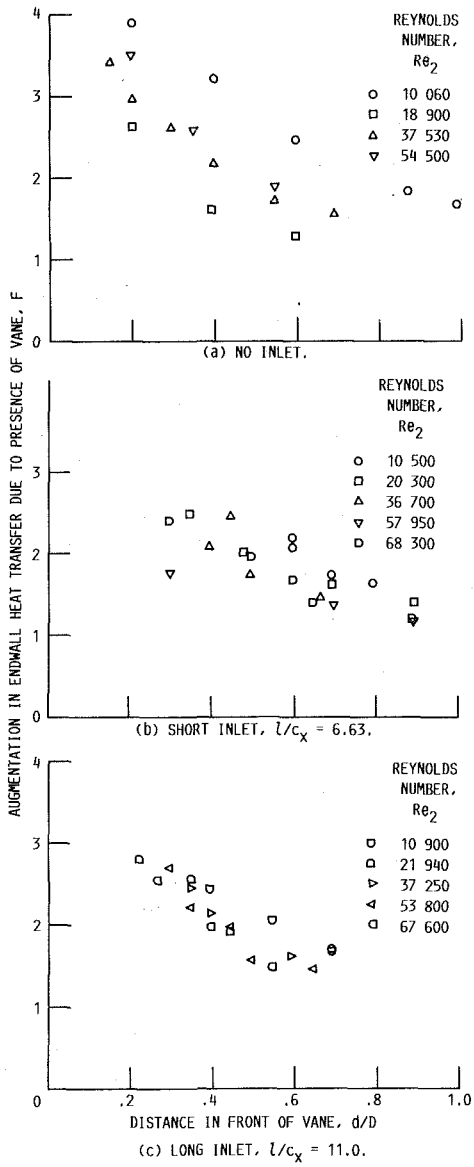

Fig. 8 Heat transfer augmentation in leading edge region

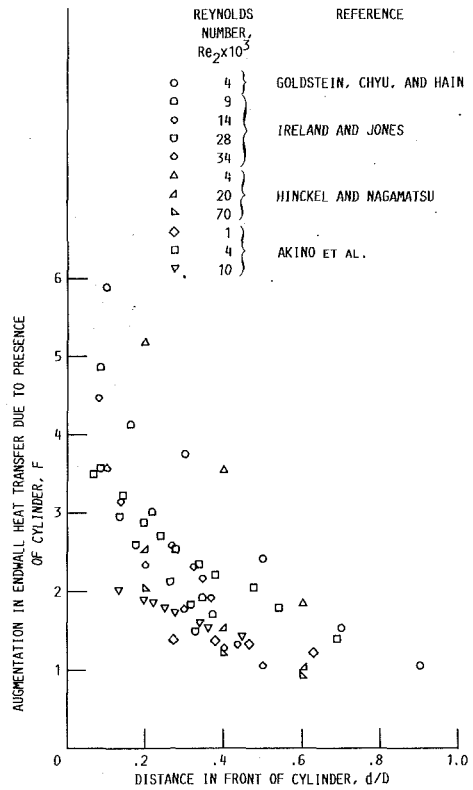

Fig. 9 Endwall heat transfer augmentation due to presence of cylinder; *previous investigations*

a shock tube. Goldstein et al. (1985) used a mass sublimation technique. Both Ireland and Jones (1986) and Akino et al. (1986) used liquid crystal measurement techniques to measure the heat transfer on the endwall in front of a cylinder. The data show considerable variation among the different sources. From a design standpoint it is not clear which results should be used to predict endwall heat transfer near a cylinder. This question also applies to the leading edge region of a turbine vane or rotor blade. The data in Fig. 8 indicate that the condition of the endwall boundary layer may affect the degree of augmentation caused by a cylinder or blade. The data in Fig. 8(*a*) show the highest augmentation for the lowest Reynolds number results. It will be shown that only for the lowest Reynolds number did the flow remain laminar up to the vane leading edge, even with no inlet section. The highest augmentations shown in Fig. 9 are for low Reynolds number cases. This may have been the result of the flow being laminar up to the region of the cylinder. The experimental results for the heat transfer in the leading edge region are in good agreement with the data of Goldstein and Spores (1988). The data of this reference are for heat transfer measurements on the endwall of a rotor configuration. Their data indicate a turbulent boundary layer upstream of the rotor blade. The data of Goldstein and Spores show peak endwall heat transfer augmentation in front of the leading edge to be somewhat in excess of 3.25. The data shown in Fig. 8 show that an extrapolation of the augmentation to a point at the leading edge gives nearly the same augmentation.

Unheated Starting Length. It was expected that the heat transfer upstream of the leading edge would correlate well with the heat transfer for flow over a flat plate with an unheated starting length. Because of the vane blockage it was not known how far upstream of the leading edge the experimental data would diverge from the flat plate correlation. Figure 10 compares the experimental data with the correlation. Figure 10(*a*) is for the case with no inlet (where the bellmouth entrance is adjacent to the heated section). The correlation given in this figure is for laminar flow. Only at the lowest Reynolds number do the data agree with the laminar correlation. At higher flow rates the heat transfer data indicate transition even before the leading edge plane. The boundary layer is turbulent before the heated section is reached.

Figure 10(*b*) shows the results for the two different inlet sections. The inlets are sufficiently long that the flow is turbulent before the heated section is reached. The correlation for the long inlet is only slightly lower than the correlation for the short inlet. Also shown in this figure is the heat transfer prediction using the STAN5 finite difference code of Crawford and Kays (1976). The experimental data were measured along a line midway between the vanes. The experimental data are somewhat higher than the predicted heat transfer. This may be due to conduction loss in the axial direction at the start of the heated section. A two-dimensional conduction analysis was done for the region close to the start of the heated test section. The analysis showed that at a distance of $x/c_x = 0.1$, at a Reynolds number of 76,000, the Stanton number would be reduced 20 percent. This is the result of axial heat flow to the unheated section upstream of the heated section. When the distance from the start of the heated section was increased to

Downloaded 01 Jun 2010 to 171.66.16.66. Redistribution subject to ASME license or copyright; see http://www.asme.org/terms/Terms_Use.cfm

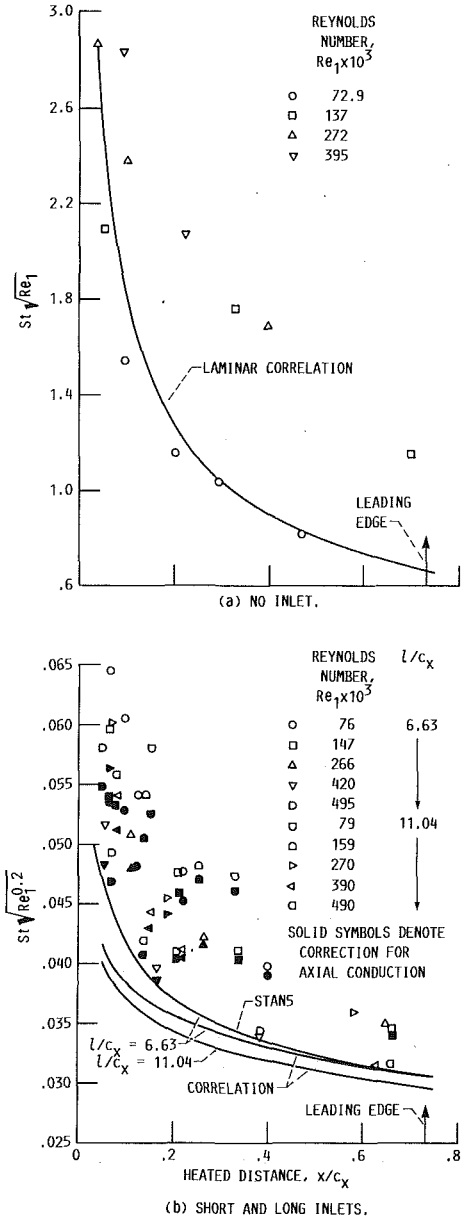

Fig. 10 Endwall heat transfer upstream of the vanes

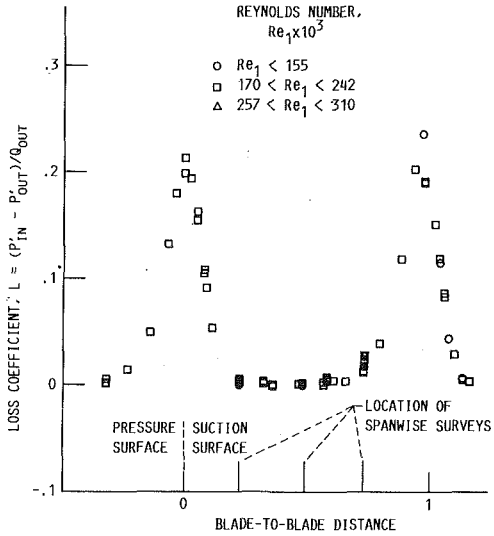

Fig. 11 Pressure loss coefficient at midspan

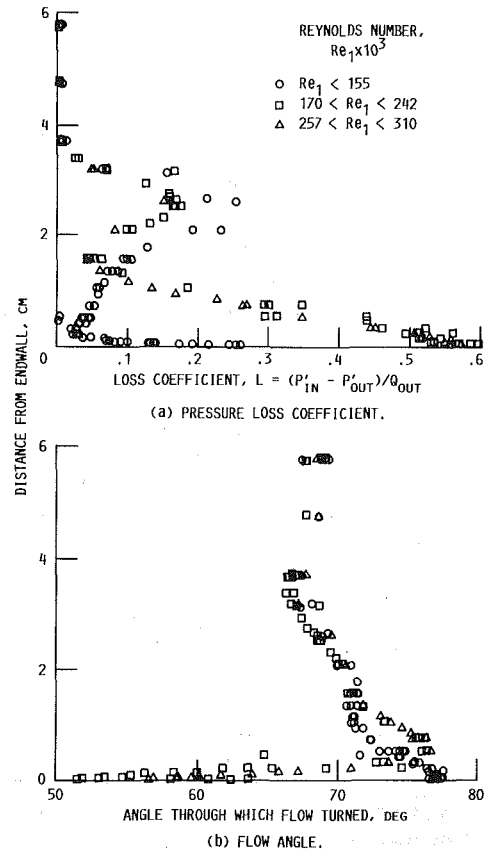

Fig. 12 Spanwise survey results near suction surface

$x/c_x = 0.5$, the Stanton number would be reduced by less than 5 percent as the result of including the effects of axial conduction. As the Reynolds number is increased the effect of axial conduction decreases. At a Reynolds number of 150,000 and $x/c_x = 0.1$ the decrease in Stanton number due to axial conduction was 10 percent. The solid symbols in Fig. 10(*b*) show the Stanton number when the effect of axial conduction is included.

At $x/c_x \approx 0.3$ the experimental data are significantly higher than the predictions at low Reynolds numbers. This is probably the result of underpredicting the heat loss through the Bakelite insulation in the normal direction. The thermocouples on the exterior of the insulation were placed opposite the test passage. The same exterior temperature was used to correct the Stanton numbers upstream of the vane. Effectively this assumed the *same external natural convection heat transfer coefficient*. Since the external geometry was different in this region due to the supporting structure, this was a bad assumption. Calculations were done to determine the correction in Stanton number when the exterior insulation and ambient temperatures were equal. The results showed changes in Stanton number more than enough to account for the differences between the prediction and experimental data. Since both axial and normal conduction are important at low Reynolds numbers, a lower conductivity material would have to be used to reduce heat loss to a negligible level. Just increasing insulation thickness would allow for more axial conduction. Alternatively, a complete map of *the external and upstream boundary temperatures could* be used to account properly for heat losses at low Reynolds numbers. Near the leading edge the experimental and predicted Stanton numbers are in good agreement over a wide range of Reynolds numbers. This indicates that the corrections applied to the measured heat flux were appropriate when the external insulation temperatures were known. As discussed in the ap-

Downloaded 01 Jun 2010 to 171.66.16.66. Redistribution subject to ASME license or copyright; see http://www.asme.org/terms/Terms_Use.cfm

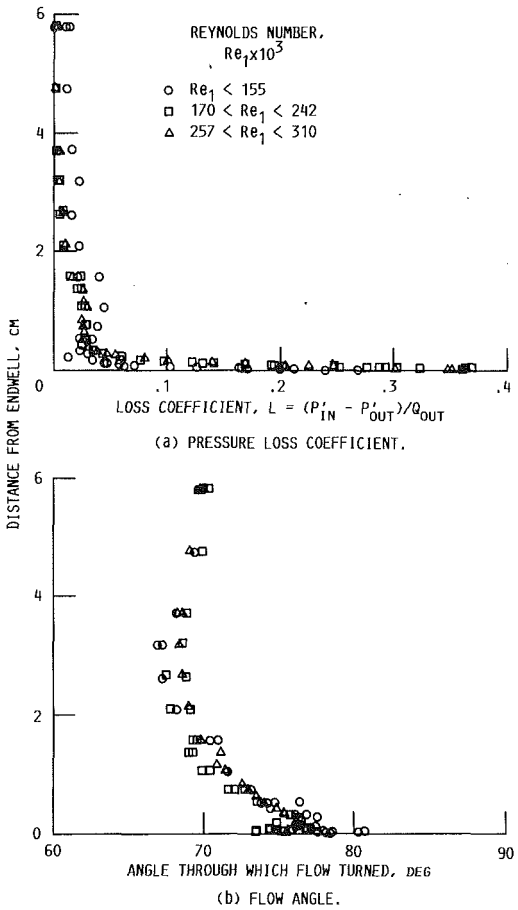

Fig. 13 Spanwise survey results midway between vanes

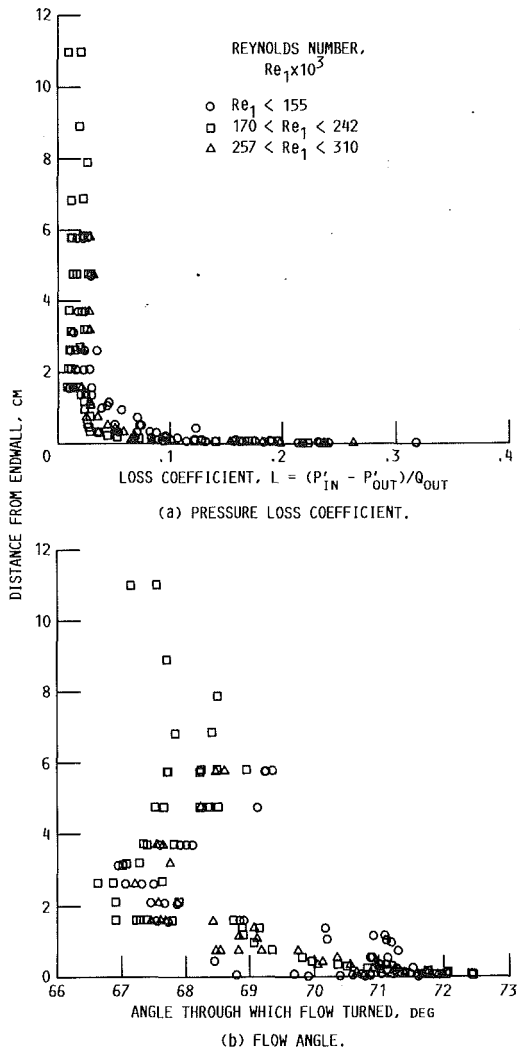

Fig. 14 Spanwise survey results near pressure surface

pendix, the corrections to the heat flux were substantial for some test conditions. At the combination of lowest heat flux and Reynolds number the corrected Stanton number was approximately 20 percent less than the uncorrected value. This was the result of heat loss through the Bakelite insulation and radiation to the surroundings. At the combination of highest heat flux and Reynolds number the corrected Stanton number was approximately 30 percent greater than the uncorrected value. This was primarily caused by temperature drop across the cover sheet used to seal the liquid crystal.

Exit Surveys. Figure 11 shows the results of a pitchwise total pressure survey. The survey was made 0.11 axial chord downstream of the vane trailing edge. This was fairly close to the trailing edge of the vane. This survey was made at midspan, so that endwall effects would be at a minimum. The high total pressure loss wake regions are clearly shown. Between the wakes the loss level is nearly zero. Shown along the abscissa of this figure are three pitchwise locations at which spanwise boundary layer surveys were made.

Figure 12 shows the results of spanwise surveys made downstream of the vane near the suction surface. This is the leftmost location given in Fig. 11. Figure 12(*a*) shows the total pressure loss coefficient as a function of the distance from the endwall, and Fig. 12(*b*) shows the flow angle that was measured simultaneously with the total pressure. Results are given for different Reynolds numbers. While the probe was near the suction surface, it was outside of the midspan wake region. The distributions of loss as well as flow angle were strongly influenced by Reynolds number. Data were taken over a range of Reynolds numbers, and for convenience they have been grouped into three ranges. The data in the lowest Reynolds number range differ markedly from the data in the other two ranges. The two higher Reynolds number ranges show very similar behavior in terms of both loss and flow angle turning. Only in the lowest Reynolds number range is relaminarization of the flow likely to have occurred. For this range of flows the boundary layer adjacent to the wall is thinner, and the flow is overturned toward the suction surface. While the endwall boundary layer is thinner, the loss at 2 cm from the endwall is greater for the lowest Reynolds number range. This loss is associated with the vortices formed within the passage.

Figure 13 shows the same data as Fig. 12, but for a pitchwise location midway between the suction and pressure surfaces. The results show that Reynolds number effect is still present. The effect is much less pronounced, and is primarily evidenced by differences in the flow angle adjacent to the wall. Figure 14 shows the same data as Fig. 12, but for a location near the pressure surface. At this pitchwise location there is no difference among the results for the different Reynolds numbers.

Conclusions

The results of the experimental investigation showed that the heat transfer distribution on the endwall of a turbine stator vane cascade was strongly influenced by the flow through the cascade. At low Reynolds numbers the heat transfer contours are somewhat aligned with the inviscid flow streamlines. At

Downloaded 01 Jun 2010 to 171.66.16.66. Redistribution subject to ASME license or copyright; see http://www.asme.org/terms/Terms_Use.cfm

high Reynolds numbers the heat transfer distributions are significantly different. At high Reynolds numbers the local endwall heat transfer coefficient correlates well with the local freestream velocity.

The pattern of the Stanton number contour lines was noticeably affected by changes in Reynolds number. The pattern of the Stanton number contour lines was not affected by changes in the thickness of the incoming boundary layer. There was a change in the level of the Stanton number with changes in the thickness of this boundary layer. This change was of the same magnitude as would be expected due to the thicker inlet boundary layers. This was expected upstream of the vane leading edge. The same change was seen within the vane passage as well.

Spanwise total pressure loss and flow angle surveys were made at different pitchwise locations. These surveys were done at a distance of 0.11 axial chord behind the vane trailing edge. Near the vane suction surface the spanwise distribution of both loss and flow angle was strongly influenced by Reynolds number. At the midpitch location the Reynolds number effect was still noticeable, but much less pronounced. There was no noticeable Reynolds number effect near the pressure surface. The results of the spanwise surveys indicated that relaminarization of the turbulent endwall boundary layers significantly affected the boundary layer development within the passage. The survey data support the inference that flow relaminarization significantly affects the pattern of the endwall Stanton number contours.

References

Akino, N., Kunugi, T., Ichimiya, K., Mitsushiro, K., and Ueda, M., 1986, "Improved Liquid Crystal Thermometry Excluding Human Color Sensation, Part II—Application to the Determination of Wall Temperature Distributions," in: *Pressure and Temperature Measurements*, ASME HTD-Vol. 58, pp. 57–62.

Bailey, D. A., 1979, "Study of Mean- and Turbulent Velocity Fields in a Large-Scale Turbine-Vane Passage," NASA CR-3067.

Blair, M. F., 1974, "An Experimental Study of Heat Transfer and Film Cooling on Large-Scale Turbine Endwalls," ASME *Journal of Heat Transfer*, Vol. 96, pp. 524–529.

Brooks, A. J., Colbourne, D. E., Wedlake, E. T., Oldfield, M. L. G., Schultz, D. L., Jones, T. V., and Loftus, P. J., 1985, "The Isentropic Light Piston Annular Cascade Facility at RAE Pyestock," in: *Heat Transfer and Cooling in Gas Turbines*, AGARD Pub. No. 390.

Crawford, M. E., and Kays, W. M., 1976, "STAN5—A Program for Numerical Computation of Two-Dimensional Internal and External Boundary Layer Flows," NASA CR 2742.

Dunn, M. G., and Hause, A., 1982, "Measurement of Heat Flux and Pressure in a Turbine Stage," ASME *Journal of Engineering for Power*, Vol. 104, No. 1, pp. 215–223.

Dunn, M. G., Martin, H. L., and Stanek, M. J., 1986, "Heat-Flux and Pressure Measurements and Comparison with Predictions for a Low-Aspect-Ratio Turbine Stage," ASME JOURNAL OF TURBOMACHINERY, Vol. 108, pp. 108–115.

Georgiou, D. P., Godard, M., and Richards, B. E., 1979, "Experimental Study of the Iso-Heat-Transfer-Rate Lines on the End-Wall of a Turbine Cascade," ASME Paper No. 79-GT-20.

Goldstein, R. J., Chyu, M. K., and Hain, R. C., 1985, "Measurement of Local Mass Transfer on a Surface in the Region of the Base of a Protruding Cylinder With a Computer-Controlled Data Acquisition System," *Int. J. Heat Mass Transfer*, Vol. 28, No. 5, pp. 977–985.

Goldstein, R. J., and Spores, R. A., 1988, "Turbulent Transport on the Region Between Adjacent Turbine Blades," ASME *Journal of Heat Transfer*, Vol. 110, No. 4, pp. 862–869.

Hinckel, J. N., and Nagamatsu, H. T., 1986, "Heat Transfer in the Stagnation Region of the Junction of a Circular Cylinder Perpendicular to a Flat Plate," *Int. J. Heat Mass Transfer*, Vol. 29, No. 7, pp. 999–1005.

Hippensteele, S. A., and Russell, L. M., 1988, "High Resolution Liquid Crystal Heat Transfer Measurements on the Endwall of a Turbine Passage With Variations in Reynolds Number," in: *Proceedings of the 1988 National Heat Transfer Conference*, ASME HTD-96, Vol. 3, pp. 443–453.

Ireland, P. T., and Jones, T. V., 1986, "Detailed Measurements of Heat Transfer on and Around a Pedestal in Fully Developed Passage Flow," *Proceedings of the 8th Int. Heat Transfer Conference*, San Francisco, CA, Vol. 3, Hemisphere Pub. Corp., pp. 975–980.

York, R. E., Hylton, L. D., and Mihelc, M. S., 1984, "Experimental Endwall Heat Transfer and Aerodynamics in a Linear Vane Cascade," ASME *Journal of Engineering for Gas Turbines and Power*, Vol. 106, pp. 159–167.

APPENDIX

Corrections to Measured Heat Flux

The measured heat flux is given by

$$q_m = I^2R/A_f$$

The net heat flux is given by

$$q_{nei} = q_m - q_c - q_{rad}$$

The actual heat transfer coefficient is given by

$$h = q_{net}/(T_M - T_r)$$

The conduction through the Mylar cover of the insulation is given by

$$q_M = k_M(T_M - T_{lc})/t_M$$

The heat flux through the Mylar cover sheet equals the net heat flux. Therefore

$$k_M(T_M - T_{lc})/t_M = h(T_M - T_r)$$

The heat flux through the Bakelite insulation material is given by

$$q_c = k_i(T_{lc} - T_i)/t_i$$

The value of T_i was obtained by interpolating the measured temperatures on the outside of the insulation. Since there was a thermal resistance between the insulation and ambient, this temperature was higher than the ambient temperature. The radiant heat flux is given by

$$q_{rad} = \sigma(T_M^4 - T_a^4)$$

While the Mylar cover sheet is transparent to visible light, it is opaque and nonreflective in the infrared region of the test temperatures. The heat balance can be rearranged to give

$$k_M(T_M - T_{lc})/t_M = I^2R/A_f - k_i(T_{lc} - T_i)/t_i - \sigma(T_M^4 - T_a^4)$$

The recovery factor was taken as one, so that $T_r = T_a$. The above equation is then solved to determine the outer temperature of the Mylar cover sheet, T_M. Once T_M is determined the net heat flux can be calculated. The heat transfer coefficient is determined from the net heat flux. The uncorrected heat transfer coefficient h_{uc} is found from

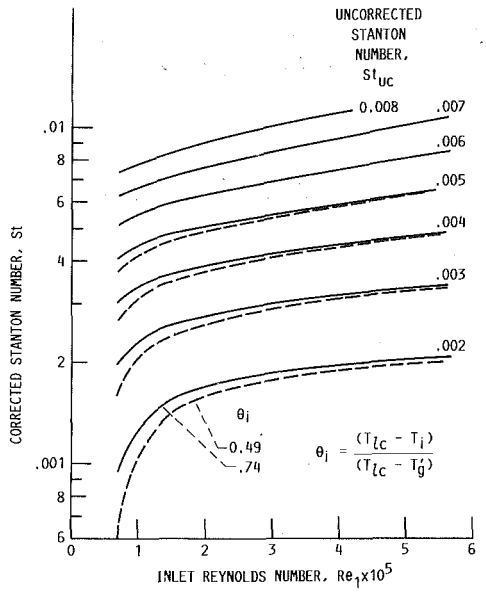

Fig. A1 Comparison of corrected and uncorrected Stanton numbers for test configuration

Downloaded 01 Jun 2010 to 171.66.16.66. Redistribution subject to ASME license or copyright; see http://www.asme.org/terms/Terms_Use.cfm

$$h_{uc} = \frac{I^2R}{A_f(T_{lc} - T_r)}$$

Once the corrected and uncorrected heat transfer coefficients have been determined, the corresponding corrected and uncorrected Stanton numbers can be calculated. Figure A1 shows the corrected Stanton number versus the test Reynolds number for a range of uncorrected Stanton numbers. Data are shown for two values of the normalized outer insulation temperature θ_i. The temperature used to correct the experimental data came from thermocouples on the outside of the insulation. The normalized temperature was within the range of θ values shown on the figure. This figure shows that at the midrange of both the Reynolds number and the uncorrected Stanton number the correction to the Stanton number is small. However, at the combination of low Reynolds number and low Stanton number the correction is substantial, being about 25 percent for the combination of lowest Reynolds and Stanton numbers. At these conditions heat loss through the Bakelite insulation as well as the radiant energy loss dominate the correction. Doubling the thickness of the Bakelite insulation would not halve the conduction loss. As the insulation becomes thicker there would be an increase in thermal conduction within the insulation. Also, at the combination of high Reynolds number and high Stanton number the correction is again substantial, again being about 25 percent. At these conditions the heat flux to the air is very high, and there is a substantial temperature difference across the Mylar cover sheet.

Downloaded 01 Jun 2010 to 171.66.16.66. Redistribution subject to ASME license or copyright; see http://www.asme.org/terms/Terms_Use.cfm

Characteristics of Partial Length Circular Pin Fins As Heat Transfer Augmentors for Airfoil Internal Cooling Passages

S. C. Arora

W. Abdel-Messeh

Structures Analysis, Turbine,
Pratt & Whitney Canada Inc.,
Longueuil, Quebec, Canada

Pin fins are commonly used as heat transfer augmentors for internal cooling of turbine airfoils. These pins may extend from one wall to the other or may be segmented to meet specific requirements of removing the airfoil's varying heat load. Three configurations of the partial pins were tested in a channel with aspect ratio 25:1 and the results are compared with those for the full pins. The array average heat transfer rate decreases linearly with increasing gap and is bounded by the value for full pins at one end and that for the smooth channel at the other. However, the local distribution of the Nusselt number and the average for each of the two walls depends on the configuration of the partial pins. The friction factor was lower for partial pins than for the full pins and also decreased with increasing gap. For the configuration with all partial pins on one wall, the friction factor was found to be the lowest, with no change in the corresponding heat transfer rate from a wall with pins.

Introduction

Modern gas turbine airfoils make extensive use of internal cooling passages augmented with pin fins to remove the excess heat load and maintain the airfoils at desired metal temperatures. These pin fins may extend from one wall to the other, especially in the trailing edge of the airfoil, or they may be segmented (Fig. 1) to meet specific requirements of varying heat load. The complete pins provide structural strength, and may add additional heat transfer surface area, while augmenting the heat transfer rates over those achieved with smooth channel flows. The internally cooled stator airfoils (Fig. 1) usually have an insert, which provides the coolant for impingement at the airfoil leading edge. The flow splits thereafter into two channels around the insert. These channels are augmented with pin fins. Since the pins are normally cast in place and the insert is fitted during assembly, the manufacturing tolerances necessitate that there be some clearance between the pins and the insert wall. This clearance is usually of the order of 15 percent of the total channel height. This, however, is likely to alter the structure of flow in the channel by forcing the flow into the gap, thereby affecting the associated heat transfer rates and the pressure gradient.

Due to the varying external heat load, the cooling requirements of the pressure and suction surfaces could be significantly different. In such applications, the designer must resort to a cooling scheme with discriminating rates of heat pickup to achieve metal temperature uniformity. This is feasible by employing partial length pin fins on the surface where high rates of heat transfer are desired. However, sufficient design information is necessary to optimize the cooling scheme properly. The available information on the pressure drop/heat transfer characteristics of such pin fin geometries is meager in comparison to that for the full pins. Peng (1984) has published some data for geometries with gaps of 20, 50, and 67 percent of the channel height at the center of the pins. Only the array average data for 8, 11, and 16 rows of pins with H/D of 4 and 6 were reported. The results showed that both the array average heat transfer and the pressure drop decreased with increasing gap size. Because of the averaged nature of the data and the large H/D ratio of the pins, these results have only limited use from the design point of view.

Steuber and Metzger (1986) have also reported heat transfer data on partial length pins epoxied to one wall, the other wall being smooth. The gap between the pins and the opposite smooth wall was maintained equal to 1/3, 1/2, and 2/3 of the channel height. In a typical gas turbine airfoil this gap is usually of the order of 15 percent. The axial pitch of the pins was $1.5D$. However, the manufacturing constraints impose a minimum pitch of the order of $2D$. Double-sided partial pins with a gap equal to 2/3 the height of the channel at the center of the pins were also tested. Although this geometry, with no full pins, is not practical, nevertheless the results do provide additional information to the designer. Results showed that from the heat transfer point of view alone, partial length pins were judged to be inferior to the full length pins.

The present study was guided by the requirements for the design optimization of airfoil cooling. The axial (X/D) and lateral (S/D) pitches were maintained at 2.83 and 2.42, respec-

Contributed by the International Gas Turbine Institute and presented at the 34th International Gas Turbine and Aeroengine Congress and Exhibition, Toronto, Ontario, Canada, June 4-8, 1989. Manuscript received at ASME Headquarters January 17, 1989. Paper No. 89-GT-87.

Copyright © 1990 by ASME
Downloaded 01 Jun 2010 to 171.66.16.66. Redistribution subject to ASME license or copyright; see http://www.asme.org/terms/Terms_Use.cfm

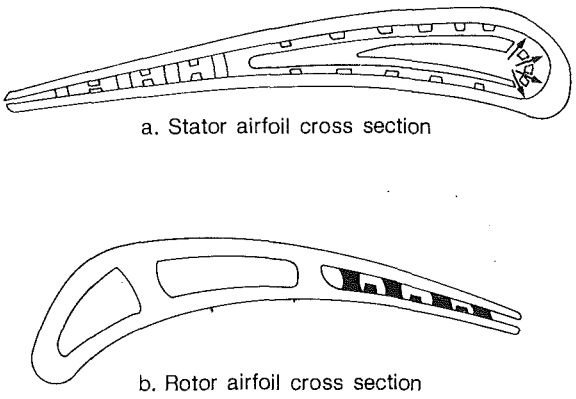

Fig. 1 Pin fin augmented cooling scheme for typical high-pressure turbine airfoils

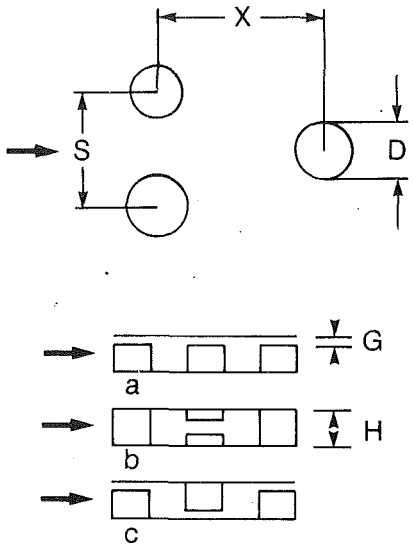

Fig. 2 Pin fin array nomenclature

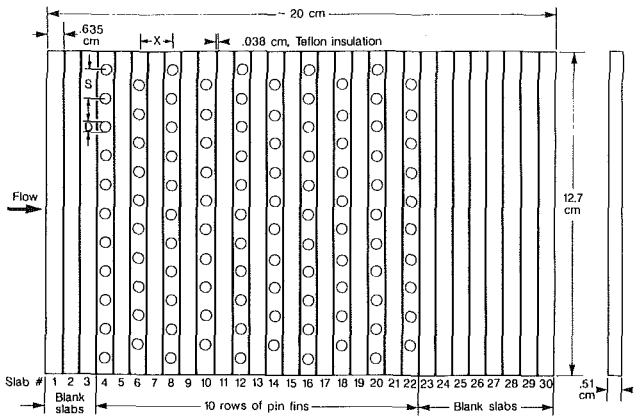

Fig. 3 Test section geometric setup

tively. The H/D ratio was 1.07. The gap ratio (G/H) for the single sided pins (Fig. 2*a*) was 15 percent of the channel height. For comparison, the same gap was maintained for the other two configurations (Figs. 2*b* and 2*c*). To evaluate the relative effect of the partial pin lengths, the corresponding full pin data were taken from the previous work reported by the authors (Arora and Abdel-Messeh, 1983). The overall performance of the array may also be influenced by the ratio of the pin to the total heat transfer surface area. Therefore it was decided to test three additional geometries of partial pins with $G/H = 0.47$, having total surface area equal to the case for the full pins. The heat transfer surface area equality with the full pins was achieved by varying the height of the partial length pins. Thus heat transfer and pressure drop data for six partial length pins and one full length pin are reported in this paper. These geometries are considered to be practical from the design point of view and the resulting data attempt to fill in the void in the existing literature.

In the present study, the local row-by-row heat transfer data were obtained for ten rows of pins mounted in a channel with aspect ratio 25:1 (Fig. 3). Because of the staggered arrangement of pins, the even numbered rows had one less pin than the odd numbered rows.

Experimental Details

A schematic layout of the test rig used for this study is shown in Fig. 4. The details of the apparatus and the test procedure have previously been described by Arora and Abdel-Messeh (1985) and therefore only a brief review is given here for completeness. Compressed air is fed to the test section through a plenum chamber (10.16×30.48 cm) to settle the flow and an entrance duct of over 50 hydraulic diameters length to provide a fully developed velocity profile at inlet to the test section. After the test section air passes through a smooth channel of over 16 hydraulic diameters length to avoid any "exit effects," followed by a mixing chamber where its bulk average temperature is measured.

Nomenclature

A = heat transfer surface area
Ac = channel cross-sectional area
Cp = specific heat of air
D = pin diameter
Dh = hydraulic diameter of the smooth channel
fr = friction factor = $\dfrac{dP}{dx}\dfrac{D}{\rho 2 V_{\max}^2}$
G = gap (clearance) between the endwall and the partial length pins
H = channel height
h = heat transfer coefficient
K = thermal conductivity of air
$\dot{m}$ = mass flow rate
Nu = Nusselt number = $\dfrac{hD}{K}$ or $\dfrac{hDh}{K}$
P = pressure
Pr = Prandtl number of air
$\dot{q}$ = heat flow rate
Re = Reynolds number = $\dfrac{\rho V_{\max} D}{\mu}$; $\mathrm{Re}_{Dh} = \dfrac{\dot{m} Dh}{Ac\mu}$
S = pin spacing in the spanwise direction
T = temperature
$V_{\max}$ = average streamwise velocity at the minimum flow area
X = pin spacing in the streamwise direction
x = axial coordinate
μ = fluid dynamic viscosity
ρ = fluid density
$\bar{}$ = indicates average quantity

Subscripts

b = bulk average; base case with full pins
f = film
m = mixing chamber
P = pin
s = surface
t = total

Downloaded 01 Jun 2010 to 171.66.16.66. Redistribution subject to ASME license or copyright; see http://www.asme.org/terms/Terms_Use.cfm

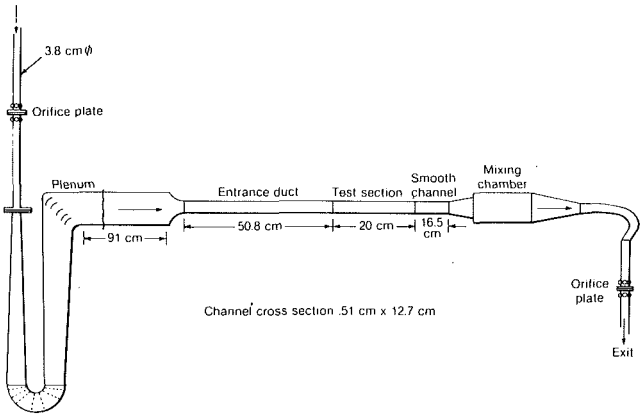

Fig. 4 Schematic layout of the test rig

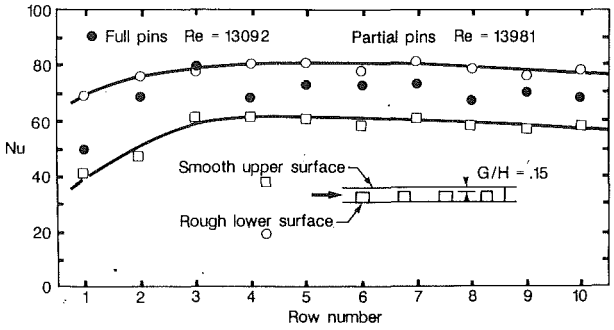

Fig. 5 Distribution of local Nusselt numbers with all pins on one wall

The top and bottom walls of the test section consisted of 30 copper slabs (Fig. 3), of which only 29 were fully instrumented. Each copper slab had two copper-constantan thermocouples to monitor its temperature during testing. A 0.318-cm square cartridge heater located at the back of each slab was used as a heat source.

The top and bottom walls were maintained at a constant channel height of 0.51 cm by two units of spacers (one for each side), which also formed the side walls of the test section. Thirty static pressure holes of 0.12 cm diameter were drilled through both spacer side wall units. In addition eight pressure taps were mounted in the entrance duct to measure the pressure distribution. The heater and thermocouple leads passed through the spacers and were then connected to multipin connectors for quick assembly and disassembly of the test section.

Copper pins ($D=0.476$ cm) were epoxied to the endwall slabs at desired locations using the technique first proposed by Arora and Abdel-Messeh (1983). The technique involves the use of a thin layer of silver-based highly conductive epoxy to bond the pins to the endwall. Ten units of copper slabs were mounted with pins to provide 10 rows of pin fins. A smooth (blank) slab was provided between two successive rows of pins to achieve the desired axial pitch. Also, no pins were mounted on the first three and the last seven slabs to avoid any end effects.

The heat transfer tests were carried out at steady state by maintaining endwalls at a constant surface temperature (~71°C). This was achieved by varying the power input to the heaters. The isothermal condition of endwall segments 1 to 29 was generally maintained to within ±0.3°C; however, the temperature of the two adjoining slabs was maintained to within ±0.14°C. The variation in the two thermocouples in each slab was also within this range (±0.14°C).

The heat transfer coefficient h for top and bottom copper slabs with or without pins was obtained from the power supplied ($\dot{q}$) to the respective heater corrected for conduction losses from the back ends of the segments and for intersegment conduction across the teflon insulation. The intersegment losses were calculated for each test run and were generally small. The back losses for each slab were measured experimentally with no flow through the test section. These losses varied from about 2 to 10 percent of the power input depending on the Reynolds number. Then using the temperature difference between the segment surface, T_s, and the air flowing over as the driving potential, the heat transfer coefficients were calculated as

$$h=\frac{\dot{q}}{A(T_s-T_b)} \tag{1}$$

The heat transfer area A for all experiments was the actual copper surface area (pin + endwall) exposed to the flow. The local bulk average temperature T_b, as a function of streamwise endwall segment position, was determined in the present experiment from an energy balance. The air temperature measured in the mixing chamber (T_{bm}) was taken as the bulk average temperature at the end of slab No. 29. Working toward the upstream end of the test section, the bulk temperature for use with the ith segment is calculated as

$$T_{bi}=T_{bm}-\frac{\dot{q}_i}{2\dot{m}Cp}-\begin{cases}\sum_{j=i+1}^{29}\dot{q}_j/\dot{m}Cp & \text{for } j\le 29\\ 0\end{cases} \tag{2}$$

The q_i and q_j include the total heat input to both the top and bottom slabs up to the ith and jth location, respectively. The calculated air temperature at the inlet to the rig using this procedure differed from the measured temperature by less than 1.5 percent.

The friction factor for the pin arrays was estimated as

$$fr=\frac{dp}{dx}\frac{D}{2\rho V_{\max}^2} \tag{3}$$

where dp/dx is the pressure gradient through the pin fin array. The pressure drop across the array normalized by the number of pin rows has been used by other researchers to compute the friction factors. However, such a definition does not take into consideration the length of the test section over which the given number of pin rows are located (i.e., the axial pitch of the array).

All relevant properties (k, ρ, μ, C_P) were evaluated at the film temperature (T_f), defined as

$$T_f=\frac{T_s+T_b}{2} \tag{4}$$

The experimental uncertainty was estimated, using the method of Kline and McClintock (1953), to be ±4.5 percent on friction factor and ±5 percent on the heat transfer coefficients.

Results and Discussion

The local row-by-row distributions of the heat transfer coefficients in terms of the Nusselt number (Nu) for the configuration with all pins epoxied to one wall and the other wall being smooth are shown in Fig. 5. The data are plotted for only one value of clearance gap ($G/H=0.15$) and for a Reynolds number (Re) of 13,981. The data for different Reynolds numbers and for the other values of the gap showed a similar pattern and therefore are not reported here. The row-by-row distribution of the Nusselt number for both walls is generally similar to that for the case with full pins; however the magnitude for the smooth wall is lower. Except for the first

Downloaded 01 Jun 2010 to 171.66.16.66. Redistribution subject to ASME license or copyright; see http://www.asme.org/terms/Terms_Use.cfm

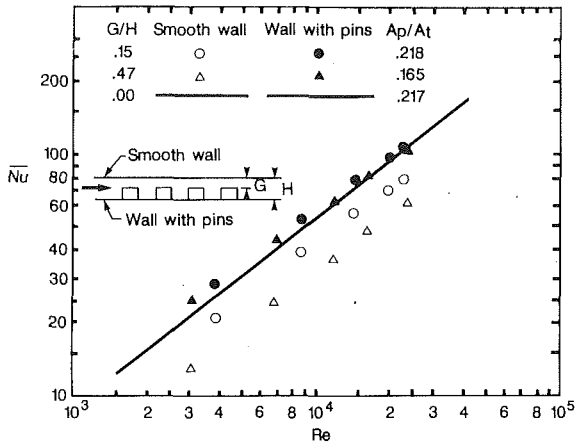

Fig. 6 Nu versus Re for the geometry with all pins on one wall

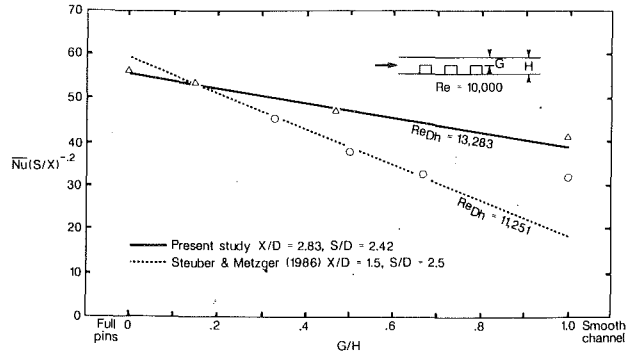

Fig. 7 Effect of the clearance on Nusselt numbers for all pins on one wall

row, the Nusselt number for the wall with partial length pins is comparable to that for the full pins; however for the smooth wall, it is much lower. Although the local Nusselt number for the partial pins is slightly higher than for the full pins, about 4 percent of this difference is due to the variations in the respective Reynolds numbers. The rest could be attributed to the experimental uncertainties in the two data sets. Thus, the local Nusselt numbers for the wall with the partial pins can be taken to be equal to that for the channel with full pins.

Sparrow and Ramsey (1979) reported that the heat transfer coefficients from the surface of partial length pin increases with increasing pin height. No data on the heat transfer from the endwall with pins or the opposite smooth wall were reported. The results of the present study show that the heat transfer rate from the endwall with pins (pins + endwalls) remains independent of the pin height. This implies that the contribution of the endwall to the heat transfer must be decreasing with the increasing pin height.

Steuber and Metzger (1986) also obtained the row-by-row local heat transfer data for a similar pin fin geometry with $X/D = 1.5$ and $S/D = 2.5$ and for clearances of 33, 50, and 66 percent of the channel height. The distribution of the local Nusselt number was presented for only two values of clearance (33 and 50 percent) and for $\mathrm{Re} = 10{,}000$. Their heat transfer data for the wall with the partial pins (epoxied to the upper wall) did not show any increase over the first three to five rows. In contrast the Nusselt number on the opposite wall (with no pins) decreased like the entry flow in a smooth duct. After the third row, the heat transfer rate on the smooth wall starts to increase as the effect of the turbulence generated by the pins on the opposite wall propagates to the wall with no pins. The turbulence generated by the pin fins should, however, first affect the rate of heat transfer from the pins and the wall to which the pins are epoxied. Its effect should eventually propagate to the opposite wall. The results of Steuber and Metzger (1986) show a trend contrary to this hypothesis; however, the present study shows physically consistent behavior.

This particular array geometry has a specific application in estimating the rate of heat transfer to the coolant from the hot gas through the wall with pins. A part of this heat is transferred to the incoming coolant through the smooth wall of the insert. Because of such a design application, the array average data were obtained separately for both walls. These array-averaged Nusselt numbers are shown in Fig. 6. Results show that the heat transfer rate from the wall with the pins is not affected by the height of the partial pins (for the range investigated here) and can be taken to be equal to the case for the full pins. However, the heat transfer rate from the smooth wall is dependent on the height of the partial pins on the opposite wall and decreases with increasing gap size.

The total heat transfer surface area (A_t) of the array with a clearance of 47 percent of the total channel height is the same as for the full pin array. However, the ratio of the pin surface area (A_p) to the total area (A_t) is different. The array with a clearance of only 15 percent has the same A_p to A_t ratio as the full pin, but the total heat transfer area is about 7 percent greater than for the full pin geometry. These differences do not appear to be significant from the heat transfer point of view. The normalized clearance (G/H), on the other hand, seems to be a more dominant factor.

To establish the effect of the clearance on the overall heat transfer for the channel (including both the walls and the pin surface), the averaged Nusselt numbers were computed. These are shown in Fig. 7 for one value of the Reynolds number ($\mathrm{Re} = 10{,}000$). The data from the work of Steuber and Metzger (1986) are also shown in the figure. The value of $G/H = 0$ indicates the case of full pins and that of $G/H = 1.0$ is for the smooth channel. The smooth channel Nusselt number was estimated from the relationship

$$\overline{\mathrm{Nu}} = 0.023\ \mathrm{Re}_{Dh}^{0.8}\ \mathrm{Pr}^{0.4} \tag{5}$$

This equation utilizes the Reynolds number based on the channel cross section and the hydraulic diameter. Therefore, the Reynolds number of 10,000 for the pin array was corrected to 13,283 (Re_{Dh}) for the present study and to 11,251 for the work of Steuber and Metzger for the same mass flow rate as for the full pin fins.

The data obtained in the present study are for a pin array configuration different from that reported by Steuber and Metzger. Therefore, to facilitate the comparison of the two data sets, the array-averaged Nusselt numbers were multiplied by a factor $(S/X)^{-0.2}$. This is based on the correlation proposed by Zukauskas (1972) for arrays of large cylinders, i.e.,

$$\overline{\mathrm{Nu}} = 0.35\ (S/X)^{0.2}\ \mathrm{Re}^{0.6}\ \mathrm{Pr}^{0.36} \tag{6}$$

The Nusselt numbers for the smooth channels were also multiplied by the respective $(S/X)^{-0.2}$ values of the two configurations. It is assumed that the S/X dependence of large cylinders will also be applicable to the pin fins of length-to-diameter ratio of unity. The function $\overline{\mathrm{Nu}}\,(S/X)^{-0.2}$ decreases linearly with increasing clearance. The rate of decrease is much higher for the array configuration with $S/D = 1.5$ than for the array with $S/D = 2.42$. Since the two curves shown in Fig. 8 for two different array configurations have different slopes, the function $(S/X)^{-0.2}$ proposed by Zukauskas (1972) may not be truly applicable to the configurations considered here.

The data from the present study show a linearly decreasing effect with increasing clearance right up to the smooth chan-

Downloaded 01 Jun 2010 to 171.66.16.66. Redistribution subject to ASME license or copyright; see http://www.asme.org/terms/Terms_Use.cfm

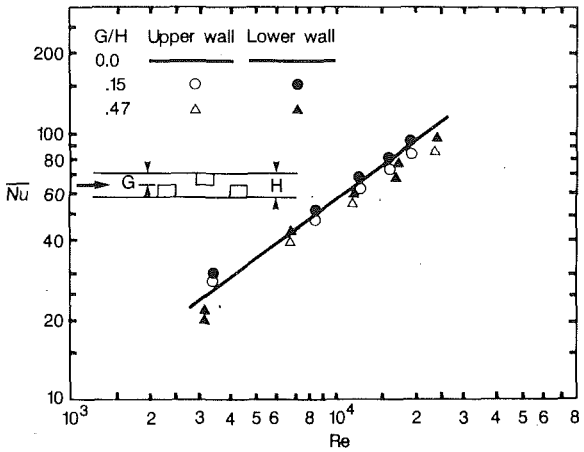

Fig. 8 Nu versus Re for staggered partial length pins

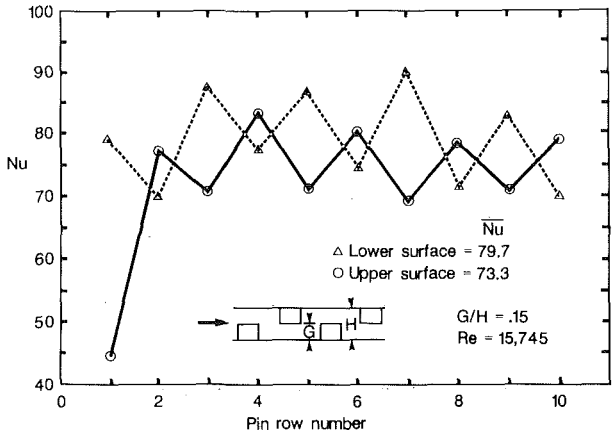

Fig. 9 Row-by-Row distribution of Nu for staggered partial length pins

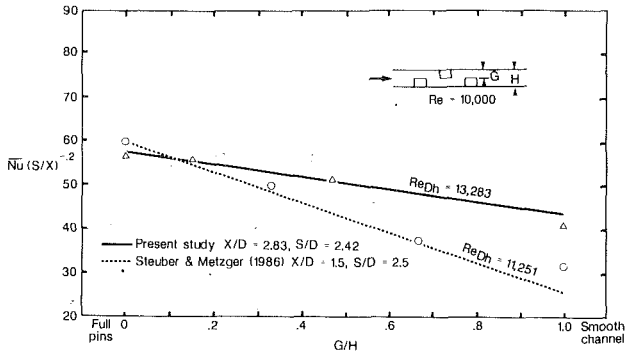

Fig. 10 Averaged Nusselt numbers as a function of clearance for staggered pins

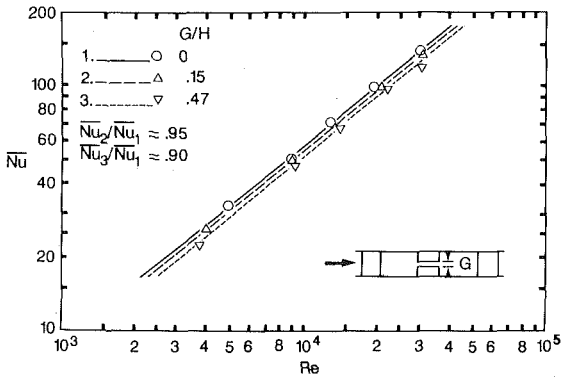

Fig. 11 Average Nusselt numbers for alternate rows segmented at the center

nel, whereas the data reported by Steuber and Metzger (1986) show that the average heat transfer rate from the partial pins of length equal to 33 percent of the channel height yield the same Nusselt number as the smooth channel. Since the pins with 33 percent of the channel height are definitely longer than the viscous sublayer thickness, the presence of these partial length pins would be expected to result in some augmentation in the heat transfer. The data of Steuber and Metzger tend, however, to contradict this reasoning.

The distribution of the array-averaged Nusselt numbers of the configuration with rows of partial pins epoxied alternatively to the bottom and top walls are shown in Fig. 8. The partial length pin fins of the first row are all epoxied to the bottom wall, whereas those of the second row are epoxied to the top wall. This is repeated for all subsequent rows of pin fins. The data in Fig. 8 are plotted separately for the top and bottom walls. The results show that the average Nusselt number for each wall decreased with decreasing pin fin height (i.e., with increasing G/H). However, the bottom wall, which has the first row of pin fins and one more pin per row than the top wall, experiences a higher rate of heat transfer than the opposite wall. This difference was of the order of 10–15 percent. Furthermore, the heat transfer coefficients for the bottom wall (with the first row of partial length pins) with $G/H=0.15$ were comparable to the case with $G/H=0$. The row-by-row distribution of the Nusselt number at $\mathrm{Re}=15{,}745$ and $G/H=0.15$ is shown in Fig. 9. The data at the other values of G/H and Reynolds numbers were similar in nature. The experimental data points are connected by lines for visual simplicity. The local Nusselt number oscillates as the flow moves through the row of partial length pins epoxied alternatively to the two walls.

The distribution of the overall array average Nusselt numbers (for both the walls) as $\overline{\mathrm{Nu}}(S/X)^{-0.2}$ for this geometry is shown in Fig. 10 as a function of the clearance (G/H). Also shown are the data taken from the work reported by Steuber and Metzger (1986). Both the data sets show that the $\overline{\mathrm{Nu}}\ (S/X)^{-0.2}$ decreases linearly with increasing clearance and is bounded by the value for full pins at one end and the smooth channel flow at the other. This suggests that the array-averaged Nusselt number for any clearance can then be interpolated from the value for the full pin fins and that for the smooth channel. The slopes of the two curves for different array geometry are, however, different, implying that the function $(S/X)^{-0.2}$ may not fully account for the effect of the array configuration for these pin fins. The full pin array with higher density of pins ($S/D=1.5$) having high Nusselt number shows higher rate of decrease with the increasing clearance (G/H) than the array with lower density of pins ($S/D=2.42$).

Figure 11 shows the array-averaged Nusselt number for the geometry where the pin fins in every second row were cut at the center. Unlike the other cases of partial pin fins, this geometry is symmetric. Therefore, the average data for the two walls were equal. Similarly, the row-by-row variations of the local data were also equal for both walls and are similar to that for the full pin fins. However, the magnitude of the Nusselt number decreases with increasing clearance. This decrease in the Nusselt number is about 5 percent for $G/H=0.15$ and 10 percent for $G/H=0.47$. The $\overline{\mathrm{Nu}}\ (S/X)^{-0.2}$ function for this geometry also showed a linear dependence on the G/H ratio. The bounding values were, as for the other geometries, the full pin array and the smooth channel. No data were available for comparison in the literature for this particular geometry of the partial length pins.

Downloaded 01 Jun 2010 to 171.66.16.66. Redistribution subject to ASME license or copyright; see http://www.asme.org/terms/Terms_Use.cfm

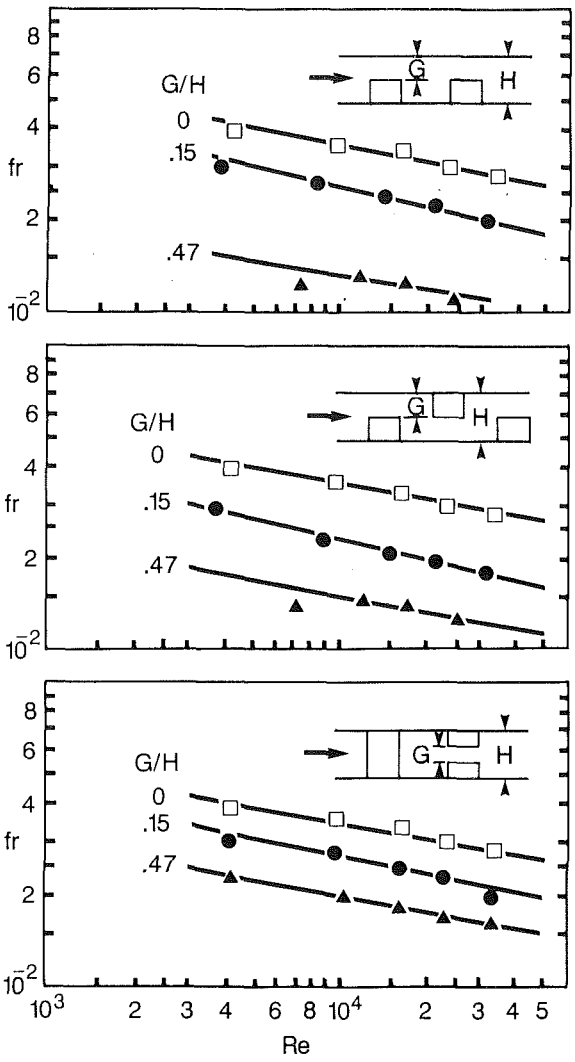

Fig. 12 Friction factor characteristics of partial length pin fins

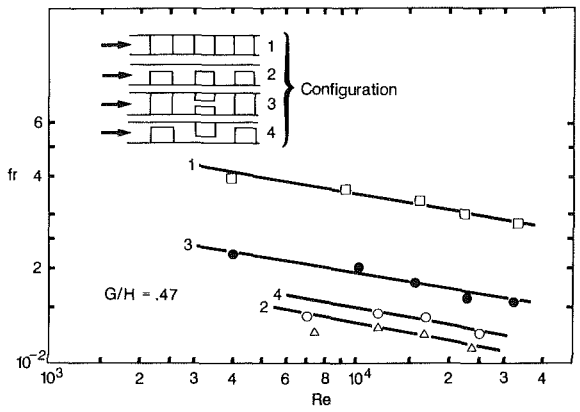

Fig. 13 Comparison of friction factors for different geometries

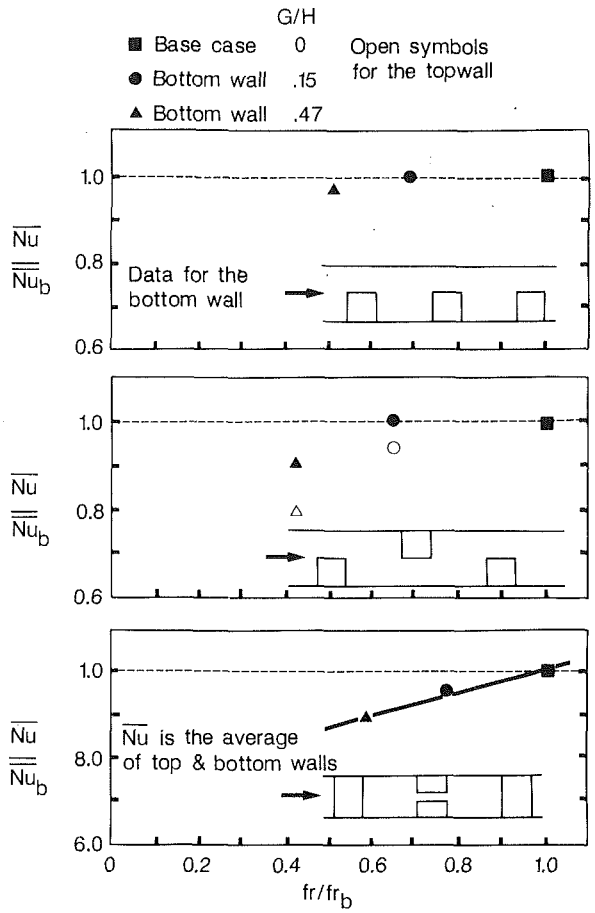

Fig. 14 Relative performance of partial length pin fins for Re = 20,000

These data show that the average Nusselt number decreases linearly with increasing clearance and the rate of decrease is dependent on the full pin array geometry. This slope can be established by drawing a straight line between the $\overline{Nu}$ for the full pin array and the smooth channel value. The resulting $\overline{Nu}$ for any clearance can then be interpolated. This suggests that the reduction in $\overline{Nu}$ due to the clearance is not affected by the geometry of partial pins, at least for the three geometries tested in this study. However, the gap not only reduces the average Nusselt number, but it also changes the distribution of heat transfer from the two walls except for the third geometry. Therefore, for design applications the relative heat transfer behavior of the two walls must be taken into consideration.

The friction factor results for the channel with pin fins are shown in Fig. 12 for all three geometries corresponding to $G/H=0$, 0.15, and 0.47. These friction factors are based on the pressure gradient in the channel with pin fins. It is evident that for all three geometries, the friction factor decreases with increasing clearance. This is consistent with the observed distribution of the averaged Nusselt numbers. A similar conclusion was also reported by Sparrow and Ramsey (1978).

Figure 13 compares the friction factors of full and partial length pin fins for a constant gap ratio of $G/H=0.47$. As expected, the full pins have the highest friction factor, followed by the geometry with every second row having gap at the center. Third is the geometry with the rows of pins bonded alternatively to the bottom and the top walls. The geometry with all pins bonded to one wall and the other wall smooth has the lowest friction factor. This ranking of the partial length pin fins on the basis of friction factor appears to be consistent with the structure of the flow that could possibly exist in the array.

To evaluate the relative performance of different pin fin geometries, the respective Nusselt number and the friction factor for each clearance normalized by the corresponding full pin fin data (the base case) at Re = 20,000 are plotted in Fig. 14. For the case with the partial pins attached only to the bottom wall, data are shown only for the wall with the pins. The heat transfer from the wall with the pins remains almost unaffected with the changing gap; however, the friction factor decreases significantly. For the case with rows of partial pins

Downloaded 01 Jun 2010 to 171.66.16.66. Redistribution subject to ASME license or copyright; see http://www.asme.org/terms/Terms_Use.cfm

bonded alternatively to the bottom and top walls, the heat transfer for the bottom wall is higher than the top wall. The friction factor for the array with $G/H=0.15$ decreases by about 35 percent, whereas the Nusselt number decreased by about 4 percent. The array with the gap at the center of the pins is geometrically symmetric and the heat transfer also shows symmetric behavior for the two walls. The corresponding Nusselt number and the friction factor ratios show a linear relationship.

Conclusions

- The array-averaged heat transfer rate decreases with increasing clearance between the partial length pins and the endwall and varies linearly from the full pin value to that for the smooth channel. Therefore the array-averaged Nusselt number for the pin fin arrays with varying gaps can be interpolated from the full pin and the smooth channel data.
- Large differences in the Nusselt numbers for the two walls were observed for the asymmetric partial length pin fin array geometries.
- The friction factor also decreases with increasing clearance. The geometry with all pins attached to one wall had the lowest friction factor with no significant change in the heat transfer for the wall with the partial length pin fins.

References

Arora, S. C., and Abdel-Messeh, W., 1983, "Heat Transfer Experiments in High Aspect Ratio Rectangular Channel With Epoxied Short Pin Fins," ASME Paper No. 83-GT-57.

Arora, S. C., and Abdel-Messeh, W., 1985, "Pressure Drop and Heat Transfer Characteristics of Circular and Oblong Low Aspect Ratio Pin Fins," AGARD Conference Proceedings 390, PEP Symposium, Bergen, Norway.

Kline, S. J., and McClintock, F. A., 1953, "Describing Uncertainties in Single Sample Experiments," *Mechanical Engineering*, Vol. 75, Jan.

Peng, Y., 1984, "Heat Transfer and Friction Loss Characteristics of Pin Fin Cooling Configurations," ASME *Journal of Engineering for Gas Turbines and Power*, Vol. 106, pp. 246–251.

Sparrow, E. M., and Ramsey, J. W., 1978, "Heat Transfer and Pressure Drop for a Staggered Wall — Attached Array of Cylinders With Tip Clearance," *Int. J. Heat Mass Transfer*, Vol. 21, pp. 1369–1377.

Steuber, G. D., and Metzger, D. E., 1986, "Heat Transfer and Pressure Loss Performance for Families of Partial Length Pin Fin Arrays in High Aspect Ratio Rectangular Ducts," *Proceedings of Eight International Heat Transfer Conference 6*, pp. 2915–2920.

Zukauskas, A., 1972, "Heat Transfer From Tubes in Crossflow," *Advances in Heat Transfer*, Vol. 8, pp. 93–160.

Downloaded 01 Jun 2010 to 171.66.16.66. Redistribution subject to ASME license or copyright; see http://www.asme.org/terms/Terms_Use.cfm